

# ***composites***

**Part A: applied science and manufacturing**

VOL. 32A 2001

**DISTRIBUTION STATEMENT A**  
Approved for Public Release  
Distribution Unlimited

**Special Issue**

Processing of Fibers and Composites

**Guest Editors**

K.K. Chawla, University of Alabama at Birmingham, AL, USA  
A. Mortensen, EPFL, Lausanne, Switzerland  
J.-A.E. Manson, EPFL, Lausanne, Switzerland

Journal homepage: <http://www.elsevier.com/locate/compositesa>



ELSEVIER

20011016 050

## Aims & Scope

*Composites Part A: Applied Science and Manufacturing* publishes original research papers, review articles, case studies, short communications and letters from a wide variety of sources dealing with all aspects of the science and technology of composite materials, including fibrous and particulate reinforcements in polymeric, metallic and ceramic matrices, aligned eutectics, reinforced cements and plasters, and 'natural' composites such as wood and biological materials.

The range of applicable topics includes the properties, design and manufacture of reinforcing fibres and particles, fabrication and processing of composite materials and structures, including process science and modelling, microstructural characterization of composites and their constituent phases, interfaces in composites, prediction and measurement of mechanical, physical and chemical properties, and performance of composites in service. Articles are also welcomed on economic and commercial aspects of the applications of composites, design with composites and case studies.

All articles published are subject to rigorous peer review and a high standard is set for both content and presentation. The Editors aim to conduct the review procedure with the minimum of delay so that prompt publication ensues.

*Composites Part B: Engineering* aims to provide a balance between mechanics and materials science aspects, basic and applied research, and high technology and high volume (low cost) composite development.

The Journal aims to provide a forum for the prompt publication of original research on all areas of composites, with emphasis being placed on evaluation and modelling of engineering details and concepts. Basic research papers are welcomed, but authors are encouraged to discuss the issues relative to application in the short or long-term in various areas, such as aerospace, automotive and other surface transportation, infrastructure, shipbuilding, off-shore, piping, and recreational products.

Current topics of interest to readers include durability, functionally gradient materials, interfaces, interlaminar fracture, joints and adhesion, smart composites, textile composites, thermoplastics, wave propagation, and non-destructive testing.

---

**Publishing and Subscriptions Offices:** Elsevier Science Ltd, The Boulevard, Langford Lane, Kidlington, Oxford OX5 1GB, UK. Tel: +44 (0) 1865 843000. Fax: +44 (0) 1865 843010.

**Advertising information.** Advertising orders and enquiries can be sent to: **USA, Canada and South America:** Mr Tino DeCarlo, The Advertising Department, Elsevier Science Inc., 655 Avenue of the Americas, New York, NY 10010-5017, USA; phone: (+1) (212) 633 3815; fax: (+1) (212) 633 3820; e-mail: t.decarlo@elsevier.com. **Japan:** The Advertising Department, Elsevier Science K.K., 9-15 Higashi-Azabu 1-chome, Minato-ku, Tokyo 106-0044, Japan; phone: (+81) (3) 5561 5033; fax: (+81) (3) 5561 5047. **Europe and ROW:** Rachel Leveson-Gower, The Advertising Department, Elsevier Science Ltd., The Boulevard, Langford Lane, Kidlington, Oxford OX5 1GB, UK; phone: (+44) (1865) 843565; fax: +44 (1865) 843976; e-mail: r.leveson-gower@elsevier.co.uk.

© 2001 Elsevier Science Ltd. All rights reserved.

This journal and the individual contributions contained in it are protected under copyright by Elsevier Science Ltd. and the following terms and conditions apply to their use:

### Photocopying

Single photocopies of single articles may be made for personal use as allowed by national copyright laws. Permission of the publisher and payment of a fee is required for all other photocopying, including multiple or systematic copying, copying for advertising or promotional purposes, resale, and all forms of document delivery. Special rates are available for educational institutions that wish to make photocopies for non-profit educational classroom use.

Permissions may be sought directly from Elsevier Science Global Rights Department, PO Box 800, Oxford OX5 1DX, UK; phone: (+44) 1865 843830, fax: (+44) 1865 853333, e-mail: permissions@elsevier.co.uk. You may also contact Global Rights directly through Elsevier's home page (<http://www.elsevier.com>), by selecting 'Obtaining Permissions'.

In the USA, users may clear permissions and make payments through the Copyright Clearance Center, Inc., 222 Rosewood Drive, Danvers, MA 01923, USA; phone: (978) 7508400, fax: (978) 7504744, and in the UK through the Copyright Licensing Agency Rapid Clearance Service (CLARCS), 90 Tottenham Court Road, London W1P 0LP, UK; phone: (+44) 20 7631 5555; fax: (+44) 20 7631 5500. Other countries may have a local reprographic rights agency for payments.

### Derivative Works

Subscribers may reproduce tables of contents or prepare lists of articles including abstracts for internal circulation within their institutions. Permission of the publisher is required for resale or distribution outside the institution.

Permission of the publisher is required for all other derivative works, including compilations and translations.

### Electronic Storage or Usage

Permission of the publisher is required to store or use electronically any material contained in this journal, including any article or part of an article.

Except as outlined above, no part of this publication may be reproduced, stored in a retrieval system or transmitted in any form or by any means, electronic, mechanical, photocopying, recording or otherwise, without prior written permission of the publisher.

Address permissions requests to: Elsevier Science Global Rights Department, at the mail, fax and e-mail addresses noted above.

### Notice

No responsibility is assumed by the Publisher for any injury and/or damage to persons or property as a matter of products liability, negligence or otherwise, or from any use or operation of any methods, products, instructions or ideas contained in the material herein. Because of rapid advances in the medical sciences, in particular, independent verification of diagnoses and drug dosages should be made.

Although all advertising material is expected to conform to ethical (medical) standards, inclusion in this publication does not constitute a guarantee or endorsement of the quality or value of such product or of the claims made of it by its manufacturer.

**Back Issues:** Back issues of all previously published volumes are available direct from Elsevier Science Offices (Oxford and New York). Complete volumes and single issues can be purchased for 1990–1997. Earlier issues are available in high quality photo-duplicated copies as complete volumes only. Back volumes on microfilm are available from UMI, 300 North Zeeb Road, Ann Arbor, MI 48106, USA.

⊗ The paper used in this publication meets the requirements of ANSI/NISO Z39.48-1992 (Permanence of Paper)

Typeset and printed by the Alden Group, Oxford



## CONTENTS

Volume 32A Number 8 2001

### Special Issue: Processing of Fibers and Composites

979 Preface

K. K. CHAWLA (USA), A. MORTENSEN & J.-A. E. MÅNSEN (Switzerland)

#### Processing research

981 Infiltration processing of fibre reinforced composites: governing phenomena

V. MICHAUD & A. MORTENSEN (Switzerland)

997 Use of electrophoretic deposition in the processing of fibre reinforced ceramic and glass matrix composites: a review

A. R. BOCCACCINI (Germany), C. KAYA (UK) & K. K. CHAWLA (USA)

1007 Fabrication of high-temperature resistant oxide ceramic matrix composites

I. A. H. AL-DAWERY & E. G. BUTLER (UK)

1013 Filament winding of bicomponent fibers consisting of polypropylene and a liquid crystalline polymer

J. HUANG, D. G. BAIRD, A. C. LOOS, P. RANGARAJAN & A. POWELL (USA)

1021 Fabrication of fiber-reinforced celsian matrix composites

N. P. BANSAL & J. A. SETLOCK (USA)

1031 Structure-property relationships for high thermal conductivity carbon fibers

N. C. GALLEG0 & D. D. EDIE (USA)

1039 Processing and characterization of barium zirconate coated alumina fibers/alumina matrix composites

M. KOOPMAN, S. DUNCAN, K. K. CHAWLA & C. COFFIN (USA)

1045 Material phenomena controlling rapid processing of thermoplastic composites

P.-E. BOURBAN, N. BERNET, J.-E. ZANETTO & J.-A. E. MÅNSEN (Switzerland)

1059 Modeling flow-induced crystallization in fiber spinning

A. J. McHUGH & A. K. DOUFAS (USA)

1067 Nextel™ 610 alumina fibre reinforced aluminium: influence of matrix and process on flow stress

B. MOSER, A. ROSSOLL, L. WEBER, O. BEFFORT & A. MORTENSEN (Switzerland)

1077 Selectively fibre-reinforced components produced by the modified investment casting process

E. NEUSSL & P. R. SAHM (Germany)

1085 Rheology and structuring in organo-ceramic composites

A. J. McHUGH & J. A. WALBERER (USA)

1095 Effect of interphase characteristics on long-term durability of oxide-based fibre-reinforced composites

B. SARUHAN, M. SCHMÜCKER, M. BARTSCH, H. SCHNEIDER, K. NUBIAN & G. WAHL (Germany)

1105 Effects of environmental conditions on mechanical and physical properties of flax fibers

A. STAMBOULIS, C. A. BAILLIE & T. PEIJS (UK)

1117 Wet layup and sintering of metal-containing microfibr0us composites for chemical processing opportunities

D. K. HARRIS, D. R. CAHELA & B. J. TATARCHUK (USA)

1127 Preparation of polycrystalline YAG/alumina composite fibers and YAG fiber by sol-gel method

A. TOWATA, H. J. HWANG, M. YASUOKA, M. SANDO & K. NIIHARA (Japan)

1133 Affordable processing of thick section and integral multi-functional composites

U. K. VAIDYA, A. ABRAHAM & S. BHIDE (USA)

1143 High performance oxide fibers for metal and ceramic composites

D. M. WILSON & L. R. VISSER (USA)

#### Industry and applications-related contributions

1155 The characterization of low cost fiber reinforced thermoplastic composites produced by the *DRIFT*™ process

T. HARTNESS, G. HUSMAN, J. KOENIG & J. DYKSTERHOUSE (USA)

1161 "Assessment of Metal Matrix Composites for Innovations" — intermediate report of a European Thematic Network

H. P. DEGISCHER, P. PRADER (Austria) & C. SAN MARCHI (Switzerland)

- 1167** Thermoplastic composite based processing technologies for high performance turbomachinery components  
V. MALLICK (Switzerland)

**Educational aspects**

- 1175** Impact of the NSF State/Industry/University Cooperative Research Center on low-cost, high-speed polymer composites processing on the research and educational programs at Michigan State University  
M. HAWLEY, K. JAYARAMAN, J. STICKLEN, B. MOORE, L. DRZAL & R. L. McCULLOUGH (USA)

- 1181** Education for a new millennium: an innovative program in fibers and films  
J. E. JACOBI, D. D. EDIE & J. M. KENNEDY (USA)

- 1185** Calendar

## Preface

A conference titled **Processing of Fibers and Composites** (Polymer, Metal, and Ceramic), under the sponsorship of the United Engineering Foundation (UEF), New York, was held during the period of May 21–26, 2000 in Barga, Tuscany, Italy. This volume contains papers presented at that meeting. The conference chair was Professor K.K. Chawla (University of Alabama at Birmingham, USA), with co-chairs, Professors A. Mortensen and Jan-Anders E. Månson (both of Ecole Polytechnique Fédérale de Lausanne, Switzerland).

The conference focused on the processing issues relevant to fibrous reinforcements and their composites. Its scope included polymeric, metallic, and ceramic fibers and their composites. The main goal was to examine aspects of processing of composites across all classes of materials, with a view toward the generation of materials featuring tailored sets of properties. The conference reflected the interdisciplinary nature of the field as well as the recent change in emphasis from defense-related to civilian applications of composites, and provided a useful forum for the exchange of ideas among researchers from academia and industry, often coming from ostensibly separate communities of research. Of course, much of what was accomplished during this conference took the shape of informal discussions at the dinner table or during recreational events, where graduate students or newly starting researchers sat side by side with more experienced researchers, and where academics sat next to members of industry; these more intangible but important benefits cannot be transcribed on paper and published in this issue. Nevertheless, it was the intention of the organizers of the conference to make a tangible piece of work presented at this conference available to the world at large. To that end, we are pleased to offer this collection of papers, duly reviewed and revised.

The papers and highlights gleaned during the discussion sessions can roughly be summarized as follows.

- **Processing Research:** This main section includes contributions on basic research on various aspects of processing of fibers and fiber-reinforced composites. In the area of fibers, there has been a considerable rate of development. For example, alumina-based fibers and carbon fibers have doubled in strength in the decade of the 1990s. Still, one must recognize that fibers are very special materials and that there is a need to model structural processes, all the way down to the molecular level.

There is also a need for a greater amount of consistency in development: a mere 1% improvement in conversion efficiency in the manufacture of carbon fibers will save millions of dollars. It was also thought that the carbon fiber production technology of today seems to have approached a theoretical limit giving reduced hopes for any significant cost reductions.

An important item that was brought up in the meeting and bears emphasizing is that of nomenclature. Although it is recognized that the term carbon fiber is a generic one, it was pointed out that there is no standardized nomenclature. Different companies use different names for their fibers. Different manufacturers produce low, intermediate, high, and ultrahigh modulus varieties of carbon fibers but these are not identical in the sense of metallic alloys produced by different manufacturers. Fibers made by different manufacturers may be similar but not identical in properties, for example, because differences in the precursor and processing routes can affect the final properties of carbon fibers; this matter should be tackled in the future.

- **Industry- and Applications-related Contributions:** The contributions in this section comprise the industry- and applications-related reports. In the area of PMCs, the thermoplastic matrix composites are fast establishing themselves as major contenders for the fast-growing composite market in the transportation sector. One of the challenges ahead is to tailor the material/process combination for reliable production-cycles of minutes. To this end, we see today an explosion in novel and innovative materials and processes aimed at capturing high-volume markets. Low-cost processing is needed, especially for penetration in sporting goods and automobile industries. In addition, attention should be focused on fast production speed and consistency. Design-relevant databases involving reliability and reproducibility aspects are also needed; in particular, the reliability issues are very important in the industry. Material qualification can also take an inordinately long time. While considerable progress has been made in the design of materials in PMCs and metal matrix composites (MMCs), there is not much to show in the area of ceramic matrix composites (CMCs). In the area of MMCs, it was pointed out that while the research community in continuous fiber-reinforced metals has decreased, the number of applications has increased. In

the area of CMCs, it is important to recognize that there are different temperature ranges of applications where different CMCs may be useful.

Among the drivers for composites are environmental concerns such as reduction in CO<sub>2</sub> emissions and recycling. A recent development that was also noted in this conference is the setting up of consortia aimed at fostering greater industrial usage of these materials; one example, a consortium on MMCs that is sponsored by the European Community, was presented at this conference.

- *Educational Aspects:* Educating future scientists and engineers in the areas of fibers and composites is an important task. The US National Science Foundation (NSF) has a number of initiatives in this regard. In particular, there are some important research centers funded by NSF at various universities. Contributions from some of these centers highlight the type and extent of work being done in educating tomorrow's specialists in fibers and composites. There is indeed a lack of trained personnel in the area of composites: one can cite examples of projects being canceled simply because of lack of trained personnel. In addition, there is an urgent need for a strong and active interaction among people coming from different disciplines and working with composites.

Two NSF centers were represented at this meeting. The Michigan State University/University of Delaware center focuses on low-cost high-speed processing of polymer composites. In particular, their work involves design paradigms and methodologies, material cost and processing, etc. It is important to recognize that design is not just mechanics. The Clemson University/MIT center focuses on virtual models and connections, long-distance courses, off-campus interaction, satellite hook-up, and research experience for undergraduates at company sites. Finally, mention should also be made of collabora-

tion between institutions outside the United States, namely the Swiss Polytechnic Institutes (ETHZ and EPFL) and the EMPA, a Swiss government laboratory in Thun and Dübendorf, in which researchers at one institution can use the equipment at other institutions by remote control.

### Acknowledgements

This conclave would not have been made possible without the generous support, financial and otherwise, of the following organizations and people:

- United Engineering Foundation
- US National Science Foundation
  - Dr. T.A. Mukherjee
  - Dr. B.A. MacDonald
- US Office of Naval Research
  - Dr. A.K. Vasudevan
  - Dr. S.G. Fishman

We are also grateful to Ms. Barbara Hickernell (UEF), Dr. N. Stoloff, Dr. A. Boccaccini (Imperial College), and D. Edie (Clemson University) for their help. KKC would like to acknowledge the skillful editorial assistance of Ms. Kanika Chawla, before and after the conference. Last but not least, we are grateful to all the participants for making this event a great success.

K.K. Chawla  
*University of Alabama at Birmingham,*  
*AL 35294-4461*  
*Birmingham, USA*

A. Mortensen  
J.-A.E. Månson  
*EPFL, Ecublens, CH-1015*  
*Lausanne, Switzerland*

## Infiltration processing of fibre reinforced composites: governing phenomena

V. Michaud<sup>a,\*</sup>, A. Mortensen<sup>b</sup>

<sup>a</sup>*Department of Materials, Composite and Polymer Technology Laboratory, Ecole Polytechnique Fédérale de Lausanne (EPFL),  
CH 1015 Lausanne, Switzerland*

<sup>b</sup>*Department of Materials, Mechanical Metallurgy Laboratory, Ecole Polytechnique Fédérale de Lausanne (EPFL), CH 1015 Lausanne, Switzerland*

Received 8 August 2000; accepted 28 November 2000

### Abstract

All three classes of fibre reinforced composite materials (polymer, metal and ceramic matrix) may be produced by flow of liquid matrix into the open spaces left within pores of a fibre preform. Even though several specific issues arise from the nature of each composite matrix class, governing phenomena apply to all infiltration processes, and include in particular: (i) capillary phenomena, (ii) transport phenomena, and (iii) the mechanics of potential fibre preform deformation. These phenomena and their governing laws are reviewed for the case of isothermal infiltration with no phase transformations. Four basic functional quantities, which need to be known to model the processes, are identified, and addressed in turn. The paper concludes with some examples of modelling methodologies and comparison with experimental data. © 2001 Elsevier Science Ltd. All rights reserved.

**Keywords:** A. Metal-matrix composites (MMCs); A. Polymer-matrix composites (PMCs); A. Ceramic-matrix composites (CMCs); E. Liquid metal infiltration; E. Resin flow

### 1. Introduction

The infiltration process has grown to become one of the most significant methods of production of composite materials. It is used industrially for both polymer and metal matrix composites, and has now also emerged as one of the most promising pathways towards the production of ceramic matrix composites.

In the most general sense, infiltration is the process whereby a fluid replaces another fluid, the latter generally being vacuum or a gas, within the open pore space a porous solid material. Infiltration, defined as such, is found in many guises in both nature and engineering: for example when it rains, when a sponge is filled with water, or when oil is extracted from the ground.

In materials processing, to produce a composite by infiltration a mechanically self-sustaining porous ‘preform’ of the composite material reinforcing phase, generally consisting of fibres or particles, is first prepared. Then, during infiltration proper, the open pore space of the preform is filled by a fluid precursor of the matrix phase; upon subsequent condensation or solidification of this fluid, the compo-

site material results. The fluid matrix can be a gas: the chemical vapour infiltration (CVI) process used to produce silicon carbide matrix composites is an important example of such a variant of infiltration. More frequently, though, the matrix is liquid or near-liquid slurry; we focus in what follows on this latter case.

As a rule, infiltration is best suited for the production of composites which contain a relatively high volume fraction of reinforcement: this is because before infiltration, reinforcing fibres or particles must percolate sufficiently for the preform to stand under its own weight. In fact, for such highly reinforced composites, infiltration is generally the most efficient and versatile processing route available for all three composite material classes.

Our aim in this paper is to provide a general overview of commonality — and also differences — in the physics of infiltration across all three major composite classes: polymer, metal and ceramic matrix composites. In order to focus this paper, we restrict ourselves to a consideration of isothermal infiltration processing of material systems free of reaction or phase change. In doing so, we do not consider the complications which arise from the influence of interfacial or matrix chemical reaction, matrix solidification, or the important underlying questions of heat and solute transport.

\* Corresponding author. Fax: +41-21-693-58-80.

E-mail address: veronique.michaud@epfl.ch (V. Michaud).

In what follows, we begin with a broad overview of the different composite infiltration processes and their associated terminology. We then review the governing laws for the mechanics and kinetics of the process, and from this we identify and specify the basic functional quantities that need to be known for modelling the process. We then address these in turn, pointing out common features and differences, which exist between the three classes of composite materials, and their incidence on processes that are used towards their production. Finally, some examples of process modelling methods and comparison with experimental results are given.

## 2. Composite infiltration processes

### 2.1. Polymer matrix composites

The form taken by infiltration processes, and also the terminology used, vary significantly according to the matrix material class. With polymer matrix composites, infiltration processes can be divided into two main classes, namely liquid composite moulding (LCM), and consolidation processes.

In LCM, the (generally thermoset) resin is injected under applied pressure into the porous reinforcement preform, itself held within a mould; most often, this mould is rigid.

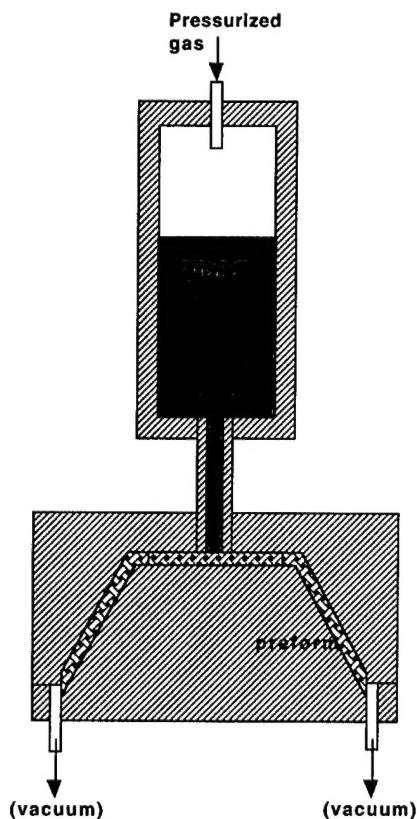


Fig. 1. Schematic description of the RTM process.

Resin transfer moulding (RTM), schematically described in Fig. 1, is the most common form of LCM. In this process, the premixed thermoset resin is injected into a preheated mould under a pressure of a few bars, applied onto the resin using either pressurised gas or a piston. Many variations of this method exist, including [1]:

- (i) Vacuum assisted RTM (VA-RTM), which consists in pulling a vacuum in the mould containing the preform during infiltration.
- (ii) Structural reaction injection moulding (SRIM) involving higher pressures applied using an injection unit to force the resin into the preform.
- (iii) Seeman composite resin infusion moulding process (SCRIMP) involving the presence of a highly permeable layer on top of the preform, encased in a vacuum bag [2,3].

This list is far from exhaustive: several additional examples of variants of RTM can be found in the literature. RTM is now widely used industrially and is the focus of a relatively large research effort (e.g. [1,4]).

*Consolidation processes* essentially consist in applying pressure and heat to an initially pre-impregnated or pre-mixed resin/fibre assembly, in order to complete infiltration and to squeeze out entrapped air, volatiles emanating from the polymer, as well as excess resin, Fig. 2. This class of processes includes the autoclave moulding of thermoset prepreps, widely used in aerospace engineering, as well as many processes designed for thermoplastic composites: examples are the film stacking process [5], the double belt press forming of Glass Mat thermoplastic blanks, as well as processes in which the reinforcement and the matrix are already intimately mixed, such as commingled yarn, pre-infiltrated yarn, or powder impregnated yarn consolidation processes [6,7]. Pultrusion, for example, is a variant of such processes, in which the consolidation step proper is

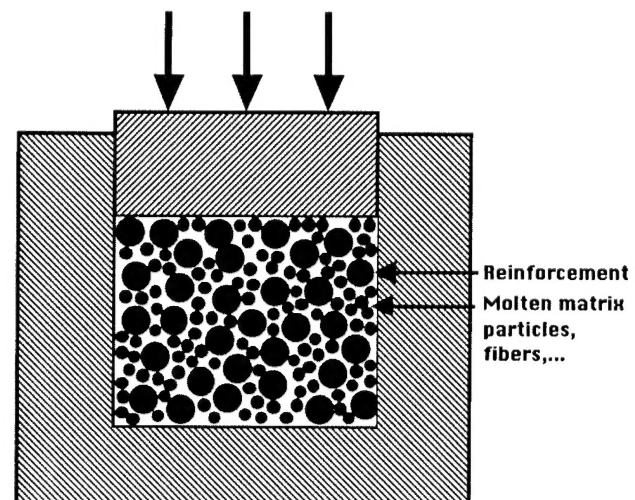


Fig. 2. Schematic description of the consolidation process.



conducted as bundled pre-infiltrated tows are pulled through a constricting die. A common feature of all consolidation processes is that the distance that must be travelled by the liquid matrix to fill pores of the preform is significantly reduced compared to massive infiltration processes such as RTM. With highly viscous polymeric melts, this is a significant advantage.

Some variants of polymer matrix composite infiltration processes belong to both classes, such as the injection-compression process wherein the resin is injected into a partially open RTM mould which is closed after infiltration [8], or a version of pultrusion in which the melt is injected directly into the die through which the fibre bundles are pulled [9].

## 2.2. Metal matrix composites

With metal matrix composites, infiltration processes are separable into two main classes, according to whether or not the matrix wets the reinforcement and can infiltrate spontaneously the preform. As with polymer matrix composites, infiltration is, for metal matrix composites, now an industrially significant process: automotive engine components [10–14], as well as electronic substrates [15] are currently mass-produced by infiltration processes.

The former case, of spontaneous infiltration, is naturally rare: principal examples are in the infiltration of tungsten or iron with copper [16], or the high-temperature infiltration of boron carbide particulate preforms with aluminium [17]. For other systems, spontaneous infiltration by a molten metal requires deliberate tailoring of matrix, reinforcement, and infiltration atmosphere chemistry: the Lanxide Primex™ process provides the best known and probably the most significant current engineering example [18].

Although spontaneous infiltration is in some cases feasible, molten metals generally do not wet typical metal matrix composite reinforcement phases, such as carbon, oxides and carbides. Then, to produce the composite by infiltration, force must be provided by external means to drive the molten metal matrix into the porous reinforcement preform. This is generally obtained by pressurization of the melt to pressures on the order of 10 or a 100 MPa.

Several of these metal matrix composite pressure infiltration processes are derivatives of pressure casting processes used for the mass-production of unreinforced metals and alloys, most typically of aluminium or magnesium. These often use a piston to drive the molten metal into a mould, and include squeeze-casting, illustrated in Fig. 3(a), in which the piston forms a significant part of the mould, and pressure die casting, in which the molten metal is injected through a narrower shot chamber into a closed die.

Alternatively, pressurised gas can be used to drive the molten metal into the preform; a typical embodiment of gas-pressure infiltration is described in Fig. 3(b). Compared with piston-driven processes, this version of metal matrix composite pressure infiltration is generally less economical

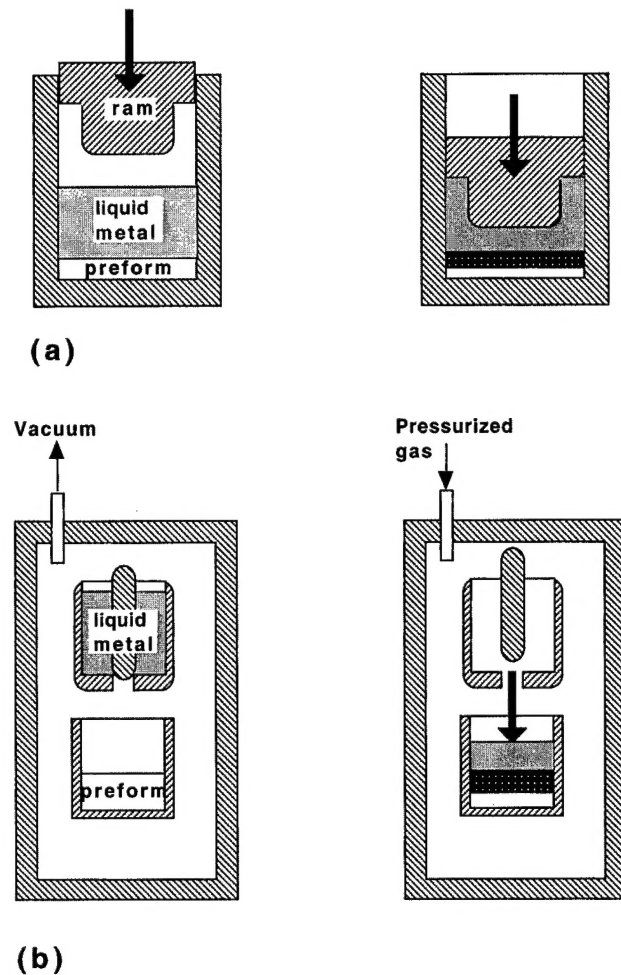


Fig. 3. Schematic description of (a) the squeeze casting, and (b) the gas pressure infiltration processes used for metal matrix composite production.

for mass-production; however, tooling required can be less extensive. Other chief differences are that in gas-driven pressure infiltration of metal matrix composites, pressures employed are typically lower (about 2–20 MPa versus about 100 MPa for piston-driven processes such as squeeze casting), and the rate of matrix solidification is also lower because dies are generally cooler in piston-driven processes (in squeeze or pressure die casting, melt temperatures are typically near 200–300°C to avoid chemical interaction between the molten aluminium and the die material, typically of tool steel). Further descriptions of process specifics for metal matrix composite infiltration can be found in Ref. [19].

Clearly, a close similarity exists between metal matrix composite pressure infiltration processes and LCM processes used for polymer matrix composites: both inject the matrix under pressure into a closed die containing the reinforcement preform using either a piston or pressurised gas, and yield net or near-net shape composites.

## 2.3. Ceramic matrix composites

Liquid phase infiltration is also an important process for



the fabrication of ceramic matrix composites; however, for these materials it takes several comparatively more complex forms, generally quite different from infiltration as practiced for metal or polymer matrix composites.

As mentioned above, CVI is one industrially significant CMC infiltration process, but several other CMC production methods exist which use liquid infiltrants. These can roughly be subdivided into a few variants [20–23]:

- (i) infiltration with the matrix in molten form, pioneered by Hillig using low-melting point ceramics [24,25], also demonstrated in pultrusion for glass matrix composite [21] and which finally includes reactive infiltration commonly used for the production of SiC/Si materials [22];
- (ii) infiltration with a slurry or a sol, or a combination thereof, which requires a subsequent densification step (e.g. Refs. [26–31]). In some cases, this latter step can involve melting of the ceramic particles followed by liquid phase consolidation; this last route is commonly used for the production of glass matrix composites [23,32];
- (iii) infiltration with a precursor of the composite matrix, such as polycarbosilane for Si–C–O matrices, and resin or pitch for carbon matrices [21,22,33]. This also requires a second series of processing steps, comprising in particular pyrolysis of the preceramic material and, frequently, a repetition of the infiltration/pyrolysis sequence to feed shrinkage that accompanies pyrolysis of the matrix precursor.

Ceramic matrix composite infiltration processes often are similar to consolidation processes used to produce polymer matrix composites: in many cases, the matrix is first brought near the reinforcement, and consolidation is then used to eliminate, or at least reduce for many CMC processes, the volume fraction of porosity in the material.

#### 2.4. Summary

Infiltration processes are thus important for all three classes of composites. Evident parallels come out upon comparison of what is practised for each class: some polymer matrix and glass matrix composites are produced similarly by liquid phase consolidation, while RTM processing of polymer matrix composites and pressure infiltration processing of metal matrix composites are essentially the same process. Spontaneous infiltration appears in all three composite classes in several forms.

There are, however, also differences across materials classes. These can be outlined and explained in general terms by consideration of the equations which govern the process: from these emerge a limited number of parameters, which influence the processes strongly and often define the process path best suited for production of the composite by infiltration.

### 3. Analysis

As in all composite manufacturing processes, the need to produce a sound and homogenous part at the lowest cost has led to research aimed at predicting the kinetics of the process, the local void and fibre content as well as, in some cases, the level of residual stresses in the final part. A large body of work has thus been conducted on the subject by the research communities of the three classes of composite materials, for the most part independently.

A major focus of this work has been to gain a quantitative understanding of the various physical phenomena which intervene in the process. General overviews of fundamental and engineering aspects of infiltration processing of polymer matrix composites can be found in Refs. [1,4], of metal matrix composites in Refs. [34–36], and of ceramic matrix composites in Refs. [20–22,24]. For the three classes of materials, the underlying physical phenomena are very similar, and include capillary phenomena, transport phenomena of fluid flow, heat, and mass transfer, the mechanics of preform deformation during infiltration, matrix solidification or reticulation, and also matrix/reinforcement chemical reaction during and after the process.

Infiltration is not only important in materials processing: several other branches of engineering science are concerned with this general phenomenon. Examples include hydrogeology, soil science, reservoir engineering, biomechanics, and chemical engineering. From this overall research community emerges a far wider body of knowledge, which can be used towards understanding, modelling, and improving infiltration processes for composite manufacturing in general.

Let us consider the infiltration by a liquid of a compressible porous preform in which all initial porosity is interconnected. In the most general case, the fluid gradually invades the pores of the preform, while capillary forces and, in many cases, applied pressure exert stress on the solid fibre preform. Hence, during the process, local volume fractions of solid fibres, of liquid, and of the initial atmosphere (generally air or vacuum) vary within the preform; in modelling the infiltration process we seek to predict these variations.

As commonly done when dealing with transport phenomena within sufficiently fine-scaled porous materials a continuum mechanics approach is used. This is based on consideration of a representative elementary volume (REV), large enough to contain representative averages of all three phases, but small enough to be considered as a differential element on the scale of the preform, Fig. 4. Within the REV, averaged values of relevant parameters, such as velocity or volume fraction, are used to derive equations for conservation of mass and momentum.

A REV contains in the most general case the initial atmosphere, fibres, and liquid, in respective volume fractions  $V_a$ ,

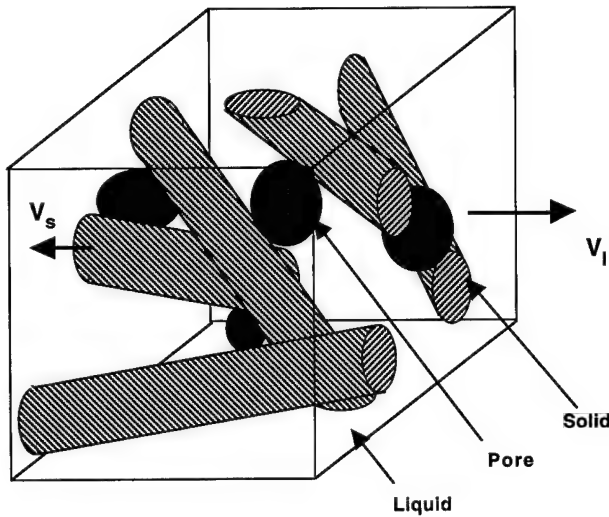


Fig. 4. Schematic of a REV used in modelling infiltration.

$V_f, V_l$ , such that

$$V_a + V_f + V_l = 1. \quad (1)$$

By similarity with soil mechanics, we also define the saturation in fluid phase  $S$  as

$$S = \frac{V_l}{(1 - V_f)}. \quad (2)$$

When the preform is empty, the saturation  $S$  is equal to 0, and when it is fully filled with fluid  $S$  equals 1; all governing equations are then those for saturated flow. It is generally assumed that the densities of liquid and solid phases are constant; in most cases of non-reactive infiltration, this is a reasonable assumption.

Mass conservation equations are written for both the solid and the fluid phase, respectively, as

$$\frac{\partial V_f}{\partial t} + \nabla(V_f u_s) = 0 \quad (3)$$

and

$$\frac{\partial((1 - V_f)S)}{\partial t} + \nabla((1 - V_f)S u_l) = 0, \quad (4)$$

where  $u_s$  is the local velocity of the solid, and  $u_l$  is the average local velocity of the liquid within the pores.

The momentum equation is generally written using Darcy's law

$$(1 - V_f)S(u_l - u_s) = -\frac{K}{\eta} \nabla P, \quad (5)$$

where  $K$  (a function of  $S$  and  $V_f$ ) is the permeability of the porous medium in  $\Delta V$ ,  $\eta$  the liquid viscosity, and  $P$  is the pressure in the liquid. Eq. (5) is valid provided the relevant Reynolds number, defined in relation to the average fluid velocity and the pore diameter, is less than about one: for all but some metal infiltration processes, this will be the case.

Finally, having neglected inertial and body forces in both

solid and liquid, stress equilibrium is written using an extension of the effective stress principle to partially saturated soils [37]

$$\nabla \sigma - \nabla(SP) = 0, \quad (6)$$

where  $\sigma$  is the effective stress acting in the solid, counted as positive in compression and averaged over a surface area comprising both solid and liquid. Initial and boundary conditions valid for each case complete the definition of the problem at hand.

When considering the simple case of fully saturated flow in a rigid porous preform, the saturation  $S$  equals one and the solid velocity is nil everywhere. All equations then reduce to the well-known two-equation set of Eqs. (4) and (5) written with  $S = 1$ . In simple cases of unidimensional flow coupled with elementary boundary conditions such as constant applied pressure or flux, these equations can then be solved analytically. In most cases, however, the set of governing equations is highly non-linear, and solution requires numerical techniques or the use of simplifying assumptions.

Four main characteristics of the fibre preform and the fluid need to be known for solution of the problem; these are

- (i) the viscosity  $\eta$ ;
- (ii) the dependence of the saturation  $S$  on the local pressure  $P$ , a function which is governed by capillarity;
- (iii) the permeability  $K$ , which depends on the local value of the solid volume fraction  $V_f$  as well as the saturation  $S$ ;
- (iv) the relevant stress-strain curve of the preform, which links, for the deformation path experienced by the preform during the process, the effective stress  $\sigma$  with the local strain as described in general by  $V_f$ .

Solution of Eqs. (3)–(6) subject to the boundary conditions at hand then provides the value of the four unknowns of the problem, namely  $u_s$ ,  $u_l$ ,  $P$ , and  $V_f$ , as functions of position and time.

With four governing equations, these four unknown quantities can in general be calculated. For a given geometry and set of boundary conditions, the solution will depend on the four parameters  $\eta$ ,  $S$ ,  $K$ , and  $\sigma$ . These four parameters and their variations with  $P$  and  $V_f$  thus embody the principal physical characteristics of the material system under consideration from the standpoint of infiltration processing; we review these in turn in Section 4.

## 4. Governing process parameters

### 4.1. Viscosity

According to Darcy's law, Eq. (5), the fluid viscosity strongly governs the infiltration kinetics, as the superficial velocity is inversely proportional to the fluid viscosity. Matrices which, at the processing temperature under consideration, have a low viscosity are obviously the most attractive.

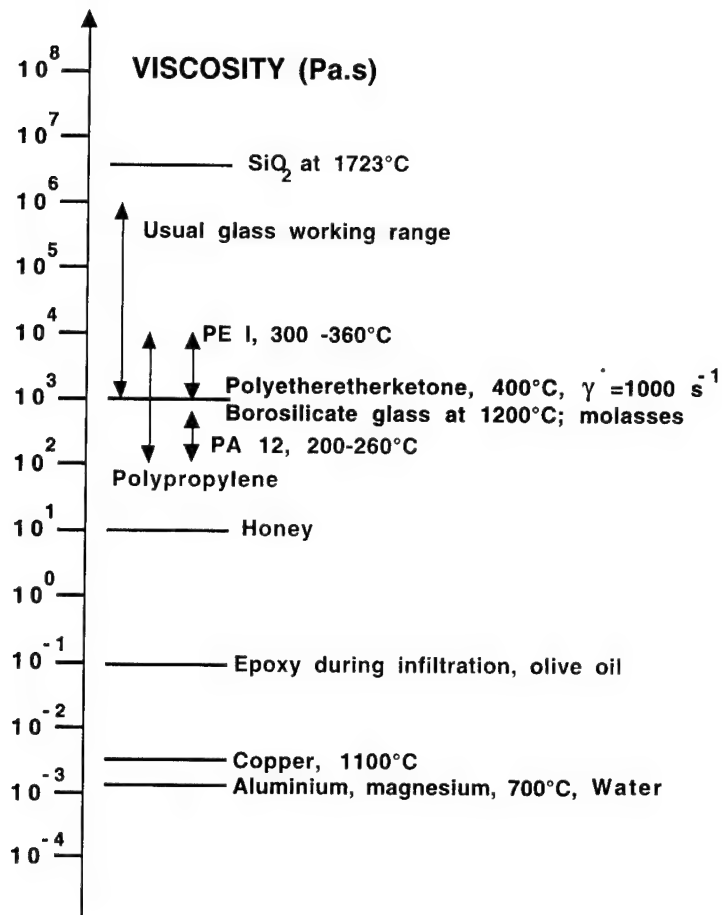


Fig. 5. Range of viscosities of matrices and various other fluids.

The range of matrix viscosities encountered in the infiltration processing of composite materials is very wide, as shown in Fig. 5. Molten metals generally have a viscosity close to that of water, whereas polymers range from 0.1 Pa s for typical uncured thermoset matrices, up to  $10^4$  Pa s for

thermoplastic polymers. Ceramic slurries are in the range of 1 Pa s, whereas glasses have viscosity values as high as  $10^6$  Pa s. The practical consequence of this fact is that, whereas it is practical to produce bulk metal matrix composite components, polymer matrix composites produced by

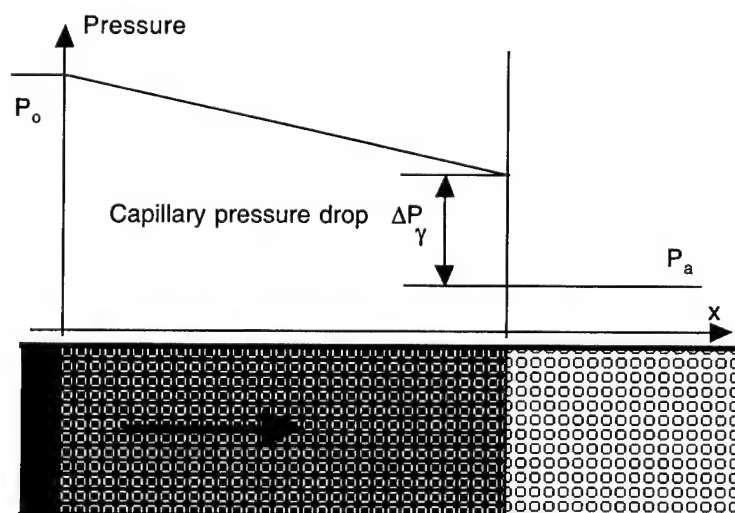


Fig. 6. Schematic description of unidirectional slug-flow infiltration, showing the pressure distribution for a preform of constant permeability.

infiltration often come under the form of thin parts or shells. Also, the high viscosity of thermoplastic matrices has fostered the development of many processes designed to reduce the infiltration path, by mingling or pre-mixing the polymer with the reinforcement.

For modelling purposes, the viscosity  $\eta$  is often considered as independent of the fluid velocity, i.e. the fluid is assumed to exhibit Newtonian flow behaviour. This is fortunately valid in most cases of metal infiltration, as well as for thermosets and some thermoplastic matrices if the shear rate is low enough. Many fluids used in the production of polymer and ceramic matrix composites are, however, shear thinning; hence, any prediction of kinetics based on consideration of a constant, low-shear, viscosity will tend to be slightly conservative. Various modifications of Darcy's law have been proposed to take into account the influence of non-Newtonian behaviour of the liquid matrix [38,39].

## 4.2. Capillary phenomena

### 4.2.1. Slug-flow assumption

As described in Section 3, in theory, the saturation  $S$  varies continuously from 0 to a finite value, equal to or less than 1, between the infiltration front and the fluid inlet. Often, however, in analysis of infiltration processes the assumption is made that the saturation versus distance curve is a step-function, equal to 0 in the non-infiltrated region, and 1 in the infiltrated part. This is known as the slug-flow assumption [19]. All capillarity-related issues are then reduced to knowledge of the pressure boundary condition at the infiltration front, as schematically depicted in Fig. 6. Capillary phenomena in composite processing can then be simply described based on thermodynamic analysis. Wetting of the reinforcement by the liquid is generally expressed using Young's equation

$$\gamma_{fm} = \gamma_{fa} + \gamma_{ma} \cos \theta, \quad (7)$$

where  $\gamma_{fm}$ ,  $\gamma_{fa}$  and  $\gamma_{ma}$  are the surface energies of the fibre-matrix, fibre-atmosphere and matrix-atmosphere interfaces, respectively, and  $\theta$  the wetting angle: the lower  $\theta$ , the better wetting is. The capillary pressure drop  $\Delta P_\gamma$ , which is by definition the difference between the pressure in the preform ahead of the infiltration front and the local pressure in the fluid phase just behind the infiltration front, is then calculated from a simple energy balance as

$$\Delta P_\gamma = \frac{A_v \gamma_{ma} \cos \theta}{(1 - V_f)}, \quad (8)$$

where  $A_v$  is the area of matrix-reinforcement interface per unit volume of composite. In Eq. (8),  $\Delta P_\gamma > 0$  indicates a non-wetting system whereas  $\Delta P_\gamma < 0$  indicates a wetting system.

Knowing that  $\cos \theta$  will generally be close to one, the surface tension of the liquid matrix therefore provides a measure of the potential magnitude of the capillary pressure drop. The surface tensions of selected polymers, metals and

ceramic slurries or melts are given in Table 1: it is seen that, as for the viscosity of matrices, these values span a relatively wide range of values. Typically, molten metals, which feature strong interatomic bonds, exhibit a high surface energy near one joule per square metre, whereas polymers, the surface tension of which is mostly governed by much weaker physical (Van der Waals) bonds, have surface tensions about two orders of magnitude lower. The presence of hydrogen bonds, in water or water-based slurries, leads to intermediate values of the surface tension. As a result, it can be inferred that capillary effects will be far more important in metal based composites: with these, capillary pressure drop values can reach up to 1 MPa (as mentioned above, generally with non-wetting conditions), whereas polymer melts typically feature capillary drop values within the kPa range.

### 4.2.2. Multiphase flow

The slug-flow approach has proven to be a very practical assumption, which is often justified if the externally applied pressure is high enough compared to the capillary pressure drop. In some cases, however, it becomes necessary to relax this assumption: when the applied pressure is low or nil, and also when one must know with precision the local amount of porosity within the part, during and after infiltration. A full analysis is then necessary, requiring the knowledge of the dependence of saturation as a function of pressure,  $S(P)$ .

Curves giving the saturation  $S$  as a function of the fluid pressure  $P$  are commonly measured in soil science or reservoir engineering, and known as drainage-imbibition curves [40–43]. In general, these curves are hysteretic: the path followed for increasing pressure and that for decreasing pressure differ, due to hysteresis in capillary phenomena which, in turn, is caused by constrictions and asperities in

Table 1

Typical surface tension values for molten composite matrices, water and ethanol

Material	Temperature (°C)	Surface tension (N/m)
Polypropylene (PP)	180	0.0208
Polyethylene (PE)	180	0.0265
Polyethylene oxide (PEO)	180	0.0307
Nylon 6.6	270	0.0303
PEI	220	0.0357
PA 12	–	0.039
Epoxy, unreacted	–	0.03–0.04
Ethanol	20	0.022
Water	20	0.073
SiO <sub>2</sub>	1800	0.31
Na <sub>2</sub> SiO <sub>3</sub>	1088	0.30
Al <sub>2</sub> O <sub>3</sub>	2050	0.63
CaSiO <sub>3</sub>	1540	0.35
Al	700	0.87
Cu	1120	1.2
Ti	1670	1.53
Ag	970	0.92
Au	1070	1.13

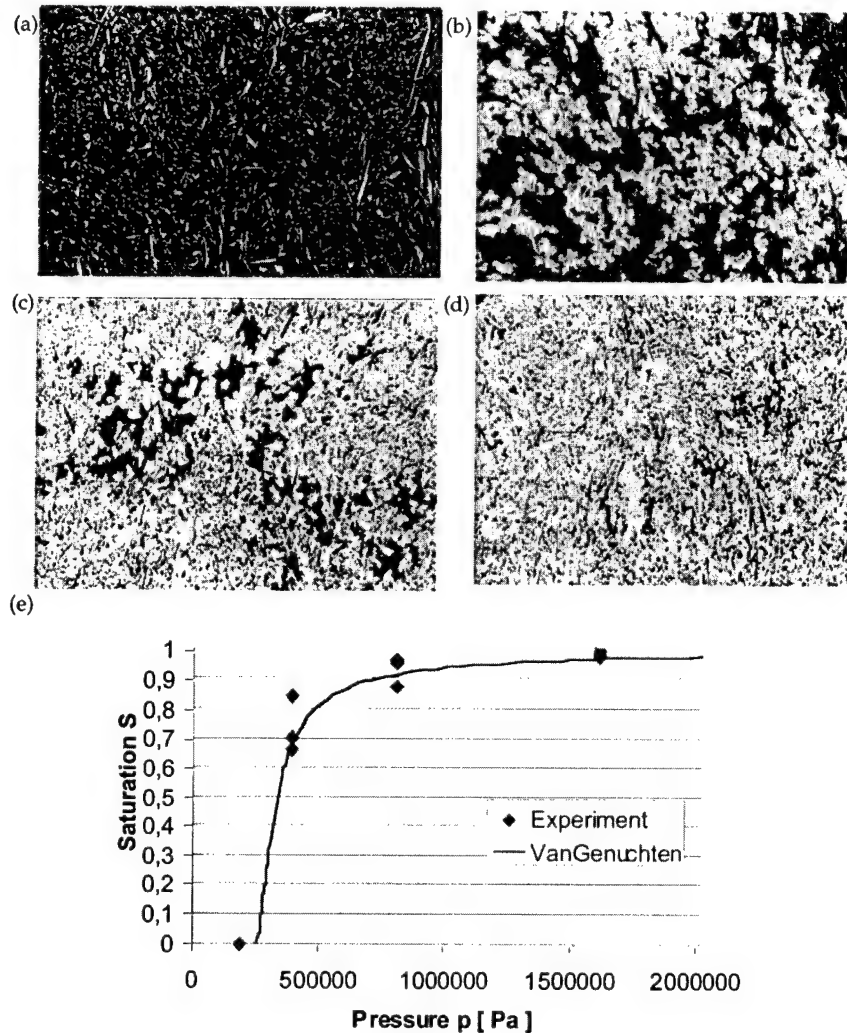


Fig. 7. Progressive nature of infiltration illustrated here for aluminium infiltrating a preform of short (Saffil™) alumina fibres: (a) applied pressure 0.2 MPa, (b) applied pressure 0.4 MPa, (c) applied pressure 0.8 MPa, (d) applied pressure 1.6 MPa, and (e) the corresponding drainage curve, showing good correlation of data with the Van Genuchten equation (Eq. (13) in the text) (from research by Dopler et al. [48]).

the porous medium, past which the displacing liquid will advance by jumps (called Haines jumps [44]), during which motion is irreversible [19,45]. Such curves have been measured for short-fibre metal matrix composites [46–48]. In polymer matrix composites, similar curves have been measured by Patel and James Lee using model fluids [49,50].

In general, the shape of the curve depends on the surface tensions of the system constituents, in a similar fashion to  $\Delta P_\gamma$ ; however, the geometry and size distribution of pores in the preform also exerts a significant influence. Given the great geometrical complexity of pores in nearly all preforms, it is very hard to predict from first principles a drainage/imbibition curve: the many attempts that have been made have therefore generally been unsuccessful. Faced with this difficulty, semi-empirical models are rather used in soil science [40]; somewhat surprisingly, these have been shown also to apply to the infiltration of short fibre preforms by molten metal [46–48]. These include the

relation proposed by Brooks and Corey [51]:

$$S = 1 - \left( \frac{P_b}{P} \right)^\lambda, \quad (9)$$

where  $P_b$  is the bubbling pressure, and  $\lambda$  is the pore size distribution index, and the relation proposed by Van Genuchten [48], shown as the solid line in Fig. 7

$$S = 1 - \frac{1}{\sqrt{1 + \alpha^2(P - P_0)^2}}, \quad (10)$$

where  $\alpha$  and  $P_0$  are the shape and the pressure parameters as well.

#### 4.3. Permeability

In the most general case of multiphase flow, permeability as defined in Eq. (5) is a function of the preform volume fraction, fibre arrangement and stress state, as well as of the degree of fluid saturation in the preform,  $S$ . For convenience,



the expression giving  $K$  is generally separated into two terms,  $K = K_r K_s$ . The saturated permeability,  $K_s$ , is the permeability tensor of the preform for fully saturated flow.  $K_s$  is a function of the fibre arrangement only. The relative permeability,  $K_r$ , is a scalar increasing from 0 to 1 as  $S$  increases between the same bounds. These two quantities are briefly reviewed in turn.

#### 4.3.1. The saturated permeability

By definition, the saturated permeability  $K_s$  is a characteristic of the preform only, which in principle does not vary with the nature of the infiltrant — provided of course that this infiltrant is an incompressible Newtonian fluid, which furthermore has fully infiltrated all open pores of the preform. A very large body of work exists on methods for measuring and modelling the permeability of porous media in saturated flow, in several instances with specific focus on infiltration processing of fibre composites [52–58].

Using Darcy's law,  $K_s$  can be measured with relative ease during a saturated flow experiment. With fibre composites, preforms are often highly anisotropic and  $K_s$  is a tensorial quantity; as a consequence, in measuring the permeability of fibre preforms flow of the fluid must be directed along selected orientations to arrive at each of the relevant component(s) of this tensor. With long-fibre preforms, the so-called *in-plane* permeability is often measured by infiltrating a model fluid through a central hole in a thin fibre preform featuring the fibre lay-up of interest and held within a flat transparent mould. The progression of the resulting elliptical flow front is measured using a CCD camera, and the two principal values of the permeability tensor in this plane are deduced from Darcy's law [54,57,58]. This relatively easy experiment may, however, lead to erroneous measurement because of the potential influence of capillarity, mentioned above in Section 4.2 [52,59,60]. Continuous flow experiments, often in one direction only, which overcome this limitation, are therefore often attractive [59]. Care must also be applied in the experiment in order to avoid the potential influence of uneven compression of the preform, as well as edge effects [61,62]. For long-fibre preforms, the permeability for flow in the third dimension, often called the *transverse permeability*, is not often measured, since flow along this direction is generally inconsequential in RTM processing of polymer matrix composites. With metal matrix composites, on the other hand, this component can be important since relatively thick components can be produced given the low matrix viscosity. Some satisfactory methods have been developed to this end, based directly on permeability measurement techniques for soils [53,63], or using flow front tracking techniques [64].

Prediction of the saturated permeability has also been the focus of a wide and long-lasting research effort, comprising many contributions from soil science and textile engineering for example. The first models proposed include the well-known Carman–Kozeny equations, based on the

assimilation of the porous preform to a bundle of capillary tubes; later refinements were subsequently added to these models, such as a variable tube diameter. These models are easy to use, can in general be fitted to experimental data, and have thus been extensively applied in composite processing [1,4]. These simple equations are, however, not well adapted for flow across fibres, and do not allow a prediction based on sole knowledge of the fibre arrangement geometry.

Other, more sophisticated and complex, models aimed specifically at fibre preforms have been developed based on the solution of fluid flow equations across cylinders, either considering the drag force around a cylinder as the resistance-creating factor for dilute systems [65], or considering the pressure drop between two parallel cylinders for concentrated systems [66–69]. These models are analytical, and generally assume a square or hexagonal array of dispersed cylinders. Numerical unit cell models have also been developed for permeability modelling [67,70]. Since most reinforcements constituting the preforms are not based on disperse fibres, but rather comprise fibre bundles which are often woven or knitted, the need to develop permeability prediction for multi-scale porous media has motivated the recent proposal of several analytical [71] semi-analytical or numerical models [72–77] for this class of geometries; possibly the most advanced model of this type is the Boltzmann lattice model developed at NIST [78].

#### 4.3.2. Relative permeability

This parameter, necessary for multi-phase flow modelling, depends on the fibre-matrix system, and is much more difficult to measure in the case of composite systems since model fluids cannot be used, or to predict theoretically given the far greater geometrical complexity of non-saturated flow. Therefore, models are again chiefly semi-empirical; such models have been proposed and validated experimentally in soil science, and take the general form

$$K_r = S^n, \quad (11)$$

where  $n$  is an exponential factor, typically between 1 and 3 for particle based soils [79]. To our knowledge, this approach has been used toward composite process modelling only in a few cases, using formulae derived from soil science [47,80], or inverse determination of the relationship from experiment [48].

#### 4.4. Stress–strain behaviour of the fibre preform

The compliance of fibrous preforms is generally measured using a compression test on the un-infiltrated preform. Oedometric tests, which are compression tests in which the porous medium is laterally constrained, have been developed to this end and are frequently used in soil science for measuring the stress–strain behaviour of granular media

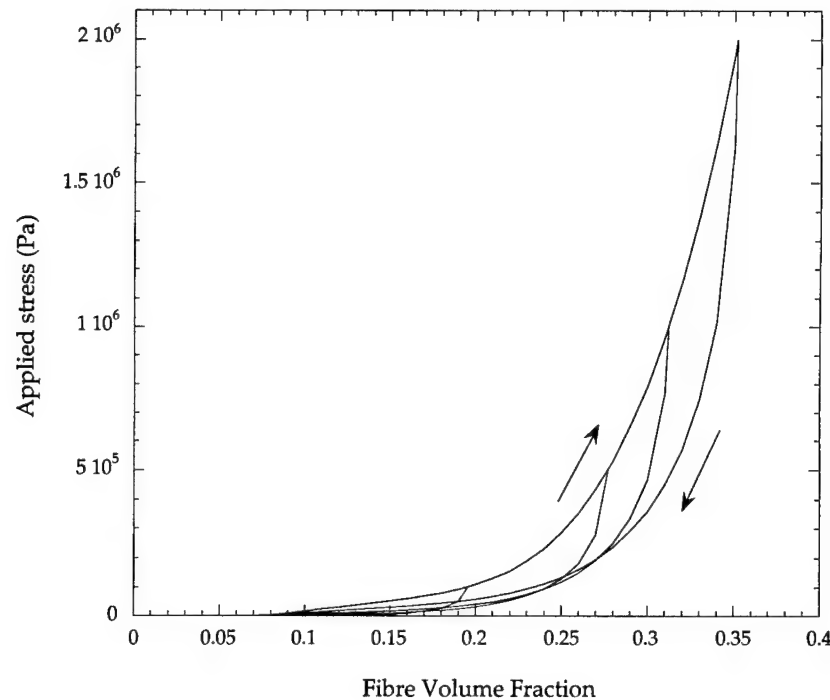


Fig. 8. Stress–strain curve (strain being represented in the form of the volume fraction fibre) for needled glass fibre mats (from research by Michaud et al. [88]).

[81]. In composite materials processing, such tests have been used for short fibre preforms [82,83]. In the case of self-sustaining long-fibre preforms, a simple compression test between two platens is useful, as very little lateral expansion occurs. Many examples of such tests are reported in the literature [4,84–86], and the resulting curves often exhibit similar shapes, an example being given in Fig. 8 for the compression of needled glass fibre mats.

Three points need to be mentioned with regard to measurement of preform compliance:

- (i) In the case of layered preforms, whether woven or knitted, the response depends on the number of stacked layers, as nesting and rearrangement occur [86]. Caution should therefore be taken to match the number of layers between the test and the infiltration process one seeks to model.
- (ii) Lubrication of the fibres often increases the compliance of the preform because it enhances sliding of the fibres past one another [87,88].
- (iii) As seen in Fig. 8, a large hysteresis may be observed, caused by fibre rearrangement, breakage and sliding during the test. In general, the hysteresis is low for fully 2D fibre arrangements; however, it may be quite appreciable when some fibres or binding material are oriented along directions orthogonal to the testing axis, as in Saffil alumina preforms [82,83] or glass mats [87].

Several models based on beam bending theory are available

in the literature towards prediction of the stress-strain behaviour during the compression phase. These include:

- (i) The model derived by Gutowski et al. [4]

$$\sigma = \frac{3\pi E}{\beta^4} \frac{(1 - \sqrt{V_f/V_{fo}})}{(\sqrt{V_a/V_f} - 1)^4}, \quad (12)$$

where  $E$  is the Young's modulus of the fibre,  $V_{fo}$  the volume fraction of the free-standing preform,  $V_a$  the maximum packing density, and  $\beta$  is a constant.

- (ii) Various forms of power law [85,89]

$$\sigma = kE(V_f - V_{fo})^n, \quad (13)$$

where  $E$  is the Young's modulus of the fibre,  $V_{fo}$  the volume fraction of the free-standing preform, and  $k$  and  $n$  are the parameters, depending on the arrangement of the fibres.

- (iii) Models developed in soil mechanics such as the Hujoux law [90]; these are currently being explored to model the behaviour of Saffil preform [91].

Most of the above relationships yield good agreement after fitting the parameters. No model has yet been proposed to model the relaxation part of the curves when hysteresis is significant; phenomenological curve fitting is then used [82,88].

## 5. Process modelling: methodology and comparison with experiments

We turn in this section to the description of a few



examples, mostly taken (for convenience) from our own work, of the application of these principles to the modelling of fibre composite infiltration processing. Our aim is to provide some insight on the solutions methods that are used, and of the level of agreement between experiment and analysis that can now be obtained.

### 5.1. Saturated infiltration of a rigid preform under constant pressure

In many practical cases of infiltration modelling, for all types of matrices, the problem can be in first approximation reduced to that of infiltration under constant applied pressure  $P_0$ . If infiltration is spontaneous, driven by a vacuum, or by pressure applied by a gas or a piston, after a transient period infiltration indeed often takes place under a constant pressure differential. In this particular case, with the additional assumption of a Newtonian fluid and if infiltration is unidirectional, solution of Eqs. (3)–(6) is self-similar: the two variables  $x$  and  $t$  are combined into a single reduced parameter  $\chi = x/\sqrt{t}$  which fully describes the problem [19,92,93].

If one makes the additional assumption of saturated flow (the slug-flow assumption defined in Section 4.2.1) and of a rigid preform, a very straightforward analytical solution is obtained, relating the position of the infiltration front  $L$  with time

$$L = \sqrt{\frac{2K(P_0 - P_a - \Delta P_\gamma)}{\eta(1 - V_f)}} \sqrt{t} \quad (14)$$

where  $P_a$  is the pressure of the atmosphere in the preform ahead of the infiltration front. This well known relationship has been widely used in composite processing analysis (sometimes with the  $(1 - V_f)$  at the denominator of Eq. (14) missing), and examples abound in all classes of composite materials where parabolic kinetics of infiltration have been experimentally observed (e.g. [30,62,94–96]). Note that if the infiltration kinetics are experimentally measured, a plot of  $L^2$  versus  $t$  then allows the determination of  $\Delta P_\gamma$  from the intercept with the  $P$ -axis, and of  $K$  from the slope [97].

If infiltration is not unidirectional or if the applied pressure is not constant, numerical methods are generally necessary. In the field of polymer composite processing, industrial applications have fostered the development of a relatively large number of simulation codes for saturated infiltration of rigid preforms. In most of these, the critical issue has often been that of precise tracking in time of the moving infiltration front location. Various methods such as the Boundary Element method have been developed to improve the precision of such software codes; these now provide useful prediction tools, in particular for the RTM process (e.g. [72,98–102]).

### 5.2. Gradual infiltration of rigid preforms

As mentioned earlier, in cases where capillary phenomena are important and the slug-flow assumption is insufficient, multi-phase flow modelling is required. So far, this approach in composite processing has focused on the case of infiltration of rigid preforms with a non-wetting fluid, for metal matrix composite infiltration modelling [47,48] as well as for polymer composite RTM modelling [103,104]. Interrupted isothermal infiltration experiments for molten aluminium flowing into Saffil alumina preforms have shown that a distribution of porosity is observed along the length of the samples [47,48]. Infiltration thus takes place in a gradual manner, the molten metal filling gradually the smaller pores as the local pressure increases.

In unidirectional infiltration, when the applied pressure is constant the similarity solution, which involves the transformation of variables for position  $x$  and time  $t$  into a single combined variable  $x/\sqrt{t}$  still obtains [47,105]. Comparison between experimental interrupted infiltration data and modelling yields satisfactory results, provided of course that the saturation curve and the dependence of the relative permeability on the saturation are known [47,48]. A numerical Finite Element model has been developed on this basis, using as a starting point a software package initially designed to treat soil-science problems, to tackle two- and three-dimensional gradual infiltration. A comparison of predictions from this simulation program with experimental porosity distributions measured for axi-symmetric infiltration of a Saffil disk by a central gate under gradually increasing pressure with a peak pressure of 0.8 MPa is given in Fig. 9 as an illustration of the predictive power of the software [48]. Some RTM modelling software packages have also started to introduce the concept of partial saturation, mostly to ease the flow front tracking issue: indeed, no sharp infiltration front need be located in multi-phase flow, and mass conservation is thus more easily obeyed [80,106].

### 5.3. Saturated infiltration of compressible preforms

As indicated in Section 4.4, fibre preforms used in composite processing, mainly in the case of polymer and metal matrix applications, can be very compliant materials. Experimental documentation of preform compression in infiltrated composites has been reported by several authors under various circumstances [55,107–110]. It is thus often necessary to take into account preform deformation during infiltration. This issue has been tackled in the field of metal matrix and polymer matrix composite processing, and several models have been proposed to predict preform deformation and account for the influence of preform deformation on the kinetics of infiltration. These can be classified into two categories, corresponding to the type of process: (i) consolidation or (ii) LCM processes.

In consolidation, the fibre assembly is compressed together with the matrix up to peak load, whereupon the

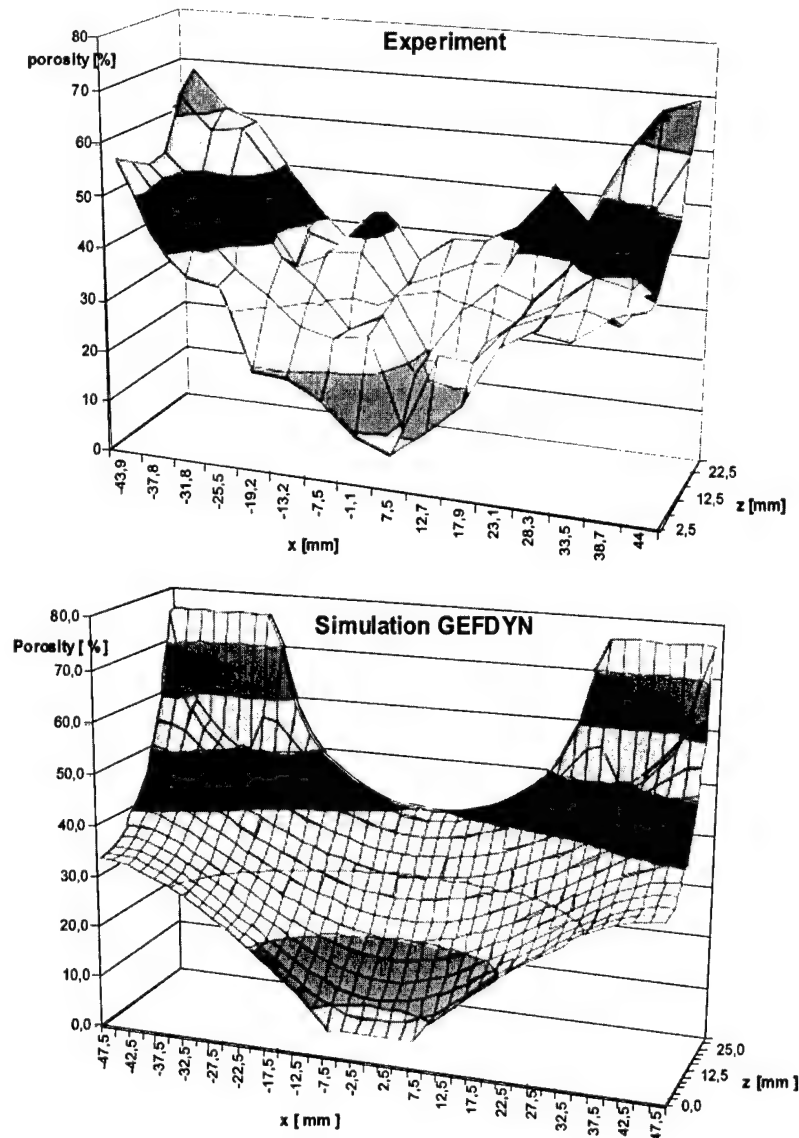


Fig. 9. Distribution of porosity in 24 volume percent dense Saffil™ (ICI, Runcorn, UK) short alumina fibre preforms infiltrated with aluminium at 973 K under a pressure of 0.8 MPa (from research by Dopler et al. [48]).

composite is solidified under load. Process modelling then requires only knowledge of the increasing stress-strain curve of the preform, since there is no deformation upon unloading. Models of this class based on soil science consolidation studies have been proposed by several authors [111–113].

In LCM processes such as RTM, and also in infiltration processing of metal matrix composites, the dry preform is also at first compressed by the incoming fluid as the pressure is applied; however, as soon as the fluid penetrates the preform, the latter starts relaxing along its decreasing stress-strain curve. Hence hysteresis in preform deformation must be taken into account in modelling. Numerical modelling of the unidirectional infiltration of compressible preforms under constant pressure has been performed using the slug flow

assumption. In this case, the similarity solution again applies, with use of the same reduced variable  $\chi = x/\sqrt{t}$ . Experimental results on the infiltration of a polyurethane sponge by ethylene glycol are compared to the predictions in Fig. 10 [114]. Good agreement is obtained after a short transient period due to the visco-elastic behaviour of the sponge. Another numerical simulation of these experimental results was also provided by Preziosi et al. [115,116].

Infiltration of compressible fibre preforms by thermoplastic matrices has been addressed along similar lines [117]. In addition, a finite difference moving boundary scheme was used to solve the equations describing the subsequent relaxation of the fibre preform that takes place in the absence of infiltration, after the fluid front has reached the end of the mould. Comparison between theory and

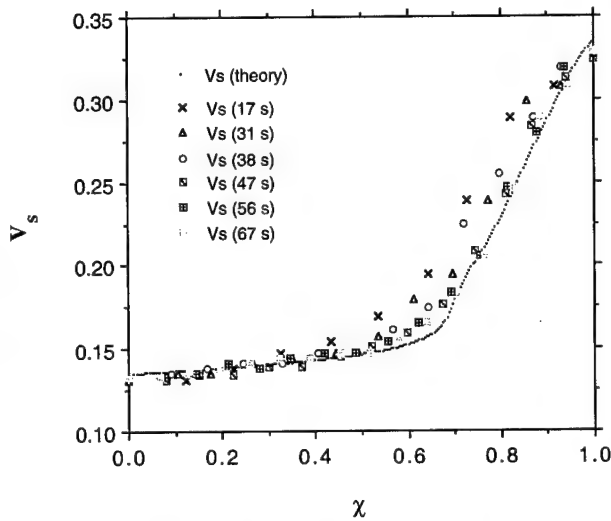


Fig. 10. Distribution of fraction solid along the infiltration path for infiltration of polyurethane foam with ethylene glycol as a function of position for various times, compared with predictions from theory: data agree with theory and show self-similar behaviour (from research by Sommer and Mortensen [114]).

experiments for the infiltration of glass fibre mats by Polyethylene Glycol (used as a model fluid) or Polypropylene (a thermoplastic polymer) showed good agreement, provided the friction at the mould walls did not prevent the preform from relaxing freely, as shown in Fig. 11 [88]. A similar influence of friction of the deforming preform along the mould wall has also been noted for metal matrix composite processing [63]; in general, this can thus be an important additional parameter in the process.

## 6. Conclusion

The infiltration process, in which the matrix in liquid form is caused to fill open pores of a preform of the reinforcing phase, has become one of the principal processes used for the production of composites across all three matrix classes: polymer, metal and ceramic.

Infiltration is governed in all cases by the same basic phenomena, which include capillarity, fluid flow, and the mechanics of potential preform deformation. These

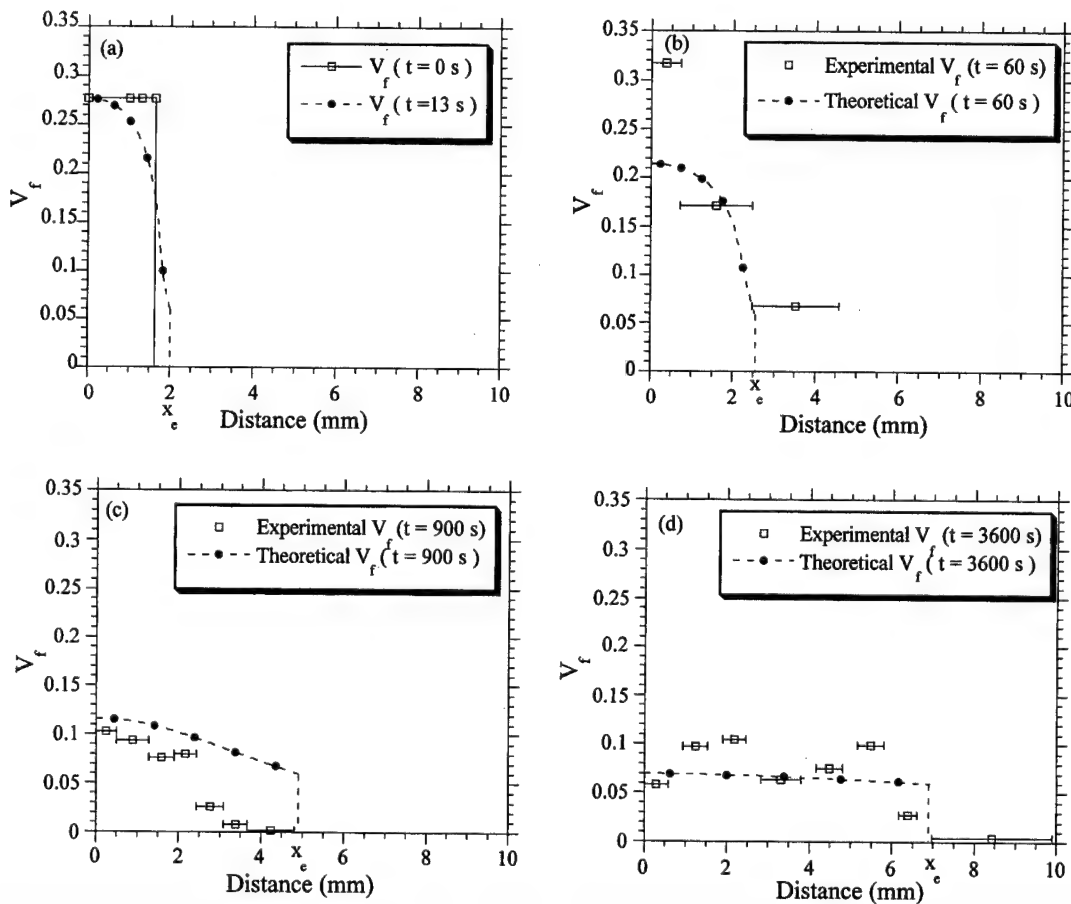


Fig. 11. Theoretical and experimental fibre volume fraction distributions at various stages during pressure impregnation of glass fibre mats with polypropylene: (a) initially and when the polymer reaches the other side of the mould (theory only), (b) after 60 s, (c) after 900 s, (d) after 3600 s (from research by Michaud et al. [88]).

phenomena, in turn, are governed by four basic parameters, namely the matrix melt viscosity  $\eta$ , the pressure-dependent melt saturation in the preform ( $S$ ) given by the relevant drainage/imbibition curve, the preform permeability  $K$  which depends both on  $S$  and on the local fibre volume fraction  $V_f$ , and finally the preform stress-strain behaviour. A comparison of these parameters, in particular of surface tension and viscosity values, across the three matrix material classes reveals significant differences; these, in turn, explain many of the differences in engineering practice from one composite matrix class to another.

The governing laws, on the other hand, are essentially the same. Application of these governing laws using both analytical and numerical methods, towards the analysis and simulation of the infiltration process is illustrated; it is in particular shown that multiphase flow in compressible media, which is highly relevant to other branches of engineering science such as soil science, is now becoming utilised towards modelling infiltration of composites. Other phenomena, which have not been considered in the present overview, can also be important in modelling infiltration. These include thermal and solutal transport phenomena, as well as phase transformations and reactions, which can govern the kinetics of the process as well as the structure of the final material obtained. For lack of space, these are not considered here; however again, similarities and differences can be drawn across materials classes. These similarities in governing phenomena of infiltration should be exploited more, and we hope that this brief overview can serve to create a few bridges across our three, often quite separate, composite research communities in addressing the fundamentals of this interesting and important process.

## Acknowledgements

We would like to acknowledge the contributions of our colleagues to the work that is cited in the present overview: at MIT Prof. M.C. Flemings, Ms L. Compton, Dr J. Sommer, and Dr J. Blucher; at the Ecole Centrale Paris Dr A. Modaressi, and Dr T. Dopler; at EPFL Prof. J.-A. Manson and Dr R. Törnqvist. We would also like to thank Dr H.P. Degischer (now at TU Vienna), Dr H. Kaufmann, and their coworkers at LKR (Ranshofen, Austria) for their participation in some of the work on metal infiltration presented in this article. We also gratefully acknowledge past sponsors of our work on the process (the Office of Naval Research, the US National Science Foundations, Alcoa, Aérospatiale Centre Commun de Recherches Louis Blériot, the European Community, and Symalit A.G.). Finally, the authors acknowledge current support of their work on the process from the Swiss National Science Foundation under contracts no. 20-52625.97 and 20-55291.98.

## References

- [1] Advani SG (Ed.). Flow and rheology in polymer composite manufacturing. In: Pipes RB, series editor. Composite Materials Series, vol. 10. Delaware. Elsevier, 1994.
- [2] Lim ST et al. Analysis of three-dimensional resin transfer mold filling process. In: Proceedings of the Fifth International Conference on Flow Processes in Composite Materials. ACMC Plymouth: Plymouth, UK; 1999. p. 137–42.
- [3] Yang H, Lee LJ. Mold filling and curing analysis in scrimp. In: ANTEC 2000, Orlando, FL. 2000. p. 2361–5.
- [4] Gutowski TG, editor. Advanced composite manufacturing. New York: Wiley, 1997.
- [5] Loos AC, MacRae JD. A process simulation model for the manufacture of a blade-stiffened panel by the resin film infusion process. *Compos Sci Technol* 1996;56:273–89.
- [6] Svensson N, Shishoo R, Gilchrist M. Manufacturing of thermoplastic composites from commingled yarns — A review. *J Thermoplastic Compos Mater* 1998;11:22–55.
- [7] Bernet N, et al. An impregnation model for the consolidation of thermoplastic composites made from commingled yarns. *J Compos Mater* 1999;33(8):751–72.
- [8] Han K, et al. Analysis of an injection-compression liquid composite molding process. *Polym Compos* 1998;19(4):487–96.
- [9] Voorakaranam S, Joseph B, Kardos JL. Modeling and control of an injection pultrusion process. *J Compos Mater* 1999;33(13):1173–203.
- [10] Donomoto T et al. Ceramic fiber reinforced piston for high performance diesel engines. Paper No. 830252SAE Technical Paper Series, Paper No. 830252, 1983, p. 10.
- [11] Ebisawa M et al. Production process of metal matrix composite (MMC) engine block. Paper No. 910835SAE Technical Paper Series, Paper No. 910835. 1991. p. 13.
- [12] Noguchi M. Aluminum composite lines cylinders. *Adv Mater Processes* 1993;143(6):20–1.
- [13] Fujine M. Aluminum composite replaces cast iron. *Adv Mater Processes* 1993;143(6):20.
- [14] Essig G, Mielke S, Bloeschies G. Anwendung Faserverstärkter Metalle in Verbrennungsmotoren. *Metall* 1990;44(5):434–7.
- [15] Premkumar MK, Hunt WH, Sawtell RR. Aluminum composite materials for multichip modules. *JOM* 1992;44(7):24–8.
- [16] Kelly A, Lilholt H. Stress-strain curve of a fibre-reinforced composite. *Philos Mag* 1969;20:311–28.
- [17] Halverson DC, et al. Processing of boron carbide-aluminum composites. *J Amer Ceram Soc* 1989;72(5):775–80.
- [18] Aghajanian MK, et al. Properties and microstructure of lanxide  $\text{Al}_2\text{O}_3$ -Al ceramic composite materials. *J Mater Sci* 1989;24:658–70.
- [19] Mortensen A. Melt infiltration of metal matrix composites. In: Kelly A, Zweben C, editors. Comprehensive composite materials, volume 3: metal matrix composites. Oxford, UK: Pergamon Press, 2000. p. 521–54 (Chapter 21, Volume editor: T.W. Clyne).
- [20] Cornie JA, et al. Processing of metal and ceramic matrix composites. *Bull Amer Ceram Soc* 1986;65(2):293–304.
- [21] Chawla KK. Ceramic matrix composites. London, UK: Chapman & Hall, 1993 (p. 126–61).
- [22] Fitzer E, Gadow R. Fiber reinforced silicon carbide. *Bull Amer Cer Soc* 1986;65(2):326–35.
- [23] Prewo KM, Brennan JJ, Layden GK. Fiber reinforced glasses and glass-ceramics for high performance applications. *Bull Amer Ceram Soc* 1986;65(2):305–13.
- [24] Hillig WB. Melt infiltration approach to ceramic matrix composites. *J Amer Ceram Soc* 1988;71(2):C96–9.
- [25] Hillig WB, McGuigan HC. An exploratory study of producing non-silicate all-oxide composites by melt infiltration. *Mater Sci Engng* 1995;A196:183–90.

- [26] Marple BR, Glass S, Green DJ. Ceramic composites by infiltration-processing, Processing of ceramic and metal matrix composites. Halifax, Nova Scotia: Pergamon Press, 1989 (p. 120–31).
- [27] Marple BR, Green DJ. Mullite alumina particulate composites by infiltration processing: II, Infiltration and characterisation. *J Amer Ceram Soc* 1990;73(12):3611–6.
- [28] Tuffé S, Marple BR. Graded casting: process control for producing tailored profiles. *J Amer Ceram Soc* 1995;78(12):3297–303.
- [29] Riou S, Queyroux F, Boch P. Zirconia-alumina particulate composites by infiltration processing. *Ceram Int* 1995;21:339–43.
- [30] Honeyman-Colvin P, Lange FF. Infiltration of porous alumina bodies with solution precursors: strengthening via compositional grading, grain size control, and transformation toughening. *J Amer Ceram Soc* 1996;79(7):1810–4.
- [31] Colomban P, Wey M. Sol–gel control of matrix net-shape sintering in 3D fibre reinforced ceramic composites. *J Eur Ceram Soc* 1997;17:1475–83.
- [32] Zhang E, Thompson DP. Carbon fibre reinforcement of nitrogen glass. *Compos: Part A, Appl Sci Manufacturing* 1997;28A:581–6.
- [33] Langguth K. Preparation of macro-porous SiC–Al<sub>2</sub>O<sub>3</sub> composites with polysilanes and polycarbosilanes. *Ceram Int* 1995;21:237–42.
- [34] Mortensen A, Jin I. Solidification processing of metal matrix composites. *Int Mater Rev* 1992;37(3):101–28.
- [35] Clyne TW, Withers PJ. In: Davis EA, Ward LM, editors. An introduction to metal matrix composites: Cambridge solid state science series, Cambridge, UK: Cambridge University Press, 1993.
- [36] Mortensen A, Michaud VJ, Flemings MC. Pressure infiltration processing of reinforced aluminum. *J Metals* 1993;45:36–43.
- [37] Aubry D et al. Coupled mechanical hydraulic behaviour of earth dams with partial saturation. In: Proceedings of the European Conference on Numerical Methods in Geomechanics, Stuttgart. 1986:1–13.
- [38] Bafna SS, Baird DG. An impregnation model for the preparation of thermoplastic prepreps. *J Compos Mater* 1992;26(5):683–707.
- [39] Velten K, Lutz A, Friedrich K. Quantitative characterization of porous materials in polymer processing. *Compos Sci Technol* 1999;59:495–504.
- [40] Bear J. In: Biswas AK, editor. Dynamics of fluids in porous media: environmental science series. New York: Elsevier, 1972.
- [41] Dullien FAL. Porous media, fluid transport and pore structure. New York: Academic Press, 1979.
- [42] Scheidegger AE. The physics of flow through porous media. 3rd ed. Toronto: University of Toronto Press, 1974.
- [43] Greenkorn RA. Flow phenomena in porous media. New York: Marcel Dekker, 1983.
- [44] Morrow NR. Physics and thermodynamics of capillary action in porous media. *Ind Engng Chem* 1970;62(6):32–56.
- [45] Mortensen A. Interface chemistry of inorganic composite materials. In: Proceedings of the Ninth Risø International Symposium on Metallurgy and Materials Science, Risø National Laboratory, Roskilde, Denmark. 1988. p. 141–55.
- [46] Kaufmann H, Mortensen A. Wetting of Saffil™ alumina fiber preforms by aluminum at 973 K. *Metall Trans* 1992;23A:2071–3.
- [47] Michaud VJ, Compton L, Mortensen A. Capillarity in isothermal infiltration of alumina fiber preforms with aluminum. *Metall Trans* 1994;25A(10):2145–52.
- [48] Dopler T, Modaressi A, Michaud VJ. Simulation of metal composite isothermal infiltration processing. *Metall Mater Trans* 2000;31B:225–33.
- [49] Patel N, Lee LJ. Modeling of void formation and removal in liquid composite molding, Part I: Wettability analysis. *Polym Compos* 1996;17(1):96–103.
- [50] Patel N, Lee LJ. Modeling of void formation and removal in liquid composite molding Part II: Model development and implementation. *Polym Compos* 1996;17(1):104–14.
- [51] Brooks RH, Corey AT. Hydraulic properties of porous media. Colorado State University Hydrology Papers 1964:27.
- [52] Parnas R, et al. Permeability characterization Part 1: A proposed standard reference fabric for permeability. *Polym Compos* 1995;16(6):429–45.
- [53] Wu C-H, Wang TJ, Lee LJ. Trans-plane fluid permeability measurement and its application in liquid composite molding. *Polym Compos* 1994;15(4):289–98.
- [54] Wang TJ, Wu C-H, Lee LJ. In-plane permeability measurement and analysis in liquid composite molding. *Polym Compos* 1994;15(4):278–88.
- [55] Luce TL, et al. Permeability characterization Part 2: flow behavior in multiple layer preforms. *Polym Compos* 1995;16(6):446–58.
- [56] Sadiq TAK, Advani SG, Parnas RS. Experimental investigation of transverse flow through aligned cylinders. *Int J Multiphase Flow* 1995;21(5):755–74.
- [57] Weitzenböck JR, Shenoi RA, Wilson PA. Radial flow permeability measurement Part B: application. *Composites Part A* 1999;30:797–813.
- [58] Weitzenböck JR, Shenoi RA, Wilson PA. Radial flow permeability measurement Part A: Theory. *Composites Part A* 1999;30:781–96.
- [59] Lekakou C, et al. Measurement techniques and effects on in-plane permeability of woven cloths in resin transfer molding. *Composites Part A* 1996;27A:401–8.
- [60] Parnas R, Flynn KM, Dal-Favero ME. A permeability database for composites manufacturing. *Polym Compos* 1997;18(5):623–33.
- [61] Friedman HL, et al. Visualization and quantification of forced in-plane flow through deformed porous media. *Polym Compos* 1999;20(5):613–27.
- [62] Ferland P, Guittard D, Trochu F. Concurrent methods for permeability measurement in resin transfer molding. *Polym Compos* 1996;17(1):149–58.
- [63] Sommer JL. Infiltration of deformable porous media. PhD thesis, Massachusetts Institute of Technology, 1992.
- [64] Ballata WO, Walsh SM, Advani S. Determination of the transverse permeability of a fiber preform. In: Proceedings of the 13th Annual Technical Conference on Composite Materials, Baltimore. American Society of Composites; 1998. p. 256–70.
- [65] Happel J. Viscous flow relative to arrays of cylinders. *AIChE J* 1959;5(2):174–7.
- [66] Keller JB. Viscous flow through a grating or lattice of cylinders. *J Fluid Mech* 1964;18:94–96.
- [67] Sangani AS, Acrivos A. Slow flow past periodic arrays of cylinders with application to heat transfer. *Int J Multiphase Flow* 1982;8(3):193–206.
- [68] Bruschke MV, Advani SG. Flow of generalized newtonian fluids across a periodic array of cylinders. *J Rheol* 1993;37(3):479–798.
- [69] Gebart BR. Permeability of unidirectional reinforcements for RTM. *J Compos Mater* 1992;26(8):1100–33.
- [70] Drummond JE, Tahir MI. Laminar viscous flow through regular arrays of parallel solid cylinders. *Int J Multiphase Flow* 1984;10(5):515–40.
- [71] Shih C-H, Lee LJ. Effect of fiber architecture on permeability in liquid composite molding. *Polym Compos* 1998;19(5):626–39.
- [72] Phelan FR. Simulation of the injection process in resin transfer molding. *Polym Compos* 1997;18(4):460–76.
- [73] Phelan FR. Modeling of microscale flow in fibrous porous media, Advanced composite materials: new developments and applications. Detroit, MI: ASM International, 1991 (p. 175–85).
- [74] Parnas R, et al. The interaction between micro- and macro-scopic flow in RTM preforms. *Compos Struct* 1994;27:93–107.
- [75] Papathanasiou TD. On the effective permeability of square arrays of permeable fiber tows. *Int J Multiphase Flow* 1997;23(1):81–92.
- [76] Binetruy C, Hilaire B, Pabiot J. Tow impregnation model and void formation mechanisms during RTM. *J Compos Mater* 1998;32(3):223–45.
- [77] Binetruy C, Hilaire B, Pabiot J. The interactions between flows occurring inside and outside fabric tows during RTM. *Compos Sci Technol* 1997;57:587–96.

- [78] Dunkers JP et al. Flow prediction in real structures using optical coherence tomography and lattice Boltzmann mathematics. In: Proceedings of the Fifth International Conference on Flow Processes in Composite Materials. ACMC Plymouth: Plymouth, UK; 1999. p. 291–302.
- [79] Spitz K, Moreno J. A practical guide to groundwater and solute transport modeling. New York: Wiley, 1996.
- [80] Antonelli D, Farina A. Resin transfer molding: mathematical modeling and numerical simulations. *Compos Part A, Appl Sci Manufacturing* 1999;30:1367–85.
- [81] Lambe TW, Whitman RV. Soil mechanics. New York: Wiley, 1979 (SI version).
- [82] Michaud VJ, Sommer JL, Mortensen A. Infiltration of fiber preforms by a pure metal: Part V. Influence of preform deformation. *Metall Trans* 1999;30A(2):471–82.
- [83] Dopler T. Low pressure infiltration process modeling. PhD, Laboratoire de Mecanique des Sols, Structures et Materiaux, Ecole Centrale, Paris, 1999.
- [84] Trevino L, et al. Analysis of resin injection molding in molds with preplaced fiber mats I: Permeability and compressibility measurements. *Polym Compos* 1991;12(1):20–9.
- [85] Toll S. Packing mechanics of fiber reinforcements. *Polym Engng Sci* 1998;38(8):1337–50.
- [86] Saunders RA, Lekakou C, Bader MG. Compression in the processing of polymer composites 1. A mechanical and microstructural study for different glass fabrics and resins. *Compos Sci Technol* 1999;59:983–93.
- [87] Kim YR, McCarthy SP, Fanucci JP. Compressibility and relaxation of fiber reinforcements during composite processing. *Polym Compos* 1991;12(1):13–9.
- [88] Michaud V, Törnqvist R, Månson J-AE. Impregnation of compressible fiber mats with a thermoplastic resin, Part II: Experiments. *Journal of Composite Materials* 2000, in press.
- [89] Toll S, Manson J-AE. Elastic compression of a fiber network. *J Appl Mech* 1995;62:223–6.
- [90] Aubry D et al. A double memory model with multiple mechanisms for cyclic soil behaviour. In: Proceedings of the International Symposium on Numerical Models in Geomechanics, Zurich, Balkema. 1982. p. 3–13.
- [91] Michali A et al. Work in progress, 2001.
- [92] Philip JR. The theory of infiltration: 1. The infiltration equation and its solution. *Soil Sci* 1956;83:345–57.
- [93] Billi L, Farina A. Unidirectional infiltration in deformable porous media: mathematical modeling and self similar solution. *Quarterly Appl Math* 2000;58(1):85–101.
- [94] Masur LJ, et al. Infiltration of fibrous preforms by a pure metal: Part II. Experiment. *Metall Trans* 1989;20A:2549–57.
- [95] Michaud VJ, Mortensen A. Infiltration of fiber preforms by a binary alloy Part II: Further theory and experiments. *Metall Trans* 1992;23A:2263–80.
- [96] Garcia-Cordovilla C, Louis E, Narciso J. Pressure infiltration of packed ceramic particulates by liquid metals. *Acta Mater* 1999;47(18):4461–79.
- [97] Mortensen A, Wong T. Infiltration of fibrous preforms by a pure metal: Part III. Capillary phenomena. *Metall Trans* 1990;21A:2257–63.
- [98] Bickerton S, Advani SG. Experimental investigation and flow visualization of the resin-transfer mold-filling process in a non-planar geometry. *Compos Sci Technol* 1997;57:23–33.
- [99] Kang MK, Lee WI. Analysis of resin transfer molding process with progressive resin injection. In: Proceedings of the 11th International Conference on Composite Materials, Gold Coast, Queensland, Australia. Cambridge, UK: Woodhead Publishing; 1997. p. IV-27–36.
- [100] Pillai KM, III CLT, Jr FRP. Numerical simulation of injection/compression liquid composite molding Part I. Mesh generation. *Composites Part A* 2000;31:87–94.
- [101] Lin MY, Murphy MJ, Hahn HT. Resin transfer molding process optimization. *Composites Part A* 2000;31:361–71.
- [102] Plymouth Uo. editor. Flow processes in composite materials (FPCM-5). Robbins Centre. Media Services, University of Plymouth: Plymouth, UK; 1999.
- [103] Pillai KM, Advani SG. Numerical simulation of unsaturated flow in woven fiber preforms during the resin transfer molding process. *Polym Compos* 1998;19(1):71–80.
- [104] Pillai KM, Advani SG. A model for unsaturated flow in woven fiber preforms during mold filling in resin transfer molding. *J Compos Mater* 1998;32(19):1753–83.
- [105] Philip JR. Theory of infiltration. In: Chow VT, editor. *Advances in hydrosience*, New York: Academic Press, 1969. p. 215–97.
- [106] Lin M, Hahn HT, Huh H. A finite element simulation of resin transfer molding based on partial nodal saturation and implicit time integration. *Composites Part A* 1998;29A:541–50.
- [107] Yamauchi T, Nishida Y. Infiltration kinetics of fibrous preforms by aluminum with solidification. *Acta Metall Mater* 1995;43(4):1313–21.
- [108] Jarry P, et al. Infiltration of fiber preforms by an alloy Part III: Dye casting experiments. *Metall Trans* 1992;23A:2281–9.
- [109] Han K, Lee LJ, Liou M. Fiber mat deformation in liquid composite molding II: Modeling. *Polym Compos* 1993;14(2):151–60.
- [110] Han K, et al. Fiber mat deformation in liquid composite molding I: Experimental analysis. *Polym Compos* 1993;14(2):144–50.
- [111] Gutowski TG, Morigaki T, Cai Z. The consolidation of laminate composites. *J Compos Mater* 1987;21(2):172–88.
- [112] Dave R, Kardos JL, Dudukovic MP. A model for resin flow during composite processing: Part I — General mathematical development. *Polym Compos* 1987;8(1):29–38.
- [113] Saunders RA, Lekakou C, Bader MG. Compression in the processing of polymer composites 2. Modelling of the viscoelastic compression of resin impregnated fiber networks. *Compos Sci Technol* 1999;59:1483–94.
- [114] Sommer J, Mortensen A. Forced unidirectional infiltration of deformable porous media. *J Fluid Mech* 1996;311(3):193–217.
- [115] Preziosi L. The theory of deformable porous media and its application to composite materials manufacturing. *Surveys Math. Indus* 1996;6:167–214.
- [116] Preziosi L, Joseph DD, Beavers GS. Infiltration of initially dry, deformable porous media. *Int J Multiphase Flow* 1996;22(6):1205–22.
- [117] Michaud V, Månson J-AE. Impregnation of compressible fiber mats with a thermoplastic resin, Part I: Theory. *Journal of Composite Materials* 2000, in press.



# Use of electrophoretic deposition in the processing of fibre reinforced ceramic and glass matrix composites: a review

A.R. Boccaccini<sup>a,\*</sup>, C. Kaya<sup>b</sup>, K.K. Chawla<sup>c</sup>

<sup>a</sup>*Fachgebiet Werkstofftechnik, Technische Universität Ilmenau, PF 100565, D-98684 Ilmenau, Germany*

<sup>b</sup>*Interdisciplinary Research Centre (IRC) for High Performance Applications & School of Metallurgy and Materials, The University of Birmingham, Edgbaston, Birmingham B15 2TT, UK*

<sup>c</sup>*Department of Materials and Mechanical Engineering, University of Alabama at Birmingham, Birmingham, AL 35294, USA*

## Abstract

Electrophoretic deposition (EPD) is a simple and cost-effective method for fabricating high-quality 'green' composite bodies which, after a suitable high-temperature treatment, can be densified to a composite with improved properties. In this contribution, we describe the use of EPD technique in the fabrication of fibre reinforced composites, with an emphasis on composites with glass and ceramic matrices containing metallic or ceramic fibre fabric reinforcement. EPD has been used to infiltrate preforms with tight fibre weave architectures using different nanosized ceramic particles, including silica and boehmite sols, as well as dual-component sols of mullite composition. The principles of the EPD technique are briefly explained and the different factors affecting the EPD behaviour of ceramic sols and their optimisation to obtain high infiltration of the fibre preforms are considered. In particular, the EPD fabrication of a model alumina matrix composite reinforced by Ni-coated carbon fibres is presented. The pH of the solution and the applied voltage and deposition time are shown to have a strong influence on the quality of the infiltration. Good particle packing and a high solids-loading were achieved in most cases, producing a firm ceramic deposit which adhered to the fibres. Overall, the analysis of the published data and our own results demonstrate that EPD, being simple and inexpensive, provides an attractive alternative for ceramic infiltration and coating of fibre fabrics, even if they exhibit tight fibre weave architectures. The high-quality infiltrated fibre mats are suitable prepreps for the fabrication of advanced glass and ceramic matrix composites for use in heat-resistant, structural components. © 2001 Elsevier Science Ltd. All rights reserved.

**Keywords:** A. Ceramic–matrix composites (CMCs); E. Prepreg; Electrophoretic deposition

## 1. Introduction

The development of fibre reinforced ceramic and glass matrix composites is a promising means of achieving light-weight, structural materials combining high-temperature strength with improved fracture toughness, damage tolerance and thermal shock resistance [1]. Considerable research effort is being expended in the optimisation of ceramic composite systems, with particular emphasis being placed on the establishment of reliable and cost-effective fabrication procedures. In this context, while the initial efforts were in the fabrication of unidirectional composites, they are increasingly shifting towards the more isotropic composite materials reinforced by two-dimensional (2D) and three-dimensional (3D) fibre architectures. The majority of the research undertaken so far on the 2D reinforcement of ceramics has been conducted using

ceramic fabrics, including SiC-based (e.g. Nicalon<sup>®</sup>, Nippon Carbon Co., Japan), alumina and aluminosilicate woven fibre mats [2–5]. Metallic fabrics are commercially available also [6] and are made from a variety of metals including stainless steel and special alloys (e.g. Hastelloy X). These fabrics provide interesting reinforcing elements for the fabrication of ductile phase reinforced brittle matrix composites, including glass matrix composites.

Ceramic and glass composites incorporating 2D or 3D fibre reinforcements are particularly prone to exhibiting uncontrolled microstructures and residual porosity. This is because it is extremely difficult to achieve complete infiltration of the matrix material into the fibre tows (where the intra-tow openings may be down to the order of  $\leq 100$  nm). Traditional processing routes for 2D or 3D fibre reinforced ceramic matrix composites have disadvantages. In particular, simple slurry infiltration is unable to penetrate tight fibre weaves, while chemical vapour infiltration (CVI) is an expensive technology due to the numerous re-infiltration steps required and the high-cost equipment involved [4].

Electrophoretic deposition (EPD) has been developed in

\* Corresponding author. Present address: Department of Materials, Imperial College, London SW7 2BP, UK.

E-mail address: a.boccaccini@ic.ac.uk (A.R. Boccaccini).



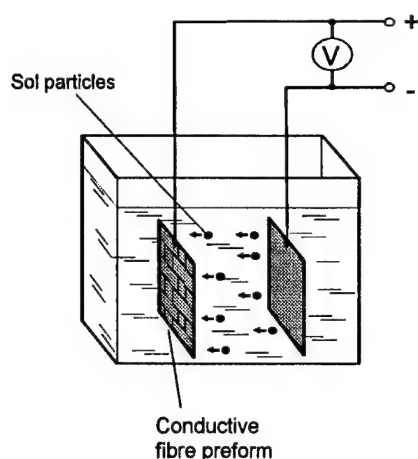


Fig. 1. Schematic diagram of the EPD cell for obtaining ceramic deposits on conductive fibre mats. The fibre mat acts as the positive electrode when the particles in the suspension are negatively charged (e.g. silica particles at pH = 9 [4]).

recent years as a novel, simple and inexpensive method for achieving complete infiltration of tightly woven fibre preforms [4,7]. The technique is based on using nanoscale ceramic particles in a stable non-agglomerated form (such as in a sol or colloidal suspension) and exploiting their net surface electrostatic charge characteristics while in suspension. On application of an electric field the particles will migrate towards and deposit on an electrode. If the deposition electrode is replaced by a conducting fibre preform, the suspended particles will be attracted into and deposited within it, providing an appropriate means of effectively infiltrating densely packed fibre bundles. A schematic diagram of the basic EPD cell is shown in Fig. 1.

The movement of ceramic sol particles in an aqueous suspension within an electric field is governed by the field strength, and the pH, ionic strength and viscosity of the solution [4]. The electrophoretic mobility (EM) of the charged particles in suspension is given by [8]:

$$EM = \frac{U}{E} = \frac{\varepsilon\zeta}{4\pi\eta}, \quad (1)$$

where  $U$  is the velocity,  $E$  the field strength,  $\varepsilon$  the dielectric constant,  $\zeta$  the zeta potential and  $\eta$  the viscosity. Accordingly, a suitable suspension for EPD should have high-particle surface charge, high dielectric constant of the liquid phase and low viscosity. Moreover, low conductivity of the suspending medium to minimise solvent transport is required.

The phenomenon of electrophoresis has been known since the beginning of the last century [9] and has found extended application in ceramic technology. In available comprehensive review articles, complete descriptions of the basics of the EPD technique and its applications in ceramics have been presented [8,10–12]. Moreover, the deep electrophoretic penetration of porous substrates, which is related to the EPD infiltration of tight fibre

preforms has been studied theoretically and experimentally [13–15].

In the present work, a complete literature review focusing on the particular use of EPD to infiltrate ceramic and metallic fibre preforms with the ultimate goal of fabricating composite materials is presented. Typical EPD experimental procedures and the results achieved are described in detail, taking as example a model alumina matrix composite reinforced by Ni-coated carbon fibres.

## 2. Literature review

Table 1 presents an overview of the published work dealing with the application of the EPD technique for the fabrication of fibre reinforced ceramic and glass matrix composites. Other types of ceramic composite systems, such as whisker reinforced composites [16,17], laminated composites [18–20], composite coatings [21], composites with porous layers [22] and functionally graded materials [22–24] have been fabricated by the EPD technique. Moreover, the use of electrodeposition to coat ceramic fibres with metals with the aim to fabricate metal matrix composites has also been investigated [25,26]. However, research on these areas will not be reviewed here, this paper being restricted to the use of EPD for the fabrication of fibre reinforced ceramic and glass matrix composites.

The feasibility of infiltrating ceramic woven fibre preforms by EPD has been demonstrated for a variety of single and mixed component ceramic sols, as summarised in Table 1. Mainly graphite [22,27–32], SiC-based [4,7,22,33–40], alumina [35,41–43] and aluminosilicate (mullite) [37,44,45] woven fibre mats have been employed. The matrices investigated have been silica, alumina, mullite, SiC,  $\text{Si}_3\text{N}_4$  and borosilicate glass. Both aqueous and non-aqueous suspensions have been used, although aqueous colloidal suspensions or sols are preferred due to environmental and cost advantages [46]. The experiments have been invariably carried out in laboratory scale, using EPD cells of small dimensions, i.e. the gap between the electrodes was between 1 and 5 cm in most studies, and the area of the fibre preforms infiltrated was smaller than  $100\text{ cm}^2$ . When EPD is used as a ceramic forming technique, it is possible to use either constant current or constant voltage conditions. An analysis of the literature showed, however, that all investigations have been conducted by using constant voltage conditions, the reason being most probably that this is the simplest mode of operation.

In the case of non-conductive fibres, such as aluminosilicate (mullite) fibres of the type Nextel<sup>®</sup> 720 (3M Co., MN, USA) or alumina fibres (e.g. Almax<sup>®</sup>, Mitsui Mining Co., Japan), a modification of the basic EPD cell must be conducted. This has been called electrophoretic filtration deposition (EFD) and it is a modification of a method used previously by Clasen [47]. Here, both electrodes are made from stainless steel and a filter metallic membrane is

Table 1  
Overview of previous research on using EPD for the fabrication of fibre reinforced ceramic and glass matrix composites

Year	System: fibre/matrix	Matrix precursors	Suspension conditions	EPD parameters		Reference
				Constant voltage (V)	Deposition time	
1991	SiC (Nicalon <sup>®</sup> ) woven fibre mat/silica	Silica sol, particle size 20 nm (+2 wt% boehmite sol)	Aqueous sol, pH 10	4	15 min	[4,7,33]
1995	SiC (Nicalon <sup>®</sup> ) woven fibre mat/mullite	Fumed silica nanoparticles, boehmite sol in mullite composition	Aqueous mixed sol, pH 4.4	4	1 min	[34,35]
1995	SiC (Nicalon <sup>®</sup> ) woven fibre mat/mullite	Polymeric mullite sol	Polymeric sol, pH 4, concentration 6 g/l	100	1 min	[36]
1995	SiC (Nicalon <sup>®</sup> ) woven fibre mat/Si <sub>3</sub> N <sub>4</sub>	Si <sub>3</sub> N <sub>4</sub> and Y <sub>2</sub> O <sub>3</sub> powders	Suspension in acetone	320	10–15 min	[37]
1995	SiC (Nicalon <sup>®</sup> ) woven fibre mat/SiC	C and Si powders	Suspension in acetone	320	20 min	[37]
1995	Aluminosilicate (Nextel-610) woven fibre cloth/Be	Be particles	Suspension in acetone	320	10–15 min	[37]
1995	C-fibre and woven fibre mat/Si <sub>3</sub> N <sub>4</sub> and Al <sub>2</sub> O <sub>3</sub>	Si <sub>3</sub> N <sub>4</sub> powder Al <sub>2</sub> O <sub>3</sub> powder	Suspension in ethanol, use of different surfactants	200	5 min	[27]
1995	Alumina (Almax <sup>®</sup> ) woven fibre mat/alumina	Boehmite sol, particle size 50 nm	Aqueous sol, pH 4	60		[35,41]
1996	C-fibre (or cloth)/SiC	$\alpha$ -SiC powder (+1 wt% Al <sub>2</sub> O <sub>3</sub> powder)	Aqueous suspension	Not-specified	Not-specified	[28]
1996	Alumina (Almax <sup>®</sup> ) woven fibre mat/mullite	Fumed silica and boehmite sol, and polymeric mullite sol	Mixed (diphasic) aqueous sol (mullite composition) and polymeric sol	60	1 min	[42]
1997	SiC (Nicalon <sup>®</sup> ) woven fibre mat/mullite	Fumed silica/alumina liquid dispersion, nanosized $\delta$ -alumina powder	Aqueous mixed sol, pH 3.1	4	1 min	[38]
1997	316L stainless steel fibre preform/soda-lime glass (with silica interface)	Soda-lime glass powder	Silica sol, pH 9, particle size 20 nm	4	1 min	[53]
1997	SiC (Nicalon <sup>®</sup> ) fibre cloth/SiC	SiC powder	Suspension in acetone, addition of surfactants	400		[39]
1997	C-cloth/YSZ, SiC (Nicalon <sup>®</sup> ) fibre cloth/alumina, stainless steel wire mesh/alumina	Non-specified	Non-specified	Not-specified	Not-specified	[22]
1998	316L stainless steel fibre preforms/alumina	Boehmite sol	Boehmite sol, pH 4	4	1 min	[50]
1998	316L stainless steel fibre preform/borosilicate glass (with silica interface)	Recycled glass powder	Silica sol, pH 4–6	5	8 min	[54]
1998	SiC (Nicalon <sup>®</sup> ) woven fibre mat/yttrium disilicate	Nanosized yttrium disilicate powder	Yttrium disilicate aqueous sol, pH 7	8	1 min	[40]
1998	C-fibre and fibre cloth/alumina, zirconia, lead zirconate titanate	Submicron alumina, zirconia and PZT powders	Suspensions in isopropyl alcohol	50–200	10 s–5 min	[29]
1998	Alumina multilayer blanket (Saffil <sup>®</sup> )/mullite	Silica nanopowder, silica sol, boehmite sol	Mixed (diphasic) aqueous sol of mullite composition, pH 4	10	2–8 min	[43]

Table 1 (continued)

Year	System: fibre/matrix	Matrix precursors	Suspension conditions	EPD parameters		Reference
				Constant voltage (V)	Deposition time	
1999	316L stainless steel fibre preform/silica	Silica sol, particle size 15 nm (+2.5 wt% B <sub>2</sub> O <sub>3</sub> , 2 wt% boehmite sol)	Aqueous sol, pH 9	4	2 min	[52]
2000	C-fibres and felts/hydroxyapatite	Submicron hydroxyapatite powder	Suspension in isopropyl alcohol	50	10 s–5 min	[30]
2000	C-fibres/alumina/316L stainless steel fibres/titania	Nanosized $\delta$ -alumina and titania powders	Suspensions in ethanol	60	1 min	[31]
2000	Aluminosilicate (mullite) fibre weaves (Nextel 720)/mullite	$\alpha$ -alumina and silica powders	Mixed suspension in ethanol; addition of surfactants containing carboxylic acid and amine	100	7 min	[44]
2000	Aluminosilicate (mullite) fibre weaves (Nextel 720)/mullite	Boehmite sol and fumed silica nano-powder	Mixed aqueous sol stable at pH 4.5	12	4 min	[45]
2000	Ni-coated C-fibres/borosilicate	Nanosized borosilicate glass powder	Aqueous colloidal sol, pH 8.5	6	4.5 min	[32]

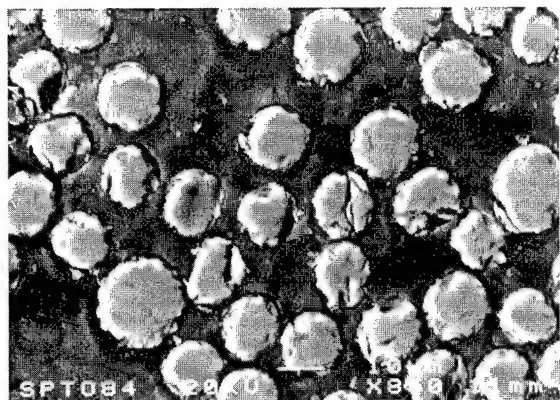


Fig. 2. SEM micrograph of EPD-infiltrated Nicalon® fibre mat using a mixed sol of mullite composition. Details of the EPD technique used are given in the original work [38]. A high level of matrix infiltration is seen. It was also shown that the deposited material fairly kept the original mullite stoichiometric composition [38].

placed between the deposition electrode and the non-conducting fibre preform [35,41,42]. On applying a relatively high voltage (e.g. 60 V for alumina sol [35]), the alumina particles migrate and deposit on to the membrane from one direction only, through the fibre preform, until a sufficient matrix thickness which envelopes the preform is achieved. The high voltage causes hydrogen evolution at the anode but the gas is prevented from becoming part of the compact by the presence of the filter membrane. In this way alumina–alumina [35] and mullite–mullite [45] woven fibre reinforced ceramic matrix composites could be fabricated.

An analysis of the published work shows that the quality of the infiltration also depended strongly on the architecture of the fibre preform employed but, in general, EPD was able to infiltrate even the very tight woven fibre mats used. The parameters of the EPD infiltration process, i.e. voltage applied and deposition time, were optimised in the different studies to obtain a high solids-loading in the intra-tow regions and firm, adherent, ceramic deposits. When using

diphasic (or mixed) sols (e.g. silica–alumina dual sols of mullite composition), the process becomes more complicated than with the single species (e.g. single silica or alumina sols). This is because it is necessary to control the mobility and zeta potential of both species in order for both of them to migrate to the same electrode and co-deposit without segregation under EPD conditions. In particular, for the fabrication of mullite matrices, it is necessary to maintain the initial silica–alumina proportion in the deposit material to warrant stoichiometric mullite composition. Several authors have shown ways to engineer the surface charge of the particles by the addition of surfactants [44] or to control short range particle–particle interactions and rheological characteristics of the colloidal suspensions by careful variation of the particle size, solids-loading and pH [48,49]. In the case of diphasic (mixed) sols of mullite composition, the pH is chosen so that both species are oppositely charged, i.e. the alumina and silica particles are positively and negatively charged, respectively. Thus, heterocoagulated particle clusters are formed, which move as single, composite particles [38,43]. An example of a Nicalon® fibre mat infiltrated by a mixed sol of mullite composition using EPD is shown in Fig. 2 [38]. A high level of matrix infiltration is seen. It was shown in this work that the deposited material fairly kept the original mullite stoichiometric composition.

One of the most critical processing steps that must be optimised, as emphasised by most authors, is the drying of the infiltrated fibre preforms. This is because extensive microcracking of the gelled ceramic matrix can occur on drying, as usually occurs in sol–gel processing. Cracking frequently develops due to the differential shrinkage of the gel network generating tensile stresses at the surface, which may lead to the catastrophic growth of microscopic flaws [50]. However, thin films ( $<1\text{--}2\text{ }\mu\text{m}$ ) can be dried without cracking because the tensile stresses developed when they shrink are insufficient to cause the growth of cracks [50]. Thus, a careful control of the thickness of the matrix materials deposited by EPD is required, as highlighted in the literature [4,35]. Fig. 3 shows the different cracking development upon drying in two Nicalon® fibre mats which have been EPD-infiltrated with mullite composition sol [34]. The sample with thicker deposit exhibits extensive microcracking, while the optimisation of deposit thickness leads to a minimisation of microcracking.

The analysis of the literature reveals that when the EPD and drying conditions were optimised, the infiltrated fibre fabrics were of sufficient quality (high infiltration, no macroporosity and minimal microcrack development) to be used as preforms for the fabrication of ceramic or glass matrix composites.

The EPD process has also been successfully applied to infiltrate metallic fibre fabrics. Boehmite, silica and titania nanoparticles have been used as precursors for the ceramic matrices [22,31,51,52]. In borosilicate and soda-lime glass matrix composites, EPD infiltration of the metallic fibre

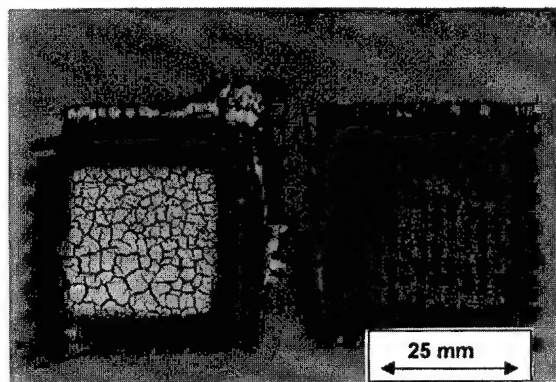


Fig. 3. Macrograph showing the development of microcracking in SiC Nicalon® fibre mats EPD-infiltrated with mullite composition mixed sol upon drying. Extensive microcracking is developed in thick deposits (left). This is minimised by depositing thin films of  $1\text{--}2\text{ }\mu\text{m}$  thickness (right) [34].

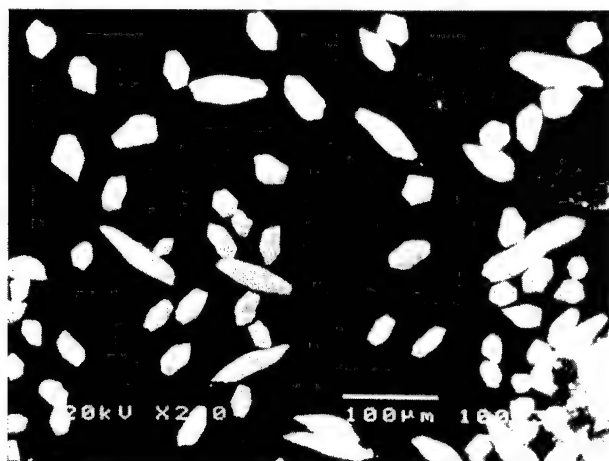


Fig. 4. SEM micrograph of a metallic fibre mat which has been fully infiltrated by silica sol using EPD. The working voltage was 4 V and deposition time 2 min [52].

preforms was conducted by using silica nanoparticles in colloidal suspensions [53,54]. In these composites, the EPD porous silica deposit was used to provide adequate matrix/fibre interfacial bonding and to avoid possible reactions between the silicate glass matrices and the metallic fibres.

Using EPD, the infiltrated metallic fabrics were sufficiently infiltrated with matrix material so as to be used as preforms for the fabrication of metal fibre reinforced ceramic or glass matrix composites. An example of a metallic fibre mat, fully infiltrated by silica sol using EPD, is shown in Fig. 4 [52]. The working voltage was 4 V and deposition time 2 min.

It must be pointed out that the reinforcement of ceramic matrices by continuous ductile elements has not been as much investigated as their ceramic–ceramic counterparts, despite the advantages they may offer. These include an increased resistance to damage during composite processing due to the intrinsic ductility of metallic fibres and the possibility of exploiting their plastic deformation for composite toughness enhancement [55].

Overall, it appears that EPD is a very versatile and cost-effective technique to infiltrate complex fibre architectures, paving the way for the development of ceramic and glass matrix composites with 2D and 3D reinforcement. Moreover, due to the high matrix homogeneity and high relative density achieved in the green bodies by EPD, several authors showed that the required subsequent densification stage can be carried out by pressureless sintering [32,35,40,42,44,51,52,53], avoiding, therefore, the cost-intensive traditional hot-pressing route. Specific experimental information about the EPD fabrication of Ni-coated carbon fibre reinforced alumina matrix composites, a system being developed currently by the authors, is given below. The objective is to describe the processing steps and to show the way for optimisation of the EPD parameters.

### 3. A case in point: Ni-coated carbon fibre reinforced alumina matrix composite

#### 3.1. Description of the EPD experimental procedure

The feasibility of fabricating Ni-coated carbon fibre reinforced alumina matrix composites via a single-infiltration EPD process is considered here, as a typical example of the application of EPD technique in the fabrication of ceramic composites.

A commercially available boehmite ( $\gamma$ - $\text{AlOOH}$ ) sol (Remet corp, USA, Remal A20) having 40 nm average particle size was used as alumina source. The sol contains 20 wt% solids-loading and the boehmite particles are in the lath shape. The as-received boehmite sol was seeded with nanosize (13 nm)  $\delta$ -alumina powder (Aluminium Oxide C, Degussa AG, Germany) containing 0.5 wt%  $\alpha$ -alumina (BDH Chemicals, UK). The seeding powder was first dispersed in distilled water, then the dispersion was added to the boehmite sol while this was stirred magnetically. Finally, the seeded boehmite sol was ball-mixed for 12 h using high purity TZP balls in a plastic container.

Ni-coated carbon fibres (Inco spp, Incofiber™, 12K50, UK) were used as reinforcement. These fibres were in the form of continuous tows of Ni-coated single carbon fibres, with 12,000 tows coated to 50% by weight with nickel. The nickel coating provided excellent conductivity which is essential for EPD, as well as ease of fibre handling and adequate wettability. The tows were unidirectionally aligned in a grooved perspex frame. EPD experiments were carried out under vacuum. Ni-coated carbon fibres held in the frame were used as the deposition electrode (cathode). Two stainless steel plates on either side of the cathode served as the positive (anode) electrodes. After the fibre preform was placed in the sol, the system was vacuum degassed to remove any entrapped air, and then the cell electrodes were connected to a 0–60 V dc power supply. EPD was performed subsequently under constant voltage conditions (5, 10, 15 and 20 V) using varying deposition times (from 50 to 500 s). An electrode separation distance of 15 mm was used in all the experiments. Under the applied electric field, the very fine boehmite particles possessing a net positive surface charge, as determined from the EM data, migrated towards the negative electrode, i.e. the Ni-coated carbon fibre tows. The particles infiltrated the fibre tows and deposited until a sufficient matrix thickness, which enveloped the fibre tows, was achieved. The fibre preform acting as electrode was connected to a balance linked to a computer. The apparatus is able to record the weight gain per milli-second during the deposition process, i.e. in real time. The dimensions of the cathode ( $25 \times 25 \text{ mm}^2$ ) were half the anode's dimensions ( $50 \times 50 \text{ mm}^2$ ) in order to eliminate the 'edge effect' which may give an inhomogeneous thickness from the centre to the edges of the cathode. The EPD-prepared green body specimens containing about 25–30 vol% fibre loading were dried under humidity controlled

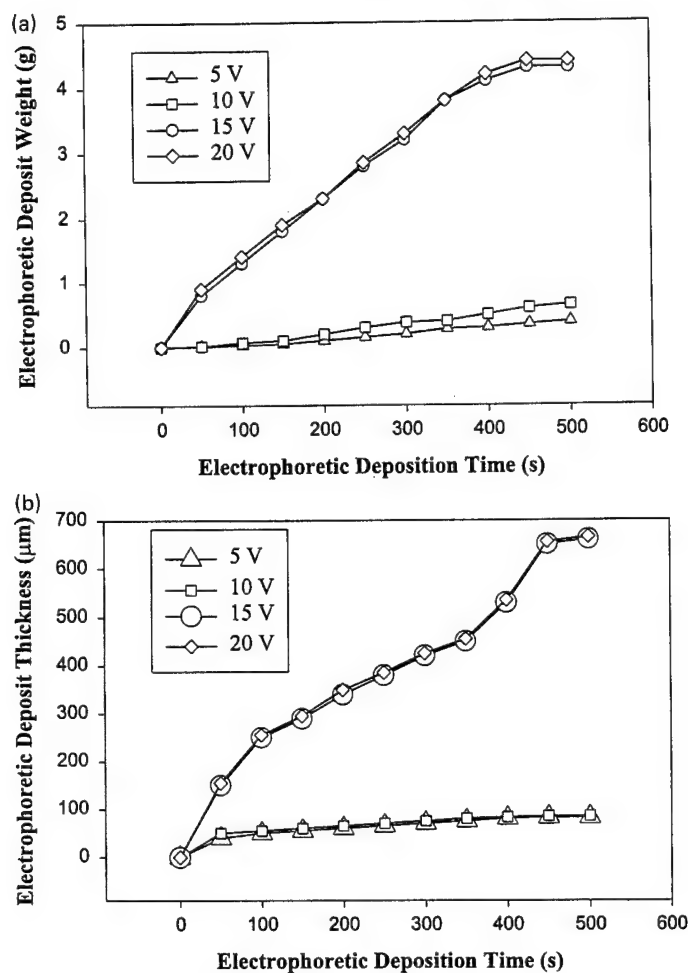


Fig. 5. EPD of boehmite sols on to Ni-coated carbon fibre mats. Graphs of the (a) electrophoretic deposit weight and (b) electrophoretic deposit thickness, as a function of deposition time for different applied voltages.

atmosphere for one day and left in normal air for another day before being pressureless sintered at 1250°C for 2 h under nitrogen atmosphere.

To prepare green and sintered fibre reinforced ceramic–matrix composite (CMC) samples for cross-sectional scanning electron microscopy (SEM), the specimens were placed in a vacuum chamber and vacuum-impregnated with Epofix resin. Impregnated green and sintered CMC samples were left to harden overnight and then cut into slices using a diamond saw. A high resolution scanning electron microscope (Field Emission Gun, FEG SEM, Hitachi S-4000, Japan) was employed to characterise the various microstructural features of the infiltrated and sintered composite bodies, including grain shape and size, porosity distribution and location, ductile interface, deposit thickness and infiltration of the matrix into the fibre architecture in both green and sintered samples.

### 3.2. Evaluation of EPD experiments

The boehmite sol used was kinetically stable and well dispersed, as there were no big heteroflocculated

agglomerates within the suspension. EPD experiments were carried out under vacuum in order to eliminate the undesirable formation and entrapment of bubbles within the deposit due to the electrolysis (evolution of gases) of the aqueous sol dispersion medium. Under vacuum, very fine boehmite particles can penetrate deep into the inter/intra-fibre tows, filling all the voids, resulting in the formation of high-quality, dense green (and sintered) composites.

The graphs in Fig. 5(a) and (b) show the results of electrophoretic deposit weight and thickness, respectively, as a function of deposition time for different applied voltages. EPD experiments were performed for up to 500 s, as this gave a deposit thickness of about 660 μm which was enough to produce a composite with an acceptable green density. The deposit thickness increased with increasing deposition time. When aqueous-based sols are used in EPD experiments, one associated problem is the electrolysis of the water. Higher voltages resulted in rapid deposit formation, but also in the undesirable formation and entrapment of bubbles within the deposit due to the electrolysis



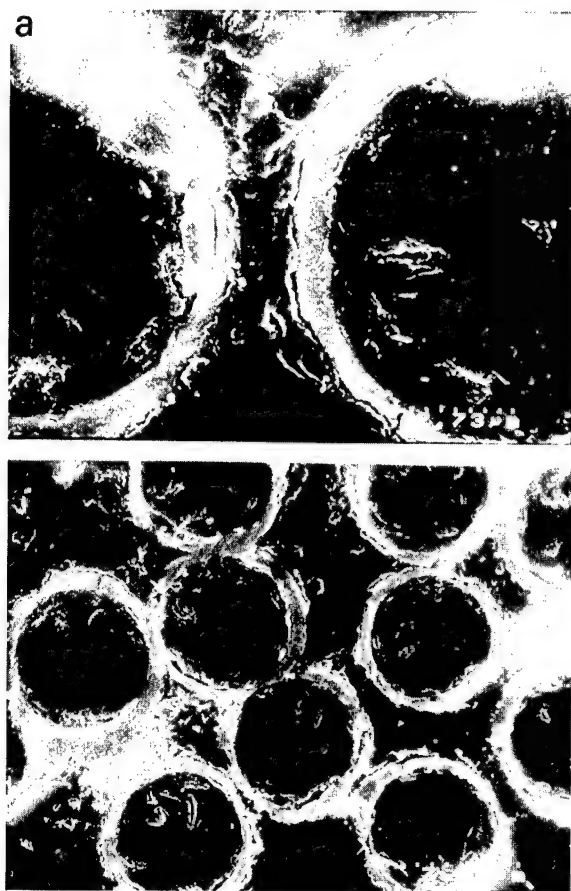


Fig. 6. SEM micrographs of EPD-infiltrated unsintered Ni-coated carbon fibre reinforced alumina matrix composite containing 30 vol% fibre loading. The fibre preform was infiltrated using an applied voltage of 15 V for 400 s. Both (a) high and (b) low magnification micrographs show that the Ni-coated carbon fibre preform was fully infiltrated with the boehmite sol. Even regions where the Ni-coated fibres were nearly touching each other have been fully impregnated by the nanosize boehmite particles, leading to high-quality green bodies.

of the aqueous sol dispersion medium, while low voltages reduced the electrolysis, but they also needed higher deposition times. Thus, a compromise had to be found and voltage and deposition time were optimised. Voltages higher than 20 V were not used. The thickness of selected electrophoretic deposits, measured from the fibre surface, is plotted against the deposition time for different voltages in Fig. 5(b). The formation of the deposit was very rapid in the first 150 s and then increased steadily.

In situ (real time) deposit weight measurements provided very reliable data to determine accurately the deposition rate. The rate of deposition was very high at the beginning (up to 150 s), and then it started to decrease with increasing deposition time. The decrease in deposition rate was attributed to the increase in the resistance of the deposit, as the current diminishes due to the increase in deposit thickness and the removal of charged boehmite particles from the sol. As a result of the decrease in the potential drop across the suspension,

the velocity and deposition rate of the charged colloidal boehmite particles also decreased.

EPD parameters were optimised in order to achieve fully infiltrated Ni-coated carbon fibre reinforced alumina composites with the minimum amount of excess material being present in the outer regions of the preform. The optimum deposition voltage and time were determined as 15 V and 400 s, respectively, for full infiltration. The full infiltration resulted in an EPD deposit thickness of  $>650\text{ }\mu\text{m}$ . Using these parameters, it was possible to produce fully infiltrated mats with only a thin ( $100\text{ }\mu\text{m}$ ) excess layer. This was beneficial as the fibre mats then have a reduced propensity to form large cracks during the drying stage. This cracking is due to the differential shrinkage of the gel network which generates tensile stresses at the surface of the deposits, as mentioned above (see Fig. 3).

The SEM pictures shown in Fig. 6 represent the green microstructures of composites produced under optimised EPD parameters. Fig. 6(a) shows an SEM micrograph of an EPD-formed green body containing 30 vol% fibre loading. High green densities (about 61% of theoretical density) were achieved at 15 V for 400 s. Green density was measured by dividing the mass of the sample by its geometrically determined volume. It can also be seen in Fig. 6(b) that the Ni-coated carbon fibre preform was fully infiltrated with the boehmite sol. Even in regions where the Ni-coated fibres were nearly touching each other, full impregnation was achieved by the nanosize boehmite powders in a very short time, i.e. 400 s, leading to high-quality green bodies. The effectiveness of the EPD providing full deposition between two fibres with a separation of 400–500 nm is clearly visible in Fig. 6(b). It must be noted that these green samples were not polished in order to avoid damaging the ductile Ni interface. Thus, some cutting effects are visible on the carbon fibres and the matrix, which resulted from the contact with the diamond saw during the very slow-speed cutting operation.

The subsequent composite preparation involved pressureless sintering of the green bodies at  $1250^{\circ}\text{C}$  for 2 h under  $\text{N}_2$  atmosphere. A fully infiltrated and dense sintered microstructure is shown in Fig. 7. Sintered densities of about 91% of theoretical density were measured by using the Archimedes technique. This result confirms that the electrophoretic processing approach is very convenient in terms of obtaining dense samples at relatively low sintering temperatures and avoiding the cost-intensive hot-pressing procedure, which has been the common practice for the fabrication of fibre reinforced ceramic matrix composites so far.

#### 4. Conclusions

A literature review on the application of the EPD technique in the fabrication of fibre reinforced ceramic and glass matrix composites was carried out. Since the first studies



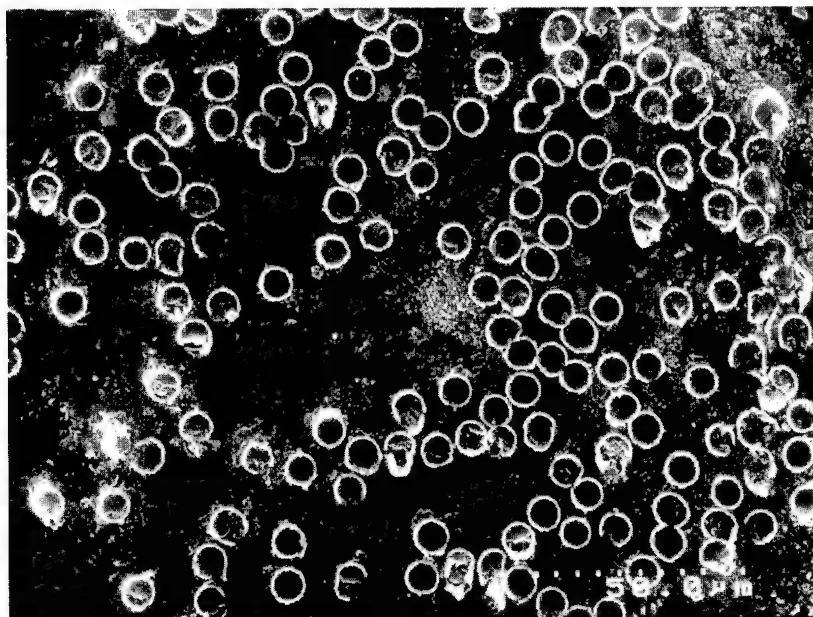


Fig. 7. SEM micrograph of vacuum EPD-infiltrated Ni-coated carbon fibre reinforced alumina matrix composite containing 30 vol% fibre loading after sintering at 1250°C for 2 h in nitrogen atmosphere. The micrograph shows the full deposition of the boehmite matrix into the fibre preform and a dense composite microstructure after sintering.

published at the beginning of the 1990s, a variety of fibre/matrix composite systems have been fabricated by EPD. Carbon, SiC (Nicalon®), alumina (Almax®) and aluminosilicate (mullite) (Nextel®) woven fibre preforms have been used, mainly with silica, alumina, mullite, borosilicate glass and SiC matrices. Overall, the analysis of the published data demonstrates that EPD, being simple and inexpensive, provides an attractive alternative for ceramic infiltration and coating of fibre fabrics, even if they exhibit tight fibre weave architectures. The high-quality infiltrated fibre mats are adequate prepreps for the fabrication of advanced glass and ceramic matrix composites for use in heat-resistant, structural components.

The parameters of the EPD infiltration process, i.e. applied voltage and deposition time, can be optimised to obtain a high solids-loading in the intra-tow regions and a firm, adherent ceramic deposit. This was shown in this paper specifically for a model Ni-coated carbon fibre reinforced alumina matrix composite.

### Acknowledgements

Helpful discussions with colleagues at the University of Birmingham, UK (Dr P. Trusty, Dr C.B. Ponton), and at the Technical University of Ilmenau (Mr U. Schindler, Dr H.G. Krüger, Prof. H. Kern) are appreciated.

### References

- [1] Chawla KK. Ceramic matrix composites. London: Chapman and Hall, 1993.
- [2] Liaw PK. Fiber reinforced CMCs: processing, mechanical behaviour and modelling. *JOM* 1995;47(7):38–44.
- [3] Davidson DL. Ceramic matrix composites fatigue and fracture. *JOM* 1995;47(7):46–52.
- [4] Illston TJ, Ponton CB, Marquis PM, Butler EG. The manufacture of woven fibre ceramic matrix composites using electrophoretic deposition. In: Duran P, Fernandez JF, editors. *Third Euroceramics vol. 1*, Madrid, Spain. Faenza Editrice Iberica, 1993. p. 419–24.
- [5] Ko FK. Preform fibre architecture for ceramic–matrix composites. *Am Ceram Soc Bull* 1989;68:401–14.
- [6] Chawla KK. *Fibrous materials*. Cambridge: Cambridge University Press, 1998.
- [7] Illston TJ, Doleman PA, Butler EG, Marquis PM, Ponton CB, Gilbert MJ et al. UK Patent no. 9124816.1, November 1991.
- [8] Brown DR, Salt FW. The mechanism of electrophoretic deposition. *J Appl Chem* 1965;15:40–48.
- [9] Hampel CA, editor. *The Encyclopedia of Electrochemistry* New York: Reinhold Publishing Corp., 1964. p. 540 (Reuss, 1807: see ‘Electrophoresis’).
- [10] Sarkar P, Nicholson PS. Electrophoretic deposition (EPD): mechanisms, kinetics and application to ceramics. *J Am Ceram Soc* 1996;79:1987–2002.
- [11] Gani MSJ. Electrophoretic deposition. a review. *Ind Ceram* 1994; 14(4):163–74.
- [12] Gutierrez CP, Mosley JR, Wallace TC. Electrophoretic deposition: a versatile coating method. *J Electrochem Soc* 1962;109(10):923–7.
- [13] Haber S, Gal-Or L. Deep electrophoretic penetration and deposition of ceramic particles inside porous substrates, I. Analytical Model. *J Electrochem Soc* 1992;139(4):1071–8.
- [14] Haber S, Gal-Or L. Deep electrophoretic penetration and deposition of ceramic particles inside porous substrates, II. Experimental Model. *J Electrochem Soc* 1992;139(4):1078–81.
- [15] Haber S. Deep electrophoretic penetration and deposition of ceramic particles inside impermeable porous substrates. *J Colloid Interface Sci* 1996;179:380–90.
- [16] Jean J-H. Electrophoretic deposition of Al<sub>2</sub>O<sub>3</sub>–SiC composite. *Mater Chem Phys* 1995;40:285–90.
- [17] Zhang Z, Huang Y, Jiang Z. Electrophoretic deposition forming of

- SiC–TZP composites in a nonaqueous sol media. *J Am Ceram Soc* 1994;77(7):1946–9.
- [18] Sarkar P, Haung X, Nicholson PS. Structural ceramic microlaminates by electrophoretic deposition. *J Am Ceram Soc* 1992;75(10):2907–9.
  - [19] Vandeperre L, Van der Biest O. Electrophoretic forming of silicon carbide laminates with graphite interfaces. In: Galassi C, editor. *Fourth Euroceramics*, vol. 1, Faenza, Italy. Gruppo Editoriale Faenza Editrice, 1995. p. 359–66.
  - [20] Fischer R, Fischer E, De Portu G, Roncari E. Preparation of ceramic micro-laminate by electrophoresis in aqueous system. *J Mater Sci Lett* 1995;14:25–7.
  - [21] Yamashita K, Nagai M, Umegaki T. Fabrication of green films of single- and multi-component ceramic composites by electrophoretic deposition technique. *J Mater Sci* 1997;32:6661–4.
  - [22] Sarkar P, Datta S, Nicholson PS. Electrophoretic deposition of controlled ceramic microstructures. *Ceram Trans* 1997;85:231–50.
  - [23] Sarkar P, Datta S, Nicholson PS. Functionally graded ceramic/ceramic and metal/ceramic composites by electrophoretic deposition. *Compos Part B* 1997;28B:49–56.
  - [24] Sarkar P, Sagakuchi S, Yonehara E, Hamagami J, Yamashita K, Umegaki T. Electrophoretic forming of functionally-graded barium/strontium titanate ceramics. In: Shiota I, Miyamoto MY, editors. *Functionally graded materials*, 1996. Amsterdam: Elsevier, 1997. p. 221–6.
  - [25] Wan YZ, Wang YL, Li GJ, Luo HL, Cheng GX. Carbon fibre felt electrodeposited by copper and its composites. *J Mater Sci Lett* 1997;16:1561–3.
  - [26] Devrajan J, Singh RN. Electrochemical processing of metal matrix composites. *Ceram Trans* 1993;38:115–25.
  - [27] Kooner S, Campaniello J, Pickering S, Bullock E. Fibre reinforced ceramic matrix composite fabrication by electrophoretic infiltration. *Ceram Trans* 1995;58:155–60.
  - [28] Kawai C, Wakamatsu S. Fabrication of C/SiC composites by an electrodeposition/sintering method and the control of the properties. *J Mater Sci* 1996;31:2165–70.
  - [29] Zhitomirsky I. Electrophoretic and electrolytic deposition of ceramic coatings on carbon fibres. *J Eur Ceram Soc* 1998;18:849–56.
  - [30] Zhitomirsky I. Electrophoretic hydroxyapatite coatings and fibres. *Mater Lett* 2000;42:262–71.
  - [31] Boccaccini AR, Schindler U, Krueger HG. Ceramic coatings on carbon and metallic fibres by electrophoretic deposition (submitted for publication).
  - [32] Kaya C, Boccaccini AR, Chawla KK. Electrophoretic deposition forming of Ni-coated carbon fiber-reinforced borosilicate glass matrix composites. *J Am Ceram Soc* 2000;83:1885–8.
  - [33] Illston TJ, Ponton CB, Marquis PM, Butler EG. Electrophoretic deposition of silica/alumina colloids for the manufacture of CMCs. *Ceram Engng Sci Proc* 1994;14:1052–9.
  - [34] Boccaccini AR, Ponton CB. Processing ceramic–matrix composites using electrophoretic deposition. *JOM* 1995;47(7):34–7.
  - [35] Trusty PA, Boccaccini AR, Butler EG, Ponton CB. Novel techniques for manufacturing woven fiber reinforced ceramic matrix composites. I Preform fabrication. *Mater and Manuf Processes* 1995;10:1215–26.
  - [36] Brown PW. Electrophoretic deposition of mullite in a continuous fashion utilising non-aqueous polymeric sols. *Ceram Engng Sci Proc* 1995;15.
  - [37] Ohkawa T, Elsner FH. Fabrication of fiber-reinforced composites. US Patent no. 5468358, 21 November 1995.
  - [38] Boccaccini AR, MacLaren I, Lewis MH, Ponton CB. Electrophoretic deposition infiltration of 2-D woven SiC fibre mats with mixed sols of mullite composition. *J Eur Ceram Soc* 1997;17:1545–50.
  - [39] Streckert HH, Norton KP, Katz JD, Freim JO. Microwave densification of electrophoretically infiltrated silicon carbide composite. *J Mater Sci* 1997;32:6429–33.
  - [40] Trusty PA, Ponton CB, Boccaccini AR. Fabrication of woven Nicalon® (NL 607) SiC fibre–yttrium disilicate CMCs using electrophoretic deposition. *Ceram Trans* 1998;83:391–8.
  - [41] Trusty PA, Illston TJ, Butler EG, Marquis PM, Ponton CB. 5. A comparison of the processing conditions for the fabrication of SiC/SiO<sub>2</sub> and Al<sub>2</sub>O<sub>3</sub>/Al<sub>2</sub>O<sub>3</sub> woven fibre reinforced composites, *Adv. Synthesis and Processing of Composites and Adv. Ceramics*, vol. 1. Ohio: The American Ceramic Society, 1995 (p. 257–62).
  - [42] Trusty PA, Boccaccini AR, Butler EG, Ponton CB. The development of mullite matrix ceramic fiber composites using electrophoretic deposition. *Ceram Trans* 1996;78:63–70.
  - [43] Kaya C, Trusty PA, Ponton CB. Electrophoretic filtration deposition (EFD) of Saffil alumina fibre-reinforced mullite multilayer nanoceramic matrix composites. *Ceram Trans* 1998;83:399–406.
  - [44] Kooner S, Westby WS, Watson CMA, Farries PM. Processing of Nextel® (720/mullite composition composite using electrophoretic deposition. *J Eur Ceram Soc* 2000;20:631–8.
  - [45] Kaya C, Gu X, Al-Dawery I, Butler EG. Processing of woven mullite fibre–mullite ceramic matrix composites using electrophoretic deposition (submitted for publication).
  - [46] Moreno R, Ferrari B. Advanced ceramics via EPD of aqueous slurries. *Ceram Bull* 2000;79(1):44–8.
  - [47] Clasen R. Forming compacts of submicron silica particles by electrophoretic deposition. In: Hausner H, Messing GL, Hirano S, editors. *Ceramic powder processing science*. Cologne, Germany: Dt. Keramische Gesellschaft, 1989. p. 633–40.
  - [48] Boccaccini AR, Trusty PA, Taplin DMR, Ponton CB. Colloidal processing of a mullite matrix material suitable for infiltrating woven fibre preforms using electrophoretic deposition. *J Eur Ceram Soc* 1996;16:1319–27.
  - [49] Kaya C, Trusty PA, Ponton CB. Preparation of heterocoagulated colloidal suspensions for fabrication of ceramic matrix composites by electrophoretic filtration deposition. *Br Ceram Trans* 1998;97(2):48–54.
  - [50] Brinker CJ, Scherer GW. *Sol–gel science*. New York: Academic Press, 1990.
  - [51] Boccaccini AR, Trusty PA. Electrophoretic deposition infiltration of metallic fabrics with a boehmite sol for the preparation of ductile-toughened ceramic composites. *J Mater Sci* 1998;33:933–8.
  - [52] Kaya C, Boccaccini AR, Trusty PA. Processing and characterisation of 2-D woven metal fibre-reinforced multilayer silica matrix composites using electrophoretic deposition and pressure filtration. *J Eur Ceram Soc* 1999;19:2859–66.
  - [53] Boccaccini AR, Ovenstone J, Trusty PA. Fabrication of woven metal fibre reinforced glass matrix composites. *Appl Compos Mater* 1997;4:145–55.
  - [54] Trusty PA, Boccaccini AR. Alternative uses of waste glasses: fabrication of metal fibre reinforced glass matrix composites. *Appl Compos Mater* 1998;5:207–22.
  - [55] Donald IW, Metcalfe BL. The preparation, properties and applications of some glass-coated metal filaments prepared by the Taylor-wire process. *J Mater Sci* 1996;31:1139–49.

# Fabrication of high-temperature resistant oxide ceramic matrix composites

I.A.H. Al-Dawery\*, E.G. Butler

*Ceramic Matrix Composites Group, Interdisciplinary Research Centre (IRC) in Materials for High Performance Applications, The University of Birmingham, Edgbaston, Birmingham B15 2TT, UK*

## Abstract

The main objectives of this work are to develop and apply new ceramic matrix materials by which a relatively high level of densification of the final composite may be achieved by pressureless-sintering at temperatures close to 1200°C. A cost-effective processing method for the production of oxide/oxide CMCs materials and components has been achieved.

A range of interphase materials is applied to Nextel™ 720 fibres. These include zirconia, neodymium and lanthanum phosphate. A combination of ZrO<sub>2</sub> and the AKP50 alumina powder have been selected as the successful candidates for the interphase and the matrix material, respectively. Work has been conducted on the preparation of slurry systems consisting of these two materials. The prime target was to establish the possibility of achieving good coating around the bulk of the fibres together with a high level of impregnation with the matrix material. Furthermore, the pressure infiltration technique has been applied and as a result composite samples with fibre volume content of 40%, and remaining porosity of around 20 vol% have been routinely produced. Composite room and high-temperature tensile strengths of around 200 MPa have been accomplished. © 2001 Published by Elsevier Science Ltd.

**Keywords:** A. Ceramic matrix composites (CMCs); Nextel™ 720

## 1. Introduction

Continuous fibre reinforced ceramic matrix composites (CMCs) with suitable interfaces can exhibit inelastic deformation behaviour, which enable these materials to retain strength in the presence of holes and notches. This damage tolerance, coupled with their inherent refractoriness, has enabled CMCs to emerge as successful candidates for many high-temperature thermostructural high performance applications [1]. Careful microstructural design has been defined as a key factor in the development of oxide/oxide CMCs. The majority of these developments have been based upon a selection of a weak interface concept, using stable oxide interphases with suitably low fracture toughness [2,3]. Furthermore, sintering kinetics suggests adequate microstructural stability for applications such as in the gas turbine engine, where initial target wall temperatures are in the range of 1100–1200°C. Here there is a processing challenge. Most matrices require sintering temperatures of or above 1200°C to achieve sufficient bonding between matrix particles. However, most commercial oxide fibres are susceptible to microstructural degradation at these temperatures [4]. High

purity ultra fine alumina offers the advantage of being sintered readily at temperature above 800°C [5]. Thus, composite materials can be processed at temperatures that minimise fibre degradation.

It is very essential during the fabrication stages that the intrinsic strength of the fibres is retained as far as possible and that the matrix material is able to translate efficiently the fibre properties into composite strength and stiffness. Normally, the reinforcement material (Nextel™ 720 fibres, 3M, USA) is first coated with a low debond energy interphase (typically using ZrO<sub>2</sub> sol). This would be followed by a second stage of incorporating the matrix material using pressure infiltration techniques. Eventually green composites are densified by pressureless sintering at 1200°C for 4 h. The method of matrix infiltration using aqueous sols and slurries is an extremely demanding challenge. Here there are two issues. The first one is that when fibre mats are coated with the ZrO<sub>2</sub> interphase a web-type solid structure, covering most voids within the fibre mats, is formed. Such formation will act as a barrier towards incoming sols and slurries aiming at filling the much bigger voids within fibre tows. As a result of this, incomplete infiltration with the matrix slurry cannot be avoided. It was therefore decided to conduct experiments through which the interphase sol and the matrix slurry were both applied in one simple and single stage. Composite samples were later made using the above approach.

\* Corresponding author. Tel.: +44-121-414-3449; fax: +44-121-414-3441.

E-mail address: i.aldawery@bham.ac.uk (I.A.H. Al-Dawery).

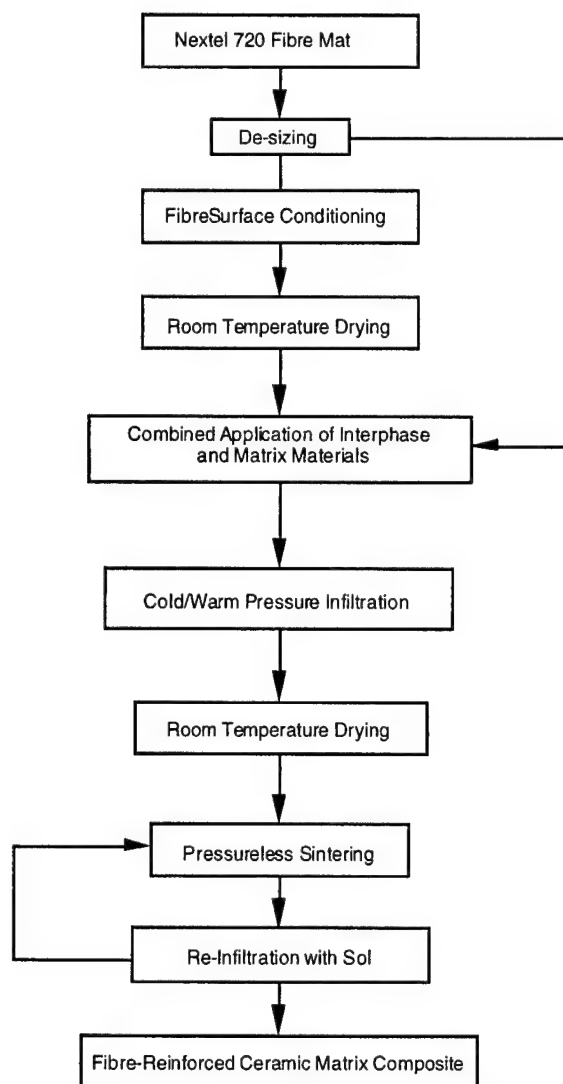


Fig. 1. Flow chart for processing oxide/oxide fibre-reinforced ceramic matrix composite.

## 2. Experimental

### 2.1. Fibre conditioning

Experimental procedures applied for processing CMCs are illustrated in Fig. 1. Organic sizing on the Nextel™ 720 fibre mats was removed by heating, in static air atmosphere, to a temperature of 600°C for 2 h. During this process, the colour of the fibres changes from light green to dark and finally to a light cream-like colour. The above conditions were found to be beneficial to allow even and sufficient de-sizing over relatively large areas of fibre mats.

### 2.2. Processing and application of zirconia interphases

The first work on interphase coating begun by using a commercially available type VP zirconia powder (Degussa Ltd). This is a hydrophilic powder with an average particle

size of 30 nm. Aqueous sols containing this powder were prepared. Sols with different solid loading were prepared and investigated. These include sols with 10, 15 and 20 wt% ZrO<sub>2</sub> powder.

As an alternative, zirconia sol was also prepared in-house using hydrothermal synthesis. The process was carried out in the medium size autoclave. 750 ml of zirconium acetate solution was placed in the autoclave, where a temperature of 220°C was reached. After 2 h of reaction, taking place at this temperature, a white slurry (zirconium oxide and acetic acid) was produced. The following step was to dry the slurry in an oven. A white powder, consisting of zirconium oxide and residual zirconium acetate, was then obtained. Calcination was carried out at 600°C for 4 h. The resultant zirconium powder was then ball milled in water.

Initial coating experiments were carried out using a method previously developed at the IRC/Birmingham University for coating Almax™ woven fabric [6]. The process begins with conditioning of fibres surfaces by immersing the fibre mat in an ammonia based surfactant with a concentration of 1.5% and a pH of 11.5. The fibre mat was left in surfactant over night and then it was dried in air. To ensure removal of entrapped air, treated fibre mats were degassed under vacuum. They were then immersed in the interphase sol. This was followed by degassing in an ultrasonic bath. Afterwards, octanol was added on the top surface of the sol. Fibre mats were then pulled out of the sol/octanol. The octanol removes excess sol from the fibre tow to prevent bridging between fibres. Finally, interphase coated fibre mats were left to dry at room temperature in air, before being fired at 700°C for 1 h.

At a later stage, an interphase coating process has been conducted using a simple dip coating technique, without pre-conditioning the fibre mats. After dipping in the sol, the fibre mat is left under vacuum for 20 min to ensure the removal of the entrapped air within the fibre mat and hence increasing the chance of the sol material to fully surround the bulk of the fibres. The coated fibre mat is then subjected to a room temperature drying over night.

### 2.3. Vacuum-assisted impregnation of fibre tows with ceramic sols

Electrophoretic deposition (EPD) process was introduced with the aim of ensuring the existence of sufficient matrix-like material filling the voids within fibre tows [7]. At a later stage, comprehensive investigation on the whole process has shown that the process was ineffective when processing large-sized samples and that densification should take place by hot-pressing [8]. Thus, an alternative process has been developed here. Simple vacuum impregnation of fibre mats with sols containing mullite composition and other suitable materials was found to be the best alternative approach to achieve full fibre-tow infiltration. The sols used here contain nano-metre sized particles. The dipping process was assisted by considerably high vacuum levels for 30 min.

#### 2.4. Processing of CMCs using pressure infiltration

Initial work involved fabrication of flat discs with a diameter of 70 mm. Progressively, the process has been adapted so that flat plates of any shape can be processed. The amounts of reinforcement material and matrix were carefully calculated so that the final thickness of the sintered composites is around 3.0 mm.

Slurries for pressure infiltration were initially prepared from alumina powders mixed with a silica sol so that the final slurry would have the composition of mullite ( $3\text{Al}_2\text{O}_3:2\text{SiO}_2$ ). Later on, mullite powder (Keith Ceramic Materials Ltd), with a mean particle size less than  $10\text{ }\mu\text{m}$  was dispersed in water and used as the matrix material. Different concentrations were used. This involved preparation of slurries with solid loading of 40 vol%. Investigation on decreasing matrix cracking over drying has led to the introduction of bi-modal systems which contain two different particle sizes of mullite powders. For this, a combination of mullite KCM 73 powder (Keith Ceramic Materials,  $10\text{ }\mu\text{m}$ ) and mullite SASM powder (Baikoski Chimie, France) with a mean particle size of  $0.70\text{ }\mu\text{m}$  has been used as the source of the matrix material.

Pressure infiltration experiments were conducted using a cylindrical die. Fibre preforms were prepared by dipping 70 mm diameter Nextel™720 fabric into a matrix slurry and laminating them within the die. A filter paper and porous stainless steel filtering plate were placed on the upper surface of the preform. The die assembly is placed within a Instron load frame model 1195 with a maximum capability of 100 kN. The pressure level was varied from 5 to 13 MPa (20–50 kN). The cross head speed was  $0.5\text{ mm/min}$ . Once the pressure reaches its required level it undergoes a cycling process. During cycling ( $\pm 5\%$  of applied load) excess liquid within the preform is removed through the porous filter plate. Upon completion of the filtration process, samples were removed from the die and then they were subjected to a room temperature drying. More details on the pressure infiltration process have been given in Ref. [9].

#### 2.5. Combined application of interphase and matrix materials

For the application of the interphase and the matrix materials in a single stage, several systems have been assessed in order to establish the best parameters through which the whole process can be put under control. For this purpose, high purity ( $>99.99$ ) and fine ( $0.1\text{--}0.3\text{ }\mu\text{m}$ ) alpha alumina powder type AKP50 (Mandoval Ltd, UK) has been investigated. This type of alumina is manufactured by hydrolysis of aluminium alkoxide. Since the  $\text{ZrO}_2$  system and the AKP50 alumina powder have been selected as the successful candidates for the interphase and the matrix material, respectively, work has been conducted on the preparation of slurries containing a mixture of both interphase and

matrix materials. The prime target was to establish the possibility of achieving good coating around the bulk of the fibres together with a high level of impregnation with the matrix material. Nextel™720 fibre reinforced composite samples were produced using combinations of interphase and matrix materials as the slurries and the pressure infiltration process was applied to consolidate green samples. The total solid loading of the final slurry was kept to the 40 vol% constant level.

Efforts have been made to investigate the best starting materials for the matrix slurries that lead to a successful fabrication of crack-free composite samples after both the drying and sintering stages. The best solution for the above challenge was found through the usage of a combination of a large and a small particle sized mullite powders. This combination system is known as a bi-modal system. It has been reported, for some composites, that to achieve maximum properties, that are required by most applications, the composite must be designed to have a reinforcement material with a volume fraction of typically 29–55% [10]. In this work, composites were fabricated with a 40% as the fibre volume fraction. This figure is applied to any given thickness of the final composite. Early pressure infiltrated and sintered composite samples were found to have a fibre volume fraction of only 30%, leading to samples with poor properties.

One of the challenges in processing CMCs is that the sintering temperature is limited to a maximum level of  $1200^\circ\text{C}$ . This is due to the fact that Nextel™720 fibres start to lose their strength at temperatures above that limit. Unfortunately, at  $1200^\circ\text{C}$  matrix materials consisting mainly of a mullite composition are difficult to sinter without application of pressure. No matter what precautions one has taken and no matter how well packed the matrix material is, if the matrix is not sintering well, appreciable properties of the final composite cannot be achieved unless materials with relatively low sintering temperature are used.

#### 2.6. Densification process

Densification of CMCs samples was carried out via pressureless sintering in static air atmosphere. Sintering was performed at  $1200^\circ\text{C}$  for 4 h, with a heating rate of  $300^\circ\text{C/h}$  and a cooling rate of  $600^\circ\text{C/h}$ . Samples were placed flat inside the furnace chamber. These conditions were carried out for our standard sintering process. In the case where re-infiltration cycles were applied, similar conditions for heat treatment were used.

#### 2.7. Sample microstructural characterisation

This mainly involves scanning electron microscopy (SEM) analysis of the prepared samples. SEM characterisation was carried out using JEOL WINSEM type JSM-6300 SEM. Thus, as received fibre mats, interphase coated fibre mats, vacuum impregnated fibre mats, and composite samples



were prepared for this analysis by vacuum impregnation of the sample with epoxy resin. This was followed by typical polishing used for any ceramic material. Fractured surfaces of composite samples were also characterised using SEM analysis.

### 2.8. Composite mechanical characterisation

Bar-shaped samples were machined for a three-point flexural test. The length of the samples was 60 mm. The test was conducted using an Instron type 4467 computer controlled machine. Furthermore, samples were also machined for room and high-temperature tensile strength analysis. The length of these samples was 120–200 mm with a width of 8–10 mm. The thickness of these samples was 2.5–3.0 mm. Tests were conducted with a strain rate of 0.5 mm/min, and the maximum testing temperature was 1150°C. Metal end-tabs were introduced to both ends of the bar-shaped samples. The test was conducted using a Zwick type 1484 computer controlled tensile machine. Tensile strengths of composite samples were later calculated.

## 3. Results and discussion

It is important to mention that the manufacturing sequence has been shown to strongly affect the properties of the final composite. Not to forget the essential role of the densification process. The whole of the sintering process, in particular the sintering temperatures for green composite samples and those for reinfiltrated components, was reviewed. Mullite emerged as an attractive matrix material, owing to its excellent creep resistance, low modulus and an adequate microstructural stability in the temperature range 1000–1200°C. However, the sluggish sintering kinetics presents a challenge in processing. That is, temperatures above 1300°C are required to achieve the required bonding between the matrix particles, yet the currently used Nextel™ 720 fibres are susceptible to microstructural degradation at these temperatures. Ideally, neck formation with minimal shrinkage should be promoted by operating in regimes dominated by surface and vapour transport mechanisms. However, this approach cannot provide the requisite strengths. Liquid precursor impregnation and pyrolysis provide another avenue to build the inter-particle necks, but the initial matrix must have sufficient strength to withstand handling. In this work, the main element of the matrix is the AKP50 type alumina powder, and the impregnation sources (secondary elements of the matrix) are diluted sols of alumina, boehmite and zirconia.

The sintering regime was selected as in the following:

1. 1200°C as the temperature for the initial heat treatment of infiltrated green samples. This is a matrix bonding treatment.
2. 1200°C as the pyrolysis temperature for heat treating reinfiltrated samples.

3. 1200°C as the sintering temperature of the final composite.

After the initial heat treatment at 1200°C for 4 h, samples were subjected to a total of five vacuum-assisted reinfiltration cycles. Sols of alumina AKP50, Condea Dispersal boehmite solution and  $\text{ZrO}_2$ , with 20 wt% solid loading, were used as the reinfiltrating materials. After each cycle, samples were heat treated under the conditions mentioned above. As for the last stage, samples were subjected to a final sintering at 1200°C for 4 h.

Results have indicated that the best and the highest levels of room temperature tensile strength for Nextel™ 720 fibre reinforced composites was 194 MPa. This figure was achieved for those samples processed with the application of the zirconia interphase and alumina matrix materials together in a single step. Furthermore, high-temperature tensile strength tests conducted at 1150°C revealed a strength level of 180 MPa. These values were obtained for composite samples processed at a temperature of 1200°C.

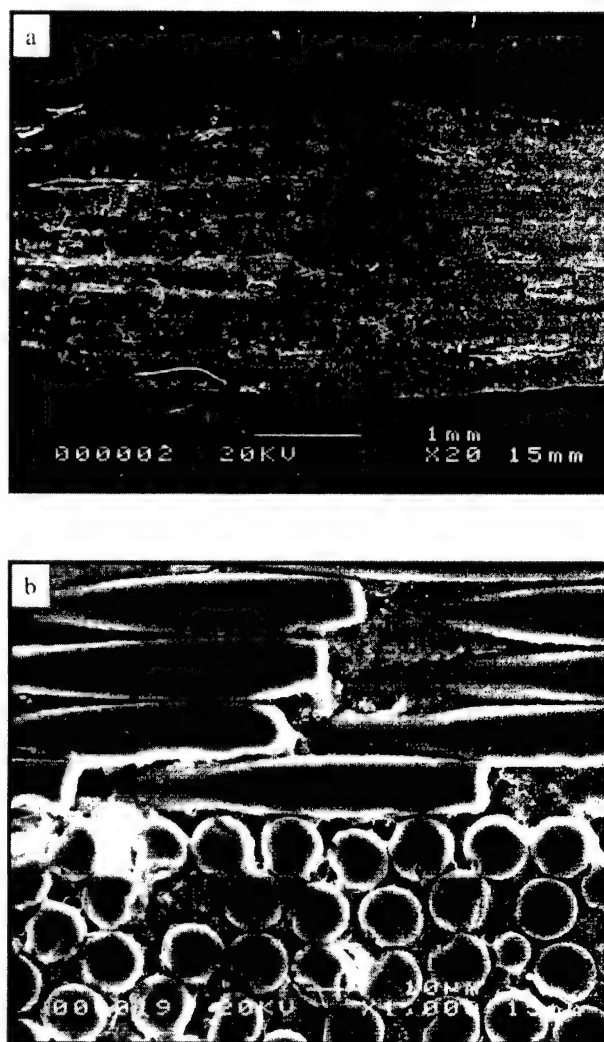


Fig. 2. SEM micrographs of: (a) low; and (b) high magnification images of a polished surface of a composite showing a high level of matrix infiltration.



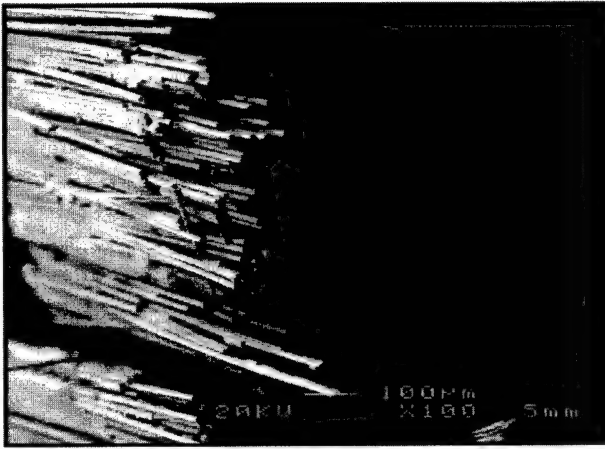


Fig. 3. SEM micrograph of a fractured surface of a standard composite. A high level of fibre pull-out is seen.

This is a significant achievement in the sense that Nextel™720 reinforced composites can still maintain a considerable level of tensile strength at such a high-temperature. It is very important to mention that the above findings can only be achieved when using zirconia as the interphase material. On the other hand preliminary studies using  $\text{NdPO}_4$  coating showed considerable damage to the fibres strength after undergoing a heat treatment at  $1200^\circ\text{C}$ , with an average of 30 MPa for the tensile strength [11]. This degradation in the tensile properties of the fibres was attributed to a possible chemical reaction between the fibres mullite composition and the deposited  $\text{NdPO}_4$  due to the acidic nature of the precursor solutions [11]. Thus, based on these results, it was decided that  $\text{ZrO}_2$  sols are the only and most suitable and stable interphase material for processing composite samples reinforced with Nextel™720 fibres.

With respect to our work on the combined application of the zirconia interphase and the alumina matrix in a single step, it was found that although near to full fibre-tow infiltration was achieved (see Fig. 2), it was difficult to establish a visible coating around the bulk of the fibres. This is due to the fact that it is possible that the thickness of the deposited coating is so small, in a nanometer scale, that it cannot be detected by SEM. However, in one way or another the existence of a zirconia solution in the alumina matrix seems to have played a role, since high strengths were only obtained for those samples fabricated with this combination. Indeed, tensile test of these composites has resulted in samples failing in a composite behaviour with a high level of fibre

pressureless-sintering, as can be seen in Fig. 3. This behaviour supports the claim of the existence of a zirconia interface that separates the fibres from the matrix material, leading to high level of fibres debonding. Composites processed with the zirconia–alumina system, as mentioned in this paper, have been found to exhibit damage tolerant mechanical properties. This is a very essential phenomenon for the development of composite components for high-temperature high performance applications.

Two important factors affecting properties of the final composite have been identified. These are processing temperature and matrix. The ultimate performance of composites processed using Nextel™720 fibres will depend on the processing temperature or on the matrix properties or on a combination of both. The temperature effect is the degradation of fibres strength as the temperature increases. The matrix effect, on the other hand, is possible chemical reactions between fibres and matrix materials. To investigate both parameters, two sets of experimental work were designed. Details of these sets and corresponding results are shown in Table 1. Results showed that there is no significant effect of matrix materials on the strength of composite samples processed at  $1200^\circ\text{C}$ . Whereas strength of the resin composite made with fibres preheated to  $1200^\circ\text{C}$  was 206 MPa, a room temperature tensile strength of 194 MPa was recorded for a ceramic composite processed at the same temperature. These results clearly indicate that: (1) there is no negative effect of the matrix materials on the final strength of the composite; and (2) only processing temperature have a significant effect on the mechanical strength.

#### 4. Conclusions

The above findings confirm that the combination of both zirconia, which is acting as an interphase, and alumina as the main constituent of the matrix, has been an excellent materials choice, since there was no chemical degradation of the final composite strength comparing to that of the reinforcement materials, i.e. Nextel™720 fibres. It is therefore decided that this combination should be used as a standard composition for the matrix material in processing of high-temperature high performance CMCs.

#### Acknowledgements

The author would like to acknowledge gratefully financial

Table 1  
Mechanical properties of ceramic and resin matrix composites. Effect of matrix and processing temperatures

Type of matrix	Ceramic	Ceramic	Resin	Resin	Resin	Resin	Resin	Resin
Composite processing conditions	$1000^\circ\text{C}$ , 1 h	$1200^\circ\text{C}$ , 1 h	As received	$200^\circ\text{C}$ , 1 h	$400^\circ\text{C}$ , 1 h	$800^\circ\text{C}$ , 1 h	$1000^\circ\text{C}$ , 1 h	$1200^\circ\text{C}$ , 1 h
Tensile strength (MPa)	275	194	231	309	195	389	259	206

support for this work from the EC (BRITE-EURAM Project BRPR-CT95-0110) and the EPSRC (UK).

## References

- [1] Richlen S. Applications of fibre-reinforced ceramic matrix composites. In: Hehman RL, El-Rahaiby SK, Wachtman JB, editors. Handbook on continuous fibre-reinforced ceramic matrix composites. J Am Ceram Soc, Westerville, OH, 1995, 495–526.
- [2] Morgan PED, Marshall DB. Ceramic composites of monazite and alumina. J Am Ceram Soc 1995;78(6):1553–63.
- [3] Lewis MH, Tye A, Butler EG, Al-Dawery I. Development of interfaces in oxide matrix composites. Key Engng Mater 1999;164:351–6.
- [4] Mouchon E, Colomban PH. Oxide ceramic matrix/oxide fibre woven fabric composites exhibiting dissipative fracture behaviour. Composites 1995;26:175–82.
- [5] Sudre O, Lange FF. Effect of inclusions on densification: I. Microstructural development in an alumina matrix containing a high volume fraction of zirconia inclusions. J Am Ceram Soc 1992;75(3):519–24.
- [6] Gu X, Trusty PA, Butler EG, Ponton CP. Deposition of zirconia sols on woven fibre preforms using a dip-coating technique. J Eur Ceram Soc 2000;20:675–84.
- [7] Boccaccini AR, Ponton CP. Processing ceramic matrix composites using electrophoretic deposition. Journal of Materials 1995;34–37.
- [8] Boccaccini AR, MacLaren I, Lewis MH, Ponton CB. Electrophoretic deposition Infiltration of 2-D woven SiC fibre mats with mixed sols of mullite composition. J Eur Ceram Soc 1997;17:1545–50.
- [9] Pearce DH, Jickells AJ, Ponton CB. Fabrication of sapphire fibre reinforced ceramic matrix composite. Br Ceram Trans 1996;95(4):141–5.
- [10] Xu HHK, Ostertag CP, Braun LM. Effects of fibre volume fraction on mechanical properties of SiC-fibre/Si<sub>3</sub>N<sub>4</sub> matrix composites. J Am Ceram Soc 1994;77(7):1897–900.
- [11] Al-Dawery I. Ultra high-temperature ceramic matrix composites. IRC Internal Report December, 1998.

## Filament winding of bicomponent fibers consisting of polypropylene and a liquid crystalline polymer

Jianhua Huang<sup>a</sup>, Donald G. Baird<sup>a,\*</sup>, Alfred C. Loos<sup>a</sup>, Priya Rangarajan<sup>a</sup>, Aaron Powell<sup>b</sup>

<sup>a</sup>Center for Composite Materials and Structures, Virginia Tech, Blacksburg, VA 24061, USA

<sup>b</sup>Luna Innovations, Inc., Blacksburg, VA 24060, USA

Received 21 August 2000; revised 20 December 2000; accepted 4 January 2001

### Abstract

This paper is concerned with novel wholly thermoplastic composite materials suitable for use in filament winding. Bicomponent fibers consisting of a sheath of polypropylene (PP) of lower melting point and a core of a thermotropic liquid crystalline polymer (TLCP) of higher melting point were produced in a ratio of 30/70(w/w) using a modification of a standard bicomponent spinning process. The modifications were required to handle the necessity of melting the TLCP at a temperature in the range of 320°C while not raising the temperature of PP above 300°C which would lead to significant degradation of PP. The tensile modulus and strength of the fibers were 38.7 GPa and 465 MPa, respectively. A methodology was developed for establishing the conditions for filament winding these bicomponent composite fibers, which would allow adequate consolidation without disrupting the molecular orientation within the TLCP component and hence reinforcing properties. Cylinders and rings were generated with winding angles of 90 and 80° under conditions in which the PP was melted but the TLCP retained its properties. The degree of consolidation was evaluated using the interlaminar shear strength test and optical microscopy. Because of the uniform distribution of the reinforcing component there was no failure observed in this test. The void content was determined to be 5.2%. The tubes generated from these materials have the potential for transport liquid oxygen and corrosive fluids. © 2001 Elsevier Science Ltd. All rights reserved.

**Keywords:** E. Filament winding; A. Polymer–matrix composites (PMCs); E. Compression molding; Liquid crystalline polymer

### 1. Introduction

Filament winding is a composites manufacturing process used to generate cylindrical structures and in some cases reinforce existing cylindrical structures [1,2]. Most frequently, carbon, glass, or aramid fibers are impregnated with thermosetting resins such as epoxies and vinyl-esters [2]. Lengthy cure times in an autoclave are required to complete the cross-linking process. In a few cases filament winding with thermoplastic composite systems are reported [3–12]. For example, filament winding with polyetheretherketon (PEEK) and carbon fibers (CF) has been reported [3,8,11]. The preparation of the tapes consisting of fibers impregnated with the thermoplastic is usually the limiting step.

Recently Baird and coworkers have reported the generation of bicomponent fibers [13] and matrix–fibril mono-

filaments [14,15] consisting of thermoplastics of lower melting point reinforced with thermotropic liquid crystalline polymers (TLCPs) of higher melting point. These materials can be used to generate wholly thermoplastic composites. In the case of the monofilaments, they have been pelletized and injection molded to form composite materials [15]. The fibers have been woven to form composite preforms suitable for compression molding [16]. For the TLCP/polypropylene (PP) sheath core bicomponent fibers, they succeeded in spinning monofilament fibers with a novel spinning pack but failed in generating quality multifilament with a conventional spinning pack [13].

Two approaches have been used to generate fibers based on thermoplastics of lower melting point reinforced with TLCPs of higher melting point [14]. One form consists of the matrix being reinforced with multiple small TLCP fibrils (of the order of one micron in diameter) which are nearly continuous. While the other consists of a sheath of thermoplastic reinforced with a core of TLCP. The former method leads to a fiber referred to as a matrix–fibril system. The matrix–fibril system is generated by a method which allows one to use a wider difference in melting points

\* Corresponding author. Address: Department of Chemical Engineering, Virginia polytechnic Institute and State University, 128 Randolph Hall, Blacksburg, VA 24061-0211, USA. Tel.: +1-540-231-5998; fax: +1-540-231-5022.

E-mail address: dbaird@vt.edu (D.G. Baird).

of the two polymers than can be done using the sheath-core approach.

In this paper we are concerned with the spinning of bicomponent fibers consisting of a PP sheath and a TLCP core and their subsequent use in filament winding. First the spinning process used to generate the multifilament bicomponent fibers is described. Because the fibers must be heated during the winding process, a procedure for establishing the appropriate processing conditions which will lead to acceptable consolidation but not destroy the reinforcing properties of the TLCP is described. Finally, the properties of filament wound tubes and rings are presented.

## 2. Experimental

### 2.1. Materials

The liquid crystalline polymer in this work was Vectra B950 (Vectra B for short in this paper) from Ticona. Vectra B is reportedly a random copolymer synthesized from 2,6-hydroxynaphthoic acid, terephthalic acid and 4'-hydroxyacetanilide using molar proportions of 58/21/21 [13]. The polymer has a glass transition temperature of 110°C, a melting temperature of 280°C and a solid density of 1.41 g/cm<sup>3</sup>. The polypropylene used is Profax 6823 purchased from the Himont Company and has a melting temperature of 161°C, flow index of 0.8 and solid density of 0.902 g/cm<sup>3</sup>.

### 2.2. Methods

The sheath-core bicomponent fiber was spun on a spinning system consisting of two Killion 1 in. extruders and a spinning pack. The spinneret has 16 die holes with the diameter of 0.7 mm. The fiber composition or sheath-core ratio was controlled through adjustment of speed of gear pumps. The composition was then tested by the burning-off method (300°C for 30 min) [17]. A Leesona take-up device (Model 966) was used to collect the fiber.

To facilitate the filament winding process a fiber band was prepared by feeding the filaments through a heated plate (225°C). A 3 mm wide fiber band was obtained and used in filament winding.

Tensile mechanical properties of the bicomponent fiber and fiber band were measured on an Instron Tensile Tester (model 4202) with 1 KN load cell. The sample grips were set 100 mm apart. When testing the fiber bundle, the ends of the bundle were fused together by heating to form a section of fiber band before testing to ensure that the tension was uniformly applied to each fiber. When testing at elevated temperature, an oven with forced convection heating was used to heat the sample. The samples were installed while the oven was hot and after the sample was installed it took less than 20 min for the oven to restore the temperature to the setting temperature. The test was made immediately after the oven reached the desired temperature. When the influence of thermal history of the fiber bands was investi-

gated, the fiber bands were let to cool down immediately after heated to desired temperature, then the mechanical properties of the sample were tested at room temperature. All mechanical properties were reported as the average of at least 5 readings.

A test was set up for measuring the fiber properties under conditions similar to those generated in the filament winding process. As schematically shown in Fig. 2, a weight was attached to one end of the sample (fiber band or fiber bundle) and the other end was clamped to the mandrel (35 mm in diameter). For fiber bundle samples, the ends of the bundle were fused together before testing to ensure the test. A heating gun was placed at a position such that the nozzle of the heating gun was 1.25 in. away from the mandrel (front surface). A thermocouple was placed on mandrel surface closing to the sample to monitor the fiber temperature. The heating gun (with constant heating power) was used to heat the sample until the polymer melted and the fiber broke. From the temperature of 16°C, the samples (sample surface as detected by the thermocouple) were heated to 100°C in 10 s, to 150°C in 25 s, to 200°C in 1 min, to 250°C in 2 min and to 275°C in 4.2 min. Changing the weight or fiber tension and recording the corresponding breaking temperature, the dependence of breaking temperature on fiber tension could be obtained.

Filament winding was performed on a model ULD computer-controlled winding machine from Composite Machine Company. A thermoplastic consolidation head assembly, including an air heater and a pressure roller, was used for filament on-line consolidation (see Fig. 4). The filament winding technique was the so-called on-line or in situ consolidation process, where the incoming filaments (fiber bands) were welded to the previously wound surface.

Compression molded samples were prepared by firstly laying out Vectra B/PP bicomponent fiber uniaxially on a 7.62 mm (3 in.) × 7.62 mm (3 in.) frame mold. The mold was then placed on the bottom press at temperature of 187°C. 1135 kg (2500 lbs) force was applied when mold temperature reached 180°C. The mold was kept for 5 min under this temperature and then was transformed to a cold press to be cooled down under pressure. The plaque obtained has thickness of about 2.9 mm.

The interlaminar shear strength (ILSS) of the TLCP/PP filament wound rings and compression molded samples was tested on a short beam bending fixture according to the ASTM standard 2344-84.

Specimens for microscopic analysis were cut from the filament wound cylinder and mounted in an epoxy-potting compound. The sample was then ground on Buehler Variable Speed Grinder-Polisher with sandpaper of 180, 240, 320, 400, and 600 grit. The polishing was performed in turn with a Textmet polishing cloth with 3 μ diamond paste and with a Trident polishing cloth with 0.05 μ colloidal silica. An Olympus BH2-UMA optical microscope was used to analyze the samples.

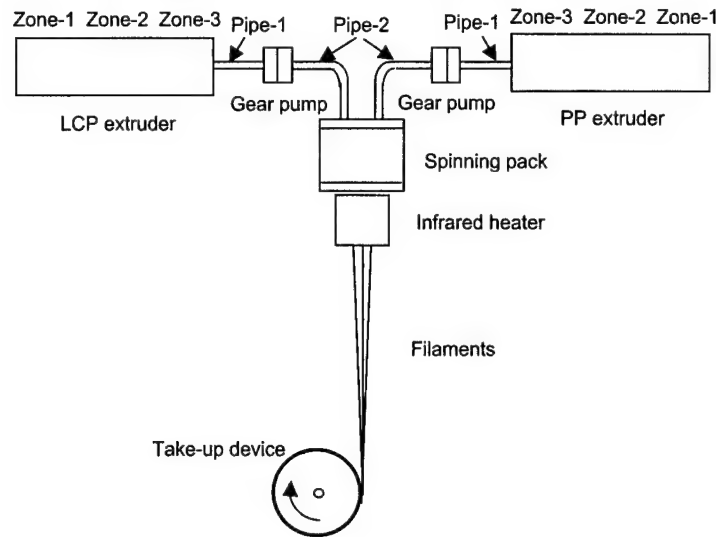


Fig. 1. Schematic diagram for the bicomponent fiber spinning system.

### 3. Results and discussions

#### 3.1. TLCP/TP system selection and fiber spinning

The features of bicomponent fiber spinning and the filament winding process determine that the requirements should be met by the TLCP/thermoplastic polymer (TP) system as a filament winding material. First, the processing temperature for TLCP and TP should overlap. This is because the TLCP and TP melts must pass through a spinning pack where the melts are joined and then extruded through the spinneret. Second, the TP should have a lower melting temperature relative to that of the TLCP so that during the filament winding process a temperature at which the TP melts but the TLCP doesn't can be used. Because a certain degree of tension is needed for filament winding, the TLCP should be strong enough at winding temperature (at least higher than the melting point of TP) to ensure appropriate tension for compaction. Finally, the TLCP should possess high modulus and strength that is not lost during filament winding. According to these requirements, Vectra B manufactured by Ticona (melting point = 280°C) was chosen as the reinforcing component while PP with a melting point of 161°C (Profax 6823 from Montell) was used as sheath component. Certainly other materials could have been used which meet these requirements.

Fig. 1 illustrates the spinning system used for generating

TLCP/PP sheath-core bicomponent fibers. The processing temperatures were listed in Table 1. The TLCP and PP were plasticized in separate extruders, and then the melts were introduced to the spinning pack. The composition of the fiber is 70 wt% of Vectra B and 30 wt% of PP. The fiber has average diameter of about 0.18 mm and apparent draw ratio of 15.

Initially it was found difficult to take up the TLCP/PP multifilament even at very low draw ratios [14]. This was believed to be caused by the solidification of TLCP melt at the early stage of the drawing process because the temperature of the spinning pack was only a few degrees higher than the melting point of the TLCP (see Table 1). However, to prevent PP from degradation, one could not solve this problem by simply increasing the temperature of the spinning pack. Although a monofilament spinning pack invented by Baird and coworkers [14] could be used at higher temperature for making fiber drawing much easier, it could not be used here because the monofilament is not the appropriate material for filament winding. Instead, in this work a multifilament spinning pack was used, but an infrared heater (a cylinder of 10.16 cm in diameter and 10.16 cm in height) was added beneath the spinneret to retard the cooling process of the fiber. It turns out that the heater could significantly increase the draw ability of the fiber and the heater temperature of 190°C was appropriate. It was also observed that the fiber surface became much smoother after the heater was added.

Table 1  
Processing temperature (°C) for generating Vectra B/PP sheath-core bicomponent fibers (refer to Fig. 1 for illustrations)

	Pack	Pipe-2	Gear pump	Pipe-1	Clamp	Zone-3	Zone-2	Zone-1
PP	290	280	260	260	260	260	260	150
VectraB	290	290	290	300	310	320	325	220

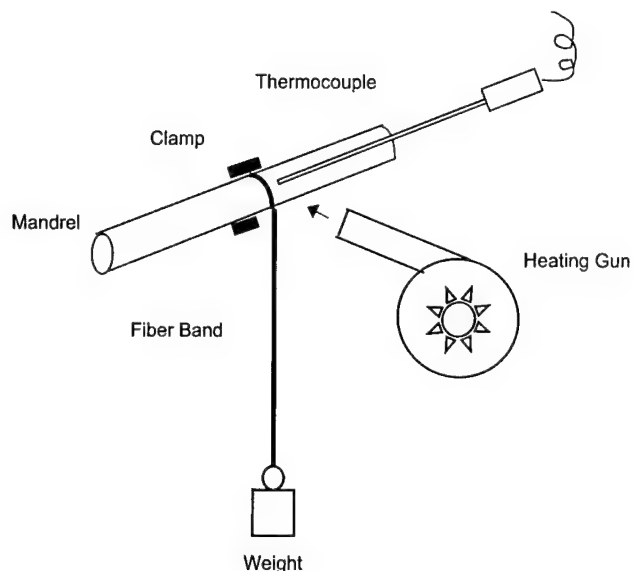


Fig. 2. Schematic diagram of the device used for thermo-mechanical testing of the fibers and fiber bands under filament winding conditions.

### 3.2. Mechanical properties of fiber and fiber band as a function of temperature and thermal history

Information on the temperature dependence of the mechanical properties of bicomponent fiber is very important to determining the appropriate filament winding conditions. The strength–temperature curve provides the information about the maximum temperature one can use for filament winding, and the impact of thermal history on

fiber properties can be used for estimating the change in properties during the consolidation process.

A simple device as shown in Fig. 2 was designed to determine the temperature dependence of the mechanical properties of the bicomponent fibers under conditions similar to that of the filament winding. The results are shown in Fig. 3. It can be seen that, if the tension of fiber band is less than 80 g, the fiber band breaks at about 280°, a temperature which is exactly the melting point of Vectra B. As the tension increases further, the breaking temperature drops dramatically and samples will break at 250°C if the tension of over 200 g is applied. Comparatively, the fiber bundles broke at much lower temperatures. When the tension is about 200 g, for example, the breaking temperature of fiber bundles is 191°C, which is 59°C lower than that of the fiber bands. Since the tension of at least 200–220 g was found necessary for the filament winding, the result mentioned above means that for the fiber bundles one could at most use 190°C as the winding temperature while for the fiber bands 60°C higher temperatures may be used. Therefore, the Vectra B/PP filaments were transformed into the fiber bands before used in the filament winding to ensure that the winding could be carried out at a temperature high enough to promote good consolidation.

It is not difficult to explain why the strength of the fiber bands is higher than that of the fiber bundles at elevated temperatures. Note that it was the consolidated filaments (consisting of 16 fibers) instead of 16 individual filaments that was surrounded by the hot air when the fiber bands were subjected to the testing or filament winding. The time

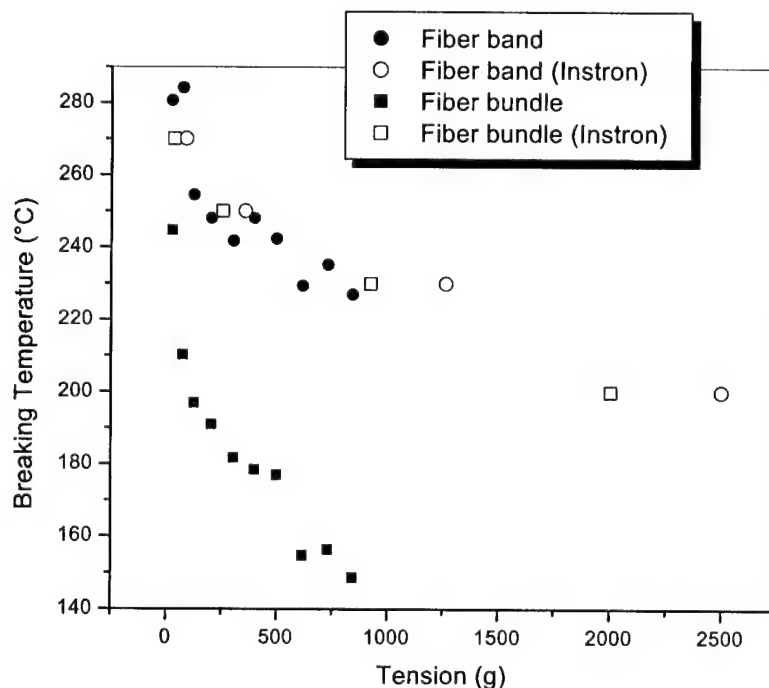


Fig. 3. Tensile strength of bicomponent fibers and fiber bands as a function of temperature. Test was performed on an Instron Tester or the device shown in Fig. 2.



Table 2

Tensile properties of 70/30(w/w) Vectra B/PP bicomponent fiber and fiber band as a function of temperature. (Note: Values in the parentheses are standard deviation of at least five readings)

Temperature (°C)	Fiber bundle			Fiber band		
	Strength (MPa)	Modulus (GPa)	Elongation (%)	Strength (MPa)	Modulus (GPa)	Elongation (%)
25	425.9 (21.1)	38.91 (0.83)	1.91 (0.16)	464.7 (24.7)	38.69 (0.50)	2.25 (0.22)
170	83.30 (14.8)	14.22 (1.05)	1.25 (0.18)	89.50 (7.45)	14.24 (0.76)	1.78 (0.49)
200	47.81 (8.30)	8.90 (1.04)	1.28 (0.33)	60.26 (8.32)	11.24 (0.82)	1.17 (0.28)
230	21.74 (4.45)	4.54 (0.62)	0.82 (0.39)	30.08 (3.39)	6.13 (0.47)	0.90 (0.12)
250	5.96 (1.25)	2.02 (1.04)	0.94 (0.28)	8.83 (1.60)	2.17 (0.77)	1.06 (0.43)
270	0.76 (0.25)	0.48 (0.47)	1.20 (0.39)	2.13 (0.50)	0.53 (0.18)	1.10 (0.29)

needed to heat up TLCP of the fiber bands should be longer than that of the fiber bundles. As a result, at the same surrounding temperatures, the TLCP in the fiber bands might actually have lower temperature and higher strength compared with that in the fiber bundles.

To compare this testing method with the standard one, the temperature dependence of mechanical properties of fibers was also determined by an Instron tester with an isothermal temperature chamber. Listed in Table 2 were the tensile strength and modulus of the fibers at different temperatures obtained from the test. To compare with the strength from tension-heating gun test, the strength data in Table 2 were transformed into the units of gram per fiber bundle or fiber band and plotted in Fig. 3, too. It was found that for fiber band the results from the two different methods agreed with each other. But for the fiber bundle, the breaking temperature determined by means of Instron was close to that of fiber band instead of fiber bundles determined by the tension-heating gun method. This apparent disagreement was actually understandable if the behavior of fiber bundles under different testing circumstances was noted. When the Instron tester was used, the whole fiber bundle inside the thermal chamber was heated uniformly. As the testing temperature was increased to 170°C or above (that is, a temperature high than the melting point of polypropylene), the fiber bundle tended to fuse and adhere with each other forming a fiber band. Hence, it was no surprise that the following test gave the results to those obtained from the pregenerated fiber bands. In contrast, the air flow (hot air from heating gun) in the tension-heating gun method was focused on a narrow region of the fiber bundle which did not lead to the formation of a fiber band as observed in Instron

chamber. Obviously, the behavior and property of the fiber bundles in this situation was closer to those in the filament winding process. These observations indicated that although both Instron and tension-heating gun tests can be used to evaluate the temperature dependence of tensile strength of the bicomponent fibers, the tension-heating gun method is much more convenient and is capable of proving results closer to those in the filament winding process.

A study on the influence of thermal history on the mechanical properties of bicomponent fiber (fiber band) is important it may provide the information about the possible changes of fiber properties which might occur during the consolidation process. The experiment was carried out by heating the fiber bands to a designated temperature (170, 200, 230 and 250°C) and then letting it cool down and testing the mechanical properties of the sample at room temperature. As shown in Table 3, within the whole temperature range (170–250°C), the degree of modulus loss is small (less than 10%). The fiber strength does not change until the temperature reaches 200°C, but immediately after that, the property starts to decline. At temperatures of 230 and 250°C, the strength of the fiber bands reduces to 84 and 75% of their original value. This property loss is attributed to the relaxation of the TLCP molecular orientation. Considering that in the filament winding process the fiber bands were exposed to hot air for a very short time (less than 5 s), the actual property loss during this process may probably be smaller than the estimation. The use of tension in filament winding may also reduce the relaxation of the TLCP molecular orientation and hence offset some of the property loss.

Table 3

Influence of thermal history on the tensile mechanical properties of 70/30(w/w) Vectra B/PP bicomponent fiber bands. (Note: Values in the parentheses are standard deviation of at least five readings)

Maximum temperature (°C)	Testing temperature (°C)	Strength (MPa)	Modulus (GPa)	Elongation (%)
25	25	464.7 (24.7)	38.69 (0.50)	2.25 (0.22)
170	25	463.4 (40.6)	36.99 (1.88)	1.71 (0.16)
200	25	461.0 (61.7)	36.74 (1.42)	1.80 (0.22)
230	25	389.8 (28.1)	36.86 (1.45)	1.62 (0.20)
250	25	349.0 (42.4)	35.35 (1.74)	1.52 (0.25)

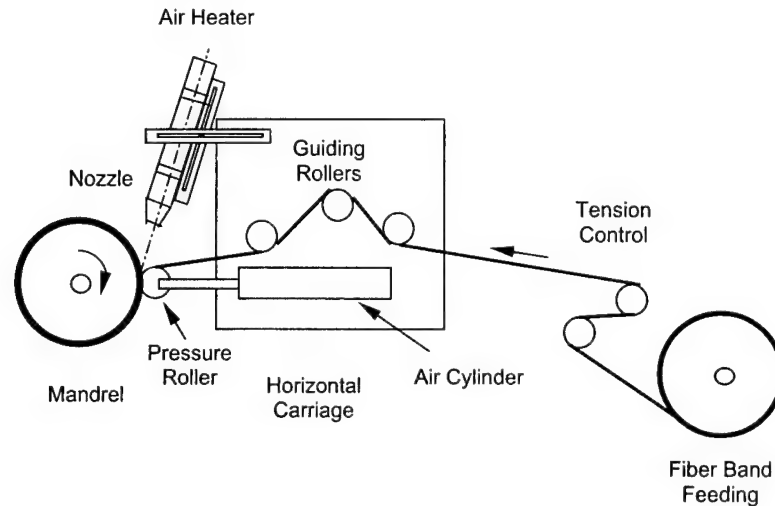


Fig. 4. Schematic diagram for on-line consolidation filament winding system.

### 3.3. Filament winding of TLCP/PP bicomponent fiber

The filament winding system used in the present work is schematically shown in Fig. 4. The system includes a computer-controlled filament-winding machine and a consolidation head (including a pressure roller and a hot air heater) mounted on the horizontal carriage of the machine [4]. A tension controlled filament delivery system was used to ensure stable delivery. Two aluminum mandrels, one having a diameter of 146 mm (5.75 in.) and the other 38.1 mm (1.5 in.), were used to form composite cylinders of different inner diameters. It was found that, as our mechanical study suggests, use of a fiber band instead of a fiber bundle in filament winding leads to less fiber breakage and better filament alignment. A 3 mm wide fiber band was prepared by feeding a fiber bundle continuously through a hot plate (225°C).

As in the case of conventional filament winding materials, the processing parameters for on-line consolidation of Vectra B/PP bicomponent fibers included heating gun temperature (nozzle temperature), nip-point temperature, winding speed, filament tension and compaction force (pressure of pressure roller). Shown in Table 4 and Fig. 5 were

Table 4  
Conditions for the filament winding of Vectra B/PP bicomponent fibers  
(refer to Fig. 5 for definition of symbols)

Winding variables	Values
Nozzle temperature $T_1$	235°C
Nip point temperature $T_2$	220°C
Heater air pressure $P_a$	41.4 kPa (6 psi)
Roller pressure $P_r$	276 kPa (40 psi)
Distance $d$	2.8 cm (1.1 in.)
Winding speed $V$	50–100 cm/min
Filament tension	$\geq 200$ g
Mandrel diameter $D$	3.81 cm (1.5 in.) 14.6 cm (5.75 in.)

processing conditions established experimentally for the Vectra B/PP bicomponent fibers. One of the most important variables was the nozzle temperature which was found to be between 235 and 240°C when placed at a distance of 2.8 cm (1.1 in.) from the nip point. The temperature around nip point was found to be about 220°C. Two filament-wound tubes (38.1 mm in diameter) with winding angles of 80 and 90° and a ring of 146 mm in diameter prepared under these conditions are shown in Fig. 6.

### 3.4. Properties of filament wound ring

To evaluate the consolidation quality of a filament wound cylinder, the ILSS of a filament wound ring (ring diameter = 146 mm, Span  $\times$  Width  $\times$  Thickness = 12.7 mm  $\times$  6.35 mm  $\times$  3.42 mm) was tested according to ASTM standard 2344-84. For comparison, the ILSS of flat sample (Span  $\times$  Width  $\times$  Thickness = 20.3 mm  $\times$  6.35 mm  $\times$  2.9 mm) prepared by compression molding was also tested using the same standard. This kind of sample is believed to have good

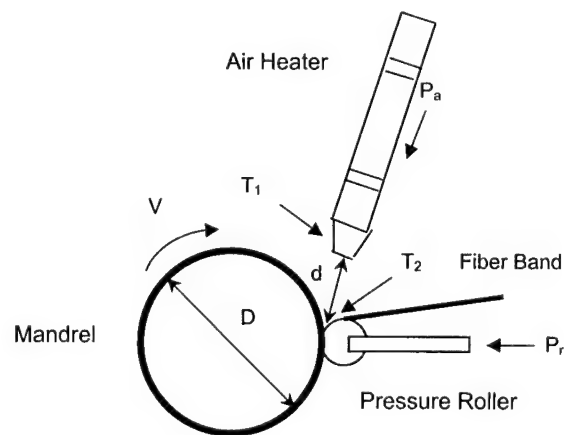


Fig. 5. Conditions for filament winding of Vectra B/PP bicomponent fibers (refer to Table 4).

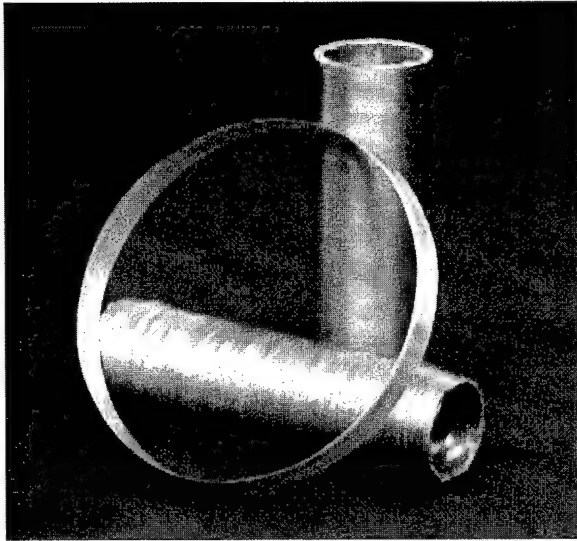


Fig. 6. Photograph of Vectra B/PP filament wound ring (146 mm in diameter) and tubes (38.1 mm in diameter) with winding angle of 90 and 80°, respectively.

consolidation under normal compression molding conditions, and the properties would serve as a baseline [4]. As can be seen from Fig. 7, the load-displacement curve of the filament wound sample is similar to that of the compression molded sample. Especially, in whole testing range, no failure or maximum load could be observed for both samples, and, hence, no ILSS value could be determined for the samples. This result was quite different from that of CF/PEEK filament wound ring reported by Shih and Loos [4]. They found that during the test an individual ply failure was

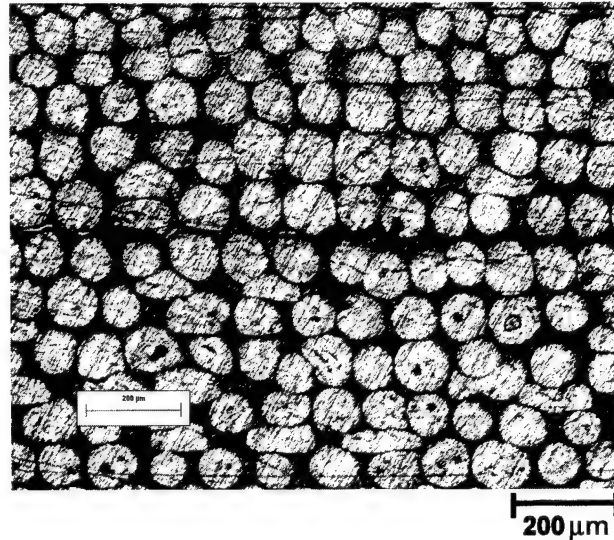


Fig. 8. Optical micrograph of the cross-section of Vectra B/PP filament wound ring.

accompanied by a sharp load decrease and an audible cracking sound, and the damaged laminate continued to carry loading until the next failure occurred. Accordingly, teeth shaped load-displacement curves were observed in their ILSS test [4].

In order to better understand why the Vectra B/PP composite cylinders did not fail in the interlaminar shear strength test, the cross-sectional morphology and quality of the filament wound samples was investigated. In Fig. 8 is shown the optical (reflection) micrographs of the cross-section of the Vectra B/PP filament wound ring. The light

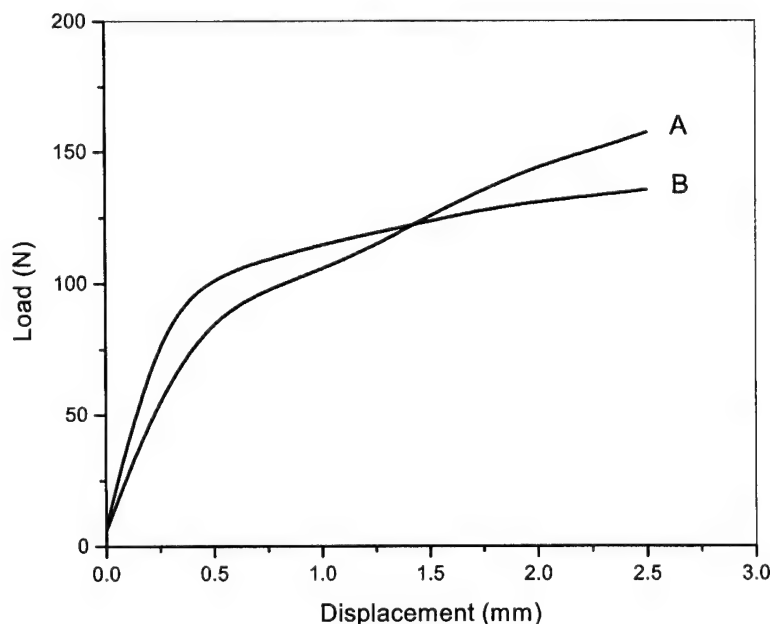


Fig. 7. Load-displacement curves from short beam bending test for: (A) filament-wound and (B) compression molded 70/30(w/w) Vectra B/PP composite materials.

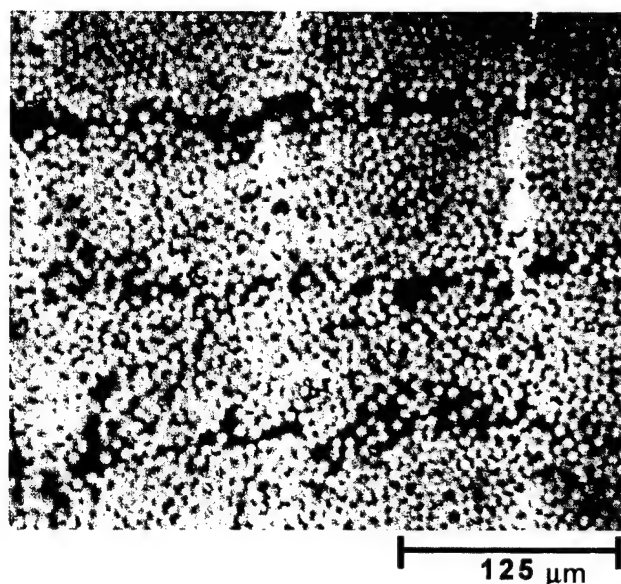


Fig. 9. Optical micrograph of the cross-section of CF/PEEK filament wound ring (cited from Ref. [4]).

regions are the Vectra B core component and the dark portion is the consolidated PP. The picture indicates that a uniform fiber distribution and an intimate layer contact were achieved during the on-line consolidation and an intimate layer contact were achieved during the on-line consolidation process. In contrast, as illustrated in Fig. 9, for a typical CF/PEEK filament-wound cylinder, periodic resin-rich regions are observed. Furthermore, it appears that little or no resin exists between some of the carbon fibers. These regions are vulnerable to shear stress due to their poor strength and modulus compared with the regions with reinforcement. One the other hand, the TLCP/PP filament-wound cylinder doesn't have such layers. This structural difference may account for the different behaviors of the two materials in the interlaminar shear test.

In general as shown in Fig. 8, the compaction is qualitatively good. Most fibers are encased in the polypropylene. There are no resin rich regions for the most part. This is in agreement with the density measurement which showed that the sample contains about 5.2% void.

#### 4. Conclusions

Bicomponent fiber with a sheath of TP and a core of TLCP can be used in filament winding to form a wholly thermoplastic product. Compared with the traditional resin impregnated fibers, the TLCP/TP sheath–core bicomponent fibers have the advantage of being prepared by a melt spinning process in which the reinforcement (TLCP) and resin (TP) are formed simultaneously. Hence the reinforcing component is fully encapsulated by the matrix, eliminating resin bath and lengthy cure cycle.

TLCP/PP bicomponent fibers were transformed into a fiber band by passing them through a heated plate. Thermo-mechanical tests showed that compared with a fiber bundle the fiber band had a higher strength at elevated temperatures which allowed the filament winding process to be carried out at a temperature high enough to promote good consolidation.

The thermo-mechanical test and filament winding process indicated that, for Vectra B/PP bicomponent fiber (fiber band), 200–230°C is a suitable filament winding temperature. At this temperature the filament could withstand the tension necessary for winding process and keep the mechanical properties fairly intact. The filament wound samples have the bonding strength and the overall quality comparable to those of compression molded samples based on the interlaminar shear strength test and optical microscopic analysis.

Since TLCP has low density and high performances including high oxygen barrier and low thermal expansion properties, the TLCP/PP filament wound materials may found application in any cases that require such properties. For example, a duct generated from these materials may be used for transport liquid oxygen as fuel for a spacecraft.

#### Acknowledgements

We gratefully acknowledge support of this work through The Science and Technology Transfer Program (Luna Innovations, Blacksburg, VA and Wright-Patterson Air Force Base).

#### References

- [1] Munro M. *Polym Compos* 1988;9:352.
- [2] Shen FC. *Mater Chem Phys* 1995;42:96.
- [3] Shih PJ, Loos AC. *J Reinforced Plast Compos* 1999;18:1103.
- [4] Shih PJ, Loos AC. Center for Composite Materials and Structures, Report CCMS-97-06, VPI-E-97-03, Virginia Polytechnic Institute and State University, Blacksburg, VA, 1997.
- [5] Mazumdar SK, Hoa SV. *J Thermoplast Compos Mater* 1996;9:35.
- [6] Haupt F, Friedrich K. *Compos Manufac* 1995;6:201.
- [7] Wagner P, Colton J. *Polym Compos* 1994;16(6):436.
- [8] Mazumdar SK, Hoa SV. 38th International SAMPE Symposium, 1993. p. 189.
- [9] Ghasemi Nejhad MN. *J Thermoplast Compos Mater* 1993;6:130.
- [10] Lauke B, Friedrich K. *Compos Manufac* 1993;4(2):93.
- [11] Colton J, Leach D. *Polym Compos* 1992;13(6):427.
- [12] Egerton MW, Gruber MB. 33th International SAMPE Symposium, 1988. p. 35.
- [13] Robertson CG, Baird DG. *Int Polym Processing* 1997;12:345.
- [14] Sukhadia AM, Datta A, Baird DG. *Int Polym Processing* 1992;7(3):218.
- [15] McLeod MA, Baird DG. *Composites Part B* 1999;30:297.
- [16] Xue TJ, Baird DG. *J Adv Mater* 2001;33:56.
- [17] Mazdlos AA, PhD Thesis, Virginia Polytechnic Institute and State University, 1994. p. 112.

# Fabrication of fiber-reinforced celsian matrix composites

N.P. Bansal<sup>a,\*</sup>, J.A. Setlock<sup>b</sup>

<sup>a</sup>National Aeronautics and Space Administration, John H. Glenn Research Center, Cleveland, OH 44135-3191, USA

<sup>b</sup>Department of Materials Science and Engineering, Case Western Reserve University, Cleveland, OH 44106, USA

## Abstract

A method has been developed for the fabrication of small diameter, multifilament tow, fiber-reinforced ceramic matrix composites. Its application has been successfully demonstrated for the Hi-Nicalon/celsian system. Strong and tough celsian matrix composites, reinforced with BN/SiC-coated Hi-Nicalon fibers, have been fabricated by infiltrating the fiber tows with the matrix slurry, winding the tows on a drum, cutting and stacking of the prepreg tapes in the desired orientation, and hot pressing. The monoclinic celsian phase in the matrix was produced in situ, during hot pressing, from the  $0.75\text{BaO}-0.25\text{SrO}-\text{Al}_2\text{O}_3-2\text{SiO}_2$  mixed precursor synthesized by solid state reaction from metal oxides. Hot pressing resulted in almost fully dense fiber-reinforced composites. The unidirectional composites having ~42 vol.% of fibers exhibited graceful failure with extensive fiber pullout in three-point bend tests at room temperature. Values of yield stress and strain were  $435 \pm 35$  MPa and  $0.27 \pm 0.01\%$ , respectively, and ultimate strengths of  $900 \pm 60$  MPa were observed. Young's modulus of the composites was measured to be  $165 \pm 5$  GPa. © 2001 Elsevier Science Ltd. All rights reserved.

**Keywords:** A. Ceramic-matrix composites (CMCs); Celsian; B. Mechanical properties

## 1. Introduction

Monoclinic celsian  $\text{BaAl}_2\text{Si}_2\text{O}_8$  (BAS) and  $\text{SrAl}_2\text{Si}_2\text{O}_8$  (SAS) are refractory materials having melting points higher than  $1700^\circ\text{C}$ . These materials are resistant to oxidation and reduction and also show reasonably good resistance to alkali attack. These materials are phase stable up to  $\sim 1600^\circ\text{C}$  and chemically compatible with alumina, mullite and silicon nitride (in inert or nitrogen atmospheres) at elevated temperatures. They show low values of dielectric constant and loss tangent which make them promising materials for electromagnetic windows or radome applications [1] at high temperatures, packaging for microelectronics, high voltage condensers and other electric insulating products. Celsian is also useful as an environmental barrier coating for SiC/SiC composites and protects against the loss of silica as volatile silicon hydroxide species in the combustion products in turbine engines at elevated temperatures [2]. Celsian is also being investigated as a matrix material for fiber-reinforced composites [3–6] for high temperature structural applications in hot sections of turbine engines.

BAS exists in three different polymorphs, the monoclinic, hexagonal, and orthorhombic phases. The monoclinic phase, commonly known as celsian, is the naturally occurring phase. The hexagonal phase, also known as hexacel-

sian, and the orthorhombic phase are found only in synthetic products. The hexacelsian phase is thermodynamically stable at temperatures between  $1590^\circ\text{C}$  and the melting point whereas the celsian phase is stable at temperatures below  $1590^\circ\text{C}$ . However, hexacelsian can exist as a metastable phase at all temperatures from  $1590^\circ\text{C}$  to room temperature. At  $\sim 300^\circ\text{C}$ , hexacelsian undergoes a rapid, reversible structural transformation [7] into the orthorhombic form, accompanied by a large volume change of  $\sim 3\%$ . Thus, hexacelsian is an undesirable phase.

In both the BAS and SAS systems, hexacelsian is always the first phase to form. However, on heat treatment at  $\sim 1200^\circ\text{C}$  or higher temperatures, its transformation into the monoclinic phase is very sluggish in BAS [8] and very rapid in SAS [9]. It is known that doping of BAS with SAS accelerates the hexacelsian to monoclinic celsian transformation [10]. Fortunately, BAS and SAS form solid solutions in the entire composition range [1,10]. The starting composition of  $0.75\text{BaO}-0.25\text{SrO}-\text{Al}_2\text{O}_3-2\text{SiO}_2$  (BSAS) was used for the synthesis of monoclinic celsian in the present study.

Processing and properties of celsian glass-ceramic matrix composites reinforced with large diameter CVD SiC SCS-6 monofilaments [3–6] and the multifilament small diameter Nicalon [11] and HPZ [12] fibers have been described earlier. The objective of this study was to develop the fabrication of small diameter, multifilament tow fiber-reinforced celsian matrix composites. Microstructures

\* Corresponding author. Tel.: +1-216-433-3855; fax: +1-216-433-5544.  
E-mail address: narottam.p.bansal@lerc.nasa.gov (N.P. Bansal).

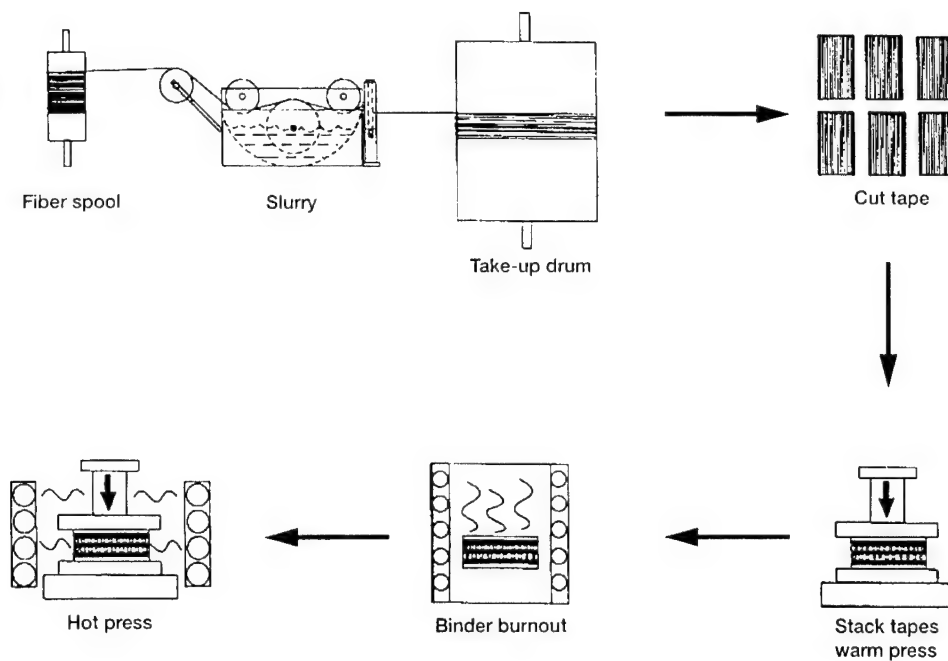


Fig. 1. Schematic of the set-up used for fabrication of small diameter, multifilament fiber tow reinforced ceramic composites by matrix slurry infiltration and hot pressing.

of the resulting FRCs were characterized and room temperature mechanical properties were measured. Strong, tough, and almost fully dense composites reinforced with BN/SiC-coated, Hi-Nicalon fibers have been obtained.

## 2. Materials and experimental procedure

The matrix of BSAS composition was synthesized by a solid-state reaction method [13]. The starting materials used

were  $\text{BaCO}_3$  (Alfa Products),  $\text{SrCO}_3$  (Alfa Products),  $\text{Al}_2\text{O}_3$  (Baikowski International Corp., high purity CR 30), and  $\text{SiO}_2$  (Cerac Inc., 99.9% purity, -325 mesh) powders. Appropriate quantities of various powders were slurry mixed in acetone and ball milled for ~24 h using alumina milling media. Acetone was then evaporated and a part of the mixture was subjected to thermogravimetric analysis (TGA) in air. The oxide mixed powder was calcined at ~900–920°C for decomposition of the carbonates into oxides, followed by cooling to room temperature and

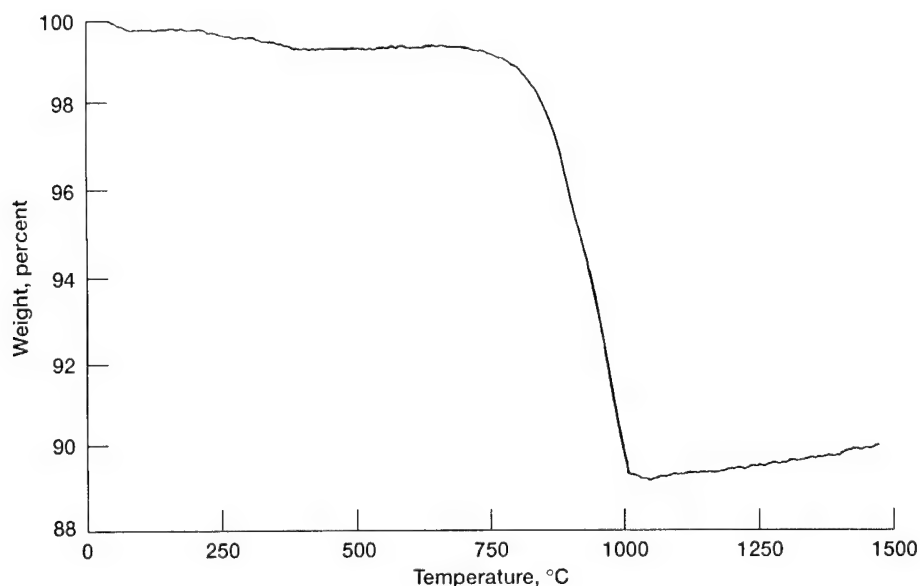


Fig. 2. TGA curve of  $0.75\text{BaCO}_3\text{--}0.25\text{SrCO}_3\text{--Al}_2\text{O}_3\text{--}2\text{SiO}_2$  mixed powder at a heating rate of 5°C/min in air.



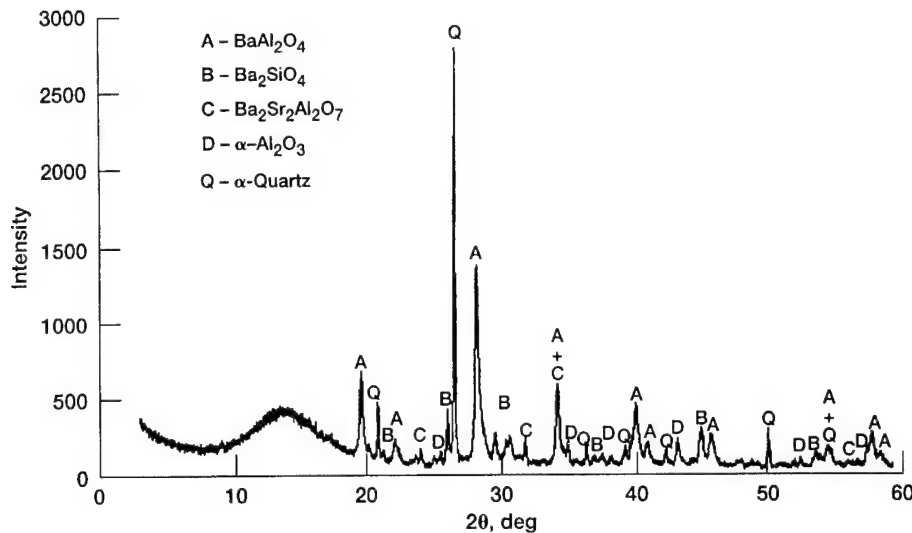


Fig. 3. Powder XRD pattern of the mixed  $0.75\text{BaCO}_3\text{--}0.25\text{SrCO}_3\text{--Al}_2\text{O}_3\text{--}2\text{SiO}_2$  powder calcined at  $915^\circ\text{C}$  for 20 h in air.

grinding. A small part of the calcined powder was loaded into a graphite die and hot pressed at  $1300^\circ\text{C}$  for 2–3 h under 27.5 MPa (4 ksi) pressure.

Polymer derived Hi-Nicalon fiber tows (1800 denier, 500 filaments/tow) with low oxygen content produced by Nippon Carbon Co. were used as the reinforcement. These fibers have an average diameter of  $\sim 14\ \mu\text{m}$ ; a reported [14,15] chemical composition (wt.%) of 62.4% Si, 37.1% C, and 0.5% O; and C/Si atomic ratio of  $\sim 1.39$ . The Hi-Nicalon fibers mainly consist of SiC microcrystals with an average grain size of 4 nm and amorphous carbon. These fibers have a density of  $2.7\ \text{g/cm}^3$ , room temperature tensile strength of  $\sim 2.8\ \text{GPa}$ , elastic modulus of 270 GPa, and an average coefficient of thermal expansion of  $3.5 \times 10^{-6}/^\circ\text{C}$  from room temperature to  $500^\circ\text{C}$ . Hi-Nicalon fibers having a

dual surface layer of BN overcoated with SiC were used in the present study. The fiber coatings were applied by a commercial vendor using a continuous chemical vapor deposition (CVD) reactor. The BN coating was deposited at  $\sim 1000^\circ\text{C}$  utilizing a proprietary precursor and was amorphous to partly turbostratic in nature. A thin overcoating of SiC was also deposited by CVD onto the BN-coated fibers. The SiC layer was crystalline. The nominal coating thicknesses were  $0.4\ \mu\text{m}$  for BN and  $0.3\ \mu\text{m}$  for SiC. The BN interfacial layer acts as a weak, crack-deflecting phase, while the SiC overcoat acts as a barrier to diffusion of boron from BN into the oxide matrix and also prevents diffusion of matrix elements into the fiber.

A sketch of the set-up used for infiltration of the matrix slurry into the fiber tows is shown in Fig. 1. This is similar to

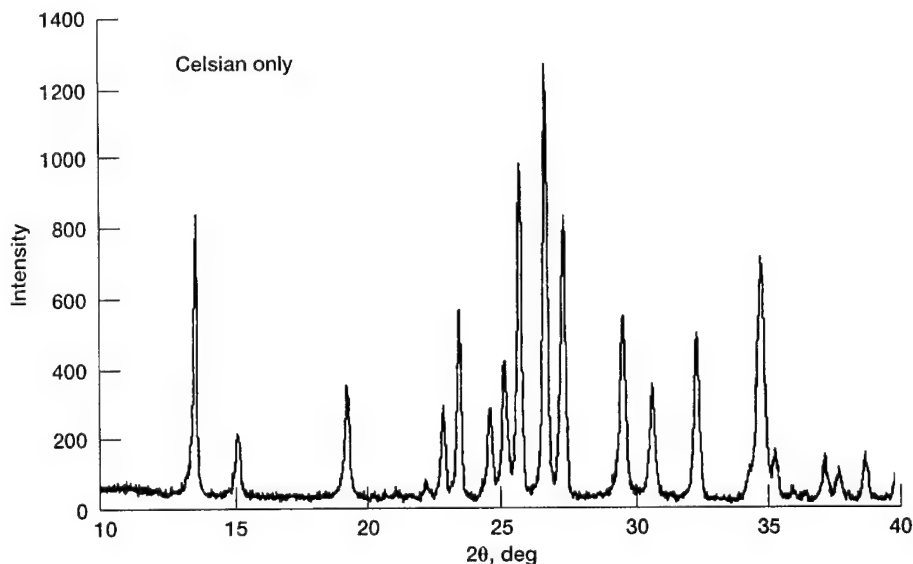


Fig. 4. XRD spectra from the surface of a hot pressed plate of  $\text{Ba}_{0.75}\text{Sr}_{0.25}\text{Al}_2\text{Si}_2\text{O}_8$ . All the diffraction peaks match with the monoclinic celsian phase.

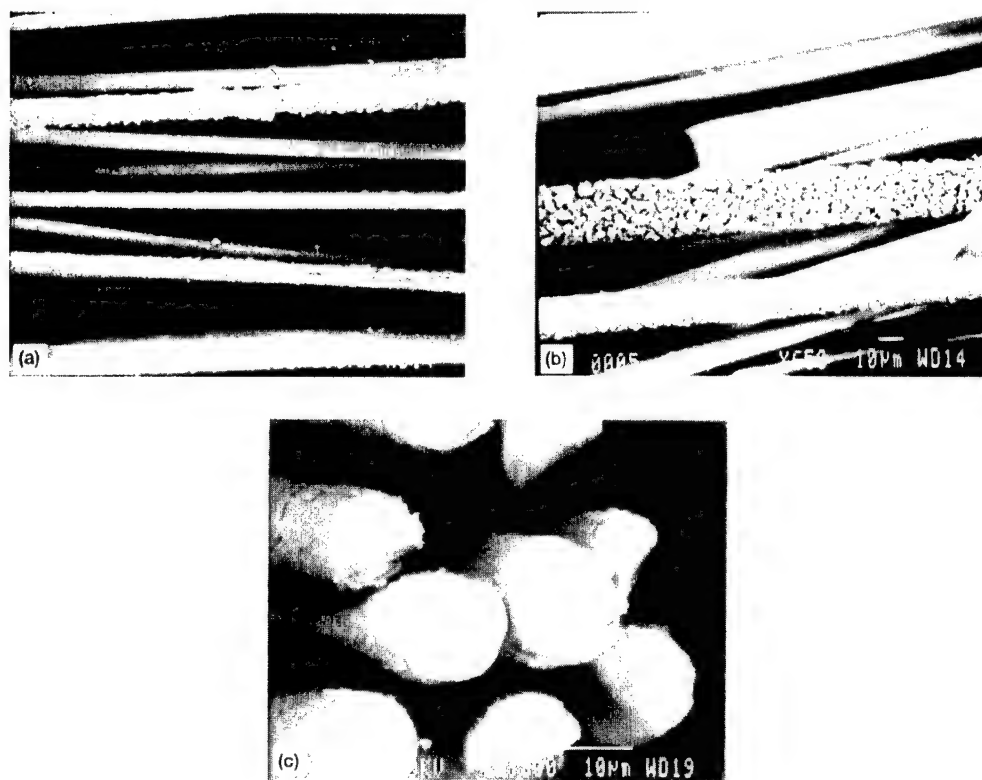


Fig. 5. SEM micrographs showing surface and cross-section of BN/SiC coated Hi-Nicalon fibers.

the set-up reported earlier by Prewo [16]. BSAS powder that had been calcined at 900–920°C for 20–24 h was made into a slurry by dispersing it in methyl ethyl ketone along with organic additives as binder, surfactant, deflocculant and plasticizer followed by ball milling. Tows of BN/SiC-coated Hi-Nicalon fibers were spread using rollers and coated with the matrix precursor by passing through the slurry. Excess

slurry was squeezed out of the fiber tow before winding at 0.977 mm tow spacing (26 fiber tows/inch) on a rotating drum. After drying, the prepreg tape was cut to size. Unidirectional fiber-reinforced composites were prepared by tape lay up (12 plies) followed by warm pressing at ~150°C to form a 'green' composite. The fugitive organics were slowly burned out of the sample in air at ~500°C,

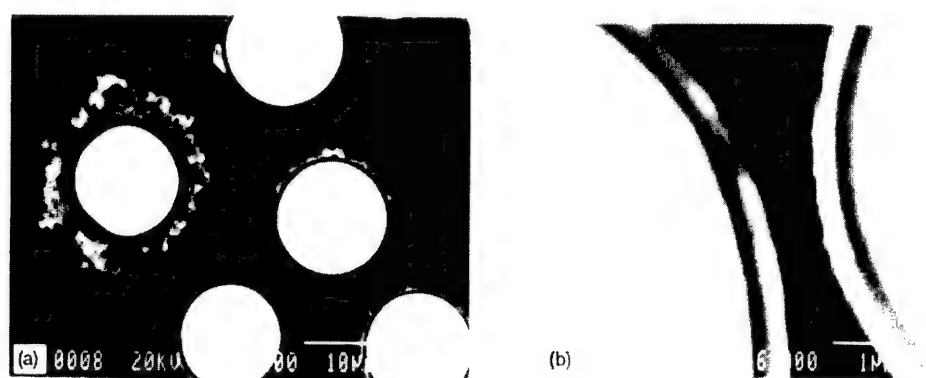


Fig. 6. SEM micrographs showing polished cross-sections of Hi-Nicalon fibers with a duplex CVD BN/SiC coating.

Table 1  
Hi-Nicalon fiber-reinforced  $\text{Ba}_{0.75}\text{Sr}_{0.25}\text{Al}_2\text{Si}_2\text{O}_8$  celsian composites (Unidirectional; 12 Plies)

Sample #	Fiber coating	Fiber content, $V_f$	Density, $\rho$ ( $\text{g}/\text{cm}^3$ )	Phase from XRD
HI-NIC-BSAS-1-29-96	BN/SiC	0.42	3.05	Monoclinic celsian
HI-NIC-BSAS-1-31-96	BN/SiC	0.42	3.09	Monoclinic celsian

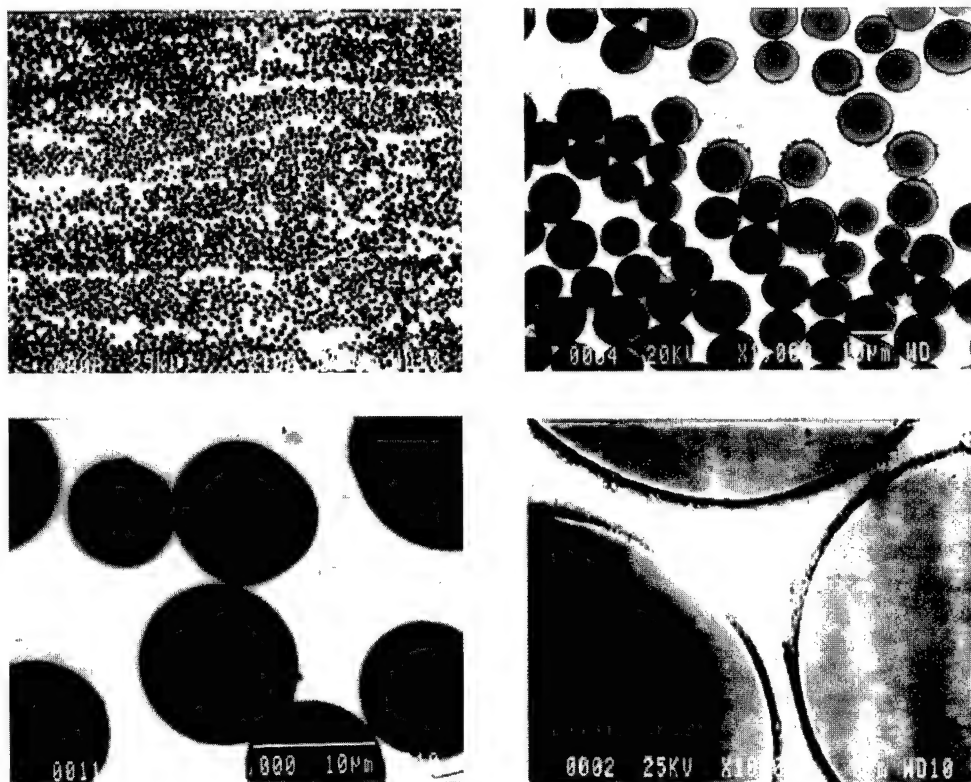


Fig. 7. SEM micrographs showing polished cross-section of a unidirectional Hi-Nicalon/BN/SiC/BSAS composite.

followed by hot pressing under vacuum in a graphite die. The hot pressed fiber-reinforced composite panel was surface polished and sliced into test bars ( $\sim 50.4 \text{ mm} \times 6.4 \text{ mm} \times 1.9 \text{ mm}$ ) for mechanical testing.

TGA of the calcination process was carried out at a heating rate of  $5^\circ\text{C}/\text{min}$  under flowing air ( $\sim 60 \text{ ml}/\text{min}$ ) from room temperature to  $1500^\circ\text{C}$  using a Perkin–Elmer TGA-7 system which was interfaced with a computerized data acquisition and analysis system. X-ray diffraction (XRD) patterns were recorded at room temperature using a step scan procedure ( $0.02^\circ/2\theta$  step, time per step 0.5 or 1 s) on a Philips ADP-3600 automated diffractometer equipped with a crystal monochromator employing  $\text{CuK}_\alpha$  radiation. Density was measured from dimensions and mass as well as by the Archimedes method. Microstructures of the polished cross-sections and fracture surfaces were observed in an optical microscope as well as in a JEOL JSM-840A scanning electron microscope (SEM). For transmission electron microscopy (TEM), thin foils of the composite samples were prepared by slicing, polishing, dimple grinding, and argon ion beam milling. A thin carbon coating was evaporated onto the TEM thin foils and the SEM specimens for electrical conductivity prior to analysis. The thin foils were examined in a Philips EM400T operating at 120 keV. X-ray elemental analyses on the TEM were acquired using a Kevex thin window energy dispersive spectrometer (EDS) and analyzer. Mechanical properties were determined from stress–strain

curves recorded in three-point flexure using an Instron 4505 universal testing instrument at a crosshead speed of  $1.27 \text{ mm}/\text{min}$  ( $0.05 \text{ in.}/\text{min}$ ) and support span ( $L$ ) of 40 mm. Strain gauges were glued to the tensile surfaces of the flexure test bars. Stress was calculated using beam theory. The yield stress was calculated from the stress–strain curves from the point where the curve deviates from linearity. Elastic modulus of the composite was determined from the linear portion of the stress–strain curve up to the yield point using linear interpolation.

### 3. Results and discussion

The TGA curve of the mixed BSAS powder consisting of metal carbonates and oxides is shown in Fig. 2. Minor weight loss near room temperature is due to evaporation of the residual moisture and acetone. A major event showing a large weight loss, due to the decomposition of barium and strontium carbonates into oxides, is observed between  $\sim 750$  and  $1000^\circ\text{C}$ . A calcination temperature of  $900\text{--}920^\circ\text{C}$  was chosen for decomposition of the carbonates. The mixed powder was calcined at this temperature for 20–24 h in air. TGA analysis of this calcined powder showed no further weight loss indicating complete decomposition of the metal carbonates during the calcination step.

The XRD pattern of the mixed powder, calcined at  $\sim 915^\circ\text{C}$  for 20 h in air, is presented in Fig. 3.  $\text{SiO}_2$

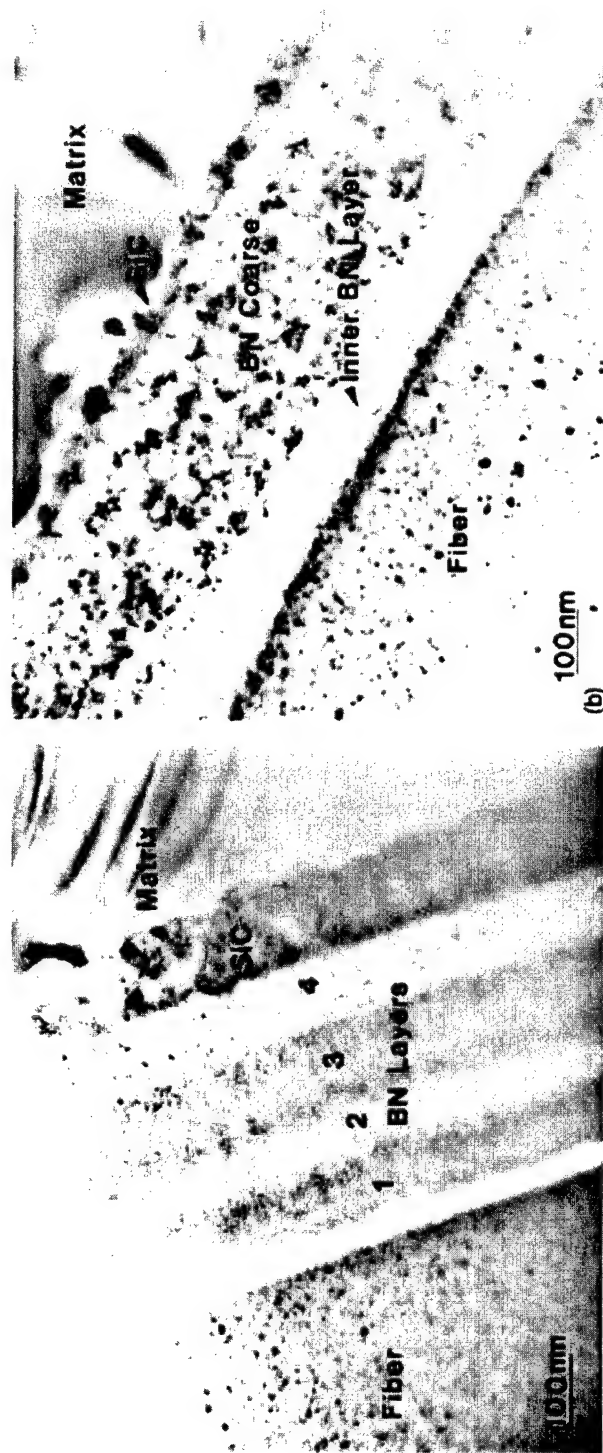


Fig. 8. TEM bright field image from cross-section of Hi-Nicalon/BN/SiC/BSAS composite showing (a) multiple BN layers and (b) coarsening of the outer three BN layers. The inner BN and the SiC interface layers are unaffected.

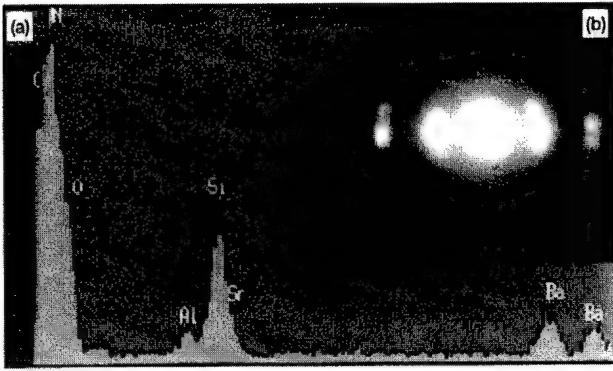


Fig. 9. EDS spectra from (a) the coarsened BN region and (b) the corresponding microdiffraction pattern.

( $\alpha$ -quartz) and  $\text{BaAl}_2\text{O}_4$  were the major phases present. Small amounts of  $\text{Ba}_2\text{SiO}_4$ ,  $\alpha\text{-Al}_2\text{O}_3$ , and  $\text{Ba}_2\text{Sr}_2\text{Al}_2\text{O}_7$  were also identified. Fig. 4 shows the XRD pattern taken from the surface of a monolithic sample made by hot pressing the precalcined powder at  $1300^\circ\text{C}$  for 2 h under 27.5 MPa (4 ksi). All the XRD peaks correspond to the monoclinic celsian phase with complete absence of the undesirable hexacelsian phase.

SEM micrographs showing the surface and the cross-sections of the BN/SiC coated Hi-Nicalon fibers are given in Fig. 5. The coatings on some of the fibers appear to be smooth and of uniform thickness whereas on other fibers the coating is very thick and granular. SEM micrographs taken from the polished cross-sections of the fibers are shown in Fig. 6. The double coating on the fiber surface is clearly visible. The dark layer is BN and the bright layer is SiC.

Some of the composite physical characteristics are given

in Table 1. The fiber volume fraction in the composites was calculated to be  $\sim 42\%$ . From their densities, the composites appear to be almost fully dense. The XRD pattern taken from the polished surface of the hot pressed composite was similar to that shown in Fig. 3. Monoclinic celsian was the only crystalline phase present and the undesired hexacelsian phase was not detected from XRD. This implies that the desired, thermodynamically stable, monoclinic celsian phase is formed in situ, from the mixed oxides precursor, during hot pressing of the composite. Doping with SrO facilitates [9,10] the formation of monoclinic celsian in the matrix. In a recent study [17], a minor amount of hexacelsian phase has been detected in the matrix using Raman micro-spectroscopy.

SEM micrographs taken from the polished cross-section of the unidirectional hot pressed composite are shown in Fig. 7. Uniform fiber distribution and good matrix infiltration within the fiber tows is evident. Some of the filaments are of irregular shape rather than having circular cross-section. The manufacturer reports an average fiber diameter of  $\sim 14\ \mu\text{m}$ , but a large variation in the diameter of the filaments within a fiber tow can be seen. The BN/SiC surface coating has been detached from some of the fibers during metallography or composite processing. Debonding or loss of the fiber coating may lead to adverse reactions between the fibers and the oxide matrix at high temperature resulting in strong fiber–matrix bonding.

TEM micrographs showing the fiber/matrix interface region of the Hi-Nicalon/BN/SiC/BSAS composite are presented in Fig. 8. The BN coating consists of four distinct layers as seen in Fig. 8(a). From EDS analysis, the fiber/BN interface was found to be rich in C along with the presence

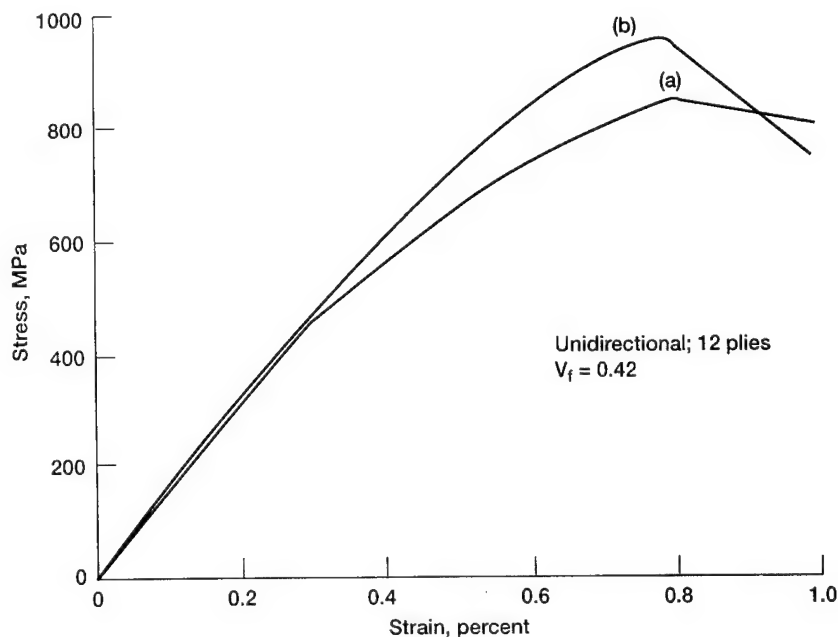


Fig. 10. Stress–strain curves recorded in three-point flexure for unidirectional Hi-Nicalon/BN/SiC/BSAS composites hot pressed under (a) less and (b) more aggressive conditions.

Table 2

Room temperature mechanical properties of Hi-Nicalon fiber-reinforced  $\text{Ba}_{0.75}\text{Sr}_{0.25}\text{Al}_2\text{Si}_2\text{O}_8$  celsian composites (Unidirectional; 12 Plies) (Measured in three-point flexure)

Sample #	Fiber coating	Fiber content, $V_f$	Elastic modulus, $E$ (GPa)	Yield stress, $\sigma_y$ (MPa)	Yield strain, $\epsilon_y$ (%)	Ultimate stress, $\sigma_u$ (MPa)	Ultimate strain, $\epsilon_u$ (%)
HI-NIC-BSAS-1-29-96	BN/SiC	0.42	168	468	0.283	958	0.661
			159	405	0.258	850	0.801
HI-NIC-BSAS-1-31-96	BN/SiC	0.42	170	436	0.264	862	0.583
			165	464	0.283	960	0.771

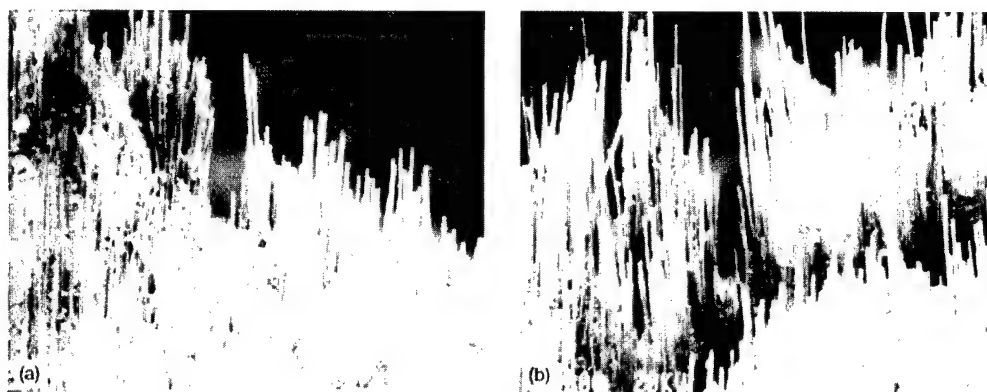


Fig. 11. SEM micrographs from the fracture surfaces of unidirectional Nicalon/BN/SiC/BSAS composites showing extensive fiber pullout; composites hot pressed under (a) less and (b) more aggressive conditions.

of Si and O. The SiC overcoating was often found to be missing from the BN/matrix interface, but was intact in this particular case. A crack running along the fiber/BN interface may also be seen. The BN coating, when viewed via the TEM, did reveal an internal reaction. Some areas show no evidence of coarsening (Fig. 8a) while others show varying amounts of reaction. Fig. 8(b) shows coarsening of three BN layers, from outside in towards the fiber, during hot pressing of the composite. However, the fiber/BN interface and the inner BN layer remain unchanged. EDS spectra obtained from the coarsened region (Fig. 9a) show no obvious chemical changes in the various BN layers. Corresponding microdiffraction patterns (Fig. 9b) show coarsening to the point where individual diffraction spots are seen. It may be pointed out that reaction through all four BN layers or visible degradation of the fiber was never observed. The SiC layer remains apparently unaffected.

Typical stress-strain curves recorded in three-point flexure for the unidirectional BSAS matrix composites reinforced with BN/SiC-coated Hi-Nicalon fibers hot pressed at two different temperatures are shown in Fig. 10. The fiber volume in the composites was  $\sim 42\%$ . Both the composites show graceful failure. The values of yield stress,  $\sigma_y$ , yield strain,  $\epsilon_y$ , elastic modulus,  $E$ , ultimate strength,  $\sigma_u$ , and ultimate strain,  $\epsilon_u$ , of the composites hot pressed at two different temperatures are given in Table 2. Values of yield stress of 400–470 MPa, ultimate strength of 850–960 MPa

and elastic modulus of 160–170 GPa were observed. The measured elastic modulus is in good agreement with a value of 169 GPa, calculated from the rule-of-mixtures ( $E_c = V_m E_m + V_f E_f$  where  $V$  is the volume fraction and the subscripts c, m, and f refer to the composite, matrix, and fiber, respectively) using  $E_m = 96$  GPa [13] and  $E_f = 270$  GPa [14,15]. Values of yield strain and the ultimate strain are  $\sim 0.26$ – $0.28\%$  and  $\sim 0.6$ – $0.8\%$ , respectively.

SEM micrographs of fracture surfaces of the two composites, after the three-point flexure tests, are shown in Fig. 11. Extensive long lengths of fiber pullout are

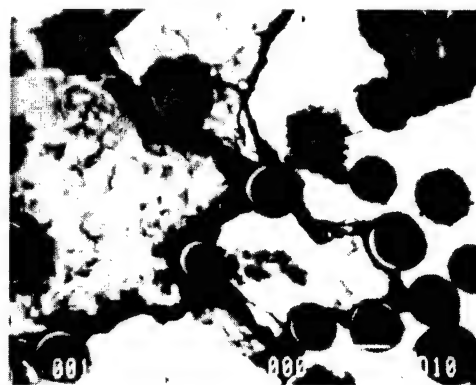


Fig. 12. SEM micrograph from the polished cross-section of a unidirectional Hi-Nicalon/BN/SiC/BSAS composite after the flexure test.



observed indicating toughening behavior. An SEM micrograph of the polished cross-section of a Hi-Nicalon/BN/SiC/BSAS composite, formed under more aggressive processing conditions and flexure tested at room temperature under ambient conditions, is presented in Fig. 12. Debonding at the fiber-matrix interface and crack deflection around the reinforcing fibers is observed, indicating a tough composite. The results of this study clearly indicate that reinforcement of BSAS matrix with Hi-Nicalon fibers having a duplex BN/SiC coating results in a strong and tough composite at room temperature.

#### 4. Summary

Hot pressing of a mixed powder of BSAS composition, obtained from calcination of metal carbonates and oxides, results in monoclinic celsian with complete absence of the undesirable hexacelsian phase. A method has been developed for the fabrication of small diameter, multifilament tow, fiber-reinforced ceramic matrix composites. BN/SiC-coated Hi-Nicalon fiber-reinforced monoclinic celsian composites have been produced by impregnation of the matrix slurry into the fiber tows, winding the tows on a drum, cutting and stacking of the prepreg tapes, and hot pressing. Strong, tough, and almost fully dense unidirectional composites having ~42 vol.% of fibers were obtained. These composites exhibited graceful failure with extensive fiber pull out in a three-point flexure test. The yield stress of ~400–470 MPa and ultimate strength as high as 960 MPa have been observed. The yield strain was ~0.26–0.28%. The Young's modulus of the composite was measured to be ~165 GPa.

#### 5. Conclusions

It may be concluded that reinforcement of the monoclinic celsian with BN/SiC-coated Hi-Nicalon fiber results in almost fully dense composites which are strong and tough at room temperature.

#### Acknowledgements

Thanks are due to Rob Dickerson, Terry Kacik, Ron Phillips and Ralph Garlick for technical assistance during this research.

#### References

- [1] Talmy IG, Haught DA. Ceramics in the system  $\text{BaO-Al}_2\text{O}_3\text{-}2\text{SiO}_2\text{-SrO-Al}_2\text{O}_3\text{-}2\text{SiO}_2$  for advanced radome application. Naval Surface Warfare Center Technical Report. NSWC TR 89-162, September, 1989.
- [2] Lee KN. Current status of environmental barrier coatings for Si-based ceramics. Presented at The International Conference on Metallic Coatings and Thin Films (ICMCTF), San Diego, CA, April 10–14, 2000.
- [3] Bansal NP. Ceramic fiber reinforced glass–ceramic matrix composite. US Patent 5,214,004, May 25, 1993.
- [4] Bansal NP. Method of producing a silicon carbide fiber reinforced strontium aluminosilicate glass–ceramic matrix composite. US Patent 5,389,321, February 14, 1995.
- [5] Bansal NP. CVD SiC fiber-reinforced barium aluminosilicate glass–ceramic matrix composites. *Mater Sci Engng, A* 1996;220(1–2):129–39.
- [6] Bansal NP. Formation of monoclinic celsian in silicon carbide fiber-reinforced barium aluminosilicate glass–ceramic matrix composites. NASA Technical Memorandum 106993, August, 1995.
- [7] Takeuchi Y. A detailed investigation of the structure of hexagonal  $\text{BaAl}_2\text{Si}_2\text{O}_8$  with reference to its  $\alpha$ – $\beta$  inversion. *Miner J Jpn* 1958;2(5):311–32.
- [8] Bahat D. Kinetic study on the hexacelsian–celsian phase transformation. *J Mater Sci* 1970;5:805–10.
- [9] Bansal NP, Drummond CH. Kinetics of hexacelsian-to-celsian phase transformation in  $\text{SrAl}_2\text{Si}_2\text{O}_8$ . *J Am Ceram Soc* 1993;76(5):1321–4.
- [10] Bansal NP, Hyatt MJ, Drummond CH. Crystallization and properties of Sr–Ba aluminosilicate glass–ceramic matrices. *Ceram Engng Sci Proc* 1991;12(7–8):1222–34.
- [11] Bansal NP, McCluskey P, Linsey G, Murphy D, Levan G. Nicalon fiber-reinforced celsian glass–ceramic matrix composites. *Proceedings of Annual HITEMP Review*, Cleveland, OH, October 23–25, 1995. NASA Conference Proceedings 10178, vol. 3, 1995. p. 41–1–41–14.
- [12] Bansal NP. Processing and properties of HPZ fiber-reinforced celsian glass–ceramic matrix composites, in preparation.
- [13] Bansal NP. Solid state synthesis and properties of monoclinic celsian. *J Mater Sci* 1998;33(19):4711–5.
- [14] Takeda M, Sakamoto J, Imai Y, Ichikawa H, Ishikawa T. Properties of stoichiometric silicon carbide fiber derived from polycarbosilane. *Ceram Engng Sci Proc* 1994;15(4):133–41.
- [15] Takeda M, Sakamoto J, Saeki S, Imai Y, Ichikawa H. High performance silicon carbide fiber Hi-Nicalon for ceramic matrix composites. *Ceram Engng Sci Proc* 1995;16(4):37–44.
- [16] Prewo KM. Fiber-reinforced glasses and glass-ceramics. In: Lewis MH, editor. *Glasses and Glass-Ceramics*. New York: Chapman & Hall, 1989. p. 336–68.
- [17] Gouadec G, Colomban P, Bansal NP. Raman study of Hi-Nicalon fiber reinforced celsian matrix composites. Part 1: distribution and nanostructure of different phases. *J Am Ceram Soc*, in press.

## Structure–property relationships for high thermal conductivity carbon fibers

N.C. Gallego, D.D. Edie\*

*Center for Advanced Engineering Fibers and Films, 301 Rhodes Hall, Clemson University, Clemson, SC 29634-0910, USA*

### Abstract

Previous work at Clemson University has shown that ribbon-shaped mesophase pitch-based carbon fibers graphitized at only 2400°C can develop thermal conductivities comparable with those of commercial round-shaped pitch-based carbon fibers graphitized at temperatures above 3000°C. The thermal and electronic transport properties (i.e. thermal conductivity and electrical resistivity) of ribbon-shaped carbon fibers produced at Clemson University are being studied. In addition, the structure of these fibers is being analyzed by electron microscopy and X-ray diffraction techniques. This paper will discuss the relationships between processing conditions, fiber structure and fiber properties. © 2001 Elsevier Science Ltd. All rights reserved.

**Keywords:** A. Carbon fibre; B. Electrical properties; B. Thermal properties; B. Mechanical properties

### 1. Introduction

Carbon fibers are perhaps the most successful new carbon product to be commercialized in the past 40 years. Their high strength and stiffness combined with their light weight makes these fibers attractive for high-volume applications ranging from sporting goods to aircraft structures.

Carbon fibers can be produced from a variety of precursors. Like other fiber products, the final properties are to a great extent determined by the material, the process and the conditions used to form the precursor fiber. Post-treatment steps (i.e. stabilization, carbonization and graphitization) merely refine and perfect the as-spun structure.

The vast majority of today's carbon fibers is produced from either polyacrylonitrile (PAN) or mesophase pitch precursors. PAN fibers have excellent strength but fairly low modulus, and their strength decreases as their modulus is increased. Typically, mesophase pitch-based fibers exhibit lower tensile strengths. However, they are capable of developing modulus levels that approach the theoretical limit of graphite (about 1000 GPa), and have much better thermal and electrical conductivity properties than PAN-based fibers. Thus, it is not surprising that PAN-based fibers are the preferred reinforcement for structural composites whereas pitch-based fibers are preferred for composite applications in which heat dissipation is critical.

The excellent transport properties of pitch-based carbon fibers are the direct result of the ordered structure created during melt-spinning and perfected during graphitization, a structure that approaches that of single-crystal graphite. It is this graphite-like structure that allows mesophase pitch-based fibers to develop high thermal conductivities, approaching values of 1000 W/m K, about 2–3 times the conductivity of copper.

Unfortunately, the high cost of current commercial high thermal conductivity pitch-based fibers (~US\$ 1000/pound) prevents their use in high-volume applications. These commercial processes melt spin precursor fibers with poorly optimized molecular orientation. Because of this, extremely high temperatures must be employed during graphitization (~3000°C) to linearize the as-spun structure, and it is this high graphitization temperature that accounts for most of the processing costs. A logical solution would be to use lower graphitization temperatures if the same or better final properties can be maintained. This might be possible if the molecular orientation can be optimized during melt-spinning.

Previous work at Clemson University has shown that the as-spun molecular orientation of rectangular (ribbon) fibers is more aligned, parallel to the fiber axis, than that of traditional commercial round fibers. Tests have indicated that these ribbon fibers graphitize more easily than round fibers, translating into lower graphitization temperatures and hence lower production costs.

However, a thorough understanding of how structure

\* Corresponding author. Tel.: +1-864-656-4535; fax: +1-864-656-0784.  
E-mail address: dan.edie@ces.clemson.edu (D.D. Edie).

develops throughout the fiber formation process (from the mesophase pitch to the melt-spinning and finally the heat treatment) is necessary if the entire process is to be optimized to achieve the desired final fiber thermal conductivity.

Section 2 begins by summarizing this previous work at Clemson. The section concludes by detailing a set of experiments performed in our ongoing study, directed at developing a fundamental understanding of the structure development of mesophase pitch-based carbon fibers. The experimental procedures used to analyze the structure and properties of these fibers are described in Sections 3–5. Section 6 discusses the results of the current study, including the relationships between process conditions and final fiber structure as well as relationships between final fiber structure and transport properties.

## 2. Structure development of mesophase pitch-based carbon fibers

Mesophase pitch is a nematic liquid-crystalline material comprised of discotic molecules. First discovered by Brooks and Taylor [1], many mesophase pitches melt below their degradation temperatures. Like other liquid-crystalline materials, mesophase pitch molecules orient when subjected to stress. Because of these characteristics, mesophase can be melt-spun to form fibers with high degrees of molecular orientation.

During the spinning of the fibers, the mesophase pitch is extruded through a spinneret capillary, causing the large planar aromatic molecules to align roughly parallel to the direction of the flow. However, the molecular orientation that develops in the cross-section of the capillary varies greatly depending on the processing conditions. Thus, many transverse microstructures have been observed in

mesophase pitch-based carbon fibers. As a study by Endo [2] demonstrated, these microstructures directly affect the thermal and mechanical properties of the fibers. Therefore, understanding the relationship between transverse structure and spinning conditions is the first step to predicting/controlling the final properties of these fibers.

The primary process variables during the melt-spinning of carbon fibers are the winding speed,  $v_L$ , the precursor extrusion rate,  $W$ , the temperature of the precursor at extrusion,  $T_0$ , the temperature of the quench air,  $T_A$ , the velocity of the quench air relative to the downward velocity of the fibers,  $K$ , the drawdown ratio,  $D_S/D_L$  and the temperature dependency of the melt viscosity of the mesophase being processed,  $E$  [3]. These variables are shown in Fig. 1. Any of these processing variables, along with the geometry of the die utilized to spin the fibers, can affect the structure and/or molecular orientation.

Several studies have analyzed the effect of these variables on the structure of fibers. However, spinning temperature [4–6] and die geometry [7–9] appear to be the most important variables.

The temperature range for successful spinning of mesophase pitch is narrower than that for melt-spun polymers. This peculiarity is caused by the extreme temperature-dependency of its viscosity. Decreasing the temperature by only a few degrees significantly increases the viscosity of mesophase and induces brittle fracture during drawdown. Conversely, increasing the temperature lowers the viscosity dramatically, causing capillary breakup of the threadline and/or thermal degradation. Therefore, accurate control of the spinning temperature is critical.

Spinning temperature not only affects fiber uniformity, it also influences molecular orientation. This is the direct result of the liquid-crystalline nature of mesophase. Mochida et al. [5] found that lower spinning temperatures induce a radial transverse structure in round-shaped fibers

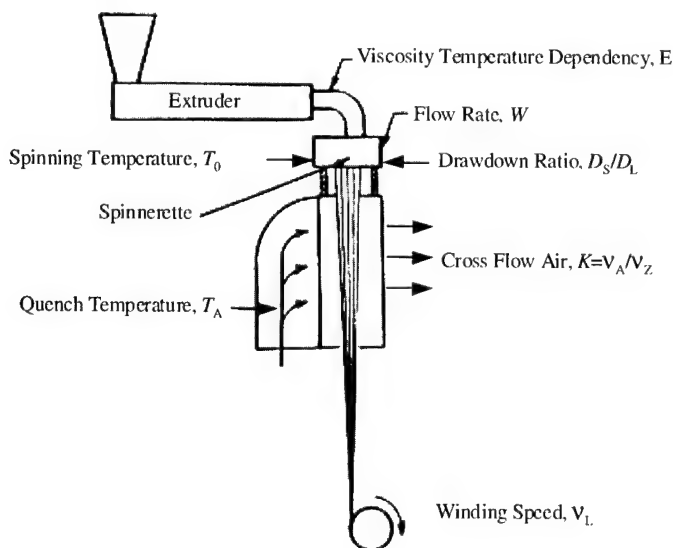


Fig. 1. Process variables in the melt-spinning of carbon fibers [3].

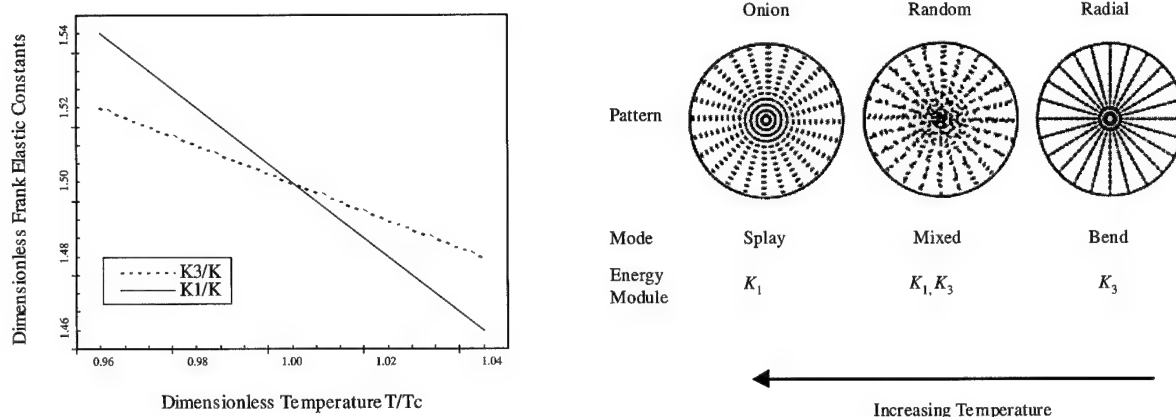


Fig. 2. Bend and splay constants versus temperature and texture versus temperature [6].

while higher spinning temperature induce an onion-like structure. Wang and Rey [6] have used liquid crystal theory to prove that either of these textures occur naturally (either during flow or in a stagnant fluid). The stable texture depends on the relative size of the elastic constants associated with bend and splay deformation of the mesophase pitch ( $K_3$  and  $K_1$ , respectively). As shown in Fig. 2, Wang and Rey [6] predicted that at low temperatures the bend elastic constant ( $K_3$ ) would be less than splay ( $K_1$ ) elastic constant. Under these conditions, the liquid-crystalline fluid would preferably deform in the bend mode, causing the pitch molecules to orient radially in the cross-section of the spinneret capillary. At high temperatures  $K_3$  should be larger than  $K_1$ , yielding a concentric, onion-skin arrangement of the molecules in the capillary.

Commercial pitch-based carbon fibers are produced by extruding the mesophase through round spinneret capillaries. As might be expected, the final fiber texture tends to be either radial or onion-skin (or a slight variation of these). However, if spinneret capillaries with non-circular cross-sectional shapes are employed, different cross-sectional textures and structures can be produced. Among the shapes that have been studied are trilobal, octalobal and rectangular fibers [10].

McHugh [9] studied the flow of mesophase pitch through rectangular channels. Using the theory of Leslie and Ericksen he proved that the mesophase molecules should

preferentially orient perpendicular to the walls of the capillary forming the cross-sectional texture shown in Fig. 3. SEM and TEM inspection of fibers melt-spun from rectangular capillaries proved that the filaments did develop this line-origin texture (as seen in Fig. 3). McHugh's measurements indicated that this highly linear texture should be more conducive to high thermal conductivity than the radial texture common to round commercial fibers. His results proved that because of the elasticity and liquid-crystallinity of mesophase pitch, the shape of the spinneret capillary influences the development of the structure during fiber formation.

### 3. Production of mesophase pitch-based carbon fiber samples

For this project five sets of ribbon-shaped carbon fibers were spun using a flat-entry spinneret with 12 capillaries, each having an aspect ratio (capillary width-to-thickness ratio) of 9:1. In past studies a range of aspect ratios were evaluated [11]. Capillaries with a 9:1 aspect ratio proved most effective for producing ribbon-shaped fibers with superior thermal and mechanical properties. All spinning variables except for spinning temperature were kept constant. The spinning temperature was varied from 305 to 325°C in 5°C increments. The same mesophase (ARA

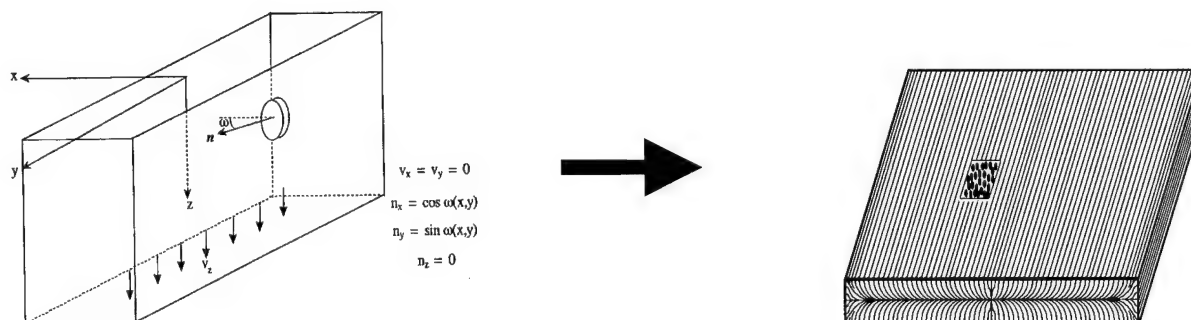


Fig. 3. Developing of the line-origin structure in ribbon-shaped carbon fibers [9].

Table 1

Spinning conditions of sets of ribbon fibers used in this project (Note: Extension ratio  $\sim 90$ ; Shear rate  $\sim 2000$  1/s; Mesophase ARA 24R 6U21; Mettler softening point  $297.6^\circ\text{C}$ )

Fiber set	Spinning temperature ( $^\circ\text{C}$ )
903-S1	305
212-S1	310
212-S4	315
212-S9	320
903-S4	325

24R-6U10, supplied by Mitsubishi Gas Chemical Company, Mettler softening point =  $297.6^\circ\text{C}$ ) was used to melt spin all fiber sets. All fiber sets were oxidized in air at  $280^\circ\text{C}$  for 30 min and graphitized in an inert atmosphere at  $2400^\circ\text{C}$ . Table 1 lists the spinning conditions and the label for all the five sets.

#### 4. Studying the structure of carbon fibers

The final properties of mesophase pitch-based carbon fibers are controlled by their internal structure. Typically, X-ray measurements such as degree of crystallinity, crystallite size (coherence length,  $L_a$ , and stack height,  $L_c$ ), interplanar spacing,  $d_{002}$ , and degree of preferred orientation, are used to quantify the structure. However, in high thermal conductivity pitch-based fibers highly oriented graphitic crystallinity develops. In these fibers small changes in crystallinity and orientation often translate into large changes in thermal conductivity. Thus, accuracy and

precision must be considered before X-ray measurements are used to construct structure/property relationships.

##### 4.1. X-ray diffraction

Spacing of the graphene planes ( $d_{002}$ ) and crystallite size were measured by performing continuous scans of fiber bundles between two theta values of  $20$  and  $90^\circ$ . The scans were performed on a symmetrical transmission mode with a Scintag XDS diffractometer equipped with a copper X-ray source. A silicon reference material, NIST 640-B, was used to correct angular position and determine the instrumental component of the peak breadth.

The degree of preferred orientation was measured by single filament analysis using beamline X27C at the National Synchrotron Light Source at Brookhaven National Laboratory. Single carbon fibers were mounted on a cardboard holder with either masking tape or cyanoacrylate glue, and the cardboard was then placed on the sample holder. The single filaments were exposed to an X-ray beam with a wavelength of  $1.37 \text{ \AA}$ . A flat plate was exposed, and the image was then digitized and analyzed using the image analysis software IMAGE TOOL<sup>®</sup>. The data were curve-fit using the software PEAKFIT<sup>®</sup> to determine the full-width-half-maximum (FWHM) or Z-value. Approximately ten single fibers from each set were examined using this method to obtain an average Z-value.

##### 4.2. Scanning electron microscopy

A Jeol JSM-IC 848 scanning electron microscope was utilized to observe the gross textural features of fractured cross-sections of all fiber types and to identify defects. Carbon fibers were mounted on aluminum stubs and

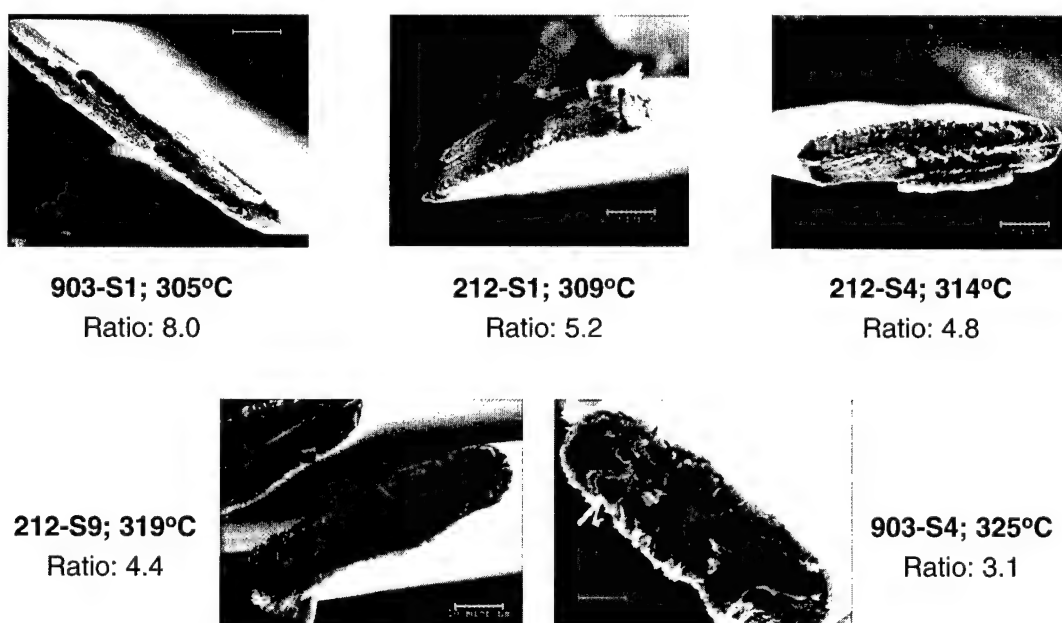


Fig. 4. Aspect ratio and texture of graphitized ribbon-shaped carbon fibers, spun at different temperatures.

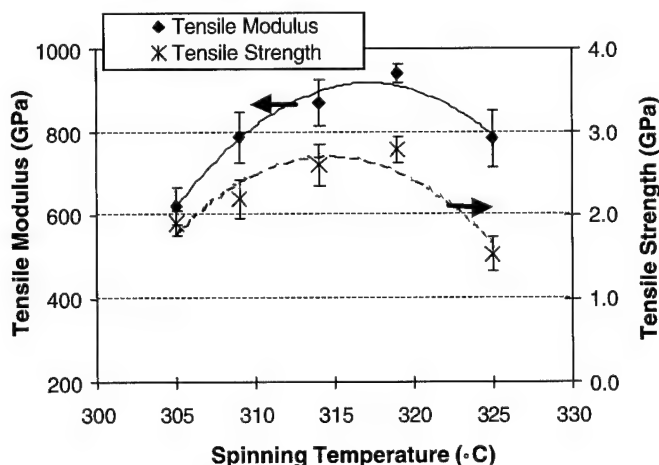


Fig. 5. Tensile modulus and tensile strength versus spinning temperature.

gold-coated using an Antech Hummer X sputter coater. The SEM was operated in the secondary electron imaging (SEI) mode at an accelerating voltage of 15 kV. For detailed procedure see Robinson et al. [12].

## 5. Properties of carbon fibers

The mechanical, electrical and thermal properties of all fiber sets were measured by standard single-filament testing techniques.

### 5.1. Mechanical properties

The mechanical properties of the ribbon fibers were measured by single-filament testing, according to ASTM standard D3544-76 procedure, using an Instron Model TM tensile-testing machine. The system compliance correction factor was calculated using tensile data obtained by testing fibers at 15, 25 and 35 mm gauge lengths; a constant gauge length of 25 mm was subsequently used for all testing. About fifty single filament tests were conducted to estimate the average tensile strength and modulus for each set. The cross-sectional area of each ribbon fiber (needed for both mechanical properties and electrical resistivity measurements), was determined using a mounting and image analysis procedure described elsewhere [13].

### 5.2. Electrical resistivity

The electrical resistivity of all fiber sets was determined using a four-point probe technique [14]. Approximately 30 single filaments were measured from each set to estimate the average electrical resistivity of the set.

### 5.3. Thermal conductivity

Because of their small size, measuring the thermal conductivity of carbon fibers is difficult and time

consuming. The high values of thermal conductivity, combined with the geometry of the sample ( $L/A \geq 10^7 \text{ m}^{-1}$ ), results in an extremely small conductance,  $C$ . Because of these complications, conventional thermal conductivity measurement techniques cannot be used [15]. However, two techniques for measuring the thermal conductivity of carbon fibers are currently available. The first method, Angstrom's apparatus, measures a fiber sample's thermal response to an oscillating heat input. The second method, the thermal potentiometer, measures a fiber sample's thermal response to a controlled thermal gradient. The Angstrom's apparatus is located at the R&D facilities of BP-Amoco in Alpharetta, GA. The thermal potentiometer is located at the University of Louvain-la-Neuve in Belgium. Description of these two methods and the procedures followed to measure the thermal conductivity is given by Gallego et al. [16].

## 6. Results and discussion

After final heat treatment the effect of spinning

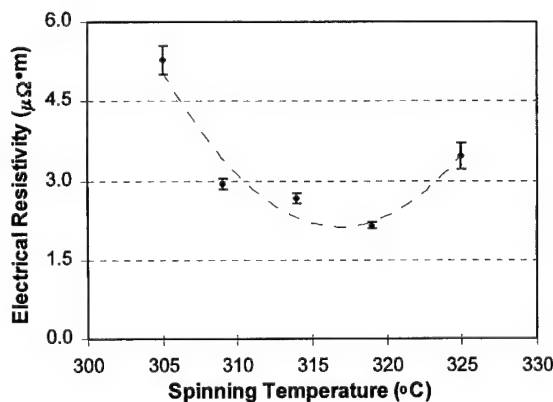


Fig. 6. Electrical resistivity versus spinning temperature.



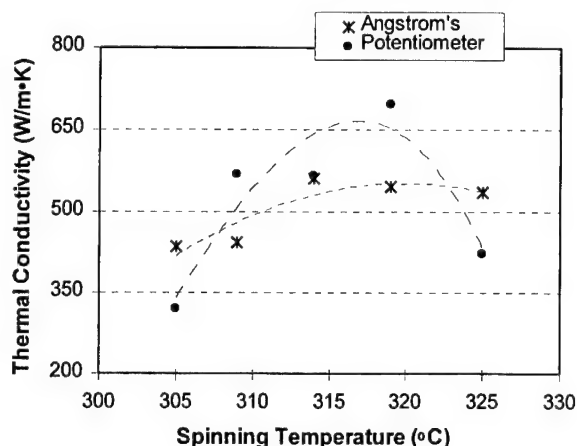


Fig. 7. Room-temperature thermal conductivity versus spinning temperature.

temperature on fiber shape, texture, mechanical properties, and thermal properties were evaluated.

#### 6.1. Effect of spinning temperature on fiber aspect ratio and texture

SEM photographs of the five sets of ribbon fibers used in this project are shown in Fig. 4. Although all fiber sets were extruded through the same capillary with an aspect ratio of 9:1, Fig. 4 shows that the aspect ratio of the graphitized fibers decreases as spinning temperature increases. As temperature increases, the viscosity of mesophase decreases and allows for more time to relax once it exits the capillary in fiber form. At the highest spinning temperature (325°C) the mesophase degrades, as indicated by the voids in the fiber. The line-origin texture also appears more pronounced as the spinning temperature increases. However, this may be merely due to increased thickness of the fiber at higher temperatures.

#### 6.2. Effect of spinning temperature on mechanical properties

The tensile strength and tensile modulus of all five sets of ribbon fibers is plotted against spinning temperature in Fig. 5. Both properties increase initially as spinning temperature is increased until they reach a maximum. Then, further increase in temperature causes a decrease in mechanical properties. However, this decrease in the tensile strength is greater than the decrease in tensile modulus.

#### 6.3. Effect of spinning temperature on electrical resistivity

Similarly, electrical resistivity decreases rapidly as spinning temperature increases until it reaches a minimum. Then, the electrical resistivity increases with additional increases in spinning temperature, as shown in Fig. 6.

#### 6.4. Effect of spinning temperature on thermal conductivity

Fig. 7 shows the room-temperature thermal conductivities of all fiber sets, as measured by the Angstrom's apparatus and the thermal potentiometer. The thermal potentiometer measurements show a more pronounced effect of spinning temperature on thermal conductivity, compared to measurements made with the Angstrom's apparatus. An analysis of the experimental errors involved in both techniques [17] indicates that data from the thermal potentiometer are more accurate; therefore, the effect of spinning temperature probably is dramatic.

#### 6.5. Effect of spinning temperature on fiber structure

Fig. 8 shows spinning temperature versus both, Z-value and  $d_{002}$  spacing. The Z-value represents the misorientation angle which is a measurement of the degree of preferred orientation of the crystallites within the fibers with respect to the fiber axis. The  $d_{002}$  spacing measures the spacing of the graphene planes within the crystallite. It can be observed

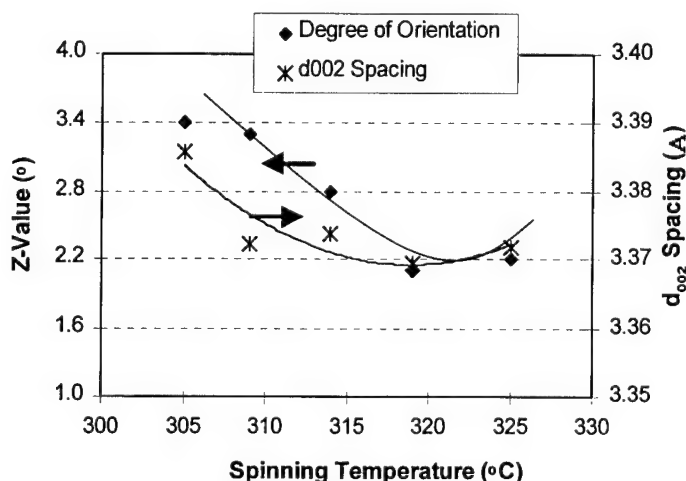


Fig. 8. Z-value and  $d_{002}$  spacing versus spinning temperature.

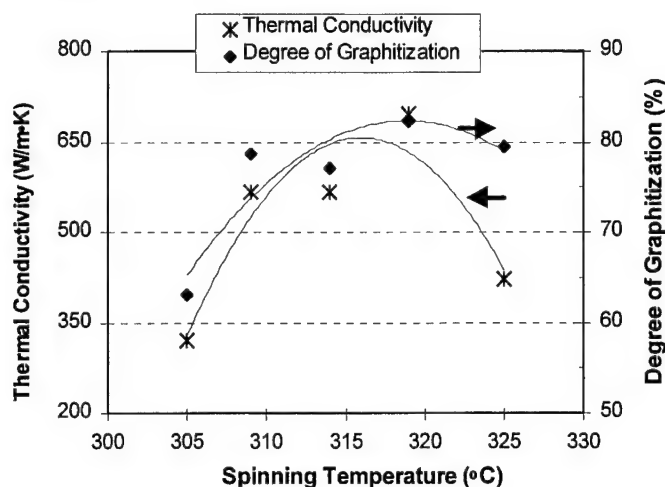


Fig. 9. Effect of spinning temperature on degree of graphitization and thermal conductivity.

that these two parameters decrease as spinning temperature increases, reflecting the development of a more ordered structure within the fiber. As these two parameters reach a minimum, further increase in spinning temperature causes them to increase.

#### 6.6. Structure versus final properties

Fig. 9 shows how both, thermal conductivity (measured by thermal potentiometer) and degree of graphitization vary with spinning temperature. Degree of graphitization ( $g_p$ ) is related to the spacing of the graphene planes ( $d_{002}$ ) by:

$$g_p = [(3.44 - d_{002}) / (3.44 - 3.35)]100, \quad (1)$$

where 3.44 Å is the spacing of the turbostratic graphite and 3.35 Å is the spacing of crystal graphite.

Initially, thermal conductivity and degree of graphitization increase as spinning temperature increases until both reach a maximum. Then, any additional increase in spinning temperature causes a decrease in thermal conductivity and degree of graphitization. However, the degree of graphitization decreases more dramatically than the thermal conductivity.

## 7. Conclusions

The molecular orientation the mesophase pitch can be improved by changing the shape of the capillary used to melt-spin fibers and this can translate into lower graphitization temperature and production cost. Ribbon fibers can develop excellent transport and mechanical properties at lower graphitization temperatures than commercial round fibers.

Mechanical and physical properties of ribbon-shaped carbon fibers improve as spinning temperature increases until they reach a maximum. These properties then begin to decrease with additional increases in spinning temperature.

## Acknowledgements

The work was supported primarily by the ERC Program of the National Science Foundation under Award Number EEC-9731680. A portion of the research was funded by the Office of Naval Research project on high thermal conductivity carbon fibers (Contract No. N0014-95-1-1345). The authors would also like to thank Drs Chris Levan and Girish Deshpande for permitting us access to the Angstrom's apparatus at BP-Amoco and Prof. Jean-Paul Issi and Dr Bernard Nysten for allowing us to use the thermal potentiometer at the University of Louvain-la-Neuve in Belgium. Finally, thanks are also due to Dr David Anderson of the University of Dayton Research Institute for his expertise and assistance in obtaining the single-filament X-ray data and to the National Synchrotron Light Source at the Brookhaven National Laboratory for access to the high energy beam used in these experiments.

## References

- [1] Brooks JD, Taylor GH. Formation of graphitizing carbons from the liquid phase. *Carbon* 1965;3:185–93.
- [2] Endo M. Structure of mesophase pitch-based carbon fibers. *J Mater Sci* 1988;23(2):598–605.
- [3] Edie DD, Dunham MG. Melt-spinning pitch-based carbon fibers. *Carbon* 1989;27(5):647–55.
- [4] Otani S, Oya A. Process of pitch-based carbon fibers in Japan. *ACS Symp Ser* 1986;303(22):323–34.
- [5] Mochida I, Yoon SH, Korai Y. Control of transversal texture in circular mesophase pitch-based carbon fiber using non-circular spinning nozzles. *J Mater Sci* 1993;28:2331–6.
- [6] Wang L, Rey AD. Pattern selection mechanism in mesophase carbon fibres. *Model Simul Mater Sci Engng* 1997;5:67–77.
- [7] Matsumoto T. Mesophase pitch and its carbon fibers. *Pure Appl Chem* 1985;57(11):1553–62.
- [8] Nazem FF. U.S. Patent 4,480,977. Apparatus for controlling the cross-sectional structure of mesophase pitch derived fibers, 1984.

- [9] McHugh JJ. The development of orientation in mesophase pitch during fiber formation. PhD dissertation, Clemson University, Clemson SC, 1994.
- [10] Edie DD, Fox NK, Barnett BC, Fain CC. Melt-spun non-circular carbon fibers. *Carbon* 1986;24(4):477–82.
- [11] Edie DD, Fain CC, Robinson KE, Harper AM, Rogers DK. Ribbon-shaped carbon fibers for thermal management. *Carbon* 1993;31(6):941–9.
- [12] Robinson KE, Edie DD. Microstructure and texture of pitch-based ribbon fibers for thermal management. *Carbon* 1996;34(1):13–36.
- [13] Edie DD, Fain CC, Robinson KE, Harper AM, Rogers DK. Ribbon-shape carbon fibers for thermal management. *Carbon* 1993;31(6):941–9.
- [14] Coleman LB. Technique for conductivity measurements on single crystals of organic materials. *Rev Sci Instrum* 1975;46(8):1125–6.
- [15] Piraux L, Issi JP, Coopmans P. Apparatus for thermal conductivity measurements on thin fibres. *Measurement* 1987;5(1):2–5.
- [16] Gallego NC, Edie DD, Nysten B, Issi JP, Treleven JW, Deshpande GV. The thermal conductivity of ribbon-shaped carbon fibers. *Carbon* 2000;38(7):1003–10.
- [17] Gallego NC. Transport properties of ribbon-shaped carbon fibers: property–structure relationship. PhD thesis, Clemson University, Clemson SC USA, 2000.

## Processing and characterization of barium zirconate coated alumina fibers/alumina matrix composites

M. Koopman\*, S. Duncan, K.K. Chawla, C. Coffin

*Department of Materials and Mechanical Engineering, University of Alabama at Birmingham, 1150 10th Avenue South, Birmingham, AL 35294, USA*

### Abstract

In an earlier work, we identified barium zirconate,  $\text{BaZrO}_3$ , as a candidate material for interfacial coating for alumina fiber/alumina matrix composites. That work involved making laminates of barium zirconate and alumina. During processing at  $1475^\circ\text{C}$ , the alumina and barium zirconate reacted to form a series of thermally stable layers, which led to crack deflection, mainly at the  $\text{BaZrO}_3/\text{ZrO}_2$  interface. In the present work, a sol–gel method was used to apply a barium zirconate coating to alumina fibers (Saphikon™ and Nextel™ 610). The coated fibers were embedded in alumina powder and hot pressed at  $1400^\circ\text{C}$  at 24 MPa for 30 min to produce alumina fiber/alumina matrix composites. Indentation cracks were produced on polished cross sections to investigate the potential for crack blunting and/or deflection. Scanning electron microscopy with energy dispersive X-ray analysis and optical microscopy were used to characterize the coatings. © 2001 Elsevier Science Ltd. All rights reserved.

**Keywords:** Ceramic matrix composites; Interface/interphase; Alumina fiber

### 1. Introduction

High temperature structural applications require strength, fracture toughness, thermodynamic stability, and in the case of an oxidizing environment, oxidation resistance. An example of such an application would be the lining for a high temperature turbine combustion chamber. Oxide fiber/oxide matrix composites have the potential of meeting the required properties. Oxide ceramics have high strength and are inherently stable in oxidizing environments. The primary obstacle to the use of such materials is their lack of toughness.

Interface engineering of component interfaces in ceramic–ceramic composites has been shown to be an effective method for increasing fracture toughness [1–3]. The basic premise is to obtain a “weak interface” between matrix and fiber, which will enable toughening mechanisms, such as crack deflection and fiber pullout to operate [4]. Examples of coatings, which have been used, include C and BN, which have easy cleavage planes. These coatings, however, are susceptible to oxidation at elevated temperatures. To overcome this obstacle, various stoichiometric oxide coatings, which produce weak interfaces, have been developed.

Examples of such coatings include  $\text{SnO}_2$  [5–7] and  $\text{LaPO}_4$  [8–11]. Both of these coatings are chemically inert with respect to common alumina-based fibers and matrices.

Recently, Gladysz et al. [12] discovered that reactions occurred at the interfaces in  $\text{Al}_2\text{O}_3/\text{BaZrO}_3$  laminates to form a series of interphase compounds between the two laminae, specifically,  $\text{ZrO}_2$ ,  $\text{BaO}\cdot\text{Al}_2\text{O}_3$  and  $\text{BaO}\cdot 6\text{Al}_2\text{O}_3$ . Fig. 1 shows a transmission electron microscope image of the reaction zones, X-ray spectra of the reaction zones and electron diffraction patterns from two of the reaction zones. The resulting interfaces between the various reaction zones were sharp, and showed evidence of being weak enough to allow for crack deflection and delamination during three-point bend tests (Fig. 2). Microstructural analysis showed that the  $\text{BaZrO}_3/\text{ZrO}_2$  interface was the most likely to deflect cracks [12]. The current work seeks to apply the  $\text{Al}_2\text{O}_3/\text{BaZrO}_3$  reactivity to an  $\text{Al}_2\text{O}_3$  fiber/ $\text{Al}_2\text{O}_3$  matrix composite, with  $\text{BaZrO}_3$  applied as an interphase coating to the fibers. The resulting interfaces after hot pressing are characterized and their ability to deflect cracks is examined.

### 2. Materials and experimental procedure

Alumina fibers for this study included both Saphikon™ and Nextel™ 610. The matrix was comprised of high purity,

\* Corresponding author. Tel.: +1-205-934-1545; fax: +1-205-934-8485.

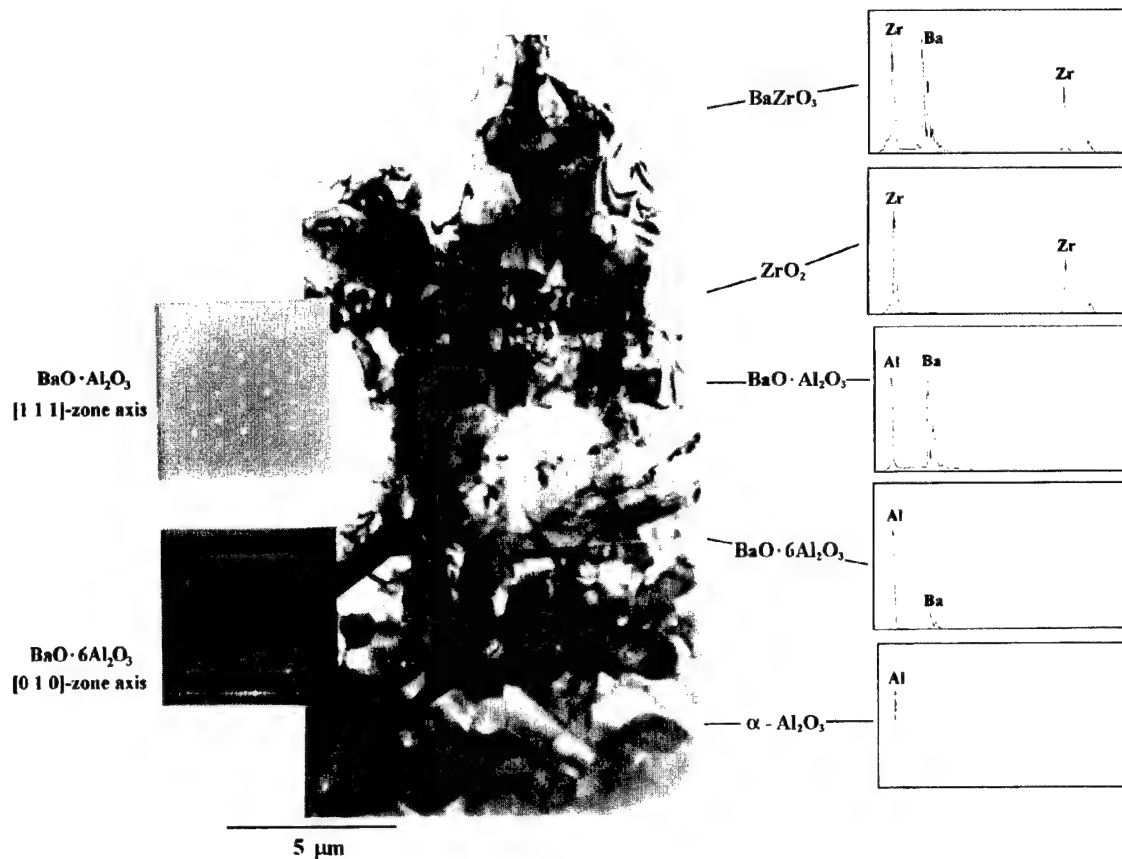


Fig. 1. Transmission electron microscope image of the reaction zones in a laminate structure of hot pressed  $\text{Al}_2\text{O}_3/\text{BaZrO}_3$ . Energy dispersive X-ray spectra of the reaction zones and electron diffraction patterns from the  $\text{BaO}\cdot\text{Al}_2\text{O}_3$  and  $\text{BaO}\cdot 6\text{Al}_2\text{O}_3$  phases contributed to identification of reaction zones present [12].

sub-micrometer alumina powder. Saphikon™ is a relatively large diameter ( $75\text{ }\mu\text{m}$ ), single crystal alumina fiber, while Nextel™ 610 is a small diameter ( $10\text{--}15\text{ }\mu\text{m}$ ), polycrystalline fiber.

Two approaches were investigated for coating the alumina fibers. A sol of barium isopropoxide and zirconium isopropoxide, obtained commercially, was used as the precursor. Ambient humidity was sufficient to

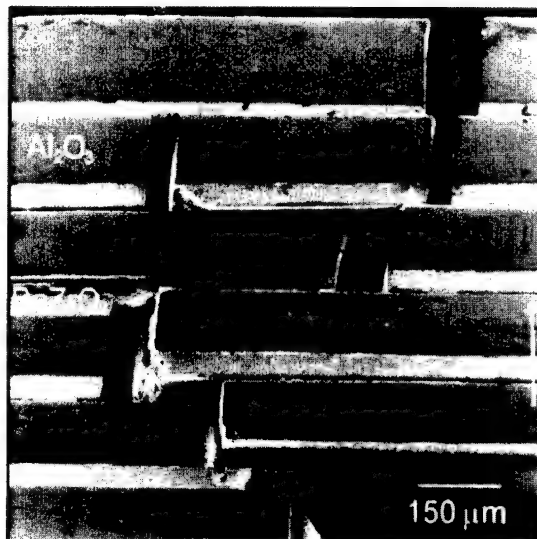


Fig. 2. Fracture path in a  $\text{Al}_2\text{O}_3/\text{BaZrO}_3$  laminate composite from a 3-point bend test, indicating crack deflection at the interfaces.

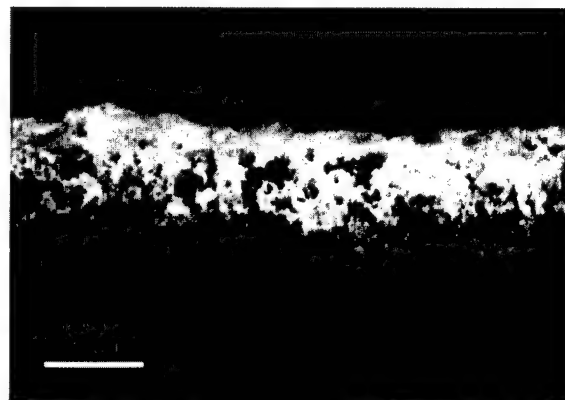


Fig. 3. The metal alkoxide technique after calcining yielded a rough coating surface with areas of uncoated fiber.

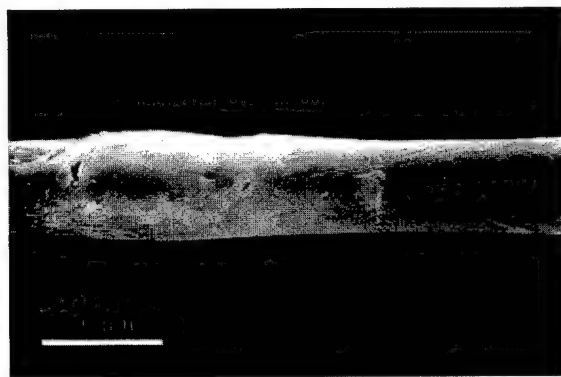


Fig. 4. The colloidal dispersion technique after calcining showed a smoother surface and more continuous coating than the metal alkoxide sol-gel techniques.

hydrolytically initiate the gel process. Fibers were dipped between 5 and 15 times to obtain variations in coating thickness. Coated fibers were heated at 3°C/min to 70°C for 1 h to drive off alcohol, to 120°C for dehydration and, finally, to 1000°C for 1 h to drive off organic compounds and increase adherence of the coating to the fiber through sintering.

A second process for coating the fibers involved a colloidal dispersion technique. Acetic acid (200 ml) was stirred continuously with methanol (200 ml) and heated to 70°C and barium acetate (38.3 g) was added. *N*-propanol (65 ml) containing 70% zirconium-*n*-propoxide was added to this solution and then poured into an open container for evaporation, until the gel appeared dry. The gel was then rehydrated and fibers were dipped 5–10 times. The dipped fibers were then calcined at 800°C for 1 h.

Coated fibers were placed in alumina powder, surrounded by BN coated Grafoil within a graphite die and hot-pressed under vacuum. Temperatures of 1350 and 1400°C, uniaxial pressures from 24 to 45 MPa and hot press hold times at temperature from 0.5 to 1 h were investigated. A heating rate of 15°C/min was used and the cooling rate was 50°C/min.

Samples were sectioned by diamond wafering, cold mounted, polished and Vickers indentations were made with 9.8 N load for 12 s to produce cracks. The samples were then prepared for scanning electron microscopy by Au–Pd sputter coating. A Philips 515 SEM, equipped with a Fison's light element energy dispersive X-ray system, EDX, was used for observing the microstructure and crack propagation paths, as well as identifying the constituent elements within the various reaction zones.

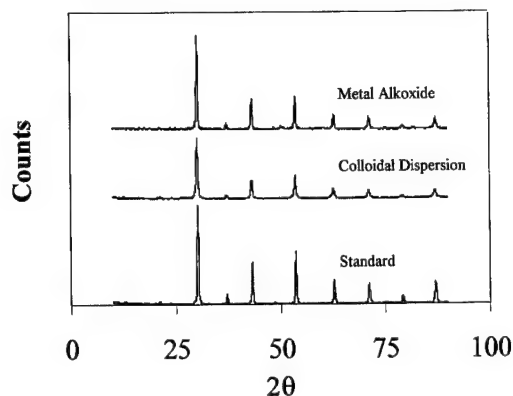


Fig. 5. X-Ray diffraction spectra from the metal alkoxide and colloidal dispersion sol-gels after calcining heat treatments, as well as a commercial high purity BaZrO<sub>3</sub> powder used as a standard. All three spectra showed a BaZrO<sub>3</sub> crystal structure.

dal dispersion sol-gel techniques after a calcining heat treatment are shown in Figs. 3 and 4. The metal alkoxide technique yielded a rough coating surface with areas of uncoated fiber. The colloidal dispersion technique showed greater promise, with a smoother and more continuous coating. Unused gel was put through the calcining heat treatment and X-ray diffraction showed BaZrO<sub>3</sub> structure for both sol-gel techniques (Fig. 5).

The goal of forming all three reaction zones between the BaZrO<sub>3</sub> interphase and the alumina matrix, while retaining unreacted BaZrO<sub>3</sub>, has not yet been reached. However, variations in the coating techniques and processing parameters have resulted in promising combinations of reaction zones around the fibers. Fig. 6 shows a partial tow of Nextel 610 fibers with greater than 10 μm of retained BaZrO<sub>3</sub>, as well as EDX analyses indicating BaO·Al<sub>2</sub>O<sub>3</sub> and BaO·6Al<sub>2</sub>O<sub>3</sub>, but lacks a ZrO<sub>2</sub> layer. This sample used the colloidal dispersion sol-gel technique and was hot pressed at 1350°C and 45 MPa for 45 min. An example of the metal alkoxide sol-gel technique resulting in the presence of ZrO<sub>2</sub> in the hot pressed microstructure is given in Fig. 7, and also indicates the presence of BaO·Al<sub>2</sub>O<sub>3</sub>, but lacks any evidence of retained BaZrO<sub>3</sub>.

Crack/coating interactions were studied by the indentation method. Fig. 8 shows a Saphikon fiber with a coating produced via the metal alkoxide precursors and an indentation induced crack propagating along the ZrO<sub>2</sub>/BaO·Al<sub>2</sub>O<sub>3</sub> interface. Similarly, Fig. 9 shows a crack being deflected along the ZrO<sub>2</sub>/6BaO·Al<sub>2</sub>O<sub>3</sub> interface around a Nextel 610 fiber. According to Gladysz et al. [12], the BaZrO<sub>3</sub>/ZrO<sub>2</sub> interface was the most likely to deflect cracks in 3-point bend tests, while interfaces between the other reaction zones might contribute to toughening. The indentation crack interactions with coated fibers in the present study indicate that the potential for toughening exists in this system.

### 3. Results and discussion

Nextel 610 fibers from both the metal alkoxide and colloidal



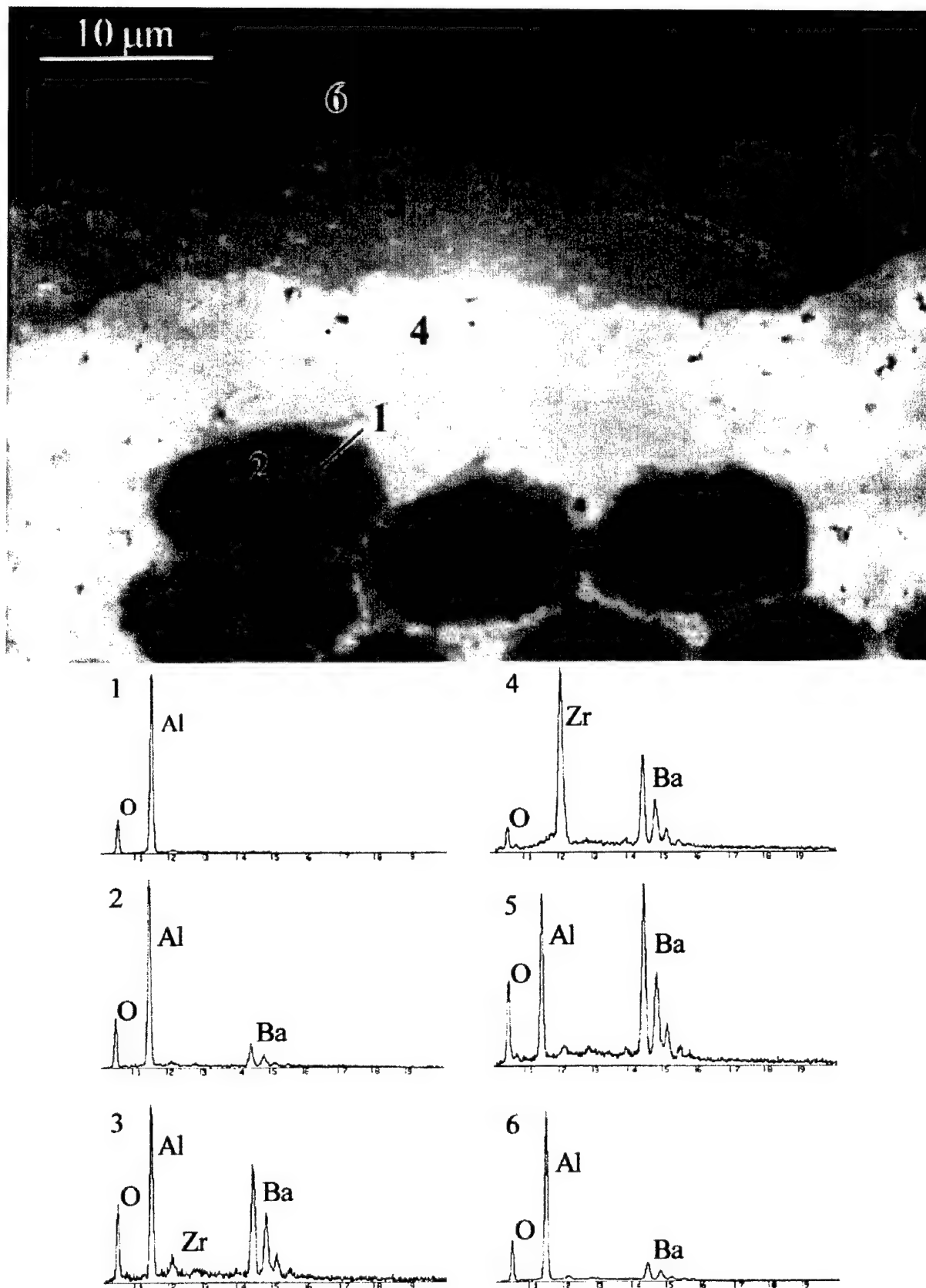


Fig. 6. A partial tow of Nextel 610 fibers with greater than 10 μm of retained BaZrO<sub>3</sub>, as well as EDX analyses indicating BaO·Al<sub>2</sub>O<sub>3</sub> and BaO·6Al<sub>2</sub>O<sub>3</sub>. Note, there is no evidence of a ZrO<sub>2</sub> layer. This sample used the colloidal dispersion sol-gel technique and was hot pressed at 1350°C and 45 MPa for 45 min.

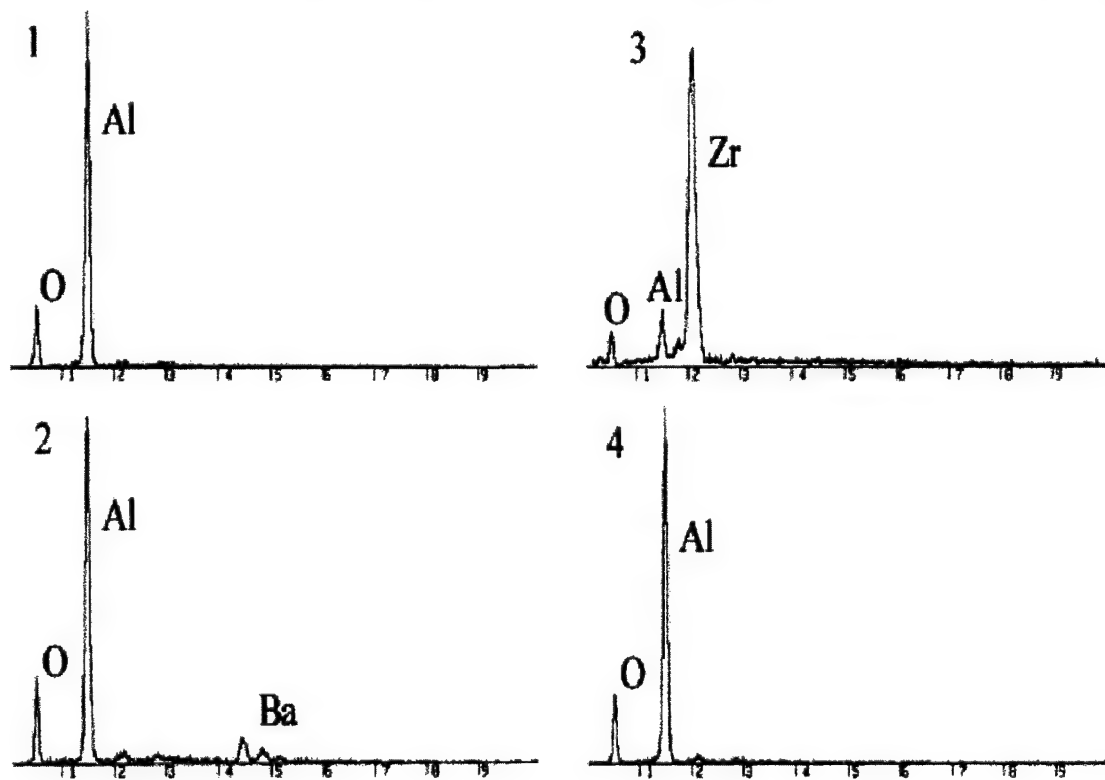
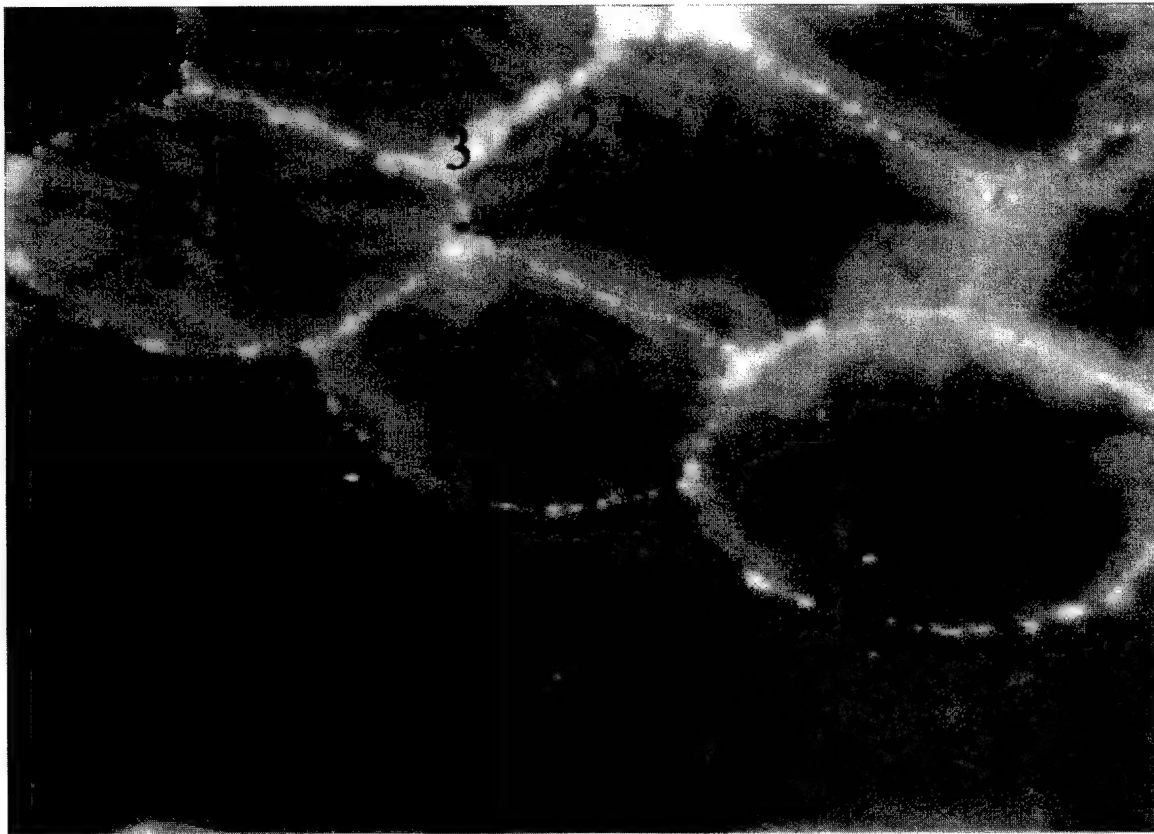


Fig. 7. The metal alkoxide sol–gel technique resulted in the presence of  $\text{ZrO}_2$  in the hot pressed microstructure. The microstructure also indicates the presence of  $\text{BaO} \cdot \text{Al}_2\text{O}_3$ , but lacks evidence of retained  $\text{BaZrO}_3$ . This sample was hot pressed at  $1400^\circ\text{C}$  and 27 MPa for 1 h.

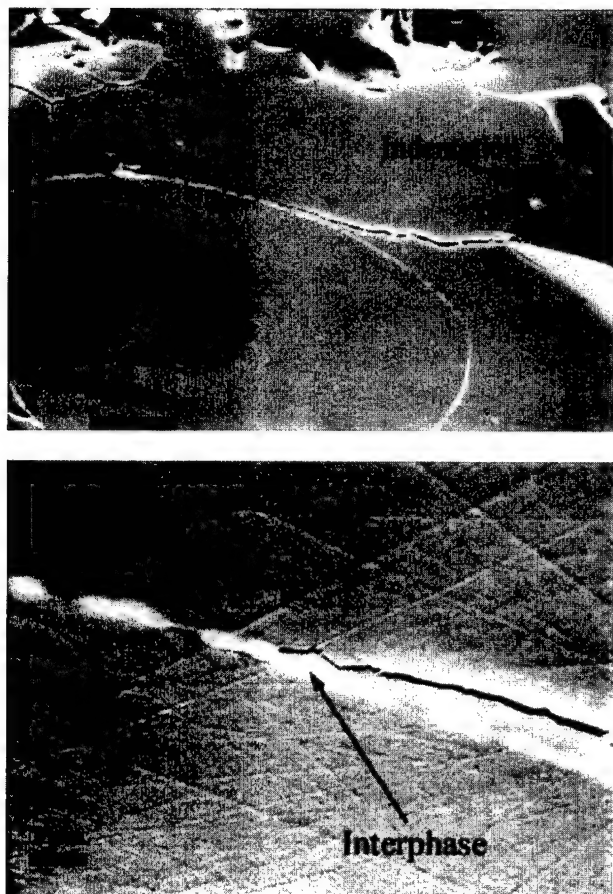


Fig. 8. (a) An indentation induced crack propagated along the  $\text{ZrO}_2/\text{BaO} \cdot \text{Al}_2\text{O}_3$  interface of a Saphikon fiber with a coating produced via the metal alkoxide precursors; (b) higher magnification image of the crack tip showed crack propagation along reaction zone interfaces.

#### 4. Conclusions

Barium zirconate coatings were applied on alumina fibers via sol–gel techniques and the coated fibers were incorporated into an alumina matrix by uniaxial hot pressing. Processing induced reaction zones were observed, however, further work is required to obtain controlled and uniform reaction zone microstructures. Indentation induced crack/reaction zone interactions showed potential for energy dissipating processes, i.e. damage tolerant fracture modes via crack deflection and crack blunting.

#### Acknowledgements

This project was funded by the US Office of Naval

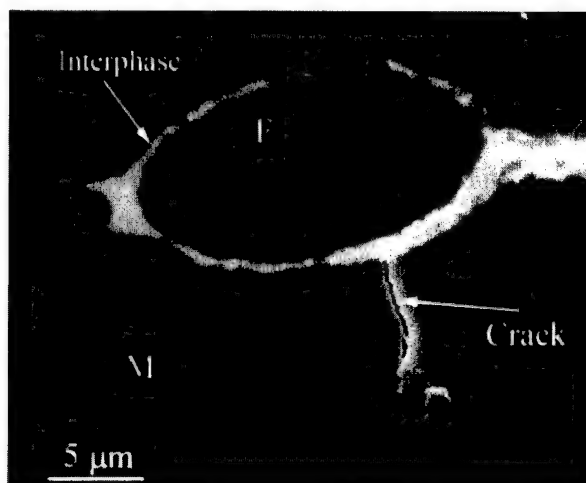


Fig. 9. An indentation induced crack deflected along the  $\text{ZrO}_2/\text{BaO} \cdot 6\text{Al}_2\text{O}_3$  interface around a Nextel 610 fiber coated via the metal alkoxide sol–gel technique.

Research, ONR Contract #N00014-99-1-0909. Dr A.K. Vasudevan and Dr. S.G. Fishman were the Program Managers.

#### References

- [1] Chawla KK. Ceramic matrix composites. London: Chapman and Hall, 1993.
- [2] Faber KT. Ceramic composite interfaces: properties and design. *Annu Rev Mater Sci* 1997;27:499–524.
- [3] Kim JK, Mai YW. Engineered interfaces in fiber reinforced composites. New York: Elsevier, 1998.
- [4] Chawla KK. Composite materials: science and engineering. 2nd ed. New York: Springer, 1998.
- [5] Chawla KK, Ferber MK, Xu ZR, Venkatesh R. Interface engineering in alumina/glass composites. *Mater Sci Engng, A* 1993;162:35–44.
- [6] Chawla KK, Xu ZR, Venkatesh R, Ha JS. Interface engineering in some oxide/oxide composites. Ninth International Conference on Composite Materials, ICCM-9, 1994. p. 788–95.
- [7] Maheshwari A, Chawla KK, Michalske TA. Behavior of interface in alumina/glass composite. *Mater Sci Engng, A* 1989;107:269–76.
- [8] Morgan PED, Marshall DB. Functional interfaces for oxide/oxide composites. *Mater Sci Engng, A* 1993;107:15–25.
- [9] Morgan PED, Marshall DB. Ceramic Composites of Monazite and Alumina. *J Am Ceram Soc* 1995;78:1553–63.
- [10] Morgan PED, Marshall DB. High-temperature stability of monazite-alumina composites. *Mater Sci Engng, A* 1995;195:215–22.
- [11] Chawla KK, Liu H, Janczak-Rusch J, Sambasivan S. Microstructure and properties of monazite ( $\text{LaPO}_4$ ) coated Saphikon fiber/alumina matrix composites. *J Eur Ceram Soc* 2000;551–9.
- [12] Gladysz GM, Schmücker M, Chawla KK, Schneider H, Joslin DL, Ferber MK. Dynamic formation of multiple barium aluminate-zirconia interface layers in alumina/alumina sandwich composites. *Mater Char* 1998;40:209–14.

# Material phenomena controlling rapid processing of thermoplastic composites

P.-E. Bourban, N. Bernet, J.-E. Zanetto, Jan-Anders E. Månson\*

*Laboratoire de Technologie des Composites et Polymères (LTC), Département des Matériaux, Ecole Polytechnique Fédérale de Lausanne (EPFL),  
MX Ecublens, CH-1015 Lausanne, Switzerland*

Received 6 September 2000; accepted 11 December 2000

## Abstract

Driven by the need for more cost-effective applications, researchers and design engineers of polymer composites are facing increasing demands for the development of faster and more environment-friendly processing methods. Rapid processing techniques require a better understanding and a more efficient control of phenomena such as heating, impregnation, bonding and solidification. Most of the new techniques promote non-isothermal and transient phenomena in order to achieve faster transformation of the materials. Material physical properties, material microstructure and processing conditions set the theoretical limits for rapid processing. The time scales of the material phenomena controlling the processing of thermoplastic composites are presented. It is shown for example, how novel composite microstructures influence the consolidation time, or how the fusion bonding time can be reduced when non-isothermal conditions are promoted. Furthermore, the application of the results to a novel integrated processing technology illustrates the new potentials of thermoplastic composites.

The description of the phenomena controlling the processing rate is useful, knowing that better tailoring and control of the material transformation, adaptation of the material constituents, and combination of process sequences are intensively required for the development of more efficient manufacturing routes for composites. © 2001 Elsevier Science Ltd. All rights reserved.

**Keywords:** Polymer composites; A. Thermoplastic resin; B. Physical properties; B. Interface interphase

## 1. Introduction

Driving forces for the development of composites have changed during the 1980s and 1990s. Appreciated for their high specific mechanical properties, composite materials are facing new demands for more cost-sensitive production. Reduction of weight and operational costs have been some of the main driving forces for the aerospace industry. Since composites have entered new application areas such as the automotive industry, demand has increased for low-cost materials and rapid processing techniques (Fig. 1), for more functional products, and for large and complex shaped parts [1,2]. At the same time, improved safety, reduction of CO<sub>2</sub> emissions and maximum return on investment capital are some of the important issues directly influencing the development of new composite materials [3]. The transportation industry is driven by reduction in weight and fuel consumption to promote lower gas emissions (Fig. 2) [3]. In this respect, the competition is severe for the implemen-

tation of new aluminium, steel or composite materials. Reduction of system costs by the integration of functions and performance is one of the unique advantages offered by polymers and composites considering their high design freedom and processing flexibility (Fig. 3) [4]. This potential will be fully exploited when complex shapes and short processing cycle times are achieved. Several composite processing techniques are starting to meet automotive production requirements. Sheet moulding compounds (SMC) and resin transfer moulding (RTM) are used for low to medium volume production, while stamping and injection moulding combined with localised placement of composites are currently being evaluated for high volume production [5].

The optimisation of processes for mass production involves the development of new material preforms, the accurate control of all the material transformation steps and an increase in processing efficiency. Processing cycles and related material transformation phenomena depend of course on the material type and composition as well as on the efficiency of the heat transfer between the material and the tools. Figs. 4a and b illustrate the temperature and time

\* Corresponding author. Tel.: +41-21-693-4281; fax: +41-21-693-5880.  
E-mail address: jan-anders.manson@epfl.ch (J.-A.E. Månson).

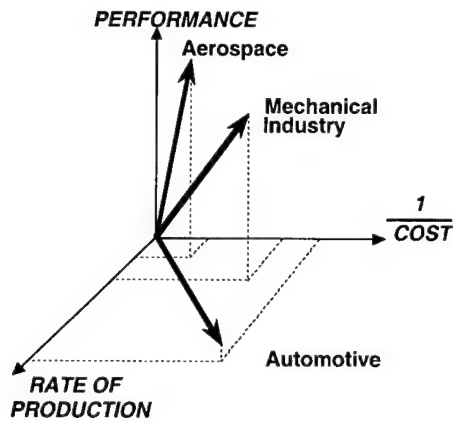


Fig. 1. Industrial sectors and related driving forces for composite materials.

cycles used for processing thermoset and thermoplastic composites. Curing kinetics and related evolution of material viscosity, impregnation kinetics, management of exothermal reactions, and finally heating and cooling strategies determine the cycle times of thermoset composites. Usually the curing chemical reaction is the time-controlling phenomenon. The processing of thermoplastic composites generally requires melting of the polymer, impregnation and then solidification. Consolidation of the composite involves: (i) removal of voids, (ii) intimate contact and healing between yarns and plies, and (iii) solidification and crystallisation when semi-crystalline polymers are involved. Material physical properties, material microstructure and processing conditions determine the time scales of the different phenomena.

Several alternative manufacturing routes have been proposed to produce composite parts. They involve different preform types and forming techniques (Fig. 5) [4]. For example, novel preforms have been developed with tailored microstructures in order to improve impregnation kinetics for thermoplastic composites. An intimate mingling of polymer powder, fibres or films with reinforcement fibres is

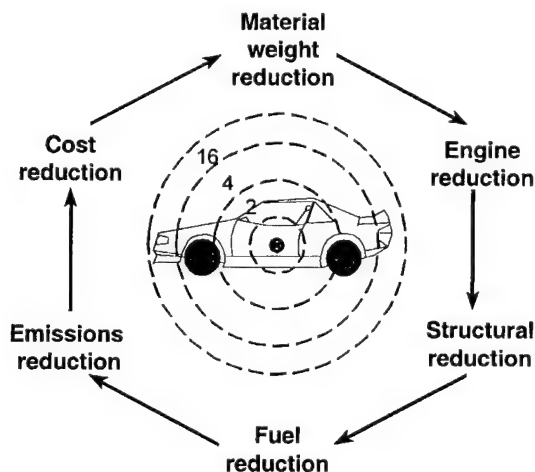


Fig. 2. Driving forces for transportation industry.

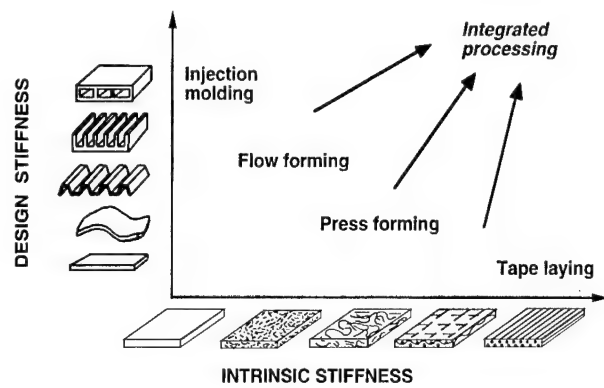


Fig. 3. Design and intrinsic stiffness of polymer composites for different processing techniques.

obtained directly in the preforms which is then consolidated using rapid and low pressure processing techniques. Thermoplastic material systems based on polyamide and polypropylene polymer are used to describe the different material transformation steps and related time scales mentioned in Fig. 4b.

## 2. Impregnation

Although thermoplastic composites offer many advantages over thermoset composites, the use of a thermoplastic matrix generally requires higher temperature and pressure in order to impregnate the fibres during the consolidation stage of the processing cycle (Fig. 4b). These processing constraints result from the high viscosity inherent in fully polymerised thermoplastic resins. The influence of the resin viscosity on the fibre impregnation rate can be analysed by Darcy's law, which is valid for the laminar flow of fluids through homogeneous porous media [6]. For one-dimensional flow, Darcy's law can be written as

$$v = \phi \frac{dL}{dt} = \frac{-K}{\eta} \frac{\partial P}{\partial z} \quad (1)$$

where  $v$  is the superficial velocity of the fluid,  $\phi$  the porosity of the porous medium,  $L$  the flow distance in the  $z$  direction,  $t$  the time,  $K$  the permeability of the porous medium,  $\eta$  the viscosity of the Newtonian fluid, and  $P$  is the pressure. From Eq. (1), the impregnation time can be evaluated as

$$t = \phi \frac{\eta L^2}{2K(P_a + P_c - P_f)} \quad (2)$$

where  $P_a$  and  $P_c$  are the applied pressure and capillary pressure, respectively; while for composite materials  $P_f$  is the pressure carried by the fibres. Eq. (2) shows that one way to obtain a short impregnation time, despite the high viscosity of the thermoplastic resin, is to reduce the flow distance,  $L$ . This has led to the development of intermediate product forms, also called preforms, in which the reinforcement is

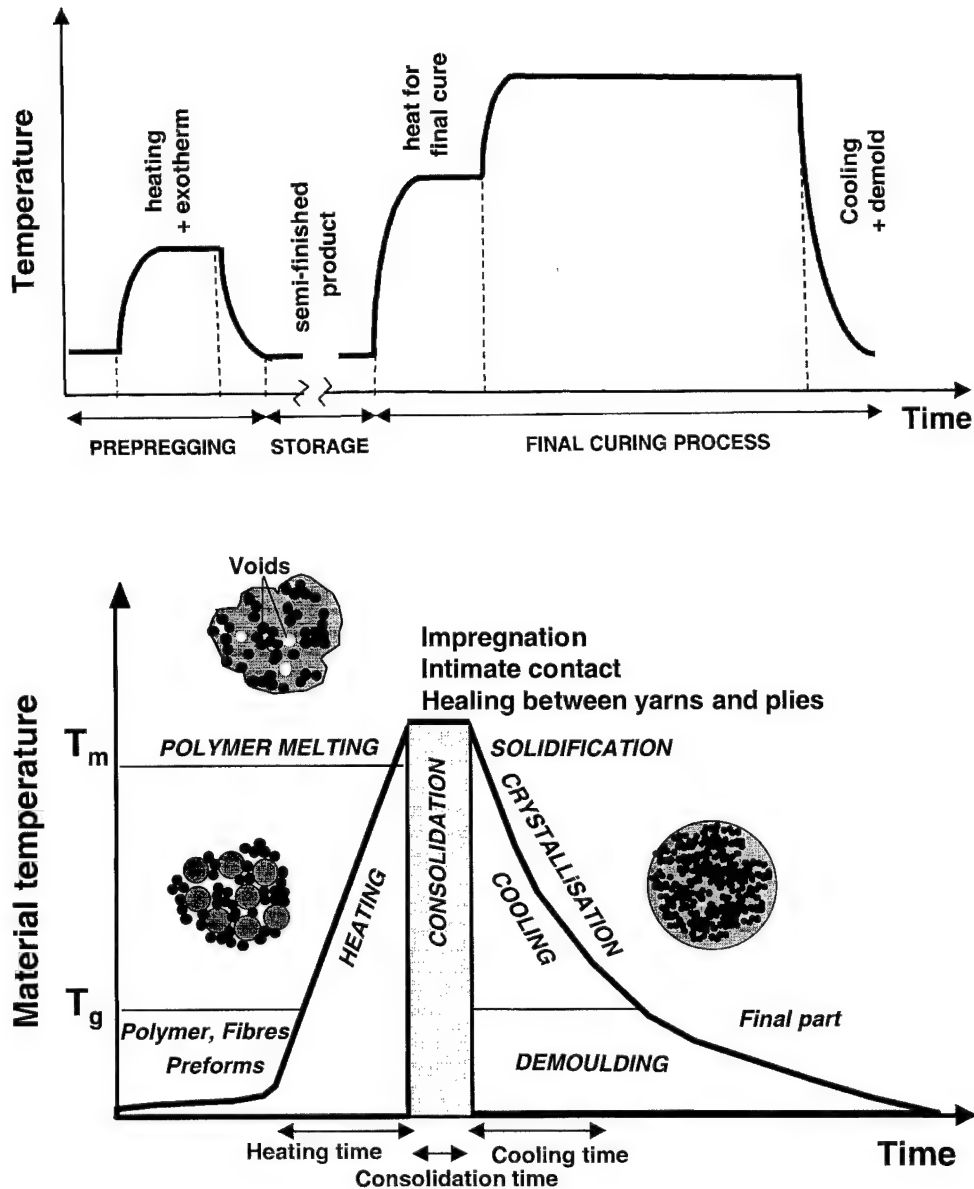


Fig. 4. Typical processing cycle and material transformation phenomena for: (a) thermoset and (b) thermoplastic materials.

already impregnated or intimately mixed with the matrix. Examples of thermoplastic composite preforms are given in Fig. 6. Preforms such as sheath-coated powder-impregnated fibre bundles (known as FIT) and commingled yarns can be converted into drapeable textile fabrics, which can then be shaped and consolidated to produce composite parts of complex geometry [7].

### 2.1. Powder-impregnated tows

A model allowing prediction of impregnation times for powder-impregnated and FIT bundles has been developed by Connor et al. [8,9]. The model assumes that each drop of molten resin powder forms a bridge between adjacent fibres. The model also assumes that all the bridges have a similar

geometry, and that each bridge is in contact with three adjacent fibres, as shown in Fig. 7. During the impregnation process, the externally applied pressure and the capillary forces drive each polymer bridge to spread along the fibres, until all adjacent bridges come into contact. Resin flow transverse to the fibres is presumed to be negligible compared to axial flow. Within these assumptions, the resin flow front velocity during impregnation is calculated as

$$\frac{d}{dt} \left( \frac{l}{L} \right) = \frac{3\pi^2}{8\eta} \left( \frac{R_f^3}{V_0} \right)^2 \left( \frac{v_{ml}}{v_{fl}} \right)^4 \left( \frac{L}{l} \right)^4 (P_a + P_c - P_f) \quad (3a)$$

where the distances  $l$  and  $L$  are defined in Fig. 7,  $R_f$  is the fibre radius,  $V_0$  the initial volume of each resin



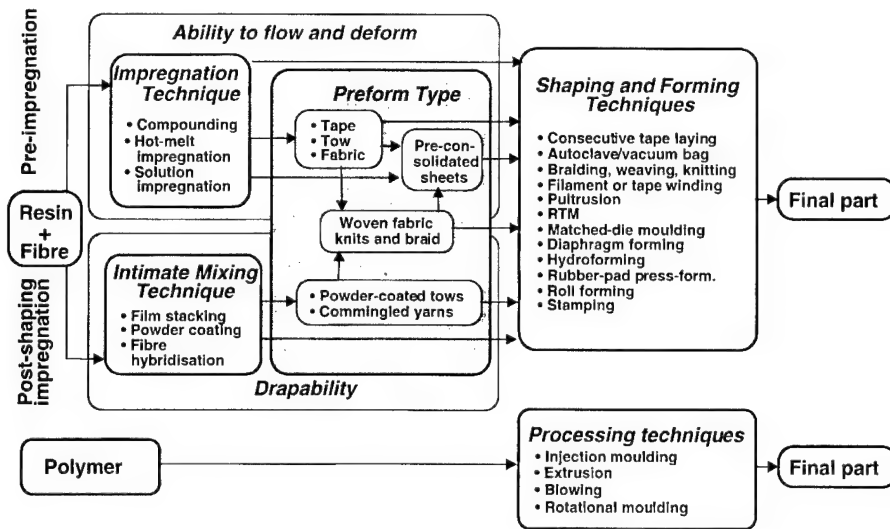


Fig. 5. Manufacturing routes for composite materials.

bridge,  $v_{m1}$  and  $v_{f1}$  the final volume fraction of the matrix and the fibres, respectively,  $P_c$  is the capillary pressure counted as positive when it enhances flow, and  $P_f$  is the pressure carried by the fibre network. When  $P_c$

and  $P_f$  can be neglected in comparison with the applied pressure  $P_a$  and  $V_0$  is expressed with the radius  $R_m$  of the polymer powder particles, the integration of Eq. (3a) leads to the following expression for the impregnation

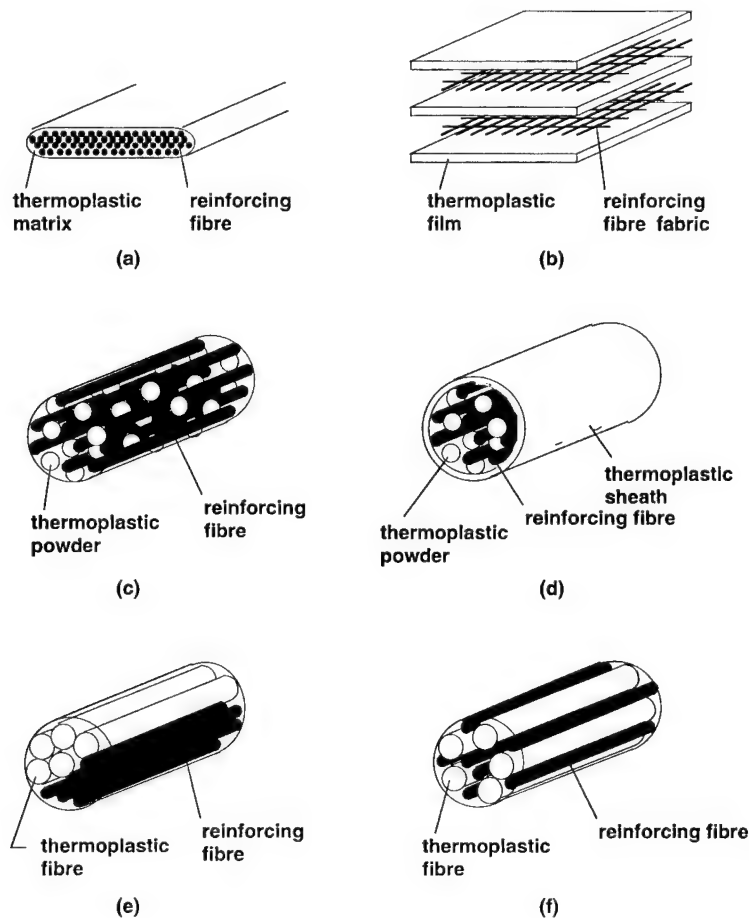


Fig. 6. Intermediate product forms for thermoplastic composites: (a) pre-impregnated tow; (b) film stacking; (c) powder-impregnated fibre bundle; (d) sheath-coated powder-impregnated fibre bundle (FIT); (e) non-commingled yarn; and (f) commingled yarn.

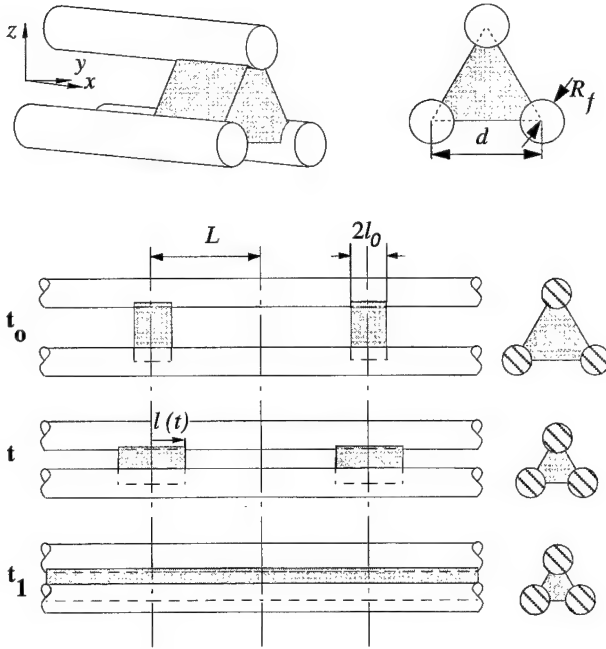


Fig. 7. Modelled geometry of fibre/matrix bridge used to describe impregnation of FIT yarns.

time:

$$t = \frac{128\eta}{135P_a} \left( \frac{v_{fl}}{v_{ml}} \right)^4 \left( \frac{R_m}{R_f} \right)^6 \left[ \left( \frac{l}{L} \right)^5 - \left( \frac{l_0}{L} \right)^5 \right] \quad (3b)$$

The model predicts for example, that for a given viscosity and applied pressure, the impregnation time is mainly controlled by the ratio between the particle and fibre size, and the ratio between the matrix and fibre volume fraction. The void content,  $X_v$ , of a powder-impregnated or FIT bundle at any time during consolidation is calculated from the bridge geometrical parameters as

$$X_v = \frac{1 - (l/L)}{1 + (l/L)(v_{fl}/v_{ml})} \quad (4)$$

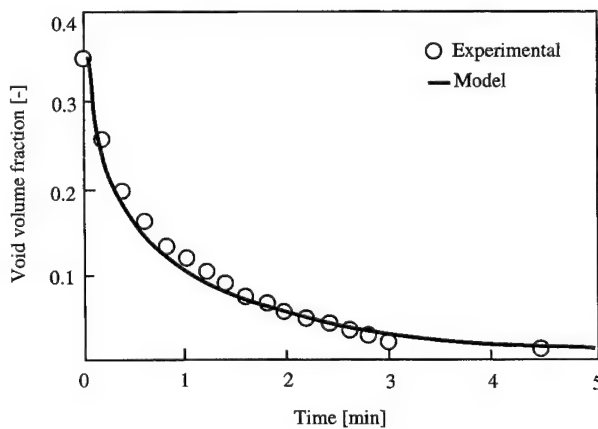


Fig. 8. Consolidation curve for a Carbon/PEEK composite processed at 380°C under a pressure of 5 MPa.

This model was applied to composites made from FIT bundles of several thermoplastic polymers, which were consolidated by matched-die compression moulding. An example is shown in Fig. 8, demonstrating the good agreement between the experimental void content measurements and the model predictions.

## 2.2. Commingled yarns

An impregnation model was also recently developed by Bernet et al. [10] for describing the consolidation of thermoplastic composites made from commingled yarns. This model relies on a geometrical description of the yarn structure. At the onset of impregnation, the latter is depicted as a molten resin pool surrounding cylindrical dry fibre bundles of different diameters, as schematically represented in Fig. 9. Assuming that the resin flows only in the direction transverse to the fibres, and that the impregnation rate obeys Darcy's law, the time increment  $\Delta t$  necessary for the flow front to advance from radial position  $R_i$  to radial position  $r_i$  in a given fibre bundle is determined as

$$\Delta t = \frac{\eta(1 - v_f)}{K(P_a + P_c - P_v(r_i))} \times \left[ \frac{r_i^2}{2} \ln \left( \frac{r_i}{r_0} \right) - \frac{R_i^2}{2} \ln \left( \frac{R_i}{r_0} \right) - \frac{r_i^2}{4} + \frac{R_i^2}{4} \right] \quad (5)$$

where  $v_f$  is the fibre volume fraction of the dry fibre bundle (i.e.  $v_f = 1 - \phi$ ),  $P_v(r_i)$  the internal void pressure varying with the flow front position  $r_i$ , and  $r_0$  is the initial radius of the dry fibre bundle. Assuming that the commingled yarn is composed of a distribution of  $n$  different bundle sizes, a size group  $k$  comprising  $N_b^k$  bundles, the flow front position in each bundle at a given time is related to the total void content of the commingled yarn as follows:

$$X_v = \frac{\sum_{k=1}^n \pi N_b^k r_k^2 (1 - v_f)}{A_t + \sum_{k=1}^n \pi N_b^k r_k^2 (1 - v_f)} \quad (6)$$

where  $A_t$  is the cross-sectional area of the completely consolidated yarn, as indicated in Fig. 9. The accuracy of the model predictions was demonstrated for carbon fibres/polyamide 12 (CF/PA12) composites consolidated by rapid processing techniques, including bladder inflation moulding, integrated processing and stamp forming [7,11]. A comparison between predictions and experimental results is shown in Fig. 10, confirming the validity of the model and the possibility of achieving short consolidation times.

Impregnation and consolidation models are relevant in that they provide useful information on how to tailor the materials and design the preform in order to minimise the residual void content or the consolidation time. For instance, impregnation models derived from Darcy's law indicate that the impregnation time is directly proportional to the resin

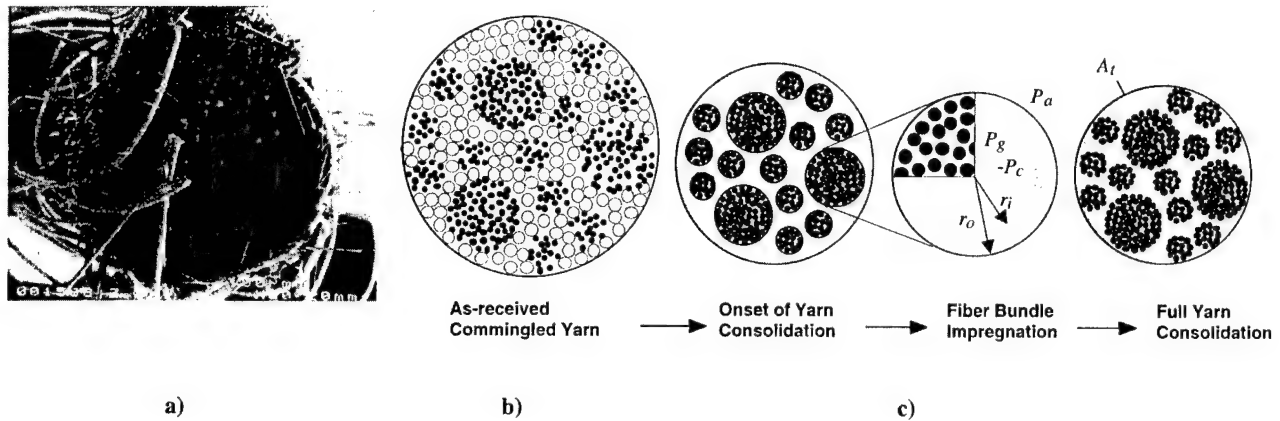


Fig. 9. SEM micrograph of a CF/PA12 commingled yarn (a). Schematic of a commingled yarn fabric (b), of a representative yarn cross-section and the assumed consolidation process (c).

viscosity, which reveals the importance of selecting a resin of low molecular weight. Such models also allow a quantitative analysis of the effects of a variation in powder particle diameter, fibre diameter or fibre/matrix mixing quality. For example, Fig. 11 illustrates the influence of the CF agglomeration size on the consolidation rate of CF/PA12 commingled yarns, showing clearly the advantage of producing yarns with a high degree of commingling. Impregnation models can also be used beneficially to predict the different processing conditions leading to the same void content. As an example, Fig. 12 presents several curves of iso-void content (to 0.1 and 1.0%) for composites made from CF/PA12 commingled yarns. For a chosen processing temperature, the time and pressure conditions must be selected so as to be on the curve in order to obtain the required void content after consolidation. In practice, the optimal processing condition, from among all the suitable combinations defined by the curves of iso-void content, is determined by considering the material and process limitations and the manufacturing cost associated with each condition.

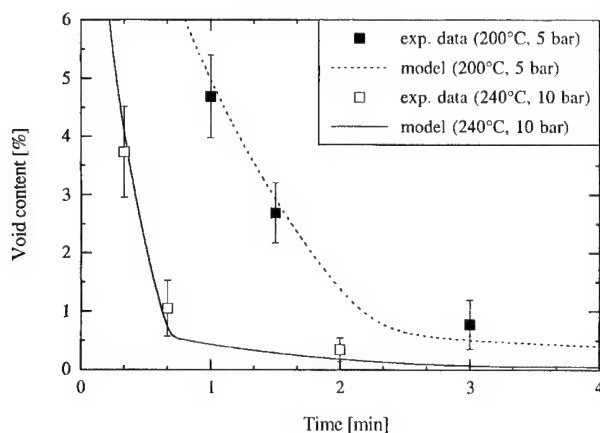


Fig. 10. Variation of void content with consolidation time for tubular braids of CF/PA12 commingled yarns processed by bladder inflation moulding.

### 3. Fusion bonding

Fusion bonding is mainly known for its application in assembling and repairing thermoplastic materials [12,13]. Nevertheless, manufacturing of thermoplastic composites involves fusion bonding processes which take place at different scales in the material structure. Intimate contact and molecular diffusion occur at several interfaces, such as between the different yarns and plies of a laminate or between different elements assembled to form the final part (Fig. 13). The main phenomena controlling the creation of such interfaces are listed in the Fig. 14 on a temperature and time cycle. It is of prime importance for the control and optimisation of the fusion bonding process to investigate the different parameters influencing interfacial intimate contact, interdiffusion and solidification.

An adequate intimate contact between two surfaces to be bonded is mainly provided by wetting and resin flow mechanisms. Due to the roughness of most adherents, geometric rearrangement of the surfaces must take place

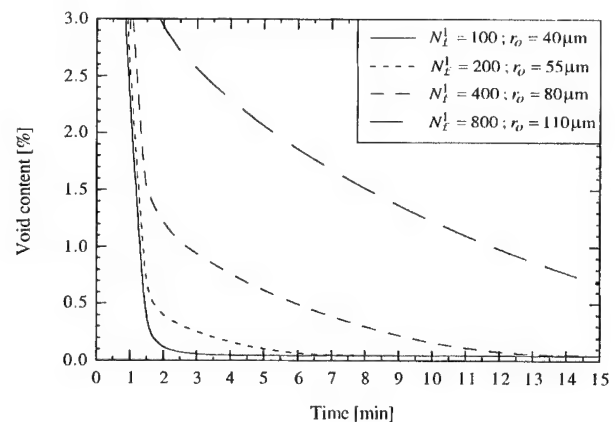


Fig. 11. Effect of reinforcing fibre bundle dimension on consolidation rate of CF/PA12 commingled yarns processed at 210°C under 10 bar, with  $N_f^l$  the number of fibres in the largest bundles and  $r_0$  the corresponding bundle radius.

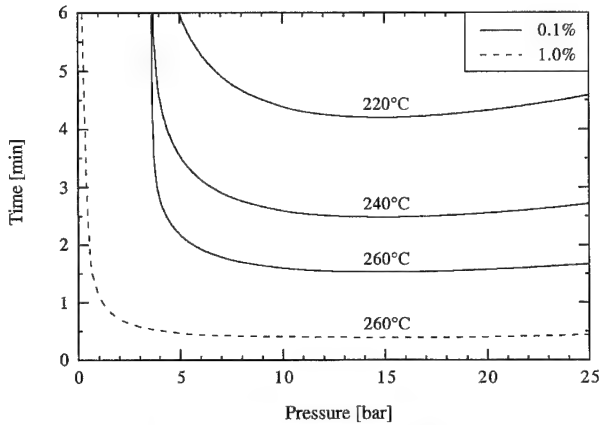


Fig. 12. Predicted combinations of processing parameters leading to a void content of 0.1 or 1.0% after consolidation of CF/PA12 commingled yarns.

by deformation of asperities or resin flow before any physical and chemical interactions can occur at the interface. The first intimate contact models focused on the deformation of the surface asperities which were simulated by rectangular elements. Then, resin squeeze-flow models have been used to model the evolution of the surface roughness as a function of temperature, pressure and material viscosity [14–16].

Using a similar approach and considering the idealised surface roughness given in Fig. 15, the evolution of intimate contact can be expressed by

$$D_{ic}(t) = \frac{f_{ic}(t)}{f_0 + \omega_0},$$

$$D_{ic}(t) = \frac{1}{1 + \omega_0/f_0} \left[ 1 + 5 \left( 1 + \frac{\omega_0}{f_0} \right) \left( \frac{a_0}{f_0} \right)^2 \int_0^{t_p} \frac{P(t)}{\eta(T(t))} dt \right]^{1/5} \quad (7)$$

where  $f_0$  and  $\omega_0$  are geometric parameters defined in Fig. 15 and  $f_{ic}(t)$  is the contact surface at time  $t$ .  $t^p$  represents the

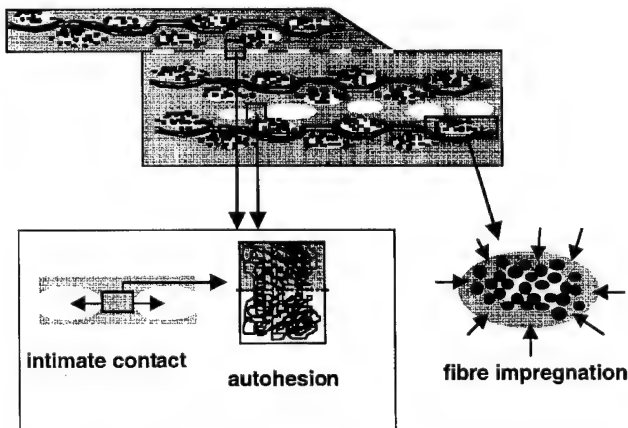


Fig. 13. Fusion bonding processes control the interface between assembled elements, between yarns and plies, and between composite and surface layers.

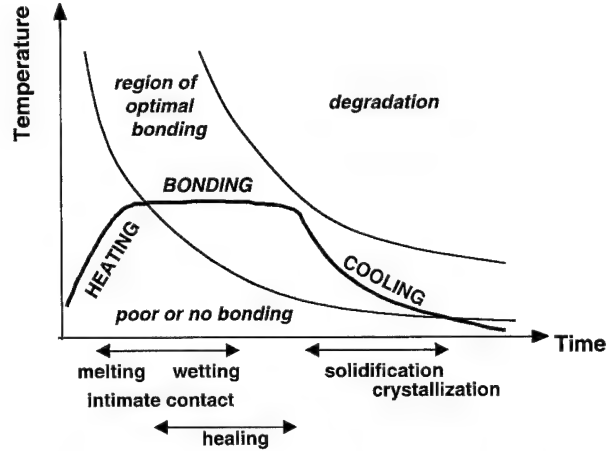


Fig. 14. The different material phenomena controlling the fusion bonding thermal cycle.

time during which the pressure  $P(t)$  is applied,  $\eta(T(t))$  is the material viscosity.

The time to reach a full intimate contact, that is  $D_{ic} = 1$ , can thus be expressed as

$$t_{ic}(T) = \frac{\eta(T)}{5P} \left( \frac{f_0 + \omega_0}{f_0} \right)^{-1} \left( \frac{a_0}{f_0} \right)^{-2} \left[ \left( \frac{f_0 + \omega_0}{f_0} \right)^5 - 1 \right] \quad (8)$$

Such a model illustrates, for example, the importance of

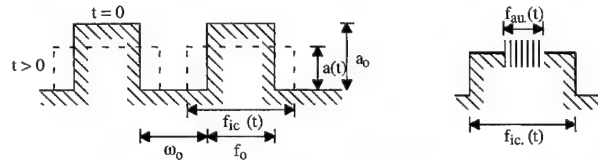


Fig. 15. Intimate contact is modelled by deformation of idealised surface roughness.

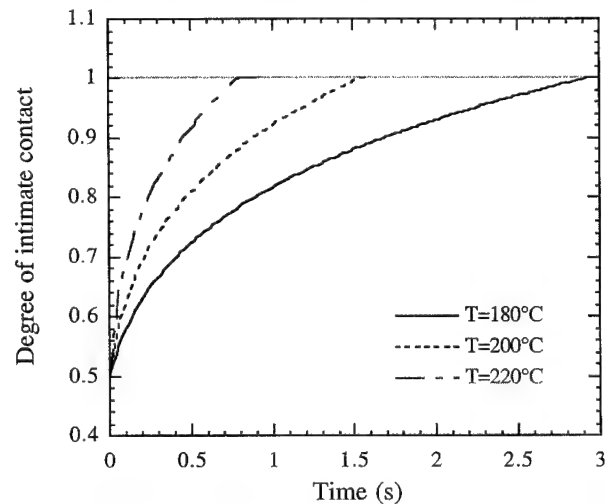


Fig. 16. Evolution of the intimate contact between two plates of polyamide 12 as a function of the interfacial temperature;  $a_0 = 0.69 \mu\text{m}$ ,  $f_0 = w_0 = 14 \mu\text{m}$ ,  $P = 2 \text{ MPa}$ .

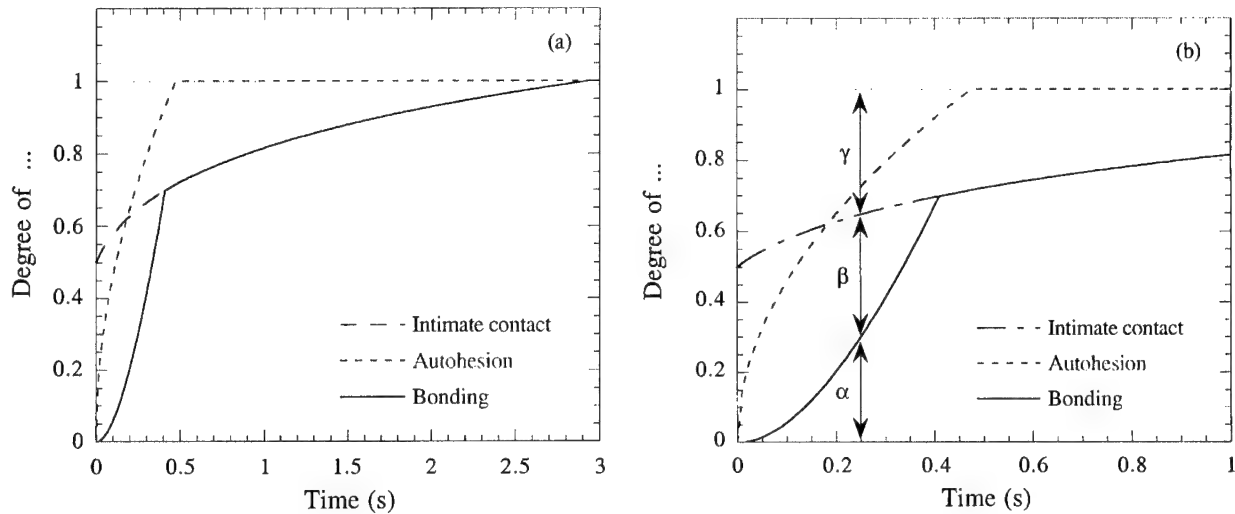


Fig. 17. Degree of progression for intimate contact, autohesion and thus bonding for polyamide 12 at 180°C under 2 MPa of contact pressure.

the temperature dependence of the viscosity on the time scale of the intimate contact mechanisms (Fig. 16). The time can further be reduced by using polymer grades with lower molecular weights.

When a good intimate contact between two compatible adherent surface is established and when temperatures are above the glass transition temperature, the bond strength is mainly determined by the interdiffusion of the polymer chains across the interface. Such healing mechanism has been extensively studied for amorphous polymers [17–20]. On the other hand, semi-crystalline polymers must be maintained at temperatures above their melting temperature in order to promote the formation of efficient bonds. Crystalline structures presumably influence interdiffusion phenom-

ena, and crystallisation mechanisms determine the final interface microstructure. Bonding mechanisms of semi-crystalline polymers are complex and not yet well understood.

As illustrated in Fig. 15, the degree of autohesion, that is the extent of chain interdiffusion between two adherents of the same polymer, can be described by

$$D_{au}(t) = \frac{f_{au}(t)}{f_{ic}(t)} \quad (9)$$

Several works [17,20] have shown that bond strength provided by healing mechanisms can be related to bonding and reptation times by the following equation:

$$D_{au}(t) = \left( \frac{t}{\tau_r} \right)^{1/2} \quad (10)$$

where  $\tau_r$  is the characteristic time to get maximum bond

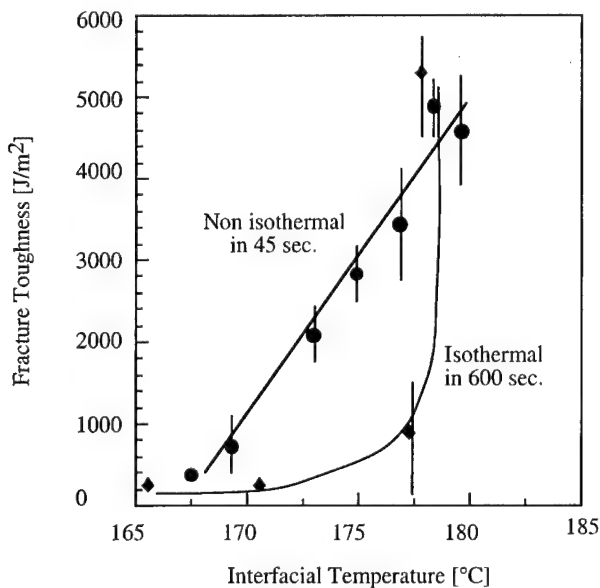


Fig. 18. Bond strengths for iso and non-isothermal bonds of polypropylene as a function of the interface temperature. Bonding times were 40 and 600 s for, respectively, the non-isothermal and isothermal conditions.

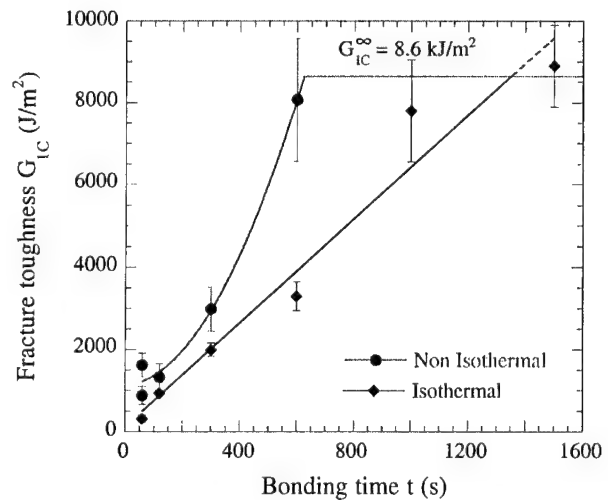


Fig. 19. Influence of the bonding time on the strength of bonds performed iso and non-isothermally between polyamide 12 adherents. The interface temperature was 180°C and the pressure 2 MPa.

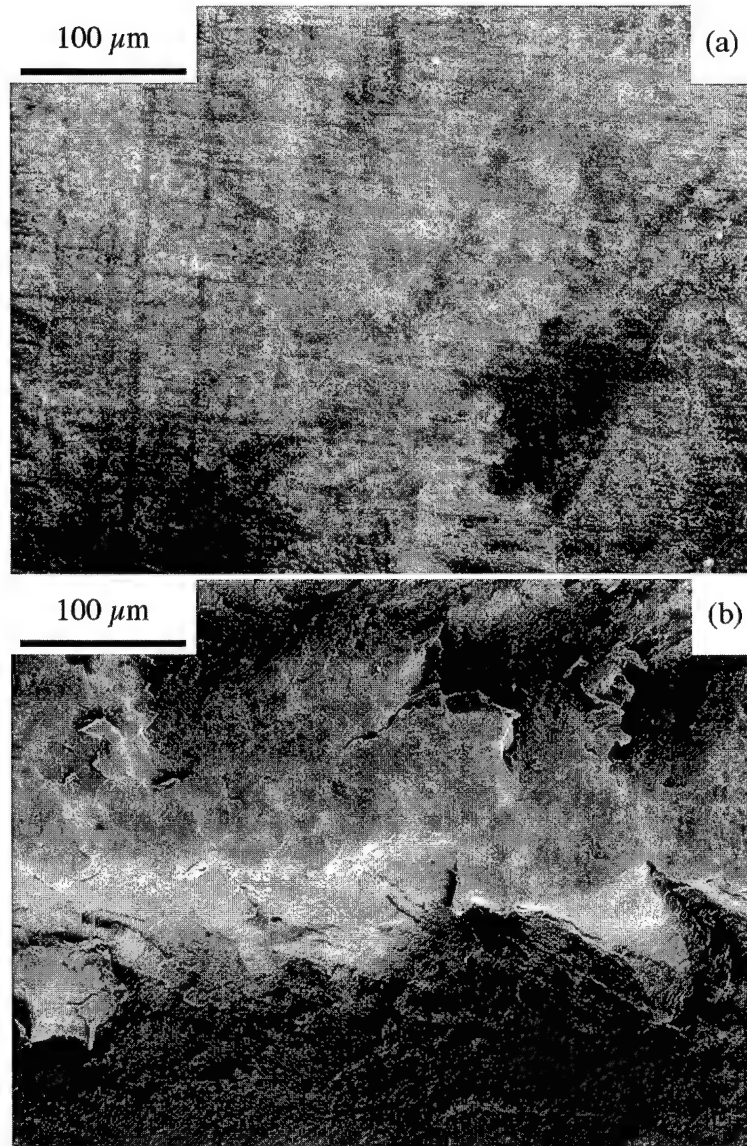


Fig. 20. Fracture surface of a polyamide 12 samples bonded: (a) isothermally and (b) non-isothermally.

strength, and is often assimilated to a polymer reptation time. Theoretical times  $\tau_r$  required to fully heal an interface come from the reptation theory of polymer chains [21–23] and can be expressed, for example, by

$$\tau_c = \left( \frac{\pi^2}{4} \right) \tau_v \left[ 1 - 1.47 \sqrt{4/5} (M_e/M)^{1/2} \right]^2 \quad (11)$$

where  $\tau_c$  is in fact the time for a chain to completely lose its initial configuration and  $\tau_v$  is the viscoelastic relaxation time which can be determined experimentally by visco-symmetry.  $M$  is the molecular weight, and  $M_e$  is the average molecular weight between two chain entanglements.

Intimate contact and autohesion are coupled [24]. As soon as the two heated surfaces are in contact, interdiffusion mechanisms begin and evolve in parallel with the intimate contact (Fig. 15). The degree of bonding is sometimes used

to indicate that intimate contact and autohesion are coupled

$$D_b(t) = \frac{f_{au}(t)}{\omega_0 + f_0} \quad (12)$$

$$D_b(t) = D_{ic}(t) D_{au}(t) \quad (13)$$

The bonding process can thus be described by the evolution of the degrees of intimate contact and autohesion (Fig. 17). The  $\gamma$  area corresponds to the region where the intimate contact is not yet activated. The  $\beta$  area shows where intimate contact is secured but autohesion is not completed; it is associated with the  $(f_{ic} - f_{au})$  zone of Fig. 15. In the  $\alpha$  area, which corresponds to the  $f_{au}$  region of Fig. 15, intimate contact and autohesion happen simultaneously.

The results described here show that bonding phenomena are complex and do interact. The variation of one bonding parameter influences several mechanisms. For example, the



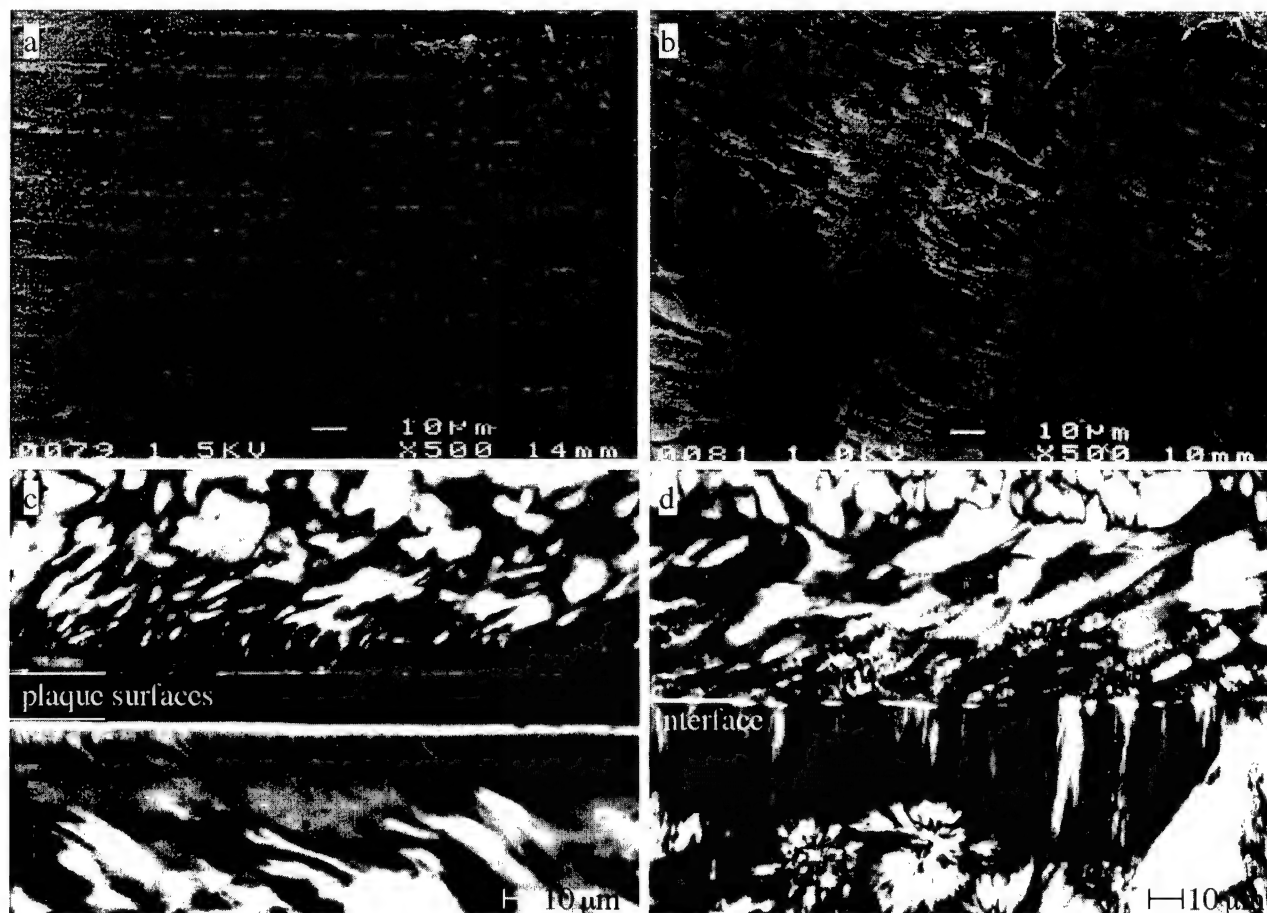


Fig. 21. Fracture surfaces and transverse section of polypropylene bonds obtained (a,c) isothermally and (b,d) non-isothermally. The interface temperature was 170°C, the bonding times and bond strengths are given in Fig. 18.

bonding temperature modifies the polymer viscosity and the chain interdiffusion kinetics, and thus the intimate contact kinetics and the autohesion mechanisms, respectively.

The material and the process determine the relative importance of one phenomenon in comparison with the others. For example, when the surface roughness is pronounced or the viscosity too high, the autohesion time becomes negligible compared with the time required to establish intimate contact. On the contrary, when high pressures are applied, intimate contact is rapid and the autohesion time may start to be significant specially if the temperature is not high enough. Furthermore, additional phenomena, such as surface degradation and diffusion of additives may modify the kinetics of the described bonding processes.

### 3.1. Non-isothermal fusion bonding

Fusion bonding of semicrystalline thermoplastics has recently been studied for the non-isothermal processing of polymers and composites, that is when two adherents of either neat polymer or composite are heated to two different temperatures prior to being assembled. These conditions are

met in processes such as tape placement, overinjection, integrated processing, etc. Fracture energy of the bonds was determined using the double cantilever beam test on samples bonded with different temperatures, pressures and holding times. For the non-isothermal cases, the lower beam was molten while the upper beam was heated but kept in the solid phase. In a first approximation, the interface temperature was taken as the average value between the upper and lower part temperatures.

More rapid and efficient bonding was observed when non-isothermal conditions were used, rather than when both components were kept at the same temperature (Figs. 18 and 19). Both polypropylene and polyamide 12 systems showed the same behaviour [25–27]. For a given interface temperature, the fracture surfaces revealed more plastic deformation and probably more melting for the surfaces submitted to non-isothermal conditions (Figs. 20, 21a,b). Furthermore, a micrograph of transverse section indicated that the crystalline structure of the bonded zone was affected by shear deformation (Fig. 21c) and that a transcrystalline zone occurred across the initial interface (Fig. 21d). It was further noticed that non-isothermal conditions might induce a modification of the initial structure over a significant zone

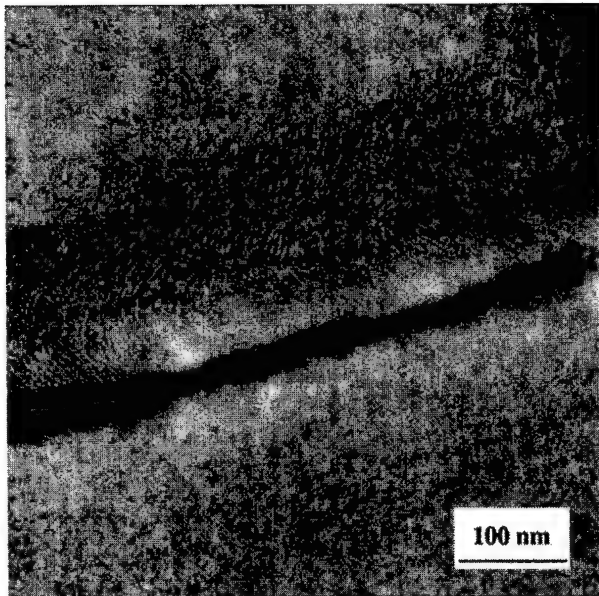


Fig. 22. TEM micrograph from the crack type zone of a polyamide specimen bonded non-isothermally. The lower part was molten at 200°C and the upper was kept solid at 160°C before to contact. The arrow indicates the zone of the solid part influences thermally by the non-isothermal bonding process.

of the upper solid beam, where thick crystalline lamellae were observed (Fig. 22). This zone was probably induced by the heat provided by the lower part kept at higher temperatures.

Several phenomena have been observed at the non-isothermal interfaces of thermoplastic bonds and it is yet difficult to propose a final explanation for the more rapid bondings obtained under non-isothermal conditions. It seems that for low and medium bond strengths the intimate contact might be favoured by non-isothermal conditions, where a lower viscosity polymer wets better the solid surface. Moreover, changes of the crystalline microstructure at and behind the interface certainly influence crack propagation mechanisms and promote the more cohesive failure modes observed in non-isothermal bonds. Nevertheless, the results clearly show that non-isothermal bonding is a way to promote faster processing of polymer and composite materials.

#### 4. Crystallisation

As far as semicrystalline thermoplastics are concerned, the crystallisation of the polymer occurs during the solidification phase (Fig. 4). Usually, crystallisation from the melt proceeds by nucleation and growth of spherulites. Adequate microscopic observations and DSC data provide satisfactory descriptions for both isothermal and non-isothermal crystallisation. Crystallisation kinetics have been extensively studied and several models have been proposed. Most of them

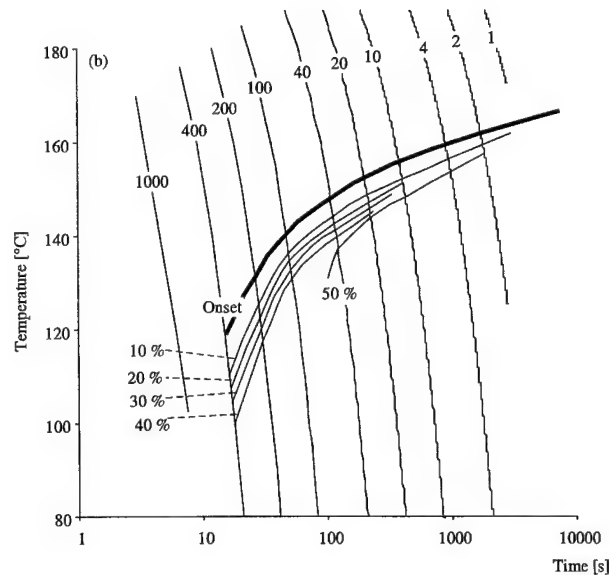


Fig. 23. Non-isothermal time-temperature-transformation diagram for polyamide 12 showing the absolute degree of crystallinity in % for different cooling rates indicated in  $K min^{-1}$ .

are based on the classical Avrami's approach [28–30]. For example, the degree of conversion for non-isothermal crystallisation is given by

$$X(t) = 1 - \exp \left[ -\frac{4\pi}{3} N_0 (\tau_d) \left( \int_{\tau_d}^t G(\xi) d\xi \right)^3 \right]; \quad t \geq \tau_d \quad (14)$$

$$X(t) = 0; \quad t < \tau_d$$

where  $N_0$  is the number of nuclei per unit volume,  $\tau_d$  a dynamic incubation time,  $G$  the radial growth rate and  $\alpha$  is the nucleating rate of spherulites. Crystallisation mechanisms are complex and not yet fully understood. Modifications of the Avrami model have been proposed to take into account additional phenomena such as secondary crystallisation [31,32].

Fig. 23 shows the non-isothermal time-temperature-conversion diagram for polyamide 12 [33]. The conversion curves were calculated from Eq. (14) mentioned above and provide the onset temperature and time for different cooling rates. This information is used to define the optimum cooling conditions considering the desired material structure and properties versus the most cost-effective cooling strategy.

#### 5. Application to integrated processing

Integration of materials and processes (Fig. 3) is very attractive in order to enhance design freedom, improve reinforcement efficiency and to add functions to composite parts [34–38,5]. During integrated processing, neat polymers and composites are combined in a single operation to reduce the

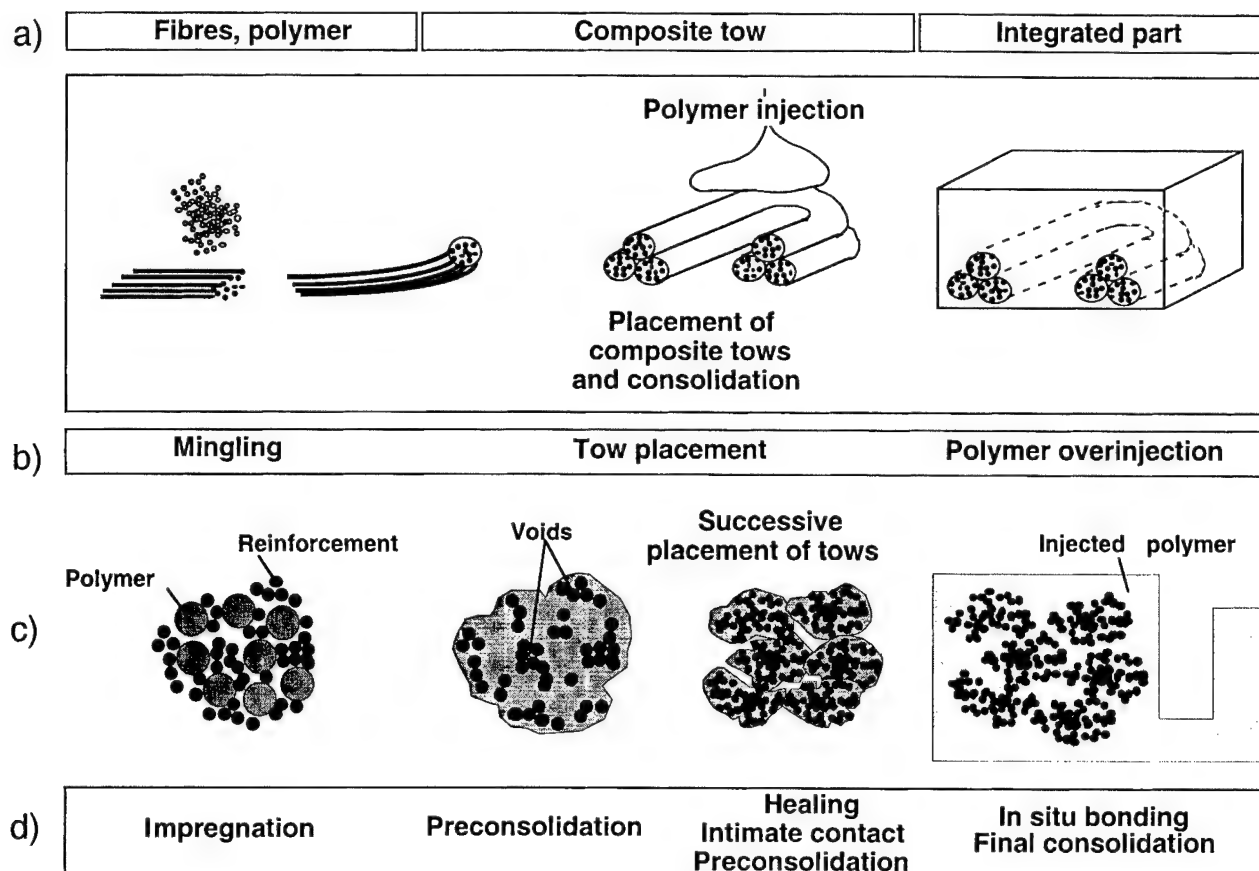


Fig. 24. (a) Materials, (b) processes and (d) material transformation steps integrated to produce samples with selective reinforcement, (c) evolution of cross-sections from initial tow to the final integrated part.

manufacturing cost by the suppression of intermediate processing and assembly steps. Each processing sequence combines different material transformation steps (impregnation, placement, and consolidation of composite reinforcement, polymer overinjection, etc.). For example, the integration of selective composite reinforcement was evaluated by the local placement of commingled yarns and powder impregnated tows into an injected polymer part (Fig. 24). Efficient combinations of the materials require in situ formation of optimum interfaces, and production of well consolidated part. By applying the results obtained on the non-isothermal fusion bonding of thermoplastic it was possible to tailor the bond strength of the integrated part and to reduce the processing cycle time. Furthermore, the evolution of the composite void content during the different processes was determined and can be tailored using the consolidation models presented above in order to optimise the total processing time [38]. It was shown, for example, that impregnation and placement speeds can be higher when tow consolidation is achieved during the final polymer overinjection. This application example illustrates how the synergy obtained during the combination of the material transformation steps can reduce the production time.

## 6. Conclusion

Material properties such as viscosity, fibre content, molecular weight, etc. were linked with processing time, temperature and pressure in order to determine the main factors controlling the impregnation, fusion bonding, and crystallisation of thermoplastic composites. For example, it was shown that for novel composites based on powder-impregnated tow and commingled yarns, the impregnation time was set by the diameters of the powder particles and fibres, and respectively by the mingling quality. It was also observed that when non-isothermal processing conditions were used, faster and more efficient bonding mechanisms occurred. Both examples illustrate how the material microstructure and transformation phenomena control rapid processing of thermoplastic composites.

## Acknowledgements

The authors would like to thank the Swiss Priority Program on Materials Research. We also acknowledge the contributions of Dr C.J.G. Plummer, Dr V. Michaud and Dr G.D. Smith.

## References

- [1] Månson JAE. New demands on manufacturing of composites materials. In: Chawla KK, editor. TMS, 1994.
- [2] Kelly A, Zweben C, editors. Comprehensive composite materials. Amsterdam/Oxford: Elsevier/Pergamon, 2000.
- [3] Månson JAE, Wakeman MD, Bourban PE, Sunderland PW. In: Plenary Lecture of 12th International Conference on Composite Materials. Paris: Woodhead Publishing, 1999.
- [4] Månson JAE. In: Kausch HH, editor. Advanced thermoplastics and their composites. Munich: Carl Hanser, 1992.
- [5] Wakeman MD, Bourban PE, Bonjour F, Månson JAE. SAMPE-ACCE-DOE, Advanced composites conference. Detroit: SAMPE, Covina, 1999.
- [6] Scheidegger AE. The physics of flow through porous media. Toronto: University of Toronto Press, 1974.
- [7] Bernet N. Commingled yarn composites for rapid processing of complex shapes. PhD thesis (2154), Lausanne, Switzerland: Swiss Federal Institute of Technology, 2000.
- [8] Connor M, Toll S, Månson JAE, Gibson AG. A model for the consolidation of aligned thermoplastic powder impregnated composites. *J Thermoplast Compos Mater* 1995;8:138–62.
- [9] Connor M. Consolidation mechanisms and interfacial phenomena in thermoplastic powder impregnated composites. PhD thesis (1413), Lausanne, Switzerland: Swiss Federal Institute of Technology, 1995.
- [10] Bernet N, Michaud V, Bourban PE, Månson JAE. An impregnation model for the consolidation of thermoplastic composites made from commingled yarns. *J Compos Mater* 1999;33(8):751–72.
- [11] Bernet N, Michaud V, Bourban PE, Månson JAE. Commingled yarn composites for rapid processing of complex shapes. *Composites: Part A* 2001, in press.
- [12] Benatar A, Gutowski TG. *SAMPE J* 1986;19:33.
- [13] Bourban PE, Gillespie JW, Tierney JT. Joining of composites. In: Kelly A, Zweben C, editors. Comprehensive composite materials. Amsterdam/Oxford: Elsevier/Pergamon, 2000.
- [14] Dara PH, Loos AC. Processing of thermoplastic matrix composites. *Rev Prog Quant Nondestruct Evaluat* 1987;B6:1257–65.
- [15] Lee WI, Springer GS. A model of the manufacturing process of thermoplastic matrix composites. *J Comp Mater* 1987;21(11):1017–55.
- [16] Mantell SC, Springer GS. Manufacturing process models for thermoplastics composites. *J Comp Mater* 1992;26(16):2348–77.
- [17] Jud K, Kausch HH, Williams JG. Fracture mechanics studies of crack healing and welding of polymers. *J Mater Sci* 1981;16:204–10.
- [18] De Gennes PG. Sur la soudure des polymères amorphes. *CR Acad Sci Paris Sér B* 1980;291:219–21.
- [19] Bastien LJ, Gillespie JW. A non-isothermal healing model for strength and toughness of fusion bonded joints of amorphous thermoplastics. *Polym Engng Sci* 1991;31(24):1720–30.
- [20] Wool RP. Polymer interfaces: structure and strength. Munich: Hanser, 1995.
- [21] De Gennes PG. Reptation of a polymer chain in the presence of fixed obstacles. *J Chem Phys* 1971;55(2):572–9.
- [22] De Gennes PG, Leger L. Dynamics of entangled polymer chains. *Ann Rev Phys Chem* 1982;33:49–61.
- [23] Doi M, Edwards SF. The theory of polymer dynamics. Oxford: Oxford University Press, 1986.
- [24] Butler CA, McCullough RL, Pitchumani R, Gillespie JW. An analysis of mechanisms governing fusion bonding of thermoplastic composites. *J Thermoplast Comp Mater* 1998;11:338–63.
- [25] Smith GD. PhD Thesis 1597, Ecole Polytechnique Fédérale de Lausanne, 1997.
- [26] Smith GD, Plummer CJP, Bourban PE, Månson JAE. Non-isothermal fusion bonding of polypropylene. *Polymer* 2001, in press.
- [27] Zanetto JE, Plummer CJP, Bourban PE, Månson JAE. Fusion bonding of polyamide 12. *Polymer Eng and Sci* 2001, in press.
- [28] Avrami MJ. *J Chem Phys* 1941;9:177.
- [29] Avrami MJ. *J Chem Phys* 1940;8:212.
- [30] Avrami MJ. *J Chem Phys* 1939;7:1103.
- [31] Hillier IH. *J Polym Sci* 1965;A3:3067.
- [32] Phillips R, Månson JAE. *J Polym Sci Part B, Polym Phys* 1997;35(6):875.
- [33] Plummer CJP, Zanetto JE, Bourban PE, Månson JAE. The crystallization kinetics of polyamide-12. *Colloid Polym Sci* 2001, in press.
- [34] Månson JAE, Bourban PE, Bonjour F. Patent PCT/1B96/00467, 1995.
- [35] Bourban PE, Bonjour F, Månson JAE. Proc ECCM7, 14–16 May, London, UK, 1996;201.
- [36] Bourban PE, Bögli A, Bonjour F, Månson JAE. *Comp Sci Technol* 1998;58:633–7.
- [37] Bourban PE, Bonjour F, Bernet N, Wakeman MD, Månson JAE. In: Proceedings of 12th International Conference on Composite Materials. Paris: Woodhead Publishing, 1999.
- [38] Wakeman MD, Bourban PE, Bonjour F, Berguerand P, Månson JAE. In: Proceedings of 12th International Conference on Composite Materials. Paris: Woodhead Publishing, 1999.

# Modeling flow-induced crystallization in fiber spinning

A.J. McHugh\*, A.K. Doufas

*Department of Chemical Engineering, University of Illinois at Urbana–Champaign, 600 S. Mathews, Urbana, IL 61801, USA*

## Abstract

A brief review is given of the microstructural/constitutive model for flow-induced crystallization (FIC), developed by the authors that couples polymer microstructure (molecular orientation and crystallinity) with the macroscopic velocity/stress and temperature fields. Application of the model to melt spinning of nylons and poly(ethylene terephthalate) (PET) under both low- and high-speed spinline conditions is described. The fiber spinning model includes the combined effects of FIC, viscoelasticity, filament cooling, air drag, inertia, surface tension and gravity, and simulates melt spinning from the spinneret down to the take-up roll device (below the freeze point). For both nylons and PET, model fits and predictions are shown to be in very good quantitative agreement with spinline data for the fiber velocity, diameter and temperature fields at both low- and high-speed conditions, and, with flow birefringence data available for high speeds. The model captures the necking phenomenon for nylon and PET quantitatively and the associated extensional softening at high-speed conditions and the occurrence of the freeze point naturally at both low- and high-speed conditions. © 2001 Elsevier Science Ltd. All rights reserved.

**Keywords:** A: Fibres; B: Microstructure; D: Thermal analysis; Flow-induced crystallization

## 1. Introduction

Fiber spinning of semi-crystalline materials is an industrial polymer process of great commercial importance. High-speed non-isothermal melt spinning (i.e. take-up speeds in excess of ~4000 m/min for nylon and poly(ethylene terephthalate) (PET) melts) is associated with a concentrated neck-like deformation process and the development of high tensile stresses that result in flow-induced crystallization (FIC). A key issue in the modeling of both high- and low-speed spinning is proper accounting for the role of FIC in the spinline dynamics. The parameter that most strongly correlates with as-spun properties is the stress at solidification. Thus an important characteristic of any mathematical model is its ability to quantify accurately the stress at the solidification, as well as other microstructural properties, such as the degree of transformation and crystal orientation, for a wide range of processing conditions.

In the past modeling efforts have been limited to “single-phase” approaches in which either a single Newtonian or viscoelastic constitutive equation is used for the polymer melt. A major shortcoming of these models is that crystallization is decoupled from the fiber deformation and stress fields, and the solidification point, rather than arising naturally in the model formulation, is forced externally (e.g. at the glass transition temperature for PET spinning). More-

over, such single-phase models are not able to predict naturally plateaus in fiber spinning velocity profiles at the end of the spinline [1,2]. In the case of the Newtonian model assumption, the “single-phase” models force the rate of deformation tensor to zero at the “solidification” point and, therefore, cannot predict the leveling-off of the tensile stress after this point. In some “single-phase” modeling approaches, the effects of crystallization are introduced through the dependence of the melt zero-shear viscosity on the crystallinity. However, such approaches are pathological, not being able to predict necking under high-speed conditions despite the completion of crystallization and the prediction of quite high zero-shear viscosities (see Ref. [1]).

We recently developed a microstructural model for FIC [3], which we have applied to the simulation of high- and low-speed melt spinning of nylons [1,4] and PET [2]. Our simulations include the combined effects of crystallization, viscoelasticity, filament cooling, air drag, inertia, surface tension and gravity. The underlying microstructural/constitutive model we developed is based on a “two-phase” approach in which the melt (untransformed) phase is modeled as a concentrated suspension of flexible macromolecules described by a modified Giesekus fluid with finite chain extensibility, and the semi-crystalline phase is approximated as a collection of rigid rods that grow and orient in the flow field. The crystallization rate is approximated by a non-isothermal Avrami equation with a frame-invariant enhancement factor — based on nucleation and polymer kinetic theory arguments — to mimic the effect of

\* Corresponding author. Tel.: +1-217-333-1178; fax: +1-217-333-5052.  
E-mail address: a-mchugh@uiuc.edu (A.J. McHugh).

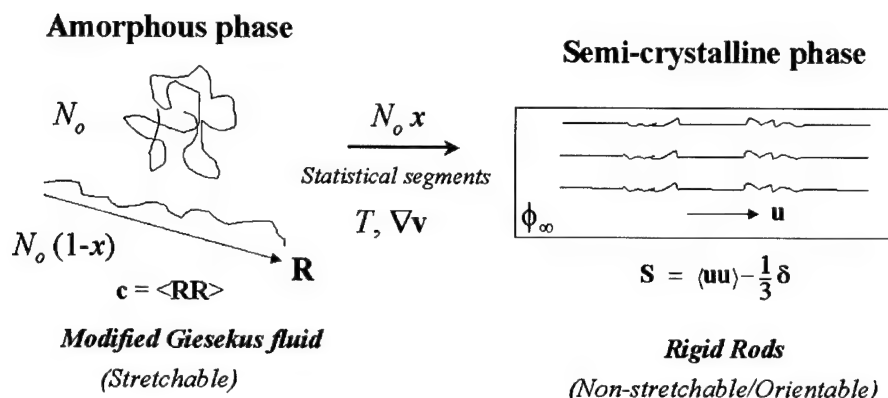


Fig. 1. Schematic representation of the molecular-based FIC microstructural model.

flow on the kinetics of the phase transition. The two phases are consistently coupled through the stress in combination with the momentum and energy balance and the feedback of crystallinity on the system relaxation times.

The purpose of this paper is to review the basics of our model and illustrate, through examples, its applicability to both high- and low-speed spinning experimental data (velocity, diameter, temperature and flow birefringence profiles) for nylon and PET.

## 2. Theory

### 2.1. Model and equations

Fig. 1 shows a schematic of our microstructural model for FIC [1,3]. The microstructural variables are the conformational tensor,  $\mathbf{c}$  ( $= \langle \mathbf{RR} \rangle$ , where  $\mathbf{R}$  is the end-to-end vector for the untransformed amorphous (melt) phase and the brackets imply averaging over the molecule conformation space), the orientational tensor,  $\mathbf{S}$  ( $= \langle \mathbf{uu} \rangle - 1/3\delta$ , where  $\mathbf{u}$  is the unit orientation vector and  $\delta$  is the identity tensor) for the semi-crystalline phase, and the degree of transformation  $x$  ( $0 < x < 1$ ). Together these determine the constitutive stress at any time and position in the computational domain. Crystallization under a given set of temperature,  $T$ , and flow conditions (i.e. velocity gradient,  $\nabla \mathbf{v}$ ), results in the transfer of  $N_0 x$  statistical segments from the melt phase to the semi-crystalline phase. In the absence of a fundamental theory for FIC, the equilibrium degree of crystallinity of the semi-crystalline phase,  $\phi_\infty$ , is taken to be a constant, independent of the flow conditions. The relation of the molten and semi-crystalline phase continuum extra stresses (i.e.  $\tau_m^*$  and  $\tau_{sc}^*$ , respectively) to the microstructural parameters shown in Fig. 1, are derived from molecular rheology considerations [1] and are given by the following

$$\tau_m^* = \frac{E}{1-x} \mathbf{c}^* - \delta \quad (1)$$

and

$$\tau_{sc}^* = 3\mathbf{S} + 6\lambda_{sc}(\nabla \mathbf{v})^T : \langle \mathbf{uuuu} \rangle \quad (2)$$

In these expressions, superscript  $*$  is used to denote either the non-dimensional stress (with respect to the melt shear modulus,  $G$ ) or the non-dimensional conformational tensor (with respect to  $K_0/k_B T$ , where  $K_0$  is the Hookean spring constant for the macromolecule before the onset of crystallization and  $k_B$  is the Boltzmann constant) and  $\lambda_{sc}$  is the semi-crystalline phase relaxation time.  $E$  is the non-linear force factor following the Peterlin approximation [1,3] and accounts for the fact that the molecular force-extension response becomes highly non-linear with either increased stretching (due to flow) or decreased amorphous chain length (due to loss of chain segments caused by crystallization). The two phases are consistently coupled through the total extra stress,  $\tau^* (= \tau_m^* + \tau_{sc}^*)$ , in combination with the overall momentum and energy balances for the system, and the feedback of crystallinity on the system relaxation times. The microstructural parameters satisfy the following evolution equations:

Conformation tensor,  $\mathbf{c}^*$  (melt):

$$\mathbf{c}_{(1)}^* = -\frac{1-x}{\lambda_a(x, T)} \left( (1-\alpha)\delta + \alpha \frac{E}{1-x} \mathbf{c}^* \right) \left( \frac{E}{1-x} \mathbf{c}^* - \delta \right) \quad (3)$$

where  $\lambda_a(x, T)$  is the relaxation time of the amorphous (melt) phase, given by

$$\lambda_a(x, T) = \lambda_{a,0}(T)(1-x)^2 \quad (4)$$

where  $\alpha$  is the molecular (Giesekus) mobility parameter that lies between unity and zero and  $\lambda_{a,0}(T)$  is the temperature-dependent Hookean relaxation time of the melt which, for a constant shear modulus, is given by the temperature dependence of the zero-shear viscosity,  $\eta_0$ .

Oriental tensor,  $\mathbf{S}$  (semi-crystalline phase):

$$\mathbf{S}_{(1)} = -\frac{\sigma}{\lambda_{sc}(x, T)} \mathbf{S} + \frac{1}{3} (\nabla \mathbf{v} + (\nabla \mathbf{v})^T) - 2(\nabla \mathbf{v})^T : \langle \mathbf{uuuu} \rangle \quad (5)$$

where,  $\sigma$  is an anisotropic drag parameter. The semi-crystalline relaxation time is related to the degree of transformation



and temperature by

$$\lambda_{sc}(x, T) = c\lambda_{a,0}(T)\exp(Fx) \quad (6)$$

where  $c$  and  $F$  are model fitting parameters. The subscript (1) in Eqs. (3) and (5) denotes the upper-convected Oldroyd derivative. The bracketed fourth-order tensor for the orientation vector  $\mathbf{u}$  in Eqs. (2) and (5) is evaluated using a hybrid decoupling approximation [1,2,4].

*Degree of transformation,  $x$ :*

$$\frac{Dx}{Dt} = mK_{av}(T)[- \ln(1-x)]^{(m-1)/m}(1-x)\exp(\xi \text{tr} \boldsymbol{\tau}^*) \quad (7)$$

Eq. (7) is a non-isothermal version of the Avrami equation, where  $K_{av}$  is the temperature-dependent Avrami coefficient (obtained from quiescent kinetics measurements), and the exponential term represents the frame-invariant enhancement factor — based on nucleation and polymer kinetic theory arguments — to account for the effect of flow on the phase transition kinetics. In the absence of a fundamental theory relating the growth exponent,  $m$ , to the flow, a value of unity is used in order to capture the lowering of the growth dimensionality, and the constant  $\xi$  is taken as a model fitting parameter. Moreover, in their studies of the kinetics of strain-induced crystallization of lightly cross-linked fibers under quite low stretch ratios ( $<1.4$ ), McHugh and Yung [12,13] reported that the in situ measured crystallization data were well fit with an Avrami exponent of approximately 1. At low-speed spinning conditions ( $<3000$  min), the molecular stretch ratio of the amorphous chains, defined as the chain extension relative to the quiescent coiled state, is calculated to be  $<3$ , and therefore a value of  $m = 1$  appears to be reasonable. At high-speeds conditions,  $m = 1$  is also a reasonable approximation, since the crystal growth is expected to be one-dimensional. The derivative on the left-hand side of Eq. (7) is the substantial derivative.

The model (Eqs. (1)–(7)) along with the macroscopic transport equations (mass, momentum and energy) of the polymer process contain quantities and parameters that fall into three categories: (i) properties that can be determined a priori from measurements of the melt. These include the stress-deformation rate rheological properties of the melt (the zero-shear-rate viscosity,  $\eta_0$ ,  $\alpha$  and  $G$ ), physical properties such as the polymer density, thermal conductivity, surface tension and heat capacities and quiescent crystallization parameters, such as the equilibrium melting point,  $T_m^0$ , and the Avrami crystallization parameter ( $K_{av}$ ); (ii) variables that relate to the processing conditions being modeled. In the case of fiber spinning, these include the take-up speed, mass flow rate, quench air velocity and temperature; and (iii) parameters that are material dependent and are calibrated from experimental data for the given process. These include the model parameters  $c$ ,  $F$ ,  $\xi$  and  $\sigma$ . The model predictions (velocity, temperature, stress profiles and location of freeze point) are most sensitive to the parameters  $F$ ,  $\xi$  [1,4]. A very extensive discussion of the

evaluation of these variables and parameters and a listing of values used for modeling the melt spinning of the nylons and PET to be discussed in the following sections is given elsewhere [1,2,4].

## 2.2. Fiber spinning equations

Fig. 2 shows a schematic that defines the single filament model and coordinate system used for steady fiber spinning, and the relevant process variables. The latter include the capillary diameter  $D_0$ , the mass flow rate  $W$ , the exiting melt temperature  $T_0$ , the spin line length  $L$ , the take-up velocity  $v_L$  and the fiber diameter at the take-up  $D_L$ . In addition, the quench air velocity,  $v_c$ , and temperature,  $T_c$ , are also noted. Shear stresses developed in the spinneret are assumed to have relaxed at the point of maximum die swell ( $z = 0$ ), and the flow field during spinning ( $0 \leq z \leq L$ ) is considered to be a locally homogeneous uniaxial extension, which at constant density, gives the following expressions for the velocity gradient and total extra stress tensors.

$$\nabla \mathbf{v} = \begin{bmatrix} \frac{dv_z}{dz} & 0 & 0 \\ 0 & -\frac{1}{2} \frac{dv_z}{dz} & 0 \\ 0 & 0 & -\frac{1}{2} \frac{dv_z}{dz} \end{bmatrix} \quad (8)$$

and

$$\boldsymbol{\tau} = \begin{bmatrix} \tau_{zz} & 0 & 0 \\ 0 & \tau_{rr} & 0 \\ 0 & 0 & \tau_{\theta\theta} \end{bmatrix} \quad (9)$$

Due to axial symmetry, the  $rr$  and  $\theta\theta$  components of the extra stress tensor are identical. The combination of uniaxial tensile forces acting on the filament during flow and the cooling of the spinline will induce crystallization (at a point where the filament temperature drops below  $T_m^0$ ) and an eventual locking-in of the fiber diameter at the freeze point. The spinline tension varies along the fiber length due to the combined effects of air drag and inertia, and is also strongly influenced by structural changes brought about by the FIC. As noted in the figure, for high-speed conditions, a concentrated deformation (necking) process occurs over some short region of the spinline, immediately prior to the freeze point, after which filament deformation ceases and the neck stabilizes. As noted earlier, the objective of the model calculation is to predict the complete dynamics (filament cooling, crystallization, neck formation and freeze point) for the given set of material parameters and process conditions. The defining equations for the cross-sectional averaged (thin filament approximation) steady state transport balances are the following [1]:

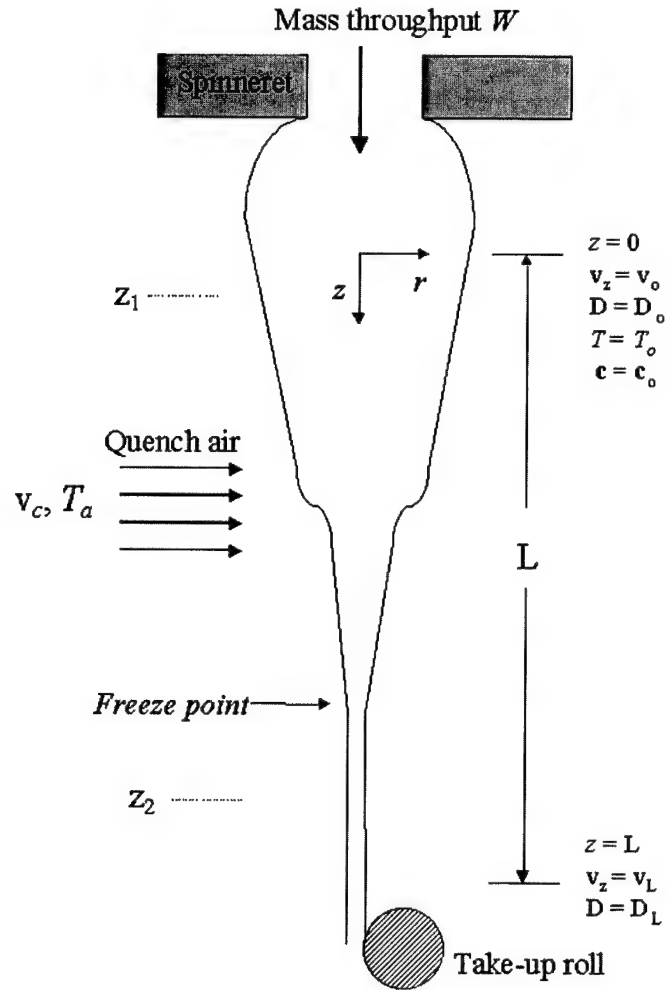


Fig. 2. Schematic representation of the melt spinning process.

*Mass balance*

$$W = \rho \frac{\pi D^2}{4} v_z \quad (10)$$

where  $\rho$  is the constant polymer density.

*Momentum balance*

$$W \frac{dv_z}{dz} = \frac{d}{dz} [A(\tau_{zz} - T_{rr})] - \pi B \mu_a (v_z - v_d) + \rho g A + \frac{1}{2} \pi s \frac{dD}{dz} \quad (11)$$

In Eq. (11), the term on the LHS is the inertia. On the RHS,  $F_t = A(\tau_{zz} - \tau_{rr})$  is the cross-sectionally averaged tensile force at an arbitrary position  $z$ . The second term is the air drag with  $B$  being the so-called Bingham number [1], characterizing the dimensionless quench air drag force per unit length of the filament,  $v_d$  is the downward component of the quench air and  $\mu_a$  is the viscosity of the quench air evaluated at the film temperature (arithmetic average of quench air and filament temperature). Finally,  $g$  is the

acceleration of gravity,  $A = \pi D^2/4$  is the cross-sectional area of the fiber and  $s$  is the surface tension of the filament.

*Equation of energy*

$$\rho C_p v_z \frac{dT}{dz} = -\frac{4}{D} h(T - T_a) + (\tau_{zz} - \tau_{rr}) \frac{dv_z}{dz} + \rho \Delta H_f v_z \frac{d\phi}{dz} \quad (12)$$

In Eq. (12),  $C_p$  is the heat capacity of the total system, which is temperature and crystallinity dependent in general. The first term on the RHS is the convective heat transfer term between the filament and the quench air, with  $h$  being the convective heat transfer coefficient. The second term expresses the viscous dissipation, and the last term is related to the release of latent heat with  $\Delta H_f$  being the heat of crystallization per unit mass and  $\phi$  the average absolute degree of crystallinity of the system (mass fraction of crystals) at the axial position  $z$ .

Substitution of the constitutive equations (Eqs. (1)–(7)) into the transport equations (Eqs. (10)–(12)) along with Eqs. (8) and (9), leads to a set of highly coupled, non-linear differential equations for the microstructural variables ( $\mathbf{c}^*$

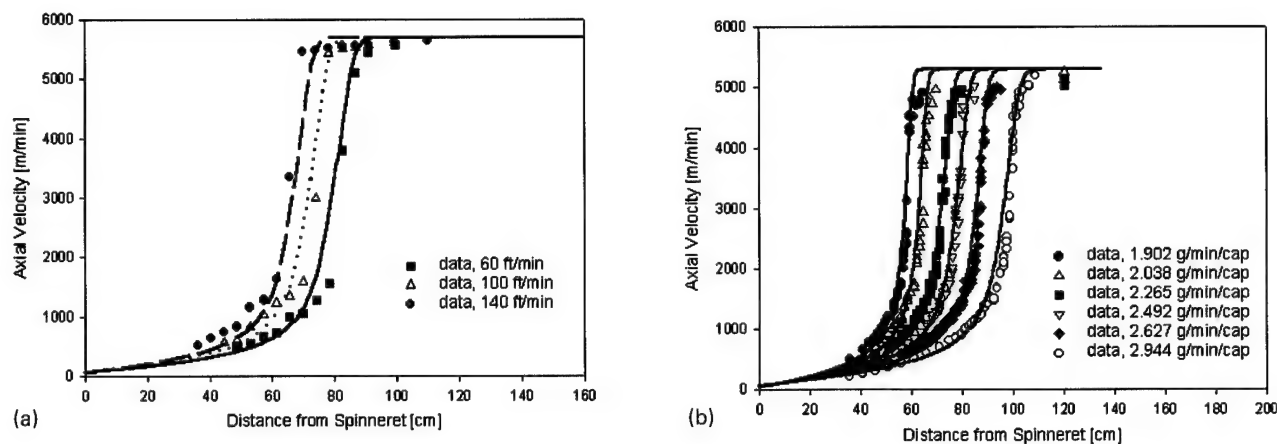


Fig. 3. (a) Effect of quench air velocity; and (b) mass flow rate on the spinline velocity profile for a 52.5 RV nylon and 70 RV nylon, respectively, at high-speed conditions. Lines represent model fittings and predictions. For (a) the take-up speed is 5700 m/min and the mass flow rate is 2.22 g/min/cap and for (b) the take-up speed is 5300 m/min. The data were taken from DuPont [5].

and  $S$  tensors and  $x$ ) and the macroscopic velocity and temperature fields. These are solved as an initial value problem with a fourth-order, Runge–Kutta algorithm combined with a shooting method [1].

### 2.3. Input parameters

All input physical and rheological properties, processing parameters, and model parameters for our simulations of nylon and PET melts are given elsewhere [1,2,4]. For the convective heat transfer coefficient,  $h$ , and Bingham number,  $B$  (related to the air drag), DuPont proprietary improvements to existing heat transfer and air drag relations in the literature were used [5]. With regard to the heat transfer and air drag correlations, we have found that the overall features (e.g. the appearance of necking at high speeds, and the general shape of the temperature profile) of the model predictions are qualitatively similar using standard published correlations. However, quantitative agreement between experimental data and predicted trends was found to be best using the Dupont correlations. Correlations for the material properties of the quench air (density, viscosity and thermal conductivity), needed in the simulations, are also listed elsewhere [1]. Model parameters for the various fiber spinning runs used in the simulations are given elsewhere [2,4].

## 3. Results and discussion

The effects of the cross flow quench air velocity for a 52.5 RV (relative viscosity) Nylon-66 melt and the mass flow rate for a 70 RV Nylon-66 melt on the filament velocity profile are shown in Fig. 3a and b, respectively. In what follows, the cross flow quench air velocity,  $v_c$ , will be referred to as “quench air velocity” and the downward velocity,  $v_d$ , is set to zero. The RV is typically used as a measure of the molecular weight and was obtained using 8%

solutions of the polymer in formic acid [5]. On varying the quench air velocity, as indicated, the data corresponding to 60 ft/min quench air velocity were used to obtain values for the model parameters. As seen, the model is able to fit the data very well. Moreover, the ability to predict the behavior of the runs corresponding to 100 and 140 ft/min quench air velocity based on those parameters is seen to be excellent. This shows the model reliability. Increases in quench air velocity are predicted to result in faster cooling rates (figure not shown) and this causes the semi-crystalline structure to lock-in faster, and therefore, the freeze point to move towards the spinneret (Fig. 3a).

Because of technical and time constraints [5], measurements for the tests presented in Fig. 3b were made on filaments a few rows back from the quench screen. Although profiles for these filaments differed considerably from those closer to the screen (differences as large as tens of degrees in the temperature profiles, and more than 10 cm in the location of the neck point), in the simulations, quench conditions for the exit of the quench screen were used. As a result, the model parameters for the same nylon (homopolymer of 70 RV) had to be changed for the different tests in order to fit the experimental velocity profiles. Fig. 3b shows the excellent model fitting capability of velocity spinline profiles at high-speed conditions. As shown earlier [1,4,6], increasing the mass throughput slows down the spinline dynamics (including the cooling process) and moves the freeze point away from the spinneret (Fig. 3b). Model predictions of the temperature profiles based on the parameters used in Fig. 3b were also found to be in very good agreement with the experimental data (figure not shown).

Comparisons of the model output with experimental profiles of diameter, temperature and flow birefringence under high-speed conditions [7] are shown in Fig. 4. Moreover, using the same model parameters as those of Fig. 4, predictions were found to be in very good quantitative agreement for the diameter, temperature and flow

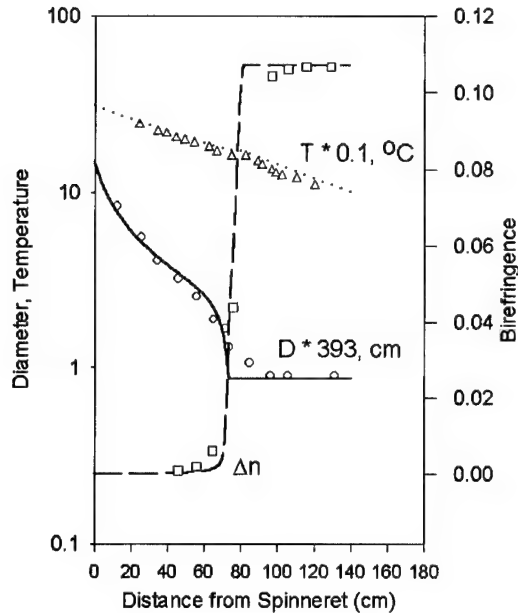


Fig. 4. Birefringence, diameter and temperature profiles along the spinline for PET at high-speed conditions. Model parameters obtained from fit of diameter data (solid line). Dashed curves represent predictions for the temperature and birefringence based on the same parameters. Take-up velocity: 5490 m/min, mass flow rate: 2.8 g/min/cap. The data were taken from Vassilatos et al. [7].

birefringence profiles for the other high-speed run of Vassilatos et al. [7] (figure not shown). Flow birefringence was calculated from the degree of transformation  $x$  and the microstructural tensors  $c$ ,  $S$  according to the methodology described previously [4].

The model captures the necking phenomenon at high-speed conditions quantitatively, where the diameter is rather suddenly reduced by a factor of approximately 1.3 in the vicinity of 70 cm (Fig. 4). On the other hand, conventional single-phase viscoelastic models with a crystallinity-dependent viscosity (e.g. the model recently proposed by Ziabicki et al. [8]) are unable to predict necking at high-speed condi-

tions. As was established in Doufas et al. [1], the single-phase viscoelastic models are pathological in that they cannot cease the deformation and lock-in the velocity field despite the completion of FIC and existence of extremely large characteristic relaxation times. Application of such a single-phase model in simulation of PET melt spinning gave aphysical results (for example for a quite high take-up speed of 10,000 m/min the velocity does not reach a plateau) [8].

As indicated by the experimental data and our model predictions (Fig. 4), the flow birefringence has relatively small values between the spinneret and the freeze point, a result of low crystallinity and isotropy in orientation. The birefringence rises sharply in the vicinity of the freeze point and finally attains a plateau value.

Our model does capture the fact that the freeze point under high-speed conditions occurs in the semi-crystalline state at temperatures well above the glass transition temperature, namely  $\sim 177^\circ\text{C}$  (Fig. 4). Therefore, crystallization plays an important role in the dynamics under high-speed conditions and cannot be neglected.

Model comparisons with experimental velocity profiles for low-speed conditions for a 0.675 IV (intrinsic viscosity) PET melt (data of George [9]) and a 72 RV Nylon-66 melt [5] are shown in Fig. 5a and b, respectively. IV was determined from the solution viscometry at  $25^\circ\text{C}$  of 0.25 g PET in 100 ml of a 60/40 mixture of phenol/tetrachloroethane [11] and is routinely used as a measure of the molecular weight for PET, similar to RV for nylon. The same set of model parameters was used for all the runs for a given polymer. Fig. 5 shows the excellent fitting and predictive capability of our model with respect to velocity profiles at low-speed conditions. The profiles exhibit a smooth increase in velocity towards a plateau value without the occurrence of a concentrated, neck-like deformation. In contrast, single-phase viscoelastic models that enforce the freeze point at the glass transition temperature for PET [10] cannot capture the smoothness of the velocity profiles towards their final values. Model predictions of temperature

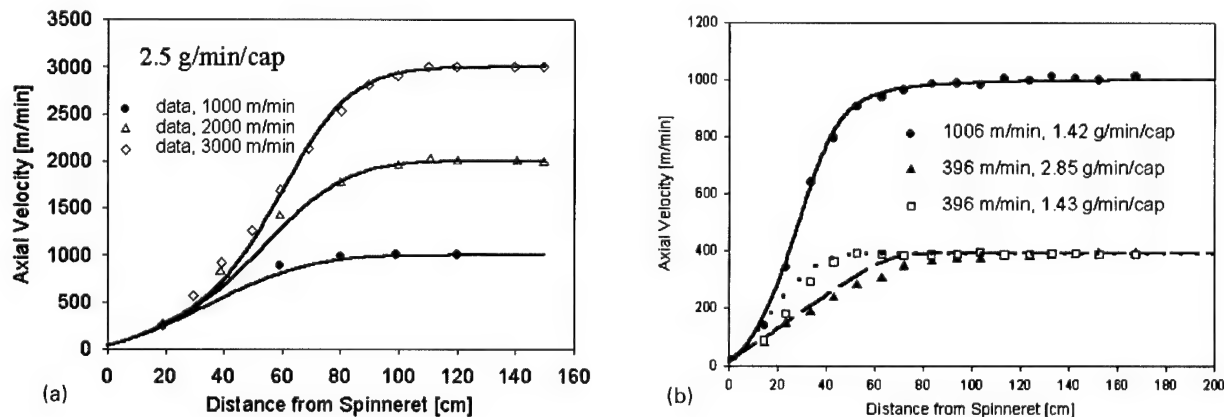


Fig. 5. Spinline velocity profiles at low-speed conditions for 0.675 IV PET (a) and 72 RV nylon. Model parameters are the same for all processing conditions for a given polymer. The PET data were taken from George [9] and the nylon data from DuPont [5].

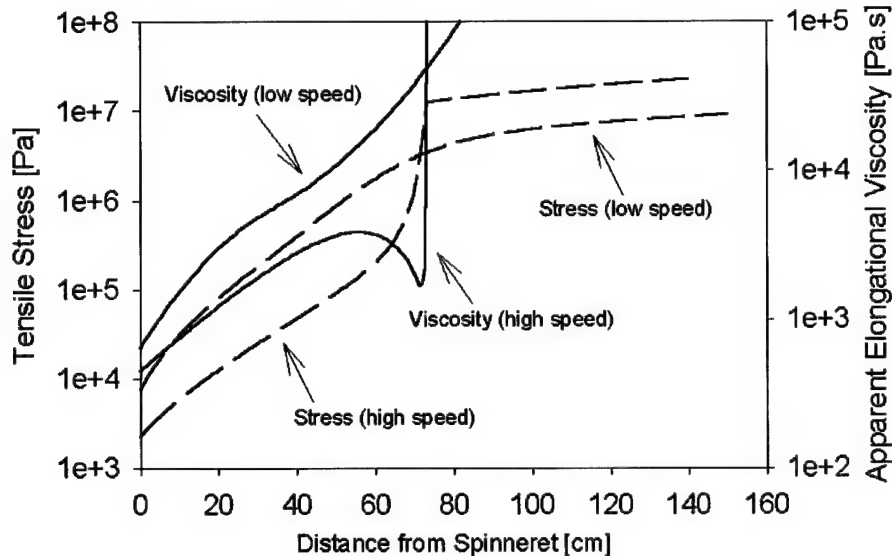


Fig. 6. Predicted tensile stress and apparent elongational viscosity profiles for PET at both low- and high-speed conditions. The low-speed profiles correspond to the 3000 m/min run of Fig. 5a and the high-speed profiles correspond to the PET run of Fig. 4. The tensile stress is defined as the normal stress difference in the axial and radial directions including both amorphous and semi-crystalline contributions.

are also in favorable agreement with the experimental data for both nylon and PET (figure not shown). The temperature profiles exhibit a monotonic decrease of temperature, typical of low-speed spinning [4,9].

Fig. 6 shows the predicted tensile stress and apparent elongational viscosity profiles for high- and low-speed conditions for PET, corresponding to Figs. 4 and 5a (speed of 3000 m/min), respectively. Near the spinneret, the elongational viscosity is predicted to follow Trouton's ratio (ratio of elongational viscosity over shear viscosity is approximately three) for all speeds investigated implying Newtonian behavior at that location. The high-speed stress and viscosity profiles are typical of neck-like deformation [1,4,6]. The elongational viscosity passes through a maximum, then drops off sharply (extensional softening), and finally rises rapidly due to FIC. Since temperature rise is not observed or predicted under these conditions, the decrease in elongational viscosity clearly reflects non-linear viscoelastic effects, which produce an apparent strain softening effect. This behavior is consistent with necking of nylon, where both experiment [6] and simulations [1] show that the temperature rise occurs after the softening of the elongational viscosity. The model captures the rapid increase of the tensile stress in the neck region and its leveling-off due to the occurrence of FIC and the cessation of the deformation. The slight increase of the stress below the freeze point is attributed to air drag. For low-speed conditions, the stress profiles are smooth, consistent with the low-speed velocity profiles (Fig. 5), and the extensional viscosity shows purely strain hardening behavior (i.e. no neck-like deformation). The model predicts the stress at the freeze point (defined as the position along the spinline where the velocity reaches its final value), which is believed to be the

most important variable related to the physical properties of the as-spun fibers [9].

The stress and elongational viscosity profiles for nylon are qualitatively similar to those of PET under both low- and high-speed conditions. Corresponding to Fig. 3b, the tensile stress at the freeze point is predicted to be almost independent of the flow rate (figure not shown), in agreement with Haberkorn et al. [6] and Doufas et al. [1].

#### 4. Conclusions

The application of our "two-phase" microstructural/constitutive model for FIC to fiber melt spinning has been shown to produce fits and predictions that are in excellent quantitative agreement with nylon and PET spinline data for velocity, diameter, temperature for both low- and high-speed conditions and flow birefringence available at high speeds. Experimental data for a given polymer are accurately predicted under different processing conditions using the same set of model parameters. An important feature of our model is that it captures the occurrence of the freeze point naturally for both low- and high-speed conditions. Under low-speed conditions, the freeze point is predicted naturally, without the use of a glass transition temperature criterion typically used for PET by conventional melt spinning models. The model quantitatively captures the necking phenomenon under high-speed conditions and the associated strain softening of the elongational viscosity. We suggest that our model can be a useful tool for optimization of melt spinning processes connecting the final product properties with the processing conditions through the prediction of the tensile stress at the freeze point and

microstructure of the semi-crystalline system (molecular orientation and crystallinity).

### Acknowledgements

This work is being supported in part by the ERC program of the National Science Foundation under Award No. EEC-9731680, and, in part, by a grant from E.I. DuPont de Nemours and Company.

### References

- [1] Doufas AK, McHugh AJ, Miller C. Simulation of melt spinning including flow-induced crystallization. Part I. Model development and predictions. *J Non-Newtonian Fluid Mech* 2000;92:27–66.
- [2] Doufas AK, McHugh AJ. Simulation of melt spinning including flow-induced crystallization. Part III. Quantitative comparisons with PET spinline data. *J Rheol*, to be published.
- [3] Doufas AK, Dairanieh IS, McHugh AJ. A continuum model for flow-induced crystallization of polymer melts. *J Rheol* 1999;43:85–109.
- [4] Doufas AK, McHugh AJ, Miller C, Immaneni A. Simulation of melt spinning including flow-induced crystallization. Part II. Quantitative comparisons with industrial spinline data. *J Non-Newtonian Fluid Mech* 2000;92:81–103.
- [5] E.I. DuPont de Nemours and Company. Private communication, 1999.
- [6] Haberkorn H, Hahn K, Breuer H, Dorrer H-D, Matthies P. On the neck-like deformation in high-speed spun polyamides. *J Appl Polym Sci* 1993;47:1551–79.
- [7] Vassilatos G, Knox BH, Frankfort HRE. Dynamics, structure development, and fiber properties in high-speed spinning of polyethylene terephthalate. In: Ziabicki A, Kawai H, editors. *High-speed fiber spinning, science and engineering aspects*. New York: Wiley-Interscience, 1985.
- [8] Ziabicki A, Jarecki L, Wasiak A. Dynamic modelling of melt spinning. *Comput Theor Polym Sci* 1998;8:143–57.
- [9] George HH. Model of steady-state melt spinning at intermediate take-up speeds. *Polym Engng Sci* 1982;22:292–9.
- [10] Gagon DK, Denn MM. Computer simulation of steady polymer melt spinning. *Polym Engng Sci* 1981;13:844–53.
- [11] Gregory DR. Departure from Newtonian behavior of molten poly(ethylene terephthalate). *Trans Soc Rheol* 1973;17:191–5.
- [12] McHugh AJ, Yung WS. Strain-induced crystallization of swollen, crosslinked polyethylene. *J Polym Sci, Polym Phys Ed* 1989;43:1–42.
- [13] McHugh AJ, Yung WS. The influence of chain constraints on the kinetics of oriented crystallization under low stress. *Polymer* 1992;33:3670–4.



# Nextel™ 610 alumina fibre reinforced aluminium: influence of matrix and process on flow stress

B. Moser<sup>a,\*</sup>, A. Rossoll<sup>a</sup>, L. Weber<sup>a</sup>, O. Beffort<sup>b</sup>, A. Mortensen<sup>a</sup>

<sup>a</sup>Laboratory for Mechanical Metallurgy, Swiss Federal Institute of Technology, 1015 Lausanne, Switzerland

<sup>b</sup>Swiss Federal Laboratory for Materials Testing and Research, 3602 Thun, Switzerland

## Abstract

Continuous alumina fibre reinforced aluminium matrix composites are produced using two different liquid metal infiltration methods, namely direct squeeze casting and gas pressure infiltration. Net-shape fibre performs for longitudinal parallel tensile bars are prepared by winding the Nextel™ 610 alumina fibre (3M, St Paul, MN) into graphite moulds. High purity aluminium, two binary (Al–6% Zn and Al–1% Mg) and one ternary (Al–6% Zn–0.5% Mg) aluminium alloys are used as matrix materials. The composite is tested in uniaxial tension–compression, using unload–reload loops to monitor the evolution of Young's modulus. A linear dependence between Young's modulus and strain is observed; this is attributed, by deduction, to intrinsic elastic non-linearity of the alumina fibre. This conclusion is then used to compare on the basis of the in situ matrix flow curve the influence of matrix composition and infiltration process on the composite stress–strain behaviour. © 2001 Elsevier Science Ltd. All rights reserved.

**Keywords:** A. Ceramic fibre; B. Elasticity; D. Mechanical testing; E. Liquid metal infiltration; In situ matrix flow curve

## 1. Introduction

Industrial applications of aluminium unidirectionally reinforced with continuous alumina fibres call for cost-effective production methods for the composites. Two liquid metal infiltration methods offer potential for industrial production of such composites, namely direct squeeze casting and gas pressure infiltration; these are compared in Table 1.

The flow stress of resulting composites parallel to their fibres is strongly dominated by the elastic properties of the fibre reinforcement, since the fibres are far stiffer than the matrix and remain elastic. Comparatively, the contribution of the matrix along this direction is small; however, matrix composition and flow stress are nonetheless known to exert a significant influence on overall properties of infiltrated continuous fibre reinforced metals [1–8].

It is of interest, therefore, to gain an understanding of the in situ matrix plastic flow stress within fibre composites, and to assess variations in this stress with matrix nature and composite processing method. Indeed, within a composite, the flow stress of metals and alloys can generally not be assumed to be similar to that which

is measured in the unreinforced condition, even after analogous processing.

For fibre reinforced composites the matrix in situ flow curve can be back-calculated with relative ease from the composite flow curve [1,9]. This method yields the least ambiguous measure of matrix flow stress as a function of strain but requires care, because the resulting matrix flow curve is calculated by subtraction of two far larger numbers (the composite and fibre stresses). Hence, the result obtained is highly sensitive to input parameters such as fibre volume fraction and fibre Young's modulus, such that highly accurate values for these parameters are needed.

We present in what follows an investigation of the influence of matrix composition and of composite infiltration process on the in situ matrix flow stress within continuous alumina fibre reinforced aluminium and aluminium alloys. We explore the behaviour of higher strength matrices, which are attractive because these offer the possibility to improve the composite transverse strength and allow the fabrication of components containing stress-bearing unreinforced regions. We also provide a first comparison of the influence of process route on the matrix flow stress for pure aluminium. Finally, we present an improvement in the method of deriving the matrix in situ stress–strain curve from that of the composite, which yields higher quality data than in earlier work on the subject for similar composites [1,10].

\* Corresponding author. Fax: +41-21-693-46-64.

E-mail address: benedikt.moser@epfl.ch (B. Moser).

Table 1

Comparison of important parameters between gas pressure infiltration and direct squeeze casting

Direct squeeze casting	Gas pressure infiltration
High maximum pressure applied (100 MPa)	Moderate maximum pressure (10 MPa)
Short contact time between liquid metal and reinforcing phase	Longer contact time between liquid metal and reinforcing phase
Wide variety of matrix systems (including reactive systems)	Limited to systems that do not display excessive interfacial reactivity or matrix evaporation
Partially controlled preform atmosphere	Preform heated under vacuum
Mechanically strong preform housing necessary	Gas-tight preform housing necessary

## 2. Experimental

### 2.1. Materials

Alpha-alumina fibres, Nextel™ 610 from 3M (St Paul, MN, USA), were combined with four different aluminium matrices: 99.99% pure aluminium, two binary alloys (Al–1% Mg, Al–6% Zn), and a ternary alloy (Al–6% Zn–0.5% Mg).

The alumina fibre properties are listed in Table 2; its chemical compatibility with aluminium and its high strength and high elastic modulus are attractive properties for the reinforcement of aluminium and its alloys. The matrices selected differ in their reinforcing mechanisms, and also their reactivity with alumina.

### 2.2. Preform preparation

Net-shape fibre preforms for parallel tensile bars were produced by winding the fibre tow directly onto a graphite mould. During this winding process the fibre tow was wetted with an aqueous suspension of small alumina particles (Sumicorundum AA-07 from Sumitomo, Japan, mean particle diameter 0.86  $\mu\text{m}$ ) to improve the handling of the fibre tow and to create a separation of the fibres from each other in the composite [11,12].

The use of net-shape graphite moulds avoids machining of the composite. This in turn enables accurate determination of the fibre volume fraction within the composite (see below) and minimizes fibre damage at the surface of the tensile specimen (compared to machined specimens).

### 2.3. Liquid metal infiltration

The preforms were infiltrated using two different liquid metal infiltration processes, namely direct squeeze casting and gas pressure infiltration. Processing parameters for these infiltration steps are listed in Table 3.

For the direct squeeze casting technique the preform is

Table 2

Properties of the Nextel™ 610 alumina fibre [25,26]

Composition	> 99.99% $\alpha\text{-Al}_2\text{O}_3$
Mean UTS at $l = 25.4$ mm	3200 MPa
Weibull modulus	10–12
Young's modulus	373 GPa [24]
Density	3.82 g $\text{cm}^{-3}$ [24]
Diameter	11.64 $\mu\text{m}$
CTE	$7.1 \times 10^{-6} \text{ K}^{-1}$
Poisson ratio	0.27

preheated under an atmosphere of forming gas, and is then transferred rapidly into the die cavity. The liquid matrix is poured over the preform and the squeeze ram moves down under speed control until the maximum pressure is reached. The load is then held for a preset solidification time. Directional solidification is achieved due to the temperature gradient that is introduced during preheating between the bottom of the die cavity and the squeeze ram.

In gas pressure infiltration the graphite moulds containing the fibre preforms are placed at the bottom of a gas-tight alumina crucible, together with a cast matrix billet resting on top of the preform. The whole assembly is placed in a vacuum-pressure furnace and evacuated. After heating under vacuum to the infiltration temperature, pressurized argon is slowly introduced into the pressure vessel until the maximum desired pressure is reached. After 5 min holding time, the pressure is reduced and the crucible is lowered and rested onto a copper chill, in order to induce directional solidification. The maximum pressure is then reapplied and held during solidification.

### 2.4. Testing

Samples were extracted from their graphite moulds and tested without machining. Aluminium tabs were glued on both ends of the parallel tensile bars, so as to avoid damage from gripping during the tensile tests. Tensile tests were performed using a fully computer-controlled screw-driven MTS tensile testing machine (Alliance RT/50) equipped with hydraulic wedge grips. Tests were run at a crosshead speed of 5  $\mu\text{m/s}$ . As strain measurement is known to be strongly affected by bending in these materials [13,14] two strain gauges on opposite sides of the specimen, together with a double-sided extensometer rotated at 90° to the strain gauges, were used to measure the strain. All four strain channels were averaged to compute the composite axial strain.

The composite was cycled twice between 1000 and –600 MPa. During this cycle each 50 MPa three unload–reload cycles over a range of 150 MPa were performed in order to monitor the evolution of the Young's modulus of the composite. Finally the composite was loaded in tension to failure, still performing the unload–reload cycles each 50 MPa.

Samples of unreinforced matrix material cast by direct

Table 3  
Processing parameters for the liquid metal infiltration

	Direct squeeze casting	Gas pressure infiltration
Melt temperature	750°C	750°C
Preform preheating temperature	820°C	750°C
Die temperature bottom to top	150–350°C	–
Preform atmosphere	Forming gas, Noxal3 (Ar/H <sub>2</sub> )	Vacuum
Maximum pressure	100 MPa	9 Mpa
Time under maximum pressure at 750°C	–	5 min
Time under maximum pressure including solidification	4 min	Several hours

squeeze casting similarly to the composite materials were also produced, and tested after machining by electroerosion into dog bone specimens. Tests were performed strain rate controlled with a strain rate of  $10^{-4} \text{ s}^{-1}$ .

### 3. Results

#### 3.1. Microstructure and fibre volume fraction of the composites

All composites feature a homogeneous fibre distribution, regardless of the infiltration technique used, and of the matrix employed. Some fibre–fibre contacts and particle agglomerates are present in all systems, Fig. 1.

Given that the composites were not machined, the fibre volume fraction in the composite samples can be directly computed knowing the number of fibre tows laid up in the mould, the mass of a fibre tow per m (measured separately), the geometry of the mould, and the density of the alumina fibre. This computation yields  $59.9 \pm 0.4 \text{ vol\%}$  for all present composites. The particle content in the composite

was determined in the same way, and is  $1.36 \pm 0.02 \text{ vol\%}$  in the composite, corresponding to  $2.28 \pm 0.04 \text{ vol\%}$  in the matrix. According to the generalized self-consistent method of calculation of particle reinforced composite modulus [15,16] this particle content leads to an increase in the Young's modulus of the matrix of about 3 GPa.

#### 3.2. Tensile test results of the unreinforced matrix

Fig. 2 shows the stress–strain curve for the squeeze cast unreinforced matrix material samples. The four matrices are seen to differ markedly in yield strength, strain hardening, ultimate tensile strength and strain to failure. For instance, the yield stress varies from about 15 MPa for the pure aluminium samples to 150 MPa for the Al–6% Zn–0.5% Mg alloy. It is noted, however, that data for the pure aluminium and the binary alloys feature significant uncertainty because the grain size was large in comparison to the specimen cross-section.

#### 3.3. Tensile test results of the composites

Fig. 3 shows a typical composite stress–strain curve. A

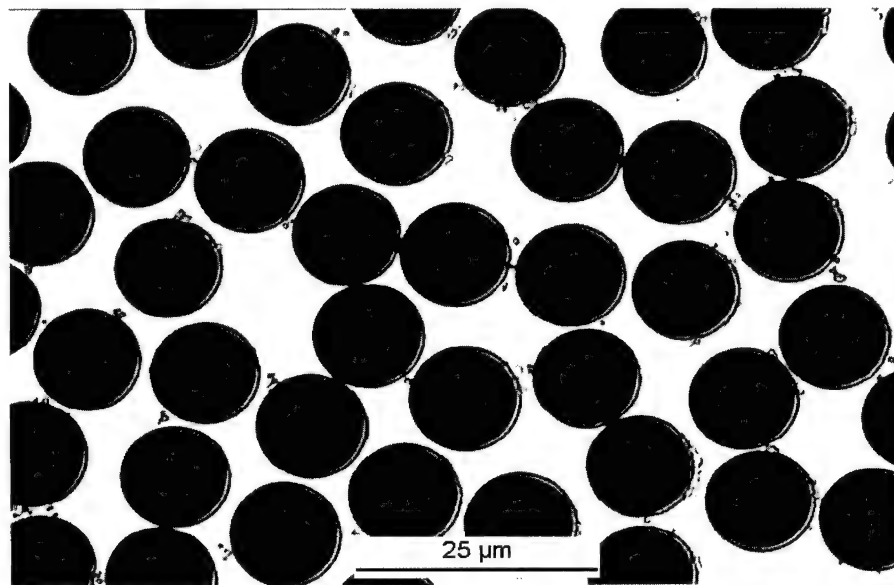


Fig. 1. Optical micrograph of a hpAl/Nextel™ 610 composite produced by direct squeeze casting. The alumina particles acting as spacers between the fibres are clearly visible.

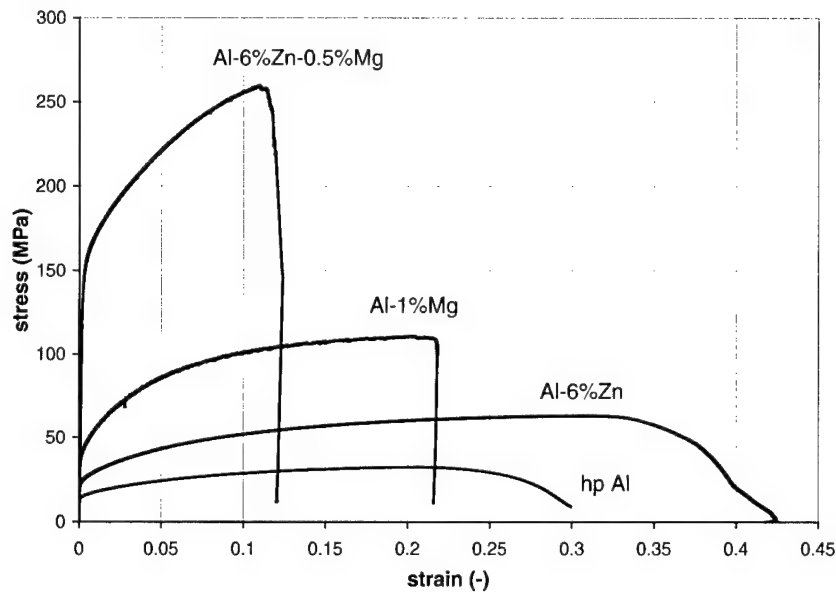


Fig. 2. Stress–strain response of the direct squeeze cast unreinforced matrix materials specimens.

clear knee-point at a strain of about 0.06% for the first loop can be seen, representing the matrix tensile elastic–plastic transition. Apart from this feature the first and the second loop between 1000 and –600 MPa are almost congruent with each other.

Fig. 4 represents the Young's modulus of the composite measured as a function of strain. One observes a linear variation of the modulus as a function of strain, in both compression and tension. This observation is consistent for all composite systems investigated in this study, Fig. 5. Additionally, some tests on commercially available aluminium wire from 3M (St Paul, MN, USA) unidirectionally reinforced with Nextel™ 610 continuous alumina fibre confirmed this result. Finally,

this behaviour was found to be completely reversible within the performed stress–strain loop.

#### 4. Discussion

##### 4.1. The evolution of Young's modulus

To explain the observed evolution of the composite Young's modulus, different hypotheses can be proposed. These comprise:

1. Progressive fibre fragmentation. An increasing amount of internal damage, including specifically an increasing

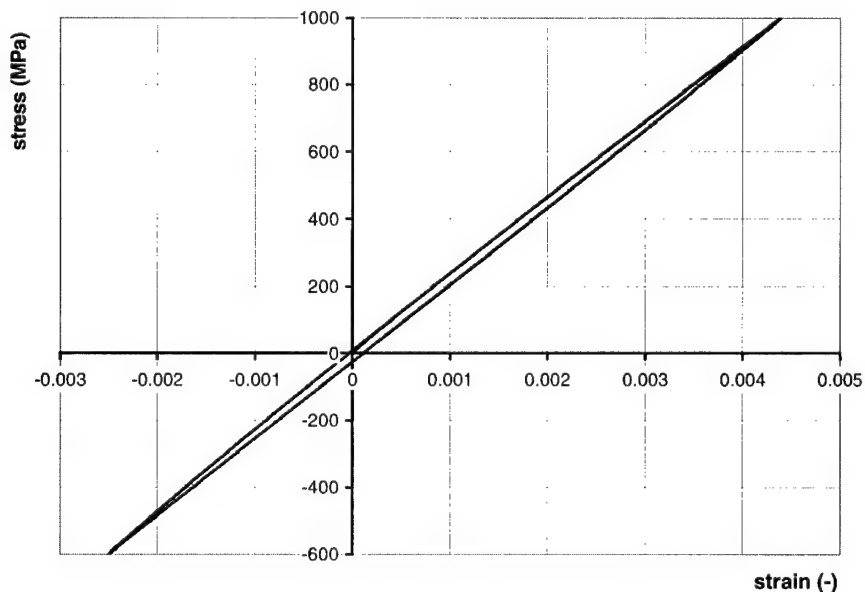


Fig. 3. Typical stress–strain response of hpAl/Nextel™ 610 composite with a fibre volume fraction  $V_f = 59.9$  vol% produced by gas pressure infiltration.

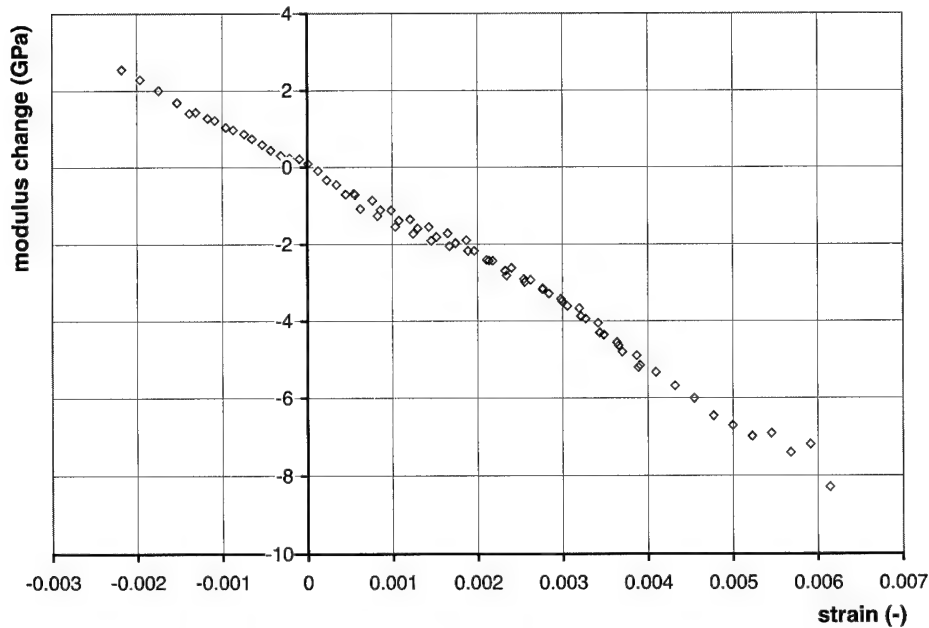


Fig. 4. Young's modulus evolution of a hpAl/Nextel™ 610 composite with a fibre volume fraction  $V_f = 59.9$  vol% produced by gas pressure infiltration.

number of broken fibres, would lead to a decrease of the composite modulus with strain. The complete reversibility of the measured modulus evolution (Fig. 4) and the continued linear evolution of the modulus in compression both make this hypothesis very unlikely.

2. Constant damage. Interestingly, a *constant* number of fibre breaks can also be invoked to explain such variations in the Young's modulus of the composite. Indeed, assume the composite contains a given fraction of fibre

breaks per unit fibre length. The effective contribution of the fibre bundle to the composite tensile modulus can be estimated using shear lag analysis as developed for a plastic matrix [17]: from each broken fibre end (where the fibre carries zero load), the fibre tensile stress is built up linearly over a certain length, known as the ineffective fibre length, from zero to the stress that would be borne by a break-free fibre (the remote fibre stress, roughly equal to  $E_f V_f \varepsilon$ ). The ineffective fibre length is thus

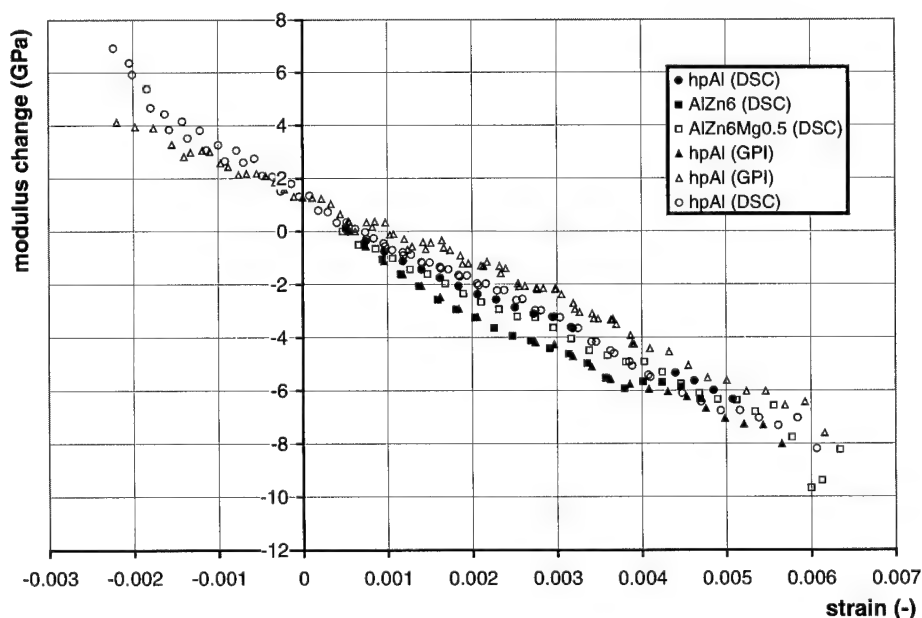


Fig. 5. The Young's modulus evolution for different matrix systems as a function of applied strain.

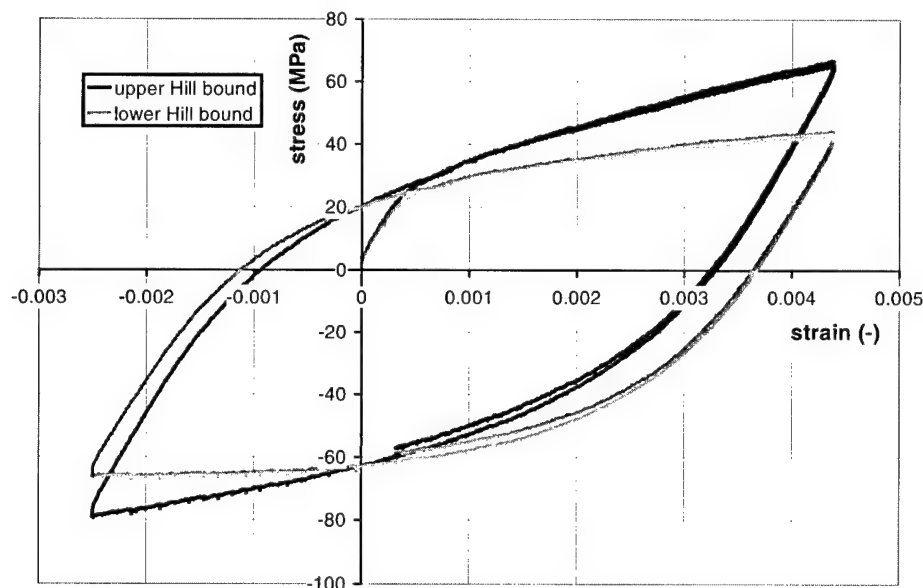


Fig. 6. In situ matrix flow curve of hpAl/Nextel™ 610 composite derived using upper and lower Hill bounds.

roughly a linear function of the strain  $\varepsilon$ . Hence, the deficit in the contribution of the fibres to the composite modulus caused by broken fibres is predicted to be linear with strain, in agreement with observations. In this sense, this analysis agrees with the data; however, this explanation can be excluded by comparison of composites with different matrices. Indeed, the ineffective fibre length is also inversely proportional to the yield stress of the matrix: the higher the matrix flow stress, the faster stress is built up in the fibres and the lower the modulus deficit is for a given strain and number of fibre breaks. The fact that the measured modulus decrease is independent of the matrix composition, Fig. 5, thus invalidates this hypothesis as an explanation of the present data.

3. Elastic non-linearity of alumina. The Young's modulus evolution can also be attributed to the intrinsic elastic non-linearity of the ceramic fibres. Non-linear elastic stress–strain behaviour (as also thermal dilatation) is a known direct consequence of the anharmonicity of interatomic potentials, which can be described via third-order elastic constants. Extensive literature exists on this subject, comprising compilations of single-crystal second [18–20] and higher order [19,20] elastic constants. From single-crystalline data (most such data are measured on whiskers), polycrystalline constants can be derived, e.g. with the classical Voigt–Reuss–Hill approximations (usually the arithmetic average of the Voigt and Reuss bounds is used). Values derived by this approach for second-order elastic constants in polycrystalline materials can be found in Ref. [18]. For alumina, values derived in this manner from tests on single-crystalline alumina [18] correspond very well to values derived from tests on polycrystalline alumina [21] if the latter are corrected for porosity. For uniaxial stress,

the third-order elasticity for the tensile modulus of an isotropic material can be described using the following equation:

$$\sigma_f(\varepsilon) = E_f \varepsilon + \frac{k}{2} \varepsilon^2 \quad (1)$$

Taking elastic constants from Refs. [18–20] leads to  $E_f = 403$  GPa and  $k = -3506$  GPa at  $\rho = 3.98$  g cm<sup>-3</sup>. This is somewhat higher, but of the same order of magnitude, as the value of  $k$  measured here for the Nextel™ 610 alumina fibres ( $k = -2540$  GPa). The discrepancy can in part be ascribed to the somewhat lower density of the Nextel™ 610 fibres (their nominal modulus of 373 GPa is somewhat lower than 403 MPa for this reason).

#### 4.2. In situ matrix stress–strain curves

The equistrain rule of mixtures is only exact if the Poisson ratios of the two phases (matrix and reinforcement) are identical. As these two ratios differ, additional stresses are built up in the fibre due to the lateral contraction mismatch between fibre and matrix; these cause the composite stress–strain curve to exceed that predicted by the equistrain rule of mixtures. Hill [22,23] gives finite positive bounds for the resulting deviation of the Young's modulus of the composite from the value predicted according to the equistrain rule of mixtures, valid for all unidirectional continuous reinforcements. These bounds are smaller for an elastic matrix than for a perfectly plastic matrix (for which the effective Poisson ratio is  $\nu_m = 0.5$ ).

For simplicity, we take the matrix as perfectly plastic and assume a random fibre spatial distribution. The resulting



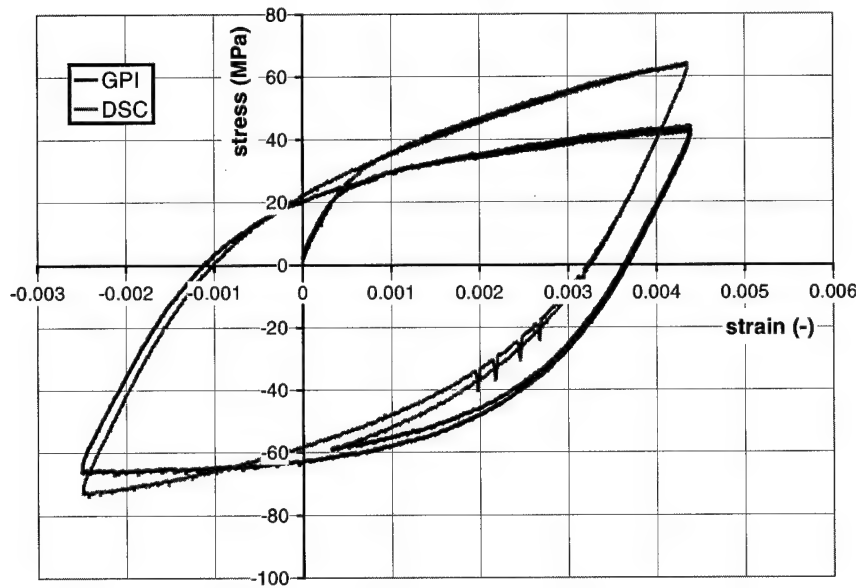


Fig. 7. Comparison between gas pressure infiltrated (GPI) and direct squeeze cast (DSC) hpAl/Nextel™ 610 composites (lower Hill bounds for both composites). The curve for the direct squeeze cast matrix is slightly tilted upward.

bounds are the widest possible and therefore conservative:

$$\begin{aligned} \frac{V_f V_m (1 - 2\nu_f)^2}{\left( \frac{V_f}{K_m} + \frac{V_m}{k_f^p} + \frac{1}{G_m} \right)} &\leq (E_c - E_f V_f) \\ &\leq \frac{V_f V_m (1 - 2\nu_f)^2}{\left( \frac{V_f}{K_m} + \frac{V_m}{k_f^p} + \frac{1}{G_f} \right)} \end{aligned} \quad (2)$$

For the system at hand, these bounds are respectively near 1.9 and 4.0 GPa. As in Ref. [1], we treat these as a source of uncertainty, by evaluating the composite flow stress as:

$$\sigma_c = \sigma_m (1 - V_f) + \sigma_f V_f + (h \pm \Delta h) \varepsilon \quad (3)$$

where  $h = (4.0 + 1.9)/2$  GPa = 2.95 GPa and  $\Delta h = (4.0 - 1.9)/\text{GPa}^2 = 1.05$  GPa.

Using Eq. (1) for  $\sigma_f$  yields:

$$\sigma_m = \frac{\sigma_c - \left( E_f \varepsilon + \frac{k}{2} \varepsilon^2 \right) V_f - (h \pm \Delta h) \varepsilon}{1 - V_f} \quad (4)$$

which is used to calculate the in situ stress–strain curve for the matrix behaviour.

This computation comprises computing the difference between two big numbers; it is therefore very sensitive to second-order variations in these two numbers. In particular, the input values for the fibre volume fraction  $V_f$  and the fibre Young's modulus at zero strain  $E_f$  influence the result strongly. The following input values were used for all subsequent calculations:  $V_f = 59.9 \pm 0.4\%$  (calculated from counted fibre tows, measured fibre mass per length, mould

geometry and density [24],  $E_f = 373$  GPa [24],  $k = -2538$  GPa (measured value).

It is found that the values for fibre volume fraction and initial composite Young's modulus correspond well to the measured Young's modulus for the composite at zero strain; this is indicative of the greater accuracy of this computation as conducted here compared with earlier work, where such agreement could not be found [1,10].

Fig. 6 shows the upper and lower Hill bounds for the in situ matrix flow curve computed using Eq. (4) from a composite stress–strain curve, measured on a hpAl/Nextel™ 610 composite produced by gas pressure infiltration. The curve exhibits an elastic regime with a clear elastic–plastic transition at a strain near 0.06% for the first loop, which corresponds to the knee-point in the composite curve. The plastic part of the curve shows a roughly linear strain hardening. This curve shows that the separation within the bounds calculated using Hill's approach creates significant uncertainty in the derived in situ matrix stress–strain curve; to this uncertainty must be added that resulting from uncertainty in  $V_f$  and  $E_f$ .

It is reasonable to suppose, however, that for these composites, the average volume fraction and deviation from the equistrain rule of mixtures does not vary much from composite to composite. Therefore, to compare matrices, we use one single curve, namely (somewhat arbitrarily) that computed with  $V_f = 59.9\%$  using the lower Hill bound of 4.0 GPa for the deviation from the equistrain rule of mixtures.

The comparison between the high-purity aluminium matrix of samples produced by the two infiltration methods is shown in Fig. 7: there is a small, but noticeable difference between the two curves. The curve for the direct squeeze

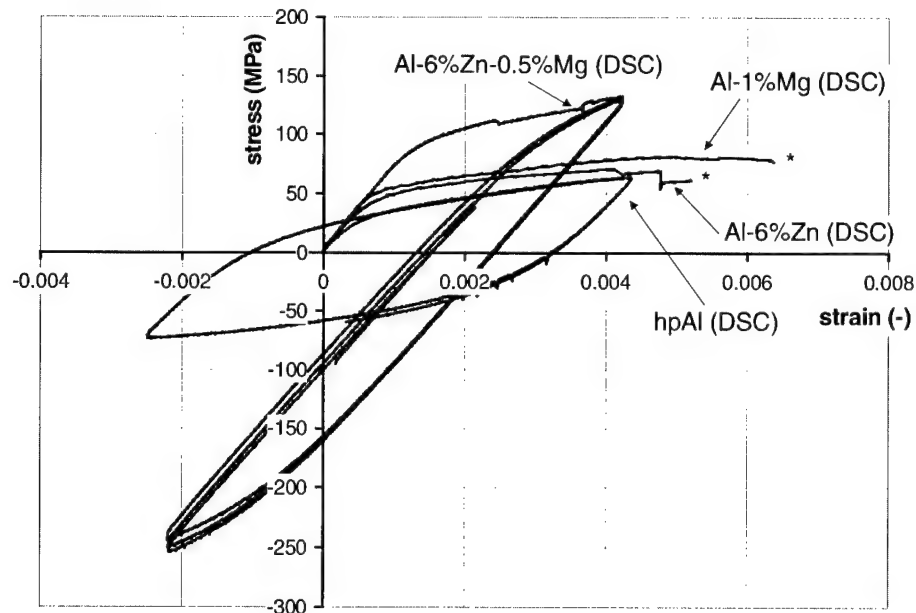


Fig. 8. In situ flow curves of the different matrix systems back-calculated from composite data using Hill's lower bound. The \* marks composite failure.

cast matrix seems to be tilted compared to the gas pressure infiltrated matrix curve; however, the shape and the size is the same. This tilt can be attributed to an elastic contribution that is higher in the case of the infiltration by direct squeeze casting, perhaps due to a greater degree of infiltration under the higher pressure applied. The residual stresses resulting from the two infiltration methods used, of about 15 MPa, are quite similar. The matrix plastic flow stress, of about 40 MPa for both composites, significantly exceeds that of the unreinforced matrix, Fig. 2. This observation, and also values for residual and plastic flow stresses, are in overall agreement with what is found for this composite in Ref. [1].

A comparison between the different matrices in direct squeeze cast composites is shown in Fig. 8. This comparison shows a somewhat higher flow stress for the solid-solution hardened binary matrices compared with pure aluminium; however, the difference found between these, and with the curve obtained for pure aluminium, is relatively small. This is a result of the significant dislocational hardening of the matrix caused by thermal mismatch during cool-down, which brings the unalloyed aluminium matrix closer to the two solid-solution strengthened alloys. Comparatively, the precipitation hardenable ternary alloy shows a far higher matrix flow stress (~150 MPa) and, as a consequence, also a far higher residual stress, in the region of about 70 MPa. This matrix, and as a consequence the composite, can deform elastically over a significantly higher strain interval.

## 5. Conclusions

- Nextel™ 610 alumina fibres (and possibly other high-

strain ceramic fibres) exhibit an elastic non-linearity that can be fairly well described for uniaxial deformation using one additional parameter for the Young's modulus. Due to the high contribution of fibre stress to longitudinal composite stress, this phenomenon cannot be neglected when the damage is investigated by means of Young's modulus evolution or when the matrix in situ flow stress curve is back-calculated from that of the composite.

- From mechanical test data, there is no evidence for fibre-related damage in the present composites at flow stresses below 1 GPa (corresponding to about 70% of the mean composite UTS).
- The difference in in situ flow curve of Nextel™ 610 fibre reinforced 99.99% pure aluminium between direct squeeze cast and gas pressure infiltrated composites is slight, and corresponds to enhanced purely kinematic hardening in the former.
- Despite dislocational hardening effects due to thermal mismatch strains, the precipitation hardened Al-6% Zn-0.5% Mg matrix features a significantly higher in situ flow stress compared with pure, and with solid-solution strengthened, aluminium matrices.

## Acknowledgements

The authors would like to thank the 3M Company (St Paul, MN, USA) for providing the fibre material. We also wish to express our gratitude to Dr Colin McCullough, Mr Tracy Anderson and Dr David Wilson from 3M for helpful advice and several stimulating discussions over the course of this work.

This research is financially supported by the EMPA–EPFL joint thesis program and core laboratory funding within EMPA and EPFL.

## References

- [1] Bystricky P, Bjerregård H, Mortensen A. Plasticity of continuous fibre reinforced metals. *Metall Mater Trans A* 1999;30A:1843–66.
- [2] McCullough C, Galuska P, Pittman SR. Criteria for matrix selection in continuous fibre aluminum matrix composites. Design fundamentals of high temperature composites, intermetallics and metal–ceramics systems. Proceedings of TMS Annual Meeting, California, February, 1996. p. 15–28.
- [3] McCullough C, Deve HE, Channell TE. Mechanical response of continuous fibre-reinforced  $Al_2O_3$ –Al composites produced by pressure infiltration casting. *Mater Sci Engng* 1994;A189:147–54.
- [4] Neussl E, Fettweis D, Sahn PR, Yong S, Flower HM. High strength Al–Zn–Mg matrix-alloy for continuous fibre reinforcement. Metal matrix composites and metallic foams. Proceedings of Euromat 99, Munich, Germany, vol. 5, October, 1999.
- [5] Hu M-S, Yang J, Cao HC, Evans AG, Mehrabian R. The mechanical properties of Al alloys reinforced with continuous  $Al_2O_3$  fibres. *Acta Metall* 1992;40(9):2315–26.
- [6] Nolte M, Neussl E, Sahn PR, Carré C, Hornung B. Progress in the development of cost-efficient MMCs with selective continuous fibre reinforcement. In: Poursartip A, Street K, editors. Proceedings of the Tenth International Conference on Composite Materials, Whistler, Canada, vol. 2, 1995. p. 115–22.
- [7] Degischer HP, Schmitt Th, Leitner H, Mundl A. Faserverstärkte Aluminiummatrix-Proben hergestellt mittels Druckinfiltration. In: Speidel, Uggowitzer Hrsg. Ergebnisse der Werkstoff-Forschung, Zürich, 3, 1990.
- [8] Chen AS, Bushby RS, Scott VD. Deformation and damage mechanisms in fibre-reinforced aluminium alloy composites under tension. *Compos Part A* 1997;28A:289–97.
- [9] Kelly A, Lilholt H. Stress–strain curve of a fibre-reinforced composite. *Philos Mag* 1969;20:311–28.
- [10] Isaac JA, Mortensen A. Structure and room-temperature deformation of alumina fibre-reinforced aluminum. *Metall Trans* 1992;23A:1207–19.
- [11] Yamada S-I, Towata S-I, Ikuno H. Mechanical properties of aluminum alloys reinforced with continuous fibers and dispersoids. In: Fishman SG, Dhingra SK, editors. Cast reinforced metal composites. Proceedings ASM Chicago, 1988. p. 109–14.
- [12] Towata S-I, Yamada S-I. Mechanical properties of aluminum alloy composites with hybrid reinforcements of continuous fiber and whisker or particulate. In: Kawata, Umekawa, Kobayashi, editors. Composites '86: recent advances in Japan and the United States. Proceedings CCM-III, Tokyo, 1986.
- [13] Lord JD, Roebuck B, McCartney LN, Cooper PM. Tensile testing of fibre reinforced metal matrix composites. The materials revolution through the 90s. In: Proceedings of the BNF 7th International Conference, Oxford, paper 26, vol. 2, 1989.
- [14] Roebuck B, Gorley TAE, McCartney LN. Mechanical property test procedures for metal matrix composites. *Mater Sci Technol* 1989;5:105–17.
- [15] Christensen RM, Lo KH. Solutions for effective shear properties three phase sphere and cylinder models. *J Mech Phys Solids* 1979;27:315–30.
- [16] Christensen RM, Lo KH. *J Mech Phys Solids* 1986;34:639 (erratum).
- [17] Kelly A, Tyson WR. Fibre-strengthened materials. In: Zackay VF, editor. High-strength materials. Proceedings of the Second Berkeley International Materials Conference, vol. 13, 1964. p. 578–602.
- [18] Simmons G, Wang H. Single-crystal elastic constants and calculated aggregate properties: a handbook. 2nd ed.. Cambridge, MA: MIT Press, 1971.
- [19] Landolt-Börnstein. In: Hellwege K-H, editor. Numerical data and functional relationships in science and technology, new series, vol. III/11. Berlin: Springer, 1979.
- [20] Landolt-Börnstein. In: Hellwege K-H, editor. Numerical data and functional relationships in science and technology, new series, vol. III/18. Berlin: Springer, 1984.
- [21] Chung DH, Simmons G. Pressure and temperature dependence of the isotropic elastic moduli of polycrystalline alumina. *J Appl Phys* 1968;39:11.
- [22] Hill R. Theory of mechanical properties of fibre-strengthened materials: I. Elastic behaviour. *J Mech Phys Solids* 1964;12:199–212.
- [23] Hill R. Theory of mechanical properties of fibre-strengthened materials: II. Inelastic behaviour. *J Mech Phys Solids* 1964;12:213–8.
- [24] McCullough C, Wilson D. Personal communication, May 2000.
- [25] 3M Ceramic Fibre Products, Nextel™ Ceramic Fibre Technical Notebook, St Paul, MN, USA.
- [26] Wilson DM. Statistical tensile strength of Nextel™ 610 and Nextel™ 720 fibres. *J Mater Sci* 1997;32:2535–42.

# Selectively fibre-reinforced components produced by the modified investment casting process

E. Neussl\*, P.R. Sahn

*Giesserei-Institut, RWTH Aachen, Intzestr. 5, 52056 Aachen, Germany*

## Abstract

A process based on the investment casting process (lost wax process) for the production of selectively fibre-reinforced castings has been developed at the Giesserei-Institut in Aachen. Besides the production of simple-shaped test specimens, the production of complex-shaped components has been demonstrated. The adaptation of a core technique allows cavities to be made in the final casting.

In addition to the process development itself, the development of a suitable matrix alloy was one of the main targets in the past. Neither commercial alloys nor pure aluminium can be used for selectively reinforced castings owing to insufficient mechanical properties of the fibre-reinforced, or of the unreinforced, section of the casting. Only some alloy compositions of the system Al–Zn–Mg show satisfactory mechanical behaviour in the MMC and in the unreinforced sections. © 2001 Elsevier Science Ltd. All rights reserved.

**Keywords:** A. Metal–matrix composites (MMCs); A. Fibres; B. Mechanical properties; E. Filament winding

## 1. Introduction

Nowadays, all light metals are used for structural applications and are competing with polymer matrix composites in this field. Metal–matrix composites (MMCs) have been developed for the past 20 years or more for the improvement of specific properties of these metals including the coefficient of thermal expansion (CTE), wear resistance, ultimate tensile strength (UTS), elastic modulus, etc. MMCs can be classified as particulate, short fibre or continuous fibre-reinforced material depending on the geometry of the reinforcement. The particulate reinforcements can be considered as the least expensive with reference to continuous fibres as the most expensive.

The use of continuous fibre-reinforced metals (CFRMs) is currently restricted largely because of inadequate fibre and processing costs. The application of filament winding techniques, selective reinforcement of the components and cost-efficient casting routes open up new possibilities to surmount these limitations.

The modified investment casting process developed at the Giesserei-Institut in Aachen, which we present in the following, represents a combination of two well-known processes, both well established for industrial production of high-quality components. The filament winding technique is widely used for the production of polymer matrix

components and the investment casting process is used for the production of complex-shape metallic components.

The selective reinforcement of aluminium castings with continuous ceramic fibres was the aim of this process development. This means that the material has to fulfil minimum requirements in the fibre-reinforced as well as in the unreinforced conditions. In an ongoing EU-project, these dual requirements have been defined as shown in Fig. 1. Note that, contrary to polymer matrix composites, the compressive strength of the CFRMs is much higher than their tensile strength. Due to the metallic matrix, the transverse strength is also significantly higher. Therefore a unidirectional reinforcement can be applied to multiaxially loaded components.

In addition to the production process development, the development of a suitable matrix represents one of the challenges that must be overcome for the success of this approach. Indeed, if commercial aluminium alloys are used as matrix material, the optimal tensile strength of the MMC cannot be reached. On the other hand, pure aluminium or other optimal composite matrices often do not fulfil the property goals for the unreinforced material.

## 2. The investment casting process

The newly developed precision casting process [1] is based on the investment casting route, which is well established for the manufacture of high-quality components

\* Corresponding author. Tel.: +49-241-805903; fax: +49-241-8888276.  
E-mail address: eric@gi.rwth-aachen.de (E. Neussl).

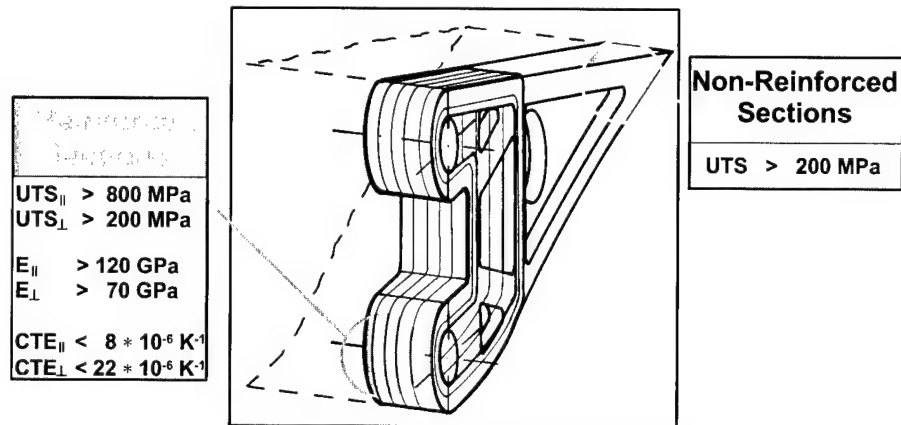


Fig. 1. Minimum property goals of selectively fibre-reinforced aluminium investment castings.

primarily for the aerospace sector. The main benefits of the investment casting process are high design freedom, near-net-shape production and cost-efficiency for small to medium lot sizes. For the incorporation of the ceramic fibres into this process, the filament winding technique has been modified towards the use of wax instead of polymer resins. Compared to the conventional investment casting technique, certain modifications have been made in the wax-pattern manufacture and in casting substeps (see flow chart in Fig. 2).

Processing comprises three main substeps: pattern-making with organic wax as pattern material, ceramic shell mould fabrication, and liquid metal infiltration. The continuous fibres are delivered as multifilaments of about 1000 fibres/tow on bobbins. These are placed into a spool

facility, which bundles a number of individual tows for the subsequent impregnation with liquid wax. The tow is drawn out of the wax bath and shaped into the geometry required for fibre reinforcement of the component. Shaping can be achieved either by filament winding techniques or by pressing a number of aligned fibre tows in a die. Component sections, which are intended to be non-reinforced, are added by conventional wax injection techniques. Finally, the completed wax pattern is fixed to a sprue and gating system, also commonly made of wax. The second main substep employs conventional dipping and sanding cycles to build up a ceramic shell mould. Now the wax has to be removed from the mould (lost wax process). Most of it is removed in a steam autoclave. A subsequent firing process burns out the remaining wax and strengthens the ceramic

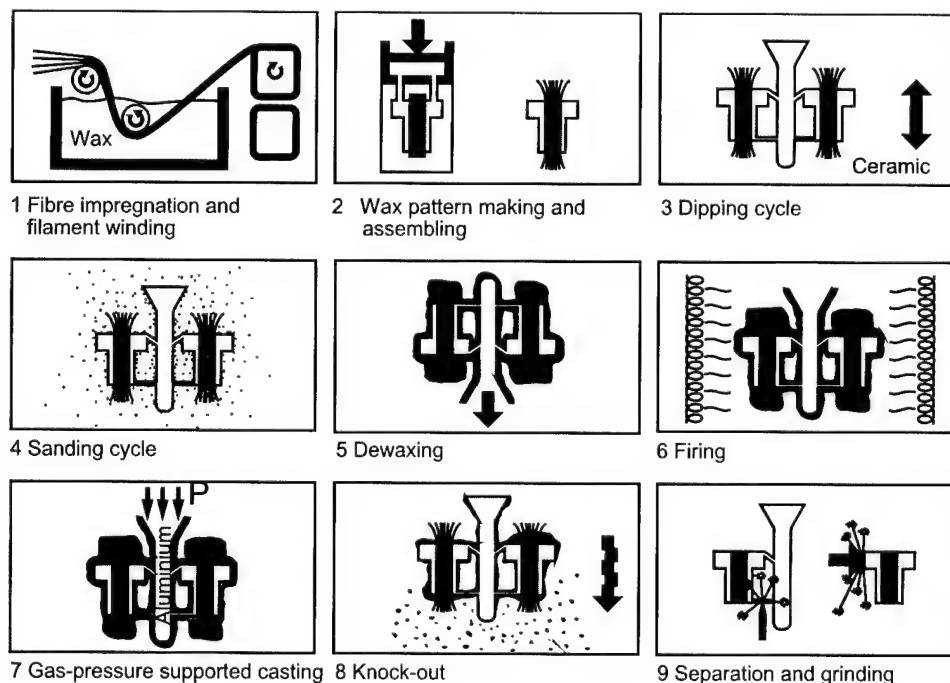


Fig. 2. Flow diagram of the modified investment casting process for production of CFRM parts. The wax pattern fabrication substeps can be combined with flexible filament winding techniques.

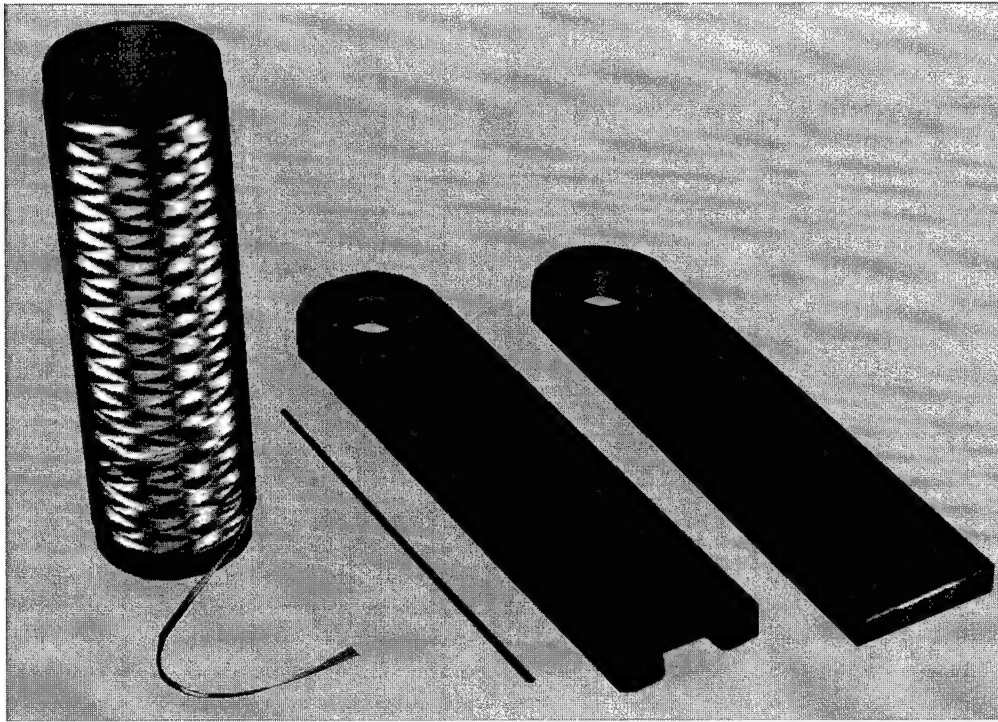


Fig. 3. Production route for selectively fibre-reinforced investment castings; fibres as received on spools, wax impregnated fibre tow, wax pattern and finished casting.

mould. The fibres are now found inside the cavity of the mould without any binder. Carbon fibres cannot be used for this process owing to the firing step and the low oxidation resistance of carbon fibres.

The melt infiltration substep uses an inert gas support of about 1 MPa. The aluminium melt is poured into the cavity of the mould and is pressurised immediately. The pressure

allows the melt to flow into the fibre bundles. After cooling down to room temperature, the mould is removed from the casting, which can be sandblasted and machined to its final geometry if necessary (Fig. 3).

The flow diagram (Fig. 4) shows the principal set-up of the casting unit that has been designed at the Giesserei-Institut for the production of fibre-reinforced investment

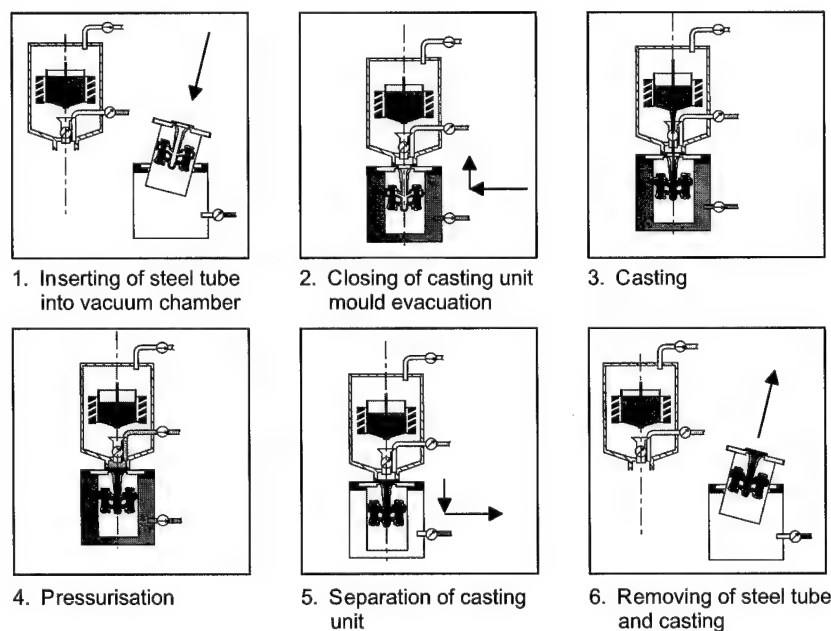


Fig. 4. Schematic flow chart of the new casting unit with a melting chamber at the top and the shell mould placed in a vacuum vessel at the bottom.



castings. A ceramic mould, backfilled with plaster material in a stainless steel case is placed into a vacuum chamber. The vacuum chamber is then attached to the melting and casting unit and evacuated. The capacity of the melting furnace is up to 10 kg of aluminium.

The crucible is equipped with a plug to allow controlled filling of the mould. After filling, a valve is closed separating the furnace from the high-pressure chamber. Then the pressure for infiltration is applied ( $\sim 1$  MPa). Next, the vacuum chamber is detached from the furnace unit and the steel case including the mould is withdrawn. The casting unit is process controlled and the most important parameters (temperature, pressure and time) are recorded.

### 3. The matrix alloy

For the successful production of selectively reinforced fibre–metal composite components, the development of a suitable matrix alloy is one of the most important issues. We have found, after extensive experimentation (thousands of experiments), that none of the commercial aluminium casting alloys can successfully be used as matrix for alumina-based fibres.

The influence of all alloying elements commonly used with aluminium has systematically been investigated. Zinc is the only alloying element that can be added to aluminium without substantial losses of tensile strength in the MMC. For alumina-based fibres as reinforcement and almost any Al-alloy composition as matrix, the bonding between fibre and matrix can be considered as strong if no surface treatment is applied to the fibres. Contrary to published views of other researchers [2,3], a strong aluminium matrix with a good bonding between fibre and matrix can produce a high-strength composite if a precipitate-free fibre–matrix inter-

Table 1

Mechanical properties of Al–Zn–Mg with and without fibre reinforcement (50 vol.% Altex) after heat treatment

	Al–Zn6–Mg1–Ag1 matrix	
	No reinforcement	50 vol.% reinforcement
Density ( $\text{g/cm}^3$ )	2.8	3.1
UTS $0^\circ$ (MPa)	> 350	> 900
UTS $90^\circ$ (MPa)	( $R_p$ 0.2 > 320)	> 200
Compression strength $0^\circ$ (MPa)	–	> 2000
Compression strength $90^\circ$ (MPa)	–	> 450
Modul tension $0^\circ$ (GPa)	75	135
Modul tension $90^\circ$ (GPa)		80

face can be created. No commercial aluminium alloy fulfils this requirement.

Our investigations led to the use of a Al–Zn6–Mg1–Ag1 alloy, which shows high strength in the fibre-reinforced as well as in the unreinforced areas after heat treatment [4]. Some mechanical properties of the alloy and the composite to be used for component layout are summarised in Table 1.

### 4. First components

Various test specimen geometries and some prototype components have been produced with this process (Fig. 5). As a demonstrator for the selective reinforcement of components, a bicycle crank was selected. The standard loading for certification of bicycle cranks is dynamic with a maximum of  $F = 1000$  N and a ratio of  $R = 0$  as shown in Fig. 6. It was designed as a hollow elliptical profile selectively

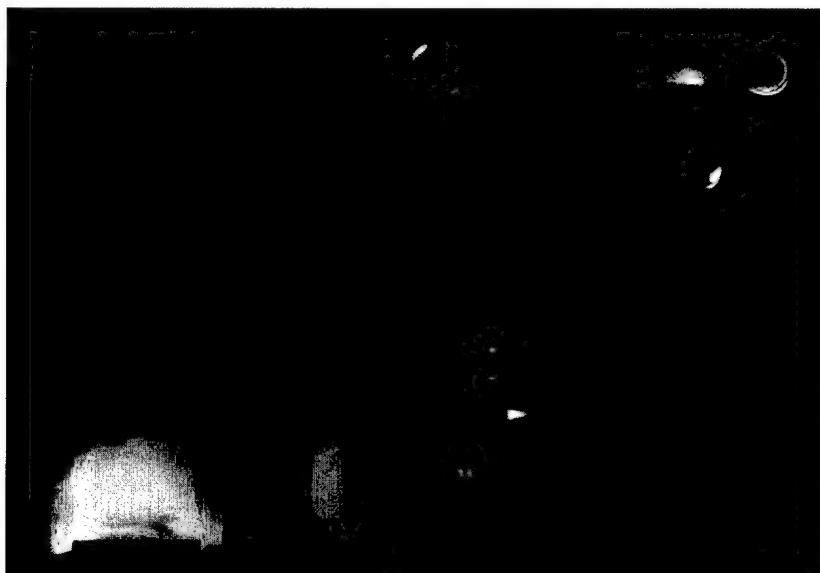
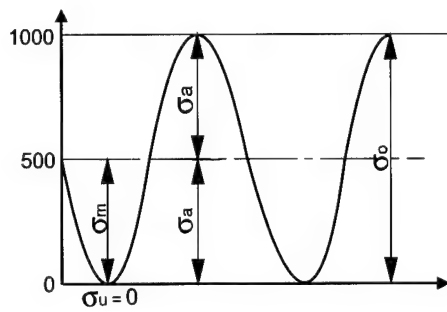


Fig. 5. Castings produced by the modified investment casting process.



Dynamic loading

$$R = \sigma_u / \sigma_o = 0$$

$$F = 1000 \text{ N}$$

$$L = 170 \text{ mm}$$

$$\alpha = 45^\circ$$

$$B = 57,5 \text{ mm}$$

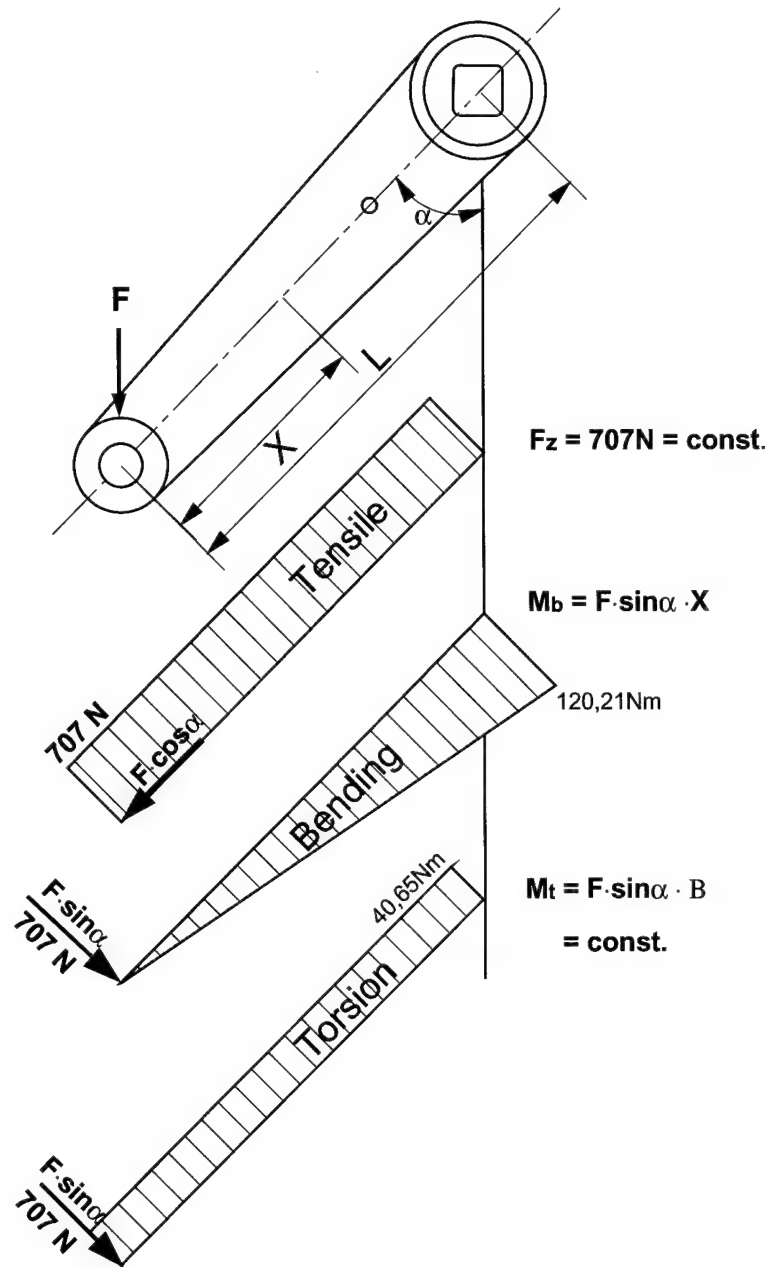
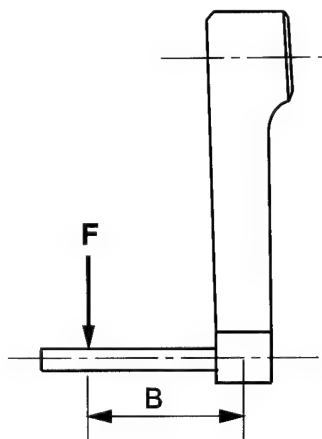


Fig. 6. Geometry and external loads of the bicycle crank.

reinforced with unidirectional fibres. The bending moment is taken by the fibre reinforcement, the torsion is taken by the unreinforced material itself. Additionally, the two sections at the tips are reinforced with circumferential windings (see Fig. 7). Altogether three ceramic cores and three windings are used for one component.

First-generation components have been tested under fatigue and failed after 224,000 cycles. The crack was initiated in the unreinforced sections at the holes result-

ing from the core prints of the central core. It grew at an angle of  $45^\circ$  indicating that the torsion moment was not successfully taken owing to shortcomings of this first design. An improved geometry will be tested in the near future.

The weight of the component has been reduced to 187 g compared to 250 g of a conventionally designed component. Numerical simulations of the component may achieve additional weight savings.



## 5. Conclusions

A production process has been developed which enables the production of selectively reinforced fibre–aluminium composite investment castings of high design flexibility. With respect to real applications, the modified investment casting process seems to be suitable as an economical and flexible production strategy and thus can allow CFRMs to be used for a broader spectrum of industrial applications.

The mechanical properties of this material fulfil the minimum requirements in the fibre-reinforced as well as in the unreinforced sections if a matrix alloy from the system Al–Zn–Mg is used. In this system, there are favourable alloy compositions showing an ultimate tensile strength higher than 350 MPa in the unreinforced section and higher than 900 MPa in the composite combined with a reasonable castability. First prototypes have successfully been produced by the modified investment casting process.

## Acknowledgements

The authors would like to acknowledge the funding of the EU that enabled them to perform the work presented above.

## References

- [1] Nolte M, Neussl E, Sahm PR. Design opportunities yielded by investment-cast continuous-fiber-reinforced metals. *Trans Am Foundrymens Soc* 1994;102:949.
- [2] Cornie JA, Argon AS, Gupta V. Designing interfaces in inorganic matrix composites. *MRS Bull* 1991;April:32–7.
- [3] Deve HE, McCullough C. Continuous-fiber reinforced Al composites: a new generation. *JOM* 1995;47(7):33–7.
- [4] Neussl E, Fettweis D, Sahm PR, Yong S, Flower HM. High strength Al–Zn–Mg matrix alloy for continuous fibre reinforcement. *EURO-MAT-99*, vol. 5, 1999. p. 119.

# Rheology and structuring in organo-ceramic composites

A.J. McHugh\*, J.A. Walberer

*Department of Chemical Engineering, University of Illinois at Urbana–Champaign, 600 S. Mathews, Urbana, IL 61801, USA*

## Abstract

The processing–structure–property relationships for calcium aluminate based organo-ceramic composites are reviewed. Processing behavior was measured with a torque-outfitted Banbury mixer, structuring behavior was analyzed with electron microscopy, and mechanical properties were determined using flexural strength measurements. These results are discussed for composites composed of either a polyvinyl alcohol or phenol formaldehyde resin organic phase. The two materials have different processing behaviors, driven by different paste formation mechanisms, but are observed to have similar microstructure and mechanical properties. The rheology of model, non-calcium aluminate based composites was studied using a lubricated squeezing flow rheometer. The relaxation modulus following a step strain was measured for reactive systems that stiffened due to a crosslinking polymer phase or a polymerizing polymer phase and compared to that measured for non-reactive polydimethyl siloxane (PDMS) systems with filler fractions from 0 to 65% by volume and 65% filled PDMS of differing molecular weights. Comparison of the normalized relaxation moduli of the model reactive and non-reactive materials suggests similarities between the effect of filler amount and crosslinking amount and between the combined effects of molecular weight and filler amount and the degree of polymerization. © 2001 Elsevier Science Ltd. All rights reserved.

**Keywords:** A. Ceramic–matrix composites (CMCs); B. Mechanical properties; D. Electron microscopy; Rheology

## 1. Introduction

Reactive organo-ceramic composites consisting of calcium aluminate particles embedded in a dense polymer matrix represent an important new class of high-strength materials. These systems have the advantage that they can be fabricated at or near room temperature as extrudable pastes, prior to low temperature heat treating, to produce hardened materials with properties similar to fired ceramics. The paste state is generated by chemical and/or physical interactions that take place between the organic and ceramic phases during high-shear processing, leading to rheological properties similar to those of highly-filled polymer melts. A unique but essential feature of these pastes is that due to the progression of chemical and/or physical interactions taking place, the processing behavior of the paste changes with time, i.e. the paste becomes stiffer and its viscosity increases as it is mixed or processed. In order to take advantage of the continuous processing possibilities of these pastes, one needs to understand how the paste rheology evolves with the processing time.

These composites were first developed by Birchall et al. [1] as a means to improve the flexural strength of hydraulic cement. By combining a small amount of a polyvinyl

alcohol (PVA) polymer with a calcium aluminate cement (CAC) in a high-shear mixing environment, they produced hardened materials with flexural strengths in excess of 200 MPa. By comparison, a cast and dried cement paste has a typical flexural strength of 3–10 MPa. Since then, many combinations of cement and polymer have been reported in the literature, but the CAC–PVA composite has the highest flexural strength and has been the most extensively studied. Due to problems with the durability of the PVA composite, Pushpalal et al. [2] replaced the PVA with a hydrophobic phenol formaldehyde resin (PR) and were successful in making a more durable, but still high-strength composite.

Previous studies on CAC–PVA and CAC–PR composites have shown that quantitative information on the mixing chemistry and resultant properties of the polymer-particle network can be generated using Banbury mixing. This type of processing protocol, in conjunction with mechanical testing and microscopy studies of hardened composite, has been used as part of a comprehensive study in the authors' laboratory on the processing–property–structure relationship in these composites [3–7]. In an attempt to generalize the work on these two specific systems and to understand better the evolving paste rheology of these reactive composites, the authors have studied two model reactive systems whose mechanism of paste stiffening is known [8].

The objective of this study is to review the processing–

---

\* Corresponding author. Tel.: +1-217-333-1178; fax: +1-217-333-5052.  
E-mail address: a-mchugh@uiuc.edu (A.J. McHugh).

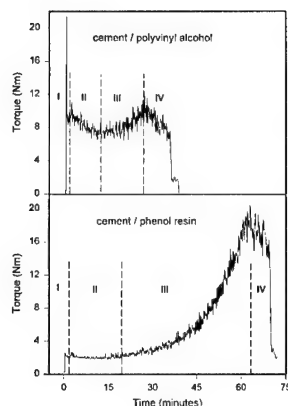


Fig. 1. Torque versus mixing time plot of CAC–PVA (top) and CAC–PR (bottom) composites at 100 rpm.

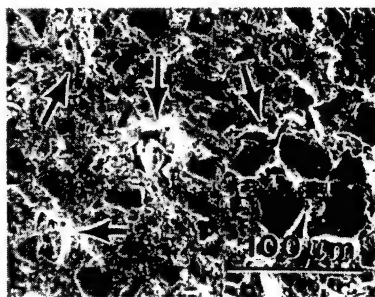
property–structure relationship for the CAC based composites and to present some new information on the rheological and processing characterization of model highly-filled reactive composites.

## 2. Organo-ceramic composites

Two different composite systems, both based on CAC, have been extensively studied. Their formulation and strength in the hardened state are compared to that of the ordinary portland cement in Table 1. The pastes are prepared by pre-blending the components in a planetary mixer and then feeding them into a high-shear Banbury mixer. In the mixer the material is transformed from a damp powder into a viscoplastic paste within about 30 s. The torque required to maintain a constant mixing rate is measured by the Banbury mixer. As the pastes react and stiffen in the mixer, the mixing torque increases. Monitoring of the torque versus time profile gives an insight into the kinetics of the mechanism(s) responsible for the paste stiffening. Generic examples of torque versus time profiles for the two CAC systems are shown in Fig. 1. Both pastes show the general feature of stiffening, or structuring, as evidenced by a torque rise. The maximum in torque represents a state of maximum structuring of the paste beyond which the



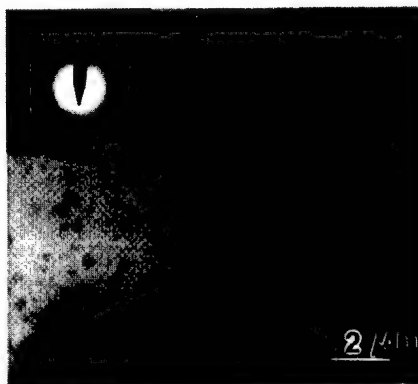
(a)



(b)



(c)



(d)

Fig. 2. SEM micrographs of hardened CAC–PVA composites processed at 100 rpm for: (a) 10 min and (b) 24 min. TEM micrographs of hardened CAC–PVA composite: (c) processed at 30 rpm for 15 min and (d) quiescently formed.



Table 1  
Formulation (by mass) and strength of hardened cement based composites

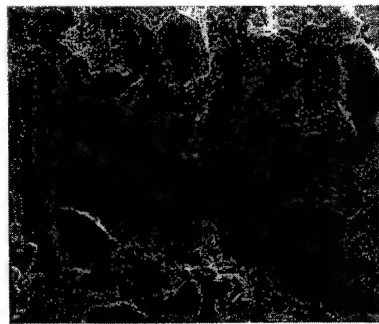
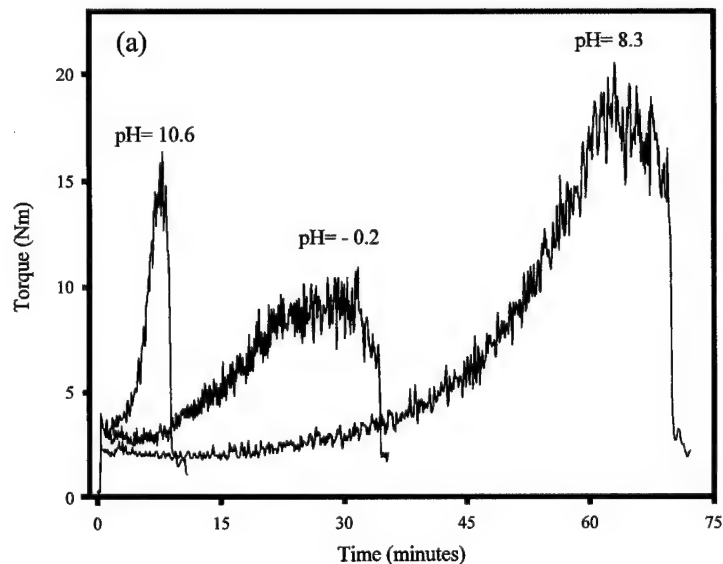
Portland cement	CAC-PVA	CAC-PR
Cement 67%	Calcium aluminate 84%	Calcium aluminate 80%
Water 33%	PVA 5.9%	PR 11%
	Water 9.5%	Methanol 7%
	Glycerin 0.6%	Glycerin 2%
Flexural strength = 5 MPa	Flexural strength = 200 MPa	Flexural strength = 170 MPa

material becomes too stiff to support deformation and simply breaks down into a crumbly powder. To make a hardened composite with favorable strength properties, one needs to remove the paste during region II or III as labeled in the figure, form it into a desired shape, and then heat it under pressure to either dry it in the case of the PVA system or polymerize the resin in the case of the PR system.

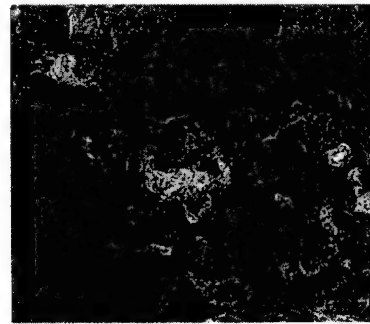
Fig. 2(a) and (b) shows scanning electron micrographs (SEM) of pastes processed for times falling within region II or III of Fig. 1 and those processed longer, to region IV.

The composites within regions II and III (Fig. 2(a)) show a continuous microstructure, free of holes and voids, whereas the composite processed in region IV exhibits macropores and large areas where the underlying matrix is degraded (arrows in Fig. 2(b)). The presence of the macrovoids in the region IV composite (Fig. 2(b)) reduces the flexural strength of the composite from a level of 200 MPa measured for the macrovoid-free composites of regions II and III (Fig. 2(a)) to 80 MPa [4].

In addition to the creation of macrovoids at the SEM



(b)



(c)

Fig. 3. (a) Torque versus mixing time plot of CAC-pH modified PR composites processed at 100 rpm. SEM micrographs of hardened composites processed at 100 rpm. Samples are: (b) CAC-high pH PR and (c) CAC-low pH PR.

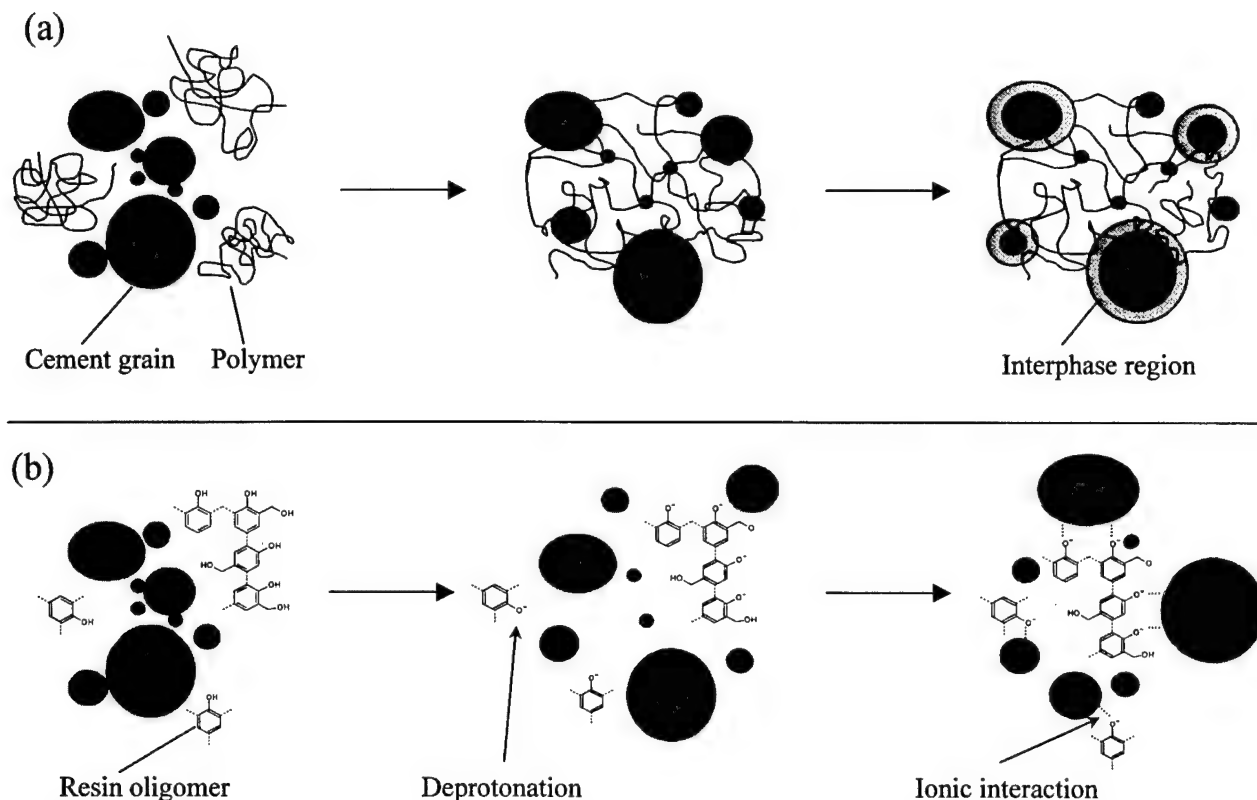


Fig. 4. Cartoon representation of the paste formation mechanism for: (a) CAC-PVA paste and (b) CAC-PR paste. The size of the polymer in (a) and the resin oligomer in (b) is greatly exaggerated.

level, the mixing time also influences the structural development of the CAC-PVA composite at the transmission electron microscopy (TEM) level. Fig. 2(c) shows a TEM micrograph of a hardened composite processed for 15 min (Fig. 1, region II). The regions of light and dark contrasts represent the polymer and cement phases, respectively. Surrounding the dark cement particles is a well-defined 0.2  $\mu\text{m}$  thick interphase region which contains cement hydration products and PVA [4]. This region is present in composites processed within regions II and III of the torque-mixing curve at mixing rates of 30–200 rpm. By contrast, Fig. 2(d) shows a TEM micrograph of a quiescently formed CAC-PVA composite, where hydrated calcium aluminate particles were suspended in a PVA film. Again, the polymer film appears as the light contrast in the background while the ceramic phase is indicated by the dark particles. Conspicuously missing from this figure is the interphase zone surrounding the cement particles. Tan and coworkers [4,5] conclude from these results and others that high-shear mixing is required for the formation of an interphase region around the cement particles and that the presence of a well formed interphase zone correlates with the measured composite flexural strengths on the order of 200 MPa.

While the processing variables of mixing time and mixing rate were probed, Tan and McHugh [6] also investigated the role of the material variables of cement particle size and polymer molecular weight in the CAC-PVA composites.

The length of regions II and III in the torque-mixing curve of Fig. 1 was shown to increase as the average cement particle size was increased from 2.8 to 36  $\mu\text{m}$ . The decrease in the total particle surface area with increasing particle size decreased the reaction rate in the system and resulted in longer regions II and III. In a similar manner, an increase in the molecular weight of the PVA was shown to reduce the lengths of regions II and III but the four regions of mixing behavior observed in Fig. 1 remained intact.

While the combination of CAC and PVA produced a high-strength hardened composite, the presence of the hydrophilic PVA made the material susceptible to water-induced degradation of its mechanical properties. This problem was eliminated by Pushpalal et al. [2] by replacing the PVA with hydrophobic PR and temperature curing the resin after mixing.

As seen in Fig. 1, the CAC-PR torque-mixing behavior differs considerably from the PVA based paste. Whereas regions II and III of the CAC-PVA paste show a fall and then a linear rise in torque with time, region II of the CAC-PR paste is flat and region III shows a power-law-like torque rise. Walberer and McHugh [7] have shown that the two regions have different mixing temperature dependencies suggesting that different mechanisms are active in each of the two regions. DSC and NMR analysis of the paste at several points along the mixing curve support this, and show no evidence of PR polymerization during region II

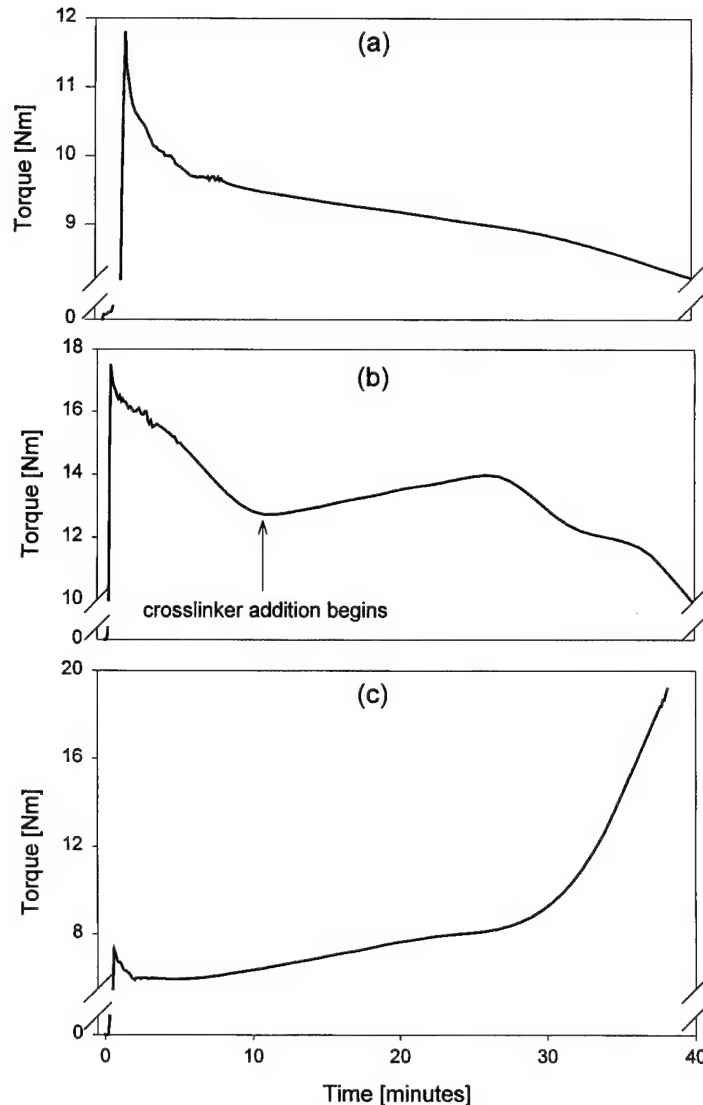


Fig. 5. Torque versus mixing time plot of: (a) PDMS SE30 filled with 45% glass beads processed at 100 rpm; (b) PVA and water filled with 51% glass beads processed at 100 rpm with the addition of a crosslinking agent, addition beginning at 10 min; and (c) epoxy-amine resin filled with 65% glass beads processed at 100 rpm.

and an increase in the degree of polymerization during region III. While the degree of polymerization of the resin is partially responsible for the stiffening in this paste, it was shown that the changes in the paste pH with mixing time are likely to have played the dominant role in the power law stiffening of region III.

Fig. 3 shows the effect of the initial resin pH on the mixing behavior of the CAC-PR paste. The unmodified resin has a pH of 8.3 and it was observed that higher or lower pH levels quickened the stiffening. The pH-induced rapid stiffening has a detrimental effect on the microstructure and flexural strength of the hardened composite. As seen in the SEM micrographs of Fig. 3, large discontinuities are present in the paste of pH 10.6 and large voids are present in the paste of pH -0.2. The associated flexural strengths of these composites were 18 and 80 Mpa, respectively [7].

In summary, it is clear that both CAC-PVA and CAC-PR hardened composites have similar mechanical properties, but very different paste processing histories. The differing processing behavior is due to differing mechanisms of paste formation. Fig. 4 shows a cartoon representation of the likely paste stiffening mechanisms active in the two systems. The CAC-PVA paste is thought to stiffen by PVA polymer chains which adsorb or chemically react within the interphase around the cement particles and later stiffen due to bulk crosslinking of the PVA phase by the ionic species generated by the partial dissolution of the cement grain surfaces. The CAC-PR paste initially does not stiffen during region II, when the ionic species from the CAC particles dissolve into solution and increase the solution pH. During region III, the now partially deprotonated resin oligomers ionically interact with the

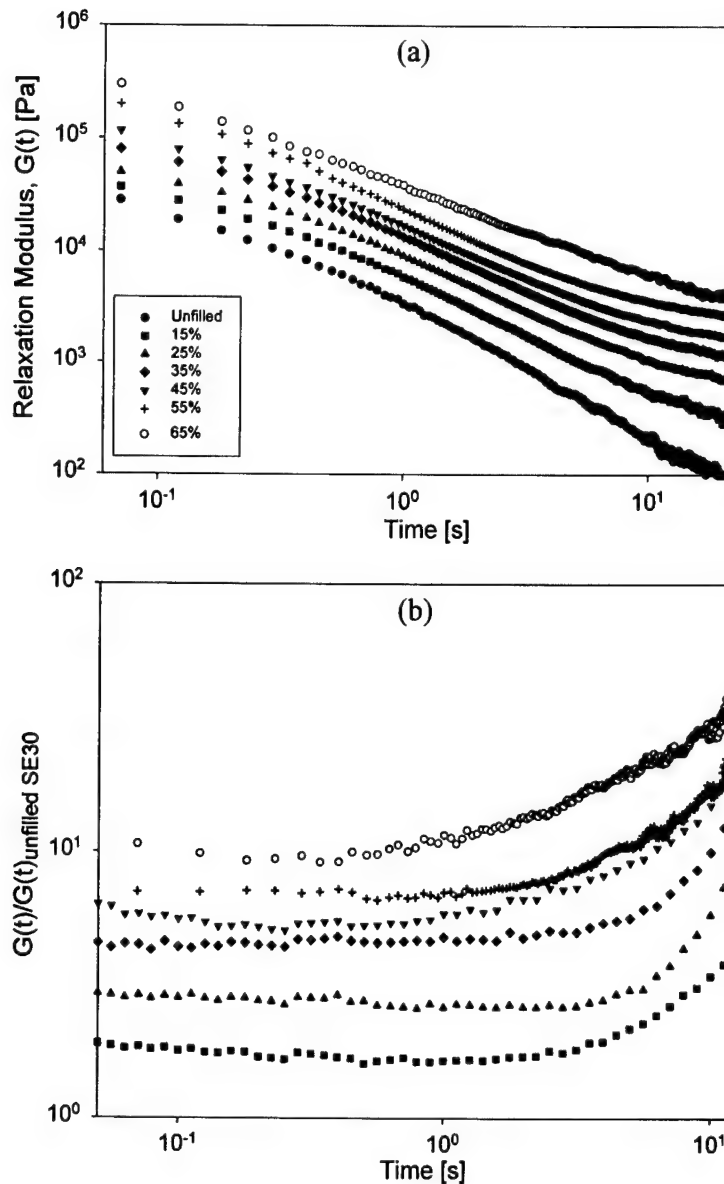


Fig. 6. (a) Linear viscoelastic relaxation modulus  $G(t)$  measured in biaxial extension of PDMS SE30 at various glass bead filler fractions. (b) Linear viscoelastic relaxation modulus for SE30 measured in shear for 15 to 45% filler and in biaxial extension for 55–65% filler, normalized with respect to the linear relaxation modulus of unfilled SE30. The symbols for (b) are the same as in (a).

positively charged cement grain surface and the resin particles polymerize partially into a growing interpenetrating network.

### 3. Rheological studies of model highly-filled systems

From the work with the CAC–PVA and CAC–PR systems, it becomes clear that each candidate combination of polymer and ceramic is likely to require its own Edisonian investigation in order to understand and optimize its processing and rheological behavior. In an attempt to avoid this, and to build a general understanding of the processing behavior of the entire class of materials, the

authors have worked with four model systems. Each model system is a combination of ceramic particles and an organic phase that is designed to stiffen as it is processed due to a specific mechanism. The four mechanisms were chosen based on the strong likelihood of their appearance in these systems. The four model systems stiffen due to: (1) polymerization of the polymer phase; (2) crosslinking of the polymer phase; (3) flocculation of the ceramic phase particles; and (4) bonding of the polymer of the organic phase to the surfaces of the ceramic particles.

In order to process these materials with a continuous technique such as extrusion, one needs to understand the evolving paste rheology. Since the Banbury mixer is not a rheometric flow field, the measured mixing torque is not

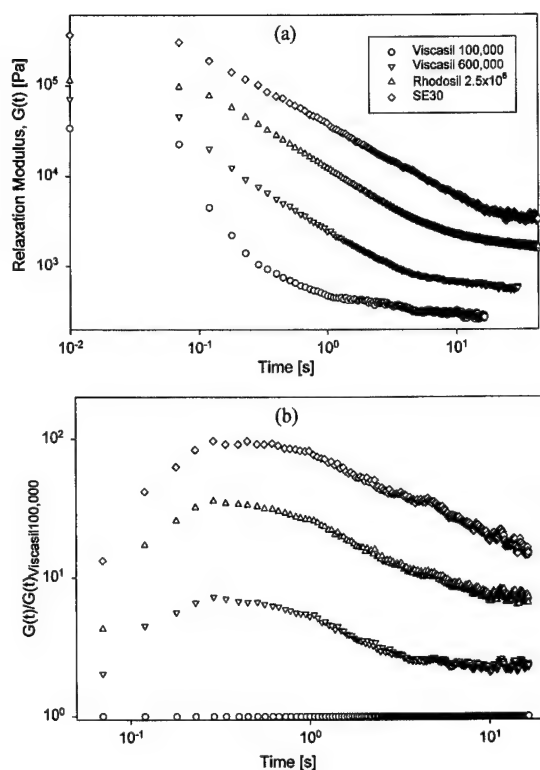


Fig. 7. (a) Linear viscoelastic relaxation modulus  $G(t)$  of 65% glass bead filled PDMS of various molecular weights. (b) Linear relaxation modulus normalized with respect to the linear relaxation modulus of 65% filled Viscasil 100,000. The symbols for (b) are the same as in (a).

uniquely related to the rheometric properties of the paste such as modulus and viscosity. However, measuring the rheological behavior of these stiff pastes presents a number of challenges. At high loading fractions, as encountered here, the materials are typically so stiff that the range of most shear rheometers is exceeded and, if measurements are possible, wall slip is commonly encountered. An additional challenge for these reactive pastes is the difficulty of quickly forming and loading samples into a device to capture its time evolving behavior accurately. A rheometric technique particularly suited for studying stiff materials is the lubricated squeezing flow, which produces an equibiaxial extensional flow. With this technique, experimental specimens can be quickly formed and loaded into the device, at which time either the linear viscoelastic relaxation modulus following a step strain or the equibiaxial extensional viscosity can be measured.

We examined the rheological trends associated with pastes that stiffen as they are processed. Here we present the results of model systems that stiffen due to: (1) polymerization of the polymer phase; and (2) crosslinking of the polymer phase. In both cases, the polymer and ceramic phases are mixed in a Banbury mixer and the subsequent time evolution of stiffening is monitored by the torque–time profile. To measure the progression of the paste rheological properties, samples are extracted from the Banbury mixer at

progressively longer mixing times and measurements of the relaxation modulus after a step strain are taken using a lubricated squeeze flow rheometer. The data from these reactive systems are compared with the effects of filler concentration in a polydimethyl siloxane (PDMS) melt, and the effect of molecular weight in a filled PDMS melt. See reference [8] for the complete experimental details.

Fig. 5 shows smoothed torque–time profiles that illustrate the mixing behavior of the systems of interest here. The slowly declining torque of Fig. 5(a) for a 45% filled PDMS, SE30, is characteristic of a non-reactive, non-stiffening system that exhibits shear thinning. Fig. 5(b) for the crosslinking system shows similar thinning behavior during the first 10 min, until the addition of the crosslinking agent begins. From 10 through about 30 min, the torque rises slightly as the crosslink density of the polymer increases. Stiffening of the paste ceases at about 30 min, indicating that crosslinking is no longer sufficient to overcome the paste breakup. Fig. 5(c) for the polymerizing epoxy system shows a slight linear increase in torque over the first 30 min, followed by a steep, power-law-like rise until the run was stopped near 40 min. For both the reactive systems, the torque profiles can be increased or decreased with changes in the mixing volume; however, the general features of a linear, steady rise in torque for the crosslinking system and an initially linear rise followed by a steep rise in torque for the polymerizing system are still apparent.

Fig. 6(a) shows the effect of filler volume fraction on the relaxation behavior of a PDMS gum, SE30. As expected, as the filler amount is increased from 0 to 65% by volume, the magnitude of the modulus shifts upward and the relaxation time grows longer. To facilitate comparison of the modulus growth among all the systems studied, the relaxation moduli were normalized with respect to that of the least stiff paste. Fig. 6(b) shows the normalized modulus from Fig. 6(a). The relative modulus of each filled paste increases more or less linearly with time at short times and then starts to grow more rapidly at longer times.

Fig. 7(b) shows the normalized modulus growth curves for filled PDMS of progressively higher molecular weights. The unnormalized modulus data are shown in Fig. 7(a). Increasing the molecular weight increases both the modulus and the relaxation time. In comparing the unnormalized data of Fig. 7(a) to those of Fig. 6(a), one might conclude that the effects of filler and molecular weight are similar; however, comparison of the normalized modulus of Fig. 6(b) with that of Fig. 7(b) shows that this is not the case. Fig. 7(b) shows that the relative modulus for each molecular weight paste passes through an intermediate maximum near 0.5 s, and then starts to decrease with time. This is fundamentally different from the effect of adding filler in which the relative moduli steadily grow with time, and, together with Fig. 6(b), provides two alternative benchmarks for interpreting the behavior of the reactive systems.

Fig. 8(a) shows the progression of the relative modulus for the crosslinking system in which the pastes were

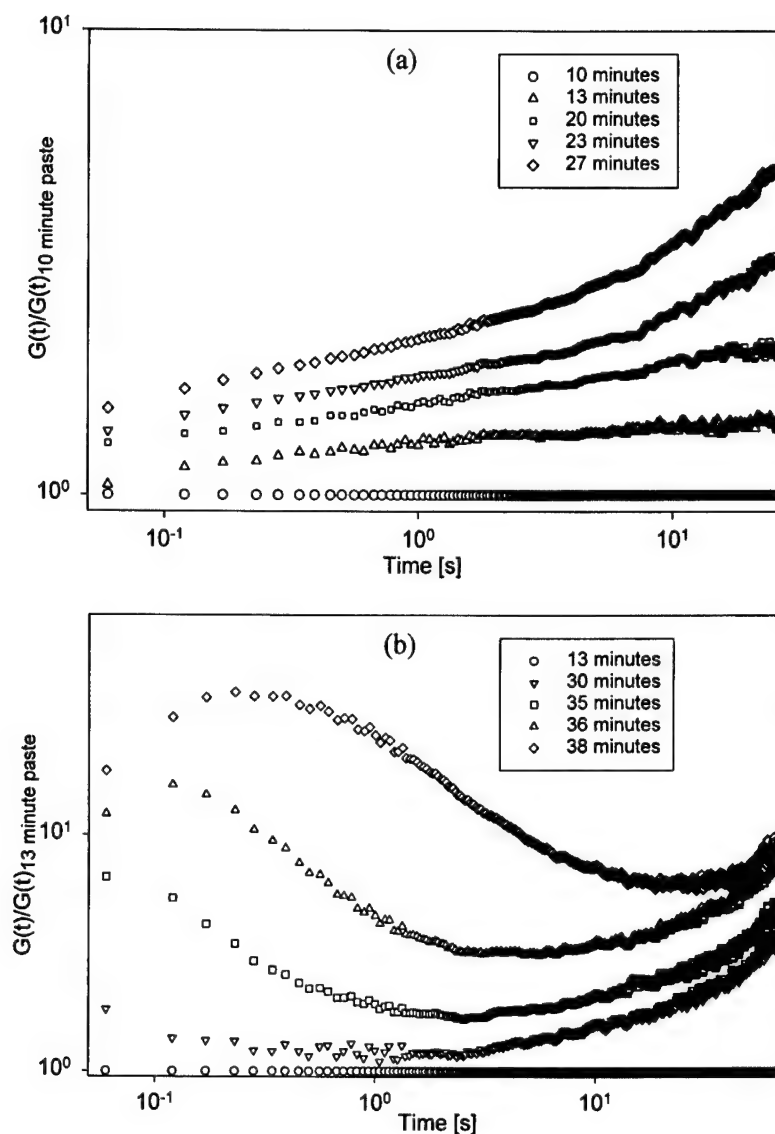


Fig. 8. (a) Linear viscoelastic relaxation modulus  $G(t)$  of 51% glass bead filled PVA pastes of various mixing times normalized with respect to the linear relaxation modulus of the paste mixed for 10 min. (b) Linear viscoelastic relaxation modulus  $G(t)$  of 65% glass bead filled epoxy-amine resin pastes of various mixing times normalized with respect to the linear relaxation modulus of the paste mixed for 13 min.

removed from the mixer at various times between 10 and 27 min. As the mixing time/degree of crosslinking increases, the modulus and relaxation time increase. The relaxation moduli of these pastes were normalized with respect to a paste processed for 10 min. The trend of a linear increase in the relative modulus followed by a greater than linear rise at longer times shows strong similarities to the behavior observed in Fig. 6(b) for an increase in filler amount. The similarity between the two systems suggests that an increase in the crosslink density of a filled polymer paste has a similar effect on the relaxation modulus as that of adding more filler to the system.

Fig. 8(b) shows the relative modulus for the polymerizing filled epoxy system. The moduli of these pastes were normalized with respect to the paste processed for 13 min, the least polymerized paste in this series. As the mixing

time/polymerization progresses, the relative modulus of each paste grows at short times, falls at intermediate times and then continues to grow at long relaxation times. The initial maxima of the pastes shifts to a longer time for the 35, 36, and 38 min pastes, and the 36 and 38 min pastes show intermediate maxima very similar to those observed in the non-reactive molecular weight varied pastes of Fig. 7(b). Comparison of Fig. 8(b) with Figs. 7(b) and 6(b) suggests that at short and intermediate times, the increasing molecular weight of the polymerizing polymer controls the relaxation behavior whereas at long relaxation times, paste stiffening shows a trend similar to an increasing filler amount. Thus the relative modulus continues to grow at long relaxation times as it was observed in Fig. 6(b).

The relative relaxation modulus gives useful insights into the changing viscoelastic behavior of the pastes as they

stiffen. Equally important for understanding paste processability is the direct measurement of the paste viscosity. The authors have shown that the lubricated squeezing flow is able to measure the evolving rheology of both the reactive and non-reactive pastes discussed above. In addition, they have demonstrated that the viscosity data can be quantified using a rheological constitutive model for highly-filled polymers that exhibit yield stress [8].

#### 4. Conclusions

Organo-ceramic composites based on CACs have mechanical properties in the range of fired ceramics but are able to be processed at or near room temperature. The relationship among processing behavior, property development, and structure development has been studied with Banbury mixing, mechanical testing, and electron microscopy. Composites based on both PVA and PR are seen to have very different torque-mixing time behavior in the Banbury mixer indicating differing mechanisms of paste formation. Despite differing formation mechanisms, the microstructure and flexural strength of the hardened materials are very similar. The rheological behavior of two model, non-CAC, organo-ceramic systems was measured using a lubricated squeezing flow technique. Because of its reliance on a wall slip condition and the ability to quickly form and load samples into the device, it is uniquely able to capture the time evolving rheology of these reactive systems. Measurements of the relaxation modulus after a step strain revealed similarities between the relaxation behavior of systems that stiffen due to crosslinking and systems that were stiffened by an increase in the volume fraction of filler particles. Further similarities were observed between the systems that stiffen due to polymerization and the systems that were stiffened by an increase in molecular weight at

short relaxation times, and between the systems that were stiffened by an increase in the volume fraction of the filler at long relaxation times. Discussions of the potential applications of these materials as thermal insulators and in structural applications can be found elsewhere [9,10].

#### References

- [1] Birchall JD, Howard AJ, Kendall K. Flexural strength and porosity of cements. *Nature* 1981;289:388–90.
- [2] Pushpalal GKD, Kawano T, Kobayashi T, Hasegawa M. Chemical characterization of calcium aluminate–phenol resin composite. *Adv Cem Bas Mater* 1997;6:45–52.
- [3] McHugh AJ, Tan LS. Mechano-chemical aspects of the processing/property/structure interactions in a macro-defect-free cement. *Adv Cem Bas Mater* 1993;1:2–11.
- [4] Gulgun MA, Kriven WM, Tan LS, McHugh AJ. Evolution of mechano-chemistry and microstructure of a calcium aluminate–polymer composite: Part I. Mixing time effects. *J Mater Res* 1995;10(7):1746–55.
- [5] Tan LS, McHugh AJ, Gulgun MA, Kriven WM. Evolution of mechano-chemistry and microstructure of a calcium aluminate: Part II. Mixing rate effects. *J Mater Res* 1996;11(7):1739–47.
- [6] Tan LS, McHugh AJ. The role of particle size and polymer molecular weight in the formation and properties of an organo-ceramic composite. *J Mater Sci* 1996;31:3701–6.
- [7] Walberer JA, McHugh AJ. Processing/property/structure interactions in a calcium aluminate–phenol resin composite. *Adv Cem Bas Mater* 1998;8:91–100.
- [8] Walberer JA, McHugh AJ. A comparison of the rheology of reactive filled systems using lubricated squeezing flow. *J Rheol* 2000;44:743–58.
- [9] Young JF. Organo-cement composite (MDF cements): current status. MAETA Workshop on High Flexural Strength Polymer–Cement Composite. Proc. Sakata, Japan, 1996. p. 1–11.
- [10] Pushpalal GKD, Maeda N, Kawano T, Kojima H. High-strength phenol-resin cement composite. Part 3. Applications. MAETA Workshop on High Flexural Strength Polymer–Cement Composite. Proc. Sakata, Japan, 1996. p. 35–47.



# Effect of interphase characteristics on long-term durability of oxide-based fibre-reinforced composites

B. Saruhan<sup>a,\*</sup>, M. Schmücker<sup>a</sup>, M. Bartsch<sup>a</sup>, H. Schneider<sup>a</sup>, K. Nubian<sup>b</sup>, G. Wahl<sup>b</sup>

<sup>a</sup>German Aerospace Centre, Institute for Materials Research, D-51147 Köln, Germany

<sup>b</sup>Technical University of Braunschweig, Institute of Surface Technology, D-38108 Braunschweig, Germany

Received 26 May 2000; revised 26 November 2000; accepted 30 November 2000

## Abstract

Mullite based fibre-reinforced composites having double layer fibre-coatings were produced and characterised. The multi-layer interphases were produced by a CVD-process (carbon(fugitive)/ZrO<sub>2</sub> or Al<sub>2</sub>O<sub>3</sub>) on aluminosilicate Nextel™ 720 fibres. Composites were fabricated by infiltration of coated fibres with a pre-mullite slurry and hot-pressing in argon at 1300°C. Short term heat-treatment of composites in air yielded a gap between the fibre and the oxide layer by oxidation of the carbon layer (so-called fugitive layer). The composites were statically and cyclically heat-treated at 1300°C for 1000 h in order to identify the mechanical and microstructural changes. Mechanical characterisation of the heat-treated composites was carried out by three-point bending. The effectiveness of the fugitive layer is determined by the oxide layer and its high-temperature stability in interaction with the matrix but it also depends on the loading condition. Under cyclic heat-treatment conditions the composites are found to be more stable and damage tolerant than under constant high-temperature exposure. © 2001 Elsevier Science Ltd. All rights reserved.

**Keywords:** B. Interface/interphase; B. Mechanical properties; E. Chemical vapour deposition (CVD); B. Damage tolerance; Mullite

## 1. Introduction

Relying on the outstanding physical, chemical and thermal properties, mullite based fibre-reinforced composites became favourite candidates for the high-temperature application in the combustion chambers of gas turbine engines. These applications require damage tolerant, temperature- and oxidation-resistant ceramic components. In order to realise damage tolerance in ceramics, it is necessary to employ continuous fibre-reinforcement and possibly an inert interface material (interphase). Thus, a suitable weak bonding, debonding and sliding at the fibre/matrix-interface can be achieved, which leads to fibre pull-out and consequently to the damage tolerance. These properties are to be realised and maintained not only at room temperature, but also at elevated temperatures and over long terms. Non-oxide interphases (e.g. BN and C) are structurally suitable, however, do not survive under long-term exposure at high temperatures, due to the lack of oxidation resistance [1]. Among many suggested concepts, the fugitive coating, resulting in a gap at the fibre/matrix-interface delivered promising results. One drawback is the closure of the gap

at very high temperatures, owing to the high diffusion rates of the oxides [2].

In this study, two interphase combinations, based on the multi-layer principle were used. The double layer interphase systems, having carbon + ZrO<sub>2</sub>- and carbon + Al<sub>2</sub>O<sub>3</sub>-double layers were produced by Chemical vapour deposition (CVD)-coating of Nextel™ 720 fibres successively. The mechanical and microstructural effects of the double layer interphase systems were compared with that of a reference composite which had only a carbon (fugitive)-layer at the fibre/matrix-interface.

## 2. Materials and methods

Coating of Nextel™ 720 fibre fabrics (8 harness Atlas) were produced by a CVD-process, with special evaporation and deposition equipment. The starting precursors were zirconium and aluminium tetramethylheptandionate (tmhd)<sub>4</sub> for oxide coating and propane for carbon coating. Carbon coating of the woven fibre mats was carried out with pure propane at 950°C under 12.5 mbar pressure. Subsequently the ZrO<sub>2</sub> and Al<sub>2</sub>O<sub>3</sub>-oxide coatings were vapour-deposited at about 510 and 610°C in a mixture of oxygen and argon under 5 mbar, respectively. After completion of the fibre

\* Corresponding author.

E-mail address: bilge.saruhan@dlr.de (B. Saruhan).

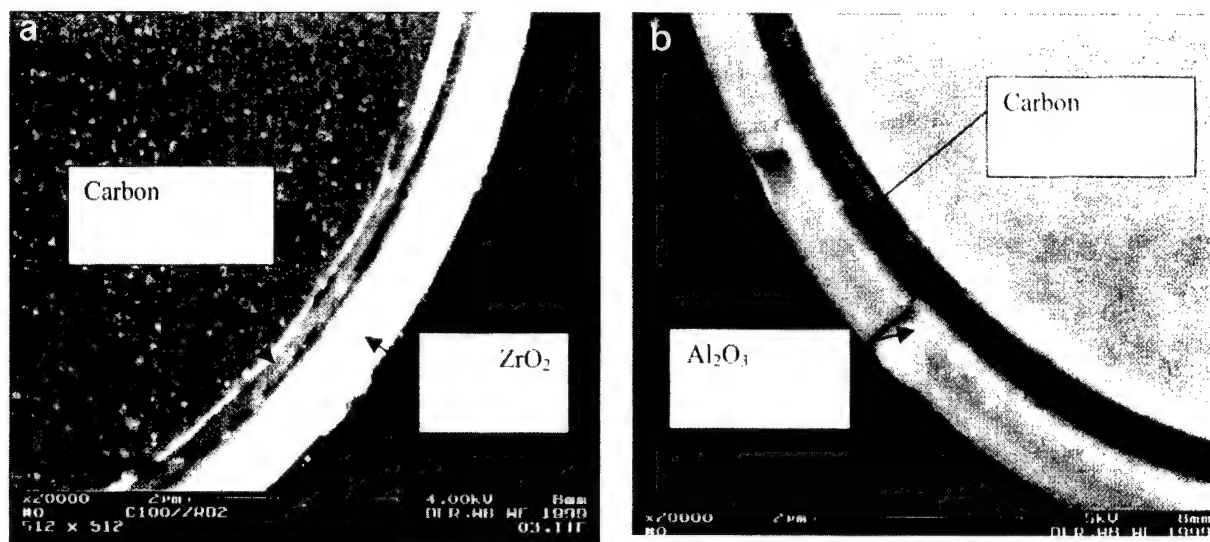


Fig. 1. Scanning electron micrographs of coated fibres: (a) carbon/ZrO<sub>2</sub>-double coating; and (b) carbon/Al<sub>2</sub>O<sub>3</sub>-double coating.

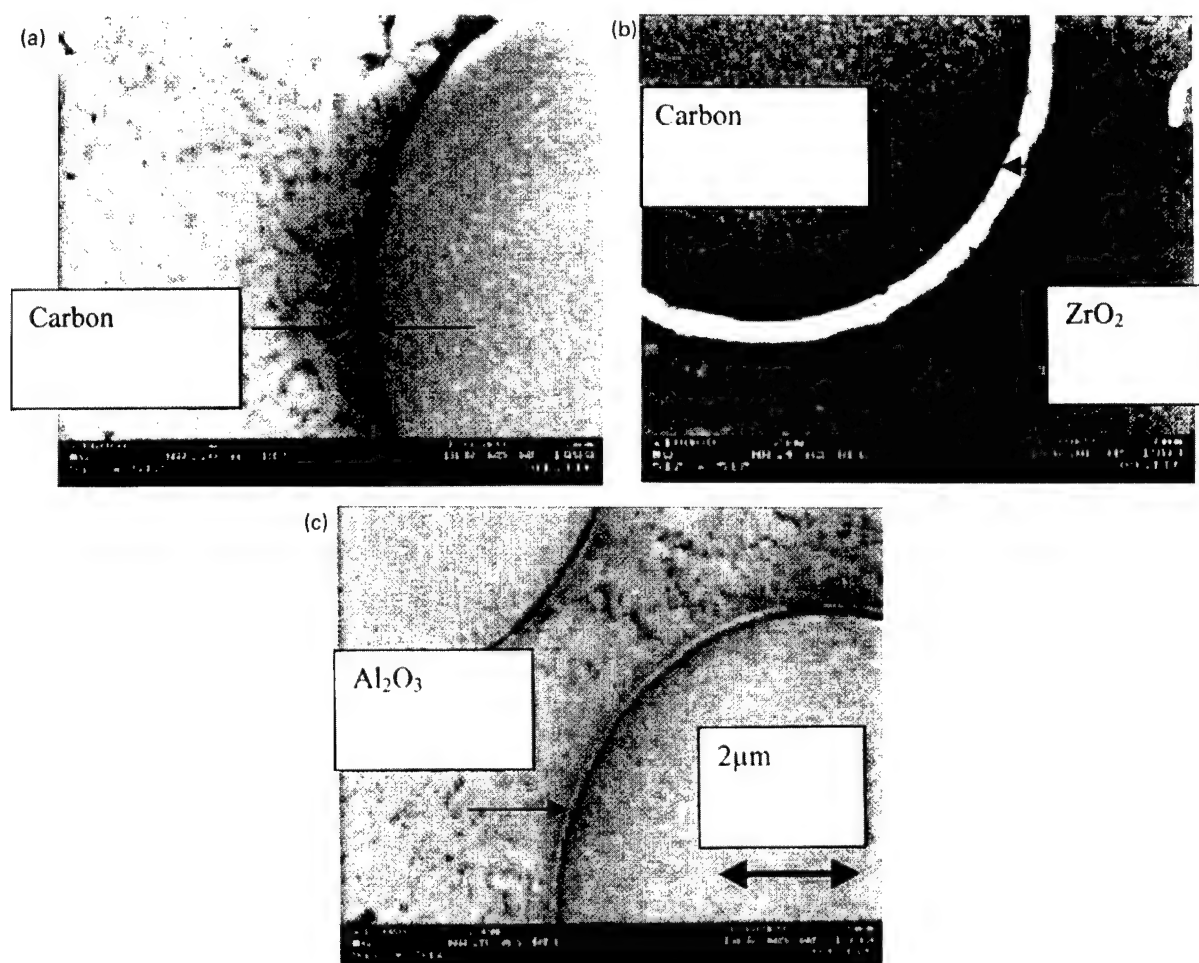


Fig. 2. Scanning electron micrographs of the interphases after hot-pressing at 1300°C for 15 min under 10 MPa pressure. (a) Reference sample; (b) carbon/ZrO<sub>2</sub>; and (c) carbon/Al<sub>2</sub>O<sub>3</sub>.

coating, the thickness of carbon coating was measured to vary between 100 and 200 nm. The thickness of oxide coatings was in turn approximately 800 nm (Fig. 1(a) and (b)).

The composites were prepared by aqueous slurry infiltration of a submicrometer pre-mullite powder (Siral, Condea, Germany) into the unidirectional laid double-coated fibre tows and hot-pressing the composites in argon at 1300°C, for 15 min, under 10 MPa uniaxial pressure. The pyrolytic carbon layer was intact after hot-pressing. The composites were heat-treated at 1200°C for 2 h in air in order to obtain a gap between the fibre and the oxide layer (so-called fugitive layer). Considering the application temperatures for the composites in combustion chambers, the composites were heat-treated at 1300°C for 1000 h under continuous- and cycling-heating conditions. Thermal cycling was carried out by heating up at a rate of 10 K/min to 1300°C and holding at this temperature for 1 h before cooling down to room temperature. This cycle was repeated 1000 times.

The mechanical and microstructural changes in the composites were determined by microstructural investigations and mechanical testing. The composites were characterised microstructurally with a scanning electron

microscope (Leitz LEO 982, Germany) and tested mechanically at room temperature by a three-point-bending test with a span of 20 mm, using a UTS-10 testing equipment with a 200 N load cell. The displacement in the middle of the 20 mm span was measured with one inductive strain gauge, neglecting the system compliance of the testing machine which was estimated to be very small compared with that of the test samples.

### 3. Results

After hot-pressing in argon, the composites contained intact carbon, carbon/monoclinic  $\text{ZrO}_2$  and carbon/ $\text{Al}_2\text{O}_3$ -interphases (Fig. 2(a)–(c)). The reference composite contained a 200 nm thick carbon interphase, after hot-pressing in argon (Fig. 2a). The thickness of the double layer-coating varied after hot-pressing such that the carbon layer in carbon/monoclinic  $\text{ZrO}_2$ -composite was reduced to 100 nm (initially 180 nm) and that of monoclinic  $\text{ZrO}_2$ -layer to 400 nm (initially 800 nm). The morphology of monoclinic  $\text{ZrO}_2$ -layer became somewhat porous (Fig. 2b).

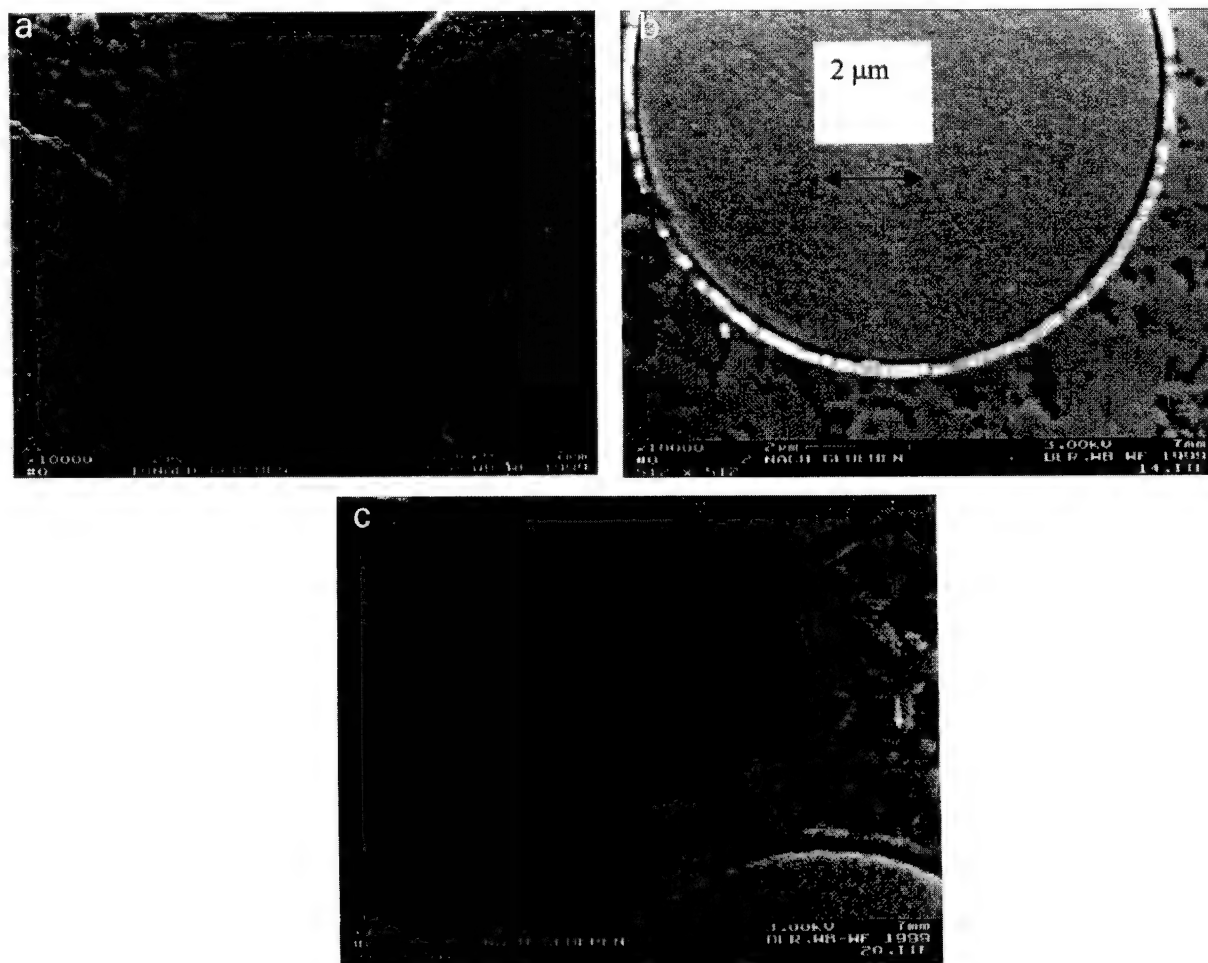


Fig. 3. Scanning electron micrographs of the interphases after heat-treatment at 1200°C for 2 h in air: (a) reference sample; (b) carbon/ $\text{ZrO}_2$ ; and (c) carbon/ $\text{Al}_2\text{O}_3$ .

Table 1

Mechanical data of the composites and the thickness of the layers before and after heat-treatment

		Fiber coating (nm)	As-hot-pressed	Heat-treated at 1200°C for 2 h	Continuous heat- treated at 1300°C for 1000 h	Cyclic heat- treated at 1300°C for 1000 × 1 h
Carbon (fugitive)	Thickness of C-layer	200	200 nm	80 nm	none	< 50 nm
	Fracture strength		80 MPa	68 MPa	120 MPa	160 MPa
	Young's modulus		42.4 GPa	27.1 GPa	84.6 GPa	84 GPa
Carbon (fugitive)/ZrO <sub>2</sub>	Thickness of C-layer	180	100 nm	80 nm	None	< 50 nm
	Thickness of oxide-layer	800	400 nm	200 nm	150 nm	150 nm
	Fracture strength		230 MPa	200 MPa	140 MPa	150 MPa
	Young's modulus		106 GPa	87 GPa	81 GPa	117 GPa
Carbon (fugitive)/Al <sub>2</sub> O <sub>3</sub>	Thickness of C-layer	180	150 nm	150 nm	≤ 50 nm	50 nm
	Thickness of oxide-layer	800	150 nm	150 nm	100 nm	100 nm
	Fracture strength		179 MPa	170 MPa	170 MPa	200 MPa
	Young's modulus		75 GPa	74.5 GPa	91 GPa	92 GPa

The carbon layer in carbon/Al<sub>2</sub>O<sub>3</sub>-composites after hot-pressing was about 150 nm, being only slightly thinner than the thickness of the as-coated layer. The thickness of the Al<sub>2</sub>O<sub>3</sub>-layer was reduced to 150 nm (initially 800 nm). The morphology of the Al<sub>2</sub>O<sub>3</sub>-layer showed

no change compared with that of the as-coated one (Fig. 2(c)).

Heat-treatment of composites at 1200°C for 2 h in air yielded a gap between fiber and oxide layer by oxidation of the carbon layer (fugitive layer) (Fig. 3(a)–(c)). This

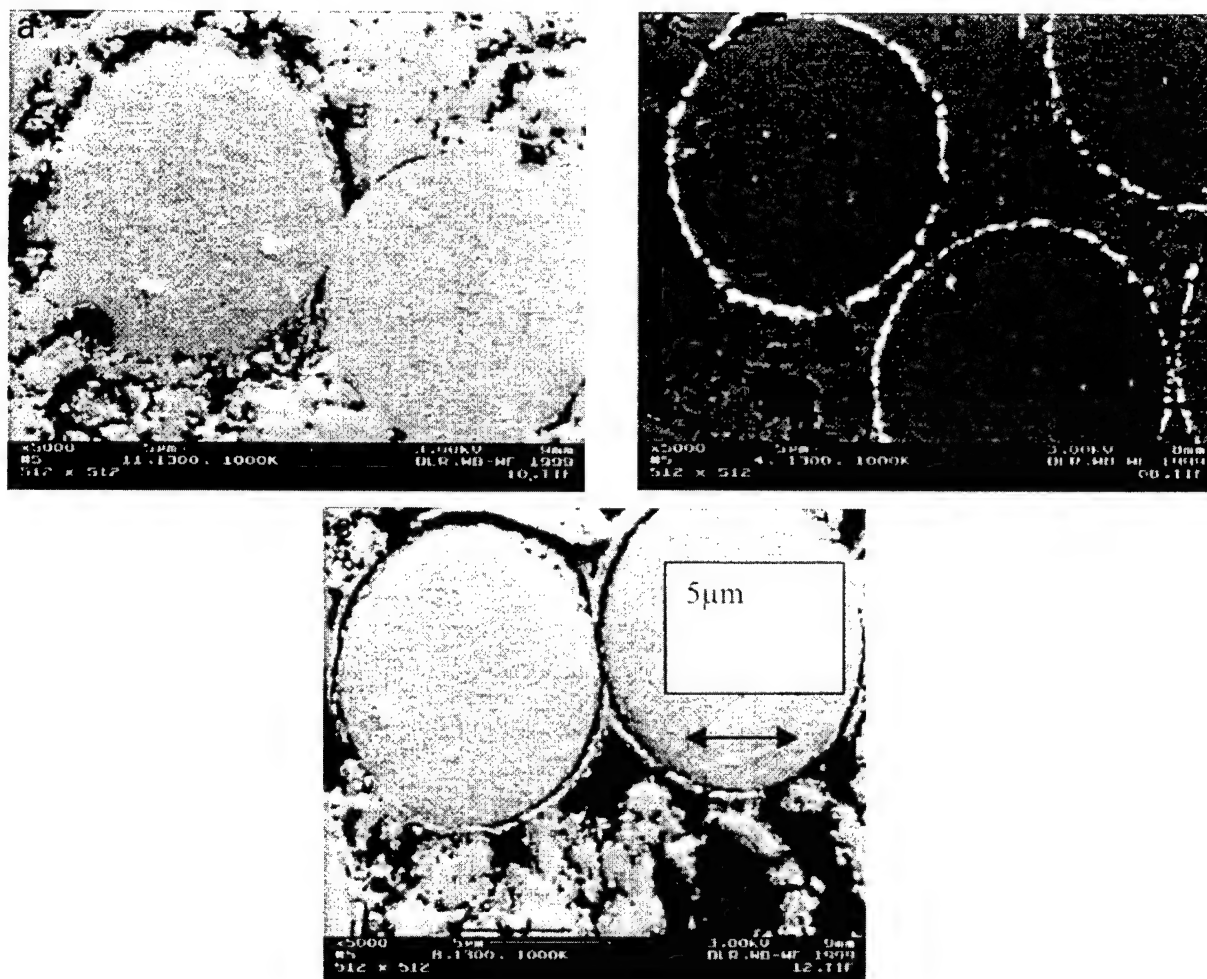


Fig. 4. Scanning electron micrographs of the interphases after continuous exposure at 1300°C in air for 1000 h: (a) reference sample; (b) fugitive/ZrO<sub>2</sub>; and (c) fugitive/Al<sub>2</sub>O<sub>3</sub>.

process did not cause any warping or cracking of the composites. The thickness of the fugitive layer in the reference composite was significantly smaller than the carbon layer after hot-pressing (about 80 nm compared to 200 nm), immediately after the oxidation of carbon layer at 1200°C/2 h. The thickness of the fugitive and  $\text{ZrO}_2$ -layers in the fugitive/ $\text{ZrO}_2$ -composites were reduced to 80 nm and 200 nm, respectively. The thickness of the fugitive layer in the fugitive/ $\text{Al}_2\text{O}_3$ -double layer composites showed no change. The thickness variations of the interphases as well as numerical mechanical data to the composites before and after heat-treatment are listed in Table 1.

Generally the fugitive layer is thermally unstable and closes progressively as the heat-treatment temperature and duration increases. This is mainly because the matrix as well as the oxide layer maintains a substantial sintering activity after hot-pressing. At the interface of the reference composite between the matrix and the fibre, substantial sintering necks form at 1300°C after 1000 h continuous exposure in air. This interaction between the fibre and the matrix reduces the amount of alumina on the surface zone of the

fibre and causes formation of notch-like damage on fibres (Fig. 4(a)).

The gap closure at the interface of the fugitive/ $\text{ZrO}_2$ -double layer composites was very advanced already after hot-pressing but led to a complete disappearance of the gap at 1300°C, after 1000 h of continuous heating. The  $\text{ZrO}_2$ -layer showed sintering-related morphological changes, resulting in a rough surface development and thickness reduction (Fig. 4(b)). In the fugitive/ $\text{Al}_2\text{O}_3$ -double layer-composites also sintering necks formed after 1000 h continuous heating at 1300°C. However, in this case, the interaction was not only between the fibre and the  $\text{Al}_2\text{O}_3$ -layer, but also between the matrix and the  $\text{Al}_2\text{O}_3$ -layer. So that the thickness of the gap was heterogeneous; larger where sintering-related contacts between the  $\text{Al}_2\text{O}_3$ -layer and the matrix took place, thinner or closed where the fibre and the  $\text{Al}_2\text{O}_3$ -layer were sintered together (Fig. 4(c)).

The interfacial relations after cyclic treatment at 1300°C differ from those under continuous heat-treatment at the same temperature and same exposure time, (Fig. 5(a)–(c)). The fugitive layer appeared to be maintained in all composites, although to different extents in each composite. The

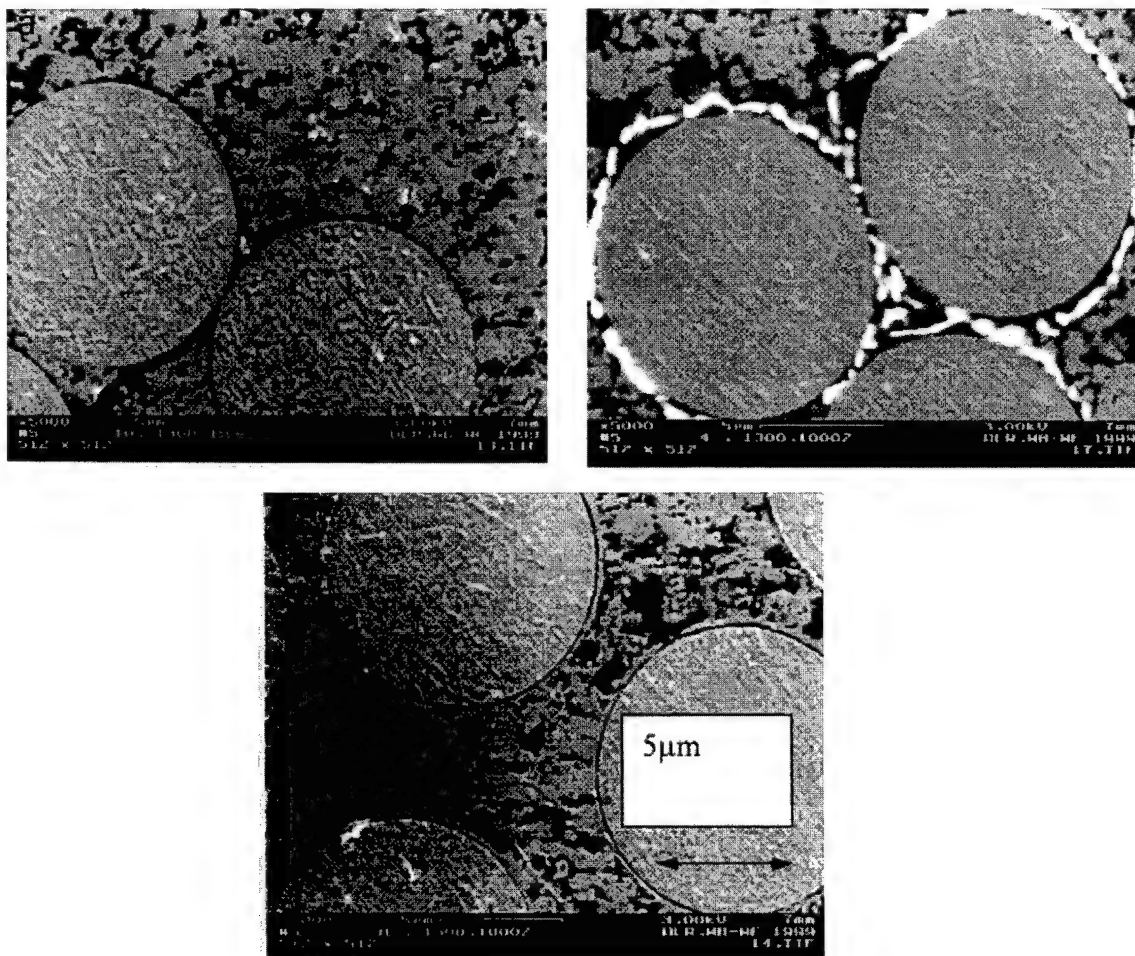


Fig. 5. Scanning electron micrographs of the interphases after 1000 thermal cycles at 1300°C in air: (a) control sample; (b) fugitive/ $\text{ZrO}_2$ ; and (c) fugitive/ $\text{Al}_2\text{O}_3$ .

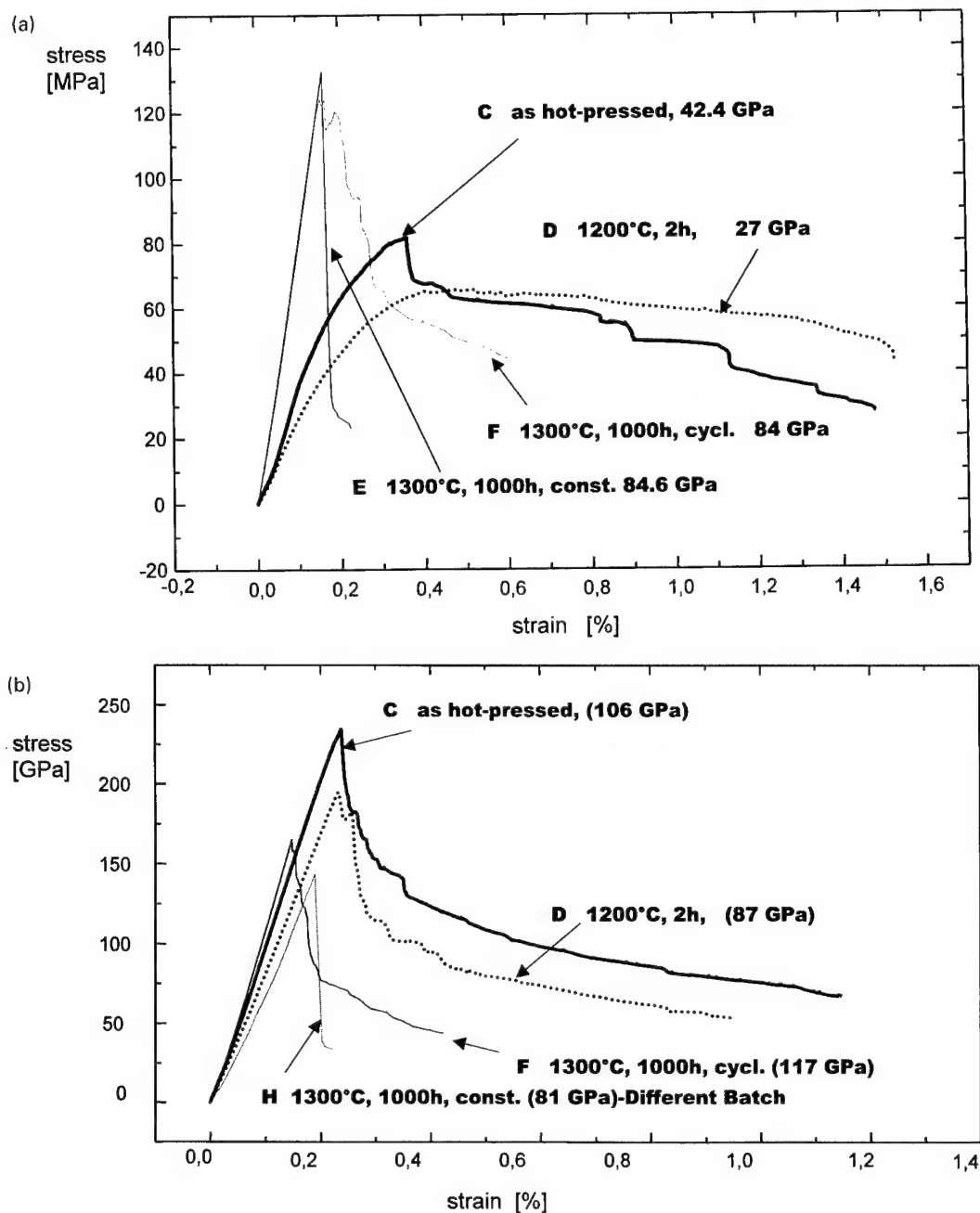


Fig. 6. (a) Three-point bending curves of the composites with carbon (fugitive)-interphase after (C) hot-pressing, (D) after heat-treatment at 1200°C for 2 h (E) after heat-treatment at 1300°C for 1000 h, cons., and (F) after heat-treatment at 1300°C for 1000 × 1 h, cycl. (b) Three-point bending curves of the composites with carbon (fugitive)/ZrO<sub>2</sub>-interphase (C) after hot-pressing, (D) after heat-treatment at 1200°C for 2 h (H) after heat-treatment at 1300°C for 1000 h, cons., and (F) after heat-treatment at 1300°C for 1000 × 1 h, cycl. (c) Three-point bending curves of the composites with carbon (fugitive)/Al<sub>2</sub>O<sub>3</sub>-interphase after (C) hot-pressing, (D) after heat-treatment at 1200°C for 2 h (H) after heat-treatment at 1300°C for 1000 h, cons. and (F) after heat-treatment at 1300°C for 1000 × 1 h, cycl.

ZrO<sub>2</sub>-layer displayed a rather unique behaviour under cyclic conditions, yielding a less tighter appearance compared with the continuously heated specimen (Fig. 5(b)).

The mullite matrix in all as-hot-pressed composites was homogeneously packed, but contained many finely distributed pores (approx. 40% porosity). Heat-treatment of the composites led to localised sintering and an extensive pore diffusion within the matrix, starting already at

1200°C after 2 h of exposure. This led to the formation of dense matrix islands and the locally cumulated large pores, due to the pore diffusion and growth. Under cyclic heat-treatment at 1300°C, the extension of sintering was less obvious. In these composites, the pore volume distribution remained homogeneous and the size of dense islands was relatively small.

The stress/strain behaviour of the composites after



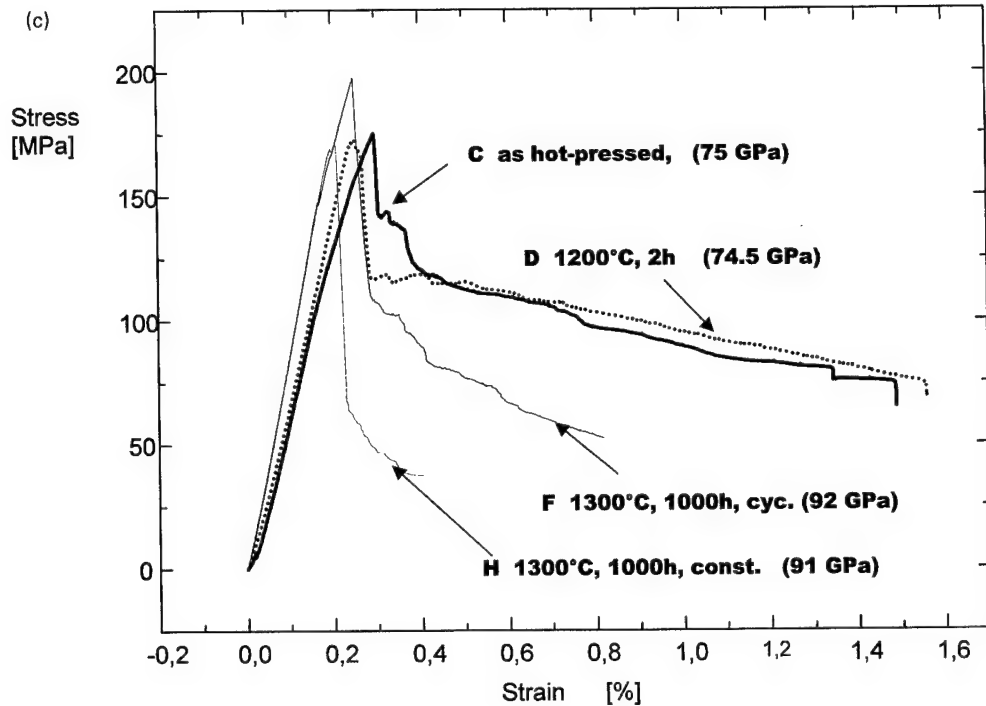


Fig. 6. (continued)

hot-pressing as well as after heat-treatments was determined by three-point-bending tests of the composites at room temperature. For the calculation of the Young's modulus for each composite, the linear elastic part of the stress/strain curves was taken. The stress/strain curves and calculated Young's modulus are shown in Fig. 6(a)–(c).

For the reference composite with initial carbon mono layer and the carbon/ $\text{Al}_2\text{O}_3$ -double layer composite, the 1200°C heat-treatment resulted in slight changes in ultimate fracture strength and Young's modulus compared with their counterparts as-hot-pressed composite (Fig. 6(a) and (c)).

Both hot-pressed and 1200°C/2 h heat-treated reference composites exhibited some load capability during further straining after reaching the load maximum. In contrast, the prolonged (1000 h) and continuous heat-exposure at 1300°C resulted in the reference composite an increased Young's modulus (84 GPa) and strength (120 MPa) but fully brittle fracture. Cyclic heat-treatment of the composite at 1300°C for 1000 × 1 h gave the same elastic modulus and almost the same fracture strength (160 MPa) as continuously heat-treated composite, however, it should be noted that after reaching the load maximum, some load capability remains during further straining of the cyclic tested sample. Both composites with double layer interphase gave remarkably higher ultimate fracture strength and Young's modulus, compared to the reference composite (only carbon mono layer) before and after prolonged heat-treatment.

Somewhat different stress/strain behaviour was observed for the carbon(fugitive)/ $\text{ZrO}_2$ -double layer composite (Fig. 6b), compared with the 1200°C/2 h heat-treated

composite. The Young's modulus was reduced from 106 to 87 GPa (after 1200°C/2 h) and strength from 230 to 200 MPa. Whereas cyclic prolonged heat-treatment at 1300°C resulted in slight increase in the Young's modulus (117 GPa) but decrease in the strength (170 MPa). Continuous heat-treatment at 1300°C resulted in a severe decrease of fracture strength (140 MPa). Some load capability after the load maximum was maintained in all carbon(fugitive)/ $\text{ZrO}_2$ -double layer composites except for the prolonged continuously heat-treated composite.

#### 4. Discussion

For the interpretation of the fibre/matrix-interaction in a composite, the Young's modulus of the composite may be considered. Assuming that the interphase fulfils the requirement for a good load transfer between the fibre and the matrix, the Young's modulus of the composite can be calculated using the rule of mixtures. For our composites, having 35 vol.% Nextel™ 720-fibers with a modulus,  $E_f$ , of 260 GPa and 65 vol.% porous matrix with a modulus,  $E_m$ , of 46 GPa, Young's modulus of the composite,  $E_{CMC}$ , is then:

$$E_{CMC} = E_f V_f + E_m V_m \quad (1)$$

$$E_{CMC} = 260 \text{ GPa} \times 0.35 + 46 \text{ GPa} \times 0.65 = 121 \text{ GPa}.$$

Young's modulus,  $E_f$ , for the Nextel 720-fibers were determined experimentally in a study after heat-treating



the fibres at 1300°C for 2 h [3]. The calculated composite Young's modulus of 121 GPa should be considered as the maximum value which can be achieved if there is a perfect load transfer between the fibre and the matrix. If the modulus is fully dominated by either fibre or the matrix, then the composite modulus would have upper bounds, respectively where  $V_m = 0$  and  $V_f = 0$  in Eq. (1). This applies to the composites tested under tensile loading. Since we used three-point-bending tests to characterise our composites, the upper bound, where  $V_m = 0$ , cannot be applied. This describes the theoretical case that no matrix contribution exists for the load transfer. In such a case, the fibres cannot transfer the bending load alone. We can, however, assume that there exists no load transfer from the matrix to the fibre, in other words, the fibre does not contribute to the stiffness of the composite in bending, then with  $V_f = 0$  the composites should have a lowest Young's modulus of around 30 GPa.

The experimentally determined Young's modulus of the reference composite showed that in the as-hot-pressed reference composite and in the composite where the carbon layer was removed at 1200°C ( $E_{CMC} = 42$  and 27 GPa, respectively), there existed almost no interaction between the fibre and the matrix. Extended heat-treatment of the reference composite at 1300°C yielded a modulus of around 84 GPa, indicating that a certain load transfer through the sintering-related contact points at the fibre/matrix-interface occurred. The higher load transfer between the fibre and the matrix caused also a simultaneous increase of the strength after the 1300°C heat-treatment. Thus, the load transfer is likely due to the formation of substantial sintering necks (Figs. 4(a) and 6(a)). The fracture behaviour of the 1300°C prolonged heat-treated composite is brittle in the case of continuously heat-treated composite. Some remaining load capability in the case of the cyclic heat-treated composite is believed due to changes in matrix porosity distribution and formation of less effective sintering points between the fibre and the matrix which may break easily providing some damage tolerant behaviour. By three-point-bending tests, it is difficult to distinguish clearly, if maintenance of some load capability is due to dissipation at the fibre/matrix-interface, so called damage tolerance, or merely due to the delamination fracture within the matrix of the composite. Since, Young's modulus and strength of the as-hot-pressed and 1200°C/2 h heat-treated reference composites are almost the same as those of the matrix material we infer that the apparent damage tolerant stress/strain behaviour was merely due to the delamination fracture.

The Young's modulus of the carbon(fugitive)/Al<sub>2</sub>O<sub>3</sub>-composites in the as-hot-pressed and 1200°C heat-treated samples was reasonably higher (75 GPa) than that of the reference composite showing that some fibre/matrix-interaction was present. The modulus increased slightly to 90 GPa for the samples heat-treated at 1300°C. Considering the microstructural observations, the measured higher fracture strength of the carbon(fugitive)/Al<sub>2</sub>O<sub>3</sub>-composites compared with that of the reference composite after the

extended heat-treatment (170 MPa against 135 MPa, respectively) indicates that the load transfer between the fibre and the matrix is not due to the substantial sintering contact points, which impair the fibre strength by notch-like defects, but more due to dissipative effects in the fugitive layer (Fig. 5(a) and (b)). The maintenance of the fracture strength in the composite at all temperatures indicates that the oxide layer has a positive effect on fibre strength by reducing the damages caused by formation of the sintering necks. On the other hand, the stress/strain curve of the continuously heat-treated composite exhibited brittle fracture, indicating that there was some change in the interfacial relations. This is also supported by the SEM-observation of the composite, displaying partial closure of the fugitive layer (Fig. 4(c)).

Occurrence of a fibre-contribution into the load transfer should become noticeable as the Young's modulus of the composite approaches to that of the calculated modulus (120 GPa). This case is more obvious with carbon(fugitive)/ZrO<sub>2</sub>-composites, where the experimentally determined composite modulus lies around 106 GPa with the as-hot-pressed and reduces to 87 GPa with the 1200°C heat-treated sample. Removal of carbon layer retards the effectiveness of load transfer in these composites. On the other hand, prolonged heat-treatment at 1300°C gives a reduced strength compared with the as hot-pressed sample as a result of severe fibre damage. The increase of the Young's Modulus to 117 GPa (cyclic heat-treated composite) indicates strong interfacial bonding. The Young's modulus and strength of the continuously heat-treated composite could not be compared, since the sample was from a different batch but brittle fracture behaviour was, in this case too, obvious. This result corresponds with the microstructural observation of a totally closed gap between the fibre and the oxide layer. In the cyclic heat-treated sample, presence of a limited degree of damage tolerance can be observed (Fig. 6(b)) which is believed due to a less tight bonding between fibre and matrix (Fig. 5(b)). These observations can be explained by the repeated volume (length) change in the ZrO<sub>2</sub>-layer during cooling and heating periods of the cyclic heat-treatment.

In a previous study, Keller et al. [4] have used 20 and 40 nm thick carbon coated Nextel 720-fibers in composites having either a dense CAS (calcium aluminium silicate) glass-matrix or a porous alumina/mullite-matrix. They have demonstrated that the strength retention in porous matrix composites was not dependent on the presence and thickness of a fugitive layer. In other words, presence of a fugitive layer in porous matrix composites makes little difference to those without an interphase. In the dense matrix composites, in turn, the thicker carbon coating (40 nm) gave higher strengths and the strength was maintained after the removal of carbon. In general they observed that the decrease of strength in dense composites was a consequence of chemical interaction and formation of necks between the fibre and the matrix.

The reference composite in our study contains a matrix

with relatively high porosity and can be regarded as a porous-matrix composite. The thickness of the carbon(fugitive)-layer applied in our study is relatively large (200 nm), comparing with that of Keller et al. and therefore a lower fibre/matrix-interaction is to be expected (see Fig. 6(a)). Despite the presence of a large fugitive layer, the continuous heat-treatment at 1300°C leads to an almost total closure of the gap between the fibre and matrix.

In contrast, our carbon (fugitive)/ZrO<sub>2</sub>-interphase composite yields strength degradation after removal of the carbon as well as after heat-treatment at 1300°C. This result is comparable with that of the dense matrix composites of Keller et al. where chemical interactions at the fibre/matrix-interface were held responsible for the strength reduction. We believe, however, in the case of fugitive/ZrO<sub>2</sub>-interphase composite, the ZrO<sub>2</sub>-layer sinters and contracts in length heavily, closing the gap and causing notch-like defects on the fibre which as a result reduce the damage tolerance as well as the strength. This behaviour of monoclinic ZrO<sub>2</sub> was attributed to the high thermal expansion coefficient ( $13 \times 10^{-6} \text{ K}^{-1}$ ), compared to that of mullite ( $4.5 \times 10^{-6} \text{ K}^{-1}$ ).

Cyclic heat-treatment in turn seems to break the sintering-related contact points within the matrix and at the interface during successive cooling down periods, yielding better maintenance of the gap and the damage tolerance. In the case of ZrO<sub>2</sub>-interphase, repeated volume changes by reversible monoclinic-tetragonal phase-transformation under cyclic conditions affected the interfacial relations, resulting in better sliding ability of the fibre.

## 5. Conclusions

Presence of a dense oxide layer behind a carbon (i.e. fugitive)-layer plays a supporting role in the load transfer

from the matrix to the fibre and increases the strength of the composites significantly (for instance in carbon/ZrO<sub>2</sub>-composites 230 MPa after hot-pressing and in carbon/Al<sub>2</sub>O<sub>3</sub>-composites 180 MPa compared to 135 MPa of the reference carbon mono layer composite).

Sintering between fibre and matrix in the reference sample decreases the damage tolerance as the strength increases in expense of damage tolerance. In the case of double layers, the behaviour of the oxide layer and its interaction with the matrix and fugitive layer is decisive for the characteristics of the interphase. In those composites where a reasonable fugitive layer was maintained, crack deflection and fibre sliding at the fibre/matrix-interface were probable.

The efficiency of the fugitive/oxide-double layer system depends on the materials and the thermal loading condition (e.g. cyclic or continuous thermal exposure). This may be due to the occurrence of different interactive mechanisms within the matrix and at the interface. Under cyclic heat-treatment conditions, the composites are found to be more stable despite high temperature and relatively long exposures.

## References

- [1] Chawla KK, Xu ZR, Ha JS, Schmücker M, Schneider H. *Appl Compos Mater* 1997;4:263.
- [2] Hay RS, Petry MD, Keller KA, Cinibulk MK, Welch JR. *Mater Res Soc Symp Proc* 1995;365:377–82.
- [3] Milz C. PhD-study, Characterisation of an aluminosilicate fibre to be used at high-temperature in fibre-reinforced composites. Shaker Verlag, 2000.
- [4] Keller KA, Mah T, Parthasarathy TA, Cooke CM. Fugitive interfacial carbon coatings for oxide/oxide composites. *J Am Ceram Soc* 2000;83(2):329–36.

# Effects of environmental conditions on mechanical and physical properties of flax fibers

A. Stamboulis<sup>a,\*</sup>, C.A. Baillie<sup>a</sup>, T. Peijs<sup>b</sup>

<sup>a</sup>Imperial College of Science, Technology and Medicine, Department of Materials, Prince Consort Road, London SW7 2BP, UK

<sup>b</sup>Queen Mary University of London, Department of Materials, Mile End Road, London E1 4NS, UK

Received 9 September 2000; revised 16 December 2000; accepted 18 December 2000

## Abstract

The environmental degradation behaviour of flax fibers and their mechanical properties were investigated. Upgraded Duralin flax fibers, which have been treated by a novel treatment process for improved moisture and rot sensitivity, were studied. Results showed that upgraded Duralin flax fibers absorbed less moisture than untreated Green flax fibers, whereas the mechanical properties of the upgraded fibers were retained with moisture absorption, if not improved. In addition electrochemical studies were conducted on these fibers. These data agreed well with conventional moisture absorption data. Zeta ( $\zeta$ )-potential measurements at different pH-levels showed differences for Duralin fibers, which can be attributed to differences in morphological features. © 2001 Elsevier Science Ltd. All rights reserved.

**Keywords:** B. Environmental degradation; B. Mechanical properties; B. Physical properties; Flax fibers

## 1. Introduction

Ecological concern has resulted in a renewed interest in natural materials. Lignocellulosic natural fibers such as flax, hemp, sisal and jute are an interesting, environmentally friendly alternative to the use of glass fibers as reinforcement in engineering composites [1]. These fibers are renewable, nonabrasive and they can be incinerated for energy recovery since they possess a good calorific value. In addition these fibers give less concern with health and safety during handling of fiber products. They also exhibit excellent mechanical properties, low density and low price. This excellent price-performance ratio at low weight in combination with the environmentally friendly character is very important for the acceptance of natural fibers in large volume engineering markets such as the automotive and construction industry. An overview of some advantages and disadvantages of natural fibers is given in Table 1.

The microstructure of natural fibers is extremely complicated, in that it comprises different hierarchical microstructures [2]. The single fiber, or elongated cell, has a diameter of around 10–20  $\mu\text{m}$  and consists of a microfibrillar cellulose phase and a matrix phase, which is mainly composed of hemicellulose (branched cellulose of low molecular weight) and lignin (phenolic-like aromatic compound) (see Fig. 1).

The microfibrils have a diameter of about 10 nm and are made up of 30–100 cellulose molecules in extended chain conformation and provide mechanical strength to the fiber. A good orientation of the microfibrils and high cellulose content are essential for obtaining a fiber with good mechanical properties. The non-crystalline matrix phase of the cell wall is very complex and consists of various compounds, including hemicellulose, lignin and some pectin, which all form complicated macromolecular networks. The hemicelluloses bond to cellulose by hydrogen bonding and act as cross-linking molecules between the cellulose microfibrils forming the cellulose-hemicellulose network, which is thought to be the main structural component of the fiber cell. The hydrophobic lignin network affects the properties of the other network in such a way that it acts as a coupling agent and increases the strength of the cellulose-hemicellulose network. The outer cell wall is porous and consists also of pectin and other non-structural carbohydrates. The pores of the outer skin are the prime diffusion paths of water through the material. Each fiber cell consists of a primary cell wall and three secondary cell walls (see Fig. 2). Each cell wall contains a lignin-hemicellulose matrix surrounded by cellulose microfibrils, which are oriented in different directions in the different wall layers. The bulk of the fiber is made up of secondary cell wall. The lumen in the centre of the fiber contributes to the water uptake properties of these fibers [3]. In most applications fiber bundles or strands are used rather than individual fibers. Within a

\* Corresponding author.

E-mail address: a.stamboulis@ic.ac.uk (A. Stamboulis).

Table 1

Main advantages and disadvantages of natural fibers

Advantages	Disadvantages
Low cost	High moisture absorption
Renewable resource	Poor dimensional stability (swelling)
Low density	Poor microbial resistance
High specific properties	Low thermal resistance
High Young's modulus	Discontinuous fiber
Good tensile strength	Anisotropic fiber properties
Nonabrasive to tooling and moulds	Low transverse strength
No skin irritations	Low compressive strength
Low energy consumption	Local and seasonal quality variations
CO <sub>2</sub> neutral	Demand and supply cycles
No residues when incinerated	
Biodegradable ( $\pm$ )	

fiber bundle, fiber cells overlap and are bonded together by pectin to give strength to the bundle as a whole. However, the strength of this composite-like bundle structure is significantly lower than that of the individual fiber cell. A major restriction to the successful use of natural fibers in durable composite applications is their high moisture absorption and poor dimensional stability (swelling), as well as their susceptibility to rotting. Swelling of fibers can lead to micro-cracking of the composite and degradation of mechanical properties [4]. Recently a novel upgrading process for lignocellulosic materials has been developed to improve the poor environmental- and dimensional stability of these materials [5]. This upgrading process,

which was initially developed for wood, has also proven its applicability to natural fibers and has led to the development of upgraded flax; the so-called Duralin flax [6]. The process is currently commercialised by CERES B.V. (Wageningen, The Netherlands) and the availability of this upgrading process for natural fibers could remove one of the main restrictions to the successful application of natural fibers in high-quality engineering composites.

The aim of this paper is to study the environmental behaviour of flax fibers. The effect of the upgrading treatment is evaluated by comparing the moisture absorption and residual mechanical properties of upgraded Duralin- and Green

### Flax Fibre Cell

1. long cells.
2. tapered ends.
3. polygonal cross section.
4. narrow lumen.
5. characteristic cross markings.
6. nodes in the overlapping at the fibre ends.
7. length: 6–60 mm.
8. width: 10–30  $\mu$ m.

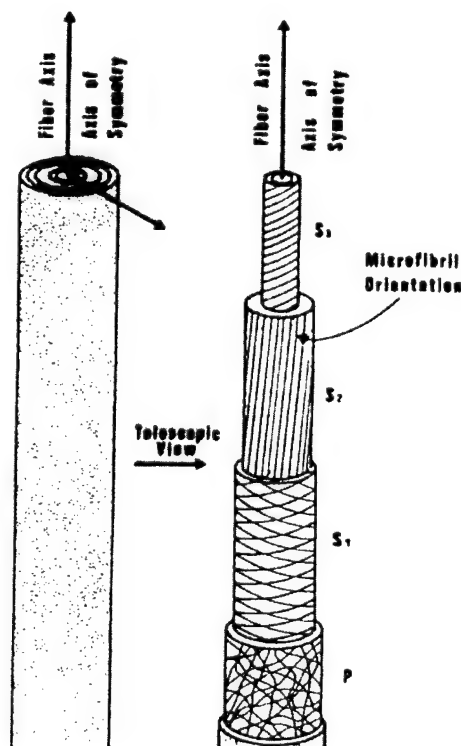


Fig. 1. The structure of a flax fiber cell.

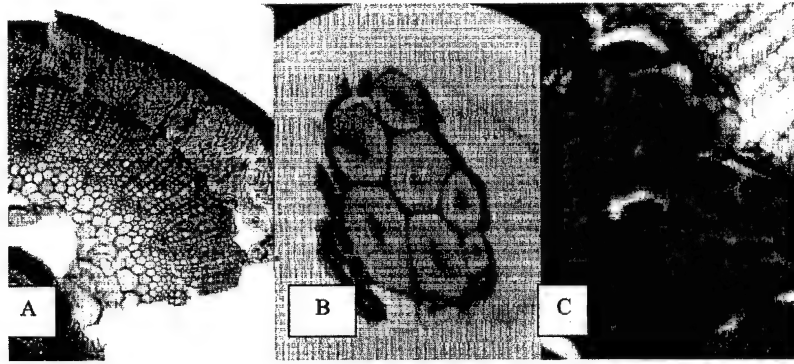


Fig. 2. The structure of flax fibers under the optical microscope: (A) Cross-section of the stem of a flax plant showing bundles of fiber cells positioned just below the surface layer. (B) Bundle of flax fiber cells, showing the lumen in the middle. (C) The internal interfaces of fiber cells. The wall layers S1, S2 and S3 are clearly visible.

flax fibers. In addition to conventional moisture absorption data, electrochemical experiments were carried out to get more insight into the effect of the Duralin treatment on the moisture uptake of flax fibers.

## 2. Materials and methods

### 2.1. Duralin treatment

The upgrading process for flax as developed by CERES B.V. uses fully rippled (deseeded) straw-flax. The use of straw-flax turned out to be beneficial for both strength and reproducibility (no dew-retting required) of the treated fibers. The Duralin treatment consists of a steam or water-heating step of the rippled straw-flax at temperatures above 160°C during approximately 30 min in an autoclave. This first step is followed by a drying step and a heating (curing) step above 150°C during approximately 2 h. During this treatment, the hemi-cellulose and lignin are depolymerised into lower molecular aldehyde and phenolic functionalities, which are combined by the subsequent curing reaction into a water resistant resin, which keeps the cellulose microfibrils together. After the treatment the fibers can easily be separated from the stem by a simple breaking and scutching operation. The fibers obtained by these procedures are fiber bundles rather than individual fibers.

### 2.2. Moisture absorption measurements

The moisture absorption of two types of flax fibers (Green and Duralin) was studied in accordance with the German specifications DIN 53495. Prior to testing the fibers were dried in an oven at 60°C for 24 h. Bundles of fibers were kept together and suspended in desiccators. The desiccators contained solutions of potassium acetate, sodium nitrate, ammonium monophosphate and distilled water and their environment had a relative humidity of 20, 66, 93 and 100%, respectively. The weight of fibers was measured at different time intervals and the moisture absorption (MC =

moisture content) was calculated by the weight difference:

$$MC(\%) = [(W - W_d)/W] \times 100\% \quad (1)$$

where  $W$  = weight of wet fibers,  $W_d$  = weight of dried fibers.

Different models have been developed in order to describe the moisture absorption of materials [1,7]. A problem, in which the temperature and the moisture distribution inside the material are to be determined, is often referred to as the 'moisture problem'. Such problems can be solved analytically and the moisture absorption can be called 'Fickian'. The following parameters need to be known in order to make 'Fickian' calculations:

1. Geometry (material thickness  $h$  in case of a one-dimensional problem).
2. Boundary conditions: ambient temperature and relative humidity (100% in case of immersion).
3. Initial conditions: temperature and moisture concentration  $M_i$  inside the material.
4. Material properties: density  $\rho$ , specific heat  $C$ , thermal conductivity  $K$ , mass diffusivity  $D$ , maximum moisture content  $M_m$  and a relationship between the maximum moisture content and the ambient conditions.

The time evolution of moisture absorption in one dimension may be described by the following equation [7]:

$$\frac{M_t}{M_m} = 1 - \frac{8}{\pi^2} \sum_{j=0}^{\infty} \frac{1}{(2j+1)^2} e^{-\frac{D(2j+1)^2 \pi^2 t}{h^2}} \quad (2)$$

where  $D$  is the diffusivity,  $h$  is the thickness of the sample,  $M_t$  is the moisture content at a time  $t$ ,  $M_m$  is its maximum moisture content, reached at equilibrium and,  $j$  is the summation index. This equation is generally used to calculate the diffusivity  $D$  and the maximum moisture content  $M_m$  of the materials.

### 2.3. Single fiber tensile testing

Individual Green- and Duralin flax fibers were carefully separated by hand from the bundles. Samples were then

prepared by fixing the fibers on special cardboard frames of gauge lengths 3.5 and 8 mm. Prior to testing, the samples were conditioned in different relative humidities for at least 5 min. The samples (15 samples of each 3.5 and 8 mm length for each fiber) were tested with the help of a specially designed microtensometer based in the Silsoe Research Institute (Silsoe, UK), with a maximum load cell of 1.0 N. The microtensometer was placed in a humidity chamber, which could create a constant environment of 30, 66 and 90% humidity at a constant temperature of 35°C. The fiber diameter was measured prior to testing with the help of an optical microscope.

#### 2.4. Zeta ( $\zeta$ )-potential measurements

The electrokinetic analyser EKA (Anton Paar KG, Graz, Austria) based on the streaming potential method [8] was used to measure the electrokinetic or  $\zeta$ -potential of different natural fibers. The streaming potential was measured as a function of time and pH at 20°C using two Ag/AgCl electrodes. The theoretical and experimental description of this technique has been reported in the recent literature [9–12]. According to Kanamaru [13], the quotient  $(\zeta_0 - \zeta_\infty)/\zeta_0$  where  $\zeta_0$  and  $\zeta_\infty$  are the  $\zeta$  potential values immediately after starting the measurement and at equilibrium, respectively, should correspond to the water up-take at a relative humidity (RH) of 100% of the investigated solid. The decrease of the  $\zeta$ -potential as a function of time due to the water uptake can be described as follows:

$$-\frac{d\zeta}{dt} = k(\zeta - \zeta_\infty) \quad (3)$$

which leads to

$$-\ln \frac{\zeta - \zeta_\infty}{\zeta_0 - \zeta_\infty} = k \cdot t \quad (4)$$

where  $k$  is a constant depending on the structure of the investigated material. The acidity and basicity of solid surfaces can be determined qualitatively by measuring the  $\zeta$ -potential as a function of the pH, if the dissociation of functional groups is the predominant mechanism forming the double-layer.

Table 2

Average maximum moisture content of flax fibers at different levels of relative humidity (RH)

Flax fiber	Maximum moisture content $M_{m,t}$ (%)			
	20% RH	66% RH	93% RH	100% RH
Green	3.61	15.03	24.0	42.58
Duralin	2.70	10.76	9.0	14.33

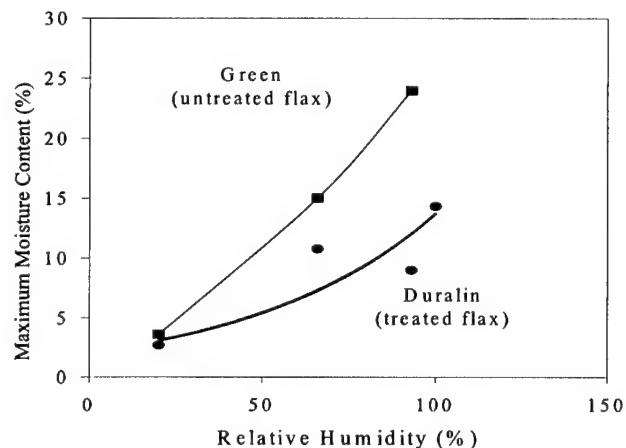


Fig. 3. The environmental relative humidity effect on the moisture absorption content of Green and Duralin flax fibers.

### 3. Results and discussion

#### 3.1. Moisture absorption

Table 2 shows the average maximum moisture absorbed by the fibers at different relative humidities. As expected, the moisture content of both Green and Duralin flax fibers increases with increasing relative humidity (Fig. 3). The moisture content of Green flax is, however, higher than the moisture content of Duralin flax fibers for all the relative humidities.

Figs. 4 and 5 show the average moisture content of Duralin and Green fibers as a function of time for 66 and 100% relative humidity, respectively. At the 66% relative humidity level, the upgraded Duralin fiber absorbs about 30% less moisture than the Green flax fiber, whereas at 100% the same fiber absorbs about 50% less moisture. The rate at which moisture diffuses into or out of any solid is governed by Fick's first law, which says that the rate of the mass of moisture that passes through a cross-section unit,

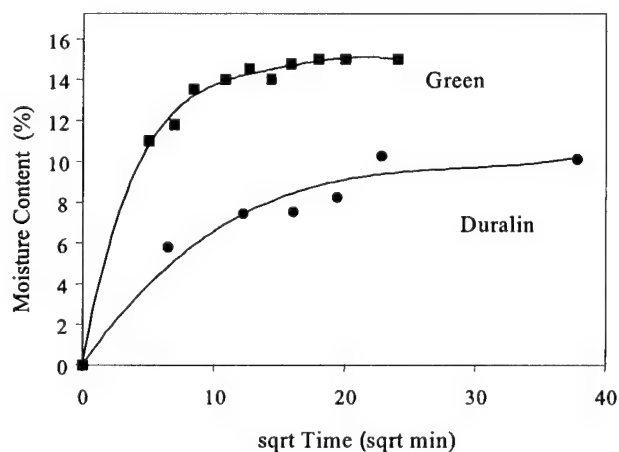


Fig. 4. Average moisture content for Green- and Duralin flax fibers at 66% of relative humidity.



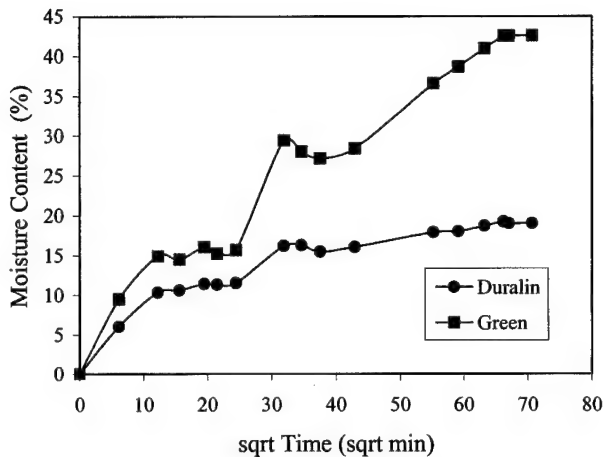


Fig. 5. Average moisture content for Green- and Duralin flax fibers at 100% of relative humidity.

called the flux, is proportional to the concentration gradient of moisture  $dc/dx$ . The proportionality constant is the diffusion coefficient or diffusivity  $D$  ( $\text{cm}^2/\text{s}$ ). In the case of the membrane problem the first Fick's law is useful because the concentration gradient is constant and at steady state  $D$  is constant as well. Most problems in diffusion such as the fiber problem have a region where the concentration of moisture changes with time. Fick's first law is not useful in this case but another expression that describes the flux is needed, which corresponds to the experimental conditions. Fick's second law may describe the moisture absorption in fibers and it is useful to determine concentration as a function of time. The analysis of the problem with Fick's second law allows us to determine the approximate time for a fiber to reach equilibrium, that is the time required to satisfy:  $x^2/4D_f$ , where  $x$  is the radius and  $D_f$  the diffusivity of the fiber [1]. From studies on the diffusivity within a hygroscopic fiber at medium humidities a value of  $10^{-7} \text{ cm}^2/\text{s}$  may be taken. The diffusivity increases rapidly with increasing concentration of water in fibers. In the dry state, diffusion is very slow but it becomes more rapid at moderate and high moisture regains. The variation in moisture content through a fiber that absorbs water shows a sharp boundary. The observation of the rate of advance of this boundary is another method to determine the diffusion coefficient in a fiber [1,14]. Another effect that may slow down the approach to the final equilibrium (as it is observed for Green fibers) is the presence of swelling stresses. The fibers swell when water is absorbed and swelling stresses build up. It has been observed that after the initial diffusion process there is a second stage where these stresses relax [1]. Consequently, the equilibrium moisture condition as diffusion proceeds is changed. Therefore the attainment of the final steady state can be delayed. During the conditioning of a bundle of fibers, diffusion takes place in three stages: during the first stage there is diffusion through the air from the water vapour to the fiber surface, the second stage involves diffusion through the air in spaces between fibers from the

surface of the bundle to the surface of a single fiber and the third stage involves diffusion from the surface of a fiber to its interior. The time needed for diffusion through air (inside or outside the specimen) depends on the size, shape and density of the specimen. Alternatively, the time needed for the diffusion in the air within the specimen is difficult to determine. However, it is expected that both effects will take place concurrently and at times of the same order of magnitude. It should be noted that the time for diffusion in air is greater than the time of diffusion within the fiber. Diffusion within the fiber occurs very fast. Consequently, in calculations involving fiber bundles, the fibers should be considered as being in equilibrium with the air at their surfaces. In our case, the fiber samples used for the moisture absorption analysis were bundles of fibers bound together. If we consider this as a single fiber with a radius of approximately 1.5 mm, the diffusivity of Green- and Duralin flax fibers at 66% relative humidity can be calculated using Eq. (2). The diffusivity  $D_f$  for Green- and Duralin flax fibers at 66% are  $4.04 \times 10^{-6}$  and  $7.8 \times 10^{-7} \text{ cm}^2/\text{s}$ , respectively. At 100% relative humidity the diffusivity of Green and Duralin fibers are  $1.93 \times 10^{-6}$  and  $1.0 \times 10^{-6} \text{ cm}^2/\text{s}$ , respectively. It is obvious that the diffusivity for Green fibers is higher compared with Duralin and this has been observed for all the examined relative humidities. Taking into consideration that in the case of fibers the time needed to reach the equilibrium is proportional to  $x^2/4D_f$  [1], the conditioning time for single flax fibers (the radius of a single fiber is considered to be approximately  $20 \mu\text{m}$ ) can be approximated. For Green and Duralin fibers at 66% relative humidity, the equilibrium time is 0.25 and 1.28 s, respectively, whereas at 100% the equilibrium time is 0.52 and 1 s, respectively. However, in real experiments the equilibrium is reached at a slower rate. The equilibrium time has been estimated for other fibers such as cotton and wool and it has always been found to be greater than the values estimated theoretically. The reason is that other factors besides the diffusion of moisture are involved. Such factors can be the heat evolved when the fibers absorb water or the structural relaxation and changes during water absorption.

Figs. 6–8 represent the relationship between the equilibrium time and the maximum moisture content in the fiber ( $M_{m,f}$ ). It can be observed that the treated Duralin fibers need more time to reach their saturation point compared with the untreated Green flax fibers with the exception of 93% relative humidity, where Duralin fibers need less time to reach their saturation point (Fig. 8). In this case, as it has been mentioned before, it is possible that at high relative humidities when the Green fibers reach a high level of moisture uptake close to their saturation point, they need more time to stabilise as the water already absorbed inhibits the process. In all cases the Green flax fibers absorb more moisture than the treated Duralin flax fibers, whereas the treatment becomes more effective at high relative humidities.

Fig. 9 shows SEM micrographs of dry and conditioned



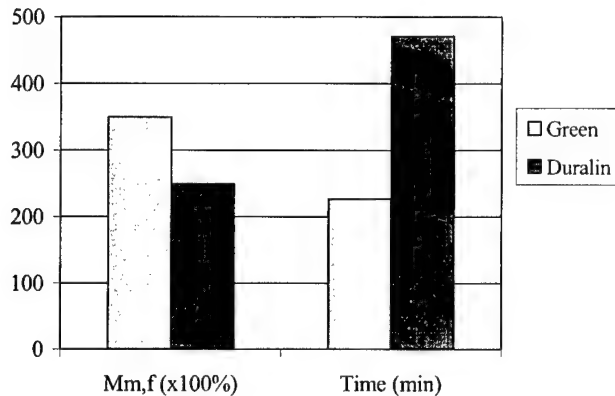


Fig. 6. Time dependence of moisture absorption for Green- and Duralin flax fibers at 20% of relative humidity.

Duralin and Green fibers. The structure of flax is made up of cellulose microfibrils bound together by a matrix of lignin and hemicellulose, which are then subsequently bound together to form larger fiber bundles. Kinks or nodes can be clearly seen at regular intervals along the fiber surface, which may be attributed to fiber cell tip overlap within the bundles or defects on the fibers surface due to compression (kink bands). The individual fibers are well connected by the pectin matrix. The fiber surface of Duralin flax fibers after conditioning at 100% relative humidity remains smooth and unchanged from its dry state. Although the individual fibers are still intact, the fiber bundle is well separated and the matrix in between the individual fibers is dissolved. The surface of dry untreated Green fibers is smooth and kink bands are visible along the fiber axis. The fiber cells are well connected by the organic matrix and form a fiber bundle. Unlike the Duralin fibers, the conditioned Green fibers (100% relative humidity) are swollen and their surface appears to be rougher than that of the dry Green fibers. Also here the individual fibers are well separated and damage is observed in the form of kink bands. After being subjected to moisture, the effects on both types of fibers are different.

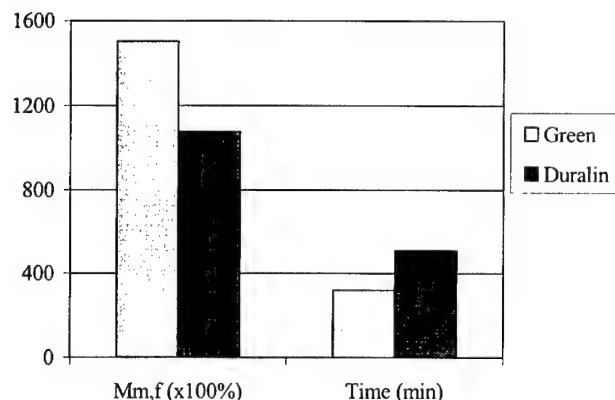


Fig. 7. Time dependence of moisture absorption for Green- and Duralin flax fibers at 66% of relative humidity.

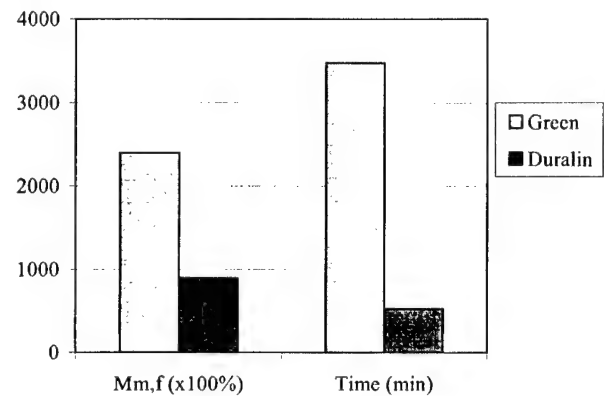


Fig. 8. Time dependence of moisture absorption for Green- and Duralin flax fibers at 93% of relative humidity.

The surface of Duralin did not appear to be damaged, whereas the surface of Green flax fibers became rougher. The matrix, which connects the fibers, was in both cases almost non-existent.

### 3.2. Influence of moisture absorption on mechanical properties

The load-displacement curves of the fibers were typical of brittle materials. Table 3 represents the results of tensile tests on humidified flax fibers. The average ultimate tensile strength of flax fibers changes as the relative humidity increases. The average tensile strength of both types of fibers at 3.5 mm gauge length is somewhat higher than those at 8 mm gauge length with the exception of Duralin, which at 90% relative humidity exhibits a lower tensile strength. The increase in strength at decreasing fiber length is expected since with increasing length the probability of critical defects causing fracture will also increase. Figs. 10 and 11 show the effect of the relative humidity on the average tensile strength of both fibers for 3.5 and 8 mm of gauge length. Surprisingly, Duralin fibers go through a maximum at a relative humidity of 66% for both gauge lengths. There seems to be two opposing effects of humidity on the fiber tensile strength. Up to a maximum of ca. 66% relative humidity, water uptake is advantageous for Duralin fibers, possibly due to a fiber plasticising effect as a result of the presence of 'free' water [15]. Excess of humidity, however, leads to an increase in the absorbed bound water and a decrease in 'free' water. Therefore, in high relative humidities the plasticising effect becomes less important, resulting in reduced fiber strength. Water is able to penetrate the cellulose network of the fiber into the capillaries and spaces between the fibrils and into less bound areas of the fibrils and it may attach itself by chemical links to groups in the cellulose molecules. The water molecules force the cellulose molecules apart destroying some of the rigidity of the cellulose structure. In this way the water acts as a plasticiser. It permits the cellulose molecules to move more freely. Consequently the mass of cellulose is softened and can

Table 3  
Average tensile strength of humidified flax fibers

Relative humidity (%)	Flax fiber	Fiber length (mm)	Average tensile strength (MPa)	Standard deviation (MPa)
30	Green	3.5	677	425
	Duralin		809	134
66	Green	3.5	799	398
	Duralin		1080	368
90	Green	3.5	818	318
	Duralin		642	344
30	Green	8	619	461
	Duralin		651	176
66	Green	8	760	390
	Duralin		913	250
90	Green	8	761	369
	Duralin		884	180

change shape more easily with an application of force [3]. It has been suggested [16,17] that the failure of cellulosic fibers under axial application of tensile stresses is controlled by the cellulose content and the microfibril angle  $\theta$  between the microfibrils and the fiber axis. The effect of the cellular content, the microfibril angle and the cellular size on the mechanical and physical properties of lignocellulosic fibers has been shown by Mukherjee et al. [18]. The spiral angle in

the case of flax fibers has been calculated to be 10%. There is a clearly defined correlation between the anisotropy of swelling and tensile properties with the wall structure of fibers. The microscopic structure of cellulose shows a significant anisotropy in that the swelling is larger in the direction perpendicular to the chains than in the direction parallel to the fiber-axis. Mainly the orientation and the angular dispersion affect this anisotropy. In other words,

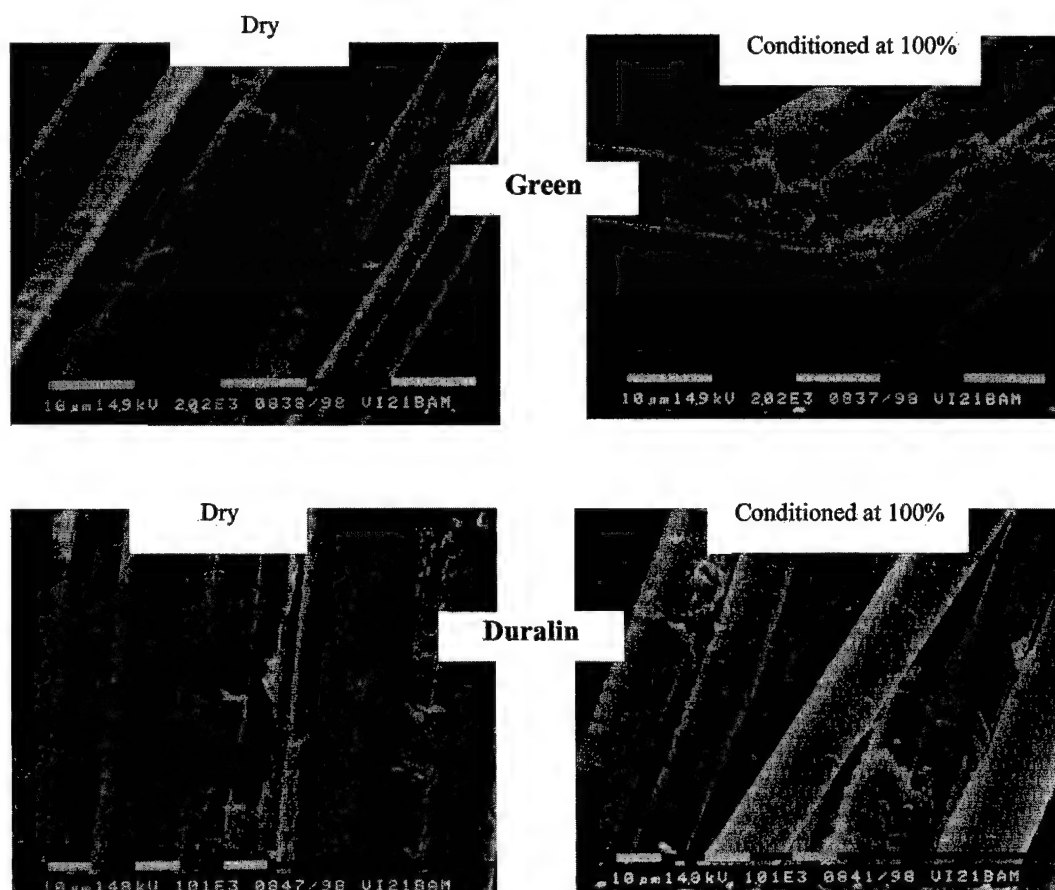


Fig. 9. SEM micrographs of dry and conditioned Green and Duralin flax fibers.

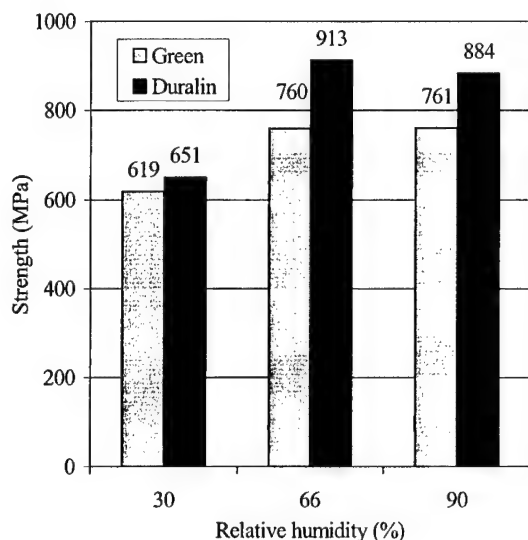


Fig. 10. Effect of relative humidity on the average tensile strength of Green- and Duralin flax fibers (8 mm gauge length).

the anisotropy can be reduced both as angular dispersion increases and as the spiral becomes flatter. The study of strength properties in natural fibers showed that flatter spirals have higher extensibility, lower Young's modulus and lower tensile strength compared with the fibers with steeper spirals. In the case that the fibers are stretched wet, the angle  $\theta$  changes in such a way that the spiral becomes steeper [16].

Green fibers seem to be less affected by the two opposing influences referred to above and maintain a more or less constant tensile strength with changing humidity with a small increase at 66 and 93% relative humidity. It is important to note that the effect of humidity on the mechanical properties of the fibers depends also on the time of exposure in certain humidity conditions. For example, it has been observed that moisture causes fungus development on the fiber surface often

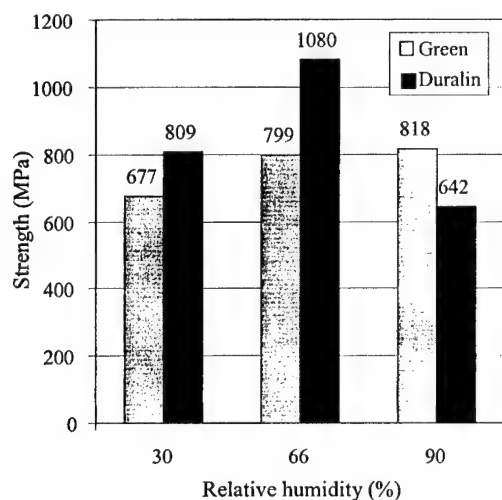


Fig. 11. Effect of relative humidity on the average tensile strength of Green- and Duralin flax fibers (3.5 mm gauge length).

after 3 days of exposure, resulting in degradation of the fibers and decrease in their mechanical properties.

### 3.3. Influence of moisture absorption on zeta ( $\zeta$ )-potential measurements

Among other surface analysis techniques, zeta ( $\zeta$ )-potential analysis has been used to characterise the surface of hydrophilic materials such as lignocellulosic fibers. Changes in the surface composition and in the water uptake behaviour due to different separation techniques or different subsequent treatments of these materials can be identified by  $\zeta$ -potential analysis.

The  $\zeta$ -potential of the hydrophilic natural fibers is strongly influenced by the water content and consequently by the swelling of the investigated fibers. The time dependence of  $\zeta$ -potential of dried Green, Dew-retted and Duralin fibers in  $10^{-3}$  mol/l KCl-electrolyte solution was measured (Fig. 12). Dew-retted<sup>1</sup> fibers have been used as the control fibers together with Green fibers in order to evaluate better the behaviour of the upgraded (industrially modified) Duralin fibers. It is clear from Fig. 12, that a decrease of the negative  $\zeta$ -potential occurs as a function of time for all fibers. More specifically, the negative  $\zeta$ -potential decreases for both Green- and Dew-retted fibers in a similar way. Compared with Duralin flax fibers, the negative  $\zeta$ -potential value for both Green and Dew-retted fibers decreases from a value  $\zeta_0$  on a different time-scale more or less asymptotically to a constant but lower negative value  $\zeta_\infty$ . The strong initial decrease of  $\zeta$ -potential with time can be attributed to the water absorption. The rate of this initial decrease depends primarily on the degree of hydrophilicity of the investigated fibers or more specifically on the swelling of the fibers. Another possible reason for the  $\zeta$ -potential decrease can be the removal of water-soluble components from the fiber bulk (for flax fibers 3.9% of water soluble components, e.g. ashes, alkali and earth metal salts [19,20]).

Comparing the  $\zeta$ -potential changes with time with the conventional moisture absorption measurement discussed earlier, it can be concluded that both methods are in a good agreement. The Green fibers absorb more water than Duralin fibers. Although the saturation point for both fibers occurs almost at the same time (about 4500 min at a relative humidity of 100%), Duralin fibers show different water uptake behaviour. Considering the time dependence of the  $\zeta$ -potential and the assumption that the quotient  $(\zeta_0 - \zeta_\infty)/\zeta_0$  should be a direct measure of the water uptake (see Table 4), it can be said that Green flax, having a higher  $(\zeta_0 - \zeta_\infty)/\zeta_0$  value compared with Duralin, absorbs more water than Duralin fibers. Duralin fibers show the lowest degree of hydrophilicity (also when compared with Dew-retted flax fibers as shown in Fig. 12 and Table 4). The

<sup>1</sup> Retting is a fermentation process that frees the fibers from the woody matter and cellular tissue that keep them together in stems. Dew-retting is a process where the crop is spread on the ground after harvesting and left for several weeks. Wetting by dew and rain encourages fermentation to take place.

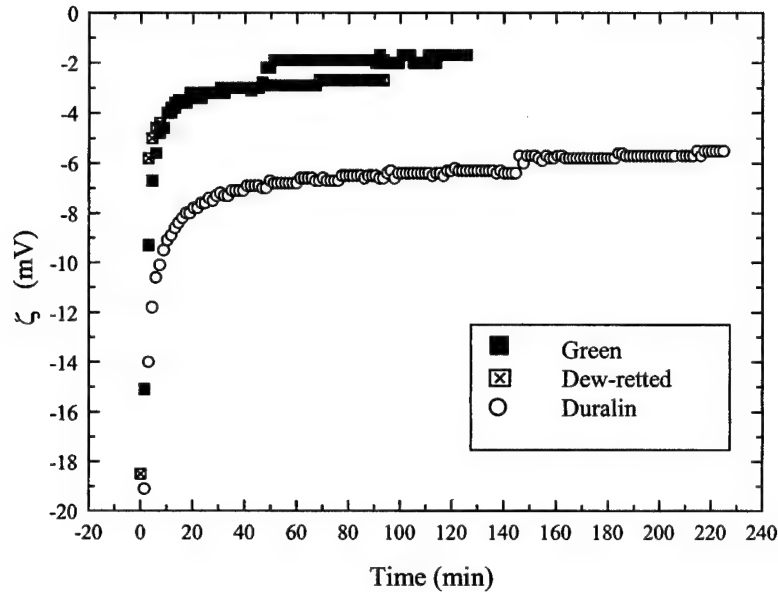


Fig. 12. Time dependence of zeta ( $\zeta$ )-potential for Green-, Dew-retted- and Duralin flax fibers measured in  $1 \times 10^{-3}$  mol/l KCl.

constant  $k$  is a measure of the velocity of the water uptake process. The smaller the constant  $k$  (see Table 4), the higher the  $(\zeta_0 - \zeta_\infty)/\zeta_0$  value and, therefore, the more water is absorbed by the fiber (in this case Green fiber). The above results confirm the potential of  $\zeta$ -potential measurements to be used as an important tool to estimate the swelling behaviour of different materials in water. These results are in line with expectations since the water up-take process should be connected with changes of the cellulose structure of fibers.

### 3.4. pH dependence of $\zeta$ -potential measurements

Fig. 13 and Table 5 summarise the pH dependence of  $\zeta$ -potential change of Green, Dew-retted and Duralin fibers. The overall trend of  $\zeta$ -potential changes with pH is very similar for Green and Dew-retted fibers with the latter slightly shifted to more negative  $\zeta$ -potential values. This indicates lower water absorbability for Dew-retted flax fibers as compared with Green flax fibers. The upgrading of Duralin fibers changes the flax fiber surface composition as the non-cellulose components were removed. The change

in flax fiber surface composition due to this upgrading process becomes more obvious in an altered  $\zeta$ -potential curve (Fig. 13). This  $\zeta = f(\text{pH})$  curve corresponds to the expected pH-dependent  $\zeta$ -potential change of materials that contain acidic dissociable surface functional groups [21]. The isoelectrical point (i.e.p.) for Duralin fibers (calculated by a simple extrapolation of the curve) lies in the pH-range of 1.6–2.2. These values are in good agreement with values measured for purified cellulose fibers [22]. Therefore it can be suggested that possibly a large number of acidic surface groups are present in Duralin fibers with the higher  $\zeta_{\text{plateau}}$ -value (Table 5) indicating improved resistance to moisture absorption as a result of the upgrading process. On the other hand, the i.e.p. for Green and Dew-retted fibers could not be estimated; negative  $\zeta_{\text{plateau}}$  were expected due to the presence of carbonyl and hydroxyl groups in cellulose, which in these fibers is higher than 64% [20,21]. The negative charge of the fibers surface leads to a preferential absorption of chloride ions resulting in a rapid increase of the negative  $\zeta$ -potential at low pH-values.

## 4. Conclusions

Upgraded Duralin fibers absorb less water than untreated

Table 4

Time dependence of  $\zeta$ -potential measured in  $1 \times 10^{-3}$  mol/l KCl electrolyte solution. ( $\zeta_0$  =  $\zeta$ -potential value measured immediately after starting the measurement,  $\zeta_\infty$  =  $\zeta$ -potential value after established equilibrium,  $(\zeta_0 - \zeta_\infty)/\zeta_0$  = calculated value that corresponds to the water up-take at 100% relative humidity,  $k$  = velocity constant of swelling process)

Flax fiber	$\zeta_0$ [mV]	$\zeta_\infty$ [mV]	$(\zeta_0 - \zeta_\infty)/\zeta_0$	$k$ [ $\text{min}^{-1}$ ]
Green	-15.1	-1.7	0.88	0.19
Dew-retted	-18.5	-2.7	0.85	0.23
Duralin	-11.8	-5.3	0.55	0.29

Table 5

$\zeta$ -potential plateau values at  $\text{pH} \geq 7$  and characteristic pH-values when rapid changes of  $\zeta$ -potential in the acidic range are observed

Flax fiber	$\zeta_{\text{plateau}} (\text{pH}7)$ [mV]	pH ( $\zeta$ changes rapid)
Green	-2.1	5.2
Dew-retted	-3.3	6.3
Duralin	-8.2	(i.e.p.(extrapolated) = 1.6–2.2)

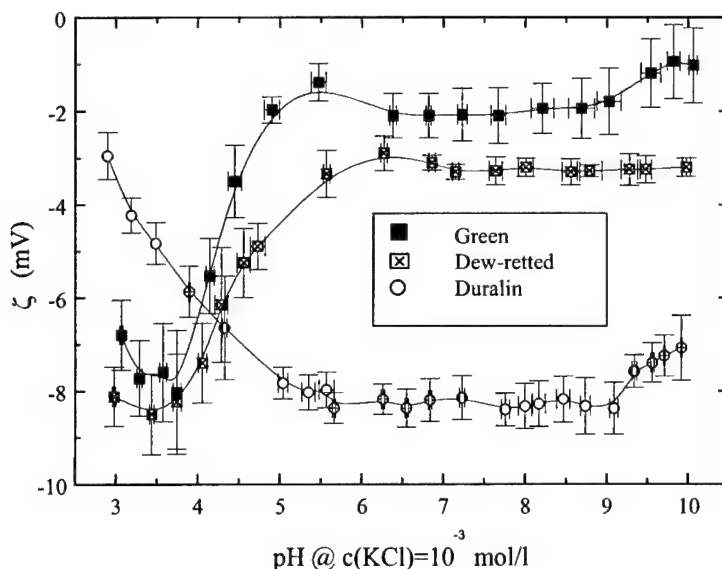


Fig. 13. pH-dependence of zeta ( $\zeta$ )-potential of Green-, Dew-retted- and Duralin flax fibers.

Green flax fibers. SEM micrographs show that Duralin fibers, even after conditioning in 100% relative humidity, retain a smooth fiber surface, whereas the individual fibers are well separated. Conditioned Green fibers appear swollen at 100% relative humidity, and their surface is rough with the individual fiber cells well separated and damage observed in the form of kink bands.

During the separation of a single fiber cell from a bundle of fiber cells, damage of the fiber may occur, which may lead to a consequent decrease in tensile strength. As the mechanical properties can be strongly affected by handling, this may well be, together with the problem of defining the exact cross-sectional area, responsible for the relatively large scatter found in the strength values of natural fibers.

Generally, the Duralin fibers exhibit a somewhat higher and more uniform strength with less scatter, i.e. the applied upgrading process not only improves their moisture resistance but also the mechanical properties of the fibers are at least retained, if not improved. The average tensile strength of flax fibers changes with relative humidity as well as test length. In almost all cases the highest strengths are observed for the shortest gauge length (3.5 mm compared with 8 mm). With increasing relative humidity, the Duralin fibers seem to go through a maximum in strength at a relative humidity of 66% due to a water plasticising effect. At high relative humidities where the largest amount of absorbed water is bound the plasticising effect becomes less important, resulting in reduced strength of the Duralin fiber. Green fibers maintain an almost constant tensile strength with humidity with a small increase at 66 and 93% relative humidity.

From the electrochemical measurements it can be concluded that the Duralin treatment leads to fibers with different surface characteristics as shown by the pH-dependent

zeta ( $\zeta$ )-potential measurements. The Green fibers are the most hydrophilic ones, whereas the upgraded Duralin fibers display a more hydrophobic surface. Finally, it is worth noticing that  $\zeta$ -potential analysis can give easy and fast information on the swelling as well as water uptake behaviour of different materials including natural fibers in aqueous solutions.

### Acknowledgements

The authors would like to thank Dr G. Pott of CERES BV (Wageningen, The Netherlands) for providing the flax fibers. Mr G. Dijon (Imperial College, Department of Materials, London) is acknowledged for providing the stained optical micrographs of the flax stem, Dr A. Bismarck for his assistance in zeta-potential measurements and Dr A.R. Boccaccini (Imperial College, Department of Materials, London) for reviewing the manuscript. One of the authors (AS) acknowledges also the financial support from the European Commission through a Marie Curie Fellowship.

### References

- [1] Morton WE, Hearle JWS. Physical Properties of Textile Fibers. 2. London, Heinemann: The Textile Institute, 1975.
- [2] Brett C, Waldron K. Physiology and biochemistry of plant cell walls. 2. London: Chapman & Hall, 1996.
- [3] Cook JG. 5. Handbook of textile fibers, 5. Shildon: Merow, 1984. p. 35–73.
- [4] Stamboulis A, Baillie CA, Garkhail SK, van Melick HGH, Peijs T. Environmental durability of flax fibers and their composites based on polypropylene matrix. Appl Comp Mater 2000;7(5-6): 273–294.
- [5] Ruyter HP, Hortulanus A. European Patent Application EP 373 726, 1993.
- [6] Pott GT, Pilot RJ, van Hazendonk JM. In: Proceedings of the 5th

- European Conference on Advanced Materials and Processes and Applications (EUROMAT 97), Vol. 2 Polymers and Ceramics, Maastricht, 21–23 April 1997, p. 107.
- [7] Springer GS. Environmental effects on composite materials. Vol. 1. Westport: Technomic Pub. Co, 1981.
- [8] Schurz J, Jorde Ch, Ribitsch V, Jacobasch H-J, Körber H, Hanke R. Cell Chem Technol 1986;20(6):575.
- [9] Grundke K, Boerner M, Jacobasch H-J. Colloids Surf 1991;58:47.
- [10] Tanhan R. PhD thesis, TU-Berlin, D83, 1997.
- [11] Bismarck A, Kumru ME, Springer J. J Coll Interf Sci 1999;210:60.
- [12] Bismarck A, Springer J, Mohanty AK, Hinrichsen G, Khan MA. Characterisation of several modified jute fibers using  $\zeta$ -potential measurements, Colloid Polym Sci 2000;278(3):229.
- [13] Kanamaru K. Kolloid-Z 1960;168:115.
- [14] Hermans PH, Vermaas D. J Polym Sci 1946;1:149.
- [15] Warner SB. In: Stenquist B, editor. Fiber Science. New Jersey: Prentice Hall, 1995. p. 134–40.
- [16] Hearle JWS, Peters RH. Fiber structure. London: Butterworth & Co Ltd, 1963. p. 255–65.
- [17] McLaughlin E, Tait RA. J Mater Sci 1980;15:89.
- [18] Mukherjee PS, Satyanarayana KG. J Mater Sci 1986;21:51.
- [19] Bledzki AK, Gassan J. Natural fiber reinforced plastics. In: Chermiansinoff NP, editor. Handbook of engineering polymeric materials. New Jersey: Marcel Dekker Inc., 1997. p. 787–810.
- [20] Ribitsch V, Stana-Kleinschek K, Jeler S. Coll Polym Sci 1996;274:388.
- [21] Bismarck A, Aranberri I, Springer J, Lampke T, Wielage B, Stamboulis A, Baillie C. Characterisation of natural fibers using zeta-potential measurements; Part B. surface properties and the water up-take behaviour of flax, hemp and cellulose fibers, submitted Coll Polym Sci.
- [22] Stana-Kleinschek K, Ribitsch V. Coll Surf A 1998;140:127.

# Wet layup and sintering of metal-containing microfibrous composites for chemical processing opportunities

Daniel K. Harris<sup>a</sup>, Donald R. Cahela<sup>b</sup>, Bruce J. Tatarchuk<sup>b,\*</sup>

<sup>a</sup>Department of Mechanical Engineering, 216 Ross Hall, Auburn University, Auburn, AL 36849-5341, USA

<sup>b</sup>Department of Chemical Engineering, 230 Ross Hall, Auburn University, Auburn, AL 36849-5371, USA

## Abstract

A new class of composite materials is prepared using traditional high speed and low cost paper making equipment and techniques. In this process,  $\mu\text{m}$  diameter metal fibers in a variety of compositions and alloys are slurried in an aqueous suspension with cellulose fibers and other selected particulates and/or fibers. The resulting mixture is then cast into a preform sheet using a wetlay process and dried to create a sheet or roll of preform material. Subsequent sintering of the preform at elevated temperatures (ca. 1000°C) removes the cellulosic binder/pore former and entraps the selected particulates/fibers within a sinter-locked network of conductive metal fibers. Unique physical properties are obtained in terms of: void volume, thermal/electrical conductivity, porosity, surface area, permeability, particle size, layer thickness, etc. To a first approximation these composites possess averaged physical properties over heretofore unavailable regions located between those of the entrapped component and those of the high void volume sintered metal carrier. For chemical processing applications the high void volume of the metallic binder/carrier (i.e. 20–99%) facilitates intralayer heat and mass transport while the ability to trap very small particulates (using the novel pore size-void volume relationship of microfibrous carriers) greatly reduces intraparticle heat and mass transport. A description of the unique and fundamental structure-property relationships and behaviors of these materials will be presented and contrasted with those of the more traditional engineering approaches and practices using fused particulates and pasted-carriers. Opportunities for significant steady-state volumetric processing improvements result when one must balance the competing demands of chemical kinetics (e.g. at the entrapped particulates) with those of the required transport processes (i.e. via the interparticle and intralayer voidage). Examples of beneficial processing applications and opportunities will be discussed in: (a) heat transfer materials, (b) catalysts and sorbents, (c) electrochemical processing and (d) filtration. © 2001 Published by Elsevier Science Ltd.

**Keywords:** A. Preform; B. Physical properties; B. Porosity; Intraparticle

## 1. Introduction

Current engineering practice often uses sintered or fused grains of microscopic materials in order to produce high surface area extrudates, particles, or sheets that facilitate the chemical and/or thermal processes underlying four application areas. Examples of such materials include catalyst pellets, sorbent extrudates, powder-binder electrode sheets, fused filter media, biosupports, heat pipe wicks, etc. While chemical and thermal processes from catalysis to thermal management often rely on kinetic phenomena, which occur at an active surface, it is generally the interstitial geometry of these same materials that provides the restricted pathways and therefore the overall rate-limitations in the transport of heat, mass, or ions to the interior active sites.

To address the steady-state interplay between surface

kinetics and intraparticle/intrabed transport, and to create new methodologies to dramatically increase the volumetric processing rate to previously unattainable values, the fundamental differences that occur in the structure-property relationships of sintered-fiber versus fused-powder structures can be exploited. As shown in Figs. 1 and 2, the fundamental differences that occur between these two systems are striking. The underlying reason for these differences results from the fact that high aspect ratio fibers allow the designer to create large void volumes with tailored/selected pore sizes which are independent of fiber diameter. In the case of sintered or fused powder materials, only narrow and fixed regimes of void volume are available, and these values are entirely dependent on the packing fractions of, e.g. spherical powders (see Fig. 1). In addition, networks of packed spheres are further restricted by the fact that the effective pore/hole size is a function of the particle diameter. Fibrous media are unique in that they can be prepared over a relatively large continuum region in pore size and void volume compared to fused powder systems

\* Corresponding author. Tel.: +1-334-844-2023; fax: +1-334-844-2065.  
E-mail address: [brucet@eng.auburn.edu](mailto:brucet@eng.auburn.edu) (B.J. Tatarchuk).



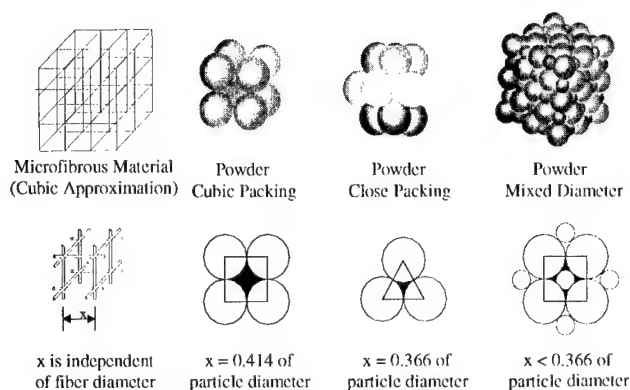


Fig. 1. Packing structures of fiber and powder based porous materials.

(see Fig. 2). This attribute provides the designer with the opportunity to ‘engineer the microfibrous properties of the media’ to the desired intraparticle or intrabed transport rates required to feed the embedded kinetics of the application.

As noted in greater detail below, exploitation of the unique pore size-void volume relationship of microfibrous media is central to the notion of increasing the steady-state volumetric reaction rate. Intraparticle transport can be increased by decreasing the size of the individual particles entrapped in the voids of the microfibrous network, while intrabed transport is increased by the ability of the mesh to separate the particles in the absence of particle–particle contact or the use of a traditional binder.

## 2. Creation of tailored microfibrous composites and structures

Efforts at Auburn University have recently led to the discovery that ‘second generation’ materials can be prepared which further capitalize on the exciting structure-

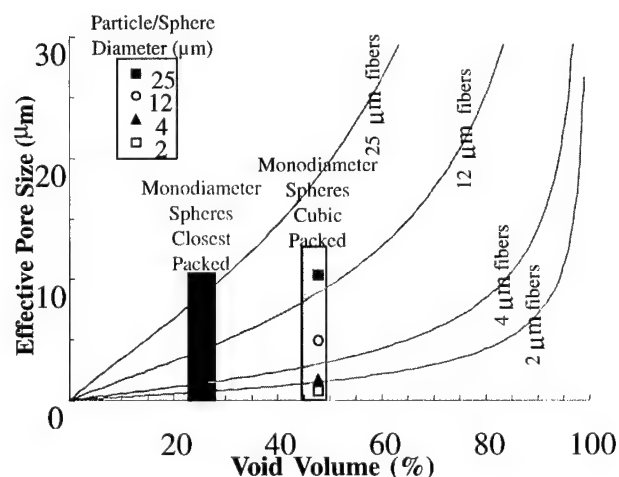


Fig. 2. Effective pore size versus void volume for fiber and powder based porous materials (data shown for fibrous media estimated using ‘cubic’ approximation shown in Fig. 1).

property foundation relationships of microfibrous materials by entrapping small grains of catalyst, electrocatalyst, biosupport, and/or sorbent within the small pore structure of the fibrous network. Examples of some of these structures are shown in Fig. 3.

During the fabrication process for these materials, micro-meter diameter metal fibers (or combinations of metal fibers and e.g. micronic catalyst/support powders) are processed into preform sheets and rolls along with cellulose fibers using traditional high-speed wet-lay papermaking techniques [1–4,14]. The resulting paper products containing microfibers of Ni, Cu, Stainless Steel, etc. are subsequently heated in a continuous hydrogen-sintering furnace at ca. 1000°C, which removes the cellulose and causes the metallic fibers to sinter-bond at their junctures thereby entrapping whatever particulates were present in the paper preform. Because there is no upper limit on the mass fraction of the cellulose binder/pore former in the ‘paper preform’, sintered fiber structures with fibrous void volumes exceeding 98% are routinely obtained after sintering. Alternatively, reducing the amount of cellulose in the preform, or introducing a simple rolling/compacting step, can be used to reduce the void volume of the sintered composite to near zero (in the absence of included refractory particulates).

In addition to the desirable physical structures and unique combinations of surface area, pore size/particle size, and void volume that are obtained; the above noted process is also attractive due to the recyclable nature of the cellulosic scraps prior to sintering and the fact that high-speed paper manufacturing and roll-to-roll handling equipment may be used. For applications that entrap small particles within the microfibrous structure (Fig. 3), intraparticle heat and/or mass transport limitations are significantly reduced. The high void volume carrier (composed of sinter-locked fibers from 95 to 98% void) also reduces intrabed heat and/or mass transport limitations. The resulting materials can further be produced in both sheet and roll form and layered or corrugated into a host of structures. These materials exhibit the high theoretical utilization, high heat transfer characteristics, and high sorptive/catalytic effectiveness factors possessed by fluidized bed reactors but at a fraction of the overall volume, mass, pressure drop, etc. and in the absence of back-mixing or typical gravitational/hydrodynamic constraints [5,6]. Particles from 10 to 100 times smaller can be entrapped within the microfibrous structure (ca. 1 μm diameter) compared to those that are applicable in normal fluid-bed reactors (ca. 100–200 μm diameter).

## 3. Chemical processing opportunities

### 3.1. Thermal management systems using microfibrous wicks for heat pipes

The ability to adapt papermaking technology to the manufacture of primary and secondary wicks, and then

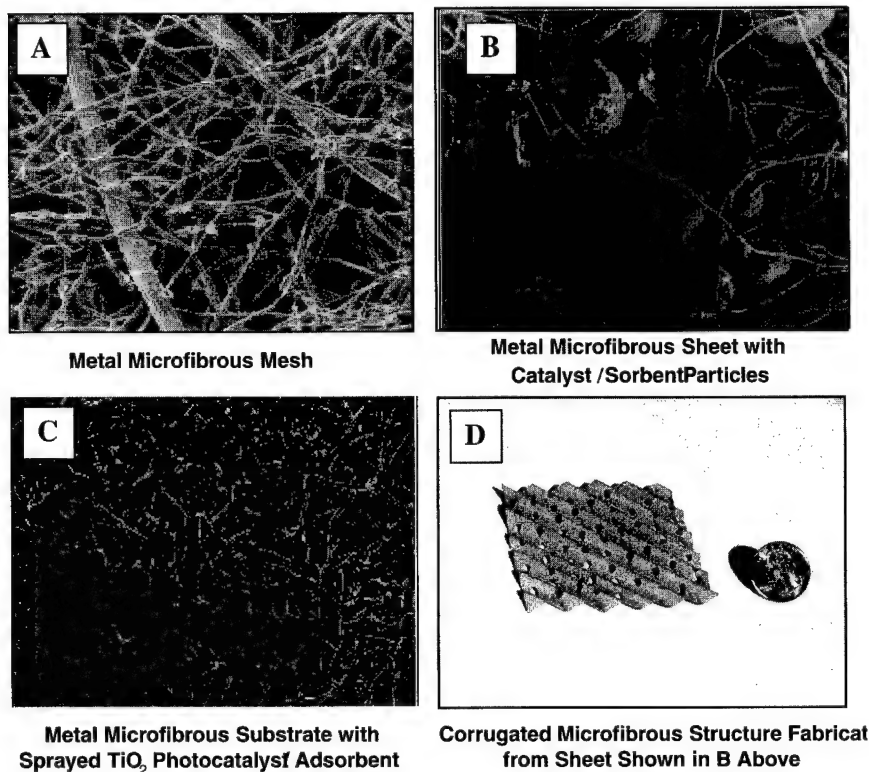


Fig. 3. Various microfibrous structures fabricated using  $2\text{ }\mu\text{m}$  (and  $8\text{ }\mu\text{m}$  in A) diameter fibers.

into integrated thermal management systems, is extremely promising and offers a vast number of applications. More importantly, heat pipe systems that incorporate microfibrous wicks may possess the unique capability to moderate or circumvent current performance barriers that are widely attributed to transport limitations. The transport limitations that can be eased include the capillary pumping limit, the evaporator boiling limit, and the entrainment limit. These system performance limits all reside within the wick, making it the single most critical element in heat pipe systems [7–13]. Ideally, the wick should have a pore size as small as possible while also possessing a large void fraction. This ideal structure would yield large capillary driving pressures while minimizing overall pressure losses within the wick as condensate flows quickly back towards the evaporator. Current generation heat pipes typically use sintered powder metal wicks in the  $1\text{--}2\text{ }\mu\text{m}$  pore size range with void volumes of only 50%. Unfortunately, small pore sizes and large void fractions are mutually exclusive properties for these systems (see Figs. 1 and 2). In the case of microfibrous wicks, however, smaller pore sizes and larger void fractions are available through the use of smaller diameter fibers (see Fig. 2). The net result anticipated using microfibrous wicks is greater heat transfer rates at lower thermal gradients.

### 3.1.1. Fabrication of near-net-shape structures

Preliminary efforts have been conducted to determine the

feasibility of using microfibrous materials in anticipated follow-on manufacturing steps. Fig. 4 shows a photograph of a complex wick structure that was formed by stacking ca. 1400 prepunched/precut preform sheets into a near-net shape article prior to sintering. The structure possesses a porous but closed end that was formed by stacking continuous disc-type preform sheets at that location while a simulated bored-hole through the center was fabricated by stacking annular prepunched sheets on top of the closed end. As this article was the first one ever attempted, the quality and processability of this procedure appears most promising at present, although a great deal of further work is obviously required. Additional efforts in our laboratory have also demonstrated that computer controlled laser-cutting operations are suitable for shaping either cellulose containing preform sheets or sheets which have been previously sintered.

The individual sheets used in the fabrication of the wick structure shown in Fig. 4 were fabricated from  $2\text{ }\mu\text{m}$  diameter nickel fibers and deliberately compressed to yield a 55% void structure with a pore size of approximately  $1.5\text{ }\mu\text{m}$ . As such, this wick was produced as an intended drop-in replacement for cylindrical wick structures currently found within capillary loop heat pipes supplied to the military, commercial and civilian space programs. It should be noted that the Auburn manufacturing approach has the potential to eliminate costly machining steps and expensive manufacturing throughput issues associated

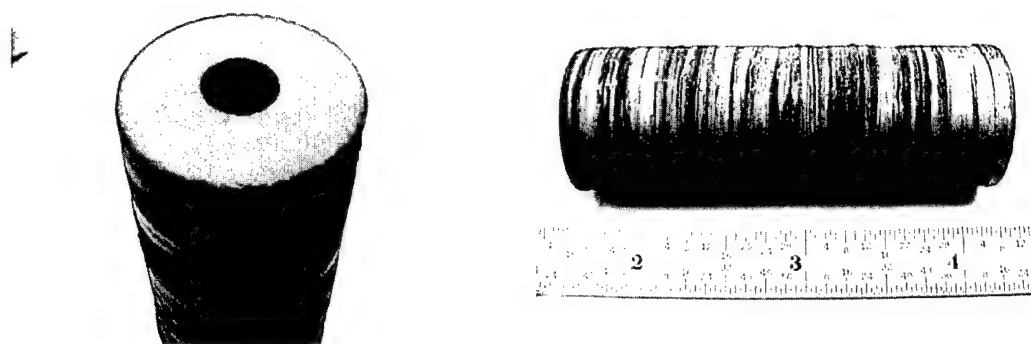


Fig. 4. Sintered fiber wick fabricated with 2  $\mu\text{m}$  by 3 mm nickel fibers for drop-in replacement capillary pumped loop primary wick; 55% porosity, 1.5  $\mu\text{m}$  effective pore size.

with the current process which starts from a block of sintered nickel powder.

The ability to independently control the physical properties of the microfibrous wick over a wide range of parameter space (e.g. pore size, void volume, thermal conductivity, permeability, etc.) provides a unique means to systematically vary these properties and subsequently observe their impact on intrawick transport behavior in the presence of system requirements and specific heat pipe applications.

Additional efforts at Auburn are currently focusing on the benefits of enhanced thermal dynamics within temperature-sensitive reactors and other unit operations. The latter activity has the potential to eliminate intrabed hot spots and improve overall catalytic selectivity obtained from various types of reactors including compact fuel processors and reformers.

### 3.2. Microfibrous entrapped catalysts and sorbents

Catalyst materials and catalyst structures similar to those shown in Fig. 3 have been studied in detail at Auburn University [5,6]. Despite intensive and successful optimization efforts there is still relatively little fundamental understanding within the body of the literature describing how these materials function in a complex reaction environment at the microscopic level. A generalized and predictive fundamental model is currently under development through a research grant with the National Science Foundation to ascertain when microfibrous entrapped-catalysts are best suited to accelerate the overall reaction process. For example, are these catalysts best suited for (a) reactions which are under heat transfer control or mass transfer control, (b) liquid, gaseous or three-phase reaction systems, (c) highly selective reactions including partial oxidations or fast partial hydrogenations? In order to address these issues, modeling and experimental activities are required to determine appropriate intrabed heat and mass transport properties, flow characteristics and pressure drop, solid thermal conductivities and convective heat transfer coefficients within the network. To the best of our knowledge, funda-

mental understanding of these transport phenomena does not currently exist for the subject materials. Armed with a predictive modeling capability, it would then be possible to match the physical attributes of these new catalysts with promising applications in specialty chemicals, food processing, and environmental and automotive catalysis, among others.

The fundamental technical challenges in sorption-based processes are closely related to those encountered in catalysis, with intraparticle mass transport and pressure drop being two major properties of interest. As with catalysis, an overall predictive model and understanding which includes surface kinetics in tandem with intrabed/intraparticle transport is required in order to design optimal structures taking fullest advantage of the microstructure.

### 3.3. Microfibrous entrapped electrocatalysts and faradaic materials

Due to the electrically conductive nature of the metallic fibers, microfibrous materials are ideal candidates for reducing intraparticle and inraelectrode resistances and transport limitations experienced in a number of industrial electrochemical cells as well as smaller devices including batteries and liquid double layer capacitors [15–17]. Since many of these applications require carbon-based electrodes or carbon-based electrocatalyst supports, small grains of these materials are entrapped within the interstitial voids of the fibers, similar to that shown in Fig. 2. Past efforts have used such microfibrous materials to prepare higher performing cathodes for: electrolysis applications (e.g. chloralkali, chlorate production, hydrogen production [18]), oxygen reduction (metal-air batteries ( $\text{OH}^-$ ) [19–24], hydrogen peroxide formation [24]), and collectors for highly dispersed faradaic materials which are coated directly onto the surfaces of the fibers to produce high surface area and low internal resistance Ni and Zn electrodes [25]. A key element of all these electrode systems is the ability to alter the loading and particle size of the active electrocatalyst/faradaic material independent of the

interparticle void volume and void size which are required to feed these sites with mass, ions, etc. In this way, the microfibrillar entrapped structure provides a unique means of balancing and meeting the steady-state heterogeneous kinetic and transport demands. To date, only one modeling effort has been undertaken in an attempt to understand the competitive kinetic and transport phenomena occurring within these promising new electrode materials [24]. Additional experimental and modeling efforts are required to more fully understand the full range of benefits, opportunities and niche applications that these materials may enjoy.

Previous measurements from oxygen electrodes in both half-cells and full Zn-air cells [19–24] have demonstrated the ability to meet or surpass the current-voltage polarization behavior of commercial electrodes at thicknesses that are only 20% those of commercial ‘button cell’ cathodes. Similar benefits have also been found for the two-electron reduction process, where favorable polarization behaviors and 95% current efficiencies to peroxide have been obtained [20,24]. In the case of these gas diffusion electrodes, high interparticle void volumes are required to permit transport of dissolved, and sparingly soluble, oxygen to the reactive site. This transport is in turn balanced against required solid/catalyst loading and surface area. Similar benefits and design strategies have also been successfully employed in our laboratories for activated/catalyzed cathodes evolving hydrogen at low overpotential as used in e.g. chloralkali and sodium chlorate production.

### 3.4. Microfibrillar metallic filters

Despite the large size of the global filtration market, relatively little is known regarding the transport mechanism of particulates and their accommodation/trapping from a superimposed liquid or gaseous flow within an asymmetric distribution of micronic interfiber voids. For low end filtration markets such as automobiles and trucks, market penetration and industrial research interest revolves around upfront media costs, regenerability studies, and analyses of life-cycle costs in comparison to disposables.

Sintered metal fiber filters currently see use in a number of commercial processes including polymer filtration [26,27], automotive airbags [28], and assorted HEPA filter applications. At present, only the higher value filtration applications use metallic filters due to the relatively high cost of the media. The Auburn manufacturing process discussed above possesses two enabling attributes that may offer a landmark opportunity to change the nature of the underlying cost-benefit relationship in selected filtration applications. The first attribute is the lower cost of media production derived from high-speed paper making processes as opposed to the much slower and less-robust air lay methods that are presently employed. It is estimated that the paper-based process may be capable of producing media at only one-third the current manufacturing cost. The second attribute involves the fact that wet-lay processing is

capable of robustly handling small fibers below 8  $\mu\text{m}$  in diameter, and can readily incorporate fibers of different diameters within the same sheet. This attribute means that asymmetric porosity can be achieved within a single layer permitting fine particle filtration and entrapment within a network of larger diameter voids formed by larger fibers. The combination of these two factors may permit finer particle filtration at lower overall pressure drop. In addition, asymmetry should permit higher dirt holding capacity at a given pressure drop and a correspondingly longer time on-stream prior to regeneration. The relatively low cost of the Auburn media also opens the possibility of using regenerable metallic filter elements for automobiles, trucks, and other low cost applications in place of the currently employed disposables. Given the fact that over 500 million oil filters are landfilled per year in the US as hazardous material [29], the latter opportunity could mediate a significant environmental and economic problem.

## 4. Microfibrillar porous media properties and permeability

### 4.1. Background

Filter materials are composed of fibrous materials and usually have a porosity greater than 80%. Usual design equations, such as the Ergun equation, for packed columns do not apply to beds with porosity greater than 50%. The reason these equations cannot be used for high porosity materials is that they do not include the form drag losses, which are the dominant contribution to the pressure drop through high porosity materials.

Bird et al. [30] derive the Ergun equation for pressure drop in a packed column. The friction factor for laminar flow inside a pipe is used to calculate the pressure drop due to friction losses. The porous media should be modeled as a collection of capillaries of length  $L_c$ :

$$\langle v \rangle = \frac{\Delta P R^2}{8\mu L_c} = \frac{\Delta P D^2}{32\mu L_c} = \frac{\Delta P R_H^2}{2\mu L_c} \quad (1)$$

where  $\Delta P$  is the pressure drop across fixed bed,  $\langle v \rangle$  the interstitial velocity,  $\mu$  the fluid viscosity,  $L_c$  the actual distance traveled by fluid flowing through fixed bed,  $R$  the capillary radius,  $D$  the capillary diameter, and  $R_H$  is the hydraulic radius. The hydraulic radius is defined as the cross-section available for flow divided by the wetted perimeter, and for a pipe it is one-fourth the diameter. The hydraulic radius for a packed bed of spherical particles is then

$$R_H = \frac{\epsilon}{a} = \frac{\epsilon}{a_v(1-\epsilon)} = \frac{D\epsilon}{6(1-\epsilon)} \quad (2)$$

The additional symbols are void fraction of packed bed ( $\epsilon$ ) and wetted surface per volume of bed ( $a$ ). The equivalent diameter of a submerged object, modeled as a sphere,

can be calculated from the volume to surface ratio of a sphere. The volume to surface ratio of an infinite fiber is one-fourth the fiber diameter, so the equivalent diameter of an infinite fiber is three-halves of its the diameter

$$D_{\text{sphere}} = \frac{6}{a_v}, \quad D_{\text{eq.fiber}} = \frac{3}{2}D_f, \quad D_{\text{eq}} = \phi D \quad (3)$$

The diameter of the non-spherical shape can be any arbitrary length, such as the width of the opening of a screen mesh used to size materials. The shape factor ( $\phi$ ) accounts for differences in the surface to volume ratio relative to that of a sphere. The shape factor for any arbitrary shape is calculated from the diameter and surface to volume ratio ( $a_v$ ) of that shape ( $\phi = 6/Da_v$ ).

Carman [31] first recognized that the interstitial velocity for a porous bed is greater than the face velocity divided by the porosity. Fluid flowing through a tortuous path has to travel a longer distance than just the length of the porous bed. For a tortuous path in a porous media, the time to travel distance  $L$  at the face velocity ( $v_0$ ) divided by the porosity has to be the same as the time to travel a tortuous path of length  $L_c$  at the interstitial velocity:

$$\frac{L\epsilon}{v_0} = \frac{L_c}{\langle v \rangle}, \quad \text{so} \quad \langle v \rangle = \frac{v_0 \tau}{\epsilon} \quad (4a)$$

The tortuosity of the porous media ( $\tau = L_c/L$ ) is estimated from a geometric model of a cubic cell with one sphere inside:  $\tau = 1 + (1 - \epsilon)/2$ .  $L$  is the actual bed thickness.

Fowler and Hertel [32] recognized that the orientation of the fibers in a fixed bed also effect the interstitial velocity. Taking the angle between the direction of flow inside the fixed bed and the perpendicular direction through the bed ( $x$ -axis) as theta ( $\theta$ ), then

$$dx = \cos(\theta) dr \quad \text{and} \quad v_x = \cos(\theta)v_r$$

The distance traveled by the fluid is greater than the thickness of the fixed bed by a factor of secant of  $\theta$ , and similarly for the velocity. The interstitial velocity is greater than that suggested by Carman by a factor of secant of  $\theta$ .

$$\langle v \rangle = \frac{v_0 \tau}{\epsilon \cos(\theta)} \quad (4b)$$

From this theory, the pressure drop due to viscous losses is proportional to one over the square of the cosine of  $\theta$ . Pressure drop data [33,34] taken on beds of fibers arranged parallel and perpendicular to the flow agree with this theory. The pressure drop for fibers arranged perpendicular to the flow is twice as large as that for those arranged parallel corresponding to  $\theta$  of  $45^\circ$ . Also, the pressure drop of beds of particles should be three-halves as large as that predicted by the Kozeny equation. A form of Kozenys' constant is given as Eq. (9), which is developed in the following section.

#### 4.2. Calculation of viscous pressure losses

The pressure drop due to friction losses in a porous media can be calculated by inserting the relationships for the interstitial velocity Eqs. (4a) and (4b) and the hydraulic radius Eq. (2) into Eq. (1). When this is done a form of the Blake–Kozeny equation is obtained

$$\frac{\Delta P}{L} = 72 \frac{\tau^2}{\cos^2(\theta)} \frac{\mu v_0}{g_c \epsilon^3} \frac{(1 - \epsilon)^2}{(\phi D)^2} \quad (5)$$

where  $g_c$  is the gravitational acceleration constant.

This equation only accounts for the friction losses in Stokes' law. The friction factor for laminar flow inside pipes is:  $f = 16/N_{Re}$ , where  $N_{Re}$  is the Reynold's number defined for packed beds as  $N_{Re} = \phi D \rho v_0 / \mu$ . The friction factor for a sphere in laminar flow is:  $f = 24/N_{Re}$ . The difference in the two friction factors is that there is no form drag for flow inside a pipe. Stokes' law for the force on a sphere in a laminar flow field is as follows [29]:

$$F = 6\pi\mu Rv = (4\pi\mu Rv)_{\text{Friction Losses}} + (2\pi\mu Rv)_{\text{Form Drag Losses}}$$

The pressure drop due to form drag losses can be calculated from the appropriate term in Stokes' law, and added to the Blake–Kozeny equation

$$F_D = 2\pi\mu Rv_\infty = \pi\mu D\langle v \rangle \quad (6)$$

Pressure loss due to form drag per length of tortuous bed is the product of the form drag force per particle ( $F_D$ ) multiplied by the number of particles per volume of bed. The number of particles per volume of bed is the volume fraction occupied by the particles divided by the volume of one particle:

$$\left(\frac{\Delta P}{L}\right)_D = 6 \frac{\tau^2}{\cos^2(\theta)} \frac{\mu v_0}{g_c \epsilon^3} \frac{(1 - \epsilon)}{(\phi D)^2} \quad (7)$$

The total pressure drop due to viscous losses is the sum of the friction losses and the form drag losses

$$\left(\frac{\Delta P}{L}\right)_{\text{Viscous Losses}} = 72 \frac{\mu v_0}{g_c \epsilon^3} \frac{\tau^2}{\cos^2(\theta)} \frac{(1 - \epsilon)}{(\phi D)^2} [1 + x_{FD}] \quad (8)$$

where  $x_{FD} = \epsilon^2/12(1 - \epsilon)$ . The Kozeny constant ( $k$ ) is a rearrangement of the pressure drop equation for viscous losses intended to eliminate effects of bed porosity and particle size and shape effects:

$$k \equiv \frac{\Delta P}{L} \frac{g_c}{\mu v_0} \frac{\epsilon^3}{(1 - \epsilon)^2} \left(\frac{\phi D}{6}\right)^2 = \frac{2\tau^2}{\cos^2(\theta)} [1 + x_{FD}] \quad (9)$$

#### 4.3. Calculation of inertial pressure losses

The inertial friction losses can be estimated by a friction factor correlation for turbulent flow inside a pipe

$$\frac{\Delta P}{(1/2)\rho\langle v \rangle^2} = \left(\frac{L_c}{R_H}\right) C_f$$

where  $\rho$  is the fluid density and  $C_f$  is the coefficient of

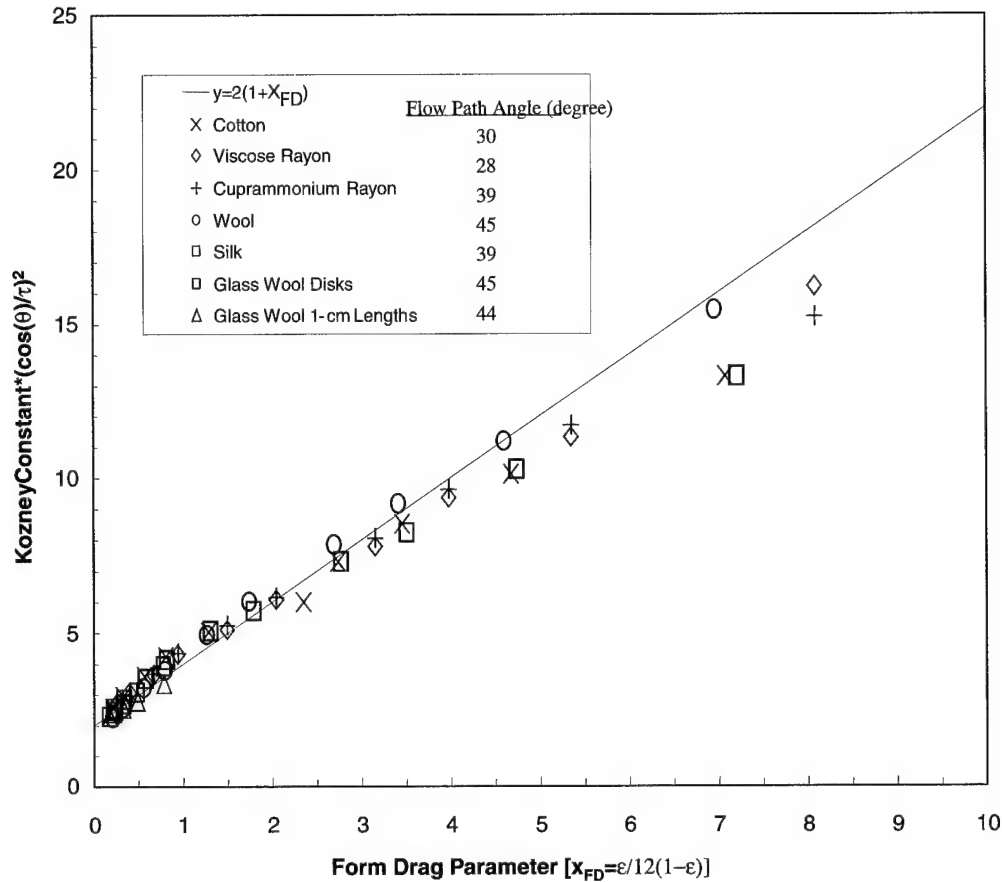


Fig. 5. Correlation of data of E. Lord with PMP equation.

friction for turbulent flow. Substituting for the hydraulic radius and the interstitial velocity results in the following expression, which is a form of the Burke–Plummer equation:

$$\left(\frac{\Delta P}{L}\right)_{\text{Inertial Friction Losses}} = 6 \frac{\tau^3}{\cos^3(\theta)} C_f \frac{\rho v_0^2}{2g_c \epsilon^3} \frac{(1-\epsilon)}{\phi D} \quad (10)$$

The inertial form drag losses can be estimated from the inertial form drag losses of a sphere in turbulent flow

$$F_D = \frac{\pi D_{eq}^2}{4} \frac{\rho \langle v \rangle^2}{2g_c} C_{FD} \quad \text{and}$$

$$\left(\frac{\Delta P}{L}\right)_{\text{Inertial Form Drag Losses}} = \frac{6}{4} \frac{\tau^3}{\cos^3(\theta)} C_{FD} \frac{\rho v_0^2}{2g_c \epsilon^2} \frac{(1-\epsilon)}{\phi D} \quad (11)$$

where  $C_{FD}$  is the coefficient of form drag of sphere in turbulent flow. The total inertial pressure losses are then given by the following equation:

$$\left(\frac{\Delta P}{L}\right)_{\text{Inertial Losses}} = 6 \frac{\tau^3}{\cos^3(\theta)} \frac{\rho v_0^2}{2g_c \epsilon^3} \frac{(1-\epsilon)}{\phi D} \left[ C_f + \frac{C_{FD}}{4} \epsilon \right] \quad (12)$$

The coefficient of form drag is the coefficient of drag minus the coefficient of friction ( $C_{FD} = C_D - C_f$ ).

#### 4.4. Calculation of pressure drop for mixtures of various shapes

Materials composed of sintered metal fibers containing particles are a new type of material useful for application in catalysis and adsorption among many other applications. These type materials have enhanced heat and mass transfer, and active material utilization compared to powder based materials. A reliable method for predicting pressure drop through mixtures of metal fibers and particulates should prove very useful for design of processes using these new sintered fiber based composites.

Formulas for the total particle surface area ( $S_p$ ) and total volume of particles ( $V_p$ ) are required to determine the equivalent diameter of the solids in the porous media for the most general form of the pressure drop equation

$$\frac{1}{D_{eq}} = \frac{S_p}{6V_p} = \sum \frac{x_i}{\phi_i D_i} \quad (13)$$

In these expressions  $x_i$  is the volume fraction of



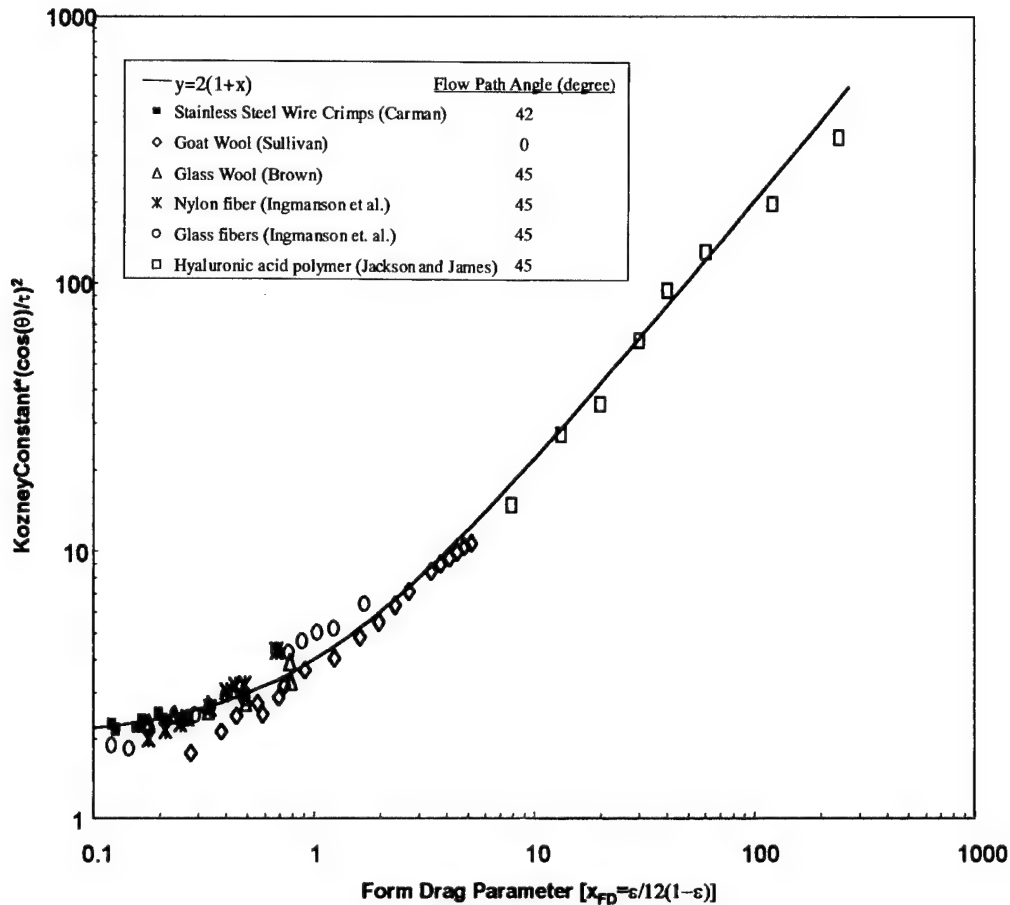


Fig. 6. Correlation of data from Jackson and James with PMP equation.

component  $i$ . The hydraulic radius is then as follows:

$$R_H = \frac{\epsilon}{6(1-\epsilon) \sum \frac{x_i}{\phi_i D_i}} \quad (14)$$

The total pressure drop for a mixture of solid particles and fibers of any shape is given by the following equation:

$$\begin{aligned} \frac{\Delta P}{L} = & 72 \frac{\tau^2}{\cos^2(\theta)} \frac{\mu v_0}{g_c} \frac{(1-\epsilon)^2}{\epsilon^3} \\ & \times \left[ \left( \sum \frac{x_i}{\phi_i D_i} \right)^2 + x_{FD} \sum \frac{x_i}{(\phi_i D_i)^2} \right] \\ & + 6 \frac{\tau^3}{\cos^3(\theta)} \frac{\rho v_0^2}{2g_c} \frac{(1-\epsilon)}{\epsilon^3} \sum \frac{x_i}{\phi_i D_i} \left[ C_f + \frac{C_{FD}}{4} \epsilon \right]. \end{aligned} \quad (15)$$

#### 4.5. Comparison to literature data

Lord [35] measured permeability of textile fibers and presented his data in the form of Kozeny constants. A comparison of the porous media permeability (PMP) equation with Lord's data is shown as Fig. 5. The data is

presented so that the theoretical equation has an intercept of two with unit slope. The parameter on the horizontal axis is the form drag parameter. The form drag parameter indicates the ratio of form drag losses to friction losses through the porous media. The flow path angle is an adjustable parameter in the PMP equation and is given in the legend. Excellent agreement of the model with the data is indicated by this figure. Jackson and James [36] tabulated Darcy permeabilities for 15 sets of data and also measured a set of permeability data that extended the range of solid fraction covered in the measurements down to  $3.45 \times 10^{-4}$  or a form drag parameter of 240. Six sets of data from Jackson and James' tabulation are presented in Fig. 6 covering three and one-half decades of the form drag parameter. The data are plotted in a log-log format since a very large range of the form drag parameter is covered by these data sets.

#### 4.6. Parameter values corresponding to the Ergun equation

Values of flow path angle and friction factor for inertial losses can be estimated by equating the Ergun equation to the one developed here. Taking the drag coefficient for a



sphere in turbulent flow to be 0.6 and a porosity of 45%, the coefficients in the modified Ergun equation, 180 for the viscous loss term and 1.8 for the inertial loss term, correspond to a flow path angle of 35.2°, and a coefficient of friction of 0.203. The viscous loss terms are most important for media composed of micron size fibers since the particle Reynolds' number is usually less than one, so these values should be useful for estimating pressure drops in microfibrinous packed beds of entrapped particles.

## 5. Conclusions and final comments

Microfibrinous materials and structures carrying small entrapped particles of catalyst, sorbent, electrocatalyst, etc. provide a novel means for matching the surface kinetics of the reaction to the required transport of heat and mass to the reaction site. This essential balancing act allows the engineer to design processes and reactors with many beneficial properties that include among others: high volumetric processing rates, improved selectivities, greater margins of safety, lower pressure drops, better interphase contacting, and higher overall thermodynamic energy efficiencies. These benefits are available as a result of the unique and advantageous structure-property relationships that microfibrinous materials possess compared to traditional contacting regimes and associated heterogeneous materials. Various chemical processing opportunities and application areas have been highlighted in this brief paper and the nature of these advantages related to specific structure-property attributes of microfibrinous materials and the corresponding demands of chemical processing reaction under consideration. Future activities in the use of microfibrinous carriers are anticipated to increase as we continue to seek increased energy efficiency, reduced processing costs, and improvements in both environmental and safety issues.

## References

- [1] Tatarchuk BJ, Rose MF, Krishnagopalan A, Zabasajja JN, Kohler D. Mixed fiber composite structures high surface area high conductivity mixtures. US Patent 5,304,330, April 19, 1994.
- [2] Tatarchuk BJ. Method of optimizing composite preparation for electrical properties: maximum capacitance electrodes. US Patent 5,102,745, April 7, 1992.
- [3] Tatarchuk BJ, Rose MF, Krishnagopalan A, Zabasajja JN, Kohler D. Mixed fiber composite structures. US Patent 5,096,663, March 17, 1992.
- [4] Tatarchuk BJ, Rose MF, Krishnagopalan A, Zabasajja JN, Kohler D. Preparation of mixed fiber composite structures. US Patent 5,080,963, January 14, 1992.
- [5] Marrión CJ, Cahela DR, Ahn S, Tatarchuk BJ. Composite fiber structures for catalysts and electrodes. *J Power Sources* 1994;47:297–302.
- [6] Meffert MW. Preparation and characterization of sintered metal microfiber-based composite materials for heterogeneous catalyst applications, PhD dissertation, College of Engineering, Auburn University, Auburn, AL, 1998.
- [7] Faghri A. Heat pipe science and technology. Washington, DC: Taylor & Francis, 1995.
- [8] Chi SW. Heat pipe theory and practice. Washington, DC: Hemisphere, 1976.
- [9] Garner SD. Heat pipes for electronics cooling applications. *Electron Cooling* 2(3).
- [10] Adkins DR, Moss T. Measuring flow properties of wicks for heat pipe solar receivers. *Solar Engr ASME Book No. H00581-90* 1990:103–8.
- [11] Acton Reay DA. Correlating equations for the properties of metal felt wicks. *Advances in heat pipe technology, Proceedings of the IV International Heat Pipe Conference* New York: Pergamon Press, 1982. p. 279–88.
- [12] Dunn PD, Reay DA. Heat pipes. 4th ed. New York: Pergamon Press, 1994.
- [13] Tien CL. Fluid mechanics of heat pipes. *J Fluid Mech* 1975;7:167–85.
- [14] Kohler D, Zabasajja J, Krishnagopalan A, Tatarchuk BJ. Carbon-metal composite materials from fiber precursors I: preparation of carbon-stainless steel composite electrodes. *J Electrochem Soc* 1990;137(1):136–41.
- [15] Cahela DR. Impedance modeling of nickel fiber/carbon fiber composite electrodes for electromechanical capacitors. *IEEE Ind Electron Soc IECON* 97 1997;3:1080–5.
- [16] Kohler D, Zabasajja J, Rose F, Tatarchuk BJ. Carbon-metal composite electrodes from fiber precursors: II. Electrochemical characterization of stainless-carbon structures. *J Electrochem Soc* 1990;137(6):1750–7.
- [17] Cahela DR. Zinc-air battery/double layer capacitor hybrid for portable communications pulse power supply. *J Power Sources* 1998.
- [18] Tatarchuk et al. Electrochemical generation of sodium chlorate. Super TAPPI Meeting, Nashville, TN, October 1997.
- [19] Poole BJ. Development of composite oxygen electrode material for use in Zn-air batteries and Zn-air/ ultracapacitor hybrids for pulse power applications, MS thesis, College of Engineering, Auburn University, Auburn, AL, 1999.
- [20] Ahn S, Tatarchuk BJ. Fibrous metal-carbon composite structures as gas diffusion electrodes for use in alkaline electrolyte. *J Appl Electrochem* 1997;27:9–17.
- [21] Ahn S, Tatarchuk BJ. 1 Air electrode: identification of intraelectrode rate phenomena via ac impedance. *J Electrochem Soc* 1995; 142(12):4169–75.
- [22] Smith RF, Ahn S, Putt R. Oxygen electrodes based on composite microfibrinous materials. *J Power Sources* 1996;37:1–4.
- [23] Poole B, Smith RF, Putt R. Composite-microfibrinous cathodes for metal-air batteries. *J Power Sources. Proceedings of the 38th Power Sources Symposium*, 1998.
- [24] Smith RF. Metal fiber-carbon electrodes for oxygen reduction, PhD dissertation, College of Engineering, Auburn University, Auburn, AL, 1998.
- [25] Johnson BA, Ferro RE, Swain GM, Tatarchuk BJ. High surface area low weight composite nickel fiber electrodes. *J Power Sources* 1994;47:251–9.
- [26] Morland C, Williams B. Selecting polymer filtration media. *Fibr Producer* 1980;8:32–9.
- [27] Shoemaker W. Critical needs of filter media part II. *Filtration News* 1995;23(2):49–55.
- [28] O'Neill B. Turning off an air bag almost never makes sense, 18. Arlington, VA: Insurance Institute for Highway Safety, 1997.
- [29] National Oil Recyclers Association ([www.noraoil.com/filters.html](http://www.noraoil.com/filters.html)).
- [30] Bird RB, Stewart WE, Lightfoot EN. Transport phenomena, 59. New York: Wiley, 1960. p. 196–200.
- [31] Carman PC. Flow of gases through porous media. New York: Academic Press, 1956. p. 12.
- [32] Fowler JL, Hertel RL. Flow of a gas through porous media. *J Appl Phys* 1940;11:496–502.

- [33] Sullivan RR, Hertel RL. The flow of air through porous media. *J Appl Phys* 1940;11:761–5.
- [34] Sullivan RR. Further study of the flow of air through porous media. *J Appl Phys* 1941;12:503–8.
- [35] Lord E. Air flow through plugs of textile fibers, part I-general flow relations. *J Text Inst* 1955;46:T191.
- [36] Jackson GW, James DF. The permeability of fibrous porous media. *Can J Chem Engng* 1986;64:364–74.

# Preparation of polycrystalline YAG/alumina composite fibers and YAG fiber by sol–gel method

A. Towata<sup>a,\*</sup>, H.J. Hwang<sup>a</sup>, M. Yasuoka<sup>a</sup>, M. Sando<sup>a</sup>, K. Niihara<sup>b</sup>

<sup>a</sup>National Industrial Research Institute of Nagoya, 462-8510, 1-1 Hirate-cho, Kita-ku, Nagoya, Japan

<sup>b</sup>The Institute of Scientific and Industrial Research, Osaka University, 567-0047, 8-1 Mihogaoka, Ibaraki, Osaka, Japan

Received 26 May 2000; revised 28 November 2000; accepted 28 November 2000

## Abstract

Polycrystalline yttrium–aluminum garnet,  $\text{Y}_3\text{Al}_5\text{O}_{12}$  (YAG) fiber and  $\alpha$ -alumina and YAG matrix composite fiber were prepared by the sol–gel method.  $\alpha$ -Alumina and YAG matrix composite fiber with fine and homogeneous microstructure could be successfully fabricated by interpenetrating YAG in alumina matrix and adding  $\alpha$ -alumina of seed particles to fibers. Effect of  $\alpha$ -alumina seed particles and YAG on crystallization and microstructure of composite fiber were discussed. The size of alumina matrix of the composite fibers heated at 1600°C for 4 h was below 2  $\mu\text{m}$ . The tensile of strength alumina fiber heat-treated at 1500°C was 0.2 GPa, while that of the composite fiber was 1.1 GPa. © 2001 Elsevier Science Ltd. All rights reserved.

**Keywords:** A. Ceramic fibre; Alumina; E. Powder processing; D. Thermal analysis

## 1. Introduction

The ceramic matrix composite has an intended use at high temperatures in several applications including advanced aircraft and gas turbine engine. Fibers used in these continuous fiber-reinforced ceramic composites are required to exhibit good thermal and mechanical properties in high temperature oxidizing environments. Oxide fibers have the potential to maintain durability and mechanical properties in oxidizing environments. However, the applications of commercially available oxide fibers are limited by the degradation of fracture strength and creep properties above 1200°C. For example,  $\text{Al}_2\text{O}_3$  fibers derived by sol–gel process, which have been commercially used for a number of years, contained a mixture of alumina spinel and amorphous silica, resulting in poor creep resistance [1]. Thus, recent research work has been focused on developing fiber materials with inherently better high-temperature properties.

The creep resistance of polycrystalline ceramics can be improved by the addition of hard second-phase particles [2–3]. The second-phase particles can affect the deformation rate of a polycrystal in two ways [4]. One is by the macroscopic modification of the continuum deformation mechanics, and the other is the microscopic change of the

interface-related deformation characteristics such as suppressing interface reactions (vacancy or interstitial creation/annihilation) or hindering grain boundary sliding. In addition, the second-phase particles may affect fiber grain growth, microstructure, and therefore creep rate by grain boundary pinning.

YAG (yttrium–aluminum garnet,  $\text{Y}_3\text{Al}_5\text{O}_{12}$ ) is a prime candidate for hardening  $\text{Al}_2\text{O}_3$  because of its excellent creep resistance [5,6]. Parthasarathy et al. [7] investigated the creep behavior of hot-pressed polycrystalline YAG with the grain size of 3  $\mu\text{m}$  and found that it indicated a lower creep rate than that calculated for polycrystalline  $\text{Al}_2\text{O}_3$  with a similar grain size. Directionally solidified  $\text{Al}_2\text{O}_3$ – $\text{Y}_3\text{Al}_5\text{O}_{12}$  eutectic composites have also been shown to exhibit better high-temperature properties.

This paper describes new fabrication process of  $\text{Al}_2\text{O}_3$  and YAG composite fiber and YAG fiber. Transformation behavior and microstructure development of  $\text{Al}_2\text{O}_3$  based composite fiber were studied. The effect of  $\alpha$ - $\text{Al}_2\text{O}_3$  and YAG seed particles and mechanical properties of these fibers were also examined.

## 2. Experimental procedure

YAG and alumina composite fiber and YAG fiber were prepared. The composite fibers had 0.5 and 40 vol% yttrium content. The aluminum isopropoxide (Nakarai Chemical

\* Corresponding author. Tel.: +81-52-911-2111; fax: +81-52-916-2802.  
E-mail address: towata@nirin.go.jp (A. Towata).

Co., Japan) and yttrium isopropoxide (High Purity Chemical Co., Japan) were dissolved in isopropyl alcohol solution with ethyl 3-oxobutanate by refluxing under air atmosphere at 60°C for 20 h according to the procedure described by Yogo et al. [8]. In the case of fiber with seed particles,  $\alpha$ -alumina (average particle size: 0.2  $\mu$ m, Taimei Chemical Co., Japan) was added to the solution. The solution was hydrolyzed by adding hydrochloric acid and water, and was condensed by refluxing at 60°C for one day. In order to control the viscosity of the precursor, the isopropyl alcohol involved in the solution was concentrated by evaporation. Viscosity of the solution increased gradually.

The solution was then spun into the precursor fiber by inserting a wire into the viscous solution and pulling it upward quickly by hand under 45% relative humidity. The resulting precursor fibers were aged and dried at room temperature for one day and with 30–60% relative humidity. Then they were put in an alumina boat and heat-treated in air at various temperatures. Heat treatment was carried out at temperatures ranging from 1200 to 1500°C with a heating rate of 10°C min<sup>-1</sup>. The holding time at the desired temperature was fixed at 4 h. After designed heat treatment the fibers were cooled in the furnace.

The crystalline phase of the composite fiber was identified by X-ray powder diffraction. The viscosity was measured by a cone viscometer.

The crystalline phase of the composite fiber was identified by X-ray powder diffraction (RU-200B, Rigaku Co. Ltd, Japan). The crystallization temperature of the fiber was investigated by DSC (Shikuu-rikou, Japan). The fiber morphology and microstructure were observed by a scanning electron microscope (SEM, JSM-6320FK, JEOL, Japan). The ratio of Y/Al of the fiber was measured by inductively coupled plasma-emission spectrometry (ICP-ES, ICAP-1000S, NIPPON Jarrell-Ash, Japan). The tensile strength of single fibers was measured using an universal mechanical testing machine (RTC-1210A, A & D Co.). Fibers were mounted with acrylic adhesive on cardboard tabs for aligning and gripping. A 5-mm gage length and a crosshead speed of 2 mm min<sup>-1</sup> were used in all tests. Owing to the non-circular cross-section of the fibers, the fracture load was converted to tensile strength by measuring the cross-sectional area of the fiber with an optical microscope.

### 3. Results and discussion

Fig. 1 shows the viscosity of polymeric precursor solution as a function of rotating speed. The precursor solution is sufficiently spinnable. The viscosity was 40 Pa s<sup>-1</sup> at 2 rpm and decreased with increasing rotating speed.

Fig. 2 shows DSC curves of the composite fibers. The transformation temperature from  $\theta$ - to  $\alpha$ -phase alumina in the case of the composite fiber with seed particles of 1.5 wt% was 1040°C. As the YAG content increased, the

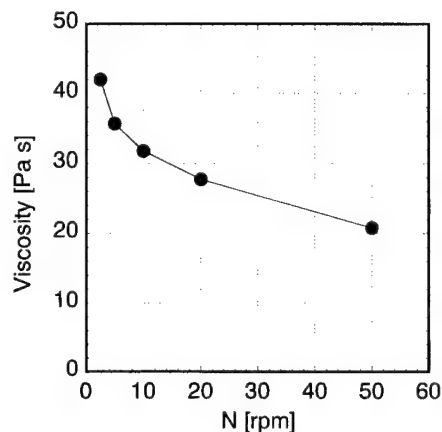


Fig. 1. Change of viscosity for precursor of solution as a function of rotating speed.

transformation temperature shifted to a higher temperature. In the case of 9.7 vol% YAG content, the transformation temperature was 1170°C. These results indicate that yttrium addition plays an important role on the crystallization behavior of  $\text{Al}_2\text{O}_3$  fibers. The transformation to  $\alpha$ -phase of the composite fiber shifted to higher temperature than for  $\text{Al}_2\text{O}_3$  fiber. This tendency was also found in the unseeded fibers heat-treated at the same temperature. It can, therefore, be inferred that yttrium inhibits the  $\alpha$ - $\text{Al}_2\text{O}_3$  crystallization.

It was probable that another peak of in this figure showed some yttrium oxide formation.

Crystallization products with  $\alpha$ - $\text{Al}_2\text{O}_3$ , YAP (yttrium–aluminum perovskite,  $\text{YAlO}_3$ ) and YAG composition were observed to follow multi-step transformations to the fully crystalline state. Crystallization of YAG appears to involve the formation of hexagonal and orthorhombic YAP as an intermediate as shown in the temperature vs. time diagram determined using X-ray diffraction analysis (Fig. 3). Crystallization of YAG depends on the yttrium content and

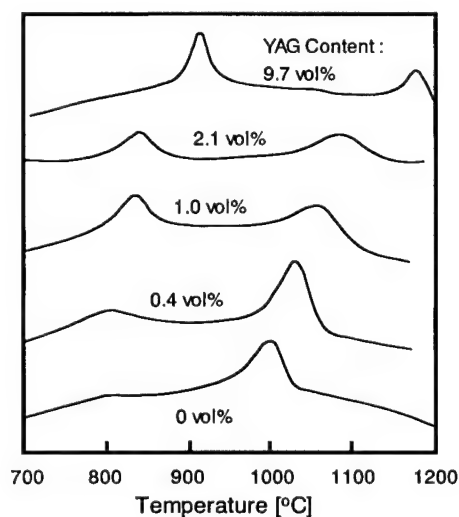


Fig. 2. DSC of the seeded (1.5 wt%) composite fibers with 0–9.7 vol% YAG. Samples were heated at the speed of 10°C min<sup>-1</sup> in air.

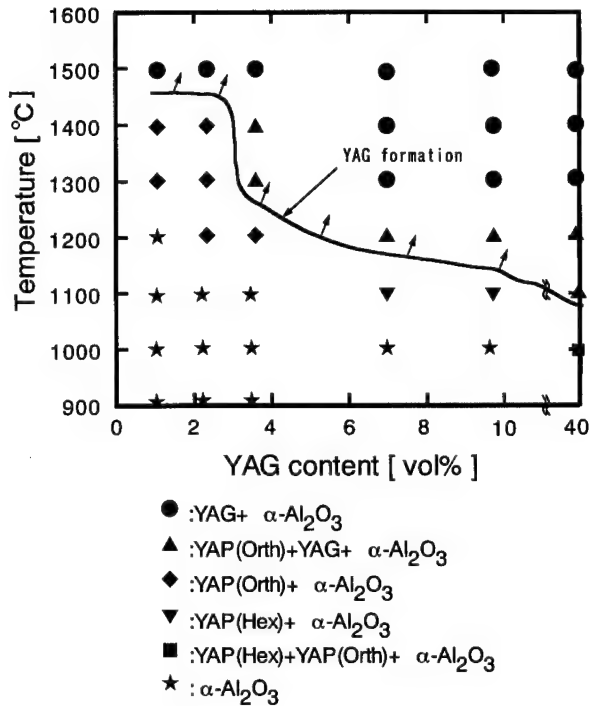


Fig. 3. Crystallization behavior of the composite fibers with different YAG content.

heat-treatment temperature. In the case of 1.0 and 2.1 vol% of YAG, orthorhombic YAP appeared at 1300°C. With the increasing temperature YAP completely transformed to YAG at 1500°C, and the composite fiber consisted of  $\alpha$ - $\text{Al}_2\text{O}_3$  and YAG at 1500°C. When the YAG content was increased up to 2.4 vol%, the crystallization of YAG shifted to a lower temperature (1300°C). However, the same

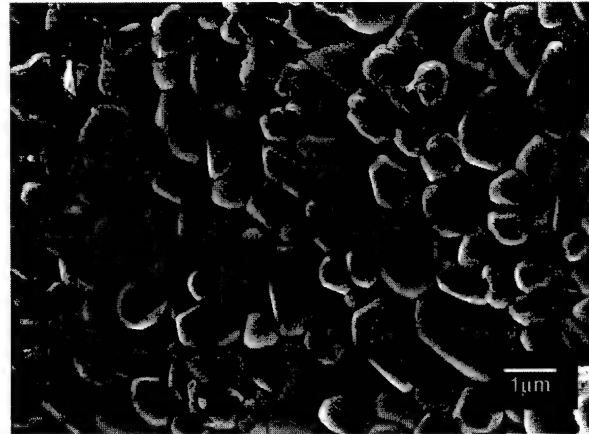


Fig. 5. SEM photograph of alumina/YAG composite fiber (YAG: 40 vol%) heated at 1600°C.

temperature (1500°C) was required to obtain the composite fiber with  $\alpha$ - $\text{Al}_2\text{O}_3$  and YAG.

The composite fiber with yttrium more than 7 vol% showed a different transformation behavior. Hexagonal YAP, which was not observed in 1.0, 2.1 and 3.5 vol% of YAG, formed at 1100°C and it disappeared above 1200°C. Crystallization of YAG was significantly accelerated with an increasing yttrium content. For example, heat treatment at 1300°C of the precursor fiber with 9.7 vol% of YAG resulted in  $\alpha$ - $\text{Al}_2\text{O}_3$  composite fiber which dispersed only with YAG. In the case of 40 vol% of YAG, YAP appeared at 1000°C.

Fig. 4 shows the X-ray diffraction patterns of alumina/40 vol% YAG composite fiber heat-treated at 1000, 1100, 1200, 1300, 1400 and 1500°C. It seemed that yttrium reacted with alumina as the heat-treatment temperature

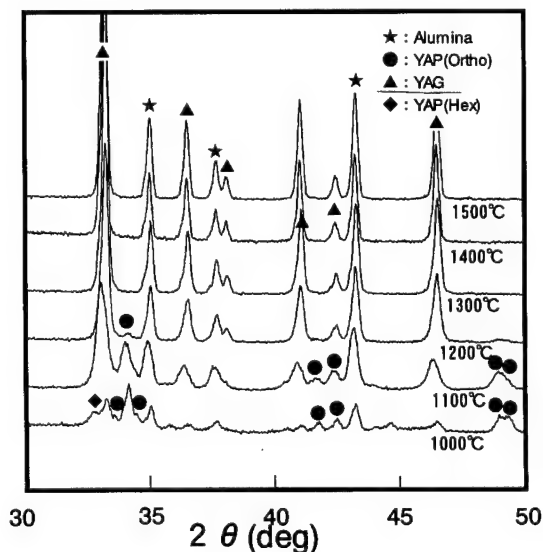


Fig. 4. X-ray diffraction pattern of  $\text{Al}_2\text{O}_3$ /YAG composite fibers (YAG: 40 vol%) heat-treated at various temperature for 4 h.

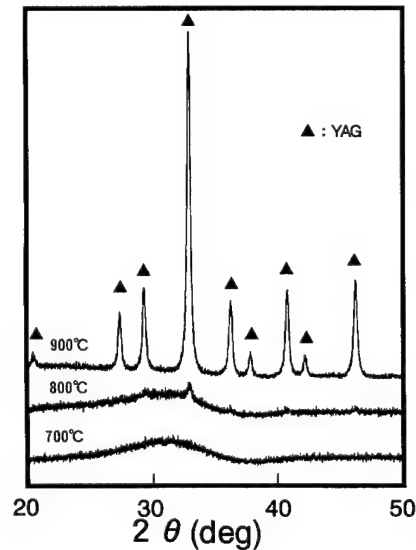


Fig. 6. X-ray diffraction pattern of YAG fibers heat-treated at various temperature for 4 h.

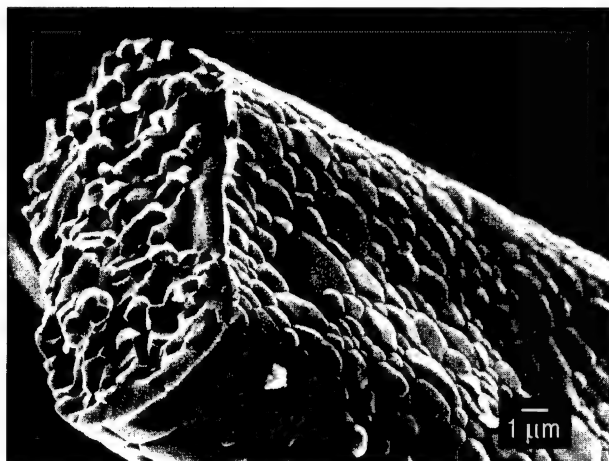


Fig. 7. SEM photograph of YAG fiber heated at 1600°C.

increased, to produce an hexagonal YAP above 1000°C. At the same time, YAG appeared at 1100°C. With increasing heat-treatment temperature, the relative intensity of YAG increased, and YAP completely disappeared at 1300°C. The composite fiber consisted of  $\alpha$ -alumina and YAG at 1300°C.

Fig. 5 shows the SEM photograph for thermally etched surface of the alumina/40 vol% YAG composite fiber heat-treated at 1600°C for 4 h. The composite fiber consisted with the 1  $\mu$ m, alumina and YAG grains were intertwined.

Fig. 6 shows the X-ray diffraction patterns of YAG fiber heat-treated at 700, 800 and 900°C. An amorphous YAG fiber was still observed at 700°C. The crystallization of YAG started at 800°C, and well-crystallized YAG fiber was obtained at as low as 900°C. A SEM micrograph of the seeded YAG fiber heated at 1600°C is shown in Fig. 7. The grain size was 1–3  $\mu$ m.

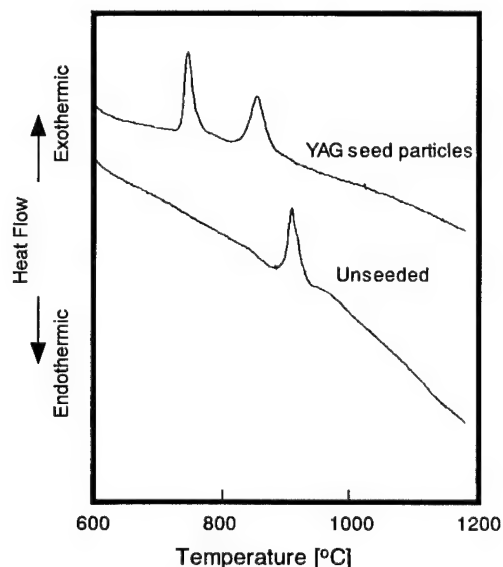


Fig. 8. DSC curve of YAG fibers heated at the speed of 10°C min<sup>-1</sup> in air.

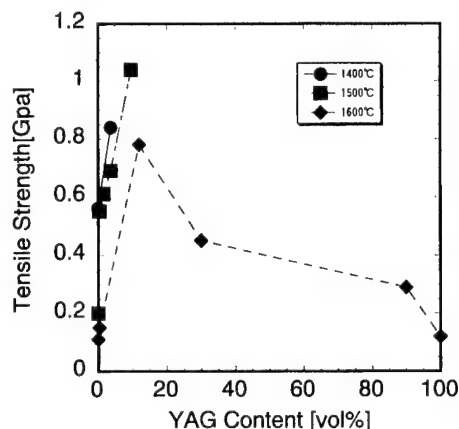


Fig. 9. Tensile strength of fibers measured at room temperature.

Fig. 8 shows DSC curves of the YAG fibers including with and without YAG seed particles. The seeded fiber had two peaks between 700 and 900°C, whereas the unseeded fiber had only one. The first peak of the seeded fiber at 740°C seems to result from the crystallization of hexagonal YAP. The second peak at 850°C is due to the transformation from hexagonal YAP phase to YAG phase [9]. The peak of the seeded fiber appeared at lower temperature than the unseeded YAG fiber.

Fig. 9 shows the tensile strength measured at room temperature of the alumina fiber and composite fiber fired at 1400, 1500 and 1600°C for 4 h. The tensile strength of alumina fiber is 0.2 GPa, while that of composite fiber is 1.1 GPa. It can, therefore, be concluded that composite fiber is stronger than alumina fiber. This result may be due to the difference of alumina size. The grain sizes of alumina and the composite fiber are 3–5, and 1  $\mu$ m, respectively. The tensile strength of the YAG-rich composite fiber and YAG are also shown in Fig. 9. YAG fiber was 0.1 GPa at 1600°C. The strength of composite fiber decreased with increasing YAG content, and may also be because of the change in the alumina grain size.

#### 4. Conclusions

Polycrystalline alumina, alumina/YAG composite fibers and YAG fiber were successfully fabricated by sol-gel process containing  $\alpha$ -alumina or YAG seed particles. The  $\alpha$ -alumina seed particle accelerated the phase transformation from  $\theta$ - to  $\alpha$ -phase. The YAG seed particle affected multi-step of the yttrium and aluminum oxide. The composite fibers with YAG (YAG = 40 vol%) consisted of alumina and YAG grains with size of 1–2  $\mu$ m at 1600°C. The tensile strength of alumina fiber heat-treated at 1500°C was 0.2 GPa, and the strength was significantly improved in the composite fiber with 10 vol% of YAG.

## References

- [1] Cooke TF. Inorganic fibers — a literatures review. *J Am Ceram Soc* 1991;74(12):2959–78.
- [2] Niihara K. New design concept of structural ceramics—ceramic nanocomposites. *J Ceram Soc Jpn* 1991;99(10):974–82.
- [3] Ohji T, Hirano T, Nakahira A, Niihara K. Particle/matrix interface and its role in creep inhibition in alumina/silicon carbide nanocomposites. *J Am Ceram Soc* 1996;79(1):33–45.
- [4] Stearns LC, Harmer MP. Particle-inhibited grain growth in  $\text{Al}_2\text{O}_3$ –SiC: I. Experimental results. *J Am Ceram Soc* 1996;79(12):3013–9.
- [5] Liu Y, Zhang ZF, King B, Halloran J, Laine RM. Synthesis of yttrium garnet from yttrium and aluminum isobutyrate precursors. *J Am Ceram Soc* 1996;79(2):385–94.
- [6] Corman GS. High temperature creep of some single crystal oxides. *Ceram Engng Sci Proc* 1991;12(9–10):1945–66.
- [7] Parthasarathy TA, Mah T, Keller K. High-temperature deformation behavior of polycrystalline yttrium aluminum garnet (YAG). *Ceram Engng Sci Proc* 1991;12(9–10):1767–73.
- [8] Yogo T, Iwahara H. Synthesis of polycrystalline alumina fibre with aluminum chelate precursor. *J Mater Sci* 1991;26:5292–6.
- [9] Yamaguchi O, Takeoka K, Hirota K, Takano H, Hayashida A. Formation of alkoxy-derived yttrium aluminum oxides. *J Mater Sci* 1992;27:1261–4.



# Affordable processing of thick section and integral multi-functional composites

U.K. Vaidya\*, A. Abraham, S. Bhide

Department of Mechanical Engineering and Applied Mechanics (MEAM), Composites Research Laboratory, North Dakota State University (NDSU), Fargo, ND 58105 USA

Received 29 May 2000; revised 20 December 2000; accepted 22 December 2000

## Abstract

The use of multi-functional integral armor is of current interest in armored vehicles and military carriers. In the present study, thick-section laminated composites and multi-layered integrated composites have been processed/manufactured with the aim of providing multi-functionality including easy reparability, quick deployment, enhanced ballistic damage and fire protection, as well as lightweight advantages. The design of an integral armor utilizes a combination of thick-section structural composite, ceramic tiles, resilient rubber, fire retardant laminate liner and a composite durability cover. Processing techniques such as automated fiber placement and/or autoclave molding are traditionally used to process dissimilar multi-layered structure, but prove to be expensive.

This work focuses on emerging cost-effective liquid molding processes such as vacuum assisted resin transfer/infusion molding (VARTM) for the production of thick-section and integral armor parts (up to 50 mm thick). While thick-section composites have applications in a variety of structures including armored vehicles, marine bodies, civil infrastructure, etc. in the present work they refer to the structural laminate within the integral armor. The processing steps of thick-section composite panels and integral armor have been presented. The integrity of the interfaces has been evaluated through scanning electron microscopy (SEM). Representative results on static and dynamic response (high strain rate, HSR and ballistic impact) of the VARTM processed thick-section composite panels are presented. Wherever applicable, comparisons are made to conventional closed-mold resin transfer molding (CMRTM). Process sensing by way of flow and cure monitoring of the resin in the fiber perform has been conducted using embedded direct current (DC)-based sensors in the thick-section preform and integral armor interfaces. The feasibility of cost-effective VARTM for producing thick-section composites and integral armor has been demonstrated. © 2001 Elsevier Science Ltd. All rights reserved.

**Keywords:** Scanning electron microscopy; E. Resin transfer moulding (RTM)

## 1. Introduction

Light weight ground combat vehicles, marine bodies and aircraft structures using advanced fabric/textile composites and/or layered material architecture are of importance because they offer improved deployability, survivability, and agility [1,2]. Components such as armored tank hull, crew capsule, rear engine bulkhead, ramp and sidewalls, etc. utilize composites with various types of fabric architectures and resin compositions (for example, S-2 glass, vinyl ester, epoxy and phenolic resins) as monocoque or sandwich hybrid constructions [1–5]. In recent years, affordability is of high interest in manufacturing composite and integrated structures. Promising techniques such as closed-mold resin transfer molding (CMRTM) and vacuum assisted resin transfer/infusion molding (VARTM) have emerged as alter-

native techniques in comparison to autoclave and/or automated fiber placement (AFP). The application of these processing techniques to thick-section and multi-layered structure lends itself to significant potential cost-savings.

### 1.1. Integral armor

A composite integral armor is designed to provide multi-interface, multi-functional capability, easy reparability, quick deployment, enhanced ballistic damage protection, and lightweight advantages. The design of the integral armor adopted in the present work is schematically illustrated in Fig. 1. The components of the armor are: (a) *Durability cover* for outer shell comprising S2-glass reinforcement (approximately 4 mm thick). (b) *Ceramic tiles* for ballistic protection of approximately 17 mm thickness. (c) *Ethylene propylene diene monomer (EPDM) rubber* for multi-hit damage tolerance (approximately 2–3 mm thick). (d) *Thick section composite structural*

\* Corresponding author. Tel.: +1-701-231-6493; fax: +1-701-231-8913.

E-mail address: uday\_vaidya@ndsu.nodak.edu (U.K. Vaidya).

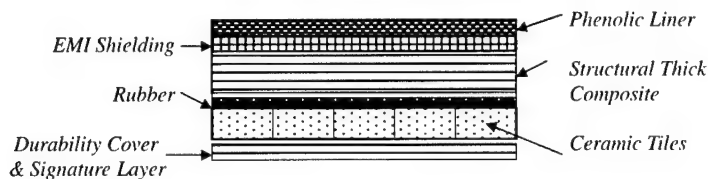


Fig. 1. Schematic of integral armor.

laminate which is the primary structural load bearing component, 20–25 mm thick comprising S2-glass reinforcement with vinyl ester or epoxy resin matrix. (e) *Electromagnetic interference (EMI) mesh* for electromagnetic shielding. (f) A *Phenolic laminate liner* for flammability protection (S2-glass/phenolic reinforcement)

In the current study, VARTM and CMRTM have been utilized in the manufacturing of the structural load bearing composite laminate (referred to as the thick-section composite) and the integral armor comprising the various layers described above. The microstructure of the resulting laminates, as well as the integral armor has been studied. The flow and cure monitoring of the liquid resin in the processing of thick-section composites, and the integral armor has been evaluated using a DC-based sensing technique [6–9]. Representative static and dynamic (high strain rate and ballistic impact) test results for the thick-section structural laminate accompanied by ultrasonic C-scan studies have been presented.

### 1.2. Vacuum assisted resin infusion/transfer molding

#### Vacuum assisted resin infusion/transfer molding

(VARTM) is of interest in low-cost innovative developments, as it uses single-sided tooling and vacuum-bag technology. It is an emerging manufacturing technique that holds promise as an affordable alternative to traditional autoclave molding and AFP for producing large-scale structural parts. In VARTM, the preform is laid on a single sided tool, which is then bagged along with the infusion and vacuum lines. The resin is infused through the preform, which causes wetting in the in-plane and transverse directions of the preform. This process is proving to be a very attractive alternative to spray-up or impregnation methods, and it is far less expensive than conventional manufacturing methods. Large structural parts with high fiber volume fractions can be produced rapidly. Other advantages of CMRTM and VARTM are low process volatile emissions, high fiber-to-resin ratios and good process repeatability [3,10].

## 2. Processing of thick composite panels

Thick-section composite panels were manufactured from S2-glass/vinyl ester epoxy resin by two methods VARTM

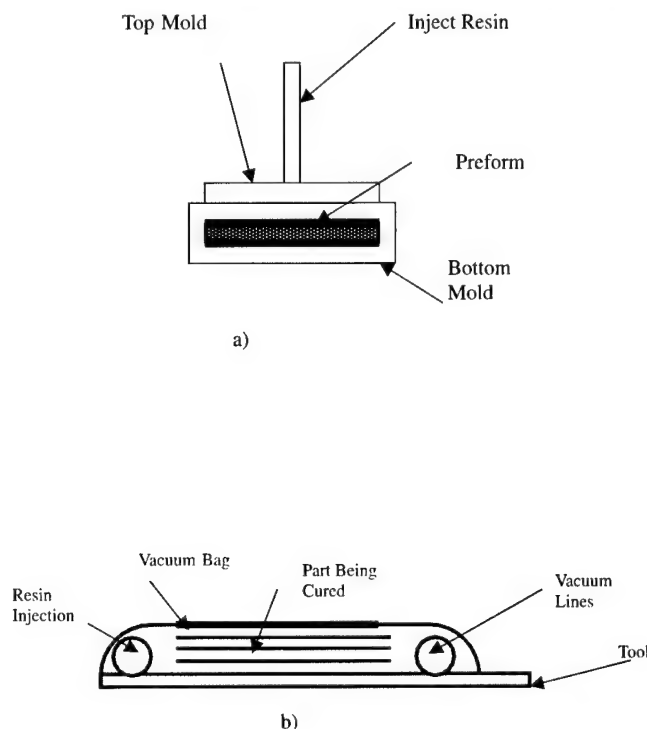


Fig. 2. Schematic of the CMRTM and VARTM processes.

and CMRTM. Fig. 2(a) and (b) provide a schematic illustration of the VARTM and the CMRTM processes. Forty-five layers (plies) of Owens Corning S2-glass fabric-twill weave architecture (0.58 mm/ply) were used to obtain the thick-section composite laminate. Dow Derakane Vinyl Ester 350 (VE350) resin system was used. The resin constituents added to the VE350 system were 6% solution of Cobalt Naphthenate/Octoate (CoNap/Oct) promoter, methyl ethyl ketone peroxide (MEKP) catalyst and dimethylaniline (DMA) accelerator, and 2,4-pentanedione (acetylacetone).

**VARTM laminates.** Forty-five layers of S2-glass preform were stacked on an aluminum caul plate. A porous teflon layer and a highly permeable nylon net (referred to as 'distribution mesh') were laid on top of the preform. Spiral tubing was used to channel the resin through the preform. Following the lay-up and bagging procedures, the preform was debulked for 3 h.

**CMRTM laminates.** A Liquid Control Corporation Positron compact variable ratio (CVR), twin flow metering, mixing and dispensing unit, in conjunction with a pneumatic press 0.41 MPa was used. A disposable mixing head was used to inject resin into the mold at its center at 0.17 MPa. The mold measured 762 mm × 863 mm × 45 mm. Spacers were used within the mold to obtain the laminate of 20 mm thickness. The typical finished dimensions of the laminates were 711 mm × 609 mm × 20 mm in both cases.

### 3. Experimental: thick-section composites

The performance of the laminates was investigated for several loading situations. (a) *Static compression tests.*

Samples of dimensions 38 mm × 25 mm × 20 mm were adopted for compression [10,11] and HSR impact testing. A 50,000 kg Mechanical Testing System (MTS) was used to conduct compression testing of the sample to failure. (b) *High strain rate impact tests.* For HSR impact testing, a compression Split Hopkinson Pressure Bar (SHPB) setup equipped with 38.1 mm diameter bar was used [12,13]. The lengths of incident and transmission bars were 1.52 m and that of striker bar was 0.3 m. These samples were subjected to high strain rate impact loading in the in-plane direction. (c) *Ballistic impact testing.* Laminates of 304 mm × 304 mm × 20 mm were subjected to ballistic testing in a light gas gun with a 76.2 mm barrel with sabo-assisted 50 caliber fragmented simulated projectile (FSP) [14,15]. Impact velocities of 400–450 m/s were adopted, which represents the ballistic limit for the 20 mm thick S2-glass/VE laminates.

## 4. Results and discussion

### 4.1. CMRTM vs VARTM processed thick section laminates

**Microstructure.** The microstructure of the VARTM route processed composites was compared to the laminates processed by CMRTM. Several microstructural differences were observed for the two processes. The extent of fiber compaction is greater in the CMRTM composites in comparison to the VARTM composites as shown in Fig. 3(a). This is attributed to the positive pressure of 0.41 MPa from the compaction provided by the pneumatic press, accompanied by 0.09 MPa or vacuum applied at the vents, in comparison to the vacuum pressure of 0.09 MPa adopted in the VARTM operation. The size of the matrix

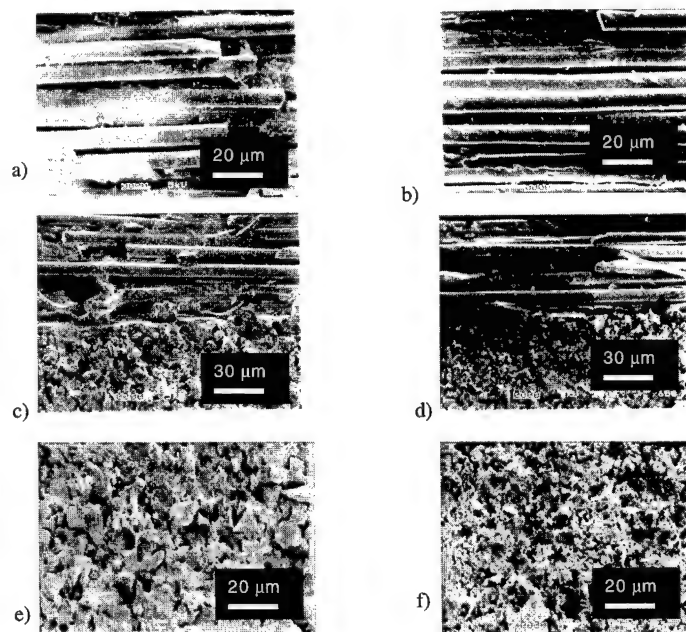


Fig. 3. CMRTM and VARTM composite. (a,b) Extent of fiber compaction, (c,d) Wetting characteristics and (e,f) Size of the matrix agglomerates.

Table 1  
Quantification of CMRTM and VARTM microstructure

	CMRTM	VARTM
Crimp angle	15°	17.5°
Matrix agglomerate size ( $\mu\text{m}^2$ )	1.43	3.4
Average no. of agglomerates	39	34
Yarn height (mm)	0.4	0.6

agglomerates for the CMRTM laminates was smaller ( $<1.43 \mu\text{m}^2$ ) as compared to VARTM where the average matrix agglomerate size was  $3.4 \mu\text{m}^2$ ) as shown in Fig. 3(b). The wetting characteristics were observed to be different as shown in Fig. 3(c). In the VARTM process, tow level wetting was noted, with several dry filaments within the tow (as resin flows around the tows), while in the CMRTM the pressure from the press aided in wet-out of the tows at the filament level.

The above observations were quantitatively studied by measuring parameters such as fiber waviness (crimp angle), yarn height, major axis, average number of matrix agglomerates, and the size of matrix agglomerates as measured with the aid of scanning electron microscopy (SEM). Table 1 summarizes these results.

**Static compression and high strain rate impact response.** Samples were subjected to in-plane loading (along the fiber direction) for static and high strain rate impact testing. The average static compression strength was determined to be 236 MPa for the VARTM samples, and 250 MPa for the CMRTM samples. The increase in compression strength of the CMRTM samples may be attributed to the localized microstructure features from variations reported in Table 1. The CMRTM samples had higher compaction, smaller matrix agglomerates (intimate wet-out) and smaller crimp angles as compared to the VARTM samples. In all the cases, the samples *failed in two ways*. In some samples, the formation of kink-bands and shear failure occurred across their thickness [13]. Failure was through collective progression of microbuckling of the fibers in the single shear plane as

Table 2  
Comparison of failure strength (MPa) and strain (mm/mm) of CMRTM and VARTM laminates

	Static	HSR: 338 (s) <sup>a</sup>	HSR: 422 (s) <sup>a</sup>	HSR: 507 (s) <sup>a</sup>
<b>Strength (MPa)</b>				
VARTM	234	310	361	322
CMRTM	250	250	298	346
<b>Strain (mm/mm)</b>				
VARTM	1.86	2.55	1.83	1.94
CMRTM	2.87	2.01	2.71	2.28

<sup>a</sup> Strain rates adopted in testing.

illustrated in Fig. 4(a). In some instances, failure initiated at two edges of the sample and forking was observed around the mid-plane as shown in Fig. 4(b).

The high strain rate impact results for both CMRTM and VARTM samples indicate an increase in dynamic compressive peak stress as compared to the static case. The characteristics of failure were similar to that observed under the static loading case, where damage initiates from the loading face, as a shear crack through collective micro buckling of the fibers a single shear plane or through forking. In a few of these samples, the samples were seen to delaminate along a weak location along the crimp. Table 2 summarizes the values of the static and high strain rate impact test results from CMRTM vs. VARTM processed panels.

**Ballistic impact tests.** The ballistic impact damage profile was seen to be fairly independent of the processing method, i.e. CMRTM or VARTM. Nearing ballistic limit, i.e. approximately 425 m/s, the CMRTM and the VARTM laminates exhibited shear plugging of the fibers on the impact side, and extended delamination damage towards the back face (Fig. 5). The spread of delamination is a conical zone, where the maximum delamination spread occurs in the inner layers nearing the back face of the laminate. Ultrasonic C-scans were obtained for different

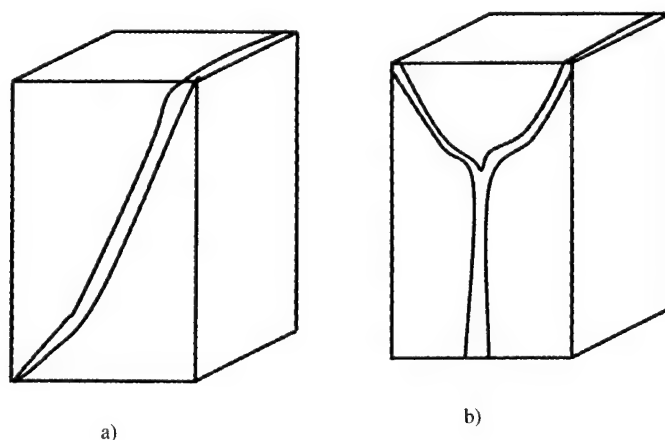


Fig. 4. Failure of S2-glass/VE in compression. (a) Single plane of fracture, and (b) forking.

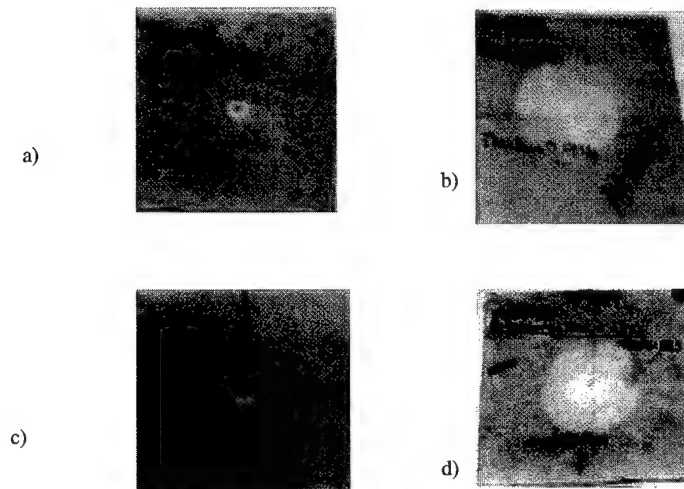


Fig. 5. Ballistic impact damage in (a,b) CMRTM (a — impact face, b — back side), and (c,d) (c — impact face, d —back side) VARTM composite laminates.

layer depths of the ballistically impacted laminates. Ultrasonic C-scans for the CMRTM and the VARTM laminates are shown in Fig. 6, which indicate that evolution of the ballistic damage is identical in both the laminate types. The local variations in microstructure (crimp angle, fiber undulation and resin agglomeration) did not affect the ballistic performance of the composites.

#### 4.2. Processing of integral armor

The integral armor was processed using multi-step hand

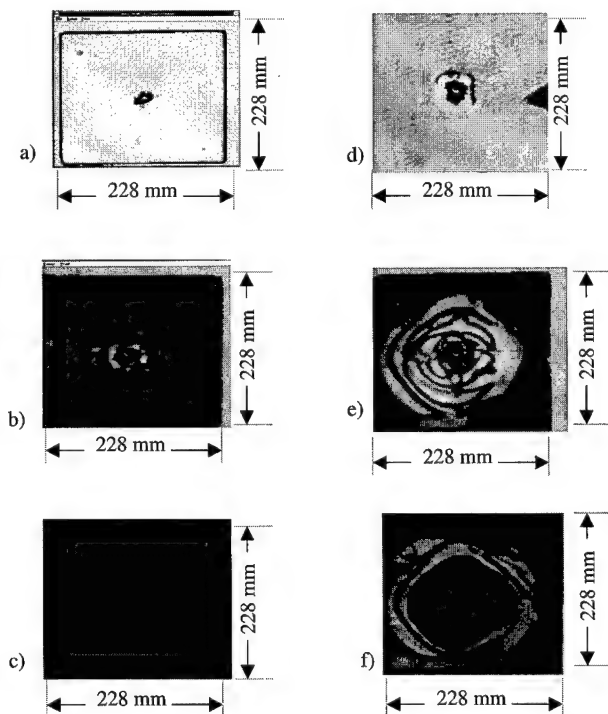
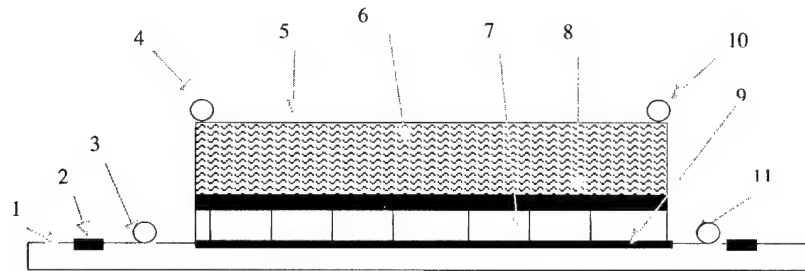


Fig. 6. Layerwise C-scans for ballistic impact damage: (a–c) CMRTM and (d–f) VARTM laminates. Note: a,b — near impact face; c,d — mid-plane of laminate; and e,f — near back side.

lay-up assist VARTM technique which was subsequently refined to a two step process including single-step VARTM infusion of all layers, followed by secondary bonding of the S2-glass/phenolic fire resistant laminate liner.

#### 4.3. Multi-step hand lay-up assist VARTM technique

The various steps of the operation involved: (a) *Preparation of the rubber layer*. EPDM rubber sheet (3 mm thick) was abraded with 600 grit sand paper on both sides. The sheet was cleaned with acetone. A thin layer of primer was applied to the rubber sheet for preparation of the side for bonding to the ceramic and the S2-glass preform. A layer of E-glass scrim cloth separated each interface. (b) *Preparation of ceramic tiles*. Hexagonal alumina ceramic tiles were cleaned with acetone and wetted with a highly compliant epoxy resin. A thin layer of primer was applied to all the edges of the tile. (c) *Resin infusion of the durability cover*. Six layers of preform for the durability cover (S2-glass layers) were laid over a mold. The hexagonal tiles were placed with small gaps (approximately 0.5 mm apart). The rubber was placed over the ceramic tiles. A vacuum bag was applied and the preform (with ceramic tiles and rubber inclusive) was debulked for about 2 h. Resin was then infused through the preform to obtain the durability cover. The part was then stripped off the bag. (d) *Resin infusion of the thick-section composite*: Forty-five layers of S2-glass, twill weave fabric were laid over the rubber side of the part (containing durability cover, ceramic tiles and rubber) and bagged. Vinyl ester VE-350 resin was then infused through the preform to produce the thick-section composite. (e) *Bonding of lay-up to emi mesh and phenolic liner*. The cured thick structural composite side of the part was lightly sanded, and bonded to an EMI screen which was sandwiched between two E-glass layers. An E-glass/phenolic laminate, 3.18 mm thick, was sanded on one side with a 600 grit sandpaper to provide a bonding surface and then cleaned with acetone. An epoxy paste adhesive was used to



1 Caul Plate. 2 Edge Sealing Tacky Tape. 3 Resin Inlet for Bottom-Side Wetting. 4 Main Resin Inlet for Top-Side Wetting. 5 Resin Distribution Media. 6 Structural Laminate Preform. 7 Ballistic Grade Ceramic Tile. 8 EPDM Rubber. 9 Durability Cover Layers. 10 Top-Side Vacuum. 11 Bottom-Side Vacuum.

Fig. 7. Layout of VARTM processing of integral armor.

bond the S2-glass/epoxy liner to the EMI mesh and the thick-section part all pressed in a pneumatic press to obtain the armor plate. The part was then trimmed on a Felker tile saw with a diamond blade.

#### 4.4. Two-step process: single-step VARTM and secondary bonding of glass/phenolic liner

A revised version of the process was developed such that the entire operation was reduced to a two-step operation. A typical layup is shown in Fig. 7. The process followed the sequence as follows: (a) Six layers of S2-glass preform were laid on the tool, (b) hexagonal ceramic tiles were placed over the perform. A finite gap of 0.50 mm was maintained between each tile, (c) EPDM rubber strips of 50 mm width

were placed over the ceramic tiles. A gap of 0.50 mm was maintained between the strips, (d) forty-five layers of S2-glass perform and the EMI mesh were laid over the rubber strips. An E-glass scrim cloth was placed at each interface (rubber–ceramic, rubber–S2-glass and ceramic–S2-glass). The scrim cloth assists in distributing resin between the layers. The part was bagged for VARTM processing. The lay-up was debulked for four hours, prior to resin infusion. Resin was infused in an end-to-end (infusion line at one end of the perform, and the vacuum line at the other end) to fill up the durability cover (the S2-glass) layers which were closest to the caul plate, and hence called bottom-side. Infusion was stopped to the durability cover layers upon its wet-out. Resin was subsequently infused to the top side (to the forty-five structural laminate forming S2-glass perform layers). The process described to bond the glass/phenolic liner was then repeated for secondary bonding. Table 3 provides a breakdown of the processing step and times for the operation steps described using the two approaches for a part size of 76 cm × 50 cm indicating a 36% time savings in adopting the latter approach.

Table 3  
Integral armor processing

Step	Number of hours	
	Multi-step hand lay-up assist VARTM	Two-step process
Preparation of rubber layers	2	2
Fabric cutting	2	2
Preparation of ceramic layers	3	3
Constituents lay-up	2 <sup>a</sup> 3 <sup>b</sup>	2
Bagging time and set-up for infusion	3 <sup>a</sup> 3 <sup>b</sup>	3
Processing time <sup>c</sup>	5 <sup>a</sup> 5 <sup>b</sup>	5
Preparation and bonding of phenolic liner	2	2
Total	30	19

<sup>a</sup> Durability cover, signature layer, ceramic tiles and rubber processing.

<sup>b</sup> Thick section composite processing.

<sup>c</sup> Includes cure time.

#### 4.5. Physical property measurements

The panels were measured for their fiber volume fraction and finished thickness. The S2-glass fiber density value was 2.49 gm/cc, and vinyl ester density value of 1.09 gm/cc. The average thickness of the thick-section composite laminated was measured to be 21 mm. The average fiber volume fractions of the laminates ranged between 48–52%. The void content of the laminate part of the thick-section armor was less than 1% (as measured through the burn-off test). Also see Table 4.

The processing integrity of various interfaces of the integral armor was evaluated by SEM. Fig. 8(a)–(d) represent the interface of the durability cover-ceramic tile, the ceramic tile-rubber interface, the rubber-structural composite interface and the structural composite-EMI, and the



Table 4  
Average physical properties measured for the armor plates

Weight (kg)	Areal density (kg/m <sup>2</sup> )	Dimensions (cm)	Volume fraction <sup>a</sup>	Weight fraction <sup>a</sup>
11.5	123	38 × 26 × 14	48–52%	62%

<sup>a</sup> Volume and weight fractions of the thick composite laminate of the armor.

phenolic laminate interfaces. As can be seen from Fig. 8(a)–(d), distinct interface zones between the dissimilar layers were observed. The bond integrity was found to be uniform through the section of integral armor plate.

#### 4.6. Process sensing: flow and cure monitoring

A DC-based sensing technique monitors the flow and cure information, thereby providing a ‘window’ into the process. A sensor grid, which comprises two orthogonal sets (‘sensing’ and ‘excitation’ lines) of conductive filaments separated by one or more preform layers, are placed between layers of the preform. As resin wets the perform during the infusion process, the gaps between the filament planes are filled with conductive resin, which completes an electrical circuit. Associated instrumentation detects the signal and can infer the resin location and cure state.

The sensors adopted in this work were copper wires (0.2 mm in diameter) insulated with E-glass fiber. The sense lines and excitation lines were woven in a glass cloth referred to as ‘scrim cloth’ to form a sensor mat that

could be placed at the interfaces of the various layers, and in the preform of the structural laminate forming layers.

The lay-up for processing consisted of durability cover layers, ceramic tiles, EPDM rubber and structural laminate forming layers as organized from the caul plate side. A layer of E-glass scrim cloth was used to separate each interface. Of these, one infusion line was placed on the top-side of the lay-up (Fig. 7), while the second line was located on the bottom-side, at one of the edges of durability cover layers. The top and bottom sides were wet-out using an end-to-end infusion-vacuum scheme. Distribution meshes were placed at the bottom of the lay-up as well as the top most position in the lay-up. The bottom side mesh was designed to carry the resin to the bottom layers (the durability cover), while the top-side mesh to spread the resin into the S2-glass layers forming the structural laminate. Resin infusion was delayed at the top-side such that the durability layers (bottom side) were wet-out first. It was expected that the resin during its course of wet-out of the durability cover layers, would simultaneously channel through the gaps in the tiles. On observing the resin emerging from the vacuum line of the bottom-side, infusion was started on the top-side of

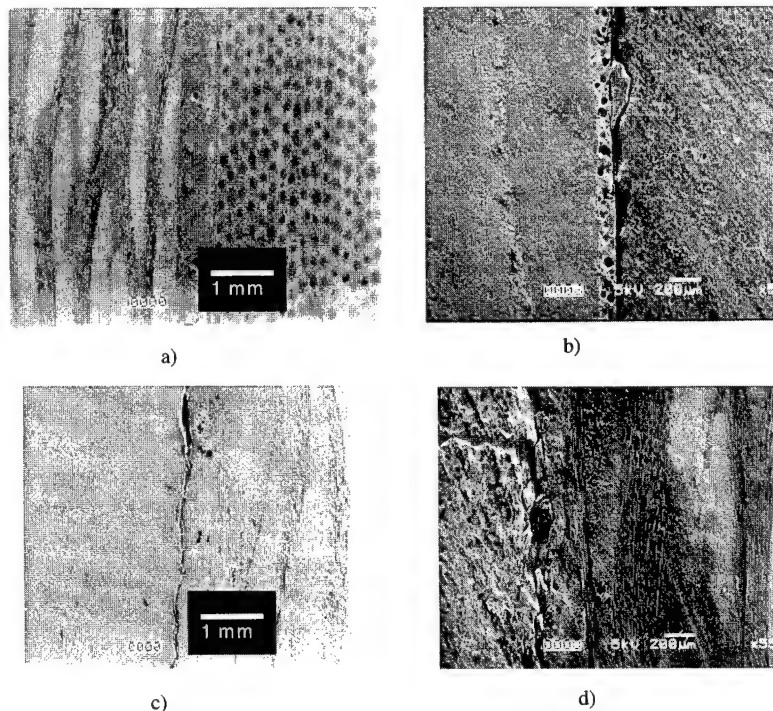


Fig. 8. Microstructure of Armor Interfaces. (a) Phenolic liner-EMI-structural laminate, (b) ceramic–rubber, (c) rubber-structural laminate, and (d) ceramic–rubber-structural laminate.



the lay-up. Four planes of excitation and sense lines (grid of  $4 \times 4$ ) were used at the interfaces between the durability cover and ceramic tile, the ceramic tile and EPDM rubber, rubber and S2-glass perform (making up the structural laminate), and at the center of the S2-glass preform.

Fig. 9(a)–(f) depicts the flow of resin at various interfaces of the integral armor during the VARTM process. Each figure (a)–(f) shows results from the four planes of sensors. The presence of resin is sensed by the increase in voltage at the respective grid. Typical voltage signals shown in Fig. 10(a) and (b) indicate the arrival of resin at a grid junction and the onset of resin cure, respectively. From Fig. 9(a), it may be observed that as the resin started flowing at the bottom-side distribution mesh, it simultaneously progressed through the gaps between ceramic tiles (time frame 815 s). As resin reached the interface between the ceramic–rubber, it started flowing rapidly. As only E-glass scrim cloth separates this interface, minimal resistance is offered at this interface, the speed of the resin flow is faster, as compared

to the durability cover layers–ceramic tile interface. As seen from Fig. 9(b), the resin wet-out nearly 75% of ceramic–rubber interface, while it had just reached 25% of durability cover layers–ceramic interface. In the latter interface, resin flows through the S-2 glass fabric on its lower side, and the ceramic tiles on its upper side.

After 1290 s (Fig. 9(b)) the entire ceramic–rubber interface was wet-out, and half of the durability cover layers–ceramic interface were wet. The resin traveled through the small gaps on either side of ceramic tiles. After 2048 s (Fig. 9(c)) it was observed that both the interfaces were wet, which indicates that resin has traveled through the durability cover layers, and through the ceramic tiles, but was yet to reach the rubber-thick laminate producing S2-glass fabric layers. After 2947 s (Fig. 9(d)) resin enters through the gaps in the rubber strips into the thick composite laminate interface. At the same time frame, the resin was seen to arrive at the bottom-side vacuum line. At this point bottom side (durability cover side) infusion was stopped, and the

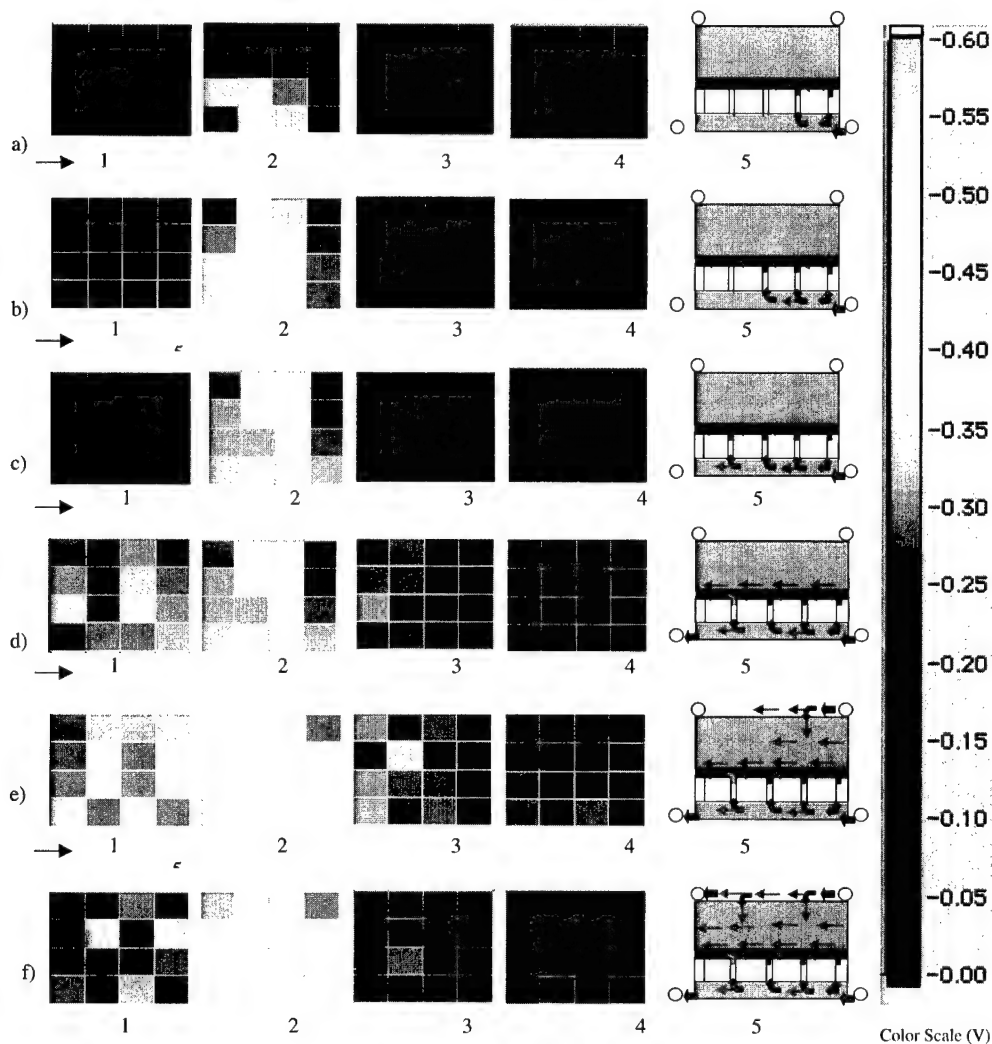


Fig. 9. DC-based sensing of resin flow at various interfaces of the integral armor during the VARTM process. (a) 815 s, (b) 1290 s, (c) 2048 s, (e) 2947 s, and (f) 5067 s.

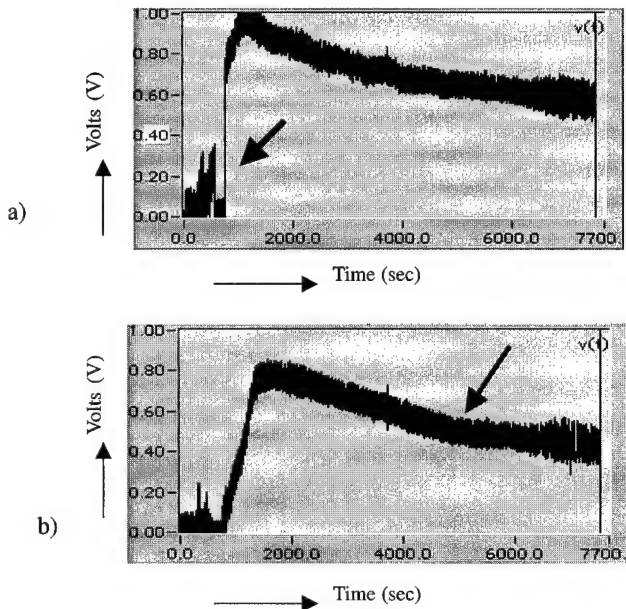


Fig. 10. Representative plots showing voltage of the signals at individual excitation lines. (a) Arrival of resin sensed (increase in voltage, and (b) resin curing starts (dropping of the voltage).

top-side vacuum lines were opened. Resin then flowed through the top-side injection line. The resin infusion lines on the top-side were sequentially activated as resin arrived at the respective infusion line. After 5067 s (Fig. 9(e)) resin was seen to nearly half of center of thick section composite. The entire panel was wet-out after 6303 s (Fig. 9(f)). The voltages diminish as a function of time indicating onset of gelation, and stabilize when the resin begins vitrification.

## 5. Conclusions

1. Thick S2-glass/vinyl ester composite panels representative of their usage in an integral armor were fabricated using low cost CMRTM and VARTM liquid molding processes.
2. The microstructure measured in terms of crimp angle and weave amplitudes was influenced according to the compaction pressures the preform was subjected to; the CMRTM panels showed 12–14% lower crimp angles as compared to the VARTM panels.
3. Process-related variations arising from a collection of factors including local fiber volume fraction and fabric crimp influenced the static compression and high strain rate impact performance. The CMRTM composites were seen to exhibit higher static compression and high strain rate impact values (5–8%) as compared to the VARTM composite samples.
4. In the case of ballistic impact performance, the processing technique used did not affect the extent of damage. If ballistic performance, is the primary design requirement, the VARTM processing offers an affordable alternative.

5. Composite integral armor panels were manufactured through liquid molding processing techniques. The two-step processing approach resulted in ~36% time savings to produce identical integral armor part as compared to a multi-step VARTM process
6. The DC-based sensing technique provided an insight into the flow and cure of the resin through the various layers of the integral armor part.

## Acknowledgements

The support provided by the Army Research Office (ARO) under the Grant No. DAAH04-95-1-0369 is gratefully acknowledged. Assistance from Dr John Gillespie Jr, University of Delaware, Center for Composite Materials (UD-CCM), and Dr Bruce Fink, Army Research Laboratory (ARL) is hereby acknowledged.

## References

- [1] Burns BP, Hoppel CPR, Newill JF, Burton LW, Tzeng JT, Bender JM, Drysdale WH. An Army perspective on composite materials. In: Whitney JM, editor. Proceedings of the 14th Technical Conference of the American Society for Composites, September. 1999. p. 223–32.
- [2] Fink BK. Performance metrics for composite integral armor. In: Whitney JM, editor. Proceedings of the 14th Technical Conference of the American Society for Composites, September. 1999. p. 252–64.
- [3] Pike T, McArthur M, Schade D. Vacuum assisted resin transfer molding of a layered structural laminate for application on ground combat vehicles. In: Proceedings of the 28th International SAMPE Technical Conference, November 04–07, Seattle, 1996; 374–80.
- [4] Faiz R. Net RTM preforming process for cost-effective manufacturing of military ground vehicle composite structures. In: Proceedings of the 28th International SAMPE Technical Conference, November 04–07, Seattle, WA, 1996; 381–92.
- [5] Vaidya UK, Abraham A, Mohamed H, Fotedar K, Haque A, Krishnagopalan J, Mahfuz H, Jeelani S. Manufacturing of composite integral armor using liquid molding processes. In: Green JE, Beckwith SW, Strong AB, editors. Proceedings of the 29th International SAMPE Technical Conference, vol. 29. 1997. p. 523–31.
- [6] Bradley JE, Fink BK, Gillespie Jr JW. On-line process monitoring and analysis of large thick-section composite parts utilizing SMART-weave in-situ sensing technology. In: Proceedings of the 43rd International SAMPE Symposium/Exhibition: Materials and Process Affordability—Keys to the Future, SAMPE, Covina, CA, 1998.
- [7] England KM, Fink BK, Gillespie Jr JW. In situ sensing of viscosity by direct current measurements. In: Moon TJ, editor. Processing and manufacturing of advanced materials and structures, ASME International Mechanical Engineering Congress and Exposition 1996.
- [8] Vaidya UK, Jadhav NC, Hosur MV, Gillespie Jr JW, Fink BK. Assessment of flow and cure monitoring using direct current and alternating current sensing in vacuum assisted resin transfer molding. *Smart Materials and Structures* 2000;9:727–36.
- [9] Rigas EJ, Mulkern TJ, Nguyen SP, Walsh SM, Granville D. Affordable thick composite processing for army applications. In: Whitney JM, editor. Proceedings of the 14th Technical Conference of the American Society for Composites, September. 1999. p. 242–51.
- [10] Davis JG. Compression strength of fiber reinforced materials.

- Composite reliability, ASTM STP 580 ASTM Philadelphia: American Society for Testing Materials, 1975. p. 364–77.
- [11] Camponeschi Jr ET. Compression testing of thick-section composite materials. In: O'Brien TK, editor. Composite materials: fatigue and fracture, STP 1110, vol. 3. ASTM Philadelphia: American Society for Testing Materials, 1991. p. 439–56.
- [12] Haque A, Ali M, Vaidya UK, Mahfuz H, Jeelani S. Rate dependent compressive response of S2-glass/vinylester composites. In: Green JE, Beckwith SW, Strong AB, editors. Proceedings of the 29th International SAMPE Technical Conference, vol. 29. 1997. p. 698–712.
- [13] Hosur MV, Vaidya UK, Abraham A, Jadhav N, Jeelani S. Static and high strain rate compression response of thick section twill weave S2-glass vinyl ester composites manufactured by affordable liquid molding processes. *ASME J Engng Mater Technol* 1999;121(4):468–75.
- [14] Bernetich KR, Fink BK, Gillespie Jr JW. Ballistic testing of affordable composite armor. In: CD-ROM Proceedings of the American Society for Composites 13th Technical Conference, Baltimore, MD, September 21–23, 1998.
- [15] Monib AM, Gillespie Jr JW. Damage tolerance of composite laminates subjected to ballistic impact. In: Proceedings of ANTEC 98, Soc. of Plastics Engineers, Brookfield, CT. 1998; 1463–67.

# High performance oxide fibers for metal and ceramic composites

D.M. Wilson\*, L.R. Visser

3M Specialty Fibers and Composites Program, St Paul, MN 55144-1000, USA

## Abstract

A family of oxide fibers, Nextel™ 610 Ceramic Oxide Fiber, Nextel™ 720 Ceramic Oxide Fiber and a new fiber, Nextel™ 650 Ceramic Oxide Fiber, has been developed specifically for the reinforcement of metal and ceramic matrix composites. This paper summarizes room and high temperature properties for these fibers. The strength of both single filaments and multi-filament rovings of Nextel 610, 650 and 720 fibers was determined between 25 and 250 mm gauge length. Weibull analysis was used to compare the statistical fracture distribution and gauge length dependence of strength. Fiber fracture statistics were in accord with Weibull theory; the effect of diameter variability on the statistical analysis was found to be small. Fractographic analysis on Nextel 610 fiber was used to identify primary fracture-causing defects; defect size was correlated with Griffith fracture predictions.

High temperature single filament strength measurements were performed on Nextel 610, 650 and 720 fibers between 800 and 1400°C. High temperature strength varied inversely with strain rate. In combination with tensile creep tests at 1100 and 1200°C, these were used to compare the elevated temperature capability of each fiber and determine maximum use temperatures. The development of crystalline yttrium aluminum garnet fibers that demonstrate further improvements in creep performance relative to Nextel 720 fibers is also discussed. © 2001 Elsevier Science Ltd. All rights reserved.

**Keywords:** A. Fibres; A. Ceramic-matrix composites (CMCs); B. Fracture; B. Microstructure;  $\text{Al}_2\text{O}_3$

## 1. Introduction

Oxide fibers are traditionally considered to have lower strength and creep resistance than covalently bonded materials such as SiC. However, in the mid 1990s, two new fibers, Nextel 610 fiber and Nextel 720 fiber, were developed that have uniquely high tensile strength and creep resistance. The high strength of Nextel 610 fiber (3.3 GPa) has allowed the development of a new generation of aluminum matrix composites that have tensile strength in excess of 1500 MPa [1]. The creep resistance of Nextel 720 fiber [2–4] allows the fabrication of oxidation-stable ceramic composites with useful load-bearing capability above 1100°C [5–7]. A new rare-earth doped alumina fiber, Nextel 650 fiber, has recently been developed that has 100 times lower creep rate than Nextel 610 fiber [8]. These fibers comprise a family of composite grade fibers specifically designed for the reinforcement of metal and high temperature ceramic matrix composites. One unique and critical difference between these fibers and other commercial fibers is that they are fully crystalline. Most commercial fibers contain silica or other non-crystalline phases, including the older Nextel™ fibers such as Nextel™ 312, 440 and

550 Ceramic Oxide Fibers. Amorphous phases become viscous at high temperatures, so are detrimental to creep performance. Equally critical for fibers designed for composite reinforcement is the reactivity of amorphous phases compared with fully crystalline fibers. Crystalline fibers containing high amounts of  $\alpha\text{-Al}_2\text{O}_3$  that are free of glassy phases are very chemically stable. High chemical stability leads to good environmental stability in corrosive atmospheres, low reactivity with respect to metal matrixes such as aluminum, and less interaction with a variety of ceramic matrices. Several successful high temperature composites utilize porous oxide matrices [5,7]. Porous oxide matrices promote crack deflection at fiber–matrix interfaces, leading to fiber debonding and pullout, thereby providing high composite toughness. This approach to composite design requires highly stable and non-reactive fibers to prevent strong matrix–fiber interactions. This type of composite, which does not require fiber coatings, is finding increasing application in part because of the significant cost advantages relative to other systems.

Nextel 720 fiber was developed for load-bearing applications at temperatures in excess of 1000°C. The superior high temperature creep performance of Nextel 720 fiber results from a high content of mullite, which has much better creep resistance than alumina. Additionally, Nextel 720 fiber consists of 0.5  $\mu\text{m}$  globular grains of mullite; this is five

\* Corresponding author.

E-mail address: davidwilson@mmm.com (D.M. Wilson).

times larger than grains in Nextel 610 fiber. In fine-grained oxides, the creep rate is inversely proportional to grain size. Lastly, the presence of acicular and globular grains of mullite and alumina reduces grain boundary sliding. However, these microstructural factors that improve creep represent a tradeoff with respect to strength. High strength fibers should preferably have a fine and uniform grain size. High contents of alumina, which has higher fracture toughness than mullite, are also advantageous for strength.

Nextel 650 fiber was recently developed for high temperature composite applications in which the presence of mullite and other silicon containing phases is not desirable. Additional information on the microstructure and properties of Nextel 650 fibers was recently published [8]. Nextel 650 fibers were developed with the goal of producing a fiber with improved strength and chemical stability relative to Nextel 720 fibers with superior creep performance relative to Nextel 610 fibers. High alumina fibers are more corrosion resistant in many environments, such as those containing alkalis, than fibers containing silica. High pressure steam environments at temperatures above 1100°C, such as in combustors in gas turbines, may also cause degradation in Nextel 720 fibers. Also, Nextel 720 fiber has a strength of only 2.1 GPa, significantly less than Nextel 610 fiber, as a result of its larger grain size. Harmer and coworkers [9] and Sato and Carry [10] have reported that doping alumina with rare-earth oxides such as  $Y_2O_3$  reduces creep in alumina by one to two orders of magnitude. The use of  $Y_2O_3$  to reduce diffusivity in  $Al_2O_3$  oxidation scales formed on metal alloys is also well known [11]. The reduction in creep is attributed to reduced grain boundary diffusivity caused by segregation of  $Y^{3+}$  to grain boundaries [12]. Since creep in fine-grained alumina is controlled by diffusion-related phenomena on grain boundaries, e.g. diffusion, grain boundary sliding, and defect elimination, rare-earth doping reduces the creep rate in alumina.

## 2. Experimental and analytical procedures

Single filament strength testing was performed by directly gripping fibers with rubber-faced clamp grips with 25 × 25 mm grip faces. For routine testing, a 25 mm gauge length and a fiber loading rate of 0.02/min was used. Filament diameters were measured using a Measure-Rite image analysis system (Model M25-6002 Dolan-Jenner Industries, Lawrence, MA), attached to a light microscope at 1000× magnification. In this system, fibers were measured end-on relative to a round template. This method has a resolution of 0.3 μm and has been determined to be accurate to within 0.3 μm relative to scanning electron microscopy (SEM) measurements.

For most single filament strength testing, filament diameter was not measured; average diameters were calculated from roving denier and the number of filaments, assumed to be 410 for 1500 denier rovings (denier =

grams/9000 m length). Calculated diameters of 11.52, 11.22 and 12.34 μm were used for 1500 denier Nextel 610, 650 and 720 fibers, respectively, and 11.98 μm for 3000 denier Nextel 610 roving (770 filaments/roving). The differences in diameter result from the different density of each fiber type.

The statistics of fiber fracture are commonly reported as a Weibull distribution. The application of Weibull theory to high modulus fibers has been reviewed [13]. The probability of failure of a material is given by:

$$P = 1 - \exp[-V/V_0(\sigma/\sigma_0)^m] \quad (1)$$

where  $m$  is the Weibull modulus,  $V$  the gauge length,  $\sigma$  the failure strength, and  $V_0$  and  $\sigma_0$  are scaling constants. For a single gauge length, Eq. (1) reduces to:

$$\ln(\ln(1/(1 - P))) = m \ln \sigma + k \quad (2)$$

where  $k$  is a constant. The Weibull modulus,  $m$ , is then determined graphically as the slope of the 'Weibull plot' of  $\ln(\ln(1/(1 - P)))$  vs.  $\ln \sigma$ . For Weibull plots,  $P = (i - 0.5)/n$  was used to estimate fracture probability, where  $n$  is the number of fibers tested and  $i$  the rank of strength for each fiber.

Another method of determining Weibull modulus is to measure fiber strength as a function of gauge length. With increasing gauge length, the chance of finding a large flaw increases, so fiber strength decreases. The effect of gauge length is given by the equation:

$$\ln \sigma = -1/m \ln L + k' \quad (3)$$

where  $L$  is gauge length and  $k'$  a constant. Thus, the slope of a log-log plot of strength vs. gauge length is  $-1/m$ .

Fractography testing was performed by breaking fibers embedded in grease to dampen vibrations, thereby preventing secondary fiber fracture. One end of a 100 mm long fiber was taped to a piece of polyethylene film. The exposed section of the fiber was coated with a water-soluble grease (Phynal, Reliance Glass Works, Bensenville, IL). The fiber section was long enough so that it protruded ~20 mm past the end of the film. The polyethylene film with fiber attached was gripped at the tape location and the protruding end of the fiber was gripped with a rubber-faced clamp grip as for standard tensile testing. The overall gauge length of fiber was 75 mm for fractography testing. After fracture, the grease was removed from the fiber by two soaks in deionized water, followed by an ethanol rinse. The matched broken end pairs were mounted vertically on SEM stubs for examination.

High temperature fiber strength testing was performed vertically using a slotted furnace with a hot zone 20 mm long. Fibers were loaded into the test frame, the hot furnace was slid around the fiber and equilibrated for 90 s before beginning the test. For strand testing, the overall gauge length was 250 mm and the strain rate was 12.5 mm/s. For single filament testing, the overall gauge length was 280 mm and the strain rate was 0.68 mm/min.

Table 1  
Properties of Nextel 610, 650, and 720 Ceramic Fibers

Property	Units	Nextel™ 610	Nextel™ 650	Nextel™ 720
Chemical composition	wt%	> 99Al <sub>2</sub> O <sub>3</sub>	89Al <sub>2</sub> O <sub>3</sub> 10ZrO <sub>2</sub> 1Y <sub>2</sub> O <sub>3</sub>	85Al <sub>2</sub> O <sub>3</sub> 15SiO <sub>2</sub>
Crystal phases		$\alpha$ -Al <sub>2</sub> O <sub>3</sub>	$\alpha$ -Al <sub>2</sub> O <sub>3</sub> + cubic ZrO <sub>2</sub>	$\alpha$ -Al <sub>2</sub> O <sub>3</sub> + mullite
Tensile strength (25.4 mm gauge)	GPa	3.3	2.5	2.1
Tensile modulus	GPa	373	358	260
Density	g/cc	3.9	4.1	3.4
Thermal expansion (100–1100°C)	ppm/°C	7.9	8.0	6.0
Maximum use temperature (1% strain/69 MPa/1000 h)	°C	1000	1080	1150
Roving denier: filament count		1500: 380–420 3000: 740–780 10000: 2500–2600	3000: 740–780	1500: 380–420 3000: 740–780

Creep testing was performed using a single filament, dead load testing system to provide an accurate and consistent load. Sample elongation was measured with a Zygo® laser extensometer (Model 1101, Zygo Corp, Middlefield, CT). The creep system used a resistance-heated, three zone alumina tube furnace with Nichrome heating elements. Hot zone temperature was accurate to within 3°C of the setpoint over the entire 106 mm gauge length. The creep rate was assumed to be uniform over this gauge length. Details of this creep system have been described previously [2].

### 3. Results

Table 1 summarizes the properties of Nextel 610 fiber, Nextel 650 fiber and Nextel 720 fiber. Nextel 610 fiber is

>99% pure  $\alpha$ -Al<sub>2</sub>O<sub>3</sub> with a grain size of  $\sim 0.1 \mu\text{m}$ . Nextel 610 has properties expected of an alumina fiber; the elastic modulus and density are slightly below theoretical (400 GPa, 3.98 g/cm<sup>3</sup>), reflecting a small amount of porosity. Thermal expansion is very close to measured values for monolithic alumina. Nextel 650 fiber has the composition Al<sub>2</sub>O<sub>3</sub> + 10% ZrO<sub>2</sub> + 1% Y<sub>2</sub>O<sub>3</sub>. The microstructure of Nextel 650 fiber consists primarily of 0.1  $\mu\text{m}$   $\alpha$ -Al<sub>2</sub>O<sub>3</sub> grains; ZrO<sub>2</sub> is present as 5–30 nm grains on both grain boundaries and within alumina grains [8]. The key additive in Nextel 650 fibers is Y<sub>2</sub>O<sub>3</sub>, which is added to reduce creep rate. ZrO<sub>2</sub> additions are used to reduce grain growth, which is accelerated by Y<sub>2</sub>O<sub>3</sub> doping. Zirconia is stabilized by Y<sub>2</sub>O<sub>3</sub> in the cubic phase. The addition of ZrO<sub>2</sub> had only a minor effect on creep rate for either rare-earth doped or undoped alumina fibers. Density and thermal expansion have not yet been directly measured, but are higher than

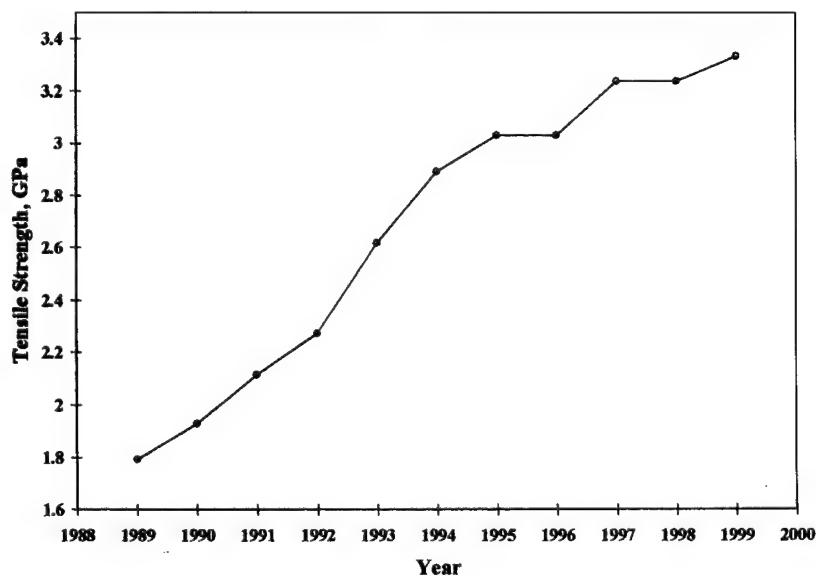


Fig. 1. Single filament strength of Nextel 610 has steadily increased to over 3 GPa (data points represent mean fiber strength for each year).



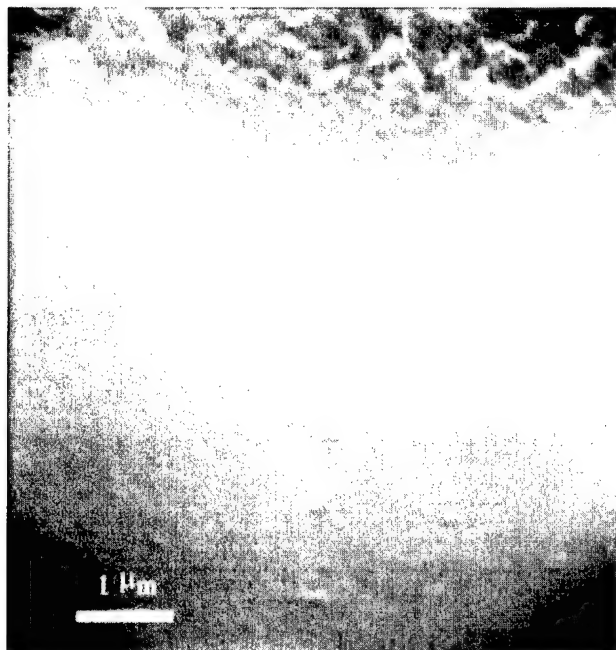


Fig. 2. SEM of fracture surface of Nextel 610 fiber from fractography testing. The fiber broke at a stress of 3.27 GPa at a weld line 0.25  $\mu\text{m}$  in depth caused by inter-filament adhesion during processing. Bar = 1  $\mu\text{m}$ .

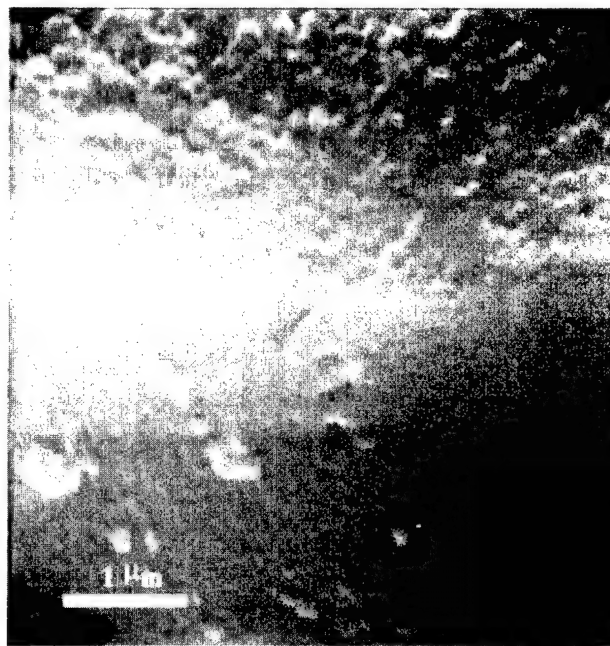


Fig. 3. SEM of fracture surface of Nextel 610 fiber from fractography testing. The fiber broke at a stress of 3.83 GPa at a surface scratch 0.5  $\mu\text{m}$  in depth. Bar = 1  $\mu\text{m}$ .

Nextel 610 fiber due to the presence of 10%  $\text{ZrO}_2$ . Elastic modulus was measured to be slightly lower than Nextel 610 fibers, as expected since  $\text{ZrO}_2$  has lower modulus than  $\text{Al}_2\text{O}_3$ . Nextel 720 fiber contains 15%  $\text{SiO}_2$  in the form of mullite; volume calculations indicate that mullite comprises 55–60% of the fiber volume. The high content of mullite lowers density and thermal expansion by 13 and 30%, respectively. These can be significant advantages for aerospace and thermally loaded applications. The microstructure of Nextel 720 fiber has been described in more detail elsewhere [14].

#### 4. Development of high fiber strength

A major application of Nextel 610 fiber is to strengthen and stiffen aluminum metal composites; therefore, high strength is a primary requirement. The high strength of Nextel 610 fibers is the result of intensive microstructural design and process development efforts. Among oxide ceramics,  $\text{Al}_2\text{O}_3$  is generally considered the most desirable structural material.  $\text{Al}_2\text{O}_3$  has excellent fracture toughness, high elastic modulus, and very good thermochemical stability. However, the fabrication of  $\text{Al}_2\text{O}_3$  in fiber form is not straightforward. The stable  $\alpha$  form of  $\text{Al}_2\text{O}_3$  has a low volumetric nucleation density, which leads to large grain size [15]. In addition to large grains, crystallization often leads to high levels of porosity which inhibit sintering. Thus, control over the nucleation process during crystallization is essential if the fine grain sizes required for high strength are to be achieved. In Nextel 610 fiber, nucleation agents are used to

produce a uniform, high-density microstructure with a grain size of 0.1  $\mu\text{m}$ .

In addition to small grain size, other defects and flaws must be minimized by careful fiber processing. The sol/gel process in combination with effective nucleation agents is uniquely suited to the preparation of such extremely fine-grained and homogeneous fiber microstructures. However, achieving this level of control is difficult. Fig. 1 shows the mean strength of Nextel 610 fibers produced during each year since 1989. Initial versions of Nextel 610 had strength below 2 GPa. During the late 1980s and early 1990s, large internal programs to develop first titanium and later, aluminum composites reinforced with Nextel 610 were performed [1,16]. Focused efforts were carried out to increase the strength of Nextel 610 fiber to greater than a target of 2.8 GPa. As shown in Fig. 1, these efforts were successful over time in increasing strength to 3.3 GPa. Keys to this effort were the development of improved nucleation agents, intensive efforts to reduce the level of internal particulate defects, and careful control of fiber spinning and heat treatment to prevent fiber damage during processing.

During fiber development, fractography testing was performed to identify fracture-causing defects in Nextel 610 fibers. Figs. 2–4 are scanning electron micrographs of fractured surfaces of Nextel 610 fibers generated during fractography testing. The mean strength of the sample of 16 fibers tested was 3.27 GPa. Fourteen of the 16 fibers fractured at defects at the fiber surface. A high proportion of surface fracture origins in Nextel 610 fibers has also been reported elsewhere [17]. Fig. 2 shows a fiber that fractured at a weld lines running down the length of the fiber surface.



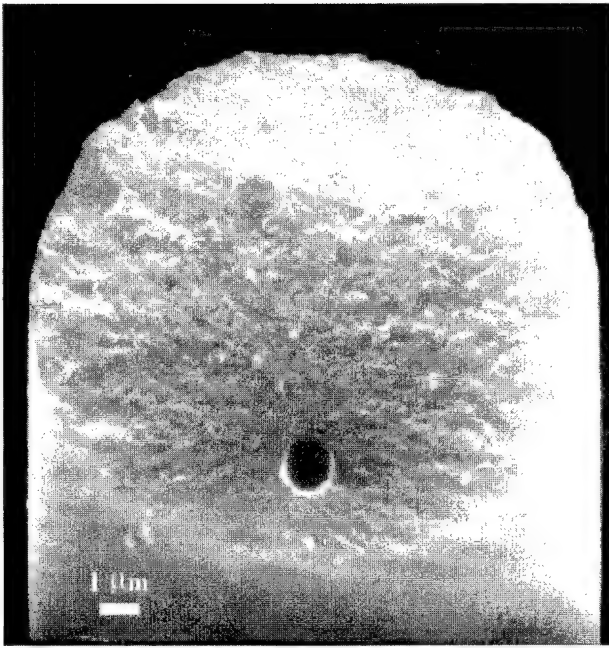


Fig. 4. SEM of fracture surface of Nextel 610 fiber from fractography testing. The fiber broke at a stress of 3.38 GPa at a 1.3  $\mu\text{m}$  round, internal pore. Bar = 1  $\mu\text{m}$ .

The weld line resulted from contact with a neighboring fiber during processing. Fracture occurred at one of the weld lines at 3.85 GPa. The weld line is 0.5  $\mu\text{m}$  in width and 0.25  $\mu\text{m}$  in depth. The fracture surface morphology has an indistinct mirror–mist–hackle appearance. Within  $\sim 1 \mu\text{m}$  of the fracture origin, the fracture surface is relatively smooth; outside of that ‘mirror’ region, the fracture surface becomes

textured, and striations lead away from the fracture origin. Fig. 3 shows a fiber that broke at a surface scratch 0.7  $\mu\text{m}$  wide and 0.5  $\mu\text{m}$  in depth (3.38 GPa). The surface scratch was probably caused by mechanical abrasion in the green (unfired) state. A fiber which broke at an internal, round, smooth pore 1.3  $\mu\text{m}$  in size is shown in Fig. 4 (3.74 GPa). This pore was likely caused by an air bubble in the sol/gel precursor used to spin the fiber.

As brittle ceramics, the strength of  $\text{Al}_2\text{O}_3$  fibers is controlled by the Griffith fracture criterion:

$$\sigma = K_{Ic}/m(\pi c)^{1/2} \quad (4)$$

where  $c$  is flaw size and  $m$  a geometrical factor. In  $\text{Al}_2\text{O}_3$ , the fracture toughness  $K_{Ic}$  is near 2.8. For a semicircular surface flaw,  $m = \pi/2$ , or 0.64 [18]. Fig. 5 shows the Griffith strength prediction for  $\text{Al}_2\text{O}_3$  as a function of flaw size. In order to achieve  $>3$  GPa strength in alumina fibers, a flaw size well below 1  $\mu\text{m}$  is necessary. Fig. 5 also shows the strength of Nextel 610 fibers during fractography testing as a function of measured defect size. In general, the width of surface flaws was twice their depth, i.e. the flaws are roughly semicircular (for the diagram in Fig. 5,  $a = b$ ). In Fig. 5, measured flaw size was plotted as the depth,  $a$ , of the flaw. As predicted by the Griffith equation, larger defects generally correlated with lower fiber strength. However, for surface flaws, measured fiber strength was somewhat less than predicted by Eq. (4). This may indicate that the fracture toughness of Nextel 610 fibers is less than larger-grained alumina; large-grained alumina is known to have higher fracture toughness due to crack–wake effects that are unlikely to be operative in a ceramic fiber. However, note

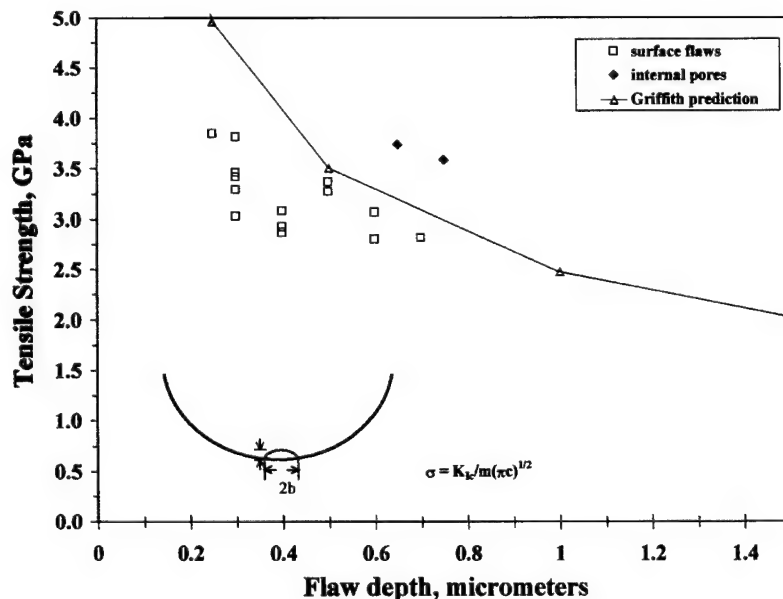


Fig. 5. Comparison of measured flaw size with the Griffith strength prediction for  $\text{Al}_2\text{O}_3$  fibers ( $K_{Ic} = 2.8$ ) with semicircular surface flaws. Flaw size must be well below 1  $\mu\text{m}$  to achieve 3 GPa strength. Measured flaw size,  $a$ , was slightly less than the predicted strength for surface flaws, but above the prediction for round, internal pores.

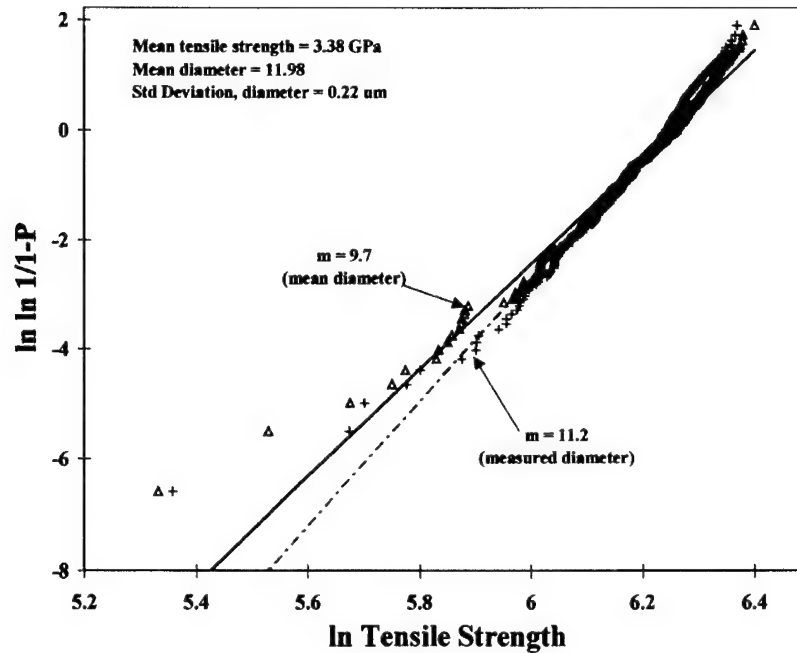


Fig. 6. Weibull plot of fracture probability as a function of failure stress using (a) measured individual filament diameters and (b) calculated mean diameter of 11.98  $\mu\text{m}$ . Using mean diameter, Weibull modulus was 15% less.

that the extremely small size of the defects and the polycrystalline nature of the fiber create some uncertainty about precise location of flaw boundaries. For instance, there may be some extension of the crack over one or two grains prior to fracture, effectively increasing the size of the flaws. The two fibers that fractured at round pores had higher strength than the Griffith prediction (for round pores, flaw size,  $c$ , was pore diameter divided by two). The smooth, round internal surface of these pores minimizes the stress concen-

tration relative to other types of defects; these pores are not sharp flaws as required by Eq. (4).

### 5. Weibull statistics of fiber strength

To determine Weibull modulus, 369 fibers from a single sample of Nextel 610 fibers were tested at 25 mm gauge length. Fig. 6 shows the data plotted as a Weibull plot.

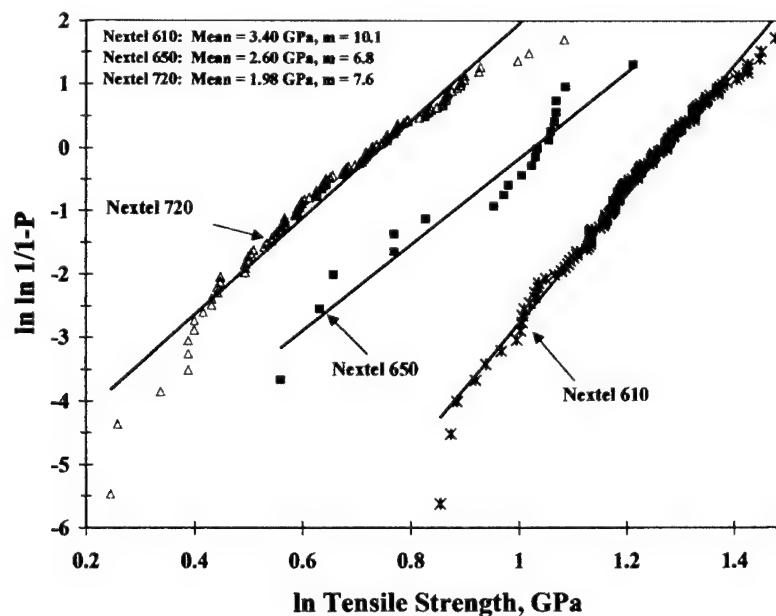


Fig. 7. Weibull plot of fracture probability. The strength of Nextel 610, 650 and 720 fibers was 1.98, 2.60, and 3.40 GPa, respectively, and the Weibull moduli were 10.1, 6.8 and 7.6.

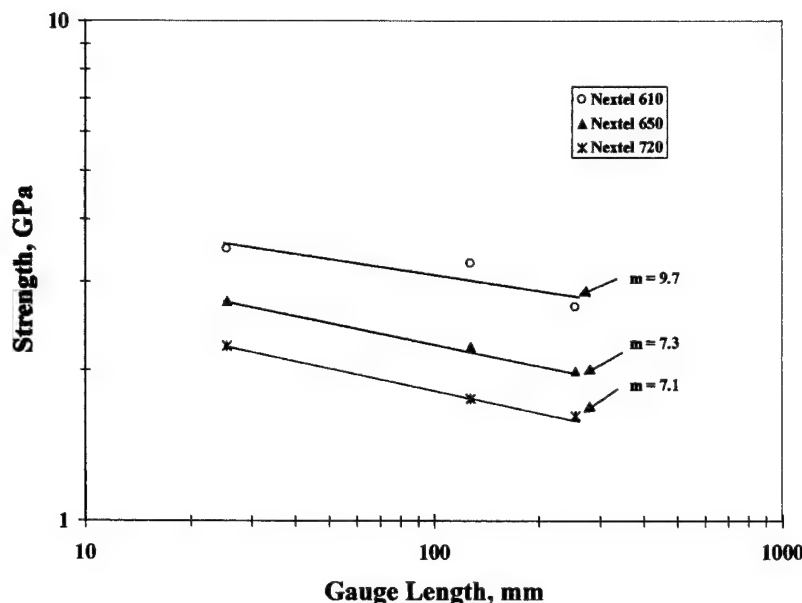


Fig. 8. Log-log plot of failure strength of Nextel 610, 650 and 720 fibers as a function of gauge length. Weibull modulus is equal to the inverse of the slope of the best-fit lines. The Weibull moduli of Nextel 610, 650 and 720 fibers were 9.7, 7.3 and 7.1, respectively.

Two methods were used for data analysis. In one data set, fiber strength was calculated using breaking load divided by the cross-sectional area, as determined from individual diameter measurements for each broken fiber. In the other data set, the mean measured diameter of  $11.98 \mu\text{m}$  was used to calculate breaking strength from the individual breaking load measurements. The correlation of the best-fit line to both data sets is only fair. The fiber fracture data deviates above the best-fit line for high strength fibers and below the line for low strength fibers for both sets of data. The cause of the poor fit appears to be an overly large effect on the least-squares fit of weakest four fibers at the end of the distribution. If the four lowest data points are removed, the fit improves greatly, and the Weibull modulus is increased  $\sim 10\%$ . Other methods of curve fitting, e.g. maximum likelihood estimator [19], have been shown to be more accurate than the least-squares method used for this data, but these methods were not applied in this study. The Weibull modulus was determined to be 11.2 for the data set with individual diameter measurements, and 9.7 for the data set using mean diameter. The lower Weibull modulus of fiber strengths calculated using mean diameter is expected; the calculated distribution will be created by the overlap of the 'true' dispersion of strength and the dispersion of fiber volume created by diameter variability. For instance, larger diameter fibers will, on average, have higher breaking loads. If mean diameter is used, then these fibers will have erroneously high calculated strength. Conversely, smaller diameter fibers will have erroneously low calculated strength. This will broaden the calculated distribution of fiber strength relative to the true distribution and therefore the Weibull modulus will be lowered. This effect has been modeled recently by Lara-Curzio and Russ [20]. For the

data in Fig. 6 (COV of diameter of (1.8%) Lara-Curzio and Russ predicts a  $\sim 5\%$  reduction in measured Weibull modulus. For more typical diameter distribution in Nextel 610 fibers (5%) [21], the predicted drop in measured Weibull modulus with the use of mean diameter is 10%. These predictions are somewhat less than measured reduction from 11.2 to 9.7 (15%), but are reasonable given uncertainties in fiber diameter measurement on the sub-micrometer level [22].

Fig. 7 is a Weibull plot that compares the strength of Nextel 610 fibers, Nextel 650 fibers and Nextel 720 fibers. Data for Nextel 610 and 720 fibers were taken from entire production lots in late 1999 and early 2000, respectively. Sets of 10 fibers were tested at periodic intervals through one production run. These sets were combined into a single population for analysis. A total of 140 Nextel 610 fibers and 120 Nextel 720 fibers were tested. Nextel 650 is currently in early stages of development and less data is available. Two sets of 10 fiber breaks were combined for this analysis. As described above, fiber strength was calculated using mean diameters; thus, the Weibull values should be conservative by 10% or more.

The strength of the fibers increased from 1.98 GPa for Nextel 720 fibers to 2.60 GPa for Nextel 650 fibers to 3.40 GPa for Nextel 610 fibers. The Weibull modulus was 10.1 for Nextel 610,  $\sim 30\%$  higher than for either Nextel 650 or Nextel 720 fibers, which had Weibull moduli of 6.8 and 7.6, respectively. These values are very similar to those reported previously for earlier lots of Nextel 610 and 720 fibers [21]. The Weibull modulus for Nextel 610 fibers is also similar to the other lot of fibers tested in Fig. 6. The expected fit to the linear Weibull relationship is good, though both Nextel 610 and 720 fibers show a deviation

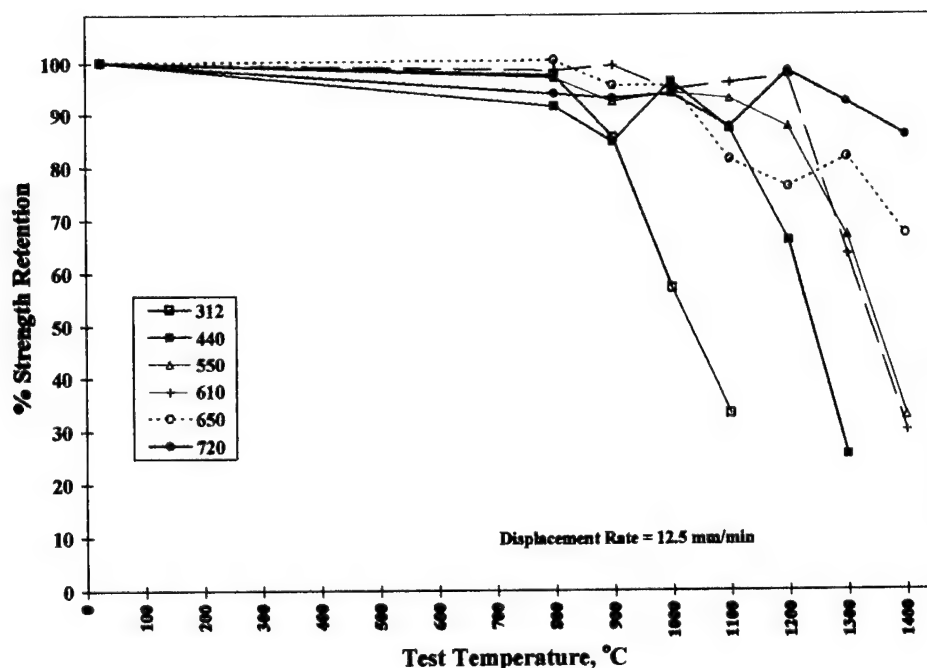


Fig. 9. Comparison of relative tensile strength retention of multi-filament strands of Nextel 312, 440, 550, 610, 650 and 720 fibers at elevated temperature.

toward high strengths at both ends of the probability range. The reason for the higher Weibull modulus for Nextel 610 fiber relative to the other fibers is not clear. One possibility is that the single-phase alumina microstructure of Nextel 610 fiber provides increased microstructural and therefore flaw homogeneity relative to the other fibers, which have multiple phases. Alternately, microscopy and fractography work has identified weld lines as critical defects in both Nextel 650 and 720 fibers; the different fiber compositions may have different intrinsic propensity toward inter-filament adhesion via sintering, which could lead to different flaw populations.

Fig. 8 shows a log–log plot of single filament strength for Nextel 610, 650 and 720 fibers as a function of gauge length in the range 25–254 mm. Ten filaments were tested at each gauge length for each type of fiber. The strength of these samples at 25 mm gauge length was 3.49, 2.75 and 2.24 GPa, respectively, for Nextel 610, 650 and 720 fibers.

Table 2  
Roving strength maximum temperature limit (70% strength retention)

Fiber	Roving strength maximum temperature limit <sup>a</sup> (°C)
Nextel 312	950
Nextel 440	1200
Nextel 550	1300
Nextel 610	1300
Nextel 650	1400
Nextel 720	> 1400

<sup>a</sup> Strain rate = 12.5 mm/min.

Fiber strength was determined using mean diameters calculated from fiber denier of 11.52, 11.22 and 12.34  $\mu\text{m}$ , as discussed above. As predicted by Eq. (3), fiber strength decreased as gauge length increased. The Weibull modulus determined from the slope of the best-fit lines was 9.7, 7.3 and 7.1 for Nextel 610, 650 and 720 fibers, respectively. These values agree very well with data from Fig. 7 using the statistics of fracture at a single gauge length. The agreement is within 7% for all three fibers. Thus, the results are consistent with a single population of flaws distributed uniformly throughout the fiber bundles. Previous results had indicated a higher Weibull modulus for gauge length measurements [21]. The reason for the difference is not clear; these measurements span a larger range of gauge lengths than the previous study.

## 6. High temperature fiber properties

High temperature fiber strength was measured in two ways. The strength of multi-filament rovings was measured for all six commercially available Nextel fibers. For the fibers most commonly used for high temperature ceramic composites, Nextel 610, 650 and 720 fibers, high temperature single filament testing was also performed.

Fig. 9 compares the relative high temperature multi-filament strand or roving strength of all available Nextel fibers. Since the number and diameter of the fibers is different for each type of fiber, the data is presented as a percentage of room temperature (RT) strength. The RT strength was measured on fibers that had the sizing removed by heat cleaning for 5 min at 700°C. All fibers retained >90% of

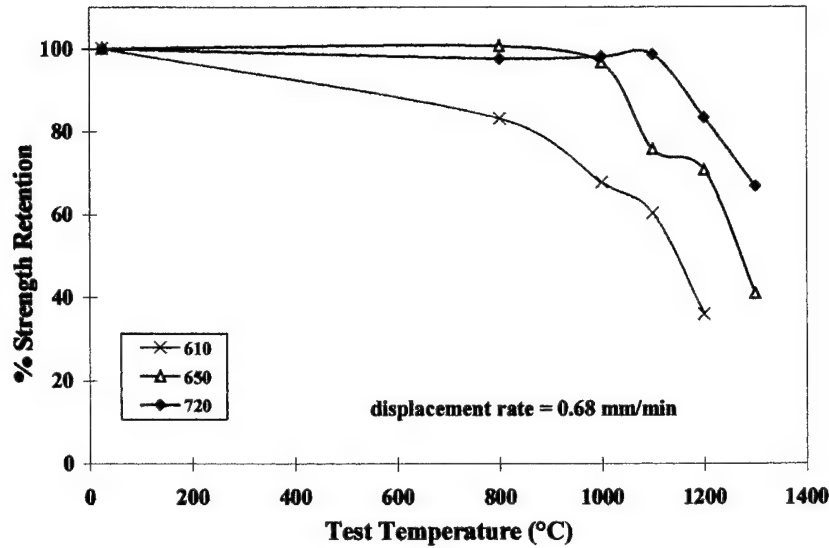


Fig. 10. Comparison of relative tensile strength retention of single filaments of Nextel 610, 650 and 720 fibers at elevated temperature. Nextel 610 fibers retained 70% of room temperature strength up to 1000°C, Nextel 650 fibers up to 1200°C and Nextel 720 fibers up to 1300°C.

their RT strength at 800°C. Using a criterion of 70% strength retention, the temperature capability of the fibers is given in Table 2. Nextel 312 fiber has the lowest temperature capability. Creep has been observed in Nextel 312 fiber at 600°C: a large component of Nextel 312 fiber is amorphous and subject to viscous deformation under load. Nextel 440 fiber, which has lower  $B_2O_3$  content, has improved temperature capability. Nextel 550 fiber, which is  $B_2O_3$ -free, has strength and creep resistance similar to Nextel 610 fiber. Both maintained 70% of RT strength at 1300°C. The high temperature strength of Nextel 650 fiber is 100°C better than Nextel 610 fiber. Nextel 720 fiber showed no

degradation in strand strength up to a maximum temperature of 1400°C used in this testing. Of the fibers most commonly used for high temperature composite applications, Nextel 610 fibers retained 60% of their RT strength at 1300°C, Nextel 650 fibers 80%, and Nextel 720 fibers, 90%.

Fig. 10 shows the high temperature single filament strength of the three composite fibers, Nextel 610, 650, and 720 fibers. The samples of fiber tested were the same as those used for gauge length testing. The relative single filament strength retention of the three fibers was similar to the strand tests. Nextel 610 fibers retained 70% of RT strength up to 1000°C, Nextel 650 fibers to 1200°C and

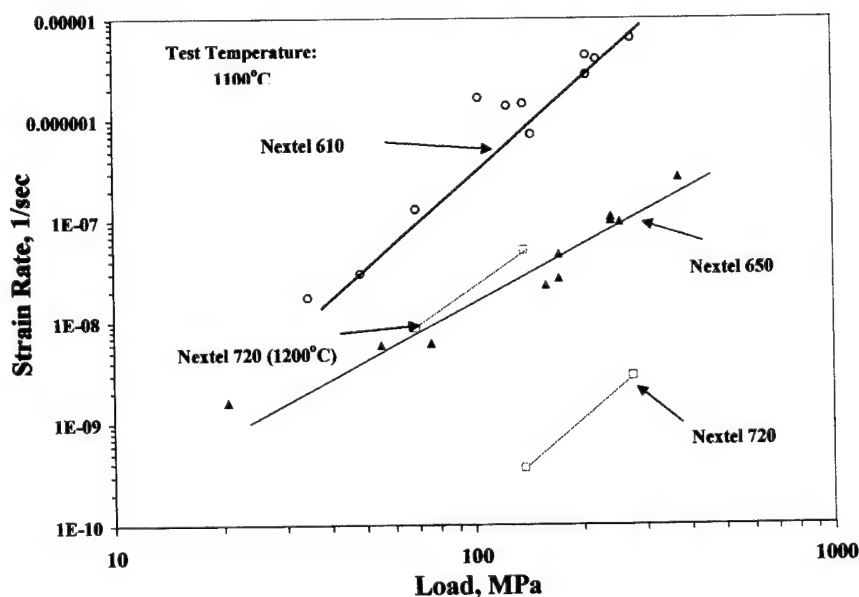


Fig. 11. Comparative creep rate of Nextel fibers at 1100°C as a function of stress. The creep rate of Nextel 610 fibers was one to two orders of magnitude higher than Nextel 650 fiber. The creep rate of Nextel 720 fiber was a further one to two orders of magnitude lower.

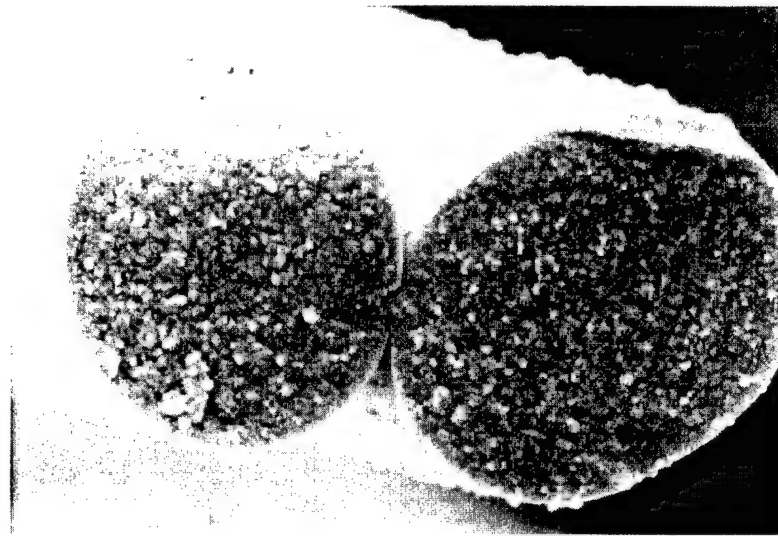


Fig. 12. Scanning electron micrograph of YAG fiber heat treated at 1200°C. Fiber grain size is near 0.1  $\mu\text{m}$ . Bar = 10  $\mu\text{m}$ .

Nextel 720 fibers to 1300°C. Overall, the strand and single filament data suggests an improvement in temperature capability for Nextel 650 fibers relative to Nextel 610 fibers of 100°C; Nextel 720 fiber has a temperature capability a further 100°C higher than Nextel 650 fiber. The relative high temperature strengths of these fibers correlated well with relative creep rates (Fig. 11).

All three composite fibers retained strength to  $\sim 200^\circ\text{C}$  higher temperature in strand testing than single filament testing. The reason for this is strain rate. The strain rate for strand testing (0.05/s) was three orders of magnitude higher than for the single filament testing ( $4 \times 10^{-5}$ /s). A reduction in high temperature strength is expected at temperatures where inelastic deformation mechanisms (i.e. creep) are active, leading to the extension of existing critical flaws and to the formation of new cracks and other flaws. At high strain rates, these time-dependent stress rupture phenomena are minimized and strength is higher. For instance, at 1100°C, the strength of Nextel 610 fiber was 70% of the RT strength of 3.47, or  $\sim 2.5$  GPa. Extrapolation of the creep data in Fig. 11 for Nextel 610 fiber at 1100°C indicates that the expected creep rate at 2 GPa stress is greater than the strain rate for single filament tensile testing ( $4 \times 10^{-5}$ /s). Conversely, for roving testing at the much slower rate of 0.05/s, significant deformation would be expected only at much higher temperature. In fact, stress-strain plots for Nextel 610 single filaments at 1200°C and higher were consistent with a large degree of inelastic deformation. For Nextel 650 fibers, a large amount of inelastic deformation was observed only at 1300°C and for Nextel 720 fibers, 1400°C.

Fig. 11 compares the creep rate at 1100°C of Nextel 610 fiber, Nextel 650 fiber, and Nextel 720 fiber. The creep rate of Nextel 720 fiber at 1200°C is also shown. The creep rate decreased in the order Nextel 610 fiber > Nextel 650 fiber > Nextel 720 fiber. The difference in creep rate was

a factor of 10–100 times between each type of fiber. At a stress of 100 MPa, the strain rate of Nextel 610 was  $1 \times 10^{-6}$ /s, Nextel 650 fiber,  $1 \times 10^{-8}$ /s, and Nextel 720,  $1 \times 10^{-10}$ /s. This magnitude of difference increases fiber temperature capability by  $\sim 100^\circ\text{C}$ . Creep data at 1200°C for Nextel 720 fiber are also included in Fig. 11. The creep rate of Nextel 720 fiber at 1200°C is very similar to Nextel 650 fiber at 1100°C. Using a criterion of 69 MPa stress, 1100°C and a 1% maximum strain in 1000 h, Nextel 610 fibers have a temperature capability of  $\sim 1000^\circ\text{C}$ . Using the same criterion, the temperature capability for Nextel 650 and Nextel 720 fiber is 1080 and 1150°C, respectively. The stress exponent for both Nextel 610 and 720 fibers was very close to 3. The stress dependence of creep for Nextel 650 fiber was 1.8, less than the other fibers. The reason for this is not known; Harmer and coworkers [12] reported no change in stress dependence with  $\text{Y}^{3+}$  doping.

Nextel 720 fiber has the best creep performance of any commercially available polycrystalline oxide fiber. However, further reductions in creep of oxide fibers are possible. For instance, yttrium aluminum garnet (YAG) fibers are the focus of a current developmental program at 3M. YAG is the most creep-resistant polycrystalline oxide [9] and also has very slow grain growth kinetics at high temperature, suggesting that YAG fibers would be an ideal fiber for high temperature composites. Short lengths of YAG fibers have been produced in the laboratory with 700 MPa strength. Bend stress relaxation measurements indicate that these fibers would have a use temperature 50°C higher than Nextel 720 fiber. Fig. 12 shows a YAG fiber heat treated to 1200°C that has a grain size of 0.1  $\mu\text{m}$ . Although not visible by SEM, this fiber contains a substantial amount of porosity. Elimination of this porosity would be expected to reduce creep rates further.

## 7. Conclusions

Nextel 610 fiber has high strength (3.3 GPa), Weibull modulus (11) and excellent thermochemical stability provided by its ultra-fine grained, single-phase  $\alpha$ - $\text{Al}_2\text{O}_3$  microstructure. It maintains excellent high temperature strength and resists creep temperatures up to 1000°C. Nextel 720 fiber comprises a majority of large, 0.5  $\mu\text{m}$ , creep-resistant mullite grains; as a result, Nextel 720 fiber has 150–200°C higher temperature capability than Nextel 610 fiber as measured by high temperature strength and creep testing. It is suitable for load-bearing applications at temperatures as high as 1200°C. The strength (2.0 GPa) and Weibull modulus (7) of Nextel 720 fiber is less than Nextel 610 fiber. Nextel 650 fiber has properties intermediate between Nextel 610 and 720 fibers. Good creep resistance is provided by  $\text{Y}_2\text{O}_3$  doping; good strength and chemical stability is provided by a fine, uniform, high alumina microstructure. Nextel 650 fiber has a strength of 2.5 GPa, a Weibull modulus of 7, and maintains strength and creep resistance as high as 1100°C. Continued improvements in the strength and high temperature performance of oxide fibers the focus of on-going research at 3M.

## Acknowledgements

The assistance of Joe Schneider, Sandy Deppe and Ruth Ann Williams at 3M and Rich Goettler of McDermott Technology in single filament testing is greatly appreciated. The efforts of Jim Reimer for creep measurements and Steve Pittman for SEM microscopy are also acknowledged. Garnet fiber work was supported by DOE under contract DE-FC02-92CE40945. Such support does not constitute an endorsement by DOE of the views expressed in the article.

## References

- [1] Deve HE, McCullough C. Continuous-fiber reinforced Al composites: a new generation. *J Met* 1995;47:33–7.
- [2] Wilson DM, Lieder SL, Lueneburg DC. Microstructure and high temperature properties of Nextel 720 fibers. *Ceram Engng Sci Proc* 1995;16:1005–14.
- [3] Wilson DM, Lieder SL, Lueneburg DC. In: Graves JA, Bowman RR, Lewandowski JJ, editors. *Intermetallic matrix composites III*, Materials Research Society Symposium Proceedings, vol. 350. Pittsburgh, PA: Materials Research Society, 1994. p. 89–98.
- [4] Goering J, Schneider H. Creep and subcritical crack growth of Nextel™ 720 aluminosilicate fibers as received and after heat treatment at 1300°C. *Ceram Engng Sci Proc* 1997;18:95–102.
- [5] Kramb VA, John R, Zawada LP. Notched fracture behavior of an oxide/oxide ceramic-matrix composite. *J Am Ceram Soc* 1999;82:3087–96.
- [6] Levi CG, Yang JY, Dalgleish BJ, Zok FW, Evans AG. Processing and performance of an all-oxide ceramic composite. *J Am Ceram Soc* 1998;81:2077–86.
- [7] Heathcote JA, Gong X-Y, Ramamurty U, Zok FW. In-plane mechanical properties of all-oxide ceramic composite. *J Am Ceram Soc* 1999;82:2721–30.
- [8] Wilson DM, Visser LR. Nextel™ 650 ceramic oxide fiber: new alumina-based fiber for high temperature composite reinforcement. *Ceram Engng Sci Proc* 2000;21:363–73.
- [9] French, Zhao J, Harmer M, Chan H, Miller J. Creep of duplex microstructures. *J Am Ceram Soc* 1994;77:2857–65.
- [10] Sato E, Carry C. Yttria doping and sintering of submicrometer-grained  $\alpha$ - $\text{Al}_2\text{O}_3$ . *J Am Ceram Soc* 1996;79:2156–60.
- [11] Pint BA, Garrat-Reed AJ, Hobbs LW. Possible role of the oxygen potential in enhancing diffusion of foreign ions on  $\alpha$ - $\text{Al}_2\text{O}_3$  grain boundaries. *J Am Ceram Soc* 1998;81:305–14.
- [12] Bruley J, Cho J, Chan HM, Harmer MP, Rickman JM. Scanning transmission electron microscopy analysis of grain boundaries in creep-resistant yttrium- and lanthanum-doped alumina microstructures. *J Am Ceram Soc* 1999;82:2865–70.
- [13] Van Der Zwaag S. The concept of filament strength and the Weibull modulus. *J Test Eval* 1989;17:292–8.
- [14] Hay RS, Boakye EE, Petry MD, Berta Y, Von Lehnden K, Welch J. Grain growth and tensile strength of 3M Nextel 720™ after thermal exposure. *Ceram Engng Sci Proc* 1999;20:153–63.
- [15] Kumagai M, Messing GL. Controlled transformation and sintering of a boehmite sol-gel by  $\alpha$ -alumina seeding. *J Am Ceram Soc* 1985;68:500–5.
- [16] Deve HE, McCullough C. Fiber coating performance in TiAl. In: Graves JA, Bowman RR, Lewandowski JJ, editors. *Intermetallic matrix composites III*, Materials Research Society Symposium Proceedings, vol. 350. Pittsburgh, PA: Materials Research Society, 1994. p. 119–24.
- [17] Cantonwine PE. Processing and properties of an alumina composite fiber. PhD thesis, University of Virginia, 1999.
- [18] Lawn BR, Wilshaw TR. Fracture of brittle solids. Cambridge: Cambridge University Press, 1975 (p. 58–61).
- [19] Sonderman D, Jakus K, Ritter JE, Yuhaski S, Service TH. Maximum likelihood estimation techniques for concurrent flaw subpopulations. *J Mater Sci* 1985;20:207–12.
- [20] Lara-Curzio E, Russ CM. On the relationship between the parameters of the distributions of fiber diameters, breaking loads, and fiber strengths. *J Mater Sci Lett* 1999;18:2041–4.
- [21] Wilson DM. Statistical strength of Nextel™ 610 and Nextel™ 720 fibers. *J Mater Sci* 1997;32:2535–42.
- [22] Hurst JB, Hong WS, Gambone ML, Porter JR. ASTM single fiber room temperature test standard development. American Society of Mechanical Engineers, paper 98-GT-567. International Gas Turbine and Aeroengine Congress, Stockholm, Sweden, 1998.



# The characterization of low cost fiber reinforced thermoplastic composites produced by the *DRIFT*<sup>TM</sup> process

Tim Hartness<sup>a</sup>, George Husman<sup>a</sup>, John Koenig<sup>a,\*</sup>, Joel Dyksterhouse<sup>b</sup>

<sup>a</sup>*Southern Research Institute, 757 Tom Martin Drive, Birmingham, AL 35211, USA*

<sup>b</sup>*Polycomp Inc., 6737 N. Lakeshore Drive, Cross Village, MI 49723, USA*

Received 10 November 2000; revised 15 February 2001; accepted 18 February 2001

---

## Abstract

A new, low cost process for hot-melt impregnation of continuous reinforcing fibers with thermoplastic polymers is described. This technique can be used to fabricate various product forms including discontinuous, long-fiber products for compression molded parts, continuous fiber products for pultrusion, filament winding, and woven fabric applications. Mechanical data are presented for composites with various fiber and polymer combinations. Effects of fiber orientation and length on mechanical properties are discussed, and the effect of fiber–polymer bonding on impact strength and microstructure are shown. It is shown that the low cost and high performance achieved with this approach has the potential to expand applications of thermoplastic composite materials. © 2001 Elsevier Science Ltd. All rights reserved.

**Keywords:** B. Mechanical properties; Thermoplastic composite

---

## 1. Introduction

Thermoplastic composites have application in a vast variety of consumer and industrial products. The current US market for these materials is over one billion pounds per year, more than half going into automotive applications. The markets for thermoplastic composites are expected to continue to grow dramatically over the next several years.

Most of the thermoplastic composite materials used today are short fiber, compounded products consisting of glass fibers (typically 10–40% by weight fiber content) in a low-cost polymer matrix, e.g. polypropylene, polyethylene, nylon, polycarbonate, polyester, etc. These compounded products are typically produced by blending chopped glass fibers and polymers in a high shear extruder, and extruding a composite rod that is chopped into pellets for injection molding processing. This process grinds the glass fibers to very short lengths (typically <2 mm). Although these composites have improved properties over the unreinforced matrix polymer, the full advantage of the reinforcing fiber is not achieved. Depending on the polymer used, these compounded products typically sell for \$0.85–1.50 per pound (\$1.87–3.30 per kg).

Several longer fiber (~10–13 mm) compounded pellet products and glass thermoplastic composite sheet products

are commercially available. The advantage of these products is that they provide better translation of fiber properties and thus higher composite structural performance. The processes used to make these products are generally more expensive than standard compounding, typically selling for \$1.20 to more than \$3.00 per pound (\$2.64–6.60 per kg). The worldwide market for these materials is estimated to be about 60 million pounds. The market for continuous fiber thermoplastic composites is very limited due to the high cost of producing these products. The market for thermoplastic composite products using fibers other than glass, such as carbon, aramids or other fibers, is also very limited by higher costs.

Recently, a novel hot melt impregnation technology has been developed that allows complete impregnation of continuous fibers with thermoplastic polymers at very high production rates, providing high quality, low cost thermoplastic composites. This technology, called *DRIFT* (Direct ReInforcement Fabrication Technology), produces products that can be made as continuous rods, tapes and pultruded shapes, or they can be chopped into pellets of any length for injection or compression molding. The process has been shown to work well with glass, carbon, aramid, and other polymer fibers and also with a wide variety of thermoplastic polymers. The superior penetration and wetting of the yarns achieved results in excellent mechanical properties and easier downstream processing

---

\* Corresponding author.

for fabricated components. The result is the ability to produce a wide variety of high-performance, thermoplastic composite products at very low costs. This paper presents the fabrication approach and the resulting microstructures and mechanical properties for various polymer/fiber combinations.

## 2. Impregnation process

The *DRIFT* process [1] is a simple, robust hot-melt impregnation technique that allows complete impregnation and wetting of continuous fibers at very high operating speeds. The process is shown schematically in Fig. 1. The components of the impregnation line consist of a fiber creel with tension control, a fiber heating oven, impregnation die which is fed polymer by a standard extrusion machine, a chiller to cool the prepreg, and a puller that controls the line speed. The impregnated product can be taken up as a continuous tape/ribbon, which is its form as it exits the impregnation die, or it can be collapsed into a continuous rod. Other product cross-sections are possible by forming the product as it is cooled. A chopper can also be put in-line to produce flakes or pellets of desired lengths, typically 0.24–1" (6.35–25.4 mm) or longer. Glass contents from 10 to 70% (by weight) have been demonstrated with a control of  $\pm 2\%$ . The limits of the process for fiber content and control have not yet been established. The ultimate result of this process is the ability to produce very high quality composite products, with a wide variety of fibers and polymers and in a variety of product forms, at costs similar to the lowest cost compounding processes.

Material selections for the impregnation process are important considerations. Polymer melt viscosity and melt stability are important factors. High melt flow polymers (melt flow index  $> 20$  g/10 min) work well in the process. Lower bounds for melt flow have not yet been determined. Melt stability of the polymer is also important to be sure that

the polymer is not degraded during the impregnation process or by downstream molding processes. While the impregnation process is quite fast, the dwell time in the impregnation die can be long. Production dies are being designed to minimize this dwell time and the die can be purged with inert gas to prevent oxidation, but high melt stability is desirable. Again, the limits on this parameter have not yet been established.

Fiber parameters are also important considerations. Yarns or rovings must be untwisted so that spreading can be achieved and all filaments can be fully wet out. Fibers must be capable of withstanding the high temperatures of the impregnation process as well as downstream molding. Glass, carbon, aramid, and LCP fibers have all been impregnated with great success. The yield of the fiber is important primarily for throughput or economic reasons. Glass rovings with yields from 750 to 113 yards/pound (1800 to 275 m/kg) have been impregnated with equal ease. Similarly both 12 and 48 K carbon impregnate easily.

Sizing on the fibers is very important for the same reasons discussed above, i.e. the sizing must allow spreading and should not be degraded by the impregnation or downstream molding conditions. Sizing is also an important consideration in the wetting and bonding of the polymer. Typically, sizing chemistries are proprietary to the fiber manufacturer. Therefore, it is important to work closely with the fiber manufacturer to determine the sizing that will be most compatible for the polymer selected.

The majority of the process and product development efforts accomplished to date have focused on E-glass impregnated with polypropylene, polyethylene, and nylon. Other fibers have been demonstrated, including S-glass, carbon, aramid, and LCP. Other polymers that have been demonstrated include polyurethane, polyphenylene sulfide, polyester, and polycarbonate.

The polypropylene material used to date has been a BP/Amoco polypropylene homopolymer, Accpro grade 9965. This is a high flow nucleated resin designed for compounding.

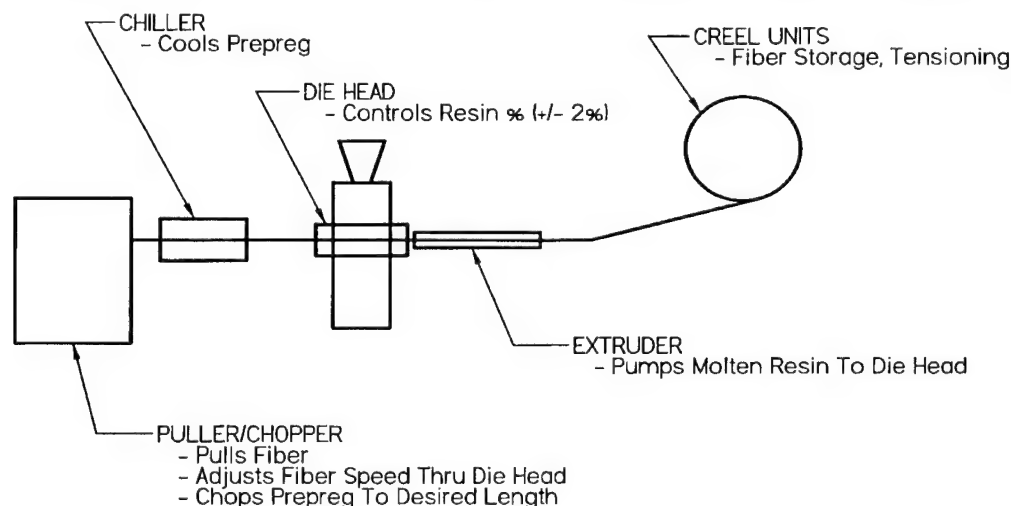


Fig. 1. *DRIFT* process.

The resin has good modulus at 2100 MPa (305 kpsi). Some limited product development has been done using a copolymer for improved toughness.

The polyethylene material used has been an injection-molding grade with high flow made by Equistar called Alathon ETP, XH5057-2. The material has a melt index of 57 g/10 min. The flexural modulus is reported to be 723 MPa (105 kpsi). There is, of course, special interest in the ability to use recycled polyethylene, and this will be pursued in the near future.

The nylon product development to date has been limited to nylon-6. A heat-stabilized grade from M.A. Hanna, 600A HS Natural A, is the virgin polymer that has been evaluated. This polymer has a reported viscosity of 50–52 (Formic Relative, ASTM D789). The dry, as-molded flexural modulus is 2651 MPa (385 kpsi). A recycled nylon-6 product from Advanced Textile Recycling, ATRON 601B, has also been evaluated.

Composite data for each of the polymers listed above are reported in this paper.

### 3. Mechanical properties

Mechanical properties of discontinuous fiber/thermoplastic composites can vary tremendously depending on the process used to fabricate the test specimens. Fiber length and orientation directly affect the mechanical properties of a composite. The process used to fabricate test specimens can directly affect the orientation and length of the fiber in the test specimen. This issue is often overlooked or unreported in testing of these materials and therefore, makes it nearly impossible to compare data from one source to another. This behavior is clearly illustrated in Table 1, which compares tensile and impact data for E-glass/polypolypropylene composites made with the *DRIFT* process. The mechanical

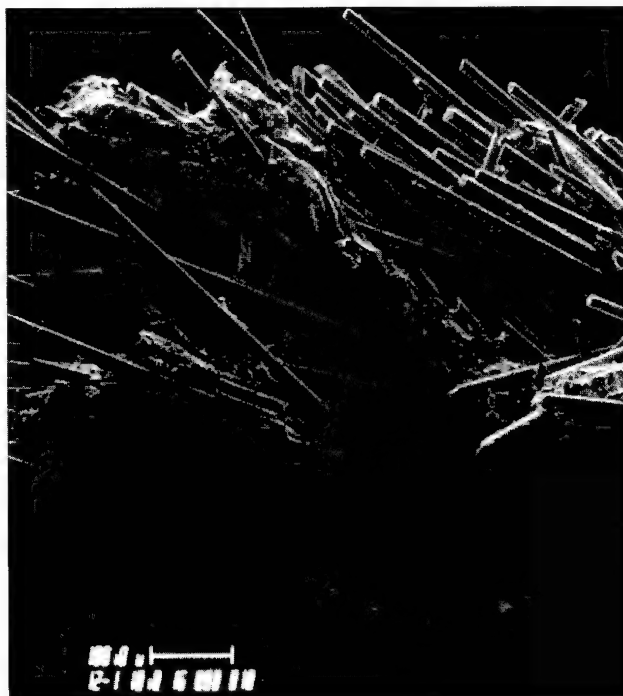


Fig. 2. Fractured surface PP/E-Glass (120 $\times$ ).

properties are also a function of the constituents, sizing, wetting and variability of bond, fiber resin distribution, and specimen/test design.

For Sample 1, test specimens were fabricated by injection molding using a standard high shear screw. Although the initial fiber length in the molding pellets was 13 mm (0.5"), the fiber length in the molded specimens was  $\sim$ 2 mm. This fiber damage caused by the molding process results in mechanical properties that compare very closely with product literature for standard compounded, short fiber composites, and thus the

Table 1  
Comparative properties 40% by weight E-glass/polypolypropylene

Sample number	Material description	Tension strength MPa (ksi)	Tension modulus GPa (Msi)	Tension strain (%)	Impact notched Izod kJ/m (ft lbs/in)
1	<i>DRIFT</i> product. Injection-molded specimens. Starting fiber length in chip 12–13 mm. Fiber length in specimens $\sim$ 2–3 mm	62.1 (9)	8.97 (1.3)	1.2	0.121 (2.26)
2	<i>DRIFT</i> product. Ram extrusion/compression-molded. Fiber length in specimens 12–13 mm	75.9 (11)	7.59 (1.1)	1.42	0.548 (10.25)
3	<i>DRIFT</i> product. Ram extrusion/compression-molded. Fiber length in specimens 25 mm	82.8 (12)	9.66 (1.4)	1.15	0.626 (11.7)
4	<i>DRIFT</i> product. Ram extrusion/compression-molded. Fiber length in specimens 25 mm. Same glass fiber but with PP compatible size	82.8 (12)	8.28 (1.2)	1.37	1.383 (25.85)

Table 2  
*DRIFT™* product data

Material description	Tension strength MPa (ksi)	Tension modulus GPa (Msi)	Tension strain (%)	Impact notched Izod J/m (ft lbs/in)
40% E-Glass/polyethylene. Ram extrusion/compression- molded. Fiber length 25 mm	110 (16)	6.9 (1)	2.23	1.360 (25.41)
40% E-Glass/Nylon-6. Injection-molded specimen. Starting fiber length in chip 25 mm. Fiber length in specimens ~2–3 mm	145 (21)	11.7 (1.7)	1.7	0.209 (3.9)
60% E-glass/polypropylene. Compression-molded. Continuous fiber/unidirectional	669 (97)	29.7 (4.3)	2.42	No break
50% S-2 glass/polypropylene. Compression-molded. Woven fabric from <i>DRIFT</i> tape. Balanced 0/90 orientation, 2 × 2 twill	455 (66)	17.4 (2.52)	3	No break

full potential benefits of the reinforcing fibers are not achieved.

For Sample 2, test specimens were machined from panels fabricated using a ram extrusion/compression molding process. Again 13 mm fiber molding pellets were used, and this fiber length was maintained in the fabricated panel. The resulting tensile modulus was slightly lower than Sample 1. This is attributed to slightly less fiber orientation in the specimens from the compression-molded panel. According to a study by Thomason and Vluc [2], which validated the modulus prediction model of Cox [3], maxi-

mum modulus of elasticity is nearly achieved when the aspect of the fiber exceeds 100. For the glass fiber diameter of these samples ( $\sim 16 \mu\text{m}$ ), near maximum modulus would occur at a fiber length of 1.6 mm. Therefore, the modulus of elasticity for both Samples 1 and 2 should be about the same, except for orientation effects. The tensile strength for Sample 2, on the other hand, is over 20% higher, and the notched Izod impact strength increased by nearly a factor of 5. These higher properties are clearly related to increased fiber length.

To look further at fiber length effects, Sample 3 panel was



Fig. 3. Fractured surface PE/E-glass (700 ×).

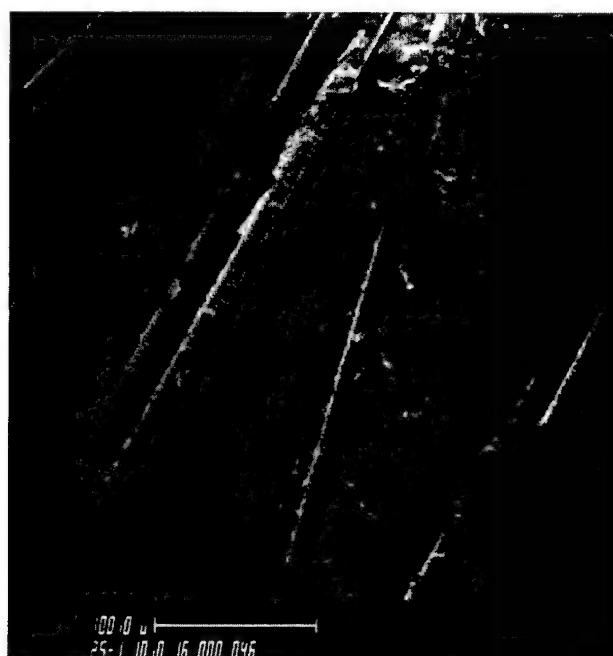


Fig. 4. Fractured surface PE/E-glass (250 ×).

prepared similar to Sample 2, except that 25 mm fiber molding pellets were used, and this fiber length was maintained in the fabricated panel. The resulting tensile properties and impact properties were basically the same as Sample 2. Higher tensile strength was anticipated for Sample 3 but did not occur. This could be more a factor of test geometry rather than true materials behavior. That is, can a 13-mm-wide test specimen measure the true tensile strength of a composite with 25 mm randomly oriented fibers? Similarly, it is not clear whether the impact data represents a limiting case for the material or a limiting case for the test.

Sample 4 panel was prepared identically to Sample 3 except that the glass fiber had a different sizing than all the other samples. This new sizing was identified as polypropylene compatible, while the sizing used in all the other samples was a high temperature size. The resulting tensile data was again basically the same as Samples 2 and 3, but the impact data more than doubled. This is attributed to increased fiber-matrix bonding, which was validated by SEM pictures taken

of the impact specimen fracture surfaces, shown in Fig. 2.

A summary of composite data with other polymers and fibers is shown in Table 2. This table also shows some data for continuous, unidirectional composites made from *DRIFT* products. These data eliminate the confusion of fiber length and orientation and demonstrate the ability of the *DRIFT* process to produce composite products that provide full translation of fiber properties.

All mechanical property data generated to date have been excellent, demonstrating predicted translation of fiber properties. Comparisons with product literature for similar composite products typically show that *DRIFT* products give equivalent or better results in all properties, with the exception of impact strength. *DRIFT* products generally have higher impact properties, which is attributed to excellent fiber wetting and bonding. This can be seen in the SEM pictures of the polypropylene composite impact specimens in Fig. 2. Similar pictures for polyethylene and nylon composites are shown in Figs. 3 and 4.

1200															
TEN-1		160 MPa		TEN-12	66 MPa	TEN-11	67 MPa	TEN-10	62 MPa	TEN-9	67 MPa	TEN-8	70 MPa	TEN-7	104 MPa
TEN-2		95 MPa													
TEN-3		95 MPa													
TEN-4		62 MPa													
TEN-5		62 MPa													
TEN-6		56 MPa													
FLEX-1		FLEX-5 (PHYSICALS)		IZOD-12	FLEX-12	IZOD-11	FLEX-11	IZOD-10	FLEX-10	IZOD-9	FLEX-9	FLEX-13 (PHYSICALS)			
IZOD-1		IZOD-5													
FLEX-2		FLEX-6													
IZOD-2		IZOD-6													
FLEX-3		FLEX-7		IZOD-16 (PHYSICALS)	FLEX-16	IZOD-15	FLEX-15	IZOD-14	FLEX-14	IZOD-13	FLEX-13				
IZOD-3		IZOD-7													
FLEX-4		FLEX-8													
IZOD-4		IZOD-8													
1200															

Fig. 5. Cutting plan showing orientation effects on tensile strength.

The properties of long fiber thermoplastic composites are strongly influenced by the orientation of the fibers as governed by the forming process. This is illustrated in Fig. 5, which shows the tensile strengths of an extruded/compression molded 40% glass/polypropylene plate. The strength is highest near the edge due to the flow pattern. It also has a preferred direction, probably due to the direction of charge placement. It is nearly isotropic at the center.

#### 4. Conclusions

The use of discontinuous, long fiber thermoplastic composites is highly desirable for a wide variety of automotive and other applications that need higher strength and impact resistance. Such applications are already increasing and are expected to accelerate dramatically over the next several years. Three key factors that are required for this growth of these products are: (1) availability of high quality, low cost products, (2) high rate molding processes that maintain the fiber length in the molded part, and (3) the development of an understanding of the mechanics of these materials. The *DRIFT* process effectively addresses the first of these factors. Companies in the molding equip-

ment industry are addressing the second factor. Boland presents a good example of this in a recent paper [4].

The successful development of *DRIFT* process and the resultant improvement in strength, impact properties and cost provide opportunities for expanded applications of thermoplastic composites. This technology provides the highest performance composite products at costs approaching the lowest cost compounded products.

The key, however to the application of *DRIFT*, and indeed, any long fiber thermoplastic, is the development of appropriate design tools and control of the key parameters that govern the behavior of these materials in application.

#### References

- [1] Dyksterhouse JA. US Patent 5,911,932.
- [2] Thomason JL, Vlug MA. Influence of fiber length and concentration on the properties of glass fibre-reinforced polypropylene. *Composites: Part A* 1996;27A:477–84.
- [3] Cox HL. The elasticity and strength of paper and other fibrous materials. *British Journal of Applied Physics* 1952;3:72.
- [4] Boland RN. Applications for extrusion deposit/compression molding, SAMPE-ACCE-DOE Advanced Composites Conference, September, 27–28, 1999.

## “Assessment of Metal Matrix Composites for Innovations” — intermediate report of a European Thematic Network

Hans Peter Degischer<sup>a,\*</sup>, Peter Prader<sup>a</sup>, Christopher San Marchi<sup>b,1</sup>

<sup>a</sup>*Institute of Materials Science and Testing, Vienna University of Technology, Karlsplatz 13/E308, A-1040 Wien, Austria*

<sup>b</sup>*Laboratoire de Metallurgie Mecanique, Ecole Polytechnique Federale de Lausanne (EPFL), CH-1015 Lausanne, Switzerland*

Received 2 September 2000; revised 29 December 2000; accepted 26 January 2001

### Abstract

The Thematic Network “Assessment of Metal Matrix Composites for Innovations” (acronym MMC-ASSESS) is a consortium of 21 partners from industry, research organisations and universities involved in research, development and application of metal matrix composites (MMC). The general goal of the project is to increase market acceptance of MMC by collecting and evaluating information related to the engineering potential of these materials. The working groups of the network are referring to production, characterisation and properties as well as modelling and applications of MMC. These topics are considered as well specifically for the four categories of MMC: particulate, short fibre and whisker, continuous fibre, and monofilament reinforced metals. A web page has been established (<http://mmc-assess.tuwien.ac.at/>) as an ongoing dissemination activity. An intermediate report on the network’s activities is presented, which started in October 1998 by funding of the European Commission for a 36 months period. © 2001 Elsevier Science Ltd. All rights reserved.

**Keywords:** A. Metal-matrix composites (MMCs); A. Fibres; B. Physical properties; E. Machining; Application

### 1. Introduction

Metal matrix composites (MMC) have been the subject of scientific investigation and applied research for about three decades, but these advanced materials have been introduced only gradually in engineering components, such as electronic heat sinks, automotive drive shafts, high speed train brake rotors, jet fighter aircraft fins or combustion engine components. Their greatest asset is the large variety of properties offered in combining many possible matrices and reinforcements, which allows to tailor material properties to meet specific and challenging requirements. On the other hand, this variety gives rise to a confusing spectrum of materials and property data, which complicates their introduction into engineering products. The main target of this network activity [1] is to increase market acceptance by collecting, evaluating and disseminating information describing the outstanding potential of MMC with their specific limitations.

The Thematic Network, bearing the acronym “MMC-

Assess” [2], has been approved by the European Community for the period between October 1998 and September 2001 within the 4th Framework Program and brings together 21 partners [3] from industry (6, one of which is SME), applied research institutions (8), universities (6) and the German Materials Society. The open structure of the network encourages the co-operation of additional experts linked to the network by their national representatives.

### 2. Working methodology

The collection and evaluation of MMC-relevant information is organised according to the main categories of MMC by the formation of material task groups referring to the four general geometries of reinforcement: particulate (PRM), short fibre and whisker (SFRM), continuous fibre (CFRM), and monofilament reinforced metals (MFRM). Different as the view points for each of the MMC categories may be, they have common methodologies, which are clustered within 11 research topics with respect to their common problems of processing, specification, test methods, modelling, reliability and marketing listed in Table 1.

Fig. 1 points out the structure of the MMC-Assess working methodology: The main working tools comprise electronic communication, regular meetings, workshops and

\* Corresponding author. Tel.: +431-58801-30811; fax: +431-58801-30899.

E-mail addresses: [sek308@pop.tuwien.ac.at](mailto:sek308@pop.tuwien.ac.at) (H.P. Degischer), [chris.sanmarchi@epfl.ch](mailto:chris.sanmarchi@epfl.ch) (C. San Marchi).

<sup>1</sup> Tel.: +41-21-693-5821; fax: +41-21-693-4664.



Table 1  
MMC-Assess working groups on material independent topics [2]

1. Primary processing (synthesis) and recycling
2. Working and final shaping (secondary processing)
3. Metallography and quantitative description
4. Bonding and interface formation
5. Modelling and simulation
6. Static/dynamic mechanical testing and properties
7. Physical properties and test conditions
8. Surface treatment, corrosion and wear resistance
9. Quality control and non destructive testing
10. Existing and potential applications: (a) aerospace, (b) automotive, (c) electronics, (d) machinery, sports, dual use
11. Pros and cons, Assessment (SWOT analysis)

seminars and aim for the generation of easily accessible information to be disseminated clearly via lectures, workshops, the Network's web page [6] and a final public presentation planned.

### 3. Activities to date

The working groups have been established, linking almost 100 experts to the Network [3]. Links are established to MMC consortia in the USA [7] as well as with Eastern European countries and the CIS [8]. Four general assemblies have taken place to date: Oct.'98/TU-Wien/AT, April '99/NPL-Teddington/GB, Oct.'99/Hamburg/DE, March 2000/Madrid/ES [4]. The first annual progress report [8] states the deliverables achieved during the first working period and the planned activities. Assessed information is openly available.

Table 2  
Index of MMC-Assess web page [6]

URL: <a href="http://mmc-assess.tuwien.ac.at/">http://mmc-assess.tuwien.ac.at/</a>	
Main pages	
"who we are"	Information about MMC-Assess and contact addresses
"what are MMC's"	MMC terminology
"applications"	Existing and potential applications
"material data"	Data and information on selected MMC
"supplier"	Producers of MMC or components (contacts)
"literature"	Selected publications correlated to topics
"conferences"	Permanently updated MMC events
"mmc-links"	Structured links to MMC on the WWW
"news"	MMC-Assess activities: meetings, seminars, workshops
"members"	Network documents (restricted for network partners)

The main outcome to date is the launching of a web page for the network [6]. This serves as a state-of-the-art presentation tool and will be expanded continuously during the duration of the project. It is maintained by the Institute of Materials Science and Testing in Vienna and is also registered by search engines for the World Wide Web. Table 2 gives an overview of its current structure, the content of which is continuously updated. The web page is used as a central tool for stimulating collaboration within the research community, and also as a publishing medium for results of the Network. It aims to enhance the dissemination of

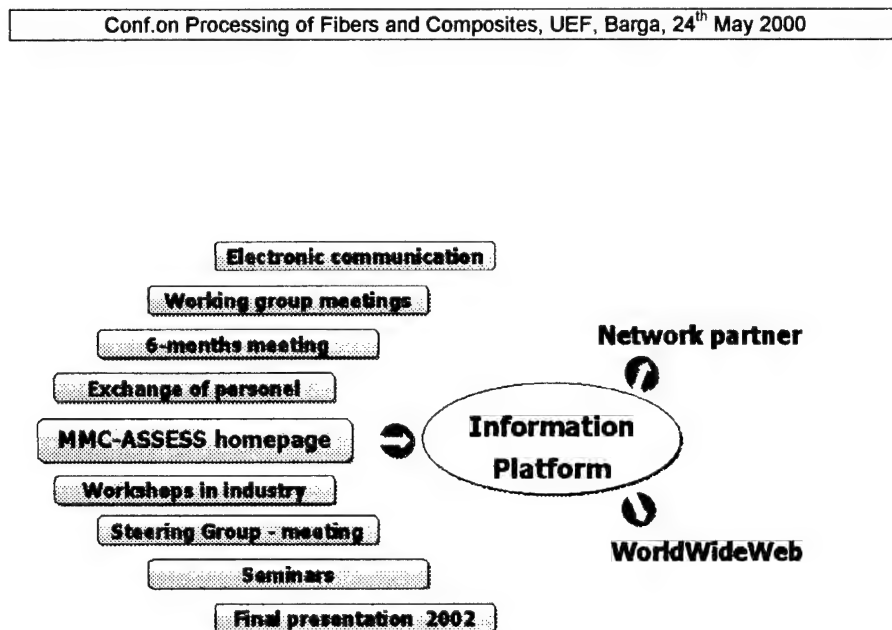


Fig. 1. Structure of working methodology and integration of web page [6].

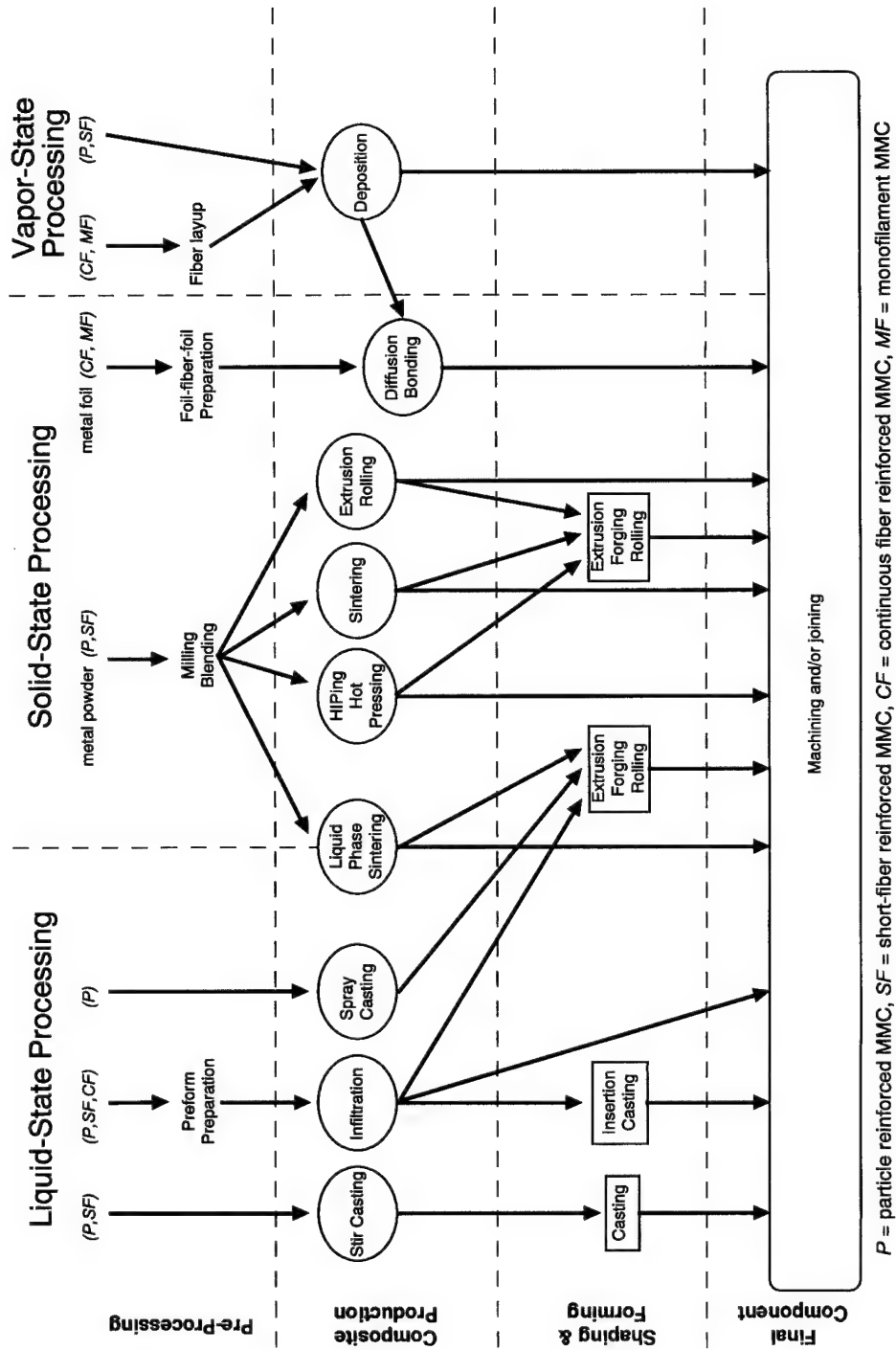


Fig. 2. Manufacturing steps and different processes for the production of metal matrix parts [6].

Table 3

Index of glossary of terms specific to MMC [9]

(1) General definitions	Composite, Hybrid composite, Metal Matrix Composite, Metal matrix, Ingredient materials, Reinforcement, Interface
(2) Reinforcement	Continuous reinforcement, Continuous fibres, Monofilaments, Discontinuous reinforcement, Discontinuous reinforcement, Particulates, Dispersoids, Platelets, Short fibres, Whiskers
(3) Types of MMC	Particulate reinforced (PRM), Dispersoid reinforced, Cermets, Short fibre reinforced (SFRM), Whisker reinforced (WRM), Continuous fibre reinforced (CFRM), Monofilament reinforced (MFRM), MMC designation, Cellular metals (metal foams)
(4) Processing steps	Pre-processing, Preform, Hybrid perform, Primary processing of composites, Continuous MMC primary process, Secondary processing, Consolidation of MMC, MMC insertion casting, Partially reinforced metal component, In-situ MMC
(5) Liquid metal processing	Stir casting, Compocasting, Semi-solid forming, Thixocasting, Infiltration (Spontaneous, Forced, Pressure, Vacuum, Gas pressure, Mechanical pressure, Squeeze casting, Pressure die), Pressure assisted investment casting, Centrifugal-, Ultrasonic-, Lorentz force-infiltration, Spray casting
(6) Solid state processing	MMC diffusion bonding, Foil-fibre-foil method, Wire winding, Powder cloth method, Powder consolidation, MMC sintering, MMC liquid phase sintering, MMC hot-, MMC cold-, MMC hot isostatic- (HIP), MMC cold isostatic pressing (CIP), MMC powder rolling, -extrusion, -forging
(7) Coating processes	Coating processes (Vapour deposition, Electrolytic, Matrix coated fibre method), Vapour infiltration, Electrolytic infiltration, Electrolytic co-deposition, Plasma spray method, Slurry tape casting
(8) Role within the production chain	Ingredient material supplier or producer, MMC supplier or producer, MMC component supplier or producer, MMC end-user, Consumer

information on MMC relevant to engineering and it is also a hub for interaction between the group members. A section for job offerings and searches has been added to promote scientists in this special field of technology.

The following indicates some examples of the provided

information referring to the topic of this conference: a glossary on MMC relevant terminology [9] has been constructed, the index of which is given in Table 3. A data bank on MMC producers, suppliers and users has been prepared at EPFL [10]. Some material suppliers and

Table 4

MMC selected for focused collection of information [4]

MMC status and category	Primary processing (supplier)	Designation
Industr. PRM (commercially available)	Stir cast (Duralcan, Hydro) Powder consolidated (AMC) Noble metal (funct.mat.)	AA6061/Al2O3/10-22 p, A35/SiC/20 p AA2xxx/SiC/25 p (To be specified)
Experiment. PRM (R and D status)	Gas pressure infiltrated Squeeze cast (GKSS) In-situ MMC (ISPRAM) PM processed (PEAK) Hot isostatic pressing (VTT)	AlSi7/SiC/>65 p Mg-matrix (to be specified) AA2618 etc./TiB2/8 p DISPAL S250 UNS31803 /Cr3C2/30 p
Industrial SFRM/WRM	Indirect squeeze casting (KS) Powder consolidation (DWA)	AlSi12CuNiMg/Al2O3-Saffil/20s AA2xxx/SiC/x w
Experiment. SFRM	Squeeze cast (GKSS) Hot press. Coated fibres (SAS)	Mg-alloy/C-T300/x s Cu/C K1100/ 40 s (chopped)
Industrial CFRM	Gas pressure infiltration (3M)	AA1099/Al2O3-N610/UD50 f
Experiment. CFRM	Squeeze cast (EMPA) Pressure assisted investment casting (RWTH) Gas pressure infiltr. (LKR)	AM10/C-T300/3D x-y-z f AlZn6Mg/Al2O3-Altex/UD50f AA1085/C-HM/UD60f
Industrial MFRM	Fibre-foil-fibre diff.bonding (ARC)	Ti6V4Al/SiC-TrimarcHSH/UD50m
Experiment. MFRM	Consolidating coated fibres (DLR, DERA)	Timetal 834/ SiC-SCS6/UD 50m Timetal 834/SiC-SM1240/UD33m

applications are presented in Ref. [6] together with the internet links to the corresponding companies. References to the literature as well as to experts in industry and research institutions are provided. A workshop on the application of X-ray computed tomography in material science has been organised by INSA/Lyon [11] dedicated to the possibilities offered by this technique to determine the three dimensional distribution of reinforcement and of defects.

A systematic overview on MMC processing was designed as shown in Fig. 2 defining four manufacturing steps:

- the pre-processing, i.e. preparation of the ingredients, eventually perform fabrication,
- the processing of the composite, i.e. establishing the bonding,
- the secondary processing of consolidation and/or shaping,
- the finishing operations of MMC components, e.g. joining, machining and surface treatments.

The processing techniques are classified by the matrix condition during composite production: solid, liquid or vapour phase. These processes can be applied in different ways to incorporate the different shapes of reinforcement: particulates (P), short fibres and whiskers (SF), continuous fibre tows (CF), and monofilaments (MF).

Some representative examples of MMC systems have

been selected to prepare a detailed description of the different MMC categories, which will demonstrate the presentation of material data. Table 4 [4] lists the materials and the abbreviations of the suppliers of industrial products and of experimental materials indicating future potential. Examples of data collected for PRM, CFRM and MFRM can be found in the material data section of the web page [6]. Some descriptions referring to the topics of processing, interfaces, modelling and mechanical properties are incorporated as well in the material data matrix [6].

Table 5 [8] indicates the deliverables achieved by the different topical working groups and the network's co-ordination after the first year of operation.

#### 4. Future activities

The web page [6] will be complemented further, especially the sections on material data and applications. A "Who's who in MMC" is in preparation. Special working group meetings and workshops will be dedicated to assess the collected information to be presented in the web page, where all activities are announced. The final presentation of the results of the network will take place during the MMC VIII conference of the British Institute of Materials on 26/27 November 2001 in London and an 'MMC school' is foreseen in 2002 to disseminate the results.

#### 5. Conclusion

The midterm of the network's program has passed: the working groups are operating with respect to the topics and the material tasks. The materials to start with the data presentation have been selected and the first data have been collected and are provided on the network's web page step by step. Although the web page is still in a preliminary stage, it is already consulted frequently from all over the world. All interested in studying, producing, supplying, designing, using, or marketing MMC are invited to visit the network's web page [6] and to provide additional information and feed back.

#### Acknowledgements

The authors acknowledge the funding by the European Commission, the assistance of the scientific officer Dr H.L. Schmidt and the effort of all the active partners and collaborating experts, particularly A. Mortensen for enabling this presentation.

#### References

- [1] A road to European Co-operation, Thematic Networks activity, IMT-Programme 1994/98, EU-Commission DGXII, EU 18197, Brussels, 1999. p. 144–145 (available via EU-CORDIS web site [5]).

Table 5  
Deliverables of the Network MMC-Assess achieved after the 1st year [8]

Topic	Intermediate results
Processing	Data base on producers, users, research laboratories Definition of MMC-terminology ('glossary')
Microstructure and interfaces	Tables of characterisation methods List of chemical reactions of constituents of MMC Workshop on computed X-ray tomography
Modelling	Description of different MMC-models (PRM, CFRM/MFRM)
Mechanical Properties	Basic references Criteria for assessing data (e.g. Young's modulus)
Physical Properties	Examples of physical property data
Corrosion, wear, surface treatment	Examples of case studies on corrosion phenomena Case studies on wear resistance of PRM and SFRM Selection of relevant surface treatments
NDT, quality control	Proposal of quality criteria List of test methods
Application	Enquiry on market penetration and further potential
Dissemination	Opening of a web page: 'mmc-assess.tuwien.ac.at' Information exchange with USA, Eastern Europe and Japan Presentations at European material conferences

- [2] Assessment of Metal Matrix Composites for Innovations (MMC Assess), Contract N(ERB BRRT-CT98-5061, work program BET2-261, TU-Wien, Nov. 1998 (Abstract available via EU-CORDIS web site [5]).
- [3] Degischer HP. Minutes of the Kick-Off Meeting in Vienna Oct. 22nd/23rd, 1998, final version, TU-Wien, 5.2.1999 (available via Ref. [6]).
- [4] Degischer HP. Minutes of the 18 Months Progress Meeting, Madrid, March 16th/17th, 2000, TU-Wien (available via Ref. [6]).
- [5] European Commission's web site on research activities: <http://www.cordis.lu/>.
- [6] Prader P, et al. Web page of MMC-Assess: <http://mmc-assess.tuwien.ac.at/>, Vienna University of Technology (opened 1999, continuously up-dated).
- [7] Hunt WH, et al. Aluminium Matrix Composites Consortium/USA, <http://www.almmc.com/> (opened 1998, continuously up-dated).
- [8] Degischer, HP. MMC-ASSESS – 12 months progress report, TU-Wien, Dec. 1999 (available via Ref. [6]).
- [9] Mortensen A, San Marchi C, Degischer, HP. Glossary of terms specific to MMC, 2nd draft, 18-08-1999, EPF-Lausanne (available via Ref. [6]).
- [10] San Marchi C, Mortensen, A. Industrial landscape on MMC; <http://dmxwww.epfl.ch/Imm>, EPF-Lausanne (Filemaker data bank opened 1999, continuously up-dated).
- [11] Baruchel J, Buffiere JY, Maire E, Merle P, Peix G. X-ray tomography in materials science. Paris: Hermes Science Publications, 2000.

# Thermoplastic composite based processing technologies for high performance turbomachinery components

Vishal Mallick\*

ABB Corporate Research, 5405 Baden-Dättwil, Switzerland

Received 2 December 2000; revised 1 March 2001; accepted 5 March 2001

## Abstract

ABB is developing new designs and processes based on thermoplastic technology in response to the lack of appropriate and affordable manufacturing methods for high performance composites parts, such as rotating machine components. A complete technology platform has been developed including design methodology, rapid thermoforming processes, robotic-based thermoplastic fibre placement (TFP) and assembly procedures based on welding. It will be shown by the way of case studies, for example, thermoplastic bandages for motors and high speed impellers for fans that these new technologies are able to deliver the required performance at an affordable manufacturing cost. However, the effort required to develop a new component remains high. It is concluded that there is now an increasing need for improved design and manufacturing simulation tools in order to bring development costs down. © 2001 Published by Elsevier Science Ltd.

**Keywords:** Thermoplastic; A. Fibre

## 1. Introduction

Increasing demands for speed, efficiency and lower costs of high-speed turbomachinery and other dynamic systems have led to increasing requirements on the material properties. Systems such as robots, where masses have to be accelerated, or rotors under centrifugal load need materials with high strength and high stiffness combined with low weight. Fibre-reinforced composites can fulfil these requirements better than standard materials such as steel, aluminium or titanium alloys due to their extraordinary strength-to-weight and stiffness-to-weight ratios (see Table 1).

Some of the industrial applications being pursued at ABB are shown in Fig. 1. For all these applications, new manufacturing processes have been developed primarily based on thermoplastic polymer composites. Details of the new technology are presented here with the aid of two case studies: (a) centrifugal impellers for high-pressure blowers, and (b) motor overhang bandages.

## 2. Centrifugal impellers for high pressure blowers

Mechanical vapour recompression (MVR) is a process used to compress vapour to a higher condensation pressure

or temperature. Such processes are used in the evaporation of dairy and food products (e.g. milk powder, soymilk, sugar, fruit juices and herbal extracts), in the pulp and paper industry or in the production of chemicals and pharmaceuticals (e.g. dye intermediates, amino acids, sodium chloride and wastewater effluent treatment). Traditionally, an MVR cycle relies on a high-speed centrifugal *compressor*. These are precision machines and can incur both high investment and maintenance costs. As an alternative, ABB is developing solutions based on high-pressure *fans*. These machines rely on a much simpler centrifugal impeller and with appropriate aerodynamic design can deliver a stage temperature rise of 7.5°C.

If fan impeller tip speeds can be further increased, even higher temperature increases can be realised and solutions can be 50% more cost effective than corresponding compressor based MVR constructions. However, modern impeller tip speeds, at 270 m/s, are close to the material limits of metals and there is little room to manoeuvre. Fibre-reinforced polymeric composites can fulfil these requirements better than steel, aluminium or titanium alloys.

### 2.1. Manufacturing process for centrifugal impellers

The slotted impeller design pursued here consists of the three basic substructures shown in Fig. 2. This consists of a back plate, inlet plate and blades with butt flanges. The manufacturing process for each of these elements is now

\* Corresponding author. Fax: +41-1-319-6363.

E-mail address: vishal.mallick@ch.abb.com (V. Mallick).

Table 1

Typical values for strength-to-weight and stiffness-to-weight ratios for different materials

Material	Strength/weight (MPa/kgm <sup>-3</sup> )	Stiffness/weight (MPa/kgm <sup>-3</sup> )
Steel	0.25	27
Aluminium alloys	0.2	26
Titanium alloys	0.2	25
AS4/PEEK	1.4	84
IM6/epoxy	2.2	128

discussed in detail, as is the assembly of the impeller. The prototype geometry was chosen to correspond with an existing impeller type with an inlet diameter of 201 mm and a tip diameter of 412 mm.

## 2.2. Materials used

Two types of composite materials have been employed in this study; carbon fibre reinforced polyetherimide (PEI) or polyetheretherketone (PEEK). These thermoplastic polymers have been selected since these are the only readily available commercial systems capable of satisfying the required service temperature conditions of 150 or 200°C. Based on these two polymers, two composite prepreg systems have been employed; the CETEX (PEI) system from TenCate and the APC2/AS4, APC2/IM7 PEEK based systems from Cytec-Fiberite. Polyimide composites were not considered since no commercial prepreg grades were readily available.

Whereas the APC2/AS4 is a high performance uni-directional (UD) prepreg system, CETEX is a plain woven fabric impregnated with PEI resin. Although CETEX does not offer the best available mechanical properties, it is easy to handle and allows prototypes to be readily manufactured. In serial production the use of UD prepreps with automated cutting and lay-up is envisaged; not only to minimise material wastage but also to achieve significantly higher

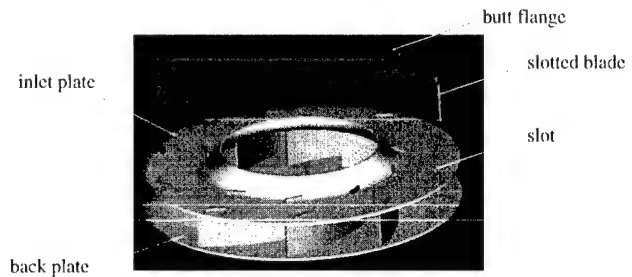


Fig. 2. Elements of the slotted blade impeller structure.

mechanical properties. The main adhesive used during the prototype manufacture was DP190 from 3M.

## 2.3. Sub-components

### 2.3.1. Inlet and back plate

If the prepreps have not been stored under dry conditions, it is advisable to dry the material at 120°C for 4 h. Thereafter the manufacturing steps are as shown in Fig. 3.

The key pressing parameters are given in Table 2. It should be noted that the cycle times reported are long due to the use of a laboratory press which did not feature cooling. If a transfer press system would be available then cycle times can be expected to be in the region of 10–15 min for these plate structures. Although the applied pressure of 1.0 MPa is less than the manufacturers recommended value of 3.0 MPa, a parallel study has shown that the achieved laminate properties are adequate.

The lay-up cutting and preparation time was typically in the order of 45 min and material wastage in the order of 35%. The manual prepreg lay-up process (Fig. 4a) can be easily automated with some form of robotic system (Fig. 4b).

The thermoplastic fibre placement (TFP) process is illustrated diagrammatically in Fig. 5. A carbon fibre tow, impregnated with thermoplastic resin, is rolled onto a

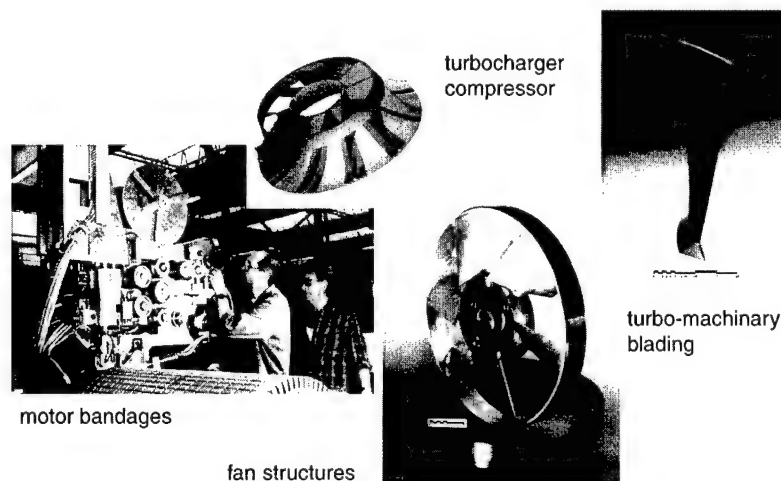


Fig. 1. Examples of high performance applications of composites at ABB.



Table 2  
Typical processing parameters for CETEX back and inlet plates

Time (min)	Pressure (MPa)	Temp. controller lower (°C)	Temp. controller upper (°C)	Temp. tool lower (°C)	Temp. tool upper (°C)	Temp. lay-up (°C)	Comment
0	0.3	330	330	–	–	22	Lay-up inserted
15	1.0	330	330	–	–	330	Pressure on
25	1.0	–	–	–	–	320	Heating off
185	–	–	–	–	–	145	Forced cooling with a ventilator to speedup the cooling down process; open tool

substrate and welded by applying localised heat at the ‘nip’ of the point of contact. Such a head has been implemented on a 6-axis ABB IRB6400 robot by the Fibre Placement equipment integrator Automated Dynamics Corporation [1]. This robotic workcell, as shown in Fig. 4b, also has

an external spindle axis to allow bodies of revolution to be processed.

It was possible to reduce material wastage by 90% and lay-up costs by 50% through the use of reduced width prepreps in the automated system.

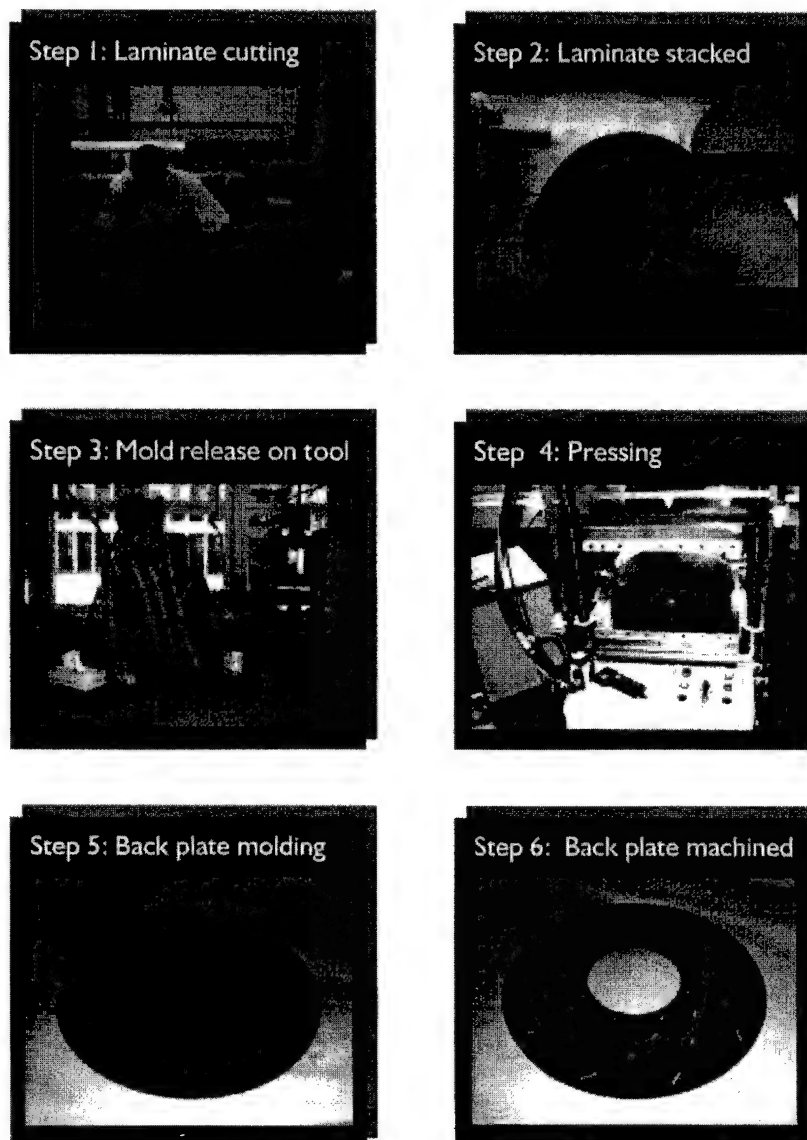


Fig. 3. Processing steps for the manufacture of impeller plates.



Fig. 4. (a) Conventional hand lay-up and (b) automated prepreg tape laying.

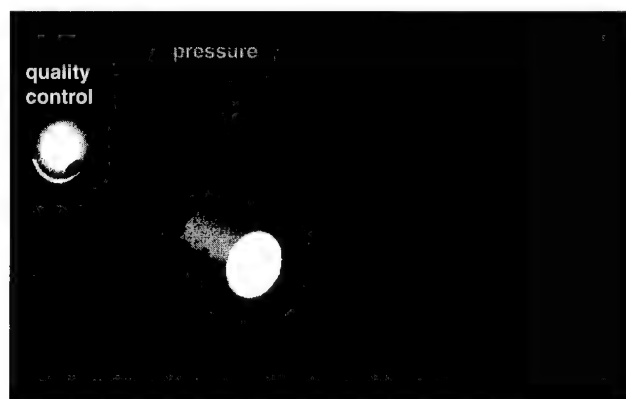


Fig. 5. Sketch of the TFP process.

**2.3.1.1. Plate machining.** To begin with, the machining of the inlet and back plates was performed by a conventional four axes CNC milling machine (Mikron WF41C). A more economical method was found to be water jet cutting. Using a locally available water jet cutting facility it was found to be possible to machine the plates within 0.1 mm accuracy. The savings due to water jet cutting over conventional machining was more than 80% in terms of time but only 60% in cost due to the higher cost of a water jet cutter.

### 2.3.2. Blade

The procedure followed for manufacturing the blade is almost identical to that of the plates except for the lay-up employed and the machining process.

Due to the use of APC2 (PEEK) material, the pressing cycle for the blade was slightly different to that of the plates. The key parameters are given in Table 3. For hand lay-up,

the material wastage was very significant at 70% case and was mainly driven by the off-cuts produced due to the angle plies extracted from the UD prepreg roll. Automatic tape laying is the only realistic solution for industrial manufacture.

### 2.4. Assembly

The adhesive used was DP190 from 3M and the main steps of the bonding operation are shown in Fig. 6..

### 2.5. Summary of costs

The costs for an impeller based on the thermoplastic composite technology described here are compared with the traditional steel impeller as well as for an resin transfer molding (RTM) version and are shown in Fig. 7. The comparison is based on the assumption of a production rate of 500 impellers per annum. Much of the cost of the steel version is due to the cumbersome welding process. RTM costs are partly high due to the long cure cycle but mainly because of the manual intensity of the awkward bagging and impregnating procedures. These might potentially be automated but would require expensive custom-built machines and thus the cost saving potential is not as large. Clearly, the thermoplastic composite-based technology is the most affordable for serial manufacturing.

## 3. Motor overhang bandages

Copper bars are usually used as the rotor windings of electrical machines to conduct the current. In the active part of the rotor the conductors are held back with keys.

Table 3  
Typical processing parameters for APC2/IM7 blade structures

Time (min)	Pressure (MPa)	Temp. controller low (°C)	Temp. controller up (°C)	Temp. tool low (°C)	Temp. tool up (°C)	Temp. lay-up (°C)	Comment
0	2.2	400	400	–	–	82	Lay-up inserted
36	2.2	400	400	–	–	390	Pressure on
51	2.2	–	–	–	–	397	Heating off
144	Off	–	–	–	–	120	Demolded

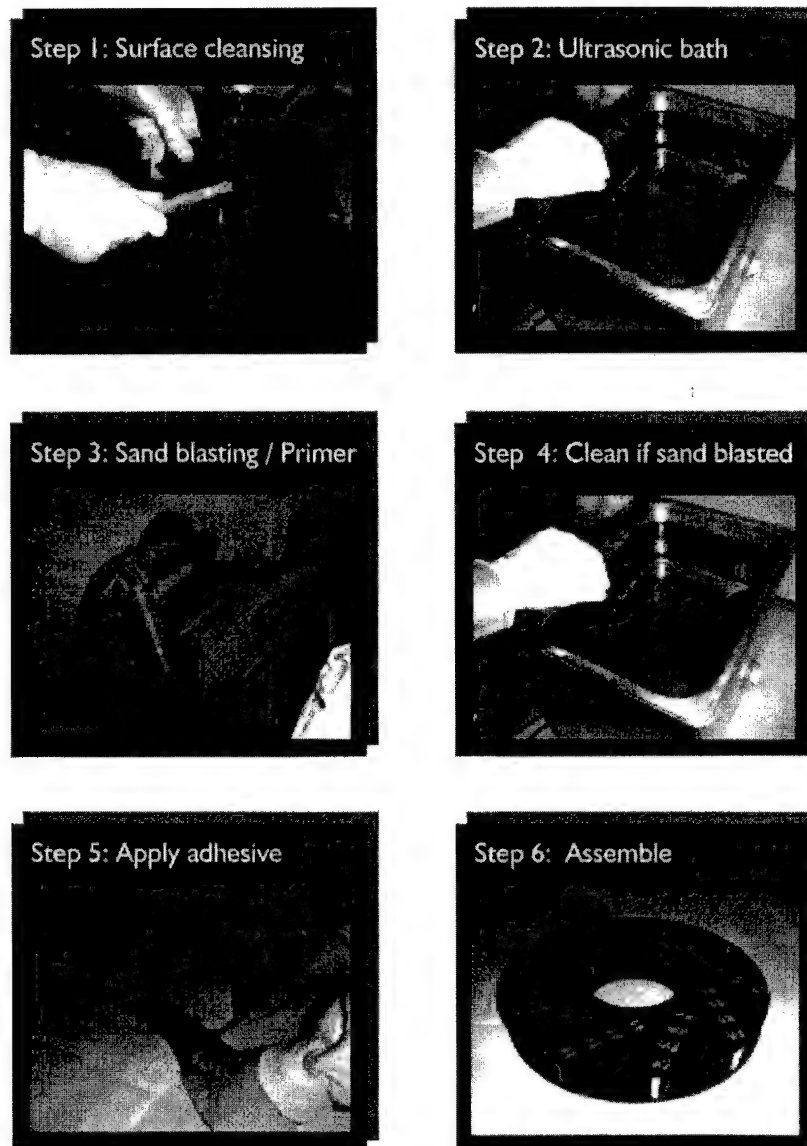


Fig. 6. Procedures for the assembly of an impeller.

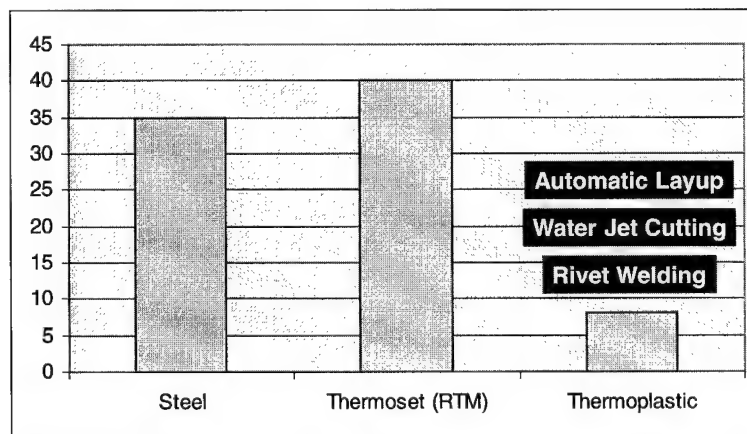


Fig. 7. Comparison of manufacturing hours for steel, thermoset and thermoplastic-composite versions of a centrifugal impeller for production rates of 500 impellers per annum.

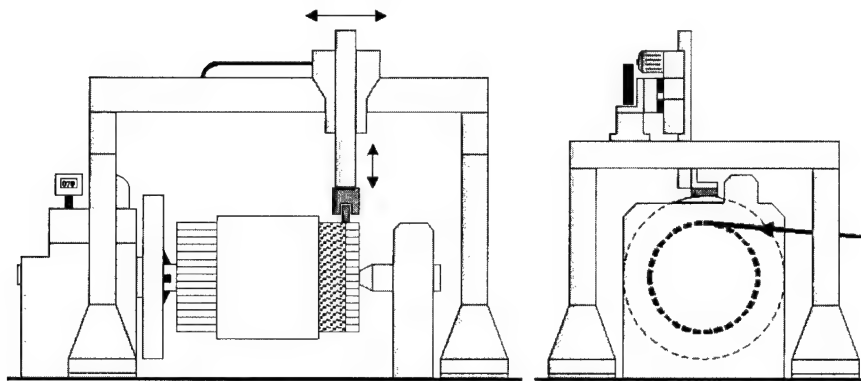


Fig. 8. Picture of TFP machine and gantry robot.

Beyond the active part, at each end of the rotor, the conductor windings overhang to accommodate the turns. This overhang is supported against centrifugal loads by a retaining ring (see Fig. 10).

Currently ABB manufactures retaining rings for its electrical motors from either wound steel wire, glass/polyester composite material or steel rings. Steel rings are used for induction motors with higher demands on the material strength. These rings are pre-machined and shrunk on the motor overhang which makes the process rather expensive. The manufacturing process for the steel wire bandages is quite slow, typically requiring a week to wind one ring on a generator rotor. The manufacturing process for the glass/polyester composite material is also laborious, requiring preheating the entire rotor in an oven, winding the ring, and then curing the rotor again in an oven. In addition the thickness of both ring designs impedes heat flow from the rotor, reducing performance.

The use of thermoplastic-matrix composite materials with the automated TFP process (Fig. 5) shows great advantages for this application:

- No need of preheating the rotor before winding or curing the rotor after winding.
- Little or no use of expendable materials.
- Material properties of carbon fibre/thermoplastic material improve performance: increased strength-to-weight ratio results in thinner, lighter rings; negative coefficient of thermal expansion promotes higher ring pretension; and higher thermal conductivity promotes rotor cooling.
- In situ consolidation process produces bandages with higher and more consistent levels of retained tension, increasing quality and reducing the need for 'overkill' designs.
- In situ consolidation process has the potential for winding geometries which are not possible with the present thermoset process.
- Rationalisation of overhang reinforcement manufacture by replacing the current three systems (glass, steel wire and steel ring) with one (thermoplastic bandage).

The TFP machine in the motor factory consists of an ABB gantry robot with a modified TFP machine head (see Figs. 8 and 9). The robot programming for normal operation is done with the robot user panel. A PC is used to control and analyse TFP process parameters.

In order to use the TFP process in a factory environment, the user interface should be easy to use. The machine is highly automated and all input for the winding of motors is done from the robot user panel.

Monitoring of process parameters, process optimisation as well as testing is done with a LabView based man-machine interface. A cost-benefit analysis [2] shows that the advantages of the TFP process using APC2/AS4 tape translate into a competitive edge over all the three existing overhang retaining methods for certain machines.

Compared to the previously used glass fibre reinforced thermoset system, the APC2/AS4 is equal in terms of cost but provides much better performance of the motor due to a lower overhang thickness and thus better cooling. The TFP process offers significant cost reduction against the steel wire wrapping system due to the reduced manufacturing

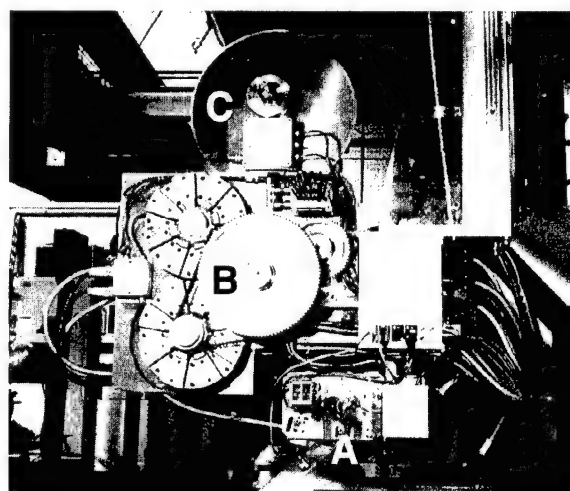


Fig. 9. Photograph of the TFP machine head used in a motor factory in ABB. (A) Compaction roller assembly, (B) brake system and (C) prepreg tape spool.

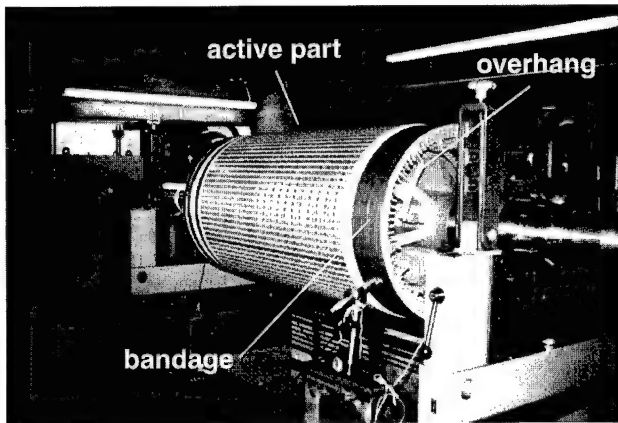


Fig. 10. Picture of an ABB motor with a thermoplastic overhang bandage.

times. Finally, against steel retaining rings, cost calculations suggest TFP is cost competitive (Fig. 10).

#### 4. Discussion and conclusions

It has been illustrated that thermoplastic-based composite technology is highly competitive against other traditional composite or metal-based processes with the aid of two case studies. Both the composite impeller and the overhang bandage are able to perform functionally better than any other system. With the impeller, higher tip speeds can be achieved than with traditional metal technology and the

composite bandage improves the price/performance ratio of a motor.

These case studies thus illustrate that serial production cost and ultimate performance are no longer barriers to the industrial application of advanced composite materials. One barrier remains however and that is the cost of application development. If application development costs are taken into account, then for both cases the economic payback period is in the region of 10 years. The high development costs can be attributed to the need to develop both the manufacturing process parameters and the component geometric and laminate design. Both require an exhaustive experimental matrix and with the application of the building block approach, development costs for composite applications are very high. It is therefore concluded that the greatest obstacle to the uptake of advanced composite technology for industrial applications are the high application development costs. Consequently, now more than ever, there is a need for the improved design and manufacturing simulation tools in order to bring these costs down.

#### References

- [1] Stover D. Tape-laying precision industrial shafts. *High Performance Compos* 1994;July/August:29–32.
- [2] Prenner H. Folgerungen aus den Untersuchungen mit thermoplastischen CFK-Bandagen, als Ersatz für Kurzschlusskäfig-Stahlschrumpfringe und duroplastische Wickelkopfbandagen, ABB, IP Note, IMD, December 22nd, 1999.

# Impact of the NSF State/Industry/University Cooperative Research Center on low-cost, high-speed polymer composites processing on the research and educational programs at Michigan State University

M. Hawley<sup>a</sup>, K. Jayaraman<sup>a</sup>, J. Sticklen<sup>a</sup>, B. Moore<sup>a,\*</sup>, L. Drzal<sup>a</sup>, R.L. McCullough<sup>b</sup>

<sup>a</sup>*Departments of Chemical Engineering, Computer Science and the Composite Materials and Structures Center, Michigan State University, Lansing, MI, USA*

<sup>b</sup>*Department of Chemical Engineering and Center for Composite Materials, University of Delaware, Newark, DE, USA*

Received 28 September 2000; accepted 29 January 2001

## Abstract

The objectives of the National Science Foundation (NSF) State of Michigan/Industry/University Cooperative Research Center on low-cost, high-speed polymer composites processing at Michigan State University (MSU) are design, development and deployment of technology and knowledge-based systems that will reduce costs of polymer composites processing by (a) insuring faster processes, (b) reducing component costs, and (c) reducing implementation times of new composite designs. Significant accomplishments have been made in research, education and technology transfer in the areas of novel processing, liquid molding, thermoplastic processing, intelligent design and process modeling, and interphases and joining. The Center's primary educational activities were supported by the National Institute of Standards and Technology-Advanced Technology Program (NIST-ATP) with General Motors and General Electric, and the Technology Reinvestment Project (TRP) with the University of Delaware and the US Department of Defense.

The Center's role in the four-year NIST-ATP was to disseminate injection-molded thermoplastics design methodologies to automotive, appliance, computer and other key US industries. The program enabled the Center to develop course material, a CD-ROM design manual, and workshop materials on state of the art thermoplastics design knowledge. To date, hundreds of individuals have participated in the workshops, and the material developed in this program is being integrated into undergraduate, graduate and continuing education offerings. The TRP program brought together the NSF Center at MSU and the composite materials center at the University of Delaware (UD) in a collaborative composite materials education and training effort for the Department of Defense and the durable goods industry. Educational developments included incorporation of knowledge derived from the TRP program into 49 new or existing engineering courses (23 at MSU and 26 at UD); six experiments for a new teaching laboratory; four workshops; four videotaped instructional modules (two each for liquid molding RTM technology and the injection molding technology); interactive WEB-based simulations and tutorials; and development of knowledge-based software. © 2001 Elsevier Science Ltd. All rights reserved.

**Keywords:** Polymer composites; B. Mechanical properties

## 1. Using computer technology to support education

Two ongoing Center projects are (1) developing a web-based tutorial for liquid molding and (2) developing an intelligent tutoring system (ITS) shell utilizing the Generic Task approach to problem solving.

The tutorial, intended for industry professionals and university students, covers molding technologies. It includes several methods of navigation, and makes use of various media types.

A recurring requirement for firms is the need to educate employees about specific subject matter. This can be an

expensive and time-consuming process. Better education and training methods, in industry as well as in academia, are needed. Web-based tutorials offer a forward-looking solution. A tutorial deliverable through the internet can be used by many users simultaneously. Additionally, it allows students to browse through material in their own order preference and to progress through the material at their individual pace. Overall, web tutorials are a very cost-effective method for the education and training of people in the manufacturing industry and in other environments.

The tutorial content is organized as four major chapters: general liquid molding, injection molding, compression molding, and new technologies and special applications. Each of these is then divided into sections and subsections.

\* Corresponding author.

E-mail address: moorebar@egr.msu.edu (B. Moore).

Several navigation techniques are provided to allow users to access the information in the manner most suitable to their needs. The current organization of material produces a tree-like structure. This makes it easy to get to major topic areas from the start of the tutorial.

To facilitate efficient navigation, each page also has a menu bar at the top. The navigational guide, always available from the menu bar, allows the user to more easily find information. The guide has four main parts: a glossary, a topical index, a list of equations, and a table of contents.

The table of contents can also become a persistent part of the interface at the user's discretion. In this mode, it becomes a vertical frame on the left side of the screen, to help more knowledgeable users who are reading the tutorial for specific information.

The goal of the ITS shell development is to create an ITS architecture that can interact with any GT-based problem solver, and effectively cover the domain knowledge represented in the problem solver. It will automatically generate tutorials in the area of molding technology from knowledge contained in current problem solvers developed in our group. ITS shells with modular designs and well-defined intercommunication strategies can be effectively reused.

The GT approach to large-grained knowledge-based problem solving [1] is one of the oldest of the task specific approaches to knowledge-based systems. The assumption of the GT approach is that there are basic 'tasks'-problem solving strategies and corresponding knowledge representation templates - from which complex problem solving may be decomposed. The backing intuition of this work is that GT problem solvers are strongly committed to both a semantically meaningful knowledge representation method and to a structured inferencing strategy. By leveraging this strong structure, automated generation of tutorial overlays is enabled.

The problem solvers developed within the Center have involved extensive knowledge acquisition from the area of polymer composites. In particular, a number of problem solvers have been developed that operate in the domains of material system design and fabrication technology selection for polymer composites. The goal in developing the tutorial overlays is to allow the accumulated knowledge that exists in the problem solvers to be available for tutorial purposes. Moreover, as new problem solvers are developed, tutorials can be automatically generated for the new domains covered. It is anticipated that this capability will prove very useful especially for industry specific systems.

As a test bed for the ITS project in molding technology, an ITS in the domain of composite material design and fabrication is being developed in conjunction with the Composite Materials and Structures Center (CMSC) at MSU, and the Center for Composite Materials (CCM) at the University of Delaware (UDEL).

These groups are working with two GT problem solvers,

both of which are utilized in the design phases of composites. The first system, COFATE [3] is a composite fabrication technology selector. The input for the problem solver consists of characteristics of the target application, as well as economic considerations. The output is a recommended set of fabrication technologies, which should be used to build the application. The second problem solver, COMADE [2] is a composite material designer. The inputs to the system are characteristics of the target application. Output from the system is a set of designs satisfying these requirements. Composites are more flexible than corresponding metals because there is a very wide range of choices for the various components of a composite. This problem solver designs a composite material by finding satisfying choices for each of these components.

Tutorials developed for these two problem-solving systems will serve to teach users the domain of knowledge embedded in the problem solving systems. These tutorials will assume that users have a working knowledge of composite material design and fabrication and will familiarize users with the systems processes.

## 2. Teaching laboratory for molding polymer composites

Several new experiments have been developed at both Michigan State University (MSU) and UDEL under a joint program between the two universities, for a teaching laboratory on molding polymers and polymer composites. The objective of this laboratory development program is to illustrate design issues in fabrication of composites and the connection between processing and performance via microstructure of the finished component. The broader objective is to integrate the latest developments in low-cost manufacturing of polymer composites into the undergraduate engineering and continuing education programs at MSU and UDEL.

These objectives have been achieved by developing a variety of courseware such as videotapes, computer-based tutorials with interactive process simulations, and manufacturing design software that emphasize the connections among characterization, processing, performance and design for manufacturing in the context of composite materials. These tools have been supplemented in the laboratory at MSU with equipment such as an instrumented press, an optical microscope with image processing software, an injection-molding machine suitable for making filled plastic components and a mechanical test frame on which students can conduct destructive mechanical testing.

The experiments include the following:

*Design of cure cycles for thick section composites based on an unsaturated polyester resin.* Prior to engaging in the laboratory work, the students are required to develop a design for a cure cycle through extensive use of existing computer simulations. The focus of the laboratory is on



evaluating the performance of the proposed cure cycle by: (a) fabricating a composite plate, (b) monitoring temperature distributions within the plate during cure, and (c) inspecting the cured plate afterwards for voids, delaminations, and poor compaction. Execution of this experiment requires the students to synthesize their knowledge of reaction kinetics, heat transfer, and fluid mechanics. This contrasts the other experiments, which are aimed at demonstrating principles in only one of these areas.

**Cure kinetics of vinyl ester/styrene.** This experiment is conducted in a junior-level chemical engineering laboratory, CHEG 345, at UDEL. Again, the focus is on resins used in resin transfer molding (RTM). The students use differential scanning calorimetry (DSC) to track heat generation during the cure of a vinyl ester/styrene system under isothermal conditions. The heat flow data is used to determine the rate of the cure reaction.

The experiment is repeated in three cycles during the semester with five groups of three students per group in each cycle. The rate constants and order of the reaction determined by preceding groups are transmitted to the current group via letters of transmittal. The data from the various groups are subjected to statistical analysis and pooled to obtain improved kinetic parameters.

**Compression molding of sheet molding compound.** The goal of this experiment is to illustrate the effect of process parameters on the microstructure of compression molded plaques. In the revised version, the students vary the initial charge area and its location in the mold; this procedure helps the students to eliminate short shots and non-uniform filling of the mold. The students are encouraged to perform a separate experiment in which the compression stroke is controlled. This results in short shots that give valuable information on the flow pattern during the compression molding process. The students then conduct mechanical property tests and inspect the microstructure in two regions: the initial charge area and areas filled later. The effect of processing on the microstructure and mechanical properties is brought out, and students are prompted to quantitatively compare the planar fiber orientation present in the SMC after compression in two distinct regions (areas) of the molded plaques. This part of the exercise illustrates the variability of orientation from region to region based on processing conditions.

**Permeation and resin cure kinetics in the SRIM process.** This laboratory exercise has two components: the permeability of a fiber preform, and the cure kinetics of a fast-curing polyurethane resin. In the first part, resin is injected through a center gate into a disk-shaped mold cavity with a preform of continuous random fiber mat. The in-plane permeability is determined from the rise in injection pressure monitored near the center of the mold during filling. Tests are conducted with different preform porosities and resin flow rates to investigate how these molding conditions affect permeability. The students learn from these tests that perme-

ability increases steeply with decreasing porosity and that is independent of the resin flow rate so long as significant crosslinking does not occur.

In the portion that focuses upon cure kinetics of a polyurethane, the students observe the cure behavior in a non-isothermal system. A sample of polyurethane resin is shot into a Styrofoam cup and the adiabatic temperature rise of the cure is monitored. The cure kinetics of the resin can then be evaluated from the temperature transient. Results from this part of the laboratory exercise enable the students to estimate the approach to gelation during reactive filling and also the time for demolding in the SRIM process.

**Inspection of molded parts.** This experiment illustrates the variability in microstructure (fiber orientation distribution and fiber length distribution) of compression molded SMC as well as injection molded specimens from fiber-reinforced thermoplastic molding compounds. This experiment involves inspecting the molded samples under an optical microscope. This serves to illustrate two sets of relationships: one between processing conditions and microstructure, and another between microstructure and mechanical properties. An optical microscope with an attached video camera was installed in the laboratory and combined with software for computerized image grabbing and image analysis. Fiber lengths and orientations relative to the dominant flow direction were determined for the specimens from the center of the plaque. This experiment helps students appreciate the importance of controlling microstructure to control properties. Students are also prompted to determine the sensitivity of the mechanical properties to the microstructure.

**Shrinkage and warpage of injection molded thermoplastic disks in a Morgan Press.** This experiment examines dimensional stability of injection molded disks. This is illustrated with the help of a Morgan press. The object is to illustrate different shrinkage and warpage behavior associated with semi-crystalline polymers such as polypropylene vs. amorphous polymers such as polycarbonate, the effect of fibers on shrinkage, and the effect of packing conditions on shrinkage. The effect of packing pressure and pack time on dimensional stability is explored with each material. Students learn to evaluate PVT data on the materials and estimate the shrinkage for comparison with observations.

### 3. Liquid and injection molding video instruction modules

Four video modules have been produced to cover, at a high level, the interactions between processing, design and performance of composites made by RTM and injection molding. The video modules are used in conjunction with workshops and classroom instruction.

The first two videos focus on liquid molding. The instructional objectives of liquid molding module I are to: (1)

explain two stages in the manufacture of composites by liquid molding, preforming and mold filling, (2) to show how preform architecture governs the cost and the performance (or strength) of the composite part, (3) to demonstrate the effect of preform architecture on resin permeation which controls the mold filling operation, and (4) to explain anisotropic permeability. This module also discusses the implications of anisotropic permeation and non-homogeneous preforms for mold filling operation and explains design choices for controlling dry spots and voids in the molded part. This volume concludes at the mold filling stage.

The second liquid molding module deals with critical issues involved in the cure stage beginning with resin selection, cure kinetics, effects of coupling agents on the mechanical properties of the finished component and mold design for heat transfer during non-isothermal cure.

The third and fourth videos are titled, 'Design for Manufacture of Injection Molded Parts' and 'Microstructure and Performance of Injection Molded Parts'. The main thrust of the third module is mold design, processing conditions and dimensional stability. The fourth module concentrates on process-induced microstructure and its influence on part performance. The instructional objectives of these modules on injection molding are to illustrate the interaction among part design, mold design and part performance in an injection molded part with the help of specific case studies.

#### 4. Thermoplastic engineering design manuals

The Thermoplastic Engineering Design (TED) Venture, a four-year program sponsored by the General Electric, General Motors and the National Institute of Standards and Technology, resulted in development of engineering-based thermoplastic design methodologies. These have been developed for use as an educational tool for a broad spectrum of industries.

The initial phases of the program were devoted to developing a scientific understanding of the relationship between processing, part geometry, material microstructure and part performance. The second phase of the TED program was to incorporate this understanding into a base of design knowledge and techniques that can be used to design thermoplastic parts 'right the first time'. The third aspect of the program is education and technology transfer to a wide range of manufacturers and future engineers.

Manufacturing industries, ranging from automotive to appliance to industrial equipment, design and introduce thousands of new thermoplastic parts every year. The ability to effectively design and manufacture these parts requires a large body of knowledge defined as 'design know-how.' This design know-how represents the interdisciplinary understanding of material properties, design methods,

manufacturing processing, assembly and recycling considerations. However, the interactions between material properties, processing conditions and part geometry are not well understood. Developing thermoplastic parts requires several cycles of analysis, design, molding trials, and redesign to correct problems in the original design. This trial-and-error or 'make it/break it' cycle adds both cost and time to the overall product development cycle. Additionally, the lack of comprehensive thermoplastic design information has resulted in poor, inefficient designs with unanticipated failures.

With active input from TED participants, the Center created an educational tool in the form of design manuals. Ten manuals have been put on CD-ROM, concentrating on seven key issues for injection molded thermoplastic parts: assembly, basic structural analysis, creep and stress relaxation, dimensional stability, fatigue, impact, and stiffness and strength. Additionally, there are manuals on design for injection molding, hot tool welding, and vibration welding. These manuals are used in conjunction with workshop presentations to train current and future engineers. They have been disseminated to TED participants and are available for use in the public domain.

#### 5. Polymer and Polymer Composites Science and Engineering courses offered at Michigan State University and University of Delaware

MSU currently offers 23 courses relating to composites which are taught by 16 faculty members from several different departments in the College of Engineering, Natural Science, and Agriculture including Chemical Engineering (CHE), Chemistry (CEM), Materials Science and Mechanics (MSM), Mechanical Engineering (ME), and Packaging (PKG). There is currently work being done to create a degree program in Polymer and Polymer Composites Science and Engineering. UDEL offers 26 composites-related courses.

#### 6. Summary

These new tools and methods being developed at MSU are being used to: (1) improve the education of future engineers and (2) keep engineers currently working in industry apprised of technological and scientific developments in their field. Additionally, the Center has provided a base of support for its students. There are approximately 20 undergraduate and 80 graduate students currently involved with research projects at the Center. These hands on research experience have provided them with an academically enriched experience in the environment of the Center. Through research at the Center, MSU is continually striving to find better ways to educate and train the workforce of today and tomorrow.

## References

- [1] Chandrasekaran B. Generic tasks in knowledge-based reasoning: high-level building blocks for expert system design. *IEEE Exp* 1986;22–30.
- [2] Lenz T, McDowell J, et al. COMADE: an intelligent decision support system for polymer composite material design. Michigan State University National Science Foundation Center on Low-Cost High-Speed Polymer Composites Processing, 1994.
- [3] Moy B, McDowell J, et al. Expansion of an intelligent decision support system for process selection and process design in polymer composites. 26th International SAMPE Technical Conference, 1994.

# Education for a new millennium: an innovative program in fibers and films

Jane E. Jacobi\*, Dan D. Edie, John M. Kennedy

*Center for Advanced Engineering Fibers and Films (CAEFF), Clemson University, Clemson, SC 29634-0910, USA*

## Abstract

The composites of tomorrow will need to be developed in advanced engineering environments. This transformation to computer-based materials design requires a transformation of traditional engineering education programs. Students need training in systems design, simulation and visualization technologies, teamwork, and communication to function effectively in distributed, diverse, collaborative work environments. The programs being coordinated and implemented by CAEFF are designed to meet these challenges and constitute a paradigm shift in engineering education. © 2001 Published by Elsevier Science Ltd.

**Keywords:** A. Fibres; Films

## 1. Introduction

A recent report by the Committee on Advanced Engineering Environments of the US National Research Council calls for the development of advanced engineering environments: computational and communications systems that create integrated virtual and /or distributed environments linking researchers, technologists, designers, manufacturers, suppliers, and customers [2]. These computer design environments would take advantage of interactive communication technologies such as distributed networking, telecommunications, multiuser computer software, and interactive virtual reality. Advanced engineering environments can be used to design products and processes as whole systems, rather than a conglomeration of subsystems or component parts.

Researchers in composites are beginning to see the possibilities of using computer simulation and visualization to design materials in these advanced engineering environments. If materials could be designed at the molecular level in a virtual design environment, composites using those materials would be radically improved. For example, carbon fibers, a common reinforcement fiber in composites, could be designed such that voids were eliminated, increasing the fibers' strength. Computer control of an in situ mixing process could produce polymer matrix composites with specific microstructures, tailored for a given application.

However, there are barriers to implementing research in advanced engineering environments. Composites engineers,

like engineers in general, traditionally prefer experimental analysis over simulation or visualization, and think of computer images as a prettified version of "real" data instead of a means of scientific discovery. As noted by the Committee on Advanced Engineering Environments, typical engineering educational practices emphasize fundamental core courses; relegate systems-level education to undergraduate capstone courses, which teach "as-is" design synthesis processes; and impart information in traditional classroom settings [3]. According to Boyer in *Scholarship Reconsidered: Priorities of the Professoriate*, the integration and application of knowledge are largely undeveloped in the academic community [1]. Students are expected to communicate with their peers, but not necessarily with researchers outside their own expertise, and certainly not with non-engineers or the general public. Few students outside of computer science or computer engineering are trained in the modeling and simulation technologies that are the essential tools of the future. Consequently, the next generation of engineers learns to be specialists, isolated by their professions and unprepared to function effectively in diverse, collaborative teams working in virtual design environments. Clearly, if the vision of designed materials is to become a reality, a cultural change in composites engineering research and education programs needs to occur.

## 2. CAEFF programs

The Center for Advanced Engineering Fibers and Films (CAEFF), a National Science Foundation Engineering Research Center, is charged with implementing just such a cultural change at Clemson University, the Massachusetts

---

\* Corresponding author.

E-mail address: jane.jacobi@ces.clemson.edu (J.E. Jacobi).

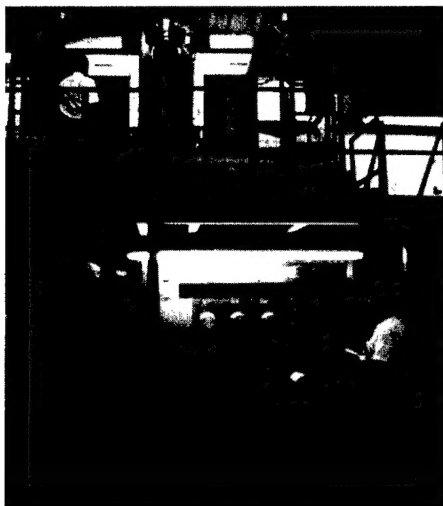


Fig. 1. The Fiber Processing Laboratory contains pilot-scale process equipment.

Institute of Technology, and other institutions conducting fiber and film research. CAEFF's mission is predicated on the belief that the fiber and film industries need to develop products and processes in collaborative virtual environments that minimize experimentation, allow manipulation of both molecular and continuum information, and maximize engineers' understanding of and control over structure formation and resultant properties. The Center is developing software packages that will allow users to input precursor specifications, processing parameters, and desired properties, and design an entire fiber or film system.

### 3. Facilities

The centralized facilities in the Center are essential to its research and education programs. Students use a Film Processing Laboratory and a Fiber Processing Laboratory (Fig. 1) to explore the interactions between process changes and product performance. Students alter processing parameters on pilot-scale equipment, observe the resulting product, and then analyze the properties of the fiber or film in the Center's adjacent Characterization Laboratory.

This traditional set of experiments is augmented by activities in a Visualization Laboratory. Students use the Center's visual simulation equipment (Fig. 2) to navigate through a virtual process, flow with the extruded material, and experience the impact of process changes. Thus students get hands-on experience with real process equipment and the opportunity to explore virtual process development.

Other central computing facilities include a Molecular Modeling Laboratory (Fig. 3), with 12 Silicon Graphics workstations and state-of-the-art molecular modeling software provided by Molecular Simulations Inc., one of the Center's industry partners. The National Science Founda-

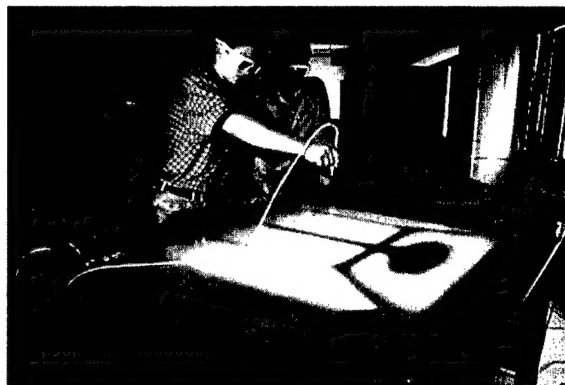


Fig. 2. The Visualization Laboratory houses computer systems capable of creating virtual environments for scientific discovery.

tion has funded the construction of a supercomputer to be used for numerical simulations. A grid of four Beowulf cluster parallel computers, providing a total of 512 processors, will be available for running parallel simulations of numerical models.

The W.M. Keck Foundation has provided \$1.3 million to CAEFF and another NSF Engineering Research Center to create a virtual visualization and design studio being called a 'collaboratory.' The gift is for the purchase of equipment that will be used for developing immersive environments for discovery and learning and visualization methodologies for the study of polymeric structure and processing. Scientists developing new materials will collaborate long-distance via a virtual network that allows them to see and use each other's data and equipment. The tools will include a graphics supercomputer, panoramic and 3-D displays, high-speed network connections and immersive haptics and audio. The Center for Advanced Engineering Fibers and Films will develop visual models that demonstrate the behavior of new classes of polymers. The University of Southern California's Integrated Media Systems Center will develop the protocol needed for off-site researchers to participate in virtual experiments. Together, the centers will simulate the development of new polymer fibers and films



Fig. 3. The Molecular Modeling Laboratory doubles as a classroom for CAEFF-developed courses.



and explore their potential uses. The imaging techniques are the first step in developing immersive environments for both research and education in the field of materials science.

CAEFF's videoconference/distance learning/smart classroom facility is heavily used for Center courses as well as communication with partner universities and member industries. All of the laboratories are also 'stages' for the myriad demonstrations, tours, workshops, and media events required of an NSF ERC.

These centralized facilities are critical to the Center's mission because they fuse experimentation with modeling and visualization, and emphasize the importance of communication to a variety of audiences.

#### 4. Curriculum innovations

Several new courses have been developed to serve the Center's mission. 'Introduction to Fiber and Film Systems,' an undergraduate technical elective/graduate course, develops students' systems-level understanding of fibers and films. The course teaches students to identify the steps in fiber and film production processes, explain the effects of process variables in a system on the structure and properties of fibers or films, and collaboratively create computer code to visualize the results of mathematical modeling. Because of the diverse educational backgrounds of the students, the course comprises both traditional lectures as well as modules. For example, students majoring in computer science take a module on polymer chemistry, while students majoring in chemical engineering take a module on visual programming language. The governing models for polymer extrusion, fiber spinning, film formation and structure—property relationships are then presented in traditional lectures. Student teams undertake interdisciplinary projects that require an integrated approach to problem-solving. The course thus provides a capstone design experience much earlier in the students' careers than would be possible in the traditional curriculum. Furthermore, the course gives students the opportunity to develop an industrial perspective by arranging site tours of local fiber and film facilities. Personnel from industry brief students on the processes and on technical issues.

Two courses in the Center focus on more advanced modeling. The first, 'Fiber and Film Systems: Modeling and Simulation,' offers a systems perspective on fiber and film processes using mathematical models, and features new models developed in CAEFF research projects. This course is team-taught by instructors from mathematical sciences and chemical engineering, and assigns students to problems requiring multidisciplinary teams. The focus of the course is the development and subsequent application of the governing equations for polymeric fluids. Topics include derivation of constitutive equations, including those based on molecular models; analytical and numerical solution of governing equations for particular cases; and capabilities

of models. Another course, "Molecular Modeling of Polymers," introduces students to atomistic simulation of polymers. Taught in the Molecular Modeling Laboratory of the Center, the course covers statistical mechanics, simulation techniques for molecular models (intra- and inter-molecular potentials, molecular dynamics, Monte Carlo methods, etc.), atomistic simulation techniques, and applications to gas transport in amorphous polymers and X-ray diffraction in crystalline polymers.

A new course, 'Diffusion through Polymers,' is team-taught by faculty from Clemson University and the University of Illinois using CAEFF's videoconference/distance learning/smart classroom facility. Such courses will be available on videotape for distribution through the continuing education program of the university.

#### 5. Research experiences for undergraduates

The Center for Advanced Engineering Fibers and Films has developed a novel Research Experiences for Undergraduates (REU) program. Each summer twelve undergraduates from different institutions and four high school students from the South Carolina Governor's School for Science and Mathematics join teams of faculty, graduate students, and industry researchers in addressing industry-defined problems. Activities in this REU program are designed to immerse the students in communications-intensive, industrially relevant, interdisciplinary research. Each team completes an annotated bibliography based on a literature search; prepares a research proposal with a detailed work plan; conducts research for a sponsoring company or funding agency; keeps laboratory notebooks; constructs Powerpoint progress reports, presented via videoconference; and presents results to different audiences in poster, oral, and written form. The individual students compile electronic portfolios that can be used in job searches, graduate school applications, and scholarship competitions. REU students can receive either English (technical writing) or engineering/science credits for their work. Students also participate in teamwork exercises; attend presentations on safety, academic and industry careers, and research methods; and tour several local fiber and film companies. Thus the REU program gives the students practice in being part of a distributed, collaborative work team that has to communicate effectively and conduct research efficiently in order to get significant results in only ten weeks.

#### 6. Teamwork and communication skills

Research projects within CAEFF are undertaken by multidisciplinary teams. These teams, which mix graduates, undergraduates, high school students, faculty, and industry researchers, give students a collaborative learning experience that will make them better scientists and engineers and more effective communicators in the industrial setting.

CAEFF is also developing a novel cascaded mentoring system—faculty mentor post docs, post docs mentor graduate students, graduate students mentor undergraduates, and the undergraduates mentor K-12 students—that develops communication among diverse groups.

CAEFF's education program emphasizes communication tools to facilitate discovery, refine understanding, enhance teamwork, and improve technology transfer. Experts in technical communication offer workshops on technical reports, oral and poster presentations, resumes and cover letters, and professional writing. Center staff members work closely with students to develop high-quality papers and presentations using the latest computer-based tools.

Center students have many opportunities to practice communicating their knowledge of and excitement about engineering to younger students. CAEFF students give presentations for National Engineers Week, Discover E, and the Junior Academy of Science, as well as for Clemson recruiting events. CAEFF students serve as science fair judges, and are developing a book of interdisciplinary, team-based fiber- and film-related science fair projects. K-12 students who choose one of the projects would be mentored by CAEFF students.

Collaboration with faculty and students involved in the Department of English's Masters in Professional Communication program and in the Center for Professional Communication will further develop the communications component of the Center. At the time of the writing of this paper, CAEFF is establishing a web-based journal of undergraduate research that will involve students from all colleges on the Clemson campus in peer-reviewed journal management and provide a forum for interdisciplinary, undergraduate research.

## 7. Conclusions

CAEFF's integrated research and education programs are developing advanced materials design techniques and implementing them both in laboratories and classrooms. Facilities are designed to further the Center's mission by supporting interdisciplinary projects that study entire fiber and film systems. Through curriculum innovation, K-12 outreach, and industrial collaboration programs, the Center is graduating students with a broad, systems-oriented technical foundation; modeling, simulation, and visualization skills; the critical thinking skills necessary to both analyze and integrate information; an appreciation of the industrial perspective; and the teamwork and communication skills necessary to function effectively in collaborative virtual design environments. Together with its academic and industry partners, CAEFF is creating a new paradigm for materials research and education.

## Acknowledgements

The research and education programs of CAEFF are supported primarily by the ERC Program of the National Science Foundation under Award Number EEC-9731680.

## References

- [1] Boyer E. *Scholarship reconsidered: Priorities of the professoriate*. Princeton, NJ: Princeton University Press, 1990.
- [2] National Research Council, Committee on Advanced Engineering Environments. *Advanced engineering environments: Achieving the vision, phase 1*. Washington, DC: National Academy Press, 1999.
- [3] National Research Council, Committee on Advanced Engineering Environments. *Advanced engineering environments: Design for the new Millennium, phase 2*. Washington, DC: National Academy Press, 2000.